AUSTRALIAN JOURNAL
OF PHYSICS

VOLUME [illegible]

[illegible]
[illegible]

QC
1
A85
V.14
1961
Science
PER

Digitized by the Internet Archive
in 2024

https://archive.org/details/australian-journal-of-physics_1961_14

AUSTRALIAN JOURNAL OF PHYSICS

VOLUME 14

MELBOURNE
1961

AUSTRALIAN JOURNAL OF PHYSICS

Published by the Commonwealth Scientific and Industrial Research Organization. Volumes 1 to 5 of the Australian Journal of Physics and the Australian Journal of Chemistry issued as the Australian Journal of Scientific Research, Series A: Physical Sciences. Issued quarterly, £2 per annum.

BOARD OF STANDARDS

The Board of Standards for this Journal is appointed by the Commonwealth Scientific and Industrial Research Organization and the Australian Academy of Science and consists of Professor Sir Macfarlane Burnet (Chairman), Dr. N. S. Noble (Editor), Professor N. S. Bayliss, Dr. J. L. Pawsey, Professor W. P. Rogers, and Professor J. S. Turner.

ADVISORY COMMITTEE

Acceptance of papers for this Journal is in the hands of an Advisory Committee appointed by the Board of Standards in consultation with The Institute of Physics and The Physical Society (Australian Branch) and consisting of Dr. N. S. Noble (Chairman and Editor), Dr. G. H. Briggs, Emeritus Professor L. G. H. Huxley, Dr. J. L. Pawsey, and Professor H. C. Webster.

All enquiries and manuscripts should be forwarded to:

The Editor,
Australian Journal of Physics,
Commonwealth Scientific and Industrial Research Organization,
314 Albert Street, East Melbourne, C.2, Victoria

MELBOURNE

CONTENTS

Number 1, March 1961

PAGE

n-Diffusion. By J. R. Philip 1

Facular Granule Lifetimes determined with a Seeing-monitored Photoheliograph. By R. J. Bray and R. E. Loughhead 14

A Study of Whistling Atmospherics. I. Occurrence. By J. Crouchley .. 22

A Study of Whistling Atmospherics. II. Diffuseness. By J. Crouchley and R. J. Finn 40

On Solving the Equation of Radiative Transfer for Conservative Nonuniform Media. By P. R. Wilson 57

Wavelengths of Krypton 86, Mercury 198, and Cadmium 114. By C. F. Bruce and R. M. Hill 64

The Characteristics of Persistent Sporadic Meteor Echoes. By J. W. Smith 89

The Distribution of Meteor Masses for Sporadic Meteors and Three Showers. By A. A. Weiss 102

The Sweep of Long Water Waves across the Pacific Ocean. By R. Green .. 120

Estimation of the Maximum Temperature in a Radially Constricted Gas Discharge between Electrodes. By P. W. Seymour 129

Average Forces in Electromagnetic Systems. By W. E. Smith 152

The Gradation and Inertia of Hurter and Driffield: A Study in Theory. By C. Candler 160

Resolution of Bremsstrahlung Experiments. By H. H. Thies 174

On the Equivalence of Current Loops and Magnetic Shells. By C. A. Hurst 188

Short Communications

The Oxidation of Polycrystalline Beryllium in Carbon Dioxide. By W. J. van Peer 191

Orientation of Polar Auroras. By J. V. Denholm and F. R. Bond .. 193

Energy Levels in ^{13}N. By V. R. McKenna, A. M. Baxter, and G. G. Shute 196

NUMBER 2, JUNE 1961

PAGE

A $\frac{1}{8}$ Å Birefringent Filter for Solar Research. By W. H. Steel, R. N. Smartt, and R. G. Giovanelli 201

Vertical Velocities in the Solar Chromosphere. By R. G. Giovanelli and J. T. Jefferies 212

A Study of Ionospherics at Macquarie Island. By B. A. McInnes .. 218

Slow Drift Solar Radio Bursts: Harmonic Frequency Ratios, Solar Longitude Dependence, and Frequency Drift Rates. By Marion B. Wood .. 234

Excited States of ^{64}Zn. By M. J. Kenny and D. E. Caro 242

Sum-coincidence Measurements on ^{154}Eu. By A. W. Parker 250

A Sky Survey of Neutral Hydrogen at λ 21 cm. I. The General Distribution and Motions of the Local Gas. By R. X. McGee and J. D. Murray .. 260

The Influence of Thermoelectric Effects on the Maximum Temperature in a Radially Constricted Gas Discharge between Electrodes. By P. W. Seymour 279

Counts of Extragalactic Radio Sources. By R. Van der Borght .. 295

Short Communications

The 5577 Å OI Emission Line of the Airglow at Brisbane. By I. J. Danziger 304

Construction of the Equivalent Electric Circuit from a Force Circuit Diagram by a Simple Graphical Method. By N. W. Tschoegl .. 307

Charged Particle Trajectories in Static Electric and Magnetic Fields. By K. J. Ausburn 310

A Phenomenological Model for Hypernuclear Binding Energies. By J. W. Olley 313

An Exact Solution to a Problem in Heat Transfer. By C. H. J. Johnson .. 317

NUMBER 3, SEPTEMBER 1961

PAGE

A Stability Criterion for a Radially Constricted Gas Discharge between Electrodes. By P. W. Seymour 321

Gamma Rays from the $^{27}\mathrm{Al}(p,\gamma)$ Reaction. By S. Bashkin and T. R. Ophel 335

Phenomena Accompanying the Birth of Sunspot Pores. By R. E. Loughhead and R. J. Bray 347

Deviations from Matthiessen's Rule for Platinum. By P. G. Klemens and G. C. Lowenthal 352

The Anomalous Thermal Expansion of Chromium. By G. K. White .. 359

Luminescence in KI:Tl. By J. E. Alderson and S. E. Williams 368

Cross-relaxation Effects in a Ruby *L*-Band (1440Mc/s) Maser at Low Magnetic Fields. By G. S. Bogle and F. F. Gardner 381

The Radio Brightness Distribution on the Sun at 21 cm from Combined Eclipse and Pencil-beam Observations. By T. Krishnan and N. R. Labrum 403

Anharmonicity and the Thermal Expansion of Solids. By G. C. Fletcher .. 420

Short Communications

Inelastic Scattering of Protons on ^{12}C. By V. R. McKenna and G. G. Shute 432

Corrigenda 435

NUMBER 4, DECEMBER 1961

PAGE

Polarization in Nuclear Collisions with Channel Coupling. By C. B. O. Mohr and C. A. Edvi-Illes 437

Gamma-radiation Absorption Coefficients of Various Materials allowing for Bremsstrahlung and other Secondary Radiations. By J. W. Allison 443

An Investigation on the Thermal Conductivity of Porous Materials and its Application to Porous Rock. By A. Sugawara and Y. Yoshizawa . . 469

The Phase Speed of a Travelling Disturbance in the *F* Region of the Ionosphere and its Comparison with Group Velocity. By L. H. Heisler and J. D. Whitehead 481

Systems for Simultaneous Image Formation with Radio Telescopes. By D. J. McLean and J. P. Wild 489

A Catalogue of Radio Sources between Declinations $-50°$ and $-80°$. By B. Y. Mills, O. B. Slee, and E. R. Hill 497

A High Resolution Galactic Survey at $19\cdot7$ Mc/s. By the Late C. A. Shain, M. M. Komesaroff, and C. S. Higgins 508

The Galactic Radio Spectrum down to $19\cdot7$ Mc/s. By M. M. Komesaroff . . 515

Free Convection in a Vertical Tube with a Linear Wall Temperature Gradient. By I. G. Donaldson 529

Short Communications

Evidence for the Transfer of Corpuscles to Distant Parts of the Sun following a Solar Radio Burst. By R. F. Mullaly 540

Index to Volume 14 545

INDEX

PAGE

Airglow, The 5577 Å OI Emission Line of the, at Brisbane 304

Alderson, J. E., and Williams, S. E.—
  Luminescence in KI : Tl .. 368

Allison, J. W.—
  Gamma-radiation Absorption Coefficients of Various Materials allowing for Bremsstrahlung and other Secondary Radiations .. 443

Aluminium : Gamma Rays from the $^{27}Al(p,\gamma)$ Reaction .. 335

Atmospherics, Whistling. I. Occurrence 22

Atmospherics, Whistling. II. Diffuseness 40

Auroras, Orientation of Polar.. 193

Ausburn, K. J.—
  Charged Particle Trajectories in Static Electric and Magnetic Fields 310

Baskhin, S., and Ophel, T. R.—
  Gamma Rays from the $^{27}Al(p,\gamma)$ Reaction 335

Baxter, A. M.—*See* McKenna, V. R. 196

Beryllium, Polycrystalline, Oxidation in Carbon Dioxide .. 191

Bogle, G. S., and Gardner, F. F.—
  Cross-relaxation Effects in a Ruby *L*-Band (1440 Mc/s) Maser at Low Magnetic Fields 381

Bond, F. R.—*See* Denholm, J. V. 193

Bray, R. J., and Loughhead, R. E.—
  Facular Granule Lifetimes determined with a Seeing-monitored Photoheliograph 14

Bray, R. J.—*See also* Loughhead, R. E. 347

Bremsstrahlung Experiments, Resolution of 174

PAGE

Bruce, C. F., and Hill, R. M.—
  Wavelengths of Krypton 86, Mercury 198, and Cadmium 114 64

Cadmium 114, Wavelengths of.. 64

Candler, C.—
  The Gradation and Inertia of Hurter and Driffield : A Study in Theory 160

Carbon : Inelastic Scattering of Protons on ^{12}C 432

Caro, D. E.—*See* Kenny, M. J.. . 242

Chromium, Anomalous Thermal Expansion of 359

Conductivity, Thermal, of Porous Materials 469

Convection, Free, in a Vertical Tube with a Linear Wall Temperature Gradient .. 529

Corrigenda 435

Crouchley, J.—
  A Study of Whistling Atmospherics. I. Occurrence .. 22

Crouchley, J., and Finn, R. J.—
  A Study of Whistling Atmospherics. II. Diffuseness .. 40

Current Loops and Magnetic Shells, On the Equivalence of 188

Danziger, I. J.—
  The 5577 Å OI Emission Line of the Airglow at Brisbane 304

Denholm, J. V., and Bond, F. R.—
  Orientation of Polar Auroras 193

Diffusion, *n*- 1

Donaldson, I. G.—
  Free Convection in a Vertical Tube with a Linear Wall Temperature Gradient .. 529

Edvi-Illes, C. A.—*See* Mohr, C. B. O. 437

Electromagnetic Systems, Average Forces in 152

Energy Levels in ^{13}N 196

PAGE
Europium: Sum-coincidence Measurements on ^{154}Eu .. 250
Expansion, Thermal, of Chromium 359
Expansion, Thermal, of Solids, Anharmonicity and the .. 420

Facular Granule Lifetimes determined with a Seeing-monitored Photoheliograph .. 14
Filter, Birefringent, $\frac{1}{8}$ Å, for Solar Research 201
Finn, R. J.—*See* Crouchley, J. .. 40
Fletcher, G. C.—
Anharmonicity and the Thermal Expansion of Solids 420
Force Circuit Diagram, Construction of the Equivalent Electric Circuit from a .. 307

Gadolinium: Sum-coincidence Measurements on ^{154}Eu .. 250
Galaxy: A High Resolution Galactic Survey at 19·7 Mc/s 508
Galaxy: The Galactic Radio Spectrum down to 19·7 Mc/s 515
Gamma-radiation Absorption Coefficients of Various Materials 443
Gamma-rays from the $^{27}\mathrm{Al}(p,\gamma)$ Reaction 335
Gardner, F. F.—*See* Bogle, G. S. 381
Gas Discharge between Electrodes, Estimation of the Maximum Temperature in a Radially Constricted .. 129
Gas Discharge between Electrodes, Influence of Thermoelectric Effects on the Maximum Temperature of a Radially Constricted .. 279
Gas Discharge between Electrodes, Stability Criterion for a Radially Constricted .. 321
Giovanelli, R. G., and Jefferies, J. T.—
Vertical Velocities in the Solar Chromosphere 212
Giovanelli, R. G.—*See also* Steel, W. H. 201
Green, R.—
The Sweep of Long Water Waves across the Pacific Ocean 120

PAGE
Heat Transfer, An Exact Solution to a Problem in .. 317
Heisler, L. H., and Whitehead, J. D.—
The Phase Speed of a Travelling Disturbance in the *F* Region of the Ionosphere and its Comparison with Group Velocity 481
Higgins, C. S.—*See* Shain, C. A. 508
Hill, E. R.—*See* Mills, B. Y. .. 497
Hill, R. M.—*See* Bruce, C. F. .. 64
Hurst, C. S.—
On the Equivalence of Current Loops and Magnetic Shells 188
Hydrogen, Neutral, Sky Survey of, at λ 21 cm 260
Hypernuclear Binding Energies, A Phenomenological Model for 313

Ionosphere, Phase Speed of a Travelling Disturbance in the *F* Region of the 481
Ionospherics at Macquarie Island 218

Jefferies, J. T.—*See* Giovanelli, R. G. 212
Johnson, C. H. J.—
An Exact Solution to a Problem in Heat Transfer 317

Kenny, M. J., and Caro, D. E.—
Excited States of ^{64}Zn .. 242
Klemens, P. G., and Lowenthal, G. C.—
Deviations from Matthiessen's Rule for Platinum .. 352
Komesaroff, M. M.—
The Galactic Radio Spectrum down to 19·7 Mc/s .. 515
Komesaroff, M. M.—*See also* Shain, C. A. 508
Krishnan, T., and Labrum, N. R.—
The Radio Brightness Distribution on the Sun at 21 cm from Combined Eclipse and Pencil-beam Observations 403
Krypton 86, Wavelengths of .. 64

PAGE

Labrum, N. R.—*See* Krishnan, T. 403

Loughhead, R. E., and Bray, R. J.—
  Phenomena accompanying the Birth of Sunspot Pores .. 347

Loughhead, R. E.—*See also* Bray, R. J. 14

Lowenthal, G. C.—*See* Klemens, P. G. 352

Luminescence in KI : Tl .. 368

McGee, R. X., and Murray, J. D.—
  A Sky Survey of Neutral Hydrogen at λ 21 cm. I. The General Distribution and Motions of the Local Gas 260

McInnes, B. A.—
  A Study of Ionospherics at Macquarie Island 218

McKenna, V. R., Baxter, A. M., and Shute, G. G.—
  Energy Levels in ^{13}N .. 196

McKenna, V. R., and Shute, G. G.—
  Inelastic Scattering of Protons on ^{12}C 432

McLean, D. J., and Wild, J. P.—
  Systems for Simultaneous Image Formation with Radio Telescopes .. 489

Magnetic Shells, On the Equivalence of Current Loops and 188

Maser, Cross-relaxation Effects in a Ruby L-Band (1440 Mc/s), at Low Magnetic Fields .. 381

Matthiessen's Rule, Deviations from, for Platinum 352

Mercury 198, Wavelengths of .. 64

Meteor Echoes, Characteristics of Persistent Sporadic .. 89

Meteor Masses, Distribution of, for Sporadic Meteors and Three Showers 102

PAGE

Mills, B. Y., Slee, O. B., and Hill, E. R.—
  A Catalogue of Radio Sources between Declinations —50° and —80° 497

Mohr, C. B. O., and Edvi-Illes, C. A.—
  Polarization in Nuclear Collisions with Channel Coupling 437

Mullaly, R. F.—
  Evidence for the Transfer of Corpuscles to Distant Parts of the Sun following a Solar Radio Burst 540

Murray, J. D.—*See* McGee, R. X. 260

Nitrogen : Energy Levels in ^{13}N 196

Nuclear Collisions with Channel Coupling, Polarization in .. 437

Olley, J. W.—
  A Phenomenological Model for Hypernuclear Binding Energies 313

Ophel, T. R.—*See* Bashkin, S. .. 335

Parker, A. W.—
  Sum-coincidence Measurements on ^{154}Eu 250

Particle, Charged, Trajectories in Static Electric and Magnetic Fields 310

van Peer, W. J.—
  The Oxidation of Polycrystalline Beryllium in Carbon Dioxide 191

Philip, J. R.—
  n-Diffusion 1

Photography—Theory : The Gradation and Inertia of Hurter and Driffield .. 160

Platinum, Deviations from Matthiessen's Rule for 352

Porous Materials, Thermal Conductivity of 469

Potassium Iodide : Luminescence in KI : Tl 368

Protons, Inelastic Scattering of, on ^{12}C 432

PAGE

Radiation, Cosmic Radio: A Catalogue of Radio Sources between Declinations −50° and −80° 497

Radiation, Cosmic Radio: A High Resolution Galactic Survey at 19·7 Mc/s .. 508

Radiation, Cosmic Radio: The Galactic Radio Spectrum down to 19·7 Mc/s 515

Radiation, Cosmic Radio: Sky Survey of Neutral Hydrogen at λ 21 cm 260

Radiative Transfer, On Solving the Equation of, for Conservative Non-uniform Media 57

Radio Brightness Distribution on the Sun at 21 cm.. .. 403

Radio Bursts, Slow Drift Solar.. 234

Radio Sources, Counts of Extragalactic 295

Radio Telescopes, Systems for Simultaneous Image Formation with 489

Seymour, P. W.—
  A Stability Criterion for a Radially Constricted Gas Discharge between Electrodes 321
  Estimation of the Maximum Temperature in a Radially Constricted Gas Discharge between Electrodes .. 129
  The Influence of Thermoelectric Effects on the Maximum Temperature of a Radially Constricted Gas Discharge between Electrodes 279

Shain, C. A., Komesaroff, M. M., and Higgins, C. A.—
  A High Resolution Galactic Survey at 19·7 Mc/s .. 508

Shute, G. G.—*See* McKenna, V. R. 196, 432

Slee, O. B.—*See* Mills, B. Y. .. 497

Smartt, R. N.—*See* Steel, W. H. 201

Smith, J. W.—
  The Characteristics of Persistent Sporadic Meteor Echoes 89

PAGE

Smith, W. E.—
  Average Forces in Electromagnetic Systems .. 152

Solar Research, $\frac{1}{8}$ Å Birefringent Filter for 201

Solids, Thermal Expansion of, Anharmonicity and the .. 420

Steel, W. H., Smartt, R. N., and Giovanelli, R. G.—
  A $\frac{1}{8}$ Å Birefringent Filter for Solar Research 201

Sugawara, A., and Yoshizawa, Y.—
  An Investigation on the Thermal Conductivity of Porous Materials and its Application to Porous Rock 469

Sun, Evidence for the Transfer of Corpuscles to Distant Parts of the, following a Solar Radio Burst 540

Sun: Facular Granule Lifetimes 14

Sun, Radio Brightness Distribution on the, at 21 cm .. 403

Sun: Slow Drift Solar Radio Bursts 234

Sun: Vertical Velocities in the Solar Chromosphere .. 212

Sunspot Pores, Phenomena accompanying the Birth of .. 347

Thallium: Luminescence in KI : Tl.. 368

Thermoelectric Effects, Influence on the Maximum Temperature of a Radially Constricted Gas Discharge between Electrodes 279

Thies, H. H.—
  Resolution of Bremsstrahlung Experiments 174

Tschoegl, N. W.—
  Construction of the Equivalent Electric Circuit from a Force Circuit Diagram by a Simple Graphical Method 307

Van der Borght, R.—
  Counts of Extragalactic Radio Sources 295

PAGE

Wavelengths of Krypton 86, Mercury 198, and Cadmium 114 64

Waves, Water, Sweep of Long, across the Pacific Ocean .. 120

Weiss, A. A.—
  The Distribution of Meteor Masses for Sporadic Meteors and Three Showers .. 102

White, G. K.—
  The Anomalous Thermal Expansion of Chromium .. 359

Whitehead, J. D.—*See* Heisler, L. H. 481

Wild, J. P.—*See* McLean, D. J. 489

Williams, S. E.—*See* Alderson, J. E. 368

PAGE

Wilson, P. R.—
  On Solving the Equation of Radiative Transfer for Conservative Non-uniform Media 57

Wood, Marion B.—
  Slow Drift Solar Radio Bursts: Harmonic Frequency Ratios, Solar Longitude Dependence, and Frequency Drift Rates 234

Yoshizawa, Y.—*See* Sugawara, A. 469

Zinc: Excited States of ^{64}Zn.. 242

n–DIFFUSION

By J. R. Philip*

[*Manuscript received September* 15, 1960]

Summary

Transfer processes in which an entity is transferred down a gradient of a concentration-like quantity satisfy the relation $\mathbf{q}=-\mathbf{A}.\mathbf{B}$, with $\mathbf{q}$ the flux density, $\mathbf{A}$ dependent on time, concentration and position, and $\mathbf{B}$ a function of the concentration gradient, $\nabla\theta$. In ordinary diffusion $\mathbf{B}=\nabla\theta$. This paper considers the more general transfer process, designated n-diffusion, for which $\mathbf{B}=|\nabla\theta|^{n-1}\nabla\theta$ $(n>0)$.

The paper deals with the simplest unsteady one-dimensional problem of n-diffusion (with $\mathbf{A}$ constant) into a semi-infinite region. The results are simply extended to the related problem in the (doubly) infinite region.

Solutions are found in terms of the incomplete beta-function, though for certain values of n solutions are expressible in terms of elementary functions. Infinite " tails " (analogous to that in 1-diffusion) occur for $0<n<1$, whilst the concentration profiles are finite for $n>1$. Distance of penetration into the region and cumulated flux vary as $(\text{time})^{1/(n+1)}$.

The present paper is intended as an introduction to later work on concentration- and space-dependent forms of n-diffusion which are immediately relevant to physical problems of interest.

I. Transfer Processes

Many branches of mathematical physics are concerned with transfer processes, in the sense that some entity is transferred down a gradient of a concentration-like quantity. For processes of this nature we have the general relation

$$\mathbf{q}=-\mathbf{A}.\mathbf{B}. \tag{1.1}$$

Here $\mathbf{q}$ is the vector flux density; $\mathbf{A}$ is a function of time, concentration, and position (and is, in the general case, a tensor of rank 2); and $\mathbf{B}$ is a vector function of the concentration gradient.

Assuming conservation of the transferred entity and differentiating, we obtain

$$\partial\theta/\partial t=\nabla.(\mathbf{A}.\mathbf{B}). \tag{1.2}$$

Here θ is the concentration and t is the time.

(*a*) *Diffusion*

In this paper we use the word " diffusion " in a mathematical sense, with no implications as to the physics of the transfer process. For diffusion, as the term is generally employed,

$$\mathbf{B}=\nabla\theta. \tag{1.3}$$

We may categorize the various types of diffusion by the form of $\mathbf{A}$. $\mathbf{A}$ is constant for linear diffusion, whereas in time-, concentration-, and space-dependent diffusion **A** is a function of the appropriate variable. In more complicated types of diffusion **A** may vary with two, or with all three, of time, concentration, and space.

---

* Division of Plant Industry, C.S.I.R.O., Canberra.

(*b*) n-*Diffusion*

In this paper we consider a generalized form of diffusion for which

$$\mathbf{B}=|\nabla\theta|^{n-1}\nabla\theta. \qquad (1.4)^*$$

The various types of *n*-diffusion, as we shall call it, may be categorized according to the form of **A** in the same way as for 1-diffusion. In this paper we confine our attention to the case **A**=constant.† This study serves as the introduction to further work dealing with concentration-dependent *n*-diffusion and certain forms of space-dependent *n*-diffusion. These more complicated types of *n*-diffusion are immediately relevant to physical problems of interest, including unsteady vertical heat transfer from a horizontal surface by (turbulent) free convection (Priestley 1954), and unsteady turbulent flow of a liquid with a free surface over a plane. The latter does not seem to have been yet formulated in the literature as a problem in *n*-diffusion; Philip (1956) gives the parallel development for non-turbulent flow.

It is of some interest that *n*-diffusion has the most general form of **B** for which solutions of the simplest unsteady problems may be found by similarity methods. We apply these methods here to the case **A**=constant; but, as we propose to show in later work, they are effective also in concentration-dependent *n*-diffusion [$\mathbf{A}=f(\theta)$] and in space [x]-dependent *n*-diffusion with $\mathbf{A}\propto x^c$ ($c<n$). The methods apply also to the more general class of *n*-diffusion with $\mathbf{A}=f(\theta).x^c$.

II. *n*-DIFFUSION IN A SEMI-INFINITE REGION

The one-dimensional form of the *n*-diffusion equation is

$$\frac{\partial\theta}{\partial t}=\frac{\partial}{\partial x}\left(A\left|\frac{\partial\theta}{\partial x}\right|^{n-1}\frac{\partial\theta}{\partial x}\right), \qquad (2.1)$$

with A and n positive constants. x is the spatial dimension. We limit ourselves to the physically interesting case of positive n because the cases $n\leqslant 0$ involve irrelevant complications.

We consider the most elementary (and perhaps most important) unsteady transfer problem, namely, transfer in the semi-infinite region $x\geqslant 0$, subject to the conditions:

$$\left.\begin{aligned}\theta=\theta_0,\quad t=0,\quad x>0\,;\\ \theta=\theta_1,\quad x=0,\quad t\geqslant 0.\end{aligned}\right\} \qquad (2.2)$$

---

[*] Of course, we could regard *n*-diffusion as characterized also by $\mathbf{B}=\nabla\theta$, but with **A** dependent on $\nabla\theta$ (as well as, in general, t, θ, and space); but the present treatment is perhaps more convenient.

[†] We shall use the term " *n*-diffusion " to describe this simple case as well as to denote the whole class of phenomena defined by (1.4). Unfortunately, we can hardly apply the adjective " linear " to the simple case. We shall avoid ambiguity by specifically labelling all types of *n*-diffusion, other than that with **A** constant, as " concentration-dependent ", " space-dependent ", etc.

It is a simple matter to modify the methods and results of this paper so that they apply to the related problem in the infinite region with the governing conditions:

$$\left.\begin{aligned} &t=0,\ x>0,\ \theta=\theta_0;\ \ x<0,\ \theta=\theta_1;\\ &t\geqslant 0,\ \int_{\theta_0}^{\theta_1} x\,\mathrm{d}\theta=0. \end{aligned}\right\} \tag{2.3}$$

The similarity substitutions

$$\vartheta=(\theta-\theta_0)/(\theta_1-\theta_0)\,;\quad \varphi=x[|\,\theta_1-\theta_0\,|^{n-1}At]^{-1/(n+1)} \tag{2.4}$$

form the generalization in n-diffusion of the "Boltzmann transformation" (Boltzmann 1894) in 1-diffusion. Applying (2.4) to (2.1), (2.2), we obtain the ordinary equation

$$\frac{\varphi}{n+1}\,\frac{\mathrm{d}\vartheta}{\mathrm{d}\varphi}=\frac{\mathrm{d}}{\mathrm{d}\varphi}\left(-\frac{\mathrm{d}\vartheta}{\mathrm{d}\varphi}\right)^n, \tag{2.5}$$

subject to the conditions

$$\varphi=0,\ \vartheta=1\,;\quad \varphi\rightarrow\infty,\ \vartheta\rightarrow 0. \tag{2.6}$$

When n is such that $\vartheta>0$ for all finite φ the second of conditions (2.6) immediately implies

$$\vartheta\rightarrow 0,\ \mathrm{d}\vartheta/\mathrm{d}\varphi\rightarrow 0. \tag{2.7}$$

But when n is such that $\vartheta=0$ at some finite φ (in fact, when $n>1$), we must consider further the behaviour of $\mathrm{d}\vartheta/\mathrm{d}\varphi$ near $\vartheta=0$. We therefore introduce the quantity $q(\vartheta)$, the flux density at the point with reduced concentration ϑ, and observe that

$$|\,q(\vartheta)\,|=A\left|\frac{\partial\theta}{\partial x}\right|^n=(A\,|\,\theta_1-\theta_0\,|^{2n}t^{-n})^{1/(n+1)}\left|\frac{\mathrm{d}\vartheta}{\mathrm{d}\varphi}\right|^n. \tag{2.8}$$

Now, since $q(0)=0$ and $A>0$ and $n>0$, we have, for $t>0$,

$$\vartheta=0,\ \mathrm{d}\vartheta/\mathrm{d}\varphi=0. \tag{2.9}$$

This result holds whether the least value of φ at which $\vartheta=0$, φ_0, is finite or not.

The substitution

$$\Psi=-\mathrm{d}\vartheta/\mathrm{d}\varphi \tag{2.10}$$

reduces (2.5) to

$$\varphi=-n(n+1)\Psi^{n-2}\mathrm{d}\Psi/\mathrm{d}\varphi. \tag{2.11}$$

This has the integrals

$$n=1\,;\quad \varphi^2=4\log[\Psi_1/\Psi]. \tag{2.12}$$

$$n\neq 1\,;\quad \varphi^2=\frac{2n(n+1)}{n-1}[\Psi_1^{n-1}-\Psi^{n-1}]. \tag{2.13}$$

Ψ_1 denotes the value of Ψ at $\varphi=0$ (i.e. at $\vartheta=1$).

A further integration of (2.12) and use of (2.6) yields

$$\vartheta = \operatorname{erfc} \varphi/2, \tag{2.14}$$

the well-known solution for $n=1$. In this case $\Psi_1 = \pi^{-\frac{1}{2}}$.

The case $n \neq 1$ needs further discussion. Referring to (2.11), we observe that, when φ and Ψ are both non-negative, $\mathrm{d}\Psi/\mathrm{d}\varphi$ is non-positive.* That is, Ψ is a non-negative monotonic function of φ, decreasing from its largest value, Ψ_1 at $\varphi=0$. It now follows from (2.13) that, for the case $0<n<1$, $\varphi \rightarrow \infty$ as $\Psi \rightarrow 0$ [i.e. as $\vartheta \rightarrow 0$: cf. (2.9)]; and that, for the case $n>1$, φ approaches the finite positive value $[\{2n(n+1)/(n-1)\}\Psi_1^{n-1}]^{\frac{1}{2}}$ as $\Psi \rightarrow 0$ (i.e. as $\vartheta \rightarrow 0$).

Integrating (2.13), and using the first of conditions (2.6), we obtain

$$n \neq 1 ; \quad \vartheta = 1 - \Psi_1 \int_0^{\varphi} \left(1 + \frac{(1-n)\varphi'^2}{2n(n+1)\Psi_1^{n-1}}\right)^{1/(n-1)} \mathrm{d}\varphi'. \tag{2.15}$$

Ψ_1 can now be evaluated.

(*a*) *The Case* $0<n<1$

In this case the substitutions

$$\alpha = \tan^{-1}\left(\frac{(1-n)\Psi_1^{1-n}}{2n(1+n)}\right)^{\frac{1}{2}} \varphi, \tag{2.16}$$

$$m = 2n/(1-n), \tag{2.17}$$

reduce (2.15) to

$$\vartheta = 1 - \left(\frac{2n(1+n)}{(1-n)\Psi_1^{1-n}}\right)^{\frac{1}{2}} \Psi_1 \int_0^{\alpha} \cos^m \alpha' \mathrm{d}\alpha'. \tag{2.18}$$

We introduce the identity

$$\int_0^{\frac{1}{2}\pi} \cos^m \alpha' \mathrm{d}\alpha' = \tfrac{1}{2}\mathrm{B}\left(\frac{m+1}{2}, \tfrac{1}{2}\right), \tag{2.19}$$

where $\mathrm{B}(p, q)$ is the beta-function $\int_0^1 x'^{p-1}(1-x')^{q-1}\mathrm{d}x'$. $\mathrm{B}(p, q)$ is expressible in terms of gamma-functions, but it is more convenient here to retain beta-function forms.

Then it follows from (2.6), (2.18), and (2.19) that

$$\Psi_1 = \left(\frac{1-n}{2n(1+n)}\right)^{1/(1+n)} \cdot \left(\frac{2}{\mathrm{B}\left(\frac{1+n}{2-2n}, \frac{1}{2}\right)}\right)^{2/(1+n)}. \tag{2.20}$$

---

* It follows at once that the family of $\varphi(\vartheta)$ curves do not possess points of inflexion.

(2.18) then reduces to the forms

$$\begin{aligned}\vartheta&=1-\int_0^{\alpha}\cos^m\alpha'\mathrm{d}\alpha'\Big/\!\!\Big/\int_0^{\frac{1}{2}\pi}\cos^m\alpha'\mathrm{d}\alpha'\\&=1-\frac{2}{\mathrm{B}\left(\frac{m+1}{2},\,\frac{1}{2}\right)}\int_0^{\alpha}\cos^m\alpha'\mathrm{d}\alpha'\\&=\int_{\alpha}^{\frac{1}{2}\pi}\cos^m\alpha'\mathrm{d}\alpha'\Big/\!\!\Big/\int_0^{\frac{1}{2}\pi}\cos^m\alpha'\mathrm{d}\alpha'\\&=\frac{2}{\mathrm{B}\left(\frac{m+1}{2},\,\frac{1}{2}\right)}\int_{\alpha}^{\frac{1}{2}\pi}\cos^m\alpha'\mathrm{d}\alpha'.\end{aligned}\tag{2.21}$$

Elimination of Ψ_1 from (2.16) yields

$$\alpha=\tan^{-1}\left[\frac{1-n}{2n(1+n)}\left\{\frac{2}{\mathrm{B}\left(\frac{1+n}{2-2n},\,\frac{1}{2}\right)}\right\}^{1-n}\right]^{1/(1+n)}\varphi=\tan^{-1}k_a\varphi.\tag{2.22}$$

We observe that, in this case, as φ goes from $0\to\infty$, α goes from $0\to\frac{1}{2}\pi$ and ϑ goes from $1\to0$.

(*b*) *The Case* n>1

In this case the substitutions

$$\alpha=\sin^{-1}\left(\frac{(n-1)\Psi_1^{1-n}}{2n(n-1)}\right)^{\frac{1}{2}}\varphi,\tag{2.23}$$

$$m=(n+1)/(n-1),\tag{2.24}$$

reduce (2.15) once again to the form (2.18), but with the factor $(1-n)$ in the denominator of the expression to power $\frac{1}{2}$ replaced by $(n-1)$.

We may now use the value of φ_0 for $n>1$ to evaluate Ψ_1 for this case. The result is

$$\Psi_1=\left(\frac{n-1}{2n(n+1)}\right)^{1/(n+1)}\cdot\left(\frac{2}{\mathrm{B}\left(\frac{n}{n-1},\,\frac{1}{2}\right)}\right)^{2/(n+1)}.\tag{2.25}$$

The forms (2.21) hold here also, and the expression for α with Ψ_1 eliminated is

$$\alpha=\sin^{-1}\left[\frac{n-1}{2n(n+1)}\left\{\frac{2}{\mathrm{B}\left(\frac{n}{n-1},\,\frac{1}{2}\right)}\right\}^{1-n}\right]^{1/(n+1)}\varphi=\sin^{-1}k_b\varphi.\tag{2.26}$$

In this case, as φ goes from $0\to1/k_b=\varphi_0$, α goes from $0\to\frac{1}{2}\pi$ and ϑ goes from $1\to0$.

III. SOLUTION IN TERMS OF ELEMENTARY FUNCTIONS

$\int_0^\alpha \cos^m \alpha' d\alpha'$ is expressible in terms of trigonometrical functions when m is integral; so that solutions for the cases

$$n=m/(2+m),\ m \text{ a positive integer;} \tag{3.1}$$

$$n=(m+1)/(m-1),\ m \text{ an integer greater than } 1; \tag{3.2}$$

can be found in terms of elementary functions.

The simplest solutions of each type are presented in Tables 1 and 2. It will be observed that, for each type, the functions entering the solution differ according as m is even or odd.

TABLE 1

THE SIMPLEST SOLUTIONS OF TYPE (3.1)

m	n	ϑ	k_a
1	1/3	$1-k_a\varphi/(1+k_a^2\varphi^2)^{\frac{1}{2}}$	$\left(\frac{3}{4}\right)^{3/4}=0\cdot806$
2	1/2	$1-\frac{2}{\pi}[\tan^{-1} k_a\varphi+k_a\varphi/(1+k_a^2\varphi^2)]$	$\left(\frac{2}{3\pi^{\frac{1}{2}}}\right)^{2/3}=0\cdot521$
3	3/5	$1-\frac{1}{2}\frac{k_a\varphi(3+2k_a^2\varphi^2)}{(1+k_a^2\varphi^2)^{3/2}}$	$\left(\frac{5^5}{2^{17}.3^3}\right)^{1/8}=0\cdot432$
4	2/3	$1-\frac{2}{3\pi}\left[3\tan^{-1} k_a\varphi+\frac{k_a\varphi(5+3k_a^2\varphi^2)}{(1+k_a^2\varphi^2)^2}\right]$	$\left(\frac{3^2}{2^2.5^3\pi}\right)^{1/5}=0\cdot356$

TABLE 2

THE SIMPLEST SOLUTIONS OF TYPE (3.2)

m	n	ϑ	k_b
2	3	$1-\frac{2}{\pi}[\sin^{-1} k_b\varphi+k_b\varphi(1-k_b^2\varphi^2)^{\frac{1}{2}}]$	$\left(\frac{\pi^2}{2^6.3}\right)^{1/4}=0\cdot476$
3	2	$1-\frac{1}{2}k_b\varphi(3-k_b^2\varphi^2)$	$\left(\frac{1}{2.3^2}\right)^{1/3}=0\cdot382$
4	5/3	$1-\frac{2}{3\pi}[3\sin^{-1} k_b\varphi+k_b\varphi(5-2k_b^2\varphi^2)(1-k_b^2\varphi^2)^{\frac{1}{2}}]$	$\left(\frac{3^5.\pi^2}{2^{17}.5^3}\right)^{1/8}=0\cdot332$
5	3/2	$1-\frac{k_b\varphi}{8}[15-10k_b^2\varphi^2+3k_b^4\varphi^4]$	$\left(\frac{2}{3.5}\right)^{3/5}=0\cdot299$

These solutions in terms of elementary functions are of some interest. However, available tables (Pearson 1934) make solution in terms of incomplete beta-functions (see following Section IV) more useful for numerical purposes, even* in the cases treated in this Section.

IV. Solution in Terms of the Incomplete Beta-function

We observe that

$$\left.\begin{aligned}\int_{\alpha}^{\frac{1}{2}\pi}\cos^m\alpha'\mathrm{d}\alpha'\Big/\int_{0}^{\frac{1}{2}\pi}\cos^m\alpha'\mathrm{d}\alpha'=I_x\left(\frac{m+1}{2},\tfrac{1}{2}\right),\\ x=\cos^2\alpha.\end{aligned}\right\}\tag{4.1}$$

Here $I_x(p, q)$ is the incomplete beta-function ratio of Pearson (1934) defined by

$$I_x(p,q)=\int_0^x x'^{p-1}(1-x')^{q-1}\mathrm{d}x'\Big/\int_0^1 x'^{p-1}(1-x')^{q-1}\mathrm{d}x'.\tag{4.2}$$

Our solutions are thus expressible in terms of this function. (2.21) may be rewritten

$$\vartheta=I_x\left(\frac{m+1}{2},\tfrac{1}{2}\right),\tag{4.3}$$

with x specified as follows:

$$0<n<1;\quad x=(1+k_a^2\varphi^2)^{-1},\tag{4.4}$$

$$n>1;\quad x=1-k_b^2\varphi^2.\tag{4.5}$$

Pearson's tabulation of $I_x(p, q)$ is for $p=\frac{1}{2}(\frac{1}{2})11(1)50$. It follows that, without interpolation, Pearson provides values of $I_x\left(\frac{m+1}{2},\frac{1}{2}\right)$ only for $m=0(1)21(2)99$. Thus, curiously enough, the table gives (without interpolation) only solutions which could be found by the elementary methods of Section III.† The table, of course, allows solutions to be computed with much less labour than would be required otherwise.

V. Power Series and Asymptotic Forms of Solution

(a) *Power Series in φ*

The power series forms in φ provide information on the behaviour of the solution near $\vartheta=1$.

Case $0<n<1$. In this case (2.15) may be rewritten

$$\vartheta=1-\Psi_1\int_0^{\varphi}(1+k_a^2\varphi'^2)^{-1/(1-n)}\mathrm{d}\varphi'.\tag{5.1}$$

---

* In fact, as we see later, Pearson's tables are directly usable *only* in cases where the solution *is* expressible in terms of elementary functions.

† A P-fold increase in the number of immediately available solutions would be provided by a tabulation of $\int_0^{\alpha}\cos^m\alpha'\mathrm{d}\alpha'$ in the interval of $0\leqslant\alpha\leqslant\pi/2$ for $m=\frac{1}{P}\left(\frac{1}{P}\right)\frac{P-1}{P}$ $\Big[$or, equivalently, by a tabulation of $I_x(p,\frac{1}{2})$ for $p=\frac{P+1}{2P}\left(\frac{1}{2P}\right)\frac{2P-1}{2P}\Big]$.

In the interval $0<\varphi<k_a^{-1}$ we may apply the binomial theorem and term-by-term integration, obtaining

$$\vartheta=1-\Psi_1\varphi\left[1-\frac{1}{3}\cdot\frac{k_a^2\varphi^2}{1-n}+\frac{2-n}{2!5}\cdot\left(\frac{k_a^2\varphi^2}{1-n}\right)^2-\frac{(2-n)(3-2n)}{3!7}\cdot\left(\frac{k_a^2\varphi^2}{1-n}\right)^3+\cdots\right]. \tag{5.2}$$

The corresponding result in the case $n>1$ is

$$\vartheta=1-\Psi_1\varphi\left[1-\frac{1}{3}\cdot\frac{k_b^2\varphi^2}{n-1}-\frac{n-2}{2!5}\cdot\left(\frac{k_b^2\varphi^2}{n-1}\right)^2-\frac{(n-2)(2n-3)}{3!7}\cdot\left(\frac{k_b^2\varphi^2}{n-1}\right)^3-\cdots\right]. \tag{5.3}$$

We observe that series (5.3) is finite whenever $1/(n-1)$ is a positive integer (i.e. whenever the integer m of (3.2) is odd). Also, since $k_b\varphi<1$ for $\varphi<\varphi_0$, series (5.3) converges throughout the interval $0\leqslant\varphi<\varphi_0$.

(b) *Asymptotic Form for* ϑ *small* $(0<n<1)$

Forms of solution discussed to this point do not readily provide a full picture of behaviour near $\vartheta=0$. Accordingly, the asymptotic form developed here for $0<n<1$ is of some interest.

We rewrite (2.15) as

$$\vartheta=\Psi_1\int_\varphi^\infty(k_a\varphi')^{-2/(1-n)}[1+(k_a\varphi')^{-2}]^{-1/(1-n)}\mathrm{d}\varphi'. \tag{5.4}$$

Then, applying the binomial theorem and term-by-term integration, we have

$$\vartheta=(1-n)\Psi_1k_a^{-2/(1-n)}\varphi^{-(1+n)/(1-n)}\left[\frac{1}{1+n}-\frac{1}{(3-n)(1-n)(k_a\varphi)^2}\right.$$
$$\left.+\frac{2-n}{2!(5-3n)(1-n)^2(k_a\varphi)^4}-\frac{(2-n)(3-n)}{3!(7-5n)(1-n)^3(k_a\varphi)^6}+\cdots\right]. \tag{5.5}$$

With some reductions involving (2.20) and (4.4), (5.5) yields the approximations, good for ϑ small (φ large),

$$\left.\begin{aligned}\vartheta&\approx\left[2n\left(\frac{1+n}{1-n}\right)^n\right]^{1/(1-n)}\varphi^{-(1+n)/(1-n)},\\ \varphi&\approx\left[2n\left(\frac{1+n}{1-n}\right)^n\right]^{1/(1+n)}\cdot\vartheta^{-(1-n)/(1+n)}.\end{aligned}\right\} \tag{5.6}$$

Although series (5.5) is conveniently (and properly) described as asymptotic, it converges in the interval $\varphi>k_a^{-1}$.

(c) *Power Series in* $(1-k_b\varphi)$ $(n>1)$

On the other hand, in the case $n>1$, behaviour near $\vartheta=0$ may be examined by means of the power series in $(1-k_b\varphi)$. Putting

$$\varepsilon=1-k_b\varphi, \tag{5.7}$$

we may here reduce (2.15) to

$$\vartheta = \frac{2^{1/(n-1)}\Psi_1}{k_b} \int_0^{\varepsilon} \varepsilon'^{1/(n-1)} (1 - \tfrac{1}{2}\varepsilon')^{1/(n-1)} d\varepsilon'. \tag{5.8}$$

Since $\varepsilon \leqslant 1$, we may apply the binomial theorem and term-by-term integration, obtaining

$$\begin{aligned} \vartheta = 2^{1/(n-1)}(n-1) \cdot \frac{\Psi_1}{k_h} \cdot \varepsilon^{n/(n-1)} \biggl[& \frac{1}{n} - \frac{1}{2n-1} \cdot \frac{\varepsilon}{2(n-1)} \\ & - \frac{n-2}{2!(3n-2)} \cdot \left(\frac{\varepsilon}{2(n-1)} \right)^2 - \frac{(n-2)(2n-3)}{3!(4n-3)} \left(\frac{\varepsilon}{2(n-1)} \right)^3 - \cdots \biggr]. \end{aligned} \tag{5.9}$$

With some reductions involving (2.25) and (4.5), (5.9) yields the approximations, good for ϑ small,

$$\left. \begin{aligned} \vartheta & \approx \frac{(2\varepsilon)^{n/(n-1)}}{\dfrac{n}{n-1} \left[\mathrm{B}\left(\dfrac{n}{n-1}, \tfrac{1}{2} \right) \right]}, \\ \varphi & \approx \varphi_0 \left[1 - \tfrac{1}{2} \left[\frac{n}{n-1} \left[\mathrm{B}\left(\frac{n}{n-1}, \tfrac{1}{2} \right) \right] \vartheta \right]^{(n-1)/n} \right]. \end{aligned} \right\} \tag{5.10}$$

It will be noted that series (5.9) is convergent throughout the interval $0 \leqslant \varepsilon \leqslant 1$.

VI. SOME GENERAL PROPERTIES OF n-DIFFUSION

In this section we discuss certain general features of n-diffusion in the semi-infinite region (subject to conditions (2.2)) which emerge from this study.

(a) *Profile Character*

We consider how the character of the concentration profiles, in the reduced form $\varphi(\vartheta)$, varies with n.

(i) *Depth of Penetration ; Order of Profiles near* $\vartheta = 0$.—An obvious feature of the profiles is the sharp distinction between the case $0 < n \leqslant 1$, for which φ_0 is infinite, and the case $n > 1$, for which φ_0 is finite. We have, for the latter case,

$$\varphi_0 = \frac{1}{k_b} = \left[\frac{2n(n+1)}{n-1} \left\{ \frac{2}{\mathrm{B}\left(\dfrac{n}{n-1}, \tfrac{1}{2} \right)} \right\}^{n-1} \right]^{1/(n+1)}. \tag{6.1}$$

φ_0 is a monotonic function of n, decreasing as n increases for $n > 1$.

When $(n-1)$ is small, but positive, we have the approximation

$$\varphi_0 \approx 2(n-1)^{-\frac{1}{2}}. \tag{6.2}$$

An approximation for n large is

$$\varphi_0 \approx (2n)^{1/(n+1)}. \tag{6.3}$$

Also

$$\lim_{n \to \infty} \varphi_0 = 1. \tag{6.4}$$

Figure 1 shows $\varphi_0(n)$, together with approximations (6.2) and (6.3).

In the case $0 > n \geqslant 1$, the rate of approach of φ to infinity as $\vartheta \to 0$ is of some interest. It is useful to introduce the notation $\varphi^{(r)}$ to denote the φ function for $n = n_r$.

We then have from (5.6) that,

$$\left.\begin{array}{c} \text{if } 0 < n_1 < n_2 \leqslant 1, \\ \varphi^{(1)} \to \infty \text{ as } \vartheta \to 0 \text{ more rapidly than does } \varphi^{(2)}. \end{array}\right\} \qquad (6.5)$$

(6.5) and the monotonic decreasing property of φ_0 for $n > 1$ supply an ordering relation for the family of $\varphi(\vartheta)$ curves close to $\vartheta = 0$. This is that,

$$\left.\begin{array}{c} \text{if } 0 < n_1 < n_2 \text{ and } \vartheta \text{ is sufficiently small,} \\ \varphi^{(1)}(\vartheta) > \varphi^{(2)}(\vartheta). \end{array}\right\} \qquad (6.6)$$

(ii) *Concentration Gradient at* x$=0$; *Order of Profiles near* $\vartheta = 1$.—Equations (2.20) and (2.25), and the known result for $n = 1$, provide the relation between Ψ'_1 (i.e. minus the concentration gradient at $x = 0$ in reduced form) and n. It is readily shown, both for $\nu > 0$ and $\nu < 0$, that

$$\text{for } n = 1 + \nu, \quad \lim_{\nu \to 0} \Psi'_1 = \pi^{-\frac{1}{2}}. \qquad (6.7)$$

It is thus confirmed that $\Psi'_1(n)$ is continuous through $0 < n < 1$, $n = 1$, and $n > 1$. We note that

$$\lim_{n \to 0} \Psi'_1 = \infty \, ; \quad \lim_{n \to \infty} \Psi'_1 = 1 \, ; \qquad (6.8)$$

and that, when n is small, we have the approximation

$$\Psi'_1 \approx 2/\pi^2 n. \qquad (6.9)$$

Figure 2 shows $\Psi'_1(n)$, together with approximation (6.9).

An important property of $\Psi'_1(n)$ is the fact that it possesses a minimum value, approximately $0 \cdot 55794$, at $n = n_* \approx 1 \cdot 29$. The existence of this minimum leads to the following relations ordering the family of $\varphi(\vartheta)$ curves close to $\vartheta = 1$.

$$\left.\begin{array}{c} \text{If } 0 < n_1 < n_2 \leqslant n_* \text{ and } (1 - \vartheta) \text{ is sufficiently small,} \\ \varphi^{(1)}(\vartheta) < \varphi^{(2)}(\vartheta). \end{array}\right\} \qquad (6.10)$$

$$\left.\begin{array}{c} \text{If } n_* \leqslant n_1 < n_2 \text{ and } (1 - \vartheta) \text{ is sufficiently small,} \\ \varphi^{(1)}(\vartheta) > \varphi^{(2)}(\vartheta). \end{array}\right\} \qquad (6.11)$$

Ordering relations (6.6) and (6.10) are in opposite senses, so that any two members of the set of profiles $0 < n \leqslant n_*$ intersect once and once only in the interval $0 < \vartheta < 1$. This set of profiles contains the sub-set $0 < n \leqslant 1$ with φ_0 infinite and the sub-set $1 < n \leqslant n_*$ with φ_0 finite. Figure 3 shows typical members of the set, the " finite φ_0 " sub-set being represented by the profile $n = 5/4$.

Ordering relations (6.6) and (6.11) are in the same sense, so that the set of profiles $n \geqslant n_*$ are non-intersecting in the interval $0 < \vartheta < 1$. φ_0 is finite for this set of profiles, which are illustrated in Figure 4 ; the profile for $n = 1$ is shown also for comparison.

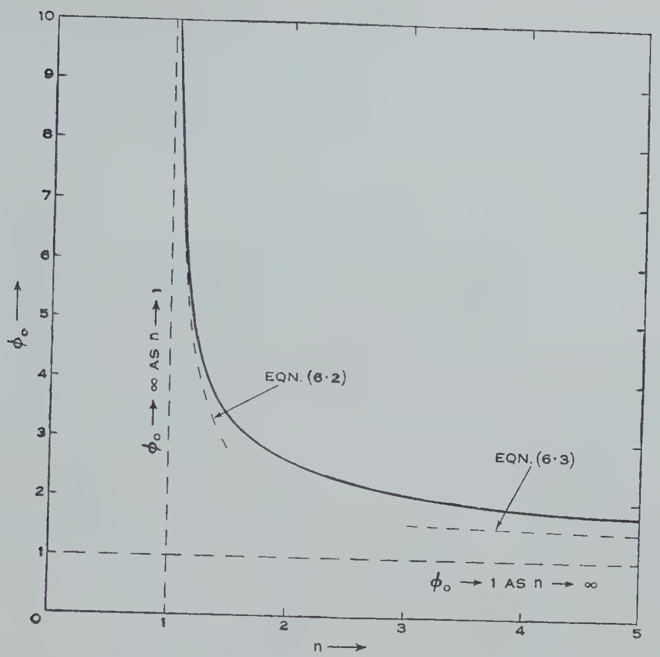

Fig. 1.—n-diffusion in the semi-infinite region. Variation with n of depth of penetration in the reduced form φ_0.

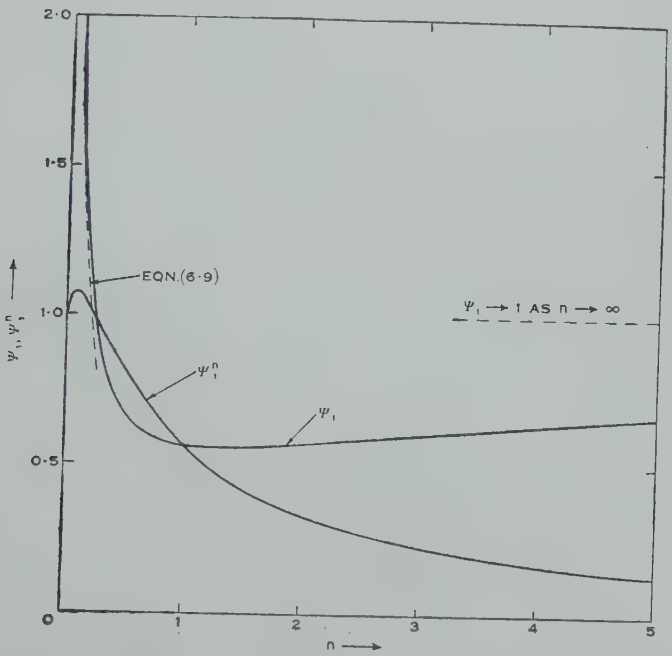

Fig. 2.—n-diffusion in the semi-infinite region. Variation with n of concentration gradient at surface $x=0$ in the reduced form Ψ_1. Also shown is Ψ_1^n, which represents flux density at $x=0$ in reduced form.

It will be understood that intersection relations between the two sets are somewhat complicated and that a representation of the whole family of profiles on the one graph would appear, at first glance, rather disorderly.

(iii) *Relationships connecting* Ψ_1 *and* k_a *and* k_b.—We note the following relationships :

$$0<n<1\,;\quad \Psi_1/k_a=2/\mathrm{B}\left(\frac{1+n}{2-2n},\ \tfrac{1}{2}\right), \tag{6.12}$$

$$n>1\,;\quad \Psi_1/k_b=\Psi_1\varphi_0=2/\mathrm{B}\left(\frac{n}{n-1},\ \tfrac{1}{2}\right). \tag{6.13}$$

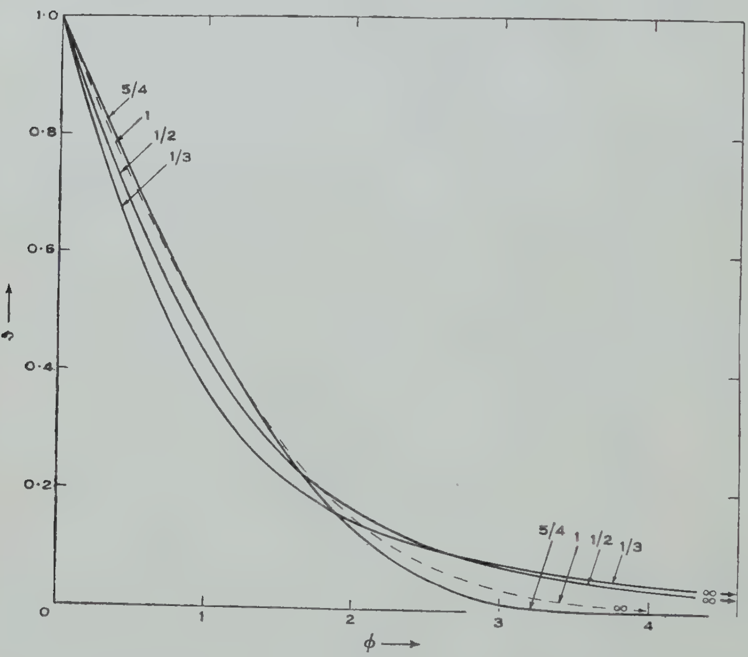

Fig. 3.—n-diffusion in the semi-infinite region. Concentration profiles in the reduced form $\vartheta(\varphi)$ for " intersecting " set $n\leqslant n_*$. Numerals on curves denote values of n. Infinite profiles are identified by the infinity sign. Profile for $n=1$ shown broken for clarity.

(*b*) *Variation with Time*

The form of the time-dependence of the phenomenon follows immediately from (2.4). We have, in particular, the following results :

$$x(\vartheta)\propto t^{1/(n+1)}, \tag{6.14}$$

$$\frac{\mathrm{d}\vartheta}{\mathrm{d}x}(\vartheta)\propto t^{-1/(n+1)}, \tag{6.15}$$

$$q_1\propto t^{-n/(n+1)}, \tag{6.16}$$

$$\int_0^t q_1\mathrm{d}t\propto\int_0^1\varphi\mathrm{d}\vartheta\propto t^{1/(n+1)}, \tag{6.17}$$

q_1 denotes the value of the flux density q at $x=0$ ($\vartheta=1$).

(*c*) *Flux Density and Integrated Flux Density*

We have the following expressions for the flux density and its time integral :

$$q_1=A^{1/(n+1)}|\theta_1-\theta_0|^{2n/(n+1)}.t^{-n/(n+1)}.\Psi_1^n, \tag{6.18}$$

$$\int_0^t q_1\mathrm{d}t=(n+1)A^{1/(n+1)}|\theta_1-\theta_0|^{2n/(n+1)}.t^{1/(n+1)}.\Psi_1^n. \tag{6.19}$$

Ψ_1^n is a measure, in reduced form, of flux density and of total transfer to time t. Some interest therefore attaches to the dependence of Ψ_1^n on n. This is illustrated in Figure 2. We note that Ψ_1^n has a maximum value approximately equal to e^{2/π^2e} $[\approx 1\cdot 08]$ at $n\approx 2/\pi^2e[\approx 0\cdot 075]$; and that $\lim\limits_{n\to 0}\Psi_1^n=1$ and $\lim\limits_{n\to\infty}\Psi_1^n=0$.

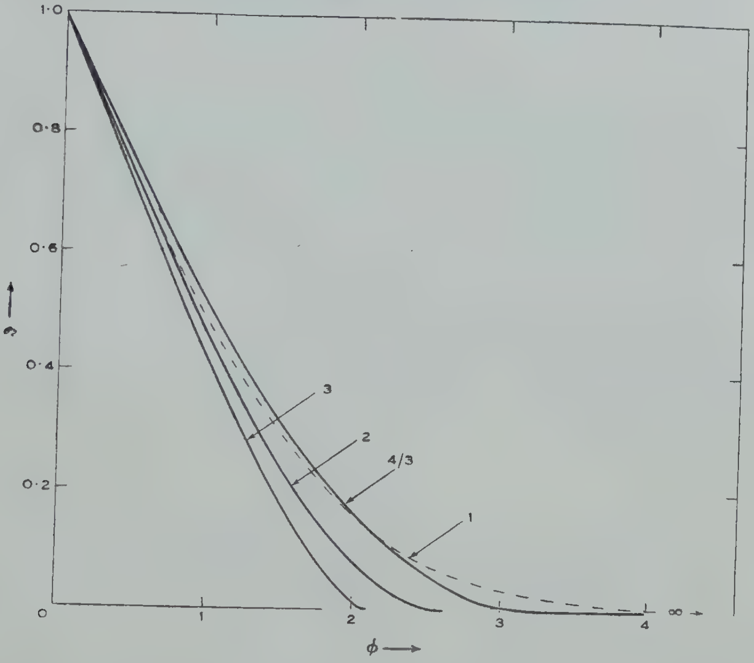

Fig. 4.—As Figure 3, but for "non-intersecting set" $n\geqslant n_*$. Profile for $n=1$ also shown for comparison (broken curve).

VII. REFERENCES

Boltzmann, L. (1894).—*Ann. Phys., Lpz.* **53** : 595.
Pearson, K. (1934).—"Tables of the Incomplete Beta-Function." (Cambridge Univ. Press.)
Philip, J. R. (1956).—*Aust. J. Phys.* **9** : 570.
Priestley, C. H. B. (1954).—*Aust. J. Phys.* **7** : 176.

FACULAR GRANULE LIFETIMES DETERMINED WITH A SEEING–MONITORED PHOTOHELIOGRAPH

By R. J. Bray* and R. E. Loughhead*

[*Manuscript received November 9, 1960*]

Summary

A telescope designed to take exposures automatically at moments of good seeing has been used to obtain a $5\frac{1}{2}$ hr sequence of high quality photographs of a facular region near the east limb of the Sun. Individual facular granules are found to be much longer lived than the photospheric granules, a result which agrees with the work of ten Bruggencate (1940) and Waldmeier (1940) but disagrees with the more recent observations of Macris (1953) and of Krat and Goldberg-Rogosinskaja (1956). Fifty per cent. of the facular granules last for over 2 hr, and 10% last for over 5 hr. In some cases, a facular granule, only 750–1500 km in diameter, occurs as an isolated bright structure, surrounded by normal photosphere and well removed from neighbouring sunspots or faculae. Apart from their greater brightness and much longer lifetimes, the facular granules differ from the photospheric granules in that they do not form a well-defined cellular pattern; these differences suggest different modes of origin.

A description is given of the method of triggering the exposures by means of a seeing monitor.

I. Introduction

Sunspot groups are invariably accompanied by white-light faculae, though sometimes faculae may be observed without attendant spots. Faculae are visible only near the limb and are composed of individual granules mostly 1–2 sec of arc in diameter. The facular granules are brighter than the surrounding photosphere and may occur singly or in clusters. High-resolution photographs (e.g. Loughhead and Bray 1960*b* : Plate 1 (*a*)) show that the facular granules are superimposed on a background of normal photospheric brightness.† In some cases isolated granules occur, well removed from neighbouring spots or faculae and surrounded by normal photosphere.

ten Bruggencate (1940) estimated the lifetimes of the individual facular granules to be of the order of 1 hr, while Waldmeier (1940) found that many facular granules last for more than 2 hr. These estimates were based on comparisons of pairs of photographs taken 1 hr and 2 hr apart. However, these results were later contradicted by Macris (1953) and by Krat and Goldberg-Rogosinskaja (1956), who found lifetimes comparable with those of the photospheric granules. The mean lifetimes of 6–7 min and 2 min found by these authors have since been quoted by Mustel (1958) and de Jager (1959) in recent monographs as representing the true values. However, the lifetimes determined

---

* Division of Physics, C.S.I.R.O., University Grounds, Chippendale, N.S.W.

† This result contradicts ten Bruggencate's conclusion that the facular granules are superimposed on a bright background (ten Bruggencate 1942).

by Macris refer, in fact, to the ordinary *photospheric* granules in the neighbourhood of a spot group near the centre of the disk ; any faculae in the neighbourhood would be invisible, since white-light faculae are visible only near the limb. Moreover, the poor quality of the photographs published by Krat and Goldberg-Rogosinskaja (1956 : cf. Plates 1 and 2) casts some doubt on the reliability of their results ; experience shows that poor seeing invariably leads to an underestimate of the lifetime of any 1–2 sec of arc photospheric detail.

The determination of the lifetimes of the facular granules described in the present paper is based on a sequence of good-quality photographs covering a period of 5½ hr. The observations were made with a 5-in. photoheliograph (Loughhead and Burgess 1958), the exposures being triggered automatically by a solar seeing monitor at the moments of best seeing. The results confirm the work of ten Bruggencate and Waldmeier in showing that individual facular granules are much longer lived than the photospheric granules : some 80% have lifetimes exceeding 1 hr, 50% exceeding 2 hr, 25% exceeding 4 hr, and 10% exceeding 5 hr. Some information has also been obtained about the modes of formation and dissolution of individual granules (Section IV).

II. OBSERVATIONS

In order to study the lifetime and evolution of the facular granules, a sequence of photographs fairly uniformly distributed over a period of several hours and consistently showing a resolution of 1 sec of arc is required. This poses an observational problem of considerable difficulty, since the seeing seldom remains at such a good level over so long a period. In fact, our experience indicates that it might take a year or more to obtain a sequence of sufficient quality and duration by the normal method of time-lapse cinematography. However, the chances of obtaining a useful sequence are considerably improved if, instead of photographing at fixed intervals, exposures are triggered off only during moments of good seeing. These moments do occur, even during long periods of otherwise mediocre seeing ; they usually last for a few seconds, occasionally for as long as a minute.

An instrument has been constructed to monitor the seeing continuously and to trigger the exposures automatically at the moments of good seeing. The principle of operation of the device is to measure photoelectrically the magnitude of the fluctuations in light intensity—due to seeing—of two narrow segments of the solar limb. The seeing monitor, which is carried on the same mounting as the 5-in. photoheliograph, has been described in detail elsewhere (Bray, Loughhead, and Norton 1959). The method used to trigger the exposures is described in Appendix I.*

The present work is based on a film taken on June 7, 1960, between 10.00 a.m. and 4.00 p.m. local time. The film shows an extended facular region surrounding a small group of sunspots near the east limb. The triggering level was set at

---

* *Note added in Proof.*—It has recently come to our attention that Siedentopf (*Die Sterne* **19** : 145 (1939)) had earlier published an account of a device to provide a quantitative measure of the solar seeing. Like the monitor described by the present authors, this device measured the distortion of the solar limb, but used a single radial slit instead of two tangential ones.

0·8 V (cf. Appendix I) throughout the film except for a period at the beginning when 92 exposures were obtained at the 0·5 V level. Out of the 800-odd photographs taken in all, 20 show a resolution of 1 sec of arc over substantially the whole frame; many others show 1–2 sec of arc resolution over more limited areas. The 20 best photographs are very uniform in quality and constitute a good sequence, fairly uniformly distributed over a period of 5 hr 33 min, for determining the lifetimes of the facular granules.

The appearance on the photographs of the faculae surrounding the spot group is typical of facular regions near the limb (cf. Waldmeier 1955). Except for the occasional appearance of bright facular streaks closely bordering small umbral areas on the *limb* side of the spot (Loughhead and Bray 1959), faculae show no close association with their attendant spots. In fact, they are distributed over a very large area in the neighbourhood of a spot group, each facular region consisting of a loose conglomeration of individual granules 1–2 sec of arc in diameter. In most cases the facular granules are not sufficiently compacted to form a pattern; even in big clusters composed of, say, 20 or more individual granules, they are often spread out along intersecting lines. For this reason it is not possible to define a mean " cell size ", or average distance between the centres of adjacent granules, similar to that measured for the photospheric and umbral granulation (cf. Loughhead and Bray 1960*a*). Not all facular granules occur in clusters: many occur as completely isolated structures, surrounded by photospheric granules of normal brightness.

An examination of a large number of limb films taken with the 5-in. photoheliograph has revealed that individual facular granules are often clearly visible only 1–2 sec of arc from the limb. On the other hand, the photospheric granules are visible only up to 4 or 5 sec from the limb (Rösch 1957; Loughhead and Bray 1960*b*). This is evidence that the facular granules extend to a greater height than the photospheric granules.

III. Lifetimes

The lifetimes of 118 individual facular granules have been determined by a method similar to that used in determining the lifetimes of other fine structures in the photosphere (see, for example, Bray and Loughhead 1958*b*). The granules selected for study were well distributed over the entire facular region, at distances from the limb ranging from 4 to 70 sec of arc. Most of the granules were members of clusters; some, however, were isolated ones. Two of the features selected—which appeared to be facular granules—were located in the penumbra of one of the associated sunspots; however, in the course of time they elongated and then merged together to form a bridge across the penumbra, so their identification as facular granules is uncertain.

In comparing maps of the facular region made from photographs taken some hours apart, some allowance must be made for the effect of solar rotation. Not only does the distance of a given facular granule from the (east) limb increase but, in addition, foreshortening causes faculae at different distances from the limb to move at different apparent rates (cf. Plate 1). However, this effect did not lead to any difficulty in following individual granules from photograph

FACULAR GRANULE LIFETIMES

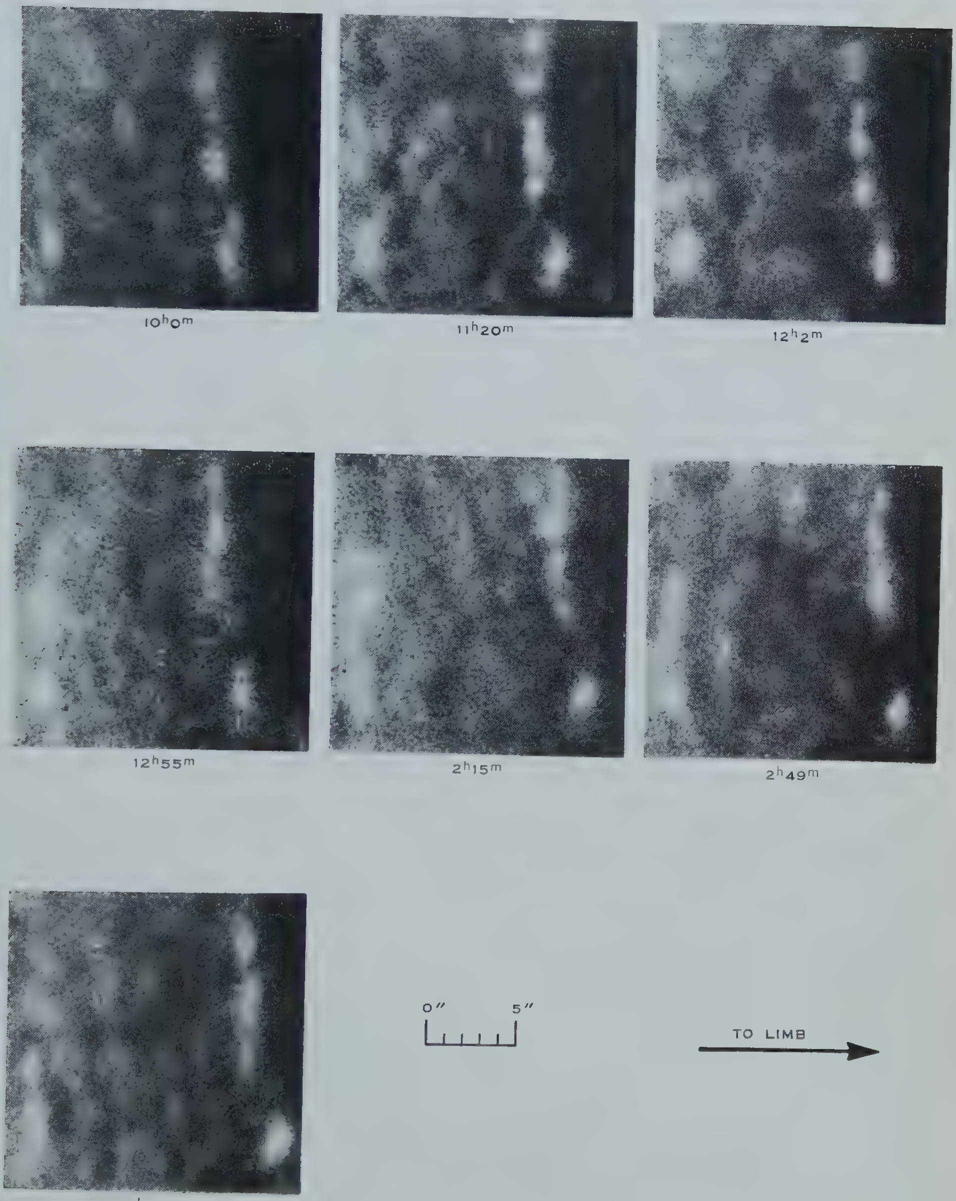
$10^{h}0^{m}$ $11^{h}20^{m}$ $12^{h}2^{m}$

$12^{h}55^{m}$ $2^{h}15^{m}$ $2^{h}49^{m}$

$3^{h}28^{m}$

Sequence illustrating stability of individual facular granules in a small region near the east limb over a period of $5\frac{1}{2}$ hr. There are some changes due to the growth of new granules, but two granules situated in the lower corners of the photographs persist throughout the sequence. The apparent increase in the separation of these granules is due to solar rotation, the heliocentric angle of the centre of the region changing from 78° at $10^{\mathrm{h}}\,0^{\mathrm{m}}$ to 75° at $3^{\mathrm{h}}\,28^{\mathrm{m}}$.

to photograph. Nevertheless, in many cases it was not possible to specify the exact times of beginning and end of a given granule ; one reason is the somewhat irregular spacing of the photographs in the sequence. In addition, the identification of a granule on maps corresponding to photographs taken several hours apart is sometimes made difficult by the growth and decay of neighbouring granules. Only in 38 out of 118 cases was it established with certainty that the granule in question both began and ended during the 5½ hr sequence. Consequently, the values obtained represent *lower limits* to the true lifetimes.

The analysis shows that the majority of the facular granules are very long-lived compared with the photospheric granules : 81% had lifetimes exceeding 1 hr, 53% exceeding 2 hr, 27% exceeding 3 hr, 25% exceeding 4 hr, and 10% exceeding 5 hr.* These figures confirm Waldmeier's conclusion that the majority of the facular granules last for at least 2 hr.

TABLE 1

LIFETIMES OF SUNSPOT AND PHOTOSPHERIC FINE STRUCTURES

Feature	Lifetime	Reference
Facular granules	2 hr	Waldmeier (1940)
	2 hr	Bray and Loughhead (this paper)
Penumbral filaments ..	~2 hr	Bray and Loughhead (1958*a*)
Umbral granules*	15–30 min	Bray and Loughhead (1959) Loughhead and Bray (1960*a*)
Photospheric granules ..	7–8 min	Macris (1953)
	~10 min	Bray and Loughhead (1958*b*)
	10 min	Rösch and Hugon (1959)

* Some umbral granules are much longer lived : 10% last for more than 2 hr.

No significant tendency has been found for short-lived granules, on the one hand, or long-lived granules, on the other, to cluster together. Isolated facular granules have lifetimes similar to those of members of clusters.

Plate 1 illustrates the stability of the facular granules in a small selected region over a period of 5½ hr. Although there are some changes due to the growth of new granules, two granules persist over the entire sequence ; these are located in the lower corners of the photographs. The apparent increase in the separation of these granules is a consequence of solar rotation (see above). The region is nearer the limb at the start of the sequence.

Reliable determinations have now been made of the lifetimes of all the basic photospheric and sunspot fine structures, namely, the photospheric and facular granules, sunspot penumbra filaments, and sunspot umbra granules.

---

* The apparent deficiency in the number of granules lasting between 3 and 4 hr is due to a gap of $1^h\,17^m$ between two neighbouring photographs occurring $2^h\,55^m$ and $4^h\,12^m$ after the beginning of the sequence. If there had been another good photograph during this interval, some of the 15 granules recorded as having a lifetime of just less than 3 hr would probably have been recorded as persisting for over 3 hr, thus smoothing the distribution curve.

These data are summarized in Table 1. It is evident that the facular granules, in common with the fine structure of sunspots, are much longer lived than the photospheric granules.

IV. Changes in the Facular Granules

In the case of the photospheric granulation, it was possible to make a systematic study of changes in the brightness, size, and shape of individual granules during their observed lifetimes (Bray and Loughhead 1958*b*). However, this is not possible for the facular granules. In the first place, since the facular granules are close to the limb, their apparent sizes and shapes depend on the degree of foreshortening which, because of solar rotation, changes during the life of a granule. Secondly, any intrinsic variations in the brightness of a granule are masked by changes due to its varying heliocentric angle. The most that can be said is that no systematic changes in brightness have been established; faint granules appear to remain faint throughout their lifetimes and, similarly, bright granules appear to remain bright.

On the other hand, some information has been obtained about the process of growth and decay of individual granules. In nine cases the spacing and quality of the photographs were such that the process of formation could be studied in detail; from these it appears that a granule develops quite suddenly in a region of hitherto normal photospheric brightness, being preceded—at least occasionally—by a patch of diffuse material of intermediate brightness some 3–4 sec of arc in diameter. The transition from a region of normal photospheric brightness to a recognizable facular granule takes place in a period short compared with the average lifetime. Twelve cases of well-defined deaths have been studied; a facular granule appears to lose its identity either by fading and being replaced by material of photospheric brightness, or by coalescing with another granule. The final fading takes place in a time short compared with the lifetime. In two cases an interesting variant was noticed: the original granule disappeared and was replaced by two facular granules on either side of its former position. These in turn were quickly replaced by ordinary photospheric material.

V. Discussion

Apart from their greater brightness, the facular granules differ from the photospheric granules in at least two important respects. Firstly, in most cases the facular granules are not sufficiently compacted to form a well-defined cellular pattern. Secondly, their lifetimes are an order of magnitude greater than those of the photospheric granules. Hence, in spite of a superficial resemblance, it is likely that the two types of granules owe their origins to different physical mechanisms. It is not yet known how the physical conditions within a facular granule differ from those of its surroundings; it is not safe to assume, for example, that the observed enhanced emission of a facular granule is due solely to a temperature excess over its surroundings.

As ten Bruggencate (1940) has pointed out, a remarkable feature of the facular granules is the extraordinary stability shown by the individual granule: a single granule, only 750–1500 km in diameter, can persist as an isolated structure—in some cases well removed from sunspots and neighbouring faculae—for a period of several hours. It is tempting to speculate that both the enhanced emission and the stability are due in some way to the influence of the magnetic field pervading the facular region. If so, the observations imply that the influence of the field is concentrated within regions no larger—and possibly much smaller—than a single facular granule.

VI. ACKNOWLEDGMENTS

The authors wish to thank Dr. C. H. B. Priestley, of the C.S.I.R.O. Division of Meteorological Physics, for correspondence concerning the interpretation of the intermittency in the solar seeing. The benefit of discussions of this paper with Dr. R. G. Giovanelli is gratefully acknowledged. The conversion of the 5-in. photoheliograph to seeing monitor control was carried out in collaboration with Mr. D. G. Norton, to whom we are also indebted for assistance in securing the observations. We are grateful to Mr. H. R. Gillett for processing the films and making the enlargements.

VII. REFERENCES

BRAY, R. J., and LOUGHHEAD, R. E. (1958*a*).—*Aust. J. Phys.* **11**: 185.
BRAY, R. J., and LOUGHHEAD, R. E. (1958*b*).—*Aust. J. Phys.* **11**: 507.
BRAY, R. J., and LOUGHHEAD, R. E. (1959).—*Aust. J. Phys.* **12**: 320.
BRAY, R. J., LOUGHHEAD, R. E., and NORTON, D. G. (1959).—*Observatory* **79**: 63.
TEN BRUGGENCATE, P. (1940).—*Z. Astrophys.* **19**: 59.
TEN BRUGGENCATE, P. (1942).—*Z. Astrophys.* **21**: 162.
ELSÄSSER, H. (1960).—*Naturwiss.* **47**: 6.
ELSÄSSER, H., and SIEDENTOPF, H. (1959).—*Z. Astrophys.* **48**: 213.
GIFFORD, F., JOHNSON, H., and WILSON, A. (1955).—*Astr. J.* **60**: 161.
HOSFELD, R. (1954).—*J. Opt. Soc. Amer.* **44**: 284.
DE JAGER, C. (1959).—"Handbuch der Physik." (Ed. S. Flügge.) Vol. 52. p. 175. (Springer: Berlin.)
KRAT, V. A., and GOLDBERG-ROGOSINSKAJA, N. M. (1956).—*Izv. Gl. Astr. Obs. Poulkovo* **20** (155): 17.
LOUGHHEAD, R. E., and BRAY, R. J. (1959).—*Aust. J. Phys.* **12**: 97.
LOUGHHEAD, R. E., and BRAY, R. J. (1960*a*).—*Aust. J. Phys.* **13**: 139.
LOUGHHEAD, R. E., and BRAY, R. J. (1960*b*).—*Aust. J. Phys.* **13**: 738.
LOUGHHEAD, R. E., and BURGESS, V. R. (1958).—*Aust. J. Phys.* **11**: 35.
MACRIS, C. (1953).—*Ann. Astrophys.* **16**: 19.
MUSTEL, E. R. (1958).—"Theoretical Astrophysics." (Ed. V. A. Ambartsumyan.) p. 301. (Pergamon: London.)
PRIESTLEY, C. H. B. (1959).—"Turbulent Transfer in the Lower Atmosphere." (Univ. Chicago Press.)
RÖSCH, J. (1956).—"Astronomical Optics." (Ed. Z. Kopal.) p. 310. (North-Holland Publishing Company: Amsterdam.)
RÖSCH, J. (1957).—*Astronomie* **71**: 138.
RÖSCH, J., and HUGON, M. (1959).—*C.R. Acad. Sci., Paris* **249**: 625.
SMITH, A. G., SAUNDERS, M. J., and VATSIA, M. L. (1957).—*J. Opt. Soc. Amer.* **47**: 755.
WALDMEIER, M. (1940).—*Helv. Phys. Acta* **13**: 13.
WALDMEIER, M. (1955).—"Ergebnisse und Probleme der Sonnenforschung." 2nd Ed. p. 205. (Geest u. Portig: Leipzig.)

APPENDIX I

*Triggering of Exposures at Moments of Best Seeing**

The principle of operation of the seeing monitor (Bray, Loughhead, and Norton 1959) is described in Section II. Figure 1 explains how the "seeing signal" is made to trigger the exposures. The vacuum-tube voltmeter is set to indicate the peak-to-peak voltage of the fluctuating signal from the amplifier-adder unit, averaged over a period comparable with the time constant of the meter. This voltage is a direct measure of the quality of the seeing on a quantitative (though arbitrary) scale. Its value fluctuates between wide limits; on the high side, very poor seeing values of 10 V or more do occur, but are fairly exceptional; on the low side, seeing better than 0·3 V has not yet been observed.

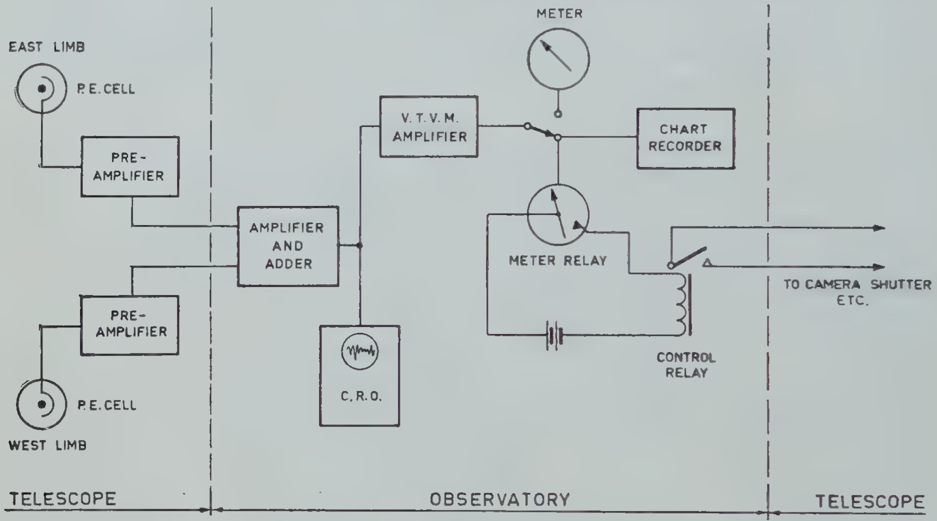

Fig. 1.—Block diagram of seeing monitor and telescope triggering system. The seeing signal from the vacuum-tube voltmeter is fed to a sensitive meter relay, whose pointer carries a contact at its lower end. This contact can close with a second contact attached to the case of the instrument. The latter can be manually adjusted so that the contacts close when the seeing signal falls to some predetermined value. This in turn closes a control relay which operates the shutters. Simultaneous tracings of the seeing signal can be obtained with a chart recorder.

There is a good correlation between the measured peak-to-peak voltage of the seeing signal and the quality of the solar image. For the purpose of obtaining direct photographs showing 1 sec of arc detail, the seeing does not become "promising" until the signal drops to 0·8 V or below. The limb of the solar image on the seeing monitor box then appears sharp and well defined, and a fairly close visual inspection is required to detect any waviness.

The actual triggering of the telescope shutters is carried out by a meter relay, which can be connected to the output of the vacuum-tube voltmeter (cf. Fig. 1). The meter relay is of the sensitive moving coil type and has a full-scale deflection corresponding to a peak-to-peak voltage at the input to the V.T.V.M. of 4 V. The lower end of the meter pointer carries a contact, which can close with a second contact attached to the case of the instrument. The second contact can be manually adjusted so that the contacts close at any predetermined value of the seeing signal voltage. An exposure is made within a small fraction of a second of the contacts closing. Should the seeing remain at the chosen level, or even improve, exposures continue automatically at the rate of one every 2–3 s (the time required for the camera to wind on).

---

* This work was carried out jointly with Mr. D. G. Norton.

On a day of generally good seeing there are typically between 50 and 200 occasions when the seeing signal drops to 0·8 V or below. Such periods usually last for a few seconds, only occasionally for as long as a minute. When a quiet period occurs the seeing signal declines with great rapidity (e.g. it may drop from, say, 5 V to only 0·5 V in a few seconds or even in less than a second) and afterwards increases to a more average value equally quickly. On the occasions when the seeing signal falls much below 0·8 V, a fair percentage of the photographs obtained show the full theoretical performance of the 5-in. objective. Under normal observing conditions the triggering level is usually set at this value. However, should a period of exceptionally fine seeing occur, the triggering level is manually reset to a lower value in order to avoid film wastage.

Dr. C. H. B. Priestley, of the C.S.I.R.O. Division of Meteorological Physics, Melbourne, has suggested (personal communication) that the intermittency in the solar seeing described above may be correlated with a similar intermittency characteristic of the temperature fluctuations in the boundary layer of the atmosphere (the first few hundred feet). The temperature traces show alternating disturbed and quiet periods (Priestley 1959 : cf. Fig. 19), the intermittency being most marked on days of light wind ; during the disturbed periods the temperature fluctuations are of the order of 1 °C, whereas during the quiet periods any residual fluctuations still present seem to be less than 0·1 °C. The quiet periods can persist from several seconds to a minute, lasting on the average somewhat longer than the moments of good seeing described above. Simultaneous velocity measurements have shown that the disturbed periods are associated with ascending air and the quiet periods with descending air. Priestley has interpreted the meteorological data as implying the existence of a regime of *convective plumes* (i.e. ascending columns of heated air) in the boundary layer of the Earth's atmosphere. There seems little doubt that the sudden moments of good seeing occur when the line-of-sight from the telescope momentarily passes through the regions of nearly uniform temperature surrounding the plumes. If this explanation is correct it implies that the quality of solar seeing is largely determined by temperature inhomogeneities in the boundary layer. This conclusion is entirely consistent with the well-known fact that temperature inhomogeneities close to a telescope (within a few hundred feet) have a marked effect both on image motion and image degradation (cf., for example, Hosfeld 1954 ; Gifford, Johnson, and Wilson 1955 ; Rösch 1956 ; Smith, Saunders, and Vatsia 1957 ; Elsässer and Siedentopf 1959 ; Elsässer 1960).

A STUDY OF WHISTLING ATMOSPHERICS

I. OCCURRENCE

By J. Crouchley*

[*Manuscript received October* 3, 1960]

Summary

The occurrence of whistling atmospherics at four Australian stations (Brisbane, Adelaide, Hobart, and Macquarie Island) over the I.G.Y. period is discussed. A strong seasonal variation is observed at each station, with the maximum occurrence during local winter, and also a strong diurnal variation with a minimum during daylight hours. Whistlers are observed more commonly at about geomagnetic latitude 45°. Autocorrelation analysis suggests recurrence tendencies in the occurrence figures and cross-correlation with sunspot numbers and Adelaide data indicates an association between the two. There is little evidence of association between whistler occurrence and magnetic planetary index.

I. Introduction

The existence of occasional audio-frequency interference, in the form of descending whistles, on single-wire telephone circuits has been reported by various observers from time to time. Eckersley (1935) suggested that the energy of these " whistlers " or " whistling atmospherics " was derived from an impulsive electrical discharge, such as a lightning flash, and that the observed frequency-time characteristic was due to the propagation of this energy as very-low-frequency electromagnetic waves in a dispersive medium. A frequency-time relationship of the form $t=Df^{-\frac{1}{2}}$ (where the zero of time is taken as the time of the initiating discharge) was predicted theoretically. D, the " dispersion ", is a constant, dependent on the path parameters, for a given whistler. This relationship is still regarded as being approximately valid for the " middle " range of whistler frequencies but requires modification at " high " and " low " frequencies.

Storey (1953) postulated that the propagation paths closely follow magnetic field lines and that reflections may, on occasions, occur at the Earth end of such a line. The simplest case, and the one giving the smallest value of dispersion and hence a " short " whistler, is a generating lightning discharge in one hemisphere and an observer in the other, while a double traverse of the path with source and observer in the same hemisphere gives rise to a whistler of twice the dispersion—a " long whistler ". If several reflections occur, alternately at opposite ends of the path, then an observer in the source hemisphere observes a " whistler train " with successive dispersions in the ratios of 2 : 4 : 6 : 8, etc.

---

* Physics Department, University of Queensland, Brisbane.

while an observer in the opposite hemisphere observes a whistler train with dispersions in the ratios 1 : 3 : 5 : 7, etc. Whistler trains are not uncommon at some stations, and Morgan and Allcock (1956), observing at two points which were approximately geomagnetically conjugate, reported the occurrence of whistlers in a train, alternately at the two stations, with time separations and dispersions appropriate to this theory.

An occasional correlation between a nearby lightning flash and the arrival of a long whistler a short time after has been reported by Morgan (1958). Helliwell, Jean, and Taylor (1958) have observed that atmospherics which are accompanied by whistlers have, on occasions, a particular type of wave-form with a large Fourier component around 5 kc/s.

This paper is concerned with an analysis of the occurrence figures for whistlers heard at Brisbane (geographic, lat. 27° 32′ S., long. 152° 55′E . ; geomagnetic, lat. 35° 8′ S., long. 226° 9′), Adelaide (34° 57′ S., 138° 23′ E. ; 44° 9′ S., 212° 5′), Hobart (42° 52′ S., 147° 20′ E. ; 51° 7′ S., 224° 6′), and Macquarie Island (54° 30′ S., 158° 57′ E. ; 61° 1′ S., 243° 1′).

II. EXPERIMENTAL DETAILS

(*a*) *Recording*

Whistlers are easily observed using a short vertical aerial, or a loop aerial, and an audio-amplifier of sufficient gain. This equipment, together with a magnetic tape recorder and timing device, constituted the basic recording apparatus (Fig. 1 (*a*)). A preamplifier was located at the base of the aerial pole and the signal fed, via coaxial cable, to the upper-track recording amplifier. Seconds pips, derived from a local oscillator triggered by the local timing device (pendulum clock, crystal clock, or chronometer), were recorded on the lower track of the $\frac{1}{4}$ in. wide magnetic tape. Recordings were made automatically from 35 to 37 minutes past each hour Universal Time (hereafter referred to as a schedule) in accordance with I.G.Y. recommendations. The local clock was compared each day with standard radio time signals.

At Brisbane, Adelaide, and Hobart a square loop aerial consisting of 12 turns of 5 m side with one corner 10 m above the ground was used. A preamplifier (Fig. 1 (*b*)) of voltage amplification 18×10^3 (±3 dB, 400 c/s to 15 kc/s) was used with filtering to minimize power mains interference and interference from V.L.F. and broadcast radio stations. Above 15 kc/s the recorder output decreased, partly because of the notch filter at 16·6 kc/s (V.L.F. station) and partly because of the fall in tape response, but a useful output was obtained to 20 kc/s. The double diode limiter (set at 1·5 V) served to clip atmospherics with a field strength of greater than about 4 mV/m. The preamplifier was calibrated by feeding a small signal in series with the loop from a very low impedance generator. Tape-recording amplifiers were of a standard pattern.

The equipment used at Macquarie Island in 1957 and early 1958 (until February 24) used a 10 m vertical aerial and a similar preamplifier to that used above but of somewhat lower gain. This equipment is estimated to have had an overall gain of one-half to one-third of those used at the other stations. It is hereafter referred to as the B-recorder. After February 24, 1958, equipment kindly lent by Dr. R. A. Helliwell of Stanford University was used. This equipment (hereafter referred to as the A-recorder) is described in ASTIA Document No. AD 110184 (Stanford University).

(*b*) *Playback and Analysis*

Tapes were played back through an amplifier of standard design. The time of occurrence (to the nearest second) of whistlers was noted as well as an aural estimate of strength on a 1–5 scale. The ear appears to be the most sensitive detector of whistlers, but the weakest whistler which can be heard varies from observer to observer and also depends on the frequency range and the dispersion of the whistler as well as the diffuseness (see Part II (Crouchley and Finn 1961)). Weak whistlers of limited frequency range, high dispersion, and large diffuseness are difficult to detect. In practice the level of observability is usually determined by the amount of noise due to high harmonics of the power mains frequency and naturally occurring noise from lightning discharges. It was not, in general, possible to distinguish between long and short whistlers by ear, owing to the large number of crash type atmospherics recorded and also to the variation in frequency range of whistlers. Without a clear-cut initiating atmospheric it is easy to confuse a short whistler, of extended frequency range, with a long whistler of more limited frequency range, but lasting about the same time. It is estimated that a signal of electric field strength about 15 μV/m would be the limit of detectability in the absence of external noise.

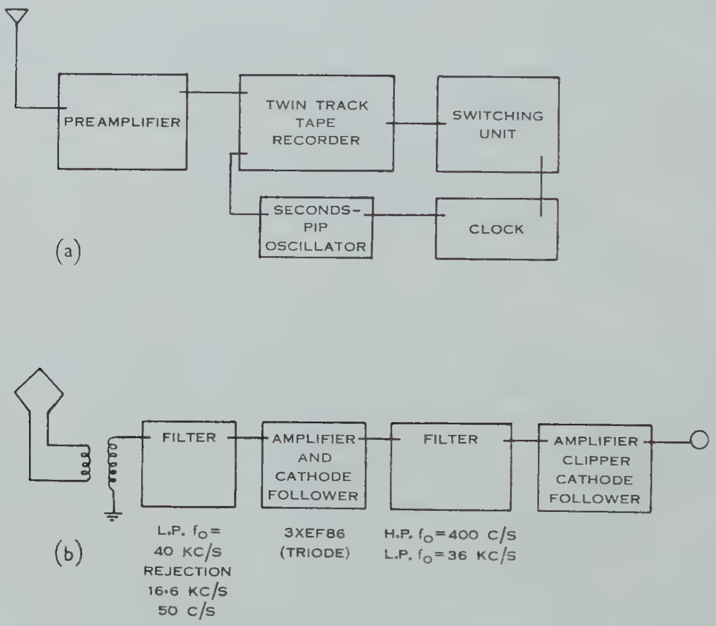
PREAMPLIFIER
TWIN TRACK TAPE RECORDER
SWITCHING UNIT
SECONDS-PIP OSCILLATOR
CLOCK
(a)
FILTER
AMPLIFIER AND CATHODE FOLLOWER
FILTER
AMPLIFIER CLIPPER CATHODE FOLLOWER
(b)
L.P. f_0= 40 KC/S REJECTION 16·6 KC/S 50 C/S
3XEF86 (TRIODE)
H.P. f_0=400 C/S L.P. f_0=36 KC/S

Fig. 1.—Apparatus for recording whistlers.

The output from the replay-amplifier was also fed to 18 tuned circuits the outputs of which were displayed on 1 in. cathode-ray tubes arranged along a straight line. The deflections of the spots of the cathode-ray tubes were photographed on slowly moving film. In this way it was possible to measure the dispersions of about one-quarter of the whistlers which could be heard. The information concerning relative abundances of short and long whistlers was obtained from these films.

III. Variations in the Number of Whistlers Observed

(*a*) *Seasonal Variation*

The four Australian stations showed a maximum whistler activity from a few weeks before the winter solstice (southern hemisphere) to a few weeks after the spring equinox, in contrast to two northern hemisphere stations of similar longitude (Toyokawa, geographic 34° 50′ N., 137° 22′ E.; geomagnetic 24° 30′ N., 203° 30′; Wakkanai, 45° 22′ N., 141° 41′ E.; 35° 20′ N., 206° 0′) for which data have been published (Fig. 2). These two stations showed a maximum of activity between winter solstice (northern hemisphere) and spring equinox. The size of this peak is clearly less in 1958 than in 1957 for Brisbane and Hobart, almost certainly so for Macquarie Island (A-recorder more sensitive than B-recorder) but the absence of recordings in July and August 1957 makes a comparison uncertain for Adelaide. Likewise the two northern hemisphere stations showed a decrease in 1958 as compared with 1957, for the period of peak activity in the southern hemisphere.

A lesser peak is apparent between summer solstice and autumnal equinox at Brisbane and Adelaide, while at Hobart it assumes an importance comparable with that of the winter peak. Macquarie Island shows no comparable increase in activity at the beginning of 1958, but December 1958 and January 1959 were months of high activity and thus this station may also have, on the average, a similar seasonal variation.

No seasonal variation in the occurrence of long whistlers was apparent at Brisbane, but only a small number was recorded. At Adelaide and Hobart long whistlers were more common in summer and at the end of winter than during the winter peak of activity. During the winter peak the number of short whistlers increased and the number of long whistlers decreased thus causing the ratio of the number of long whistlers to the number of short whistlers to fall by a factor of about four times.

(*b*) *Variation of the Number of Whistlers Observed with Geomagnetic Latitude*

As is suggested by the graphs of Section III (*a*), whistlers occur much more frequently at stations at middle geomagnetic latitudes than at the lower or higher latitude stations. This point is illustrated by Figure 3, which is a plot (full lines, dots) of the average number of whistlers per schedule (over a year) against geomagnetic latitude. For all the stations, except Adelaide, the averaging period was from the beginning of July 1957 to the end of June 1958. In the case of Adelaide the period selected was from October 1957 to September 1958, as records were not available for July and August 1957. If the 1958 months of peak occurrence were less active in 1958 than in 1957 at Adelaide, as at the other

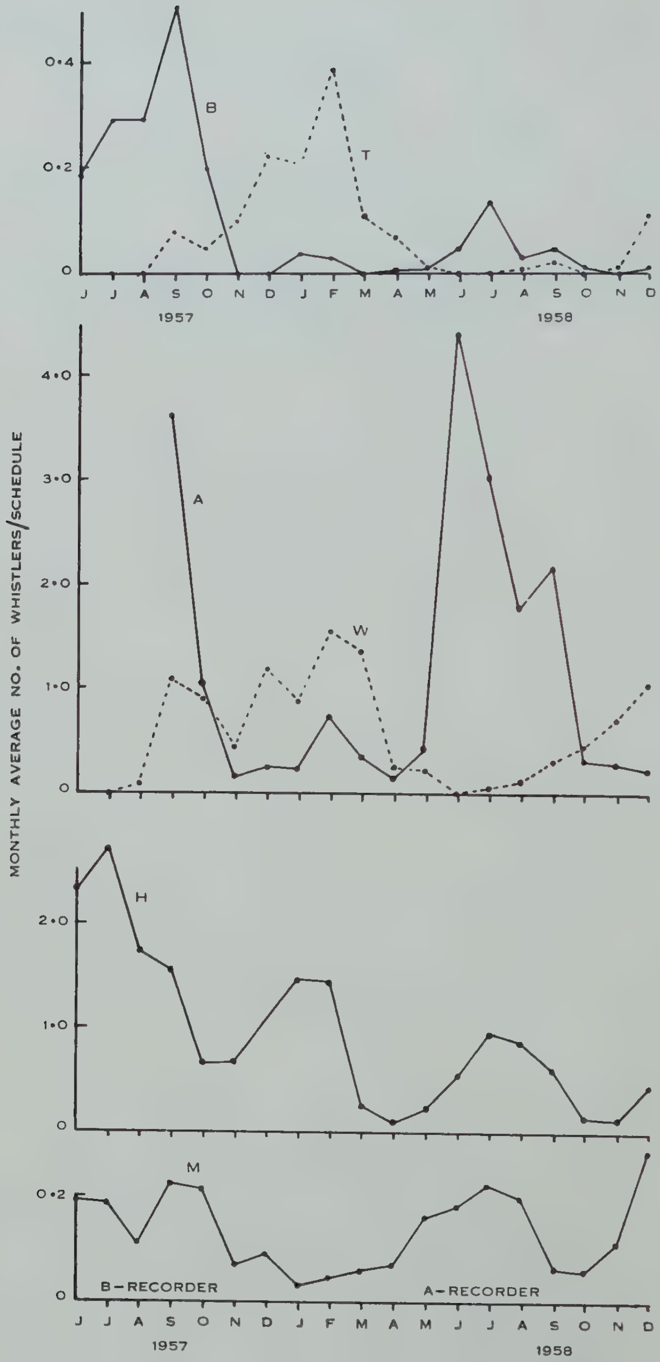

Fig. 2.—Seasonal variation of whistler occurrence. A, Adelaide; B, Brisbane; H, Hobart; M, Macquarie Island; T, Toyokawa; W, Wakkanai.

stations, then the value plotted for this station is somewhat low in comparison to the values plotted for the other stations. Included in the diagram are also values for the two Japanese stations, Toyokawa and Wakkanai (July 1957 to June 1958), for Godhavn (Ungstrup 1959) and the zero value reported by Koster and Storey (1955) for geomagnetic latitude 10°.

The discrepancy between the Brisbane and Wakkanai values is reduced by plotting against magnetic (dip) latitude rather than geomagnetic latitude (dashed line, crosses). However, subsequent work makes it appear likely that the reported values for Brisbane were unduly lowered by man-made interference.

The percentages of strong whistlers (i.e. strengths greater than 2) for the year were 3·2, 4·8, and 5·8% respectively for Brisbane, Adelaide, and Hobart. The means of the corresponding monthly percentages were 2·5, 4·0, and 6·3%, and the difference between the Hobart and Brisbane mean values was 2·3 times their combined standard error. The differences between the other pairs of means were in each case less than twice the appropriate standard error; thus only the Brisbane-Hobart difference may be considered significant at the 5% level.

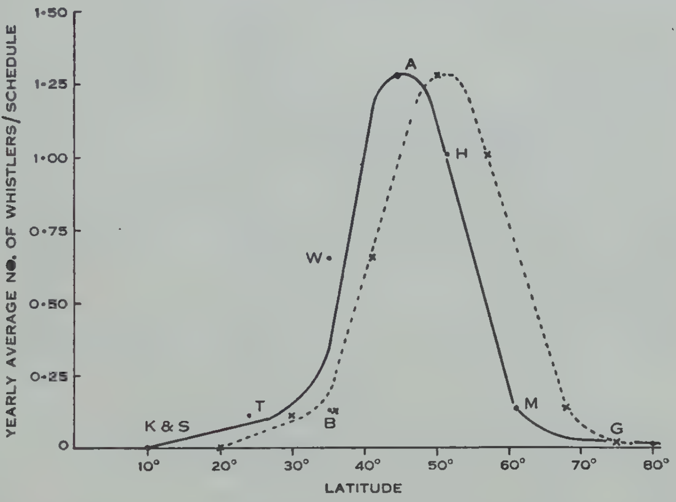

Fig. 3.—Variation in whistler occurrence with latitude. ●—— Geomagnetic; ×--- Magnetic; G, Godhavn; K & S, Koster and Storey; other abbreviations as in Figure 2.

The percentages of long whistlers were as follows: Brisbane 4%, Adelaide 12%, Hobart 36%, and Macquarie Island 40%, although the two extreme values are of lower significance than the two middle ones, due to the smallness of the samples from these two stations. Similar percentages for Toyokawa and Wakkanai are 1 and 2% respectively. The proportion of long whistlers thus seems to increase as the latitude increases and not to have a maximum at the same latitude as the maximum of whistler occurrence.

(c) *Diurnal Variation*

The average number of whistlers per schedule (over one year, as for latitude variation) against local mean time of recording is plotted in Figure 4 (*a*), and Figure 4 (*b*) shows a similar plot for the data, divided into three groups for months around the time of maximum activity, the summer submaximum, and the intermediate months. These three groups have been designated "winter-peak" (June, July, August, September), "summer-peak" (January, February, March), and "intermediate-months" (October, November, December, April, May).

Each station shows a minimum of whistler occurrence during daylight hours, and, for the winter peak, a decrease in the width of the minimum with increase in latitude. This minimum is also wider in summer than in winter. The incidence of whistlers increases to a maximum value during the evening or night hours.

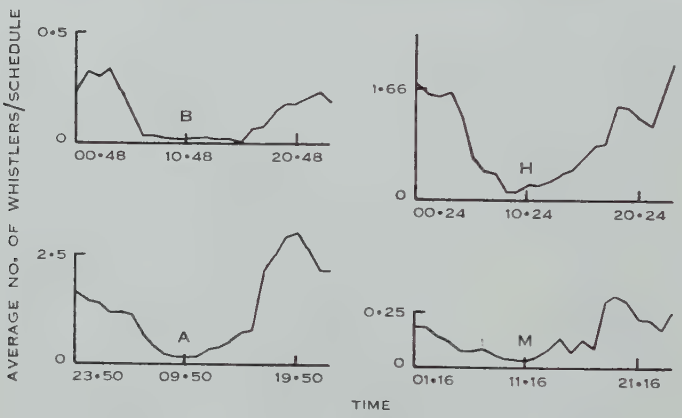

Fig. 4 (*a*).—Diurnal variation of whistler occurrence (yearly average).

At Brisbane this maximum occurs around 0200, at Adelaide around 1900, while at Hobart activity is high from late afternoon to about midnight for the winter months and is maximum two or three hours after midnight for the summer peak. Macquarie Island, which is less consistent than the other stations in behaviour from month to month, shows, on the average, a maximum of activity in the late afternoon.

At Adelaide long whistlers were very seldom observed during the day-time, although some of the short whistlers were observed during daylight hours. During the night the ratio of long to short whistlers varied somewhat erratically from schedule to schedule. At Hobart long whistlers were absent during the morning but they appeared about midday, and the ratio of long to short whistlers was somewhat higher during the night than in the afternoon, although, as for Adelaide, it varied somewhat erratically from schedule to schedule.

(d) *Day-to-Day Variation*

The total number of whistlers observed in a day (taken from midday to midday, Eastern Standard Time, in order not to assign one evening to two separate days) varied from zero up to, on a few occasions, 10 or 15 times the yearly-average for a day. Figure 5 shows a sample plot over one month for September 1959 at Brisbane.

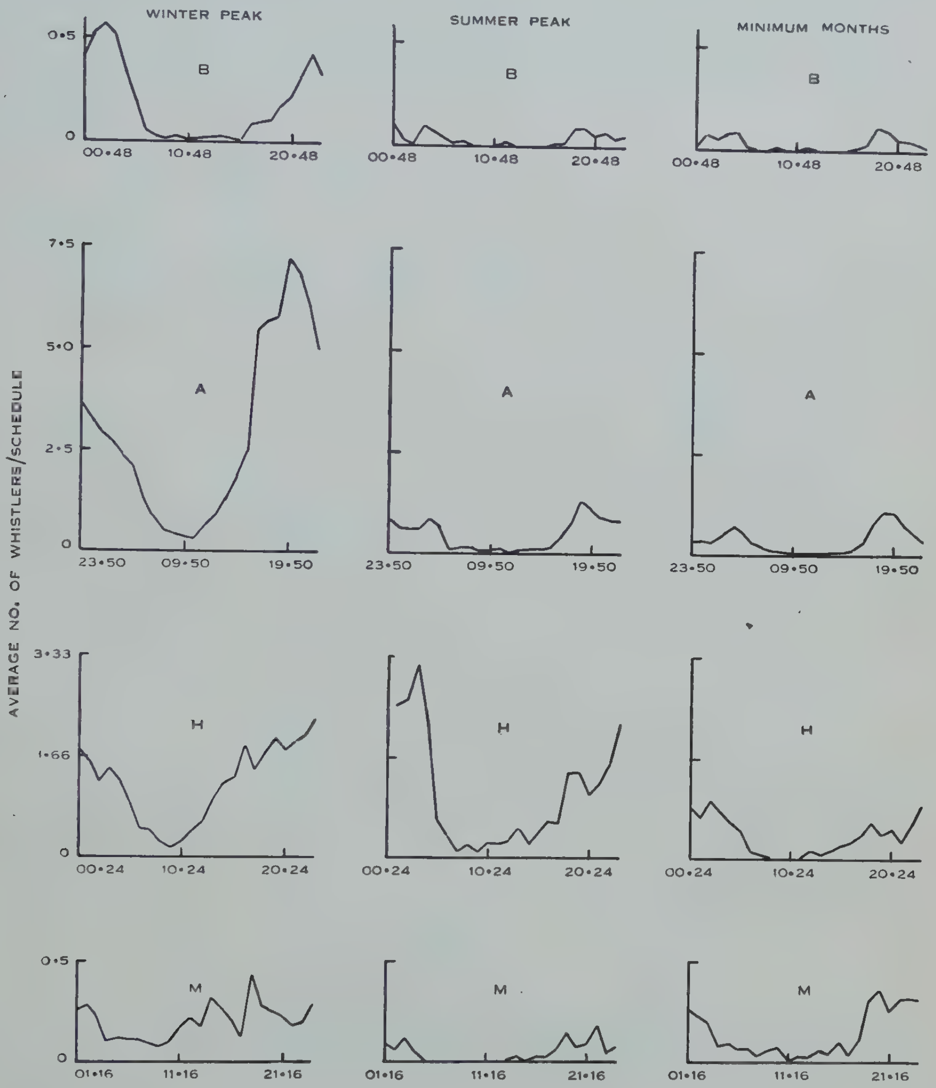

Fig. 4 (*b*).—Diurnal variation for groups of months.

IV. Correlation Analysis of Daily Total Whistler Occurrences

Approximately five months of records about the winter peak of activity in 1958 were selected for a correlation analysis. This subgroup was taken to give a reasonable size of sample and also to minimize any effect of seasonal variation.

(*a*) *Autocorrelation Analysis*

Autocorrelation coefficients for lags up to 65 days were calculated on daily totals for Brisbane, Adelaide, Hobart, and Macquarie Island and also on Adelaide day-whistlers, Adelaide night-whistlers, Adelaide weak-whistlers (strengths 1 and 2), Adelaide strong-whistlers (strengths 3, 4, and 5), Hobart daily totals, and Hobart night-whistlers (as week-end day-time recordings were not made at this station), and Macquarie Island daily totals. Figure 6 is a plot of the correlation coefficient against the number of days' lag for Brisbane daily totals,

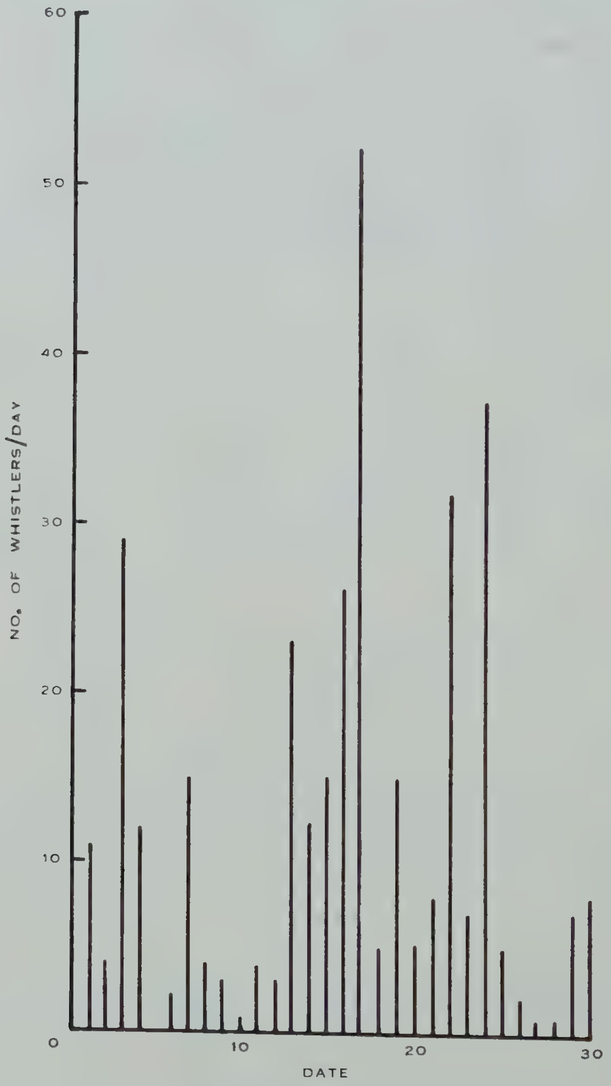

Fig. 5.—Day-to-day variation in whistler occurrence. (Brisbane, September 1957.)

Adelaide day-time values, Adelaide night-time values, Hobart daily totals, and Macquarie Island daily totals.

Both Brisbane daily totals (which because of the diurnal variation essentially represent night-time values) and Adelaide day-time values show evidence of a 17-day recurrence tendency with, for Brisbane, a possible period of about half this value. The Adelaide night-time values show a marked positive region from 26 to 29 days and this is repeated again from 55 to 58 days suggesting a recurrence period of about 27–28 days. This pattern is also apparent, but to a lesser extent, in the correlogram of Adelaide total values, Adelaide weak-whistlers, and Adelaide strong-whistlers. Hobart exhibits positive peaks at 9 days and 15 days, but these are not repeated at multiples of these values and a considerable degree of randomness is apparent over the rest of the plot. Macquarie Island shows clear-cut positive peaks at 9, 15, 54, and 63 days while several of the lesser peaks show a separation of 9 or 15 days.

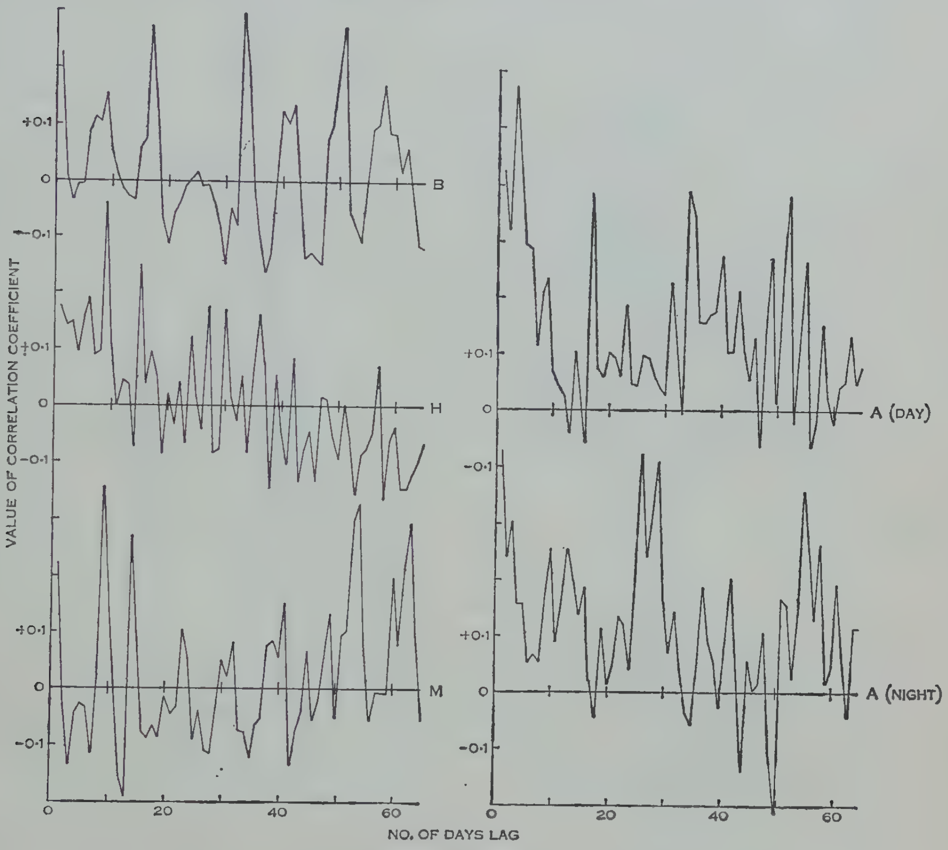

Fig. 6.—Autocorrelograms of daily totals.

Serial correlation is apparent for the first 5 days in Adelaide suggesting that at this station whistlers tend to occur or be absent for a few days at a time, but for the other stations there is little association, even over 2 days.

While it is difficult to assess the significance of individual values of the correlation coefficient in these circumstances, because of the number of coefficients calculated and of the serial correlation present in the data, the number of values used in the individual calculations (varying from 115 to 50 for Macquarie Island and 150 to 70 for the other stations) was such that the larger values would have been considered significant at the 1% confidence level if treated as isolated values.

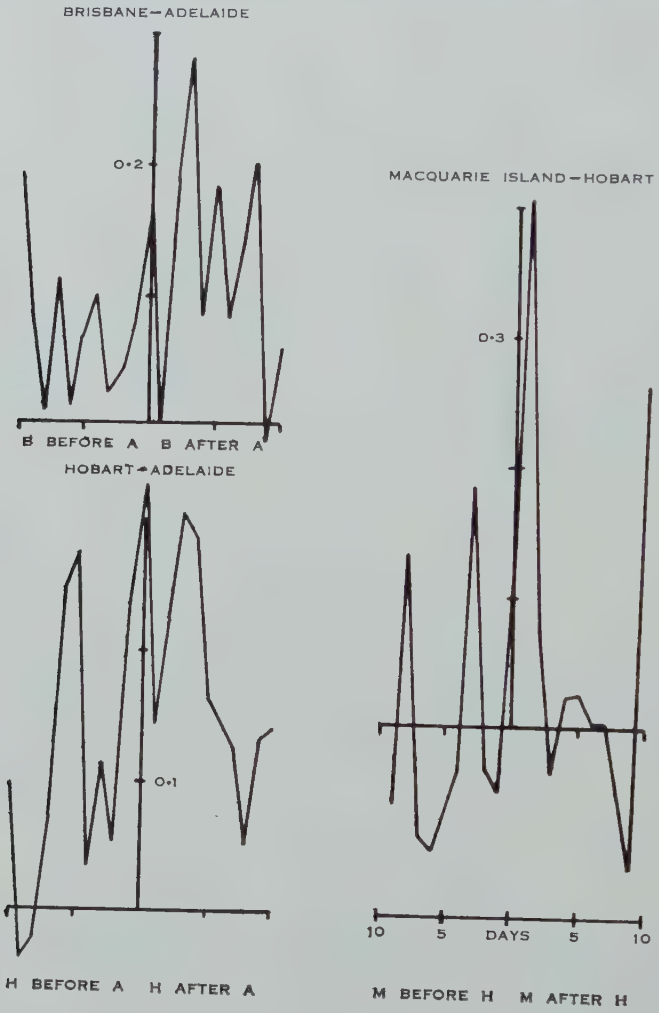

Fig. 7.—Cross-correlograms between stations.

(*b*) *Inter-station Correlation*

Figure 7 shows lag cross-correlograms with delays of up to plus and minus 10 days between the nearest pairs of stations. There are indications of activity (or lack of activity) in Adelaide being followed by a similar occurrence rate in Brisbane 2 or 3 days later, of Adelaide and Hobart occurrence rates moving in a

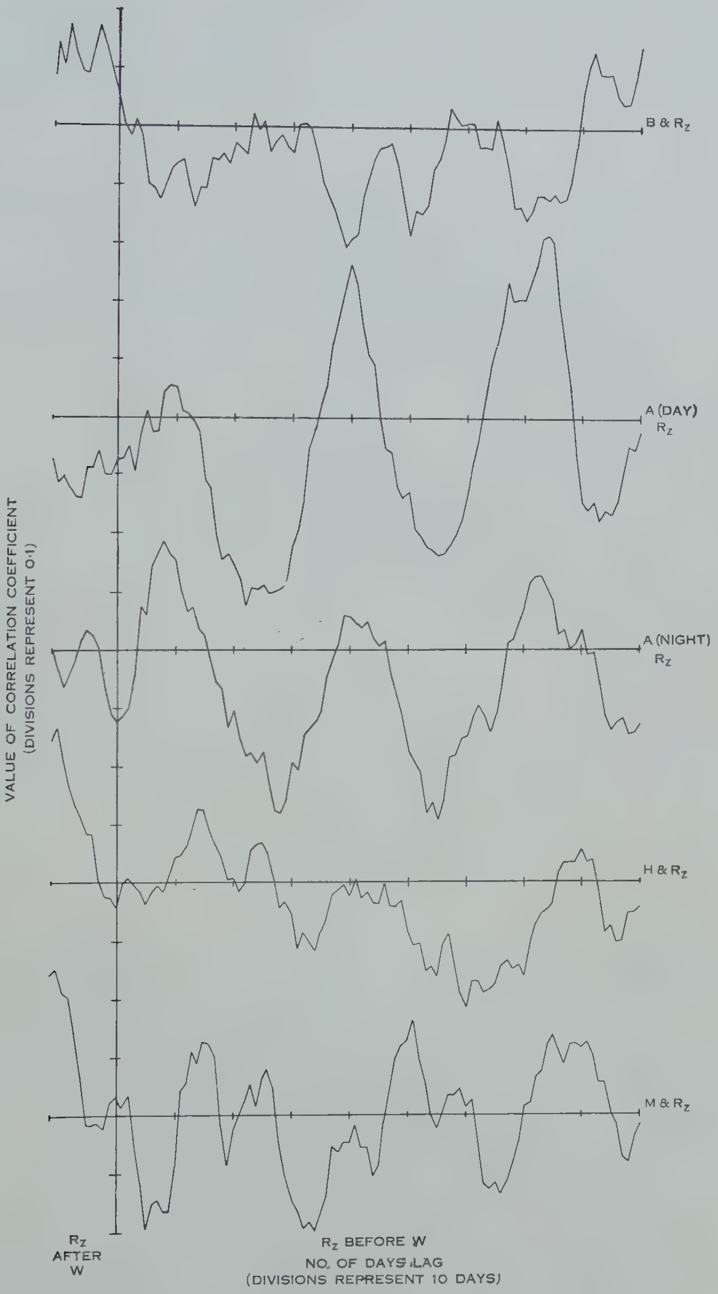

Fig. 8.—Cross-correlograms between whistler daily totals and sunspot number (R_z).

similar fashion on the same day and also of Hobart exhibiting a similar change to Adelaide 3 days after Adelaide. The largest value of correlation coefficient is observed between Hobart values and Macquarie Island values 1 day later and the effect of the 9-day recurrence tendency in the values from these stations, as demonstrated by the autocorrelograms, is apparent in the cross-correlograms.

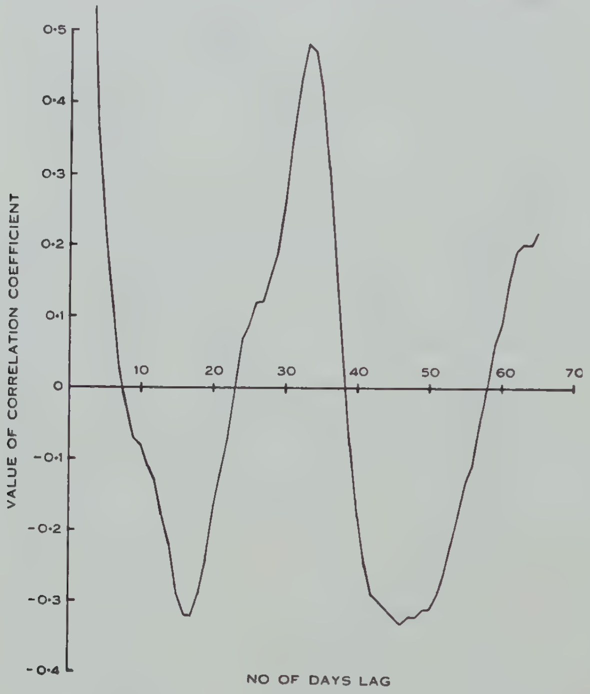

Fig. 9.—Autocorrelogram of R_z.

V. Cross-correlation between Whistler Daily Totals and Sunspot Number

The daily total values, as used for the calculation of the autocorrelograms of Section IV (*a*) were used for the calculations of correlation coefficients with Zurich Provisional Relative Sunspot Numbers (R_z) from R_z 90 days before whistler daily totals to R_z 10 days lagging on the whistler data. The cross-correlograms are shown in Figure 8, while Figure 9 shows the autocorrelograms of R_z over approximately the same period. The cross-correlogram for the Adelaide day-time values and, to a lesser extent, that for the Adelaide night-time values are similar to the autocorrelogram of R_z and suggest a possible association between whistler occurrences at this station and sunspot number. A time difference of the order of 10 days (or 10 plus a multiple of approximately 30 days) is apparent between the two variables. There is little indication of any association between whistler activity and sunspot number at the other stations.

VI. Association between Whistler Occurrence and Magnetic K-index

The lag cross-correlograms between daily whistlers totals and the daily magnetic K-index sum (SK_p) have been calculated from SK_p 60 days before to 60 days after the whistler data (Fig. 10). For zero lag Brisbane shows a significant positive correlation, Adelaide a small positive correlation, Hobart a somewhat larger positive correlation, and Macquarie Island a negative correlation. Larger values of correlation coefficient are observed with other delays but there is no

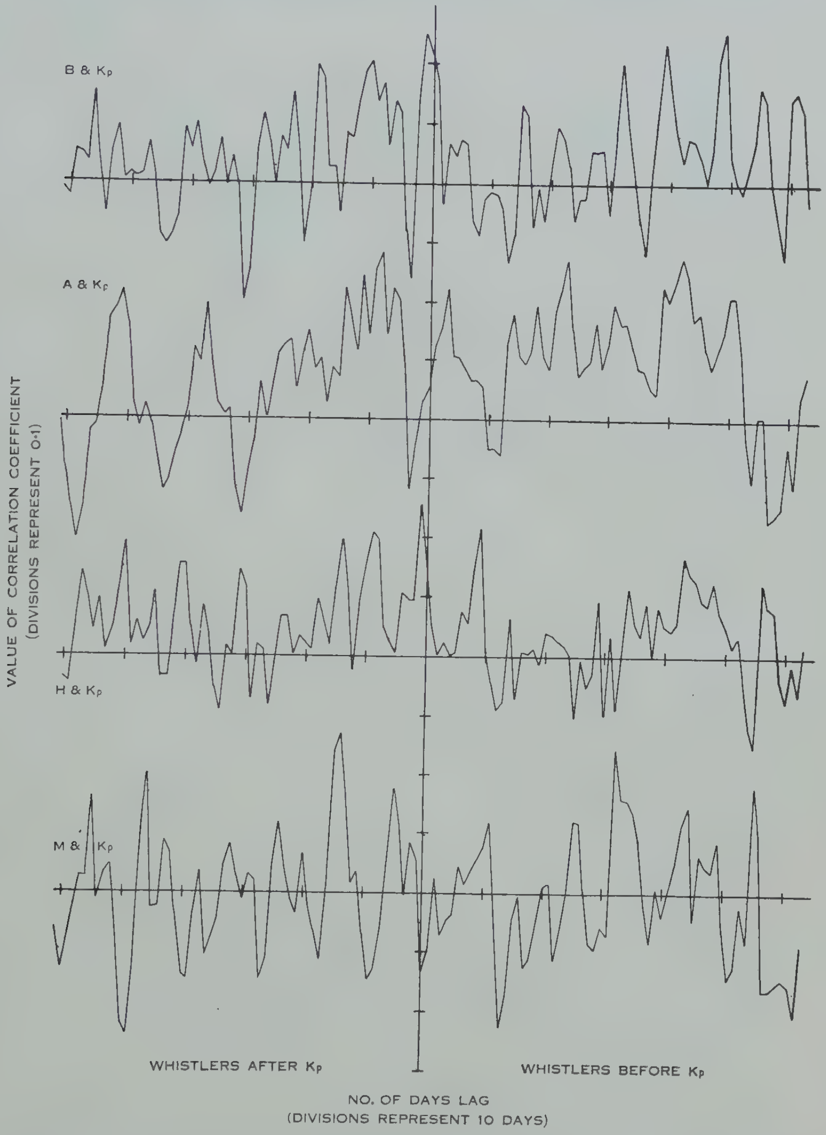

Fig. 10.—Cross-correlograms between whistler daily totals and daily sums of K_p.

systematic behaviour either between stations or for any one station. Thus there is no well-defined association between whistler occurrence and the magnetic K-index daily sums. Similar lag cross-correlograms were calculated using the K-values for Toolangi (the nearest magnetic observatory to Adelaide and Hobart) and the K-values for Macquarie Island. These cross-correlograms were very similar to those reproduced.

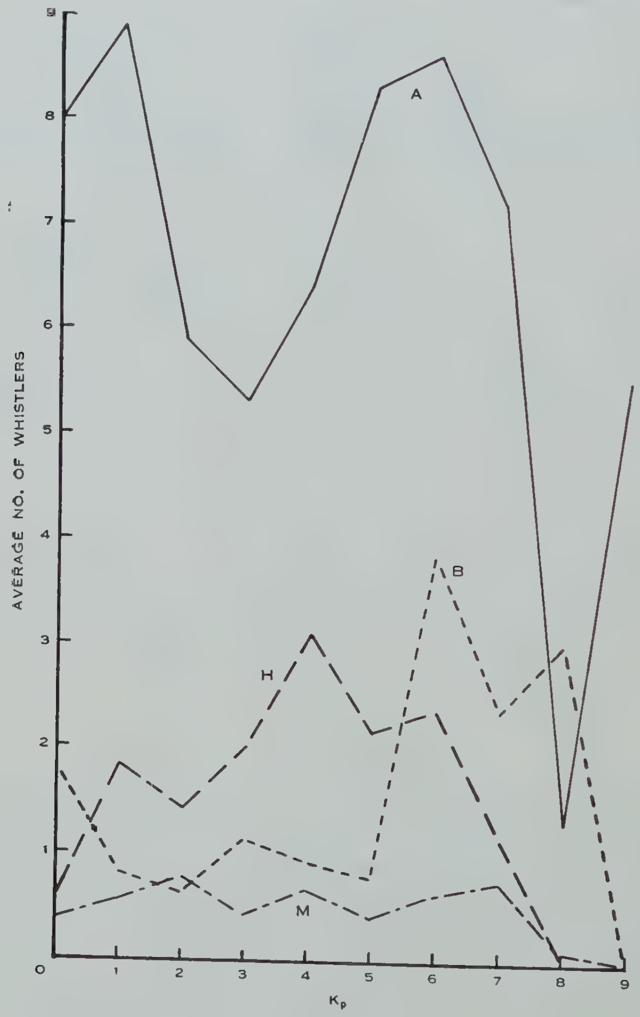

Fig. 11.—Association between K_p and average number of whistlers for each value of K_p.

A plot of the average number of whistlers observed in a 3-hr period (as used for determining the values of K_p) against the value of K_p for approximately 5 months of data is shown in Figure 11. There is a suggestion that whistlers occur more frequently for low values of K_p at high latitudes and for high values of K_p at low latitudes, but the large whistler occurrence for low value of K_p

reported for Adelaide and the relative infrequency of high values of K_p make the result inconclusive. Such a result would be in agreement with the values of correlation coefficient for zero lag reported above.

VII. Discussion

The number of whistlers observed at any station must depend on several factors, namely, the number of suitably-placed sources, the absorption in the lower ionosphere at both ends of the path, and the conditions along the path in the upper ionosphere. As individual whistlers can often be heard at stations separated by distances of the order of 1000 km and studies of diffuseness (Part II of this series) (Crouchley and Finn 1961) suggest that the actual whistler channel has a smaller cross-sectional dimension than this, then propagation conditions between the ionosphere and ground (wave-guide type propagation) or over the surface of the Earth may also be of importance.

No detailed information of thunderstorm activity is available for the conjugate points of the Australian recording stations. Even if this were available the problem is complicated by the general lack of continuous detailed correlation between lightning flashes and whistlers. Kimpara (1955) has published maps showing the distribution of sources of atmospherics in the region of the conjugate points of the Australian stations for September 1953, February 1954, and March 1954. The overall impression conveyed by these maps is that lightning is more common around the conjugate point of Brisbane than around those of Adelaide and Hobart and (as in most other locations) it is more common during the day than the night. The same author (1959) has also given values of a " thunderstorm index " for 1000 km around Wakkanai (which is of the order of 1200 km from the Adelaide conjugate point). This index shows large values for summer months (northern hemisphere) and small values for winter months. Australian meteorologists (Bath, personal communication 1959) observe a general maximum of thunderstorms in summer with submaximum late in winter. The seasonal variations of whistlers reported are thus in general agreement with the meteorological data, the large peak in whistler occurrence being due to summer thunderstorms in the opposite hemisphere producing short whistlers and the lesser peak being in part due to local summer storms in the observer's hemisphere, giving long whistlers.

The diurnal variation in whistler activity is, however, apparently at variance with the meteorological data, and one must postulate, as has been done by other workers (Helliwell and Morgan 1959), that absorption in the lower ionosphere is a significant factor in reducing the number of whistlers observed during daylight hours. If this were the only effect involved, one might expect the daylight part of the curve to be symmetrical about midday, whereas the observations indicate higher afternoon than morning values. It seems likely that this is due to the usual rise in lightning activity after midday.

The peak of whistler occurrence around geomagnetic latitude 45° is a somewhat surprising result, as is the rapid decrease in occurrence towards the equator, for the path length decreases for lower latitudes and thunderstorm activity increases. A decrease in occurrence at high latitudes is to be expected on account of the scarcity of sources and the extreme length and height of the path. While absorption in the lower ionosphere and interference from atmospherics increase at lower latitudes, it seems unlikely that these factors are adequate to explain the observed decrease. Accordingly, it is suggested that propagation conditions along the higher parts of the path are more favourable at mid latitudes than at low latitudes. The relatively large number of echoes and trains observed at middle to higher latitudes and the scarcity of even two-hop whistlers at low latitudes also substantiate this suggestion. The increase in the proportion of long whistlers at Hobart compared to Adelaide together with the decrease in thunderstorm activity with increasing latitude suggests that the most favourable conditions for whistler propagation may be at a somewhat higher latitude than that indicated by the overall occurrence figures. A line of force passing through the slot between the two Van Allen radiation belts cuts the Earth about this region. The recent work of Smith, Helliwell, and Yabroff (1960) on the guiding of whistlers by ducts explains the relative scarcity of whistlers at low latitudes in terms of the relatively large enhancements of ionization required to produce effective guiding along paths commencing at low latitudes.

The day-to-day variations in observed occurrence rates are almost certainly due in large measure to variations in source activity. However, for Adelaide there is some evidence of an association with sunspot number, particularly during daylight hours. The delay between sunspot number and whistler occurrence makes it unlikely that the effect is one of absorption. In view of the correlation between whistler dispersion and sunspot number with a lag of between one and two months reported by Allcock and Morgan (1958) it seems more likely that the reported effects are due to changes in the main body of the path rather than at the ends.

The other periodicities suggested by the autocorrelograms may be due to the same periodicity of whistler source activity or to a recurrence of favourable propagation conditions. Thus, for example, if solar disturbance produced regions of enhanced electron density on day and night sides of the Earth in the upper Van Allen radiation belt and if these regions rotated from west to east relative to the Earth with a period of 18 days but decayed appreciably in this time, then one would expect the 9-day peaks as observed in the Hobart and Macquarie Island records. The peak in the Hobart-Macquarie Island cross-correlogram for Macquarie Island data one day after Hobart data and the difference in longitude (Macquarie Island approximately 20° E. geomagnetic of Hobart) is consistent with this suggestion. Likewise, Brisbane and Adelaide-day autocorrelograms suggest a 17-day occurrence tendency. Such rotations have been suggested by Gold (1959) but with periods of the order of minutes or hours. A similar analysis of local atmospherics and of whistler data from other stations might assist the interpretation.

VIII. CONCLUSION

It seems likely that the observed variations in frequency of whistler occurrence are predominantly due to variations in the frequency of occurrence of suitable lightning flashes, but there are indications that changes in propagation conditions along the path have a significant influence. A systematic study of " whistler-mode " propagation from a suitably placed, powerful V.L.F. station, i.e. a known source, would enable the latter variations to be studied separately.

The difference between variations in whistler activity and " chorus " activity (Crouchley and Brice 1960) recorded at Australian stations confirms the view that these are separate and distinct phenomena.

IX. ACKNOWLEDGMENTS

The operation of whistler recording stations was undertaken by the University of Queensland as an International Geophysical Year Project and was assisted financially by the Australian National Committee for the I.G.Y. The equipment at Adelaide was housed and operated by courtesy of the Controller of the Weapons Research Establishment, that at Hobart by the Ionospheric Prediction Service, and that at Macquarie Island by the Antarctic Division of the Department of External Affairs. The listening to the playback of the tapes was performed by several operators and the author is indebted to them, particularly Mr. R. Hosking, Mr. N. Brice, and Mr. B. McInnes, and also to Mr. M. Andrews who wrote the SILLIAC program for the calculation of the correlation coefficients. The unfailing interest and assistance of Professor H. C. Webster is gratefully acknowledged.

X. REFERENCES

ALLCOCK, G. McK., and MORGAN, M. G. (1958).—*J. Geophys. Res.* **63**: 573.
CROUCHLEY, J., and BRICE, N. M. (1960).—*Planet. Space Sci.* **2**: 238.
CROUCHLEY, J., and FINN, R. J. (1961).—*Aust. J. Phys.* **14**: 40.
ECKERSLEY, T. L. (1935).—*Nature* **135**: 104.
GOLD, T. (1959).—*Nature* **183**: 355.
HELLIWELL, R. A., JEAN, A. G., and TAYLOR, W. L. (1958).—*Proc. Inst. Radio Engrs., N.Y.* **46**: 1760.
HELLIWELL, R. A., and MORGAN, M. G. (1959).—*Proc. Inst. Radio Engrs., N.Y.* **47**: 200.
KIMPARA, A. (1955).—*Proc. Res. Inst. Atmos. Nagoya Univ.* **3**: 1.
KIMPARA, A. (1959).—*Proc. Res. Inst. Atmos. Nagoya Univ.* **6**: 38.
KOSTER, O., and STOREY, L. R. O. (1955).—*Nature* **175**: 37.
MORGAN, M. G. (1958).—*Nature* **182**: 332.
MORGAN, M. G., and ALLCOCK, G. McK. (1956).—*Nature* **177**: 30.
SMITH, R. L., HELLIWELL, R. A., and YABROFF, I. W. (1960).—*J. Geophys. Res.* **65**: 815.
STOREY, L. R. O. (1953).—*Phil. Trans.* **246**: 113.
UNGSTRUP, E. (1959).—*Nature* **184**: 807.

A STUDY OF WHISTLING ATMOSPHERICS

II. DIFFUSENESS

By J. Crouchley* and R. J. Finn*

[*Manuscript received October* 3, 1960]

Summary

The diffuseness or spread, in time, of whistlers observed at four Australian stations is discussed. It is found to be approximately twice as large for long as for short whistlers, to be independent of season and time of day, and to be linearly related to geomagnetic latitude and whistler dispersion. The diffuseness may be accounted for by assuming that the energy travels over a range of paths in the exosphere, and estimates of this range are made (i) assuming a smooth variation of dispersion with latitude and (ii) assuming a duct-type of guiding.

I. Introduction

When one listens to whistlers replayed from magnetic tape records some sound like pure descending tones while others are much less pure or more " swishy " in character. In this paper the former are referred to as sharp whistlers and the latter as diffuse whistlers. The " diffuseness " of a whistler is herein described by the time duration of the component frequencies (rather than by the frequency band). Thus whistlers in which any particular frequency lasts more than 0·1 s sound, and are termed, " diffuse " while the remainder are classified as " sharp ". This paper discusses the diffuseness of those whistlers (discussed in Part I, Occurrence (Crouchley 1961)) which were suitable for analysis by spot-frequency tuned circuits.

II. Experimental Details

The signals, replayed from the magnetic tape (Part I), were fed to 18 parallel-tuned L-C circuits whose mid frequencies lay in the range 1·10–20·0 kc/s. The voltage outputs of these filter circuits were displayed on 18 one-inch cathode-ray tubes, equally spaced along a straight line, which were photographed with an optical reduction of 150 to 1 on film moving at 45 cm/min.

As most whistlers closely followed the frequency-time relationship $t=Df^{-\frac{1}{2}}$ (Eckersley 1935, Storey 1953 ; " D " the dispersion) over the frequency range of the analyser, it was convenient to arrange the frequencies of the individual channels in such a fashion that they responded in succession to the whistler and that the response of each channel was separated from that of the next by an equal time interval, which depended on the value of D. This may be achieved by choosing the centre frequencies of the channels so that they are equally spaced in $f^{-\frac{1}{2}}$ instead of in f. In practice, this leads to a crowding of channels at the lower frequencies and accordingly in this instrument the frequency range was covered by two sets of filters, the first containing 8 channels and covering from 20·0 to 7·10 kc/s and the second containing 11 channels and covering from 7·10 to 1·10 kc/s. A whistler which covered the whole frequency range would thus ideally appear on the film as a succession of "dots" (lower frequencies later in time) lying on two straight lines of different slope which intersected on the trace produced by the 7·10 kc/s channel. The slopes of the two intersecting straight lines are determined by D (as well as by the channel spacing) and hence a graticule marked with pairs of lines calculated for different values of D may be used to estimate this quantity from the film.

---

* Physics Department, University of Queensland, Brisbane.

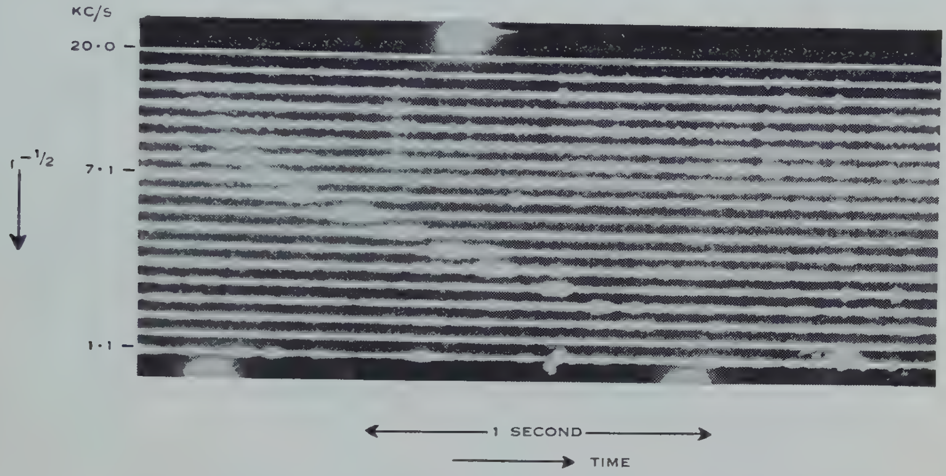

Fig. 1 (*a*).—Analyser record of sharp whistler (Brisbane, single hop).

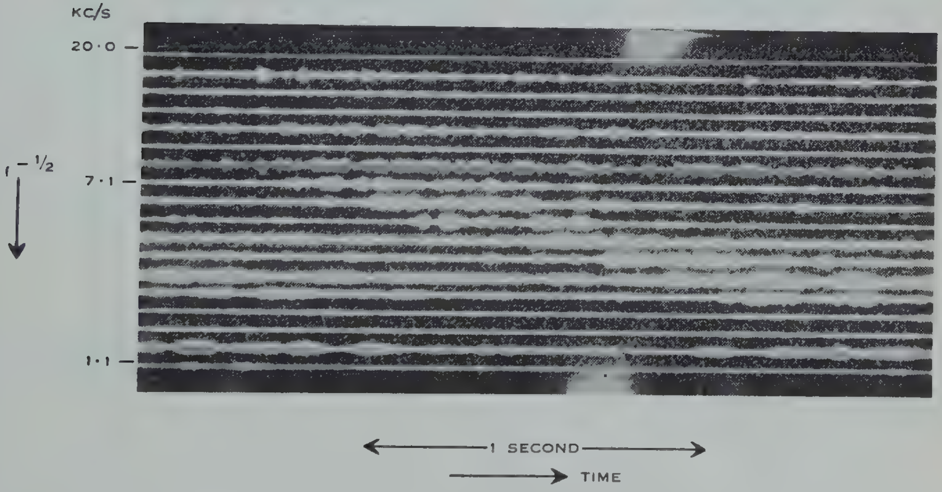

Fig. 1 (*b*).—Analyser record of diffuse whistler (Hobart, double hop).

In practice a set of 18 parallel lines was traced on the film with zero-signal input to the analyser and the response of any channel was indicated by the line corresponding to that channel being broadened. Thus an atmospheric gave rise to set of marks lying on a line at right angles to the traces and a whistler caused a set of marks lying on the pair of lines corresponding to its dispersion. A reproduction of a typical sharp whistler (Brisbane) is shown in Figure 1 (*a*) and a typical diffuse whistler (Hobart) is shown in Figure 1 (*b*).

The response of an L-C filter to a gliding tone (Storey and Grierson 1958) consists of an oscillation bounded by a relatively slowly varying envelope whose shape depends only on a single parameter k which involves the band width of the filter and the rate of change of frequency of the gliding tone. The values of k were calculated for the filters used and a whistler of dispersion of 60 $s^{\frac{1}{2}}$ and hence the times between the two " 6-dB " points for channels 4, 8, and 12 were estimated as 6, 9, and 12 ms respectively. These times, which are small compared with the durations of the observed responses on these channels and which increase only as $D^{\frac{1}{2}}$, were ignored. In practice, the bandwidths of the filters were adjusted to give approximately the best signal-to-noise ratio for whistlers of average dispersion for the station being analysed.

The following details were read from the films for each whistler:

(i) the time of occurrence of 7·10 kc/s (channel 8) to the nearest 0·05 s,

(ii) the dispersion D (accuracy about $\pm 10\ s^{\frac{1}{2}}$),

(iii) the duration (to the nearest 0·05 s) of the response on channel 4 (11·98 kc/s), channel 8 (7·10 kc/s), channel 12 (2·78 kc/s), and channel 16 (1·43 kc/s), or of such of those as showed a response,

(iv) the maximum and minimum frequencies present in the whistler.

The *diffuseness* (F) of a whistler is now defined as the average duration, in units of 0·05 s, on channels 4, 8, 12, and 16, or of such of these as responded; thus a whistler present on channels 4, 8, and 12 lasting 0·1 s, on each of these would be assigned a diffuseness of two. The F-value divided by the number of traverses of the whistler path is called the *reduced diffuseness* and denoted by F_1. A further parameter, $F'=1000F/D$, called the *diffuseness-dispersion ratio*, is also introduced.

III. Experimental Results

(*a*) *Comparison of Diffuseness of Short and Long Whistlers*

The mean values of F for the four stations, together with the standard errors of the mean (S) and the number of whistlers used (n), is shown in Table 1 for the both short ($\overline{F}_s$) and long ($\overline{F}_L$) whistlers.

The value of $\overline{F}$ for long whistlers is approximately twice that for short whistlers except for Brisbane where long whistlers are rare events. The assumption that $\overline{F}_L$ is twice $\overline{F}_s$ was tested by using the test due to Welch and Aspin (Bennett and Franklin 1954). A larger difference (i.e. $2\overline{F}_s-\overline{F}_L$) than that actually observed has probabilities of occurrence as follows: Adelaide 7%, Hobart 40%, Macquarie Island 6%. The hypothesis that $\overline{F}_L=2\overline{F}_S-0\cdot 1$ was similarly tested and gave probabilities as follows: Adelaide 25%, Hobart 30%, Macquarie Island 7%. It thus seems likely that the diffuseness for a double traverse of the whistler path is approximately twice that for a single traverse and accordingly the reduced diffuseness F_1 is adopted as a working parameter.

(b) *Occurrence of Diffuseness*

A plot of the number of whistlers with a given value of F_1 against the value of F_1 is shown in Figure 2 for the four stations, making use of data over a year. (The figures for Adelaide are scaled down by a factor of two.) The distributions for Brisbane, Adelaide, and Hobart are all skew with the mode at small values of diffuseness and with spreads up to about five times the modal value. For Macquarie Island a less peaked and more symmetrical distribution is obtained. The curves suggest that the modal value of diffuseness increases as the latitude increases.

TABLE 1

COMPARISON OF SHORT AND LONG WHISTLER DIFFUSENESS

Station	Short Whistlers			Long Whistlers		
	$\overline{F}_s$	S	n	$\overline{F}_L$	S	n
Brisbane . .	1·50	0·06	145	1·29	0·30	7
Adelaide . .	2·20	0·035	1536	4·12	0·14	150
Hobart	2·72	0·10	396	5·75	0·34	111
Macquarie I. . .	3·70	0·26	53	5·80	0·65	36

(c) *Relationship between Diffuseness and Dispersion*

A plot of the average diffuseness of whistlers with a given dispersion, $(\overline{F})_D$ versus the dispersion is shown in Figure 3 for the four stations. The results for Adelaide and Hobart and to a lesser extent those for Macquarie Island (for which fewer whistlers were recorded) suggest, within the limits of experimental error, a proportionality between diffuseness and dispersion. For Brisbane the range of the variables is small, the diffuseness, being small, is more difficult to estimate, and the two outer points of the graph were obtained from only a small number of readings, thus the line is uncertain. This approximate proportionality

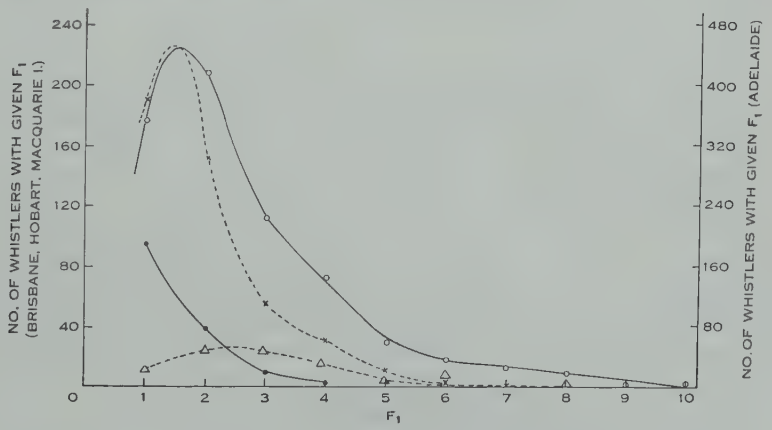

Fig. 2.—The distribution of occurrence of reduced diffusion. ● Brisbane, × Adelaide, ○ Hobart, △ Macquarie Island.

between diffuseness and dispersion and the fact that the dispersion is a property of the path (including the number of traverses) suggests the use of F/D as an alternative parameter to describe the spread of the whistler. For numerical convenience the diffuseness-dispersion ratio is multiplied by 1000 to give F'.

(*d*) *Diurnal and Month-to-month Variations*

The average diurnal variations of F_1 and F' (over one year) are shown in Figures 4 (*a*) and 4 (*b*) for hours at which sufficient whistlers were recorded. There is no evidence of a systematic variation, other than a possible small decrease in F_1 and F' after midnight at Hobart.

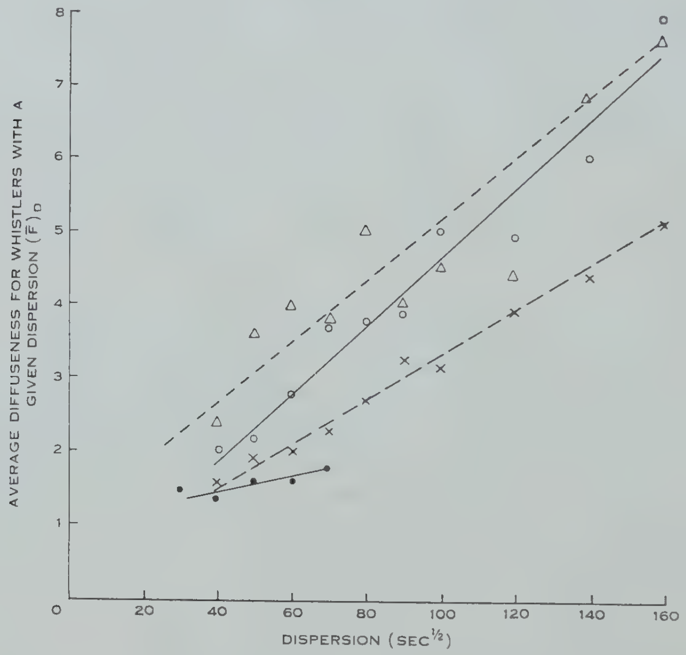

Fig. 3.—The variation of diffuseness with dispersion. ● Brisbane, × Adelaide, ○ Hobart, △ Macquarie Island.

The month-to-month changes in average reduced diffuseness and average diffuseness-dispersion ratio are plotted in Figures 5 (*a*) and 5 (*b*), where, because of the seasonal variations in the occurrence of whistlers (Part I) the points have different weights. There is no evidence for a seasonal variation in F_1 or F'. (A similar plot of diffuseness did show a seasonal variation corresponding to the variations in the relative numbers of long and short whistlers.)

(*e*) *Variation of Reduced Diffuseness and Diffuseness-Dispersion Ratio with Latitude*

Figure 6 shows a plot of mean reduced diffuseness and mean diffuseness-dispersion ratio against geomagnetic latitude. For both quantities the points lie close to a straight line passing through latitude 12°. Also shown are points obtained by using only short whistlers, which points lie close to those obtained using all whistlers except for Macquarie Island (geomagnetic latitude 61 °S.) and even here the departure of the short whistler points from the lines is less than twice the standard error of the mean. The intercept at latitude 12° is

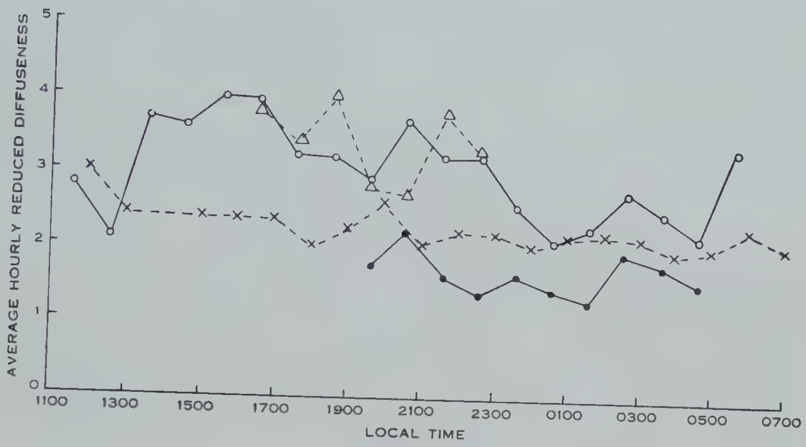

Fig. 4 (*a*).—Diurnal variation of reduced diffusion. ● Brisbane, × Adelaide, ○ Hobart, △ Macquarie Island.

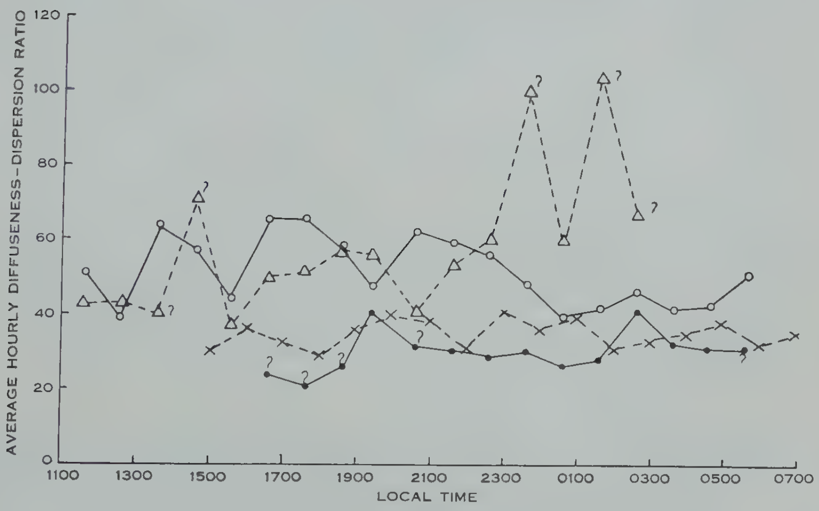

Fig. 4 (*b*).—Diurnal variation of diffuseness-dispersion ratio. ● Brisbane, × Adelaide, ○ Hobart, △ Macquarie Island.

significant as this approximately marks the boundary between lines of force which intercept the ionosphere and those which pass entirely below it.

The variation of F_1 with geomagnetic latitude may be represented approximately by the equation

$$F_1=0\cdot066(\lambda-12),$$

where λ is in degrees.

(*f*) *Dependence of Reduced Diffuseness on the Initiating Discharge*

In seeking a relationship between the duration of the initiating lightning discharge and the diffuseness or diffuseness-dispersion ratio 59 long whistlers recorded at Hobart were studied. The whistlers were classified according to the values of F or F' and the atmospherics as sharp (less than 0·1 s long), broad, or indefinite according to their duration on the film from the analyser. Table 2 (*a*) shows the number of whistlers of given F-values for the three classes of atmospherics and Table 2 (*b*) is a similar classification in terms of F'-values.

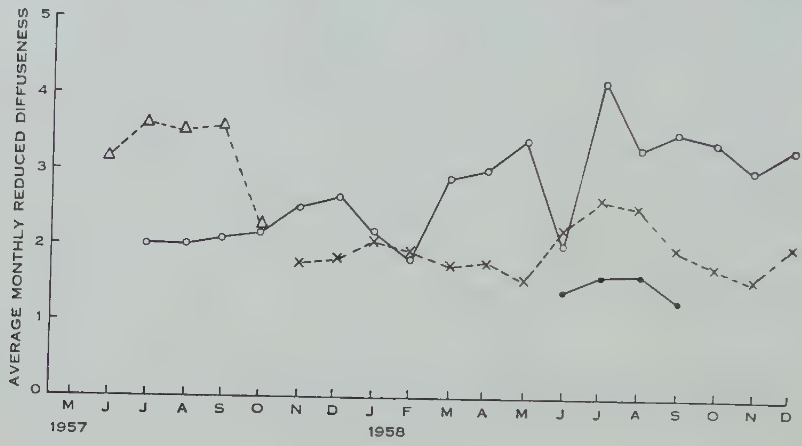

Fig. 5 (*a*).—Month-to-month variation of reduced diffuseness. ● Brisbane, × Adelaide, ○ Hobart, △ Macquarie Island.

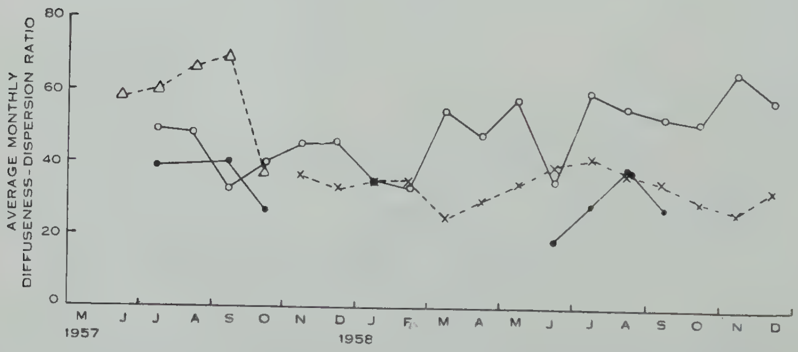

Fig. 5 (*b*).—Month-to-month variation of diffuseness-dispersion ratio. ● Brisbane, × Adelaide, ○ Hobart, △ Macquarie Island.

The assumption that the distribution of values so obtained is independent of the classification of the atmospherics was examined by means of the chi-squared test. For this purpose the tables as presented, thus giving twelve degrees of freedom (ν), were used; and also, since the number of values in the individual cells is small, a contracted table of only two columns (obtained by summing the first four values in a row and the last three values in a row) and hence two degrees of freedom was tested. The value of chi-squared so obtained and also the probability of obtaining larger values on this assumption are shown in Table 2 (*c*).

It thus seems unlikely that the diffuseness or diffuseness-dispersion ratio is dependent on the apparent time duration of the initiating discharge. Moreover, it was noted that the time duration of the atmospherics was not necessarily the same on all frequencies. There was not, however, any correspondence between the duration of a frequency in the atmospheric and of the same frequency in the whistler. Indeed on occasions a frequency present in one was apparently absent in the other.

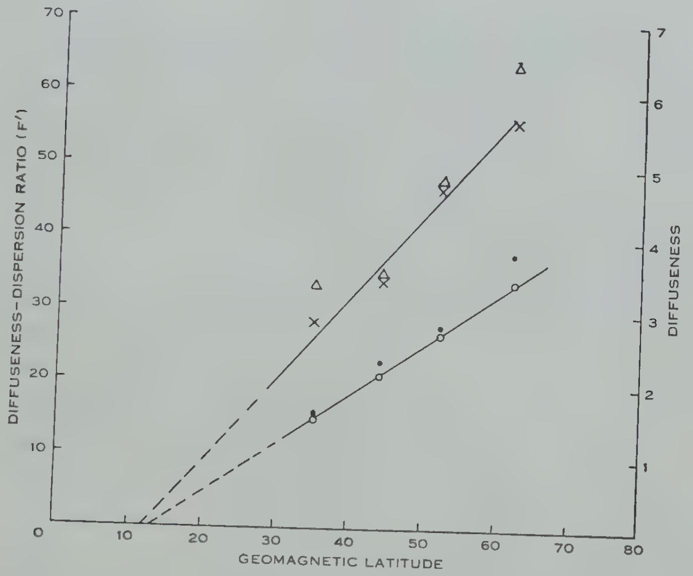

Fig. 6.—Latitude variation of diffuseness, reduced diffuseness, and diffuseness-dispersion ratio. ○ Average reduced diffuseness of all whistlers, ● average diffuseness of short whistlers, × average *F′* of all whistlers, △ average *F′* of short whistlers.

The apparent length of an atmospheric, as judged from film, will depend on its amplitude, the ringing time of the tuned circuit, and how closely it is followed by another discharge. Broad atmospherics show, in general, considerable structure, suggesting that they are due to a number of separate discharges. Any individual discharge may be expected to give a detectable trace on the film for some milliseconds after it has ceased because of the ringing of the tuned circuits, and the time to fall below the threshold of observability will depend on the strength of the discharge. It seems unlikely therefore that the clipping of the strong atmospherics (Part I) has introduced any ambiguity in classification, as the effect of this would be to tend to equalize the response produced by atmospherics of different strengths but equal time durations.

TABLE 2 (*a*)

DIFFUSENESS AND DURATION OF INITIATING ATMOSPHERIC

F Spheric	1	2	3	4	5	6	>6
Sharp ..	1	3	1	2	5	3	3
Broad ..	1	4	5	2	1	2	4
Indefinite ..	0	3	0	9	5	2	3

TABLE 2 (*b*)

DIFFUSENESS-DISPERSION RATIO AND ATMOSPHERIC DURATION

F' Spheric	0–10	10–20	20–30	30–40	40–50	50–60	>60
Sharp ..	1	1	3	3	6	1	3
Broad ..	0	4	3	4	4	3	1
Indefinite ..	1	2	1	7	7	1	3

TABLE 2 (*c*)

STATISTICAL ANALYSIS OF TABLES 2 (*a*) AND 2 (*b*)

Table	χ^2	ν	Probability (%)
F-*values*			
Whole table	18·4	12	≈10
Contracted table	2·2	2	≈35
F′-*values*			
Whole table	9·3	12	≈50
Contracted table	0·78	2	≈50

(*g*) *Dependence of Diffuseness on Ionospheric Spread*-F *and Sporadic*-E *Ionization*

An association between spread-F at Hobart (where an ionosonde operates) and F, F_1, and F' was searched for, by comparing the average values of F, F_1, and F' with values of a spread-F index which were obtained as follows. If the ionospheric observatory reports showed the presence of spread-F half-an-hour before and half-an-hour after the whistler schedule (i.e. at the regular observing times) the index 2 was assigned, if at only one of those times the index 1, and if spread-F was not present at either time the index 0 was assigned. The mean values of F, F_1, and F', together with the standard errors (S) of these means and the number of whistlers considered (n), are shown in Table 3 (*a*).

The differences of the means for spread-F index 0 and 2 was tested by means of the "Aspin-Welch test" (Bennett and Franklin 1954), and the values of "t" so calculated, together with the probability of exceeding these values of t in samples from the same population, are shown in Table 3 (b).

It seems likely that all three parameters are higher when spread-F is prevalent.

TABLE 3 (a)

DIFFUSENESS, REDUCED DIFFUSENESS, AND DIFFUSENESS-DISPERSION RATIO AND SPREAD-F

Spread-F index ..	0			1			2		
	Mean	S	n	Mean	S	n	Mean	S	n
F	2·9	(0·23)	109	3·5	(0·24)	60	3·8	(0·25)	79
F_1	2·35	(0·205)	109	2·08	(0·222)	60	3·10	(0·218)	79
F'	39·5	(2·6)	109	36·1	(3·0)	60	47·5	(2·9)	79

The procedure was extended to include spread-F one and one-half hours before and after the whistler schedule with, again, the indication that whistlers are somewhat more diffuse when spread-F is present before and after the whistler recording-period.

No evidence of a similar association with sporadic-E ionization was obtained.

TABLE 3 (b)

STATISTICAL ANALYSIS OF TABLE 3 (a)

	t	Probability of Exceeding Calculated t (%)
$\overline{F}$	2·6	≈1
$\overline{F_1}$	2·5	≈1
$\overline{F'}$	2·1	≈4

(h) *Dependence of Reduced Diffuseness on Other Geophysical Phenomena*

An autocorrelogram of average daily values of F' at Adelaide for lags of up to 65 days is shown in Figure 7. A peak in the values of the correlation coefficient around 25–27 days' lag suggests a possible recurrence-tendency in F' as in whistler occurrence (Part I) but no evidence of association with Zurich Provisional Relative Sunspot Numbers (R_z) was obtained. No indications of periodicities or of association with R_z were obtained for the Hobart data. For both stations the first few correlation coefficients of the autocorrelograms were small, suggesting that changes in F' on one day are not apparent on the following day.

Cross-correlograms between average daily values of F' for Adelaide and for Hobart with daily sums of magnetic K-index (both planetary and K-Toolangi, the nearest magnetic observatory) and Macquarie Island cosmic ray intensities showed no features of significance.

(i) *Variation of Whistler Duration with Frequency*

The majority of the whistlers studied proved to have a rather limited range of frequencies and only some 20% were present on both channels 4 and 8 while a different 10% were present on both channels 8 and 12. These two groups will be referred to respectively as upper frequency whistlers and lower frequency whistlers. The mean value of the time durations, $\overline{\delta t}$ (in seconds), for a single traverse of the path, together with the standard error of the mean and the number of whistlers involved, is shown for the two groups of whistlers and for Adelaide and Hobart in Table 4.

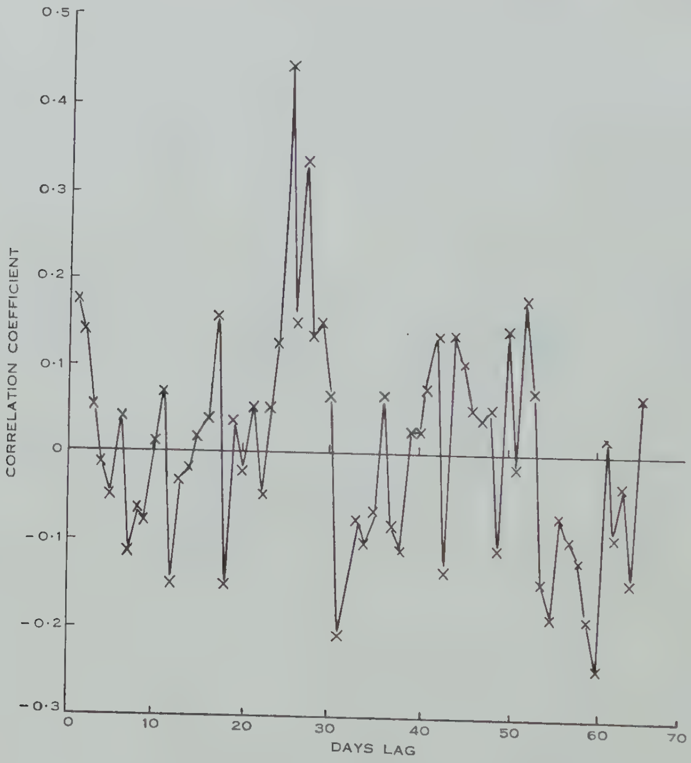

Fig. 7.—Autocorrelogram of daily average dispersion ratio for Adelaide (1958). (No. of values approximately 70.)

The assumption that the two values of $\overline{\delta t}$ at 7 kc/s are caused by taking different samples from the same population was tested by the method of Welch and Aspin. In the case of Adelaide differences greater than the observed have a probability of occurrence of about 0·03 and this probability for Hobart is less than 0·005. It thus seems likely that there is a real difference between the two groups.

TABLE 4

AVERAGE DURATIONS OF WHISTLERS AT DIFFERENT FREQUENCIES

Frequency	12·0 kc/s			7·1 kc/s			2·8 kc/s		
Station	$\overline{\delta t}$ (sec)	S.E.	n	$\overline{\delta t}$ (sec)	S.E.	n	$\overline{\delta t}$ (sec)	S.E.	n
Adelaide									
Upper frequency . .	0·087	0·003	309	0·104	0·004	309			
Lower frequency . .				0·148	0·019	34	0·128	0·015	34
Hobart									
Upper frequency	0·117	0·019	110	0·138	0·012	110			
Lower frequency . .				0·260	0·015	130	0·265	0·019	130

IV. DISCUSSION

It would be expected that the diffuseness of a whistler would be due either to the initiating discharge lasting for times comparable to those observed for the duration of individual frequencies in a whistler, or to some feature of the whistler path, or to a combination of these two factors. Since the diffuseness shows no apparent connexion with the duration of the atmospheric but is related to (i) the number of traverses of the path, (ii) the dispersion, and (iii) latitude, and the last two factors are related to path length, it seems likely that the path is the important factor. Furthermore, the fact that double-hop whistlers have approximately twice the diffuseness of single-hop whistlers (at least for middle latitudes) suggests that the reflection mechanism does not contribute markedly to the diffuseness and, thus, that the energy after reflection returns along a path close to the forward path.

In the initial discussion of whistler path Storey (1953) showed that very-low-frequency electromagnetic radiation from a lightning flash would experience a strong refraction at the base of the ionosphere and that hereafter " all the rays will follow the line of force of the earth's magnetic field fairly closely ". The time of travel (t_f) of a frequency f over a path along which the electron density N and magnetic field strength H vary was found to be

$$t_f \simeq f^{-\frac{1}{2}}\left(\frac{e}{2}\right)^{\frac{1}{2}}\int\left(\frac{N}{H}\right)^{\frac{1}{2}}\mathrm{d}l, \qquad (1)$$

and is thus dependent on electron density, magnetic field strength, and path length (l). More recently various workers (Helliwell and Gehrels 1958 ; Northover 1959 ; Smith, Helliwell, and Yabroff 1960) have suggested that guiding tubes or ducts, i.e. regions (surrounding a line of force) in which the electron density is significantly different from the surroundings, are responsible for the propagation of whistlers. The maxima and minima commonly observed in the response of the tuned circuits to a whistler thus suggest propagation of energy from one lightning flash over several ducts.

On either of the above suppositions the values of δt_f would be expected to depend on the distribution of electrons along the paths. This is still uncertain and accordingly two different models will be discussed: (*a*) one derived from experimental values of dispersion, and (*b*) one derived from the assumption that N/H is constant over a whistler path.

Model (*a*)

Treating this first from the point of view of a smooth distribution of electrons rather than a duct type of propagation, we may expect that both the finite area of "illumination" of the lower ionosphere and imperfect guiding will cause energy from one lightning flash to traverse a range of paths. The effect of both factors may be approximated to by assuming that all the energy is propagated in a region bounded in latitude by two lines of force. Unless there is a considerably greater displacement of the rays in the tangent plane to a line of force than in the diametral plane, the maximum time spread will be determined by the two rays which determine the spread in latitude, as there is no evidence of dispersion being dependent upon longitude. On these assumptions and using the equations

TABLE 5

FREQUENCY DEPENDENCE OF δx_f

Frequency	12·0 kc/s	7·1 kc/s	2·8 kc/s
Station		δx_f	
Adelaide			
Upper frequency ..	435 km	420 km	
Lower frequency ..		600 km	340 km
Hobart			
Upper frequency ..	580 km	550 km	
Lower frequency ..		1080 km	700 km

$$t_f = Df^{-\frac{1}{2}} \quad \text{(Dispersion law)},$$
$$D \simeq 2\cdot 2(\lambda - 12) \quad \text{(from graph in Allcock 1959)},$$

where λ=geomagnetic latitude, we may derive the equation

$$\delta t_f = 0\cdot 021 f^{-\frac{1}{2}} \delta x_f$$

for the difference in propagation time δt_f of a frequency f over two lines of force separated by δx_f km along the meridian of longitude. Substitution of values from Table 4 leads to estimates of δx_f for Adelaide and Hobart as in Table 5. For each station the estimates of δx_f using the higher frequency whistlers are quite close but the lower frequency whistlers require larger values of δx_f to explain the observed spread in time.

An estimate of the variation of δx with latitude may be made from the equation for the variation of $\overline{F}_1$ with latitude if the assumption is made that $\overline{F}_1$

values (which are effectively average values of δt_f for three frequencies) apply to an " average frequency " of 7·1 kc/s. The values are shown in Table 6.

Since the illuminated area at the base of the ionosphere at the source end of the path may reasonably be assumed to have a radius of at least 100 km and the field lines range in length from 9000 km (30°) to 58,000 km (60°) these results suggest that the departure from perfect guiding is much less than one degree.

If, however, the propagation of whistlers is due to the presence of ducts, then the above reasoning may be considered to apply to the ducts rather than to a continuous medium, for the observed average dispersions must then be an average property of the guiding ducts. The diffuseness would then be expected to be determined by the range of ducts " illuminated " by energy from a lightning stroke. At low latitudes the diffuseness would be expected to be small because of the relatively large enhancements of electron density needed to produce effective ducts and the consequent relative decrease in the number of ducts (Smith, Helliwell, and Yabroff 1960), and also because of the limitation of the region of illumination suggested by Iwai and Outsu (1956). At higher latitudes a larger number of ducts may be expected to be illuminated, with a consequent increase in diffuseness. The supposition of a duct type of propagation also facilitates the explanation of the occasional very sharp whistlers which are observed at high latitudes. On these premises the diameter of ducts must be considered to be only a fraction of the dimensions listed in Table 6.

Table 6

LATITUDE DEPENDENCE OF δx

Latitude ..	30°	40°	50°	60°
δx (km) ..	240	380	510	650

Model (*b*)

A model of the upper atmosphere in which the quotient of electron density and magnetic field strength is constant along a line of force has been used by Gallet (1959) in studies of V.L.F. emissions. If it is assumed that such a condition is satisfied throughout the region in which a whistler propagates, then the time of travel is, by virtue of equation (1), proportional to path length and

$$\delta t_f = (\delta l / l) D f^{-\frac{1}{2}},$$

where δl is the difference in length between the two extreme paths and l the length of the " middle path ". The quotient, $\delta l/l$, depends on latitude and also upon the separation in latitude (at the surface of the Earth) of the two extreme paths. The appropriate values may be readily estimated from tables of path length (Chapman and Sugiura 1956). These data, together with the variation of $\overline{F}_1$ with λ, the experimental values of dispersion, and the use of an " average frequency " of 7·1 kc/s, gave estimates of δx ranging from 240 km at latitude 30° to 190 km at latitude 60°. The values for higher latitudes are thus appreciably smaller than for model (*a*).

Again, if propagation is by means of ducts within which the electron density is comparable with the surroundings, it seems reasonable (failing any more detailed knowledge of the variation in properties from duct to duct) to regard the values of δx calculated above to be an approximate measure of the extent of illumination of the lower ionosphere.

For both models the numerical values calculated are dependent on the values assigned to the dispersion. The experimental values of dispersion, which are average values for a large number of whistlers observed at several different latitudes, are likely to be somewhat biased because of the variation in the occurrence of whistlers with latitude (Part I) and the distance over which a whistler may be heard (Storey 1953 ; Crary, Helliwell, and Chase 1955). It thus seems likely that the values used for D are too large for lower latitudes and too small for high latitudes and are least in error for middle latitudes where whistlers are most common. However, if such is the case, the diffuseness figures will be in error in a similar fashion and the one error will tend to reduce the other.

The smaller diffuseness of upper frequency whistlers (Section III (a)) is not explicable in terms of either of the above models. The difference noted in $\overline{\delta t}$ on the 7 kc/s channel for the two groups suggests a difference in the mode of propagation either over the ground or in the outer atmosphere. If the former were the case, then the smaller diffuseness of the upper frequency whistlers might be explained in terms of these arriving at the ground a considerable distance from the observing station and undergoing sufficient attenuation to reduce the time for which any frequency is observable. The absence of the lower frequencies might then be due to the increased absorption discussed by both theoretical and experimental workers (Wait 1957 ; Obayashi 1959). The lower frequency whistlers would then have to be considered to be those which reached the ground near to the observing station, but no explanation for the absence of the higher frequencies is apparent on this basis. Alternatively, it might be postulated that the upper frequency whistlers are guided by ducts with a lower frequency cut-off of about 5 kc/s and that the lower frequency ones are propagated, as described by Storey, in a region without ducts. The values of $\overline{\delta t}$ for 3 kc/s, which for either model suggest smaller values for δx at this frequency than at 7 kc/s, are in qualitative agreement with Storey's work which predicted " the spreading will be least for the lowest frequencies ". While a difference in the spectrum of the source could explain the difference in frequency range of the two groups of whistlers, it would not explain the difference in diffuseness.

If the data of Table 4 are considered to indicate a cut-off frequency of the order of 5 kc/s, then one may attempt to estimate the radius of the ducts (considered to be circular in cross section) in the lower atmosphere by considering them to be of the nature of a dielectric waveguide. For such a guide of radius b, permittivity ε_1, permeability μ_1, in a medium ε_2, μ_2, the cut-off frequency (Bronwell and Beam 1947)

$$f_0 = k_1 b / 2\pi b(\varepsilon_1\mu_1 - \varepsilon_2\mu_2)^{\frac{1}{2}},$$

where $k_1 b$ is approximately $2 \cdot 4$. This equation may be transformed to

$$f_0 = 2 \cdot 4 v_1 / 2\pi b(1 - N_2/N_1)^{\frac{1}{2}},$$

where v_1 is the velocity in medium 1 and N the electron density. Taking a value of 100 for the refractive index of the F layer (Storey 1953) and assuming $N_1 = 1 \cdot 1 N_2$ for latitudes of about 50° (Smith, Helliwell, and Yabroff 1960) leads to an estimate of approximately 800 m for the radius of the duct in the F layer; furthermore, this value is reduced by a factor of only about three times when N_1 is much larger than N_2.

The explanation of the increase in whistler diffuseness observed when ionospheric spread-F is prevalent must depend on the interpretation of the latter phenomenon. However, various workers have found an association between spread-F and the patches of ionization, elongated along magnetic field lines, which are considered to be responsible for radio star scintillations (Briggs 1958), and a correlation has been reported between spread-F and the occurrence of field-aligned ionization (Leadabrand 1955). Thus, it seems plausible to regard the reported increase in diffuseness as being due to there being an increase in the number of ducts illuminated when ionospheric spreading is observed.

The values calculated for δx are mean values which, for Brisbane, Adelaide, and Hobart, will be somewhat larger than the modal values as indicated by Figure 2. Values of δx several times larger than these must be postulated to exist on occasions to account for the very diffuse whistlers sometimes observed.

V. Conclusions

The diffuseness of whistlers is primarily dependent on the path over which the energy travels. It may be explained either by assuming imperfect guiding in a medium with smoothly varying properties or in terms of propagation along ducts with parameters somewhat different to those of the surrounding medium. The experimental evidence from the present study is inadequate to differentiate between the two models but suggests that ducts may be operative at higher frequencies and inoperative at lower frequencies. No significant seasonal or diurnal variations in diffuseness have been observed but diffuseness increases at times when ionospheric spread-F is prevalent.

VI. Acknowledgments

The work described herein was performed upon whistlers recorded at the several stations by courtesy of the organizations mentioned in Part I. The authors desire to thank Professor H. C. Webster for his interest and encouragement.

VII. References

Allcock, G. McK. (1959).—*J. Atmos. Terr. Phys.* **14**: 185.

Bennett, C. A., and Franklin, N. L. (1954).—" Statistical Analysis in Chemistry and Chemical Engineering." p. 177. (Wiley: New York.)

Briggs, B. H. (1958).—*J. Atmos. Terr. Phys.* **12**: 89.

Bronwell, A. B., and Beam, R. E. (1947).—" Theory and Application of Microwaves." p. 344. (McGraw-Hill: New York.)

Chapman, S., and Suguira, M. (1956).—*J. Geophys. Res.* **61**: 485.

Crary, J. H., Helliwell, R. A., and Chase, R. F. (1955).—*J. Geophys. Res.* **61**: 35.

Crouchley, J (1961).—*Aust. J. Phys.* **14**: 22.

Eckersley, T. L. (1935).—*Nature* **135**: 104.

Gallet, R. M. (1959).—*Proc. Inst. Radio Engrs., N.Y.* **47** : 211.
Helliwell, R. A., and Gehrels, E. (1958).—*Proc. Inst. Radio Engrs., N.Y.* **46** : 785.
Iwai, A., and Outsu, J. (1956).—*Proc. Res. Inst. Atmos. Nagoya Univ.* **4** : 29.
Leadabrand, R. L. (1955).—Tech. Rep. No. 98, p. 113. Radio Prop. Lab. Stanford Univ.
Northover, F. H. (1959).—*J. Atmos. Terr. Phys.* **17** : 158.
Obayashi, T. (1959).—*Nature* **184** : 34.
Smith, R. L., Helliwell, R. A., and Yabroff, I. W. (1960).—*J. Geophys. Res.* **65** : 815.
Storey, L. R. O. (1953).—*Phil. Trans.* A **246** : 113.
Storey, L. R. O., and Grierson, J. K. (1958).—*Electron. Engng.* **30** : 648.
Wait, J. R. (1957).—*Proc. Inst. Radio Engrs., N.Y.* **45** : 768.

ON SOLVING THE EQUATION OF RADIATIVE TRANSFER FOR CONSERVATIVE NON-UNIFORM MEDIA

By P. R. Wilson*

[*Manuscript received October* 14, 1960]

Summary

The equation of radiative transfer in a form suitable for non-uniform semi-infinite media in radiative equilibrium is solved for the attenuation coefficient $\varkappa$ compatible with models for total intensity J as functions of two variables, subject to the boundary condition of zero inward flux at the surface.

The method is tested in a case where a solution has been previously obtained and then applied to an axially symmetric medium.

I. Introduction

Recent studies of solar granulation and sunspot phenomena have emphasized the importance of solutions of the equation of radiative transfer for non-uniform media. Giovanelli (1959) produced the approximate form of the transfer equation, suitable for non-uniform media in radiative equilibrium,

$$\nabla^2 J = \frac{1}{\varkappa} \nabla J \cdot \nabla \varkappa, \tag{1}$$

where J, the total intensity of radiation, and $\varkappa$, the attenuation coefficient of the medium, are both functions of position.

This equation is usually solved subject to the boundary condition that the inward flux is zero at the surface. In Cartesian or cylindrical polar coordinates, if the z-axis is normal to the surface $z=0$, and positive outwards, this takes the form

$$\varkappa J + \frac{2}{3} \frac{\mathrm{d}J}{\mathrm{d}z} = 0, \tag{2}$$

when $z=0$.

In the customary method of solution of (1) and (2), a particular model for the attenuation coefficient $\varkappa$ is assumed and (1) is solved for J subject to (2). Giovanelli (1959) considered the model semi-infinite medium

$$\begin{aligned} \varkappa &= \varkappa_0(1+\alpha \cos lx) \quad && (z<0), \\ &= 0 && (z>0), \end{aligned}$$

where $\varkappa_0$, α, and l are constants. Assuming α small, he obtained the approximate solution

$$J(x,z) = Az + B + Ce^{lz} \cos lx,$$

---

* Department of Applied Mathematics, University of Sydney.

where A, B, and C are constants determined by the boundary condition, and C/A is small. Higher harmonic terms are assumed negligible. Wilson (1960), using the model

$$\begin{aligned} \varkappa &= \varkappa_0 e^{-\nu z}(1+\alpha\cos lx) \quad (z<0), \\ &= 0 \qquad\qquad\qquad\qquad\quad (z>0), \end{aligned} \tag{3}$$

where ν is constant, obtained a similar solution

$$J(x,z) = Ae^{-\nu z} + B + Ce^{pz}\cos lx, \tag{4}$$

where

$$p^2 + \nu p - l^2 = 0, \quad p>0, \tag{5}$$

and C/A is small.

As a first step towards the study of radiative transfer in non-uniform regions of the solar atmosphere, this method of solution of (1) has the disadvantage that it is necessary to propose a model for the attenuation coefficient, and assess its likelihood by comparing the solution of (1) for J with the information which can be obtained from observations of the directional intensity at the surface. In all but the simplest cases, it is by no means obvious how best to choose the models for $\varkappa$.

In the present paper a new and, for many purposes, more direct approach to equation (1) is suggested and is tested by application to the sinusoidal case (equations (3), (4), and (5)) which has already been studied. It is then applied to an exponential medium exhibiting axial symmetry.

II. THE SOLUTION OF THE TRANSFER EQUATION

Although the total intensity J is not directly observable, its variation near the surface $z=0$ in a direction parallel with the surface must be closely related to the variation in directional intensity at $z=0$. It is therefore logical to assume a model for J throughout the medium, based on observations, and use equations (1) and (2) to find the attenuation coefficient $\varkappa$ required to produce such radiation.

Assuming J and $\varkappa$ to be point functions of two variables (e.g. x and z, or, using cylindrical polar coordinates for an axially symmetric model, r and z), equation (1) may be written

$$\frac{\partial}{\partial x}\left(\frac{1}{\varkappa}\,\frac{\partial J}{\partial x}\right) + \frac{\partial}{\partial z}\left(\frac{1}{\varkappa}\,\frac{\partial J}{\partial z}\right) = 0,$$

which is a necessary and sufficient condition for the existence of a function $\varphi(x,z)$ such that

$$\frac{\partial\varphi}{\partial z} = \frac{1}{\varkappa}\,\frac{\partial J}{\partial x} + \psi(z), \tag{6}$$

$$\frac{\partial\varphi}{\partial x} = -\frac{1}{\varkappa}\,\frac{\partial J}{\partial z} + \eta(x), \tag{7}$$

where $\psi(z)$ and $\eta(x)$ are arbitrary functions of one variable. Thus if $\varphi(x,z)$ can be found, $\varkappa(x,z)$ can be determined from (6) and (7), $\psi(z)$ and $\eta(x)$ being chosen so that $\varkappa$ is unique.

Eliminating $\varkappa$ from (7) yields

$$\frac{\partial\Phi}{\partial z}\Big/\frac{\partial\Phi}{\partial x}=-\frac{\partial J}{\partial x}\Big/\frac{\partial J}{\partial z}, \tag{8}$$

where $\partial\Phi/\partial z=\partial\varphi/\partial z-\psi(z)$ and $\partial\Phi/\partial x=\partial\varphi/\partial x-\eta(x)$.
Thus

$$\Phi(x,z)=\varphi(x,z)+X(x)+Z(z), \tag{9}$$

where X and Z are again arbitrary functions of one variable.

Equation (8) yields

$$\frac{\partial\Phi}{\partial x}\,\frac{\partial J}{\partial x}+\frac{\partial\Phi}{\partial z}\,\frac{\partial J}{\partial z}=0,$$

or

$$\nabla\Phi\cdot\nabla J=0, \tag{10}$$

whence, if $J(x,z)$=constant defines a family of curves in the x,z plane, $\Phi(x,z)$=constant defines an orthogonal family. Given $J(x,z)$, therefore, we may always find Φ and hence $\varphi(x,z)$ to within arbitrary functions of one variable, and an accurate solution of (1) is thus available. It is emphasized, however, that any solution of (1) is subject to the boundary condition (2), and that if the accurate solution fails on the boundary, it is necessary to consider approximate solutions which satisfy (1) and (2) to the same order of accuracy.

III. Application to the Sinusoidal Case

It is instructive to apply this method to the model for J given by equation (5), i.e.

$$J(x,z)=A\mathrm{e}^{-\nu z}+B+C\mathrm{e}^{pz}\cos lx.$$

The family of curves $J(x,z)$=constant has gradient given by

$$\frac{\mathrm{d}x}{\mathrm{d}z}=-\frac{A\nu\mathrm{e}^{-\nu z}-Cp\mathrm{e}^{pz}\cos lx}{Cl\mathrm{e}^{pz}\sin lx}.$$

Hence the differential equation for the orthogonal family is

$$\frac{\mathrm{d}z}{\mathrm{d}x}=\frac{A\nu-Cp\mathrm{e}^{(p+\nu)z}\cos lx}{Cl\mathrm{e}^{(p+\nu)z}\sin lx}.$$

Substituting $\zeta=\mathrm{e}^{(p+\nu)z}$ yields

$$\frac{\mathrm{d}\zeta}{\mathrm{d}x}+l\lambda\zeta\cot lx=\frac{\mu}{\sin lx}, \tag{11}$$

where $\lambda=p(p+\nu)/l^2$, and $\mu=A\nu(p+\nu)/Cl$.
This equation has the solution

$$\zeta(\sin lx)^{\lambda}=\int\mu(\sin lx)^{\lambda-1}\mathrm{d}x+\Phi,$$

and the family of curves Φ=constant is given by

$$\Phi(x,z)=\mathrm{e}^{(p+\nu)z}(\sin lx)^{\lambda}-\int \mu(\sin lx)^{\lambda-1}\mathrm{d}x, \tag{12}$$

whence $\varphi(x,z)$ is determined to within arbitrary functions of one variable. Substitution in (7) yields

$$\varkappa=\frac{Cl}{(p+\nu)}\,\frac{\mathrm{e}^{-\nu z}(\sin lx)^{1-\lambda}}{[1+(Cl/A\nu)\eta(x)(\sin lx)^{1-\lambda}/\{1-(Cp/A\nu)\mathrm{e}^{(p+\nu)z}\cos lx\}]}, \tag{13}$$

while from (6)

$$\varkappa=\frac{Cl}{(p+\nu)}\,\frac{\mathrm{e}^{-\nu z}(\sin lx)^{1-\lambda}}{\{1+\psi(z)\mathrm{e}^{-(p+\nu)z}/(p+\nu)(\sin lx)^{\lambda}\}}. \tag{14}$$

A unique function for $\varkappa$ is obtained if the arbitrary functions $\eta(x)$ and $\psi(z)$ are taken to be zero. Thus

$$\varkappa=\varkappa_0\mathrm{e}^{-\nu z}(\sin lx)^{1-\lambda}, \tag{15}$$

where $\varkappa_0=Cl/(p+\nu)$.

If $p^2+\nu p-l^2=0$, as in (5), $1-\lambda=0$ and (15) becomes

$$\varkappa=\varkappa_0\mathrm{e}^{-\nu z}. \tag{16}$$

Applying the boundary condition (2) to the solution (16) at $z=0$ and $\cos lx=\pm 1$ yields

$$\left.\begin{aligned}\left(\varkappa_0-\frac{2}{3}\nu\right)A+\varkappa_0B+\left(\varkappa_0+\frac{2}{3}p\right)C=0,\\ \left(\varkappa_0-\frac{2}{3}\nu\right)A+\varkappa_0B-\left(\varkappa_0+\frac{2}{3}p\right)C=0,\end{aligned}\right\} \tag{17}$$

which may be satisfied only if C is zero. If the ratio $C/(A+B)$ is small, (17) is satisfied only if first-order terms are ignored. Thus (16), although an accurate solution to (1), is not a satisfactory solution to the problem and it is necessary to consider approximate solutions.

As a first approximation the ratio C/A is assumed small and in (13) non-zero values of $\eta(x)$ are investigated. Provided $\eta(x)$ is of order not greater than unity, (13) yields an approximation correct to first order terms

$$\varkappa=\varkappa_0\mathrm{e}^{-\nu z}\left[1-\frac{Cl}{A\nu}\eta(x)+\mathrm{O}\left(\frac{C}{A}\right)^2\right]$$

or

$$\varkappa=\varkappa_0\mathrm{e}^{-\nu z}\{1+\alpha\eta(x)\}, \tag{18}$$

where α is of order C/A and $\eta(x)$ is arbitrary but of order not greater than unity. The boundary conditions suggest the choice

$$\eta(x)=\cos lx,$$

and in this case (2) is satisfied correct to the first order provided

$$\alpha=\frac{C}{A+B}\left(1+\frac{2p}{3\varkappa_0}\right), \tag{19}$$

and B is related to A by

$$B=A\left(\frac{2\nu}{3\varkappa_0}-1\right).$$

As (18) also satisfies equation (1) to the same order, it is with (4) a satisfactory first-order solution to the problem. Equation (14) has not been used to obtain this approximate solution, since partial differentiation has eliminated the leading constant A.

This method verifies the solutions (3) and (4) previously obtained, but provides a more detailed account of the approximations used.

IV. Application to an Axially Symmetric Medium

As a first step towards a solution of the problem of radiative transfer in the neighbourhood of a sunspot, an axially symmetric model of $J(r,z)$ is chosen which has a minimum value at $r=0$ and increases to a finite limit as r approaches infinity, the dependence of $J(r,z)$ on r decreasing with depth. A function having these properties is

$$J=A\mathrm{e}^{-\nu z}+B+C\mathrm{e}^{pz-kr^2}, \tag{20}$$

where A must be positive, C negative, and p and k must be positive. Equations (6) et seq. apply provided cylindrical polar coordinates are used, x being replaced by r, and $\varkappa(r,z)$ being assumed independent of θ.

Proceeding as before, the function φ is found to be given by

$$\varphi=r^{\lambda}\mathrm{e}^{(p+\nu)z}+R(r)+Z(z),$$

where $\lambda=p(p+\nu)/2k$, and this yields the accurate solution of (1) for $\varkappa$,

$$\varkappa=\varkappa_0 r^{1-\lambda}\mathrm{e}^{-\nu z-kr^2}, \tag{21}$$

where $\varkappa_0=2Ck/(p+\nu)$.

In the special case $p^2+p\nu-2k=0$, $1-\lambda=0$, and the solution becomes

$$\varkappa=\varkappa_0\mathrm{e}^{-\nu z-kr^2}. \tag{22}$$

Applying the boundary condition (2) at $z=0$ yields

$$\varkappa_0\mathrm{e}^{-kr^2}(A+B+C\mathrm{e}^{-kr^2})+\frac{2}{3}(-A\nu+Cp\mathrm{e}^{-kr^2})=0. \tag{23}$$

For a first-order solution, the boundary condition must be satisfied at two values of the horizontal coordinate. At $r=0$ (23) yields

$$A(1-2\nu/3\varkappa_0)+B+C(1+2p/3\varkappa_0)=0, \tag{24}$$

and at any finite value $r=R$,

$$A(1-2\nu\mathrm{e}^{kR^2}/3\varkappa_0)+B+C(\mathrm{e}^{-kR^2}+2p/3\varkappa_0)=0. \tag{25}$$

Thus, provided the ratios C/A and B/A satisfy (24) and (25), (20) and (22) form a first-order solution of (1) and (2) in the axially symmetric case. Since the features of the total intensity J are determined by the attenuation coefficient and the boundary condition, it is to be expected that the solution imposes the restrictions (24) and (25) on the values of A, B, and C. The absolute magnitude of A is determined by the net flux at $z=-\infty$, and $\varkappa_0$ is given by (21).

A difficulty arises, however, in considering the limit as r approaches infinity. Equation (2) becomes

$$J=Ae^{-\nu z}+B,$$

which entails the solution

$$\varkappa=\varkappa_0 e^{-\nu z},$$

whereas in (22) the limit of $\varkappa_0 e^{-\nu z-kr^2}$ is zero. However, equation (25) requires $A=0$ when R approaches infinity, and the case is trivial. Thus the first-order solution given by (22) is available only over a restricted range of the horizontal coordinate.

An approximate solution may be obtained over the range $0\leqslant r<\infty$ by considering the discontinuous function

$$\left.\begin{aligned}\varkappa&=\varkappa_0 e^{-\nu z-kr^2}, & 0\leqslant r\leqslant R,\\ \varkappa&=\varkappa' e^{-\nu z}, & r>R,\end{aligned}\right\} \tag{26}$$

On the boundary $z=0$, equations (24) and (25) hold for the range $0\leqslant r\leqslant R$, while at $r=\infty$ equation (2) yields

$$\varkappa'(A+B)-\tfrac{2}{3}A\nu=0,$$

therefore

$$\varkappa'=\tfrac{2}{3}\nu/(1+B/A).$$

The solution is continuous at $r=R$ provided R is chosen to satisfy

$$\varkappa'=\varkappa_0 e^{-kR^2}.$$

The partial derivative $\partial\varkappa/\partial r$ is discontinuous at this point, but the discontinuity is small if R is large.

As an alternative approximate solution which is analytic at all points in the range $0\leqslant r<\infty$, equations (26) suggest

$$\varkappa=\varkappa_0 e^{-\nu z}(\beta+e^{-kr^2}), \tag{27}$$

where β is a constant. On the boundary $z=0$ this solution yields consistent equations at $r=0$, $r=R$, and $r=\infty$. Equation (1) is satisfied correct to first-order terms in C/A when r is small and when r is large. For values of r of order unity, however, it is satisfied only provided terms of order C/A may be ignored.

V. Conclusion

Giovanelli's form of the transfer equation for non-uniform media has been shown to be readily soluble for the attenuation coefficient $\varkappa$, given the total intensity J as a function of two coordinates.

The method has been applied to the case

$$J=Ae^{-\nu z}+B+Ce^{pz}\cos lx,$$

with boundary condition at $z=0$

$$\varkappa J+\tfrac{2}{3}\mathrm{d}J/\mathrm{d}z=0,$$

and the approximate solution, correct to first-order terms, is found to be in agreement with a previous solution (Wilson 1960).

The axially symmetric case for which

$$J=Ae^{-\nu z}+B+Ce^{pz-kr^2}$$

with a similar boundary condition at $z=0$ yields the solution

$$\varkappa=\varkappa_0 e^{-\nu z-kr^2},$$

which satisfies the boundary condition to the first order over a finite range of r, provided two relations hold between A, B, and C. This indicates the approximate solution in the range $0\leqslant r<\infty$ of the form

$$\begin{aligned}\varkappa&=\varkappa_0 e^{-\nu z-kr^2}, &\quad 0\leqslant r\leqslant R,\\ \varkappa&=\varkappa' e^{-\nu z}, &\quad r>R,\end{aligned}$$

where, if R satisfies

$$\varkappa_0 e^{-kR^2}=\tfrac{2}{3}\nu/(1+B/A),$$

$\varkappa$ is continuous for $0\leqslant r<\infty$, but $\partial\varkappa/\partial r$ is discontinuous at $r=R$.

VI. ACKNOWLEDGMENT

The author wishes to thank Dr. R. G. Giovanelli of the Division of Physics, C.S.I.R.O., for his continued interest in the project and for many fruitful discussions.

VII. REFERENCES

GIOVANELLI, R. G. (1959).—*Aust. J. Phys.* **12**: 164.

WILSON, P. R. (1960).—*Aust. J. Phys.* **13**: 461.

WAVELENGTHS OF KRYPTON 86, MERCURY 198, AND CADMIUM 114

By C. F. Bruce* and R. M. Hill*

[*Manuscript received October* 17, 1960]

Summary

The vacuum wavelengths and the spectral line profiles of four lines of krypton 86, four lines of mercury 198, and four lines of cadmium 114 have been measured. One line, the radiation $2p_{10}$–$5d_5$ of krypton 86 (6057 Å), has been used as the reference standard in the wavelength measurements.

A variable gap Fabry-Perot interferometer with electromagnetically controlled plate holders was used throughout under vacuum conditions. The use of photoelectric recording methods and mechanical scanning made it possible to compare wavelengths with an accuracy of better than 1 part in 10^8, and half-intensity widths of lines were measured with an accuracy of $0 \cdot 5$ mK ($0 \cdot 0005$ cm^{-1}).

The 6057 Å line of krypton 86 was examined under different operating conditions of the Engelhard-type lamp and small wavelength shifts due to variation of temperature, pressure, and current density were measured. The Doppler shift and interatomic Stark shift annul each other if the lamp is viewed in the direction cathode to anode to observer, and is operated in a liquid air bath with the temperature near the capillary surface of the lamp at 63 ± 1 °K and with a current density of $0 \cdot 28 \pm 0 \cdot 05$ A/cm^2. The Doppler shift under these conditions was found to be $+0 \cdot 014 \pm 0 \cdot 003$ m^{-1} (-50 ± 10 μÅ) and the interatomic Stark shift $-0 \cdot 014 \pm 0 \cdot 003$ m^{-1} ($+50 \pm 10$ μÅ). Under these conditions also the half-intensity width is $13 \cdot 5 \pm 0 \cdot 5$ mK, and the wavelength emitted is that for the unperturbed state of the atoms to 2–3 parts in 10^9. This line is superior to the other lines examined for sharpness and reproducibility and other wavelengths may be established in terms of it to at least 1 part in 10^8. This is the line that has been recommended as the new primary standard of length.

I. INTRODUCTION

The recommendation of the Advisory Committee of the International Committee of Weights and Measures on the Definition of the Metre (1957) that the metre be redefined in terms of a krypton 86 wavelength emphasizes the importance of obtaining exact knowledge of the characteristics of this line and other lines suitable as secondary standards in metrology and spectroscopy.

The chosen line is the radiation $2p_{10}$–$5d_5$ of krypton 86 for the unperturbed state of the atoms and by definition it has been recommended that the metre be 1 650 763·73 times the vacuum wavelength of this radiation. The vacuum wavelength is then 6057·802106 Å ($1\text{ Å} = 1 \times 10^{-10}$ m) and it is this value that has been used as a reference standard in the wavelength measurements described here.

A photoelectric Fabry-Perot interferometer was developed using mechanical scanning for the precise comparison of vacuum wavelengths and for the accurate recording of the spectral line profiles. An electrodeless cadmium 114 lamp has been prepared and shows promise as a satisfactory source of secondary standards.

---

* Division of Metrology, C.S.I.R.O., University Grounds, Chippendale, N.S.W.

II. LIGHT SOURCES

The krypton 86 lamp, supplied by E. Engelhard of the Physikalisch-Technische-Bundesanstalt (PTB) (Engelhard 1952), was of the hot cathode type and was normally operated at 20 mA d.c., the current density being 0·28 A/cm². The lamp was cooled by immersion in a bath of liquid air which was continuously evacuated. The temperature of the lamp could be satisfactorily regulated by controlling the rate of pumping. The temperatures in the liquid air bath were measured at various points, using an oxygen gas thermometer and specially calibrated thermocouples. Two thermocouple junctions were attached to different points on the capillary of the lamp and were thus very close to the gas discharge used as the light source. Another thermocouple was placed in the liquid air close to the bulb of the oxygen thermometer. Under stable conditions, with no fluctuations in the pumping rate, all three thermocouples and the gas thermometer indicated the same temperature to 1 degK. However, any variation in the pumping rate led to differences of several degrees Kelvin between the gas thermometer and the thermocouples. The cold junctions of the thermocouples were placed in an ice bath and the e.m.f.'s generated were measured with a precision potentiometer. The temperatures indicated by the thermocouples attached to the capillary of the lamp are those referred to in this report, and these are reliable to within ±0·1 degK. The lamp was viewed, in general, from the anode side. That is, the direction of propagation of light may be said to be from cathode to anode to observer (CAO). In Doppler shift measurements, the lamp was also viewed in the opposite sense (ACO). This method of designating light direction will be used throughout this article.

TABLE 1

ELECTRODELESS MERCURY LAMPS

Lamp	Mercury 198	Carrier Gas	Tube Material
NBS 32	2 mg	Argon at 3 mmHg	" Vycor "
NBS 99	1 mg	Argon at 3 mmHg	" Vycor "
NRC	2 mg	Argon at ½–1 mmHg	" Vycor "
NSL 7	1 mg	Argon at 2 mmHg	Quartz

The mercury 198 lamps consisted of a series of the electrodeless type, two of which were Meggers lamps from the National Bureau of Standards (NBS) (Meggers and Westfall 1950), one from the National Research Council (NRC), and one made in this Laboratory (NSL). All were excited at a frequency of 100 MHz and cooled with water to 10–12 °C during operation. One lamp (NSL 7) was examined at temperatures in the range 4–15 °C. The power output from the high frequency oscillator, in general, was about 60 W and the lamps were observed broadside on. The details of these lamps, as given by the makers, are in Table 1.

NBS 32 was an old lamp that had been used extensively for several years. NBS 99 was a new lamp. NRC had an isotopic content as follows: 198/98·0%; 199/1·51%; 200/0·16%; 201/0·08%; 202/0·12%; and 204/0·06%.

The cadmium 114 lamp was of the electrodeless type made in this Laboratory and consisted of a small amount of cadmium 114 in a quartz tube containing argon at a pressure of 2 mmHg. This lamp was then surrounded by a further quartz jacket which was evacuated to a pressure below 10^{-6} mmHg. Considerable care was taken in the baking and degassing of the lamp tube and its jacket to ensure that the pressure in the surrounding jacket was as low as possible. The form of the lamp is shown in Figure 1. The techniques required to make this lamp were established by first making several lamps with natural cadmium. One special form of test lamp was made with a thermocouple sealed through the outer jacket and attached to the outer surface of the quartz tube of the lamp. The temperature at this point was then measured for different power outputs from the oscillator. With about 2–3 mg of natural cadmium and with argon at 1–2 mmHg pressure, the lamp emitted the cadmium spectrum very intensely for power outputs from 40 W upwards. The intensity of the red line 6440 Å was about twenty times that emitted by a cadmium Osira-type lamp running at 1 A, and the fringes obtained with the lamp were of comparable visibility. The temperature at the centre of the lamp was in the range 180–200 °C. It was found that, with an oscillator power of about 50 W, the lamp operated very satisfactorily. Using a 2400 MHz oscillator, a lamp was life tested over 100 hr and was still continuing to emit a clean cadmium spectrum when excited at either 100 MHz or 2400 MHz. The vacuum jacket around the lamp therefore maintains the temperature quite efficiently for the satisfactory emission of the cadmium spectrum.

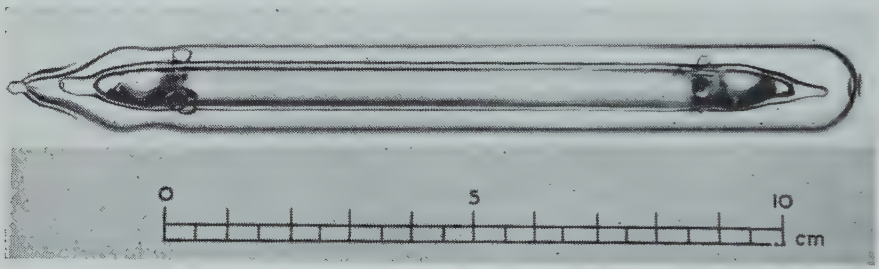

Fig. 1.—Cadmium 114 electrodeless lamp. Outer jacket evacuated to less than 10^{-6} mmHg pressure.

A lamp was then prepared using cadmium 114 isotope. The supply of this isotope had to be distilled to obtain pure metal and consequently the lamp prepared was estimated to contain only a small fraction of a milligram of the pure cadmium isotope. The lamp was filled with argon at 2 mmHg pressure. A power output from the oscillator of about 60–80 W was used to obtain an intense cadmium spectrum. The intensity of the red line was about three times as great as that of the Osira-type lamp containing natural cadmium and operating at 1 A.

The experiments with lamps containing natural cadmium indicate that a few milligrams of cadmium are desirable for a lamp of high intensity and stability, and more lamps will be made with " Vycor " glass when further supplies of cadmium 114 become available.

III. The Interferometer System

The interferometer was a variable gap Fabry-Perot type in which the optical flats were mounted in specially designed electromagnetic plate holders. The carriages for the plate holders were made of invar and supported in a V-shaped trough of invar. The plate holders could be adjusted for parallelism initially by coarse and fine mechanical controls.

One holder provided means for moving one optical flat through a small distance by remote electrical control without appreciable change in parallelism. This plate could also be oscillated at any desired frequency by applying an a.c. input to the exciting coil. A schematic diagram is shown in Figure 2. The unit consists essentially of a fixed coil in a magnetic field produced by a permanent ring magnet and soft iron ring assembly. The assembly is attached to a brass elastic member which holds the optical flat. The movement of the assembly is controlled by the current passing in the coil. The slotted elastic member was designed to give adequate displacement of the optical plate without passing too great a current through the coil and without being excessively sensitive to external vibration. A direct current of 180 mA moved the plate through about four orders of interference.

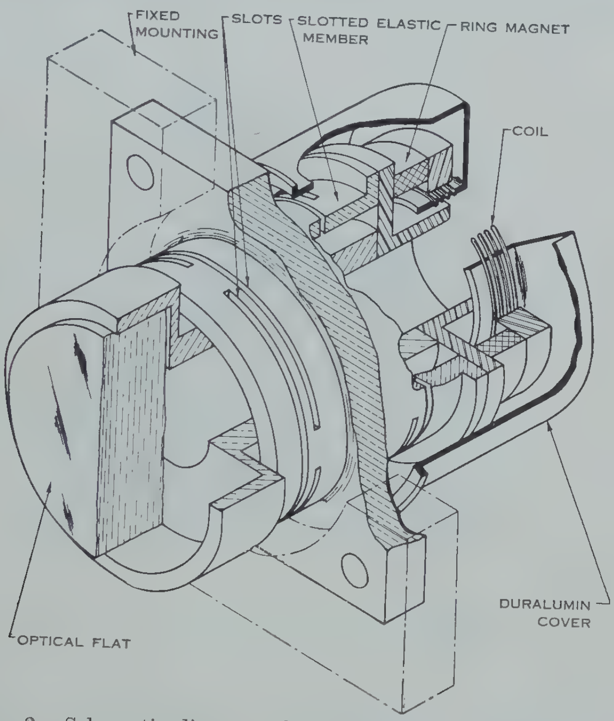

Fig. 2.—Schematic diagram of electromagnetic plate holder for translating and oscillating one interferometer plate.

The other holder provided a means of tilting the second optical flat to a very fine degree in two mutually perpendicular directions. This unit consists essentially of four electromagnets, with four polarizing magnets acting on a soft iron ring assembly. The elastic member is attached to the soft iron assembly so that it is tilted when current passes through the coils. A schematic outline is shown in Figure 3. Details of these holders will be reported elsewhere.

The whole of the interferometer assembly was mounted in a vacuum chamber from which the electrical leads passed to the electrical controller situated close to the observer. A temperature-controlled water jacket was designed to enclose the chamber, but this was not available in time for the present measurements. External vibrations were entirely eliminated by mounting the interferometer on inflated motor tubes (pressure of only a few pounds per square inch) which were sandwiched between two flat plates. The whole of this assembly was mounted on a heavy concerete block.

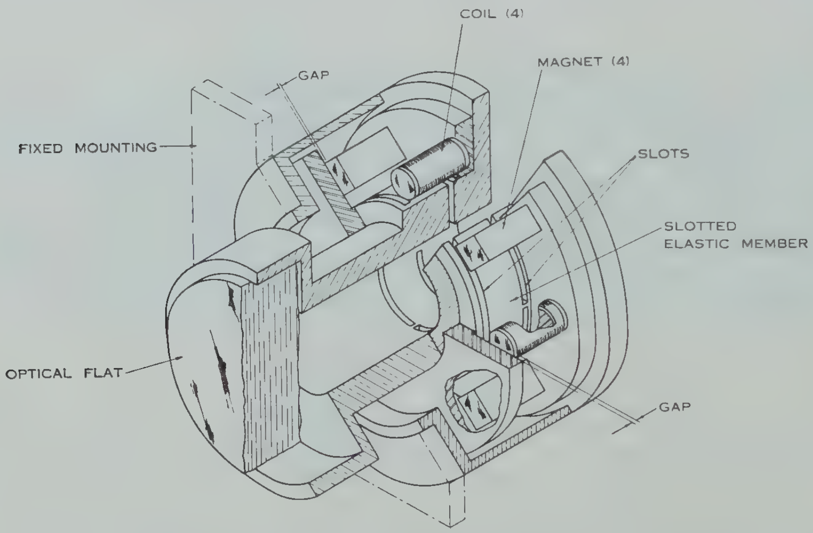

Fig. 3.—Schematic diagram of electromagnetic plate holder for tilting other interferometer plate.

The interferometer could be illuminated with either collimated or convergent light and the Haidinger fringes were projected on to the slit of a prism spectrograph. With a camera lens of focal length 640 mm the dispersion at 5000 Å was 17 Å/mm, using glass prisms.

A special photoelectric head was made to permit simultaneous observation of two spectral lines with two photomultiplier tubes. This head was substituted for the photographic plate holder. With this unit two fairly close lines could be observed, photoelectrically, at the same time. With a camera lens of focal length 1600 mm, even closer lines could be observed.

The plate separation of the interferometer was established conveniently to a few orders of interference by the use of air gauging. A double jet unit was placed between the two optical plates and held in position by means of a spring clip attached to the plate holder so that the gap between one jet and one optical flat was of a convenient value (about 5μ). The other plate could then be brought up towards the second jet by means of a micrometer head controlling the position of the plate in the chamber until a given reading was obtained on a single head Solex air controller. Figure 4 shows the arrangement. Calibration scales had been prepared for jets of different lengths corresponding to different plate separations. The air input was disconnected at the interferometer when the chamber was evacuated but the jet attachment remained in position between the optical plates during measurements. The air gauge reading was checked at the end of a series of measurements. The air jet unit is situated near the edge of the optical plates, but this is of little consequence since the final air gauge readings are taken when the plates are accurately parallel, as observed interferometrically.

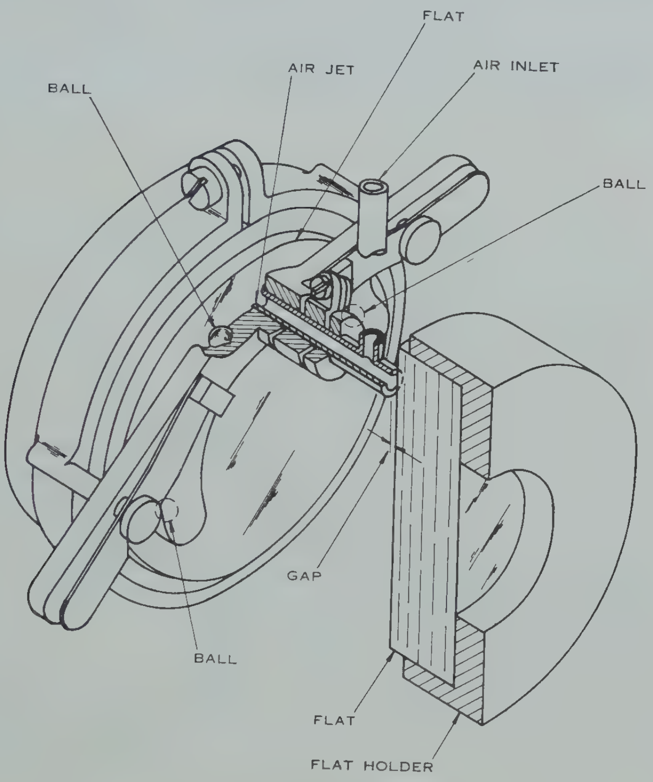

Fig. 4.—Schematic diagram of air-gauging jet unit for setting separation of interferometer plates.

The optical plates were of high quality fused quartz whose flatness over the 25 mm area used was within the limits λ/50–λ/100. Multilayer dielectric and silver films were used on the plates. The seven-layer dielectric films had a reflectance ranging from 92% at 5000 and 6500 Å to a peak of 96% over the region 5560–5880 Å. The absorption was less than 0·8%. These films were specially useful in line profile studies. The silver plates had a reflectance of about 80–85%.

The linearity of the electromagnetic plate holders used for the translation of the optical flat was carefully tested by measuring the displacement of sharp multiple-beam Fizeau fringes for given currents passing through the exciting coil. The currents were determined by measuring the potential difference across a standard resistor in the coil circuit with a high precision potentiometer. A further and final check was obtained from the recorded line profiles of the very sharp spectral lines where the abscissa was found to be strictly proportional to changes in plate separation. The plate holder behaved in a strictly linear fashion and would return to a particular position when the exciting current was switched off and then on. No deterioration in the sharpness of the Haidinger fringes was observed when the plate was moved over several orders of interference.

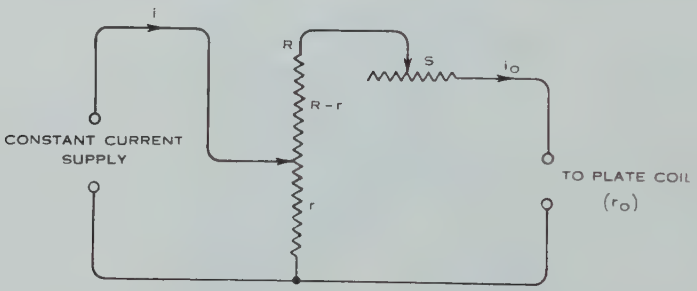

Fig. 5.—Basic electrical circuit of controller for changing plate separation.

The heating effect of the small currents in the exciting coils for the translation and tilting of the optical plates was investigated. With maximum currents of the order of 200 mA in the translation plate coils, there was an initial drift in plate separation of about 0·3 of a fringe in 30 min but a steady state was then reached. In wavelength intercomparisons, currents, on the average, did not exceed 20 mA (power dissipation 0·04 W). Further, the methods used enabled setting points for two wavelengths to be obtained almost simultaneously. The heating effects of the small currents were thus not significant in practice. This was consistently verified throughout measurements.

The current in the coils for the translation and tilt of the optical plates was controlled by variable resistances. The only requirement for the tilt mechanism is that the current control should be fine enough to obtain precise parallelism of the plates, these having already been set mechanically to quite a high degree of accuracy. The translation control is required for accurate and rapid measurement of fringe fractions in wavelength measurement and for recording spectral line profiles in which the abscissa is directly proportional to wave number or plate separation. The important requirement is linearity between the setting of the variable resistance and the current passing through the excitation coil to better than 1 in 1000. The basic circuit is shown in Figure 5, where R is the variable resistance controlling the fringe displacement, r_0 the resistance of the exciting coil, and S is the sensitivity control. The current i_0 through the exciting coil is $ir/(R+S+r_0)$ and thus, if i is constant, $i_0=Kr$, where K is a constant. A constant current power supply provided a current of 200 mA which was constant to better than 1 in 10^4.

For the recording of spectral line profiles, the resistance R was a precision helical potentiometer whose spindle was connected through gears to the drive of a pen recorder. For wavelength measurement, the resistance R became a set of three decade series of special resistors enabling fringe fractions to be measured. Two sets were built into a controller with a switch for selecting either set and with dials for reading to any desired fraction of a fringe. The sensitivity controls were designed specifically to give direct readings of fringe fractions to 0·001 fringe but appropriate changes in the design can give any desired accuracy. Subsequent work showed that a controller designed to read directly to 0·0001 fringe is justified.

IV. Spectral Line Profiles

The spectral line profiles were recorded for the main radiations of krypton 86, mercury 198, and cadmium 114 using a Sefram spot-follower recorder in conjunction with a galvanometer having a sensitivity of 10^{-9} A/mm. The Fabry-Perot etalon was *in vacuo* (less than 0·01 mmHg) and the path difference was 100 mm, giving a spectral range of 0·1 cm^{-1}. Dielectric reflecting films were used for wavelengths down to 4800 Å. Silver films were used for shorter wavelengths. The paper speed of the recorder was 120 mm/min, which through the helical potentiometer gave a uniform scanning speed for the Fabry-Perot etalon of 0·008 fringe/s at 5462 Å. The centre of the ring system of fringes was focused in the centre of a small aperture (0·4 mm diameter) by the camera lens of the spectrograph. Appropriate corrections for the error in centering of the ring system in the aperture were considered and applied to the results. It can be shown that asymmetric profiles, occurring if there is a decentering between aperture and ring pattern, can be used to find half-widths, since, for small decentering errors, only one half of the profile shows asymmetry. Figure 6 shows typical recorded spectral line profiles for the 6057 Å line of krypton 86, the 5462 Å line of mercury 198, and the 6440 Å line of cadmium 114 (nominal vacuum wavelength values).

The instrumental half-width was determined by recording the line profiles at plate separations of less than 1 mm using the various wavelengths from the isotope lamps. At this separation, the true line profile of the spectral lines makes a negligible contribution to the profile, which is purely instrumental. The true half-widths of the spectral lines were subsequently computed using the method of Minkowski and Bruck (1935).

The intensity fluctuations at the centre of the ring pattern were observed with photomultiplier tubes using low noise stabilized power supplies. A tube with a tri-alkali cathode was specially useful for the relatively weak lines in the red region. The linearity of response of the photomultipliers was measured using a calibrated wedge filter, and relative intensities for given lines under different operating conditions were also measured.

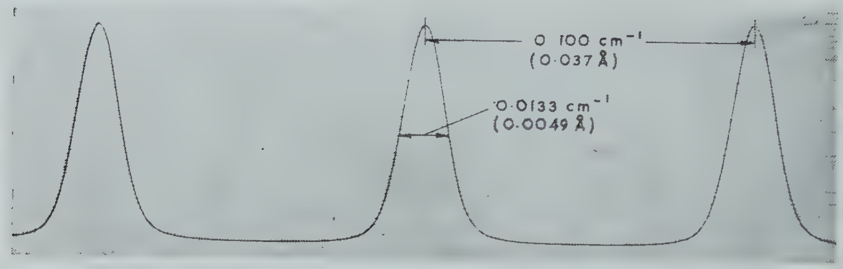

(a) KRYPTON 86 — 6057Å
SPECTRAL RANGE 0·100 cm⁻¹ (0·037Å)

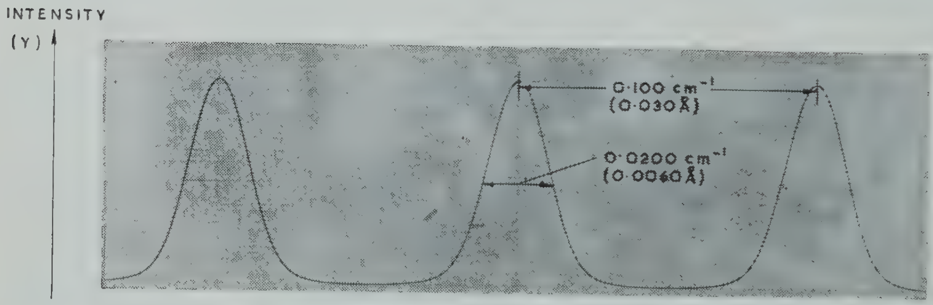

(b) MERCURY 198 — 5462Å
SPECTRAL RANGE 0·100 cm⁻¹ (0·030Å)

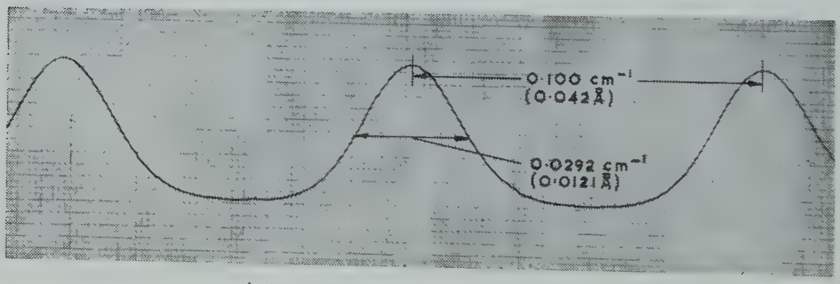

(c) CADMIUM 114 — 6440Å
SPECTRAL RANGE 0·100 cm⁻¹ (0·042Å)

CHART SCALE ⊢ 10 cm ⊣

PATH DIFFERENCE
(X)

Fig. 6.—Recorded spectral line profiles under vacuum conditions. (*a*) 6057 Å line of krypton 86 excited by direct current (current density 0·28 A/cm^2); temperature 63 °K; (*b*) 5462 Å line of mercury 198 excited at 100 MHz; oscillator output 60 W; temperature 285 °K; (*c*) 6440 Å line of cadmium 114 excited at 100 MHz; oscillator output 60–80 W; temperature about 470 °K.

The half-widths could be obtained from the profiles to 0·0005 cm^{-1} and it is considered that the values for the half-intensity widths given in Table 2 are accurate to 0·5 mK (0·0005 cm^{-1}).

The krypton 86 line 6057 Å was studied in further detail, and the effects of current density and temperature of the lamp on half-intensity width and intensity were measured from the recorded profiles. The results are shown in Figures 7, 8, 9, and 10. Results obtained by the Bureau International des Poids et Mésures (BIPM) (Terrien 1957*a*) and PTB (Engelhard 1957*a*) are indicated on the figures for comparison.

TABLE 2

HALF-INTENSITY WIDTHS

Lamp	Details	*t* (°C)	Wavelength (Å)	Half-intensity Width (mK)			
Krypton 86 Hot cathode (PTB)	Excited with d.c.; current density 0·28 A/cm²; temperature at capillary surface of lamp 63 °K; viewed end-on; light direction CAO		6458	15·8			
			6057	13·3			
			5651	14·3			
			4503	18·8			
Mercury 198 Electrodeless	Excited at 100 MHz; oscillator output 50 W; viewed broadside on; cooled with running water to *t* °C			NBS 32	NBS 99	NRC	NSL 7
		12	5792	20·1	20·6	23·1	19·5
		12	5771	19·8	20·4	23·0	20·1
		5	5462	—	—	—	19·7
		15		20·4	20·2	22·2	21·3
		12	4359	18·2	20·0	19·3	19·0
Cadmium 114 Electrodeless (NSL)	Excited at 100 MHz; oscillator output 60–80 W; viewed broadside on; lamp enclosed in outer vacuum jacket; temperature at outer surface of lamp about 200 °C		6440	29·2			
			5087	33·6			
			4801	33·3			
			4679	33·4			
Cadmium natural Osira	Excited at 140 V a.c., 1 A		6440	36·9			
			5087	49·8			
			4801	43·2			
			4679	42·5			

The effect of temperature (as measured by the thermocouples on the capillary of the lamp) on the half-intensity width is shown in Figure 7 for a current density of 0·28 A/cm². The half-width of the line at 63 °K is about 30% broader than the theoretically computed Doppler width. Further, the half-width is not proportional to the square root of the measured temperature over the range of temperatures studied (55–70 °K) but within 1 mK was proportional to the square of the temperature. If pure Doppler broadening is assumed the "emission temperature" corresponding to the energy of the excited atoms is about 108 °K when the temperature of the lamp surface is 63 °K. This was computed using the Doppler relation

$$T = M\omega^2c^2/5\cdot578R\nu^2,$$

where T=absolute temperature,
M=molecular weight of the gas,
ω=half-width in cm^{-1},
c=velocity of light,
R=universal gas constant,
ν=wave number in cm^{-1}.

The relationship for the Doppler line broadening considers only the physical properties of the gas and does not consider Stark broadening that may occur from the current density existing during measurement. Figure 8 shows the relationship between the half-width and current density, and from this graph the half-width at zero current density is about 10·8 mK, which corresponds quite closely to a temperature of 63 °K.

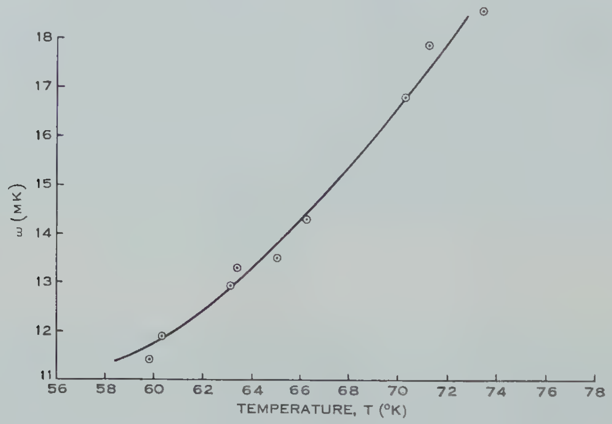

Fig. 7.—Effect of temperature T on line half-width ω for krypton 86–6057 Å ; current density 0·28 A/cm².

Over the temperature range 60–65 °K the relation between half-width and temperature is fairly linear and the relation $\omega = 0\cdot38T + 11$ (ω in millikaysers and T in degrees Kelvin) fits the curve to well within 0·5 mK. It follows that the half-width value is constant to within ±0·5 mK for a tolerance of ±1 degK on the temperature T.

The effect of current on half-width (Fig. 8) is fairly linear over the range 0–40 mA and the relation $\omega = 0\cdot12i + 11$ fits the curve to within 0·5 mK where i is in milliamperes and ω in millikaysers. As the capillary diameter of the lamp was 3 mm, a tolerance of ±0·05 A/cm² on current density would establish the half-width to within 0·5 mK.

Appropriate limits on current density and temperature as measured at the surface of the lamp would therefore be (0·25±0·05) A/cm², and (63±1) °K respectively. This establishes the half-width to within 1 mK.

The effect of temperature on the intensity of the 6057 Å line (Fig. 9) was found to be in good agreement with the results of Engelhard (1957*b*). However, the effect of current on intensity was different from that found by Engelhard (1957*c*). For this reason a second set of independent readings was taken and this is shown in Figure 10. The relation between intensity I and current i which fitted the observed points best was $I = ki^m$, where m was about 0·33.

The half-width obtained for the cadmium 114 6440 Å line as emitted by the NSL type electrodeless lamp was compared with results reported by Terrien (1957*b*), who used a lamp supplied by the Institute of Metrology (I.M.) of the U.S.S.R. (Batarchoukova, Kartachev, and Romanova 1954). The temperature of the I.M. lamp was maintained by an electric furnace and the oscillator was excited at 300 MHz. The NSL lamp, as already mentioned, maintained itself at a high enough temperature by the use of a surrounding vacuum jacket and was excited at 100 MHz. The observed half-widths and furnace temperatures reported for the I.M. lamp are plotted in Figure 11 and there is clearly a linear relationship between half-width and temperature over the range 230–270 °C. Using this graph and the observed half-width value for the NSL lamp, the temperature at the surface of this lamp would be about 195 °C. This value agrees very well with the measured value at the surface of the natural cadmium lamp in its vacuum jacket.

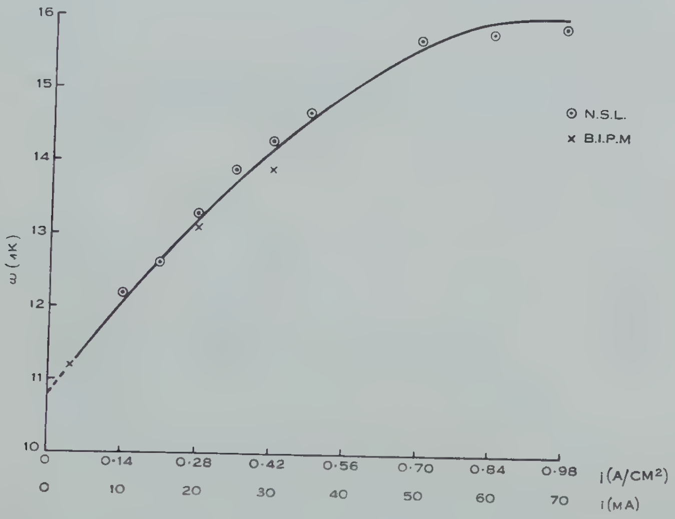

Fig. 8.—Effect of current density j on line half-width ω for krypton 86–6057 Å; temperature 63 °K.

The half-width of the 6440 Å line was about 30% sharper than the same line emitted by an Osira-type lamp containing natural cadmium and operated at 140 V and 1 A alternating current. The intensities of the lines from the cadmium 114 lamp were several times greater than those from the Osira lamp while the power required to excite the lamp was only a fraction of that used for the Osira lamp. Therefore, this lamp seems to be a very satisfactory source of secondary wavelength standards in metrology. The fact that cadmium 114 emits four strong lines well distributed and separated in the visible spectrum makes it particularly attractive as a source of working optical standards of length.

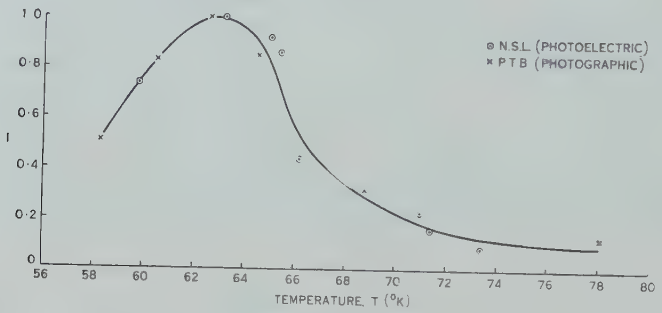

Fig. 9.—Effect of temperature T on intensity I for krypton 86–6057 Å; current density 0·28 A/cm².

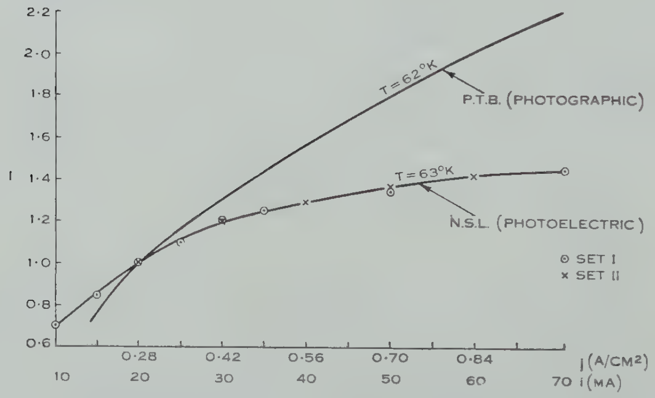

Fig. 10.—Effect of current density j on intensity I for krypton 86–6057 Å; temperature 63 °K.

V. Wavelength Measurements

(a) *Photoelectric Method*

The vacuum wavelengths of four main radiations from each of the isotope lamps were measured using the photoelectric recording method described in Section III.

Throughout, the reference wavelength was obtained from the radiation corresponding to the transition between the levels $2p_{10}$ and $5d_5$ of the atom of krypton 86. This radiation has been accepted internationally as the primary standard, and it has been recommended that the metre be defined as 1 650 763·73 wavelengths in vacuo of this radiation. The wavelength in vacuo is then 6057·802106 Å where 1 Å$=10^{-10}$ m. This is the standard value used throughout.

One interferometer plate was oscillated at a frequency of about 20 c/s, and the intensity fluctuations at the centre of the ring system were observed for two different wavelengths with two photomultiplier tubes mounted on the spectrograph. A small aperture situated at the principal focus of the telescope lens of the spectrograph restricted, to a desired amount, the area of the central spot of the fringe system observed photoelectrically. The obliquity effect due to the integration of light from the finite area was negligible. The fringes were brought to a sharp focus in the plane of the viewing aperture. The light emerging from the apertures was collimated by a small lens on to the photocathodes of the photomultiplier tubes and the output from a selected photomultiplier tube was passed through a tuned amplifier and then to the Y-plates of an oscillograph. The output from the oscillator producing the scanning frequency of the interferometer plates was connected to the X-plates of the oscillograph. The oscillograph is thus a synchronous detector that can point on a bright fringe maximum with high sensitivity.

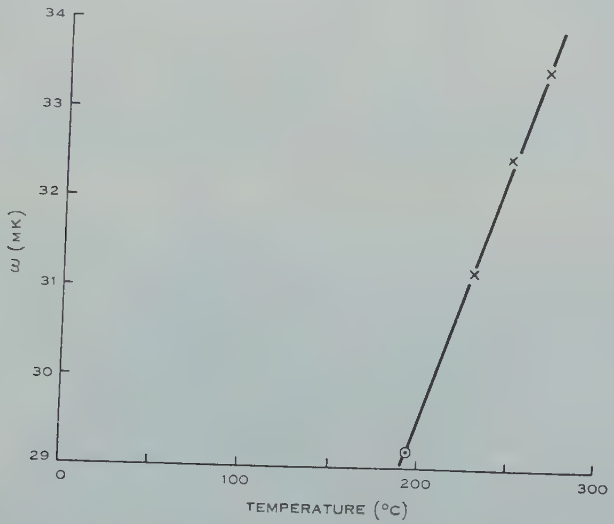

Fig. 11.—Effect of temperature I on line half-width ω of cadmium 114–6440 Å. × BIPM ; ⊙ NSL.

With one interferometer plate scanning over a double amplitude of about 0·1 fringe, the plate was gradually moved by the electrical controls until the Lissajous figure on the oscillograph indicated zero signal on the Y-plates. This indicated precise setting on the peak of a fringe. The change in interferometer plate separation, or, change in order of interference, required to set on a bright maximum could be read directly from the dials of the electrical controller.

The fine control and measurement of the change in the plate separation necessary to set on the peak of a bright fringe was obtained by replacing the resistance R, Figure 5, by three sets of 10 resistance coils making up three decades. The basic circuit is shown in Figure 12. If r is the resistance of each coil in R_1, then $R_1=10r=10R_2=100R_3$. The resistances in each decade were made equal and $R_1/R_2=10$ and $R_1/R_3=100$ to the required accuracy. The resistance R_3'

is a compensating resistance linked with R_3 in order to keep the total resistance in the circuit constant. This arrangement was duplicated and the two groups incorporated in a controller so that, by the throw of the selector switch, observations could be taken at one wavelength and then the other. Thus two wavelengths could be compared almost simultaneously.

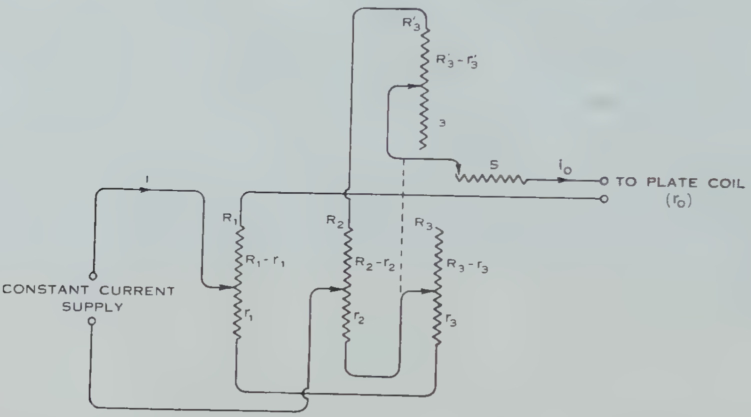

Fig. 12.—Basic electrical circuit of a single channel of the controller for precise measurement of fractional orders of interference.

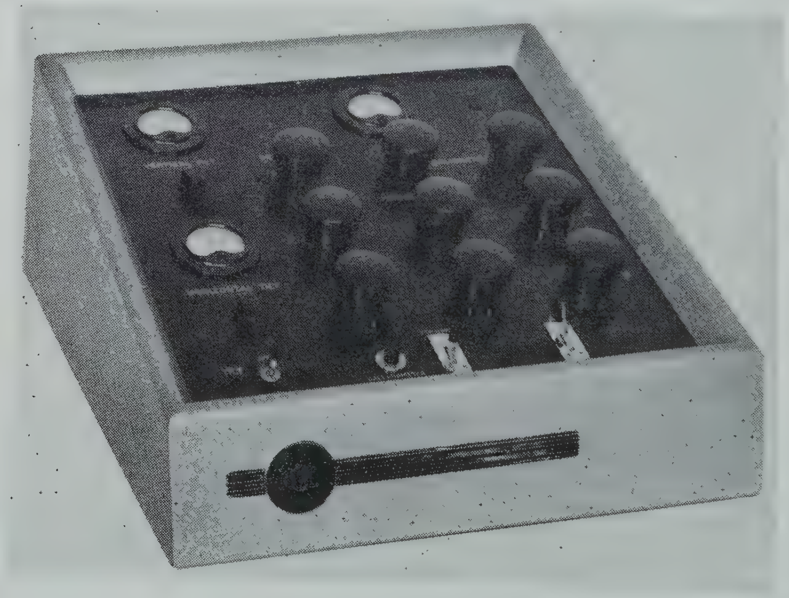

Fig. 13.—Control panel of electrical controller.

Figure 13 is a photograph of the instrument panel of the controller and Figure 14 is a block diagram of the optical, scanning, and photoelectric recording systems.

The procedure adopted was to obtain the fringe spacing for the standard wavelength before and after a set of independent settings as a calibration check for both the standard and unknown wavelengths.

If the setting on the standard λ_A is A and that on the unknown λ_B is B, then the series of settings is $A_1\ B_1\ A_2\ B_2\ A_3\ B_3\ A_4\ B_4\ A_5$. If the fringe spacing is C, then the fringe fraction for λ_A is taken to be $(A_1+A_2)/2C$, $(A_2+A_3)/2C$, etc., and the corresponding fraction for λ_B is B_1/CR, B_2/CR, etc., where $R=\lambda_B/\lambda_A$ and need only be known approximately. Obviously, by adjustment of the sensitivity of the controller, C may be made unity and then the dial readings are direct fractional orders for λ_A. In practice, it was found convenient to make C slightly less than unity. A single wavelength determination involving settings ABA took about 15 s.

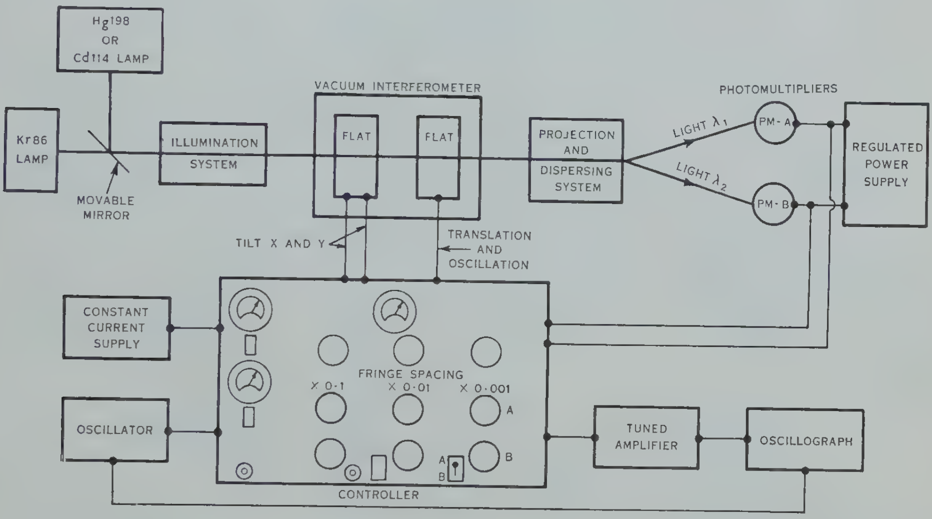

Fig. 14.—Block diagram of the optical, mechanical scanning, and photoelectric recording system used in wavelength measurement.

The measurements were done at a path difference of 100 mm, and at 16 mm to eliminate phase dispersion effects. The integral order of interference was established from the fairly exact knowledge of the plate separation by air gauging, as described earlier, and the observed fractional orders at different wavelengths.

The mean measured values of the vacuum wavelengths are given in Table 3 (*a*).

The mercury 198 wavelength values are those obtained at a temperature of 283 °K and are uncorrected for pressure shift.

The cadmium 114 wavelength values are those obtained for a temperature of about 470 °K and are uncorrected for pressure shift.

(*b*) *Photographic Method*

Some photographic measurements were done by the conventional methods in order to compare the accuracy of the photoelectric methods with them. The fringes were photographed on high speed panchromatic plates, the complete visible spectrum for each lamp being recorded in the sequence Kr 86–Hg 198–Kr 86–Hg 198–Kr 86–Hg 198–Kr 86 on one plate. This sort of sequence can be used to reduce temperature effects in comparing the Hg 198 spectrum results with the standard Kr 86 orange-red line. However, different exposure times were necessary for different lines in the one spectrum. In such cases, temperature drift during the time intervals involved (up to 60 s) could influence the position of the centre of density of the recorded image of the fringe on the photographic plate. This effect was in fact detectable on analysing the records. The photoelectric method on the other hand ensured that the observations on standard and unknown were almost simultaneous.

Table 3 (*a*)

MEASURED VACUUM WAVELENGTHS

Reference wavelength : krypton 86, $6057 \cdot 802106 \times 10^{-10}$ m

Radiation	Lamp	Measured Wavelength (Unit : 1×10^{-10} m)		Standard Deviation ∇ (10^{-10} m)	N*
		Whole Part	Fractional Part		
Krypton 86 ..	PTB	6458	07240	0·000 09	15
		5651	12851	0·000 07	15
		4503	61553	0·000 04	14
Mercury 198 ..	NSL 7	5792	26816	0·000 15	14
	NBS 99		26797	0·000 13	8
	NRC		26799	0·000 07	8
	NBS 32		—	—	—
Mercury 198 ..	NSL 7	5771	19772	0·000 08	11
	NBS 99		19826	0·000 09	14
	NRC		19856	0·000 08	15
	NBS 32		—	—	
Mercury 198 ..	NSL 7	5462	27029	0·000 03	16
	NBS 99		27064	0·000 04	8
	NRC		27053	0·000 02	8
	NBS 32		27063	0·000 02	8
Mercury 198 ..	NSL 7	4359	56227	0·000 04	16
	NBS 99		56239	0·000 03	16
	NRC		56157	0·000 06	14
	NBS 32		56145	0·000 15	8
Cadmium 114 ..	NSL	6440	24659	0·000 10	16
		5087	23849	0·000 11	8
		4801	25358	0·000 12	6
		4679	45526	0·000 40	4

* N = number of determinations.

The photographic plates were measured on two comparators by two observers using 3–5 rings in the pattern. The fractional orders of interference were obtained in the usual way by the method of least squares.

The photographic results are given in Table 3 (*b*) together with photoelectric results for the krypton 86 lines and the mercury 198 green line from three different lamps.

The krypton 86 lamp was operated as described earlier, the capillary surface temperature being 63 °K and the current density 0·28 A/cm². The light direction for viewing was CAO.

TABLE 3 (*b*)

COMPARISON OF MEASURED VACUUM WAVELENGTHS

Reference wavelength: krypton 86, $6057 \cdot 802106 \times 10^{-10}$ m

A, photoelectric; B, photographic

Radiation	Lamp	Measured Wavelength (Unit: 1×10^{-10} m)		Standard Deviation ∇	*N*
		Whole Part	Fractional Part		
Krypton 86 ..	PTB	6458 A	07240	0·000 09	15
		B	07278	0·000 37	9
		5651 A	12851	0·000 07	15
		B	12865	0·000 28	8
		4503 A	61553	0·000 04	14
		B	61567	0·000 13	10
Mercury 198 ..	NSL 7	5462 A	27029	0·000 03	16
		B	27034	0·000 39	9
	NBS 99	5462 A	27064	0·000 04	8
		B	27083	0·000 21	9
	NRC	5462 A	27053	0·000 02	8
		B	27094	0·000 19	10

VI. THE KRYPTON 86 RADIATION $2p_{10}$–$5d_5$ ($\lambda_{\text{vac.}}$=6057 Å)

The recommended value by convention of 1 650 763·73 vacuum wavelengths per metre of the krypton orange-red radiation refers to the wavelength as radiated from the atoms of krypton 86 in the unperturbed state. In practice, the wavelength actually emitted is influenced by (*a*) the motion of the radiating atoms in the line of sight (Doppler effect) and (*b*) the pressure and current density in the lamp (interatomic Stark effect).

It is of importance, therefore, to obtain exact knowledge of the change in wavelength due to the Doppler effect (Doppler shift $(\Delta\sigma)_D$) and the change due to the effect of pressure and current density (Stark shift $(\Delta\sigma)_S$). The effects are small and they may be expressed as a wavelength shift $\Delta\lambda$. However, having in mind the recommended definition of the metre, it is more appropriate to express the effects as a change in the number of waves per metre $(\Delta\sigma)_D$ and $(\Delta\sigma)_S$.

If $\Delta\lambda$ is expressed in 10^{-6} Å and $\Delta\sigma$ in m^{-1}, then $\Delta\lambda = -3669\,\Delta\sigma$ for the radiation under consideration here.

The Doppler and Stark shifts were measured using the photoelectric recording interferometer described in Section III, at different temperatures and current densities, using an Engelhard-type hot cathode krypton 86 lamp. It was operated in the same manner as already described by Engelhard and Terrien (1960), except that there was no stirrer within the liquid air.

The shift in wavelength due to a change in the direction of viewing or to a change in current density was immediately visible on the cathode-ray oscillograph. The change in fringes was read directly from the dials of the electrical controller when the adjustment was made to give zero signal. A path difference of 100 mm was used throughout and shifts of a few parts in 10^9 could be measured.

(*a*) *Doppler Shift* $(\Delta\sigma)_D$

The lamp was viewed first from the anode side of the lamp (CAO) and then from the cathode side of the lamp (ACO) and the dial readings of the controller taken for a setting on a fringe maximum for both methods of viewing. The viewing direction could be changed rapidly by the movement of a single mirror. Due precautions were taken to see that correct imaging and illumination existed for both methods of viewing.

The wavelength λ for the undisturbed state of the atom shifts to $\lambda + \Delta\lambda$ when the lamp is viewed from the cathode side (ACO). The corresponding shift in wavelength when the direction of propagation is in the opposite sense (CAO) is $\lambda - \Delta\lambda$.

TABLE 4

DOPPLER SHIFT $(\Delta\sigma)_D$ FOR KRYPTON 86–6057 Å LINE

Temperature 63 °K

No.	Laboratory	$(\Delta\sigma)_D$ (Light Direction CAO) (m^{-1})	Reference
1	NSL	+0·014	
2	PTB	+0·024	Engelhard (1957*d*)
3	NPL	+0·009	Barrel (1957)
4	NRC	+0·013	Baird and Smith (1959)
5	PTB–BIPM	+0·019	Engelhard and Terrien (1960)

With the surface of the capillary of the lamp at 63·0 °K, and a current density of 0·28 A/cm², the value of $2\Delta\lambda$ was measured and found to be 100×10^{-6} Å. The value of $\Delta\lambda$ is therefore -50×10^{-6} Å if the light direction is CAO, and $+50 \times 10^{-6}$ Å if the light direction is ACO. The standard deviation for 50 determinations was 10×10^{-6} Å. The value of $(\Delta\sigma)_D$ is therefore $+0{\cdot}014\ m^{-1}$ if light direction is CAO, and $-0{\cdot}014\ m^{-1}$ if light direction is ACO, with a standard deviation of $0{\cdot}003\ m^{-1}$. The result is compared with results from other laboratories in Table 4.

(i) *Effect of Temperature and Current Density.*—There was no significant variation in $(\Delta\sigma)_D$ with current density over the range $0\cdot1$–$1\cdot0$ A/cm^2.

The effect of temperature was also very small. Table 5 reports observed changes in $(\Delta\sigma)_D$ for a change in temperature from 63 to 61 °K for light direction CAO. Results of PTB and BIPM are also given for comparison.

TABLE 5

CHANGE IN DOPPLER SHIFT WITH TEMPERATURE

No.	Laboratory	Change in Doppler Shift for Change in Temperature from 63 to 61 °K (m^{-1})	Reference
1	NSL	$+0\cdot006$	
2	PTB	$+0\cdot001$	Engelhard and Terrien (1960)
3	BIPM	$+0\cdot006$	Engelhard and Terrien (1960)

(*b*) *Interatomic Stark Shift* $(\Delta\sigma)_S$ (*Pressure and current density effect*)

The procedure adopted here was again to use one lamp and observe the wavelength shift on changing the current density by a fixed amount over a range of temperatures and the shift on changing the current density by different amounts at a constant temperature. The direction of light propagation throughout was CAO.

The wavelength shift is towards the red and follows the approximate law

$$(\Delta\lambda)_S = K(pj)^{2/3}, \tag{1}$$

when p is the pressure of the krypton in the lamp and j is the current density. The pressure in the lamp is computed from the temperature T (°K) at the capillary surface of the lamp, using the Meihuizen (1940) formula

$$\log P_{\mathrm{cm}} = -607\cdot69/T + 7\cdot2955 - 0\cdot0026675T.$$

(i) *Absolute Value of* $(\Delta\sigma)_S$.—The absolute value of $(\Delta\sigma)_S$ was established in three ways.

(1) The wavelength shift was observed when the current density was changed from $0\cdot28$ A/cm^2 to $1\cdot12$ A/cm^2 (20–80 mA current) with the temperature at 63 °K, and the value of K calculated assuming equation (1) is valid. It was found to be 255 ($\nabla=35$, $N=15$) if $(\Delta\lambda)_S$ is in 10^{-6} Å, p in mmHg, and j in mA/mm^2. With $K=255$, the absolute value of $(\Delta\sigma)_S$ was calculated for $T=63$ °K and $j=0\cdot28$ A/cm^2.

(2) A $(\Delta\sigma)_S$–$j^{2/3}$ straight line graph was obtained from the plotted values of $(\Delta\sigma)_S$ (relative) and of $j^{2/3}$ (absolute), and the graph extrapolated to $j=0$. This established the abscissa and therefore absolute values for $(\Delta\sigma)_S$.

(3) A $(\Delta\sigma)_S$–$p^{2/3}$ straight line graph was plotted as in (2) and the graph extrapolated to $p=0$ and the absolute value of $(\Delta\sigma)_S$ again was found.

The results are given in Table 6, together with results from other laboratories.

Table 6

STARK SHIFT $(\Delta\sigma)_S$ FOR KRYPTON 86–6057 Å LINE

Temperature 63 °K, current density 0·28 Å/cm²

No.	Laboratory	Method	$(\Delta\sigma)_S$ (m^{-1})	Reference
1	NSL	(1)	—0·014	
2	NSL	(2)	—0·015	
3	NSL	(3)	—0·012	
4	NSL	Mean	—0·014	
5	PTB–BIPM	—	—0·019	Engelhard and Terrien (1960)
6	NRC	—	—0·011	Baird and Smith (1959)

The light direction for results 1–3 was CAO and for 6, ACO, but theoretically light direction should have no significance.

(ii) *Effect of Current Density.*—The results are shown in Figure 15. The full curve is the mean of the results of PTB and BIPM individually (Engelhard and Terrien 1960). There is almost exact agreement between this curve and the NSL values for the rate of change of $(\Delta\sigma)_S$ with current density. The difference in absolute values of $(\Delta\sigma)_S$ between NSL and PTB–BIPM (Table 6) is only about 3 parts in 10^9.

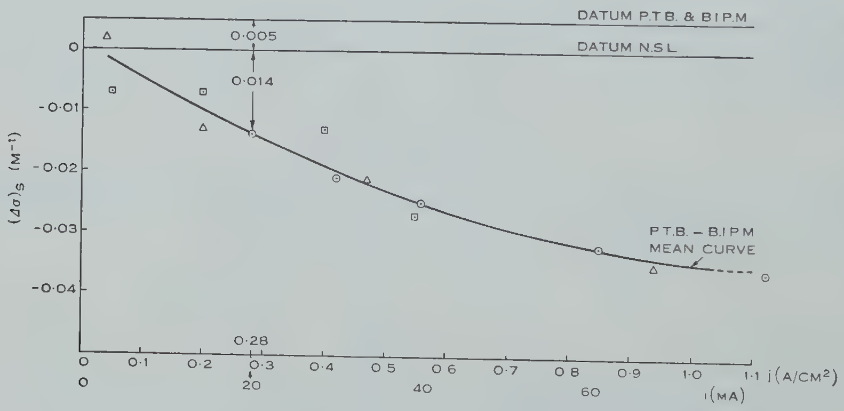

Fig. 15.—Effect of current density j on Stark shift $(\Delta\sigma)_S$ of krypton 86–6057 Å expressed as a variation in the number of waves per metre. Temperature 63 °K.
⊙ NSL, △ PTB, ⊡ BIPM.

(iii) *Effect of Temperature* (*Pressure shift*).—The Stark shift over a temperature range 59–70 °K has been measured and the results are given in Figure 16 for a current density of 0·28 A/cm². Again, comparing the graph of PTB–BIPM (Engelhard and Terrien 1960) with the NSL result (light direction CAO), values from the curves are given in Table 7.

(iv) *Effect of Temperature on the* K *Value.*—The value of K in relation (1) at different temperatures is plotted in Figure 17 and indicates the approximate nature of the relation. The variation appeared to have some correlation with the intensity of the line (see Fig. 9). This point was not pursued further.

VII. Discussion

The photoelectric recording methods described here have measured with high precision the quality of various radiations under vacuum conditions.

Small wavelength changes of 2–3 parts in 10^9 are measurable and, with photomultiplier cells of adequate sensitivity, wavelengths have been compared with the krypton 86 orange-red radiation with an accuracy of better than 1 part in 10^8. These results were obtained with the interferometer in an accurately temperature-controlled room, but without the thermostatically controlled water jacket. The work showed that as a result of the procedures and techniques used, temperature drift effects were extremely small. Nevertheless, with techniques which have been proved capable of measuring displacements to nearly 1 part in 10^9, it is anticipated that improved results will be obtained with more accurate temperature control.

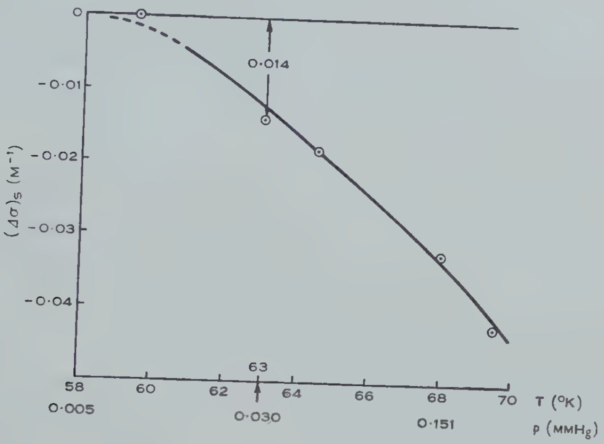

Fig. 16.—Effect of temperature T (pressure shift) on Stark shift $(\Delta\sigma)_S$ of krypton 86–6057 Å, expressed as a variation in the number of waves per metre. Current density 0·28 A/cm².

The more serious limitation on higher accuracies in the present experiments was the degree of response of the available photomultiplier tubes to some of the

Table 7

CHANGE IN STARK SHIFT WITH TEMPERATURE

No.	Laboratory	j (A/cm²)	Change in Stark Shift for Temperature Change from 63 to 62 °K (m⁻¹)	Reference
1	PTB	0·14	+0·004	Engelhard and Terrien (1960)
2	BIPM	0·14	+0·006	Engelhard and Terrien (1960)
3	NSL	0·28	+0·003*	Fig. 16

* Assuming the $j^{2/3}$ law, the NSL result for 0·14 A/cm² would be +0·002 m⁻¹.

less intense lines. The tri-alkali type of tube is excellent for this work, but only one was available, and use had to be made of other types of tubes of much lower efficiency in conjunction with this one, in the two-channel photoelectric system. The magnitude of the standard deviations for different radiations in the wavelength measurements is largely a measure of the efficiency of the photoelectric detector at that radiation. This limitation will shortly be removed and, with highly efficient temperature control, it is considered that wavelength measurements can be made reliable to a few parts in 10^9.

The superiority of the photoelectric detection methods over the conventional photographic methods is shown in Table 3 (*b*). The standard deviations stated can be improved for both the photoelectric and photographic methods, the latter by better temperature control and the former mainly by increased overall photoelectric detection sensitivity. The speed with which fractional orders of interference are observed directly and the removal of the tedium of photographic plate measurement and subsequent reduction of results in the photographic method are major advantages of the photoelectric method.

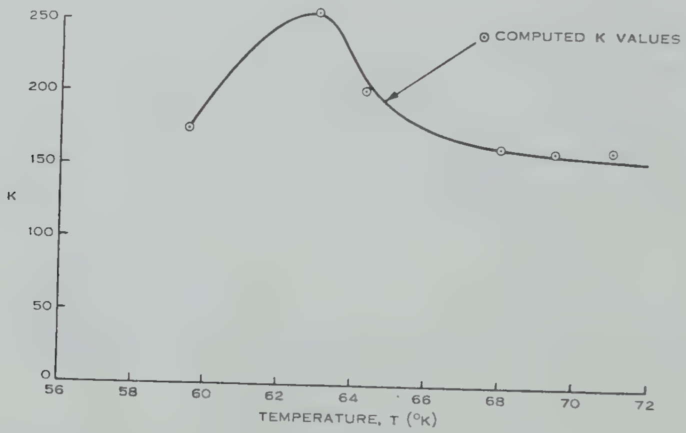

Fig. 17.—Variation of value of Stark shift constant *K* with temperature *T*.

The krypton 86 radiation $2p_{10}$–$5d_5$, which is recommended for adoption as the primary standard, has been studied in detail. The Engelhard-type lamp performs most reliably, and the pressure and current density at which it operates can be controlled and evaluated with adequate accuracy.

The line profile study of this radiation showed that its half-intensity width is constant to at least ±0·5 mK (0·0005 cm^{-1}) if the temperature at the capillary of the lamp is constant to ±1 °K and if the current density is constant to ±0·05 A/cm^2.

The Doppler shift is independent of current density and has the value +0·014 m^{-1} (−50×10^{-6} Å) when the temperature is 63 °K and when the direction of propagation of light is from cathode to anode to observer (CAO).

The Stark shift has the value $-0\cdot014\ \mathrm{m}^{-1}$ when the temperature is 63 °K, the current density $0\cdot28\ \mathrm{A/cm}^2$, and the light direction CAO. It does not vary by more than $\pm0\cdot004\ \mathrm{m}^{-1}$ if the temperature changes by ±1 °K or more than $\pm0\cdot003\ \mathrm{m}^{-1}$ if the current density changes by $\pm0\cdot05\ \mathrm{A/cm}^2$.

Thus, if the lamp is operated at a temperature of 63 ± 1 °K (at the surface of the capillary) and a current density of $0\cdot28\pm0\cdot05\ \mathrm{A/cm}^2$, (current of 20 mA for a 3 mm diameter capillary) and viewed so that the direction of propagation of light is from cathode to anode to observer, the wavelength emitted is that for the unperturbed state of the krypton 86 atoms, to 2–3 parts in 10^9. It is this wavelength that would define the metre.

There was evidence of considerable variation in the wavelength values for the mercury lines from various electrodeless lamps. There was, in addition, some evidence of quite short period variation (seconds) in the wavelength of the emitted light from a single lamp. This was particularly noticeable when an attempt was made to use the mercury 198 green radiation as a reference wavelength in studying variations in the wavelength of the krypton 86–6057 Å line for different conditions of lamp operation.

The wavelength values given for the cadmium 114 electrodeless lamp are the least reliable. As explained earlier, the amount of pure cadmium 114 metal in the lamp was inadequate, owing to insufficient supply of the isotope in proper form. Further supplies did not become available in time for other lamps to be made for use in the measurements. From the life tests on identical lamps made with natural cadmium, there is no reason to doubt that the form of electrodeless lamp described here will be satisfactory. The intensity distribution and separation of the cadmium 114 radiations are all extremely suitable for much work in length measurement. It is considered that, though the mercury 198 and cadmium 114 radiations from electrodeless lamps cannot compete with the krypton 86 orange-red radiation in quality as a primary standard, they have many attractive features as secondary working standards. Such radiations may become very strong competitors as a primary standard with the development of atomic beam sources. However, it is also possible that other parts of the electromagnetic spectrum may supply even better primary standards in the future. In all cases the principle of using a natural atomic unit as the primary standard of length is likely to remain. The best existing unit of this kind is the orange-red radiation $2p_{10}$–$5d_5$ of the krypton 86 atom which is reproducible to 2 to 3 parts in 10^9.

VIII. ACKNOWLEDGMENTS

The authors are indebted to the following colleagues for assistance with various aspects of the work.

The principle employed in the electromagnetic plate holders was one that was applied by the Division of Electrotechnology of this Laboratory in the design of a calculable capacitor operating under vacuum conditions. Mr. W. K. Clothier of that Division was responsible for the basic design and he has given much valuable advice on electrical aspects of their operation.

Mr. R. S. Fisher constructed the constant current supply and the electrical controller, and Mr. E. Phair made the mercury 198 and cadmium 114 lamps.

Mr. P. J. Sim, Mr. R. S. Brockman, Miss I. D. Herberg, and Miss W. A. Colahan also assisted in the work. The schematic diagrams were prepared by Mr. H. M. King, and the general design and constructional work was done by the drawing office and workshops of the Division.

IX. References

Advisory Committee of the International Committee of Weights and Measures (1957).—*P.V. Com. Int. Poids Més.* **26B**: M30.

Baird, K. M., and Smith, D. S. (1959).—*Canad. J. Phys.* **37**: 832.

Barrell, H. (1957).—*P.V. Com. Int. Poids Més.* **26B**: M80.

Batarchoukova, N. R., Kartachev, A. I., and Romanova, M. F. (1954).—*P.V. Com. Int. Poids Més.* **24**: 121.

Engelhard, E. (1952).—*P.V. Com. Int. Poids Més.* **23A**: 165.

Engelhard, E. (1957*a*).—*P.V. Com. Int. Poids Més.* **26B**: M66.

Engelhard, E. (1957*b*).—*P.V. Com. Int. Poids Més.* **26B**: M68.

Engelhard, E. (1957*c*).—*P.V. Com. Int. Poids Més.* **26B**: M69.

Engelhard, E. (1957*d*).—*P.V. Com. Int. Poids Més.* **26B**: M58.

Engelhard, E., and Terrien, J. (1960).—*Rev. Opt. (Théor. Instrum.)* **39**: 11.

Meggers, W. F., and Westfall, F. O. (1950).—*J. Res. Nat. Bur. Stand.* **44**: 447.

Meihuizen, J. J. (1940).—Dissertation, Leiden.

Minkowski, R., and Bruck, H. (1935).—*Z. Phys.* **95**: 299.

Terrien, J. (1957*a*).—*P.V. Com. Int. Poids Més.* **26B**: M150.

Terrien, J. (1957*b*).—*P.V. Com. Int. Poids Més.* **26B**: M141.

THE CHARACTERISTICS OF PERSISTENT SPORADIC METEOR ECHOES

By J. W. Smith*

[*Manuscript received September* 19, 1960]

Summary

This paper examines the frequency distribution of the durations of nearly 8000 persistent radio echoes from sporadic meteors recorded at Adelaide during 1957. The maximum line densities in the trails formed by these meteors exceed 10^{13} electrons/cm, corresponding to visual magnitudes $<+3$. As the echo duration increases, the numbers of echoes are found to fall progressively further below the numbers expected from a power-law distribution. No significant seasonal or diurnal variation in the mass distribution of the meteors examined is apparent.

Echo trace irregularities, which have been classified into five distinct types, are present in 43% of the persistent echoes recorded. Four of these types of irregularity are attributed to distortion of the trail due to atmospheric turbulence, whilst the fifth (leader echo) type is associated with the process of trail formation. The characteristics and diurnal variation in incidence of each type are examined in detail.

I. Introduction

A comprehensive theoretical treatment of the scattering of radio waves by the ionized column formed when a meteor enters the Earth's atmosphere has been given by Kaiser and Closs (1952). They showed that two distinct types of scattering occur, depending on whether the electron line density α of the column is less than or greater than $2\cdot4\times10^{12}$/cm. If $\alpha<2\cdot4\times10^{12}$/cm, the incident wave penetrates throughout the ionized column and the electrons scatter coherently and independently; although in the case where the incident electric vector is normal to the trail there may be an enhancement of scattering due to resonance. As the column expands the echo exhibits an exponential decay, the time τ required for the amplitude to decay to 1/e of the maximum amplitude being

$$\tau=\lambda^2/16\pi^2D, \tag{1}$$

where λ is the wavelength and D the ambipolar diffusion coefficient. This is the so-called " decay " type echo.

If, however, $\alpha>2\cdot4\times10^{12}$/cm, the incident wave does not penetrate throughout the column and the reflection process is similar to that from an expanding metal cylinder. In this case the echo will persist, with little change in amplitude, until diffusion causes the axial electron density to fall below the critical value, after which the type of scattering changes and the echo decays rapidly and exponentially as before. Echoes such as these are classed as persistent. The time for which the echo persists before its eventual decay is given approximately by

---

* Division of Radiophysics, C.S.I.R.O., at Department of Physics, University of Adelaide.

$$\tau = 1 \cdot 124 \times 10^{-12} (\lambda^2 / 16\pi^2 D)\alpha. \tag{2}$$

Theoretical curves showing the variation of the reflection coefficient with $D\tau/\lambda$ for different values of α, given by Kaiser and Closs (1952), show that, as is to be expected, there is not an abrupt change of echo type at $\alpha = 2 \cdot 4 \times 10^{12}$/cm. The transition between the two types occurs smoothly in the range $10^{12} < \alpha < 10^{13}$/cm.

Because of the exponential form of the decay, the duration measured for a decay type echo will depend on the echo amplitude. It is not until $\alpha > 10^{13}$ electrons/cm that the echo duration becomes essentially independent of amplitude and hence of equipment sensitivity.

The problem of the frequency distribution of meteor echo durations measured by radio techniques has been treated theoretically by Kaiser (1953, 1955). He has shown that for persistent echoes received from meteor trails produced by evaporation of solid meteor particles in an isothermal atmosphere, the number of echoes N_τ whose duration exceeds τ is

$$N_\tau \propto \tau^{3(1-s)/4}. \tag{3}$$

In this relation, which applies to both shower and sporadic meteors, s is the exponent in the assumed differential meteor mass distribution

$$\nu_m \mathrm{d}m = bm^{-s}\mathrm{d}m, \tag{4}$$

where $\nu_m \mathrm{d}m$ is the number of meteors in the mass range m to $m + \mathrm{d}m$, crossing unit area normal to their direction of flight per unit time ; b is a constant.

If the distribution described by the relation (3) applies in practice, it should be possible to obtain the value of s, both for the major showers and the sporadic background, by measuring the distribution of radio echo durations. Results for three of the major showers, the Perseids, Arietids, and Geminids, have been given by Kaiser (1953) and Browne *et al.* (1956). In the case of the sporadic background, however, no previous extended survey seems to have been made. The value of s for sporadic meteors has been derived from visual and photographic measurements, as well as by an alternative radio technique which involves the comparison of echo rates obtained from two equipments, identical in every respect other than sensitivity. Kaiser (1953), using results obtained by McKinley (1951), has given the value of $s = 2 \cdot 00 \pm 0 \cdot 02$ over the zenithal magnitude range +5 to +10. The visual and photographic determinations of s, which apply to bright meteors, involve large corrections for subjective factors and it is not surprising that the values obtained show considerable variation. Watson (1939) gives the same value as that obtained by Kaiser for fainter meteors ($s = 2 \cdot 0$) ; Millman (1935), however, suggests that for very bright meteors ($-7 < M_v < -2$) $s = 2 \cdot 4$. The most recent photographic determination, made by Hawkins and Upton (1958), gives $s = 2 \cdot 3$ over the range $0 < M_v < +4 \cdot 5$.

Besides measuring the value of the mass distribution parameter s, it is important to establish whether that parameter shows any real temporal variations. For instance, a knowledge of such variations is necessary before it can be decided whether the very small diurnal and seasonal changes, found in meteor height distributions by Evans (1955), reflect properties of the upper atmosphere, or are due to real variations in s, on which the measured radio echo height distribution also depends. The data used in the determinations of s mentioned above were either too fragmentary or too sparse to give any information on this point.

This paper deals with the measurement and analysis of durations of meteor echoes recorded at Adelaide during 1957, as part of an extended survey of meteor activity in the southern hemisphere. The records provide an adequate diurnal and seasonal cover, and include also the periods of activity of most of the known showers. The diurnal and seasonal variations in the mass distribution of brighter sporadic meteors are investigated in detail. An analysis of the data for showers will be presented separately (Weiss 1961*b*).

II. The Equipment

The equipment used in the Adelaide survey was essentially the 67 Mc/s narrow-beam radiant equipment described by Weiss (1955), with the transmitter power increased to 50 kW. The minimum detectable line density during the survey was close to 1×10^{11} electrons/cm. The transmitter was double pulsed with 12 μs pulses 110 μs apart, at a repetition frequency of 93/s. The film speed of the existing camera system, 12 cm/hr, was far too slow for the accurate measurement of echo durations. To obtain adequate writing speed, the receiver output was fed to a second intensity-modulated display and photographed by a camera incorporating a rocking mirror optical system, which sweeps the trace to and fro across the continuously moving 70 mm recording paper. The effective film speed so obtained was slightly greater than 4 in/min.

The shortest echo trace length which could be reliably measured was $0\cdot025$ in., corresponding to a duration of $0\cdot36$ s. This time interval was adopted as the basic unit of measurement. Using curves given by Kaiser and Closs (1952, Fig. 12) and taking the value of the ambipolar diffusion coefficient D to be 3×10^4 cm^2/s, the electron line density corresponding to an echo duration of $0\cdot36$ s, for an equipment for which $\lambda=448$ cm, is approximately 1×10^{13}/cm. This means that echo durations were measured only above the limit for which the effect of equipment sensitivity may be neglected and were therefore insensitive to the position of the echoing point within the aerial beam.

III. Analysis of Echo Durations

The radiant equipment was operated continuously throughout 1957, and durations recordings were made from the middle of February until the end of August, and again during November and December. Because they provided a good seasonal cover with freedom from interruptions due to excessive external interference and minor equipment failures, the months of March, May, July-August, and December were chosen for analysis. Every persistent echo recorded during these months was individually examined and classified according to its duration and time of occurrence, and at the same time any indication of irregularity in the form of the echo which could be attributed to distortion of the trail was noted. After periods of known shower activity and excessive interference were removed, 7825 persistent echoes (i.e. those with durations $\geqslant 0 \cdot 36$ s) remained. Of these, 3360 or 43% showed obvious sign of disturbance, as evidenced by the fact that their traces were not formed of unbroken straight lines at constant slant range. It seems highly probable that there were many more echoes in which the disturbance was not obvious, because an investigation of records from the Adelaide 27 Mc/s wind equipment (where the echoes, exhibited on an A-scope rather than an intensity-modulated display, can be examined in much finer detail) suggests that at least 60% of all echoes are disturbed to some extent.

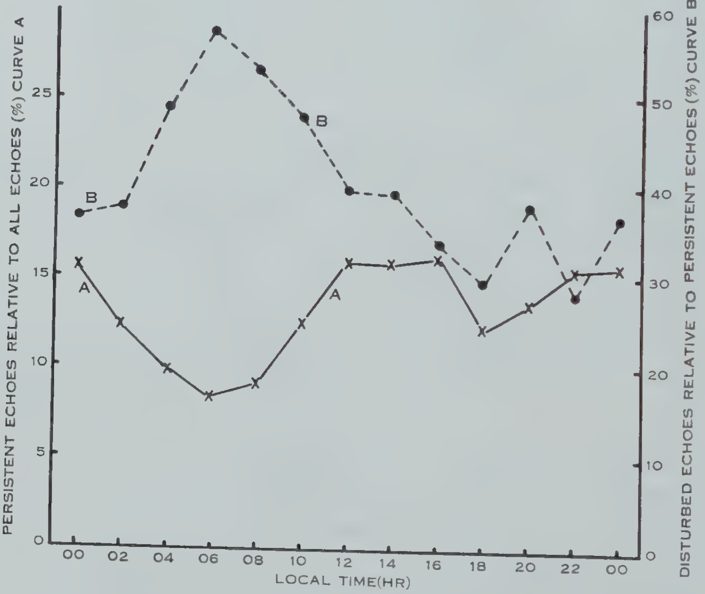

Fig. 1.—Diurnal variations in the number of persistent echoes relative to the total number of echoes received (curve A), and in the number of disturbed persistent echoes relative to the total number of persistent echoes (curve B) in each 2 hourly group.

(*a*) *Diurnal Variation in the Incidence of Persistent Echoes*

The diurnal variation in the incidence of persistent echoes relative to the total number of echoes is given in Figure 1 (curve A). Curves for individual months were almost identical, so only the average for all months is given. Also shown in Figure 1 is a plot of the diurnal variation of the ratio of the number of disturbed echoes relative to the total number of persistent echoes (curve B). Both plots show a strong diurnal variation, although of different character. The small, sharp dip in curve A near 18 hr is present in the results for every month.

There seems to be no simple explanation for the form of these diurnal variations. However, both the echo rate and the geocentric velocities of meteors tend to be highest around 06 hr and this may contribute to the low percentage of persistent echoes at this time. It is possible, too, that the higher velocities, leading to the formation of trails at greater heights, may also be responsible for the increased proportion of disturbed echoes. These are no more than suggestions, however, and more extensive information relating echo duration with trail height and trail disturbance is required before a firm explanation for the form of these diurnal variations can be sought.

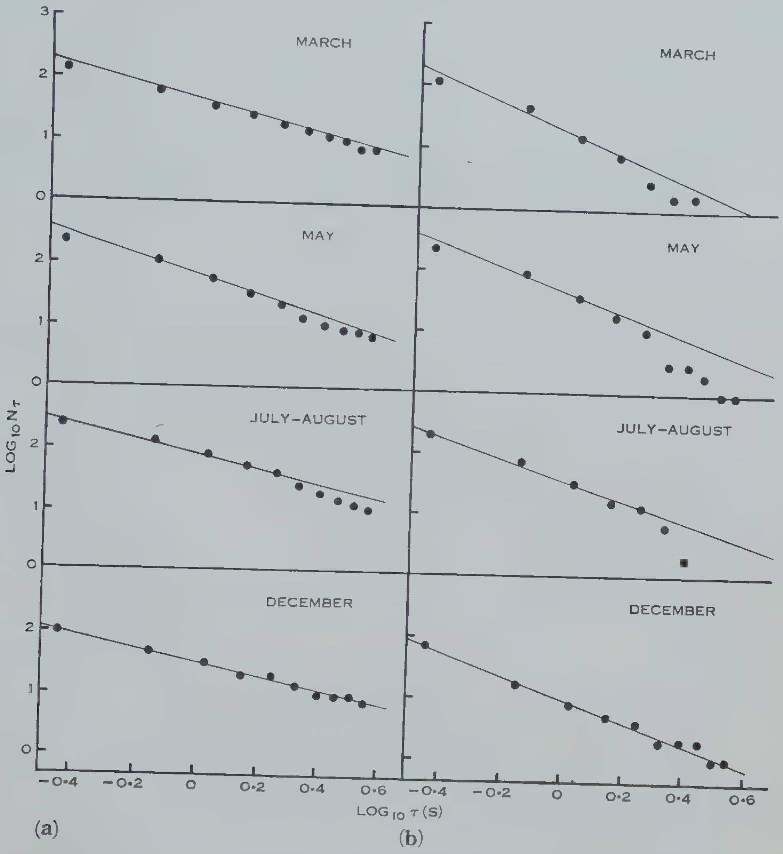

Fig. 2.—The distributions of sporadic echo durations obtained for typical 2-hr periods during 1957. N_τ is the number of echoes of duration greater than, or equal to, τ s. (*a*) All persistent echoes, 23–01 hr; (*b*) undisturbed persistent echoes, 00–02 hr.

(*b*) *The Distribution of Echo Durations*

If the theoretical distribution given by the relation (3) can be applied, a double logarithmic plot of the distribution of durations of persistent meteor echoes should result in a straight line whose gradient, $\mathrm{d}N/\mathrm{d}\tau$, is $3(1-s)/4$. Such plots were made from the results for each month, using firstly all persistent echoes collected into 2-hourly groups, and then repeating the process using only those persistent echoes showing no disturbance. Straight lines could be fitted fairly satisfactorily to a few of these plots, but more often the fit was poor and sometimes quite meaningless. Almost without exception the poor fit was caused by the number of echoes falling increasingly further below the expected number as τ increased. In Figure 2 the results for the group 23–01 hr for all persistent echoes are shown, together with those for the equivalent group (00–02 hr) of undisturbed echoes. These are quite typical examples showing perhaps rather better than average fit to straight lines. The scatter of points is much more pronounced for the early evening hours, when the echo rate is lowest. In almost every case the fall away in N_τ with increasing τ is apparent and would be even more pronounced if the end four or five points had been disregarded when fitting the lines. It is also apparent that the gradients are steeper and the fall-off more pronounced for the undisturbed echo plots than for the plots made from all persistent echoes.

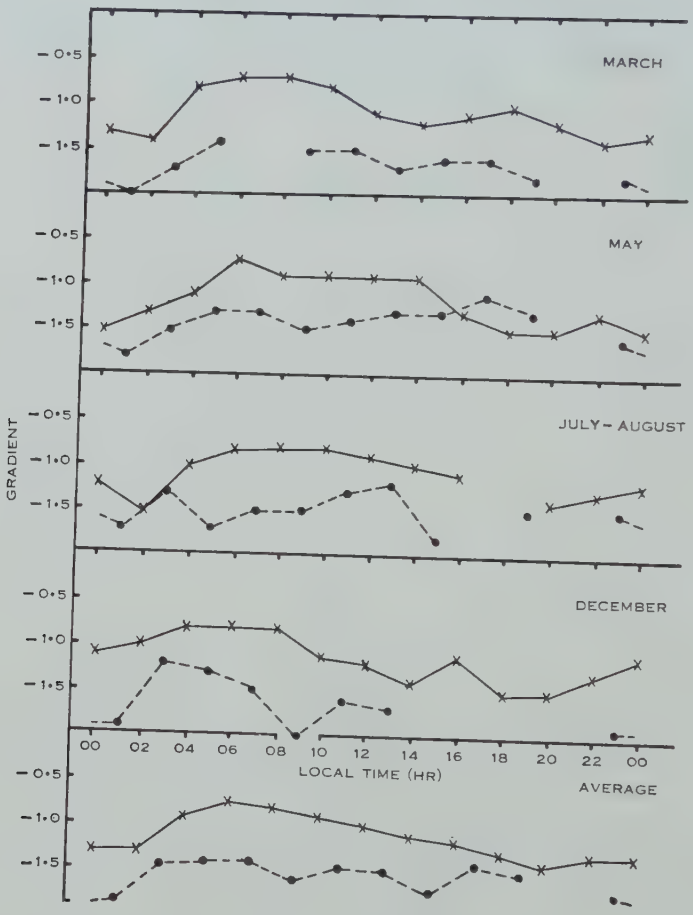

Fig. 3.—Diurnal variations in the gradients ($\delta N_\tau/\delta\tau$) of the lines fitted to the 2-hourly plots of distributions of echo durations. ×—×, All persistent echoes; ●---●, undisturbed persistent echoes only.

(c) *Diurnal Variation in Durations Distribution*

The diurnal variations in the gradients of the straight lines fitted to the plots of the distributions of echo durations similar to those in Figure 2 are shown for each month in Figure 3. Since there is no significant seasonal variation in either case, scatter can be reduced by averaging for all months; these plots are also included. The plots show that there is quite a strong diurnal variation when disturbed echoes are included, but almost none when they are excluded. As already mentioned, the results obtained using the Adelaide wind equipment suggest that at least 60% of echoes are disturbed, rather than only the 40% obvious in the durations records. This, together with the fact that the diurnal variation in the gradients of the lines fitted to the durations distribution plots parallels the diurnal variation in the relative incidence of disturbed echoes (Fig. 1), suggests that, if all the disturbed echoes could be removed, the diurnal variation in gradient (and hence in the mass distribution parameter s) would vanish altogether.

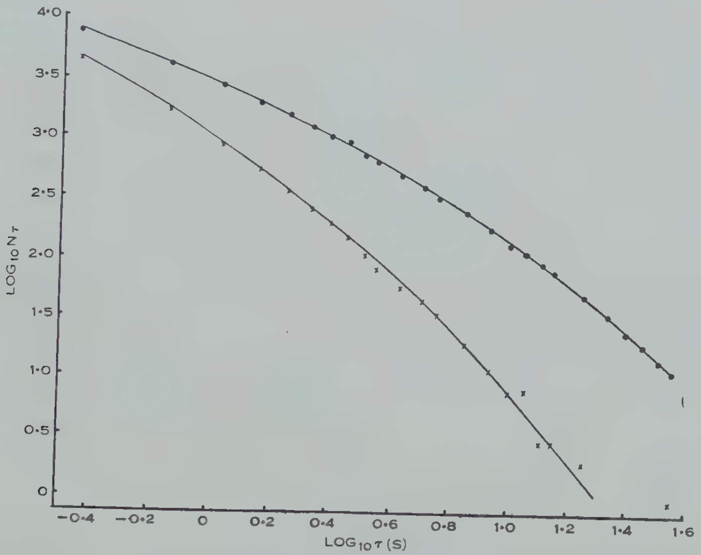

Fig. 4.—The integral distributions of echo durations obtained by adding together the echoes for all hours and all months. ●—●, All persistent echoes; ×—×, undisturbed persistent echoes only.

(d) *Average Distribution of Durations*

In Figure 4 double logarithmic plots of the distribution of all echo durations measured are shown, again one set comprising all persistent echoes and the other undisturbed persistent echoes only. It is evident that straight lines cannot be fitted to the points, but that they lie on smooth curves whose gradients are becoming more negative with increasing duration. As expected, it is the undisturbed echoes curve which throughout has the steeper and more negative gradient. In Table 1 the gradients and corresponding s values (from (3)) are given for several intervals along the curves. Even the lowest is considerably higher than the accepted s-value for fainter meteors ($s=2\cdot0$).

The meteors examined in the Adelaide durations survey all have an electron line density $\alpha \geqslant 10^{13}$/cm (corresponding to a meteor of visual magnitude $+3$) and it is known (e.g. Hawkins and Southworth 1958) that these larger meteors do not obey the evaporation theory on which the relation (3) is based. Instead the trails show evidence of fragmentation and are shorter than expected. The consequences of such a fragmentation process have been investigated by Weiss (1961*a*), who finds that starting with the assumptions $\tau \propto \alpha^q$ and $D \propto p^r$ (where p is the atmospheric pressure) the distribution of the durations of persistent echoes becomes

$$N_\tau = k\tau^{3(1-s)/(3q+r)}, \tag{5}$$

where k is an extremely slowly varying function of τ, provided $\alpha > 10^{13}$ electrons/cm. This result is independent of trail length and is expected to be insensitive to the shape of the ionization curve. Inserting the values $q=1\cdot 0$ and $r=0\cdot 35$ (Murray 1959), (5) reduces to

$$N_\tau = k\tau^{3(1-s)/3\cdot 25}, \tag{6}$$

which, although it gives lower values of s, is of the same form as Kaiser's original relation (3).

TABLE 1

THE GRADIENTS $dN/d\tau$ AND ASSOCIATED s-VALUES, DETERMINED USING EQUATION (3), FOR DIFFERENT DURATIONS INTERVALS

Duration Interval (in units of 0·36 s)	All Persistent Echoes		Undisturbed Persistent Echoes	
	Gradient	s	Gradient	s
1– 2	—0·88	2·17	—1·37	2·83
4– 5	—1·05	2·40	—1·72	3·29
8–10	—1·34	2·79	—2·72	4·63
16–20	—1·30	2·73	—2·51	4·35
32–40	—1·56	3·08	—4·40	6·87
64–80	—2·24	3·99	—	—

Davis, Greenhow, and Hall (1959) have recently drawn attention to the importance of the removal of electrons from a meteor trail, by attachment to neutral air molecules, in shortening the durations of longer persistent echoes. However, until a satisfactory analysis of the effect of trail distortion on echo duration has been made, it is not possible to determine whether the progressive departures of the observations from a linear relationship (Fig. 4) can be attributed entirely to the effects of electron attachment, or reflect a real decrease in the numbers of more massive meteors below those expected from the assumed meteor mass distribution law (4).

IV. AN ANALYSIS OF DISTURBANCES

The irregularities shown by the traces of persistent echoes are of five distinct types, although in many echoes two, or even three, of these are present together. An enlarged drawing of a typical example of each type of irregularity is shown in Figure 5. From Figure 6 it can be seen that the relative incidences of echoes showing three of these types, namely, the irregularly dotted trace echoes, those with weak beginnings and those showing range drift, have similar pronounced and regular diurnal variations, while that of the fourth type, in which the trace appears as a regular series of dashes, has a marked semi-diurnal variation. The fifth irregularity, in which the main echo is preceded by a short, strong preliminary echo, appears to have no significant diurnal variation in incidence. Since it is known that the motions in the atmosphere at meteor heights have strong diurnal and semidiurnal components (e.g. Elford 1959) it is probable that the first four types of trace irregularity are the result of distortion of originally straight trails by atmospheric disturbances. In contrast, the preliminary leader echoes presumably reflect a property of the meteors themselves; and it is suggested that they can be identified with the head echoes noted by earlier observers (e.g. McKinley 1955).

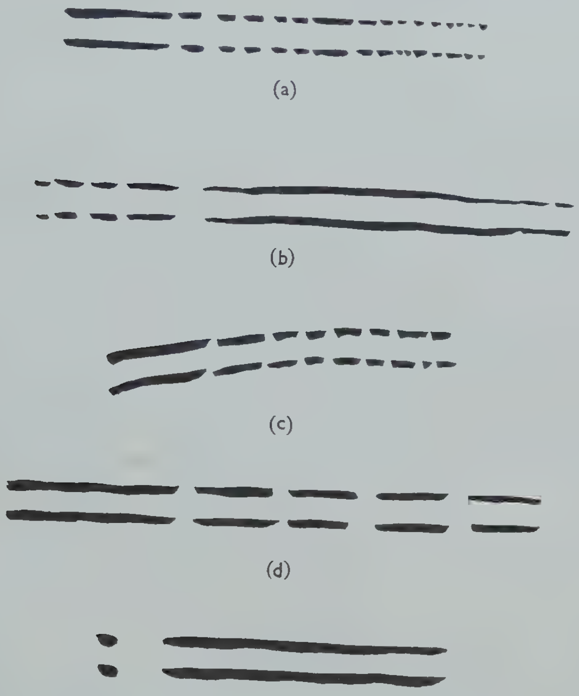

Fig. 5.—The five types of trace irregularity. (*a*) Irregularly dotted trace; (*b*) weak beginning; (*c*) range drift; (*d*) regularly dashed trace; (*e*) leader echoes.

By far the largest group of disturbed echoes are those having an irregularly dotted trace (2974 cases, 38·0%). The form of the trace, representing fairly rapid and often irregular variations in echo amplitude, is presumably due to the changing phase relationships between signals returned from separate reflecting centres along a distorted trail. The 46 echoes (0·6%) whose traces start weakly are probably special cases of dotted trace echoes, and represent trails which, although they did not satisfy the conditions of specular reflection when first formed, were subsequently distorted until some part of them did so.

The present records do not allow accurate measurements of the rate of range drift; in fact, only range drifts faster than about 2 km/s can be detected at all. It is estimated, however, that among the 310 echoes (4·0%) showing recognizable range drifts, drift rates in the vicinity of 10–20 km/s are quite common. It has been suggested (Browne 1958) that these high drift rates can be explained much more satisfactorily by assuming that the trail is being bent, so that the position of the specular reflection point moves rapidly along it, rather than by assuming that the whole trail is being bodily moved at such high speeds. It is probable, therefore, that range drifts are caused by the effects of uniform wind shear, whereas the first two types of trace irregularity discussed are more likely to represent trail distortions caused by atmospheric turbulence on a smaller scale.

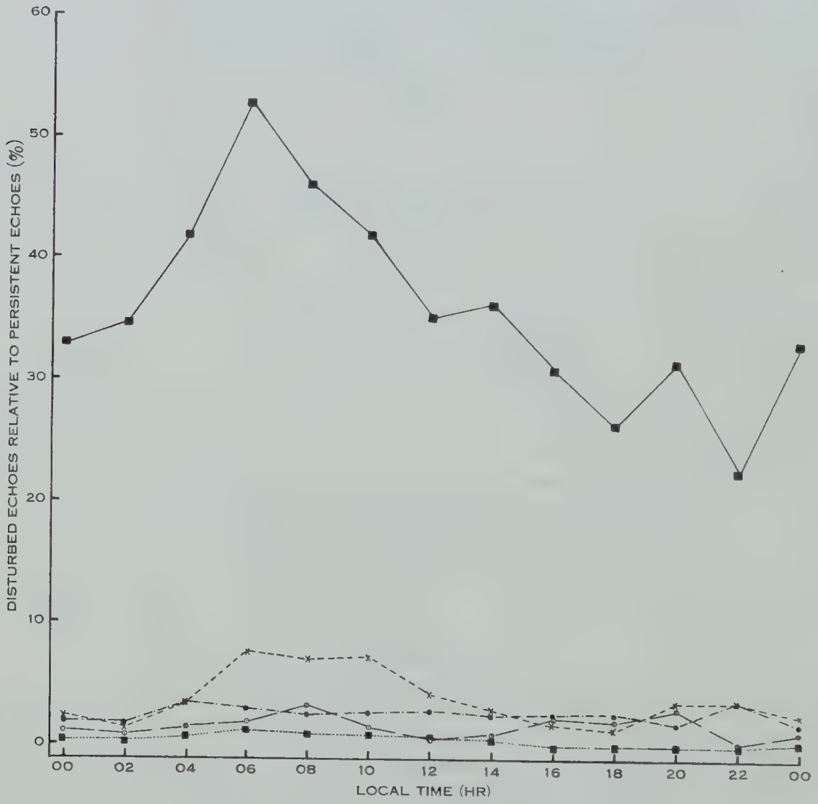

Fig. 6.—Diurnal variations in the incidence of echoes showing the various types of trace irregularities, relative to the total number of persistent echoes in each 2-hourly group. ■——■, Dotted trace echoes; ■····■, echoes with weak beginnings; ×---×, echoes showing range drift; ⊙——⊙, dashed trace echoes; ●-·-·●, echoes preceded by leaders.

The 110 echoes (1·3%) having dashed traces are quite distinct from those of the group with dotted traces, being distinguished from them both by the greater regularity and the longer period (about 1 s) of their fading. That these two disturbances are apparently different effects is further emphasized by their different diurnal variations in relative incidence (Fig. 6). An analysis of the Adelaide wind records for wind shear yielded nothing which would help to account for these differences in diurnal variations.

TABLE 2

A COMPARISON BETWEEN THE INCIDENCES OF DISTURBED ECHOES AMONGST ALL PERSISTENT ECHOES AND AMONGST LEADER ECHOES

Type of Disturbance	Percentage of Disturbed Echoes	
	All Persistent Echoes	Leader Echoes
(*a*) Short period fading	38·0	25·3
(*b*) Weak beginning	0·5	1·5
(*c*) Range drift	4·0	10·0
(*d*) Long period fading	1·4	6·3
All types	40·5	37·4

It seems unlikely that the separate preliminary echo preceding 190 of the persistent echoes (2·4%) is in any way related to trail disturbance. This supposition is strengthened by a comparison of the incidence of the four true disturbance types amongst those echoes with leaders, with that amongst all persistent echoes. The result is shown in Table 2. The only significant difference is the reduction, amongst echoes with leaders, of the relative number of echoes showing short-period fading, with a corresponding increase in all other types.

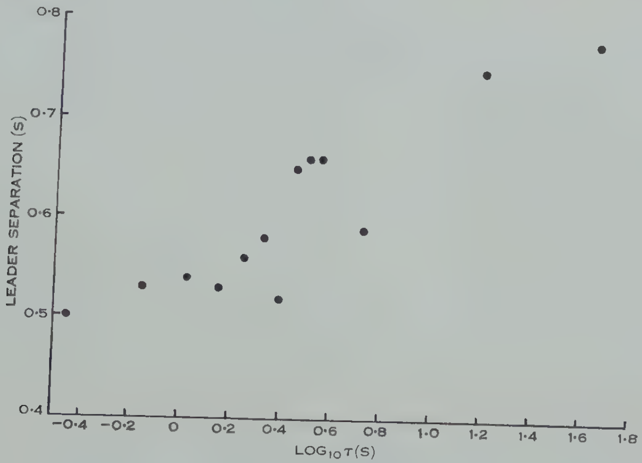

Fig. 7.—The average separation between preliminary leader echo and main echo as a function of echo duration τ.

The time separation of the leader from the main echo has been measured for each leader echo. In Figure 7 the variation of average separation with subsequent echo duration shows that there is a slow but steady increase in leader separation with increase in duration. Figure 8 is a histogram giving the distribution of leader separations; the mean separation is 0·34 s.

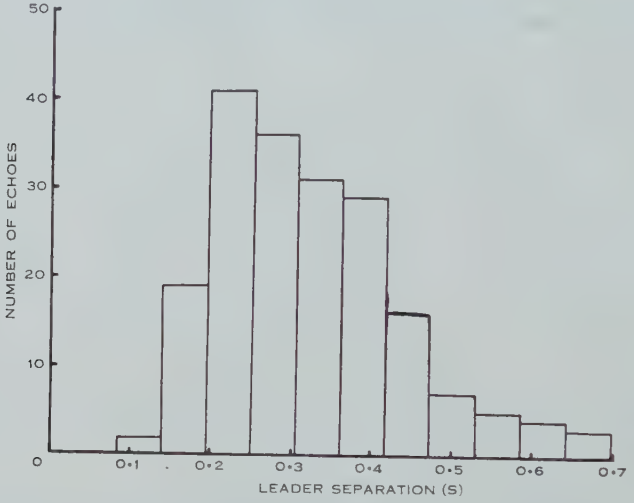

Fig. 8.—The frequency distribution of leader separations.

V. Conclusions

This survey has shown that for sporadic meteors whose trails have an electron line density $\alpha \geqslant 10^{13}$/cm (i.e. meteors brighter than visual magnitude +3) an unqualified power law such as (3) or (6) fails to describe the distribution of meteor echo durations. The departures from a power law are systematic and in the sense of an apparent increase in s with increasing meteor mass. It seems extremely unlikely that the whole of this increase is the result of trail disturbance affecting echo durations, as the removal of two-thirds of the expected number of disturbed echoes merely causes s to increase even more rapidly. Indeed, it is not impossible that the whole of the departure of the observed durations distribution for sporadic meteors from the power-law form may be attributed to the effects of the removal of electrons from the ionized columns by attachment to neutral air molecules.

From the arguments advanced in Section III (*c*) it may be concluded that if there is any seasonal or diurnal variation in the mass distribution of the brighter incident meteors it is scarcely significant.

This paper has posed a number of questions concerning the diurnal variations in the incidence of persistent echoes and in the various types of disturbed echoes which have been recognized. These questions can only be answered by a much more comprehensive recording of echo characteristics and waveform than has been possible with the simple equipment used in the present survey. In particular, the height of the echoing point, the velocity of the meteor particle, and the orientation of the trail will be required for each individual meteor, together with an understanding of the precise nature and effect of the distortion of the trail on the echo waveform and duration. A programme of observations fulfilling these requirements has been commenced at Adelaide.

VI. ACKNOWLEDGMENT

The author wishes to thank Dr. A. A. Weiss for his constant encouragement and for many discussions on the interpretation and presentation of data.

VII. REFERENCES

BROWNE, I. C. (1958).—*Jodrell Bank Ann.* **1** : 245.

BROWNE, I. C., BULLOUGH, K., EVANS, S., and KAISER, T. R. (1956).—*Proc. Phys. Soc. Lond.* B **69** : 83.

DAVIS, J., GREENHOW, J. S., and HALL, J. E. (1959).—*Proc. Roy. Soc.* A **253** : 130.

ELFORD, W. G. (1959).—*Planet. Space Sci.* **1** : 94.

EVANS, S. (1955).—" Meteors." (Ed. T. R. Kaiser.) p. 86. (Pergamon Press : London.)

HAWKINS, G. S., and SOUTHWORTH, R. B. (1958).—*Smithson. Contr. Astrophys.* **2** : 349.

HAWKINS, G. S., and UPTON, E. K. L. (1958).—*Astrophys. J.* **128** : 177.

KAISER, T. R. (1953).—*Advanc. Phys.* **2** : 495.

KAISER, T. R. (1955).—" Meteors." (Ed. T. R. Kaiser.) p. 118. (Pergamon Press : London.)

KAISER, T. R., and CLOSS, R. L. (1952).—*Phil. Mag.* **43** : 1.

MCKINLEY, D. W. R. (1951).—*Canad. J. Phys.* **29** : 403.

MCKINLEY, D. W. R. (1955).—" Meteors." (Ed. T. R. Kaiser.) p. 65. (Pergamon Press : London.)

MILLMAN, P. M. (1935).—*J. R. Astr. Soc. Canad.* **29** : 210.

MURRAY, E. L. (1959).—*Planet. Space Sci.* **1** : 125.

WATSON, F. G. (1939).—*Proc. Amer. Phil. Soc.* **81** : 493.

WEISS, A. A. (1955).—*Aust. J. Phys.* **8** : 148.

WEISS, A. A. (1961*a*).—C.S.I.R.O. Aust. Div. Radiophys. Rep. RPR 139.

WEISS, A. A. (1961*b*).—*Aust. J. Phys.* **14** : 102.

THE DISTRIBUTION OF METEOR MASSES FOR SPORADIC METEORS AND THREE SHOWERS

By A. A. Weiss*

[*Manuscript received September 20, 1960*]

Summary

Distributions of maximum line densities ($\alpha_{\text{max.}}$ electrons/cm) in meteor trails, and hence distributions of meteor masses, are derived from radio-echo data for sporadic and shower meteors. Distributions are obtained in the range $10^{11}<\alpha_{\text{max.}}<10^{12}$ from comparisons of echo rates, and for $\alpha_{\text{max.}}>10^{13}$ from durations of persistent echoes. For $\alpha_{\text{max.}}>10^{11}$ the mass distributions cannot be represented by a simple inverse power law with constant exponent s. For sporadic meteors s increases from $2\cdot0$ for $10^{11}<\alpha_{\text{max.}}<10^{12}$ to $2\cdot5$ for $\alpha_{\text{max.}}>10^{13}$. For the η-Aquarid, δ-Aquarid, and Geminid showers, $s<2\cdot0$ for $\alpha_{\text{max.}}<5\times10^{13}$, and $s\geqslant2\cdot0$ for $\alpha_{\text{max.}}\geqslant5\times10^{13}$. The δ-Aquarids exhibit a concentration of bright meteors to the centre of the stream.

It is suggested that the extent of fragmentation of shower meteors (relative to sporadic meteors) can be estimated from comparisons of the values of s found for the same shower by the echo rate method described in this paper and by the height distribution method developed at Jodrell Bank.

I. INTRODUCTION

The variation of the meteor echo rate as a function of the sensitivity of the radio equipment is determined almost entirely by the distribution of meteor masses and the form of the aerial polar diagram. Since measurements of echo rates are easily made, and there is little difficulty in making allowance for the aerial polar diagram, it seems surprising that relative echo rates have been so little exploited in the determination of the distribution of meteor masses, at least amongst the smaller meteors.

It is important to remark that the meteor parameter derived directly from the relative echo rates is not the mass distribution, but rather the distribution of the maximum electron line densities in the trails. The experimental data with which this paper is concerned are interpreted in terms of this latter parameter. However, the conclusions will apply to the mass distributions also, provided that the ionizing efficiency of an evaporated meteor atom is independent of the meteor mass.

The rate of detection of echoes by a radio equipment may be varied in two ways:

(1) By varying the limiting sensitivity of the equipment, that is, by changing the maximum line density of the weakest trail accessible to the equipment. This can be achieved, for a given aerial system, by altering either the transmitter power or the receiver sensitivity. Kaiser (1953) has used experimental values obtained by McKinley (1951), in which the transmitter power was varied, to

---

* Division of Radiophysics, C.S.I.R.O., University Grounds, Chippendale, N.S.W.

study the distribution of maximum line densities amongst faint sporadic meteors. The results described in the present paper were obtained by varying the receiver gain ; maximum line density distributions are obtained in the range 10^{11}–10^{12} electrons/cm.

(2) With limiting sensitivity held constant, by counting only those echoes whose line densities at the echoing points exceed certain selected values. Here and elsewhere (e.g. Browne *et al*. 1956) the selection has been made on the basis of echo durations. This yields distributions for maximum line densities exceeding 10^{13} electrons/cm.

The range of maximum line densities for which distributions are determined in this paper extends from 10^{11} to a little greater than 10^{14} electrons/cm. Measurements have been made for sporadic meteors and for three showers (Geminids, δ-Aquarids, η-Aquarids) over the period 1957 to 1960. Attempts were also made to derive maximum line density distributions for the June day-time showers (Arietids, ζ-Perseids) and the July Phoenicid shower, but the shower echo rates were too low, in comparison with the sporadic background, to yield useful results.

II. Equipment

During 1957 observations were made with the 67 Mc/s narrow-beam radiant equipment (Weiss 1955, 1960*a*). Calibration for equipment sensitivity using the Geminid shower echo rate gives a maximum line density in the faintest detectable meteor trail of $1\cdot3\times10^{11}$ electrons/cm (Weiss 1960*a*). A new calibration from the sporadic echo rate, which gives an almost identical result, is described in Section IV.

All the echo durations measured were recorded with this equipment, using a modified recording display whose effective writing speed was increased to 4 in/min by a combination of optical and electrical time bases. The smallest duration which could be measured reliably was 0·36 s. No attempt has been made to exclude echoes whose durations may be affected by distortion of the trail due to turbulent motion of the atmosphere.

For the 1959 and 1960 observations the 67 Mc/s equipment was replaced by a new equipment operating at 61 Mc/s, the transmitter power of 50 kW remaining unchanged. This equipment has separate transmitting and receiving aerials, each with beam axes directed due west at an elevation of 29°. The composite beamwidth is larger than for the 67 Mc/s Yagi array, but the lower aerial gain was almost completely compensated by a decrease in site noise which permitted operation at higher receiver sensitivity. Consequently, the overall equipment sensitivity for the 61 Mc/s observations is little, if any, lower than for the earlier 67 Mc/s observations.

III. Theory of the Echo Rate

(a) *The Incident Meteor Flux*

Following previous practice, it will be assumed that the flux of meteors producing trails whose maximum line densities lie in the range $\alpha_{\text{max.}}$ to $\alpha_{\text{max.}}+\mathrm{d}\alpha_{\text{max.}}$ is

$$n\,\mathrm{d}\alpha_{\text{max.}}=c\alpha_{\text{max.}}^{-s}\mathrm{d}\alpha_{\text{max.}}. \tag{1}$$

For the theoretical developments it will be assumed that s is a constant. This is known not to be the case for some showers (Browne *et al.* 1956), but the variation of s with $\alpha_{\max.}$ is sufficiently slow for the law (1) to constitute a useful definition of the line density distribution.

The definition of radio magnitude in terms of the maximum electron density in the trail and its relation to the visual magnitude scale have been discussed by Browne *et al.*

(*b*) *Echo Characteristics*

The echo is returned from a meteor trail in the vicinity of the specular reflection point, which is not in general at the point of maximum ionization. Two types of echo, depending on the line density α at the reflection point, have been recognized (Kaiser and Closs 1952). When $\alpha<2\times10^{12}$/cm, the electron volume density is sufficiently low for the incident wave to penetrate right throughout the trail (Lovell-Clegg scattering). The maximum echo amplitude A is proportional to α, and the echo duration τ, defined as the time required for the echo amplitude to fall to 1/e of its initial value, is independent of α. These are referred to as short-duration or decay-type echoes. When $\alpha>2\times10^{12}$/cm, the incident wave is no longer able to penetrate to the axis of the trail, and the nature of the reflection process changes (persistent scattering). When $\alpha>10^{13}$/cm, $A\propto\alpha^{1/4}$ and $\tau\propto\alpha$ if the decay is caused only by radial diffusion of the trail; if, in addition, removal of free electrons from the trail by attachment to neutral atmospheric molecules is significant, both A and τ are smaller, the reductions increasing rapidly as α increases. These are known as persistent echoes.

So far as echo durations are concerned, the range of α from 2×10^{12}/cm to 10^{13}/cm is a transition region in which incomplete penetration of the trail occurs, but the exponential decay characteristic of the short-duration echoes occupies an appreciable portion of the total echo duration. Consequently the echo duration is not independent of the echo amplitude and hence of the equipment parameters and of the location of the echoing point within the aerial beam. When discussing echo durations in this paper the limit $\alpha=10^{13}$/cm will be taken as the lower boundary of the region of persistent echoes.

(*c*) *The Total Echo Rate*

The theory of the radio echo rate has been given by Kaiser (1955*a*). His treatment assumes specular reflection and the evaporation theory for a solid meteor particle in an isothermal atmosphere. Expressions are derived for the instantaneous shower echo rate, when echoes are received only from the echo plane which passes through the observing station and is perpendicular to the direction of the radiant; and also for the echo rate from a distributed source such as sporadic meteors, when echoes are received simultaneously from all elements of the aerial beam.

The shower echo rates discussed in this paper were determined by summing over the whole time of passage of the radiant through the collecting area of the equipment. The second alternative above, the echo rate for a distributed source, is therefore the one to take. With the flux (1), the total echo rate given by Kaiser may be written in the form

$$N=hHI_0\int_{\alpha_0}^{\infty}W(\alpha)\alpha^{-s}\mathrm{d}\alpha, \tag{2}$$

where h=mean height of reflection points, H=atmospheric scale height, and α_0=minimum detectable line density in the direction of the beam axis. In this and subsequent equations the subscript " max." has been dropped. I_0 is an integral whose value depends only on the shape of the ionization curve of the meteor trails. $W(\alpha)$, which may be described as the aerial aperture function, is a function of α alone. It takes account of the increase, as α increases, in the volume of space within which trail segments of line density α at the echoing points are detectable.

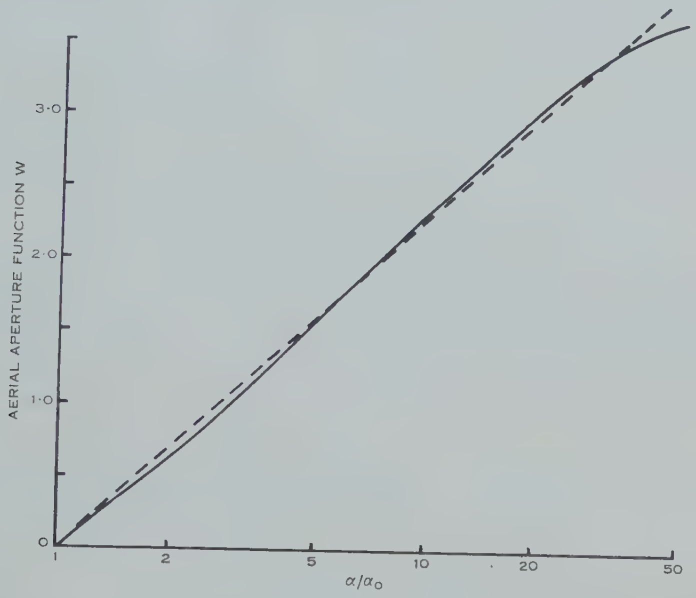

Fig. 1.—Aerial aperture function W for the Adelaide narrow-beam 67 Mc/s radiant equipment (——) compared with $W=\ln(\alpha/\alpha_0)$ (– – – –). The scale of W has been normalized for best fit to the logarithmic law. α_0 is the minimum detectable line density for the equipment.

W is determined by the aerial polar diagram and the elevation of the axis of the aerial beam. It has been evaluated numerically for the theoretical polar diagram of the Adelaide narrow-beam aerial system, under the restriction that $\alpha_{\mathrm{max.}}\leqslant 10^{12}$/cm over the greater part of the aerial beam. It is seen from Figure 1 that, apart from a multiplying constant, a very good approximation to W for the range $1\leqslant\alpha/\alpha_0\leqslant 30$ is

$$W=\ln(\alpha/\alpha_0), \quad \alpha<\alpha_t. \tag{3a}$$

This law cannot be applied beyond the point of transition, α_t, from Lovell-Clegg to persistent scattering; the appropriate forms are then

$$\left.\begin{aligned} W &= \ln(\alpha_t/\alpha_0)+\tfrac{1}{4}\ln(\alpha/\alpha_t), && \alpha>\alpha_t>\alpha_0 \\ &= \tfrac{1}{4}\ln(\alpha/\alpha_0), && \alpha>\alpha_0>\alpha_t \end{aligned}\right\}. \tag{3b}$$

It will be assumed for the present that (3b) extends into the region of persistent echoes, where $\alpha>10^{13}/\text{cm}$; its validity in this region will be examined later. Since the form of the polar diagram for the 61 Mc/s aerial system is similar to that for the 67 Mc/s array, (3a) and (3b) will be taken to apply in this case also.

The expressions (3) for W were derived by considering echo collection from a shower radiant near the zenith. However, collecting areas examined during the course of the computations proved quite insensitive to the zenith angle of the radiant. Expressions (3) will therefore be accepted for sporadic meteors also. This implies neglect of a small correcting factor which depends on the apparent distribution of sporadic radiants. This will introduce a small error into the total echo rate, but the effect on relative echo rates will be negligible.

(*d*) *Relative Echo Rates and Equipment Sensitivity*

Since we are concerned only with the relative echo rates obtained with different equipment sensitivities, the constants H and I_0 appearing in (2) and the slight change of the mean height h with equipment sensitivity may be ignored. The echo rate will therefore be written

$$N=\int_{\alpha_0}^{\infty} W(\alpha)\alpha^{-s}\mathrm{d}\alpha, \tag{4}$$

with W defined by (3a) or (3b), as appropriate. Carrying out the integrations, the dependence of the total echo rate on the limiting line density α_0 becomes

$$N=\frac{\alpha_0^{1-s}}{(s-1)^2}\left\{1-\tfrac{3}{4}\left(\frac{\alpha_0}{\alpha_t}\right)^{s-1}\right\}, \quad \alpha_0\leqslant\alpha_t, \tag{5a}$$

$$=\tfrac{1}{4}\frac{\alpha_0^{1-s}}{(s-1)^2}, \qquad \alpha_0\geqslant\alpha_t. \tag{5b}$$

These functions, suitably normalized, are sketched in Figure 2 for $s=1\cdot5$ $2\cdot0$, $2\cdot5$. The influence of the transition from persistent to Lovell-Clegg scattering is still noticeable for values of α_0 smaller than $\alpha_t/10$ when $s<2\cdot0$. With $\alpha_t\simeq10^{12}/\text{cm}$, this implies that the simple formula which is often used for the echo rate, namely, $N\propto\alpha_0^{1-s}$, is invalid for $10^{11}<\alpha_0<10^{12}/\text{cm}$. It is true that this result has been derived only for the special form (3) for the function W, but it is expected to apply to any reasonable aerial system.

It is also important to note that these results are independent of the validity of the evaporation theory. From (2) it is evident that the shape of the ionization curve may profoundly affect the *total* echo rate, but since it does not enter into the computation of W, the *relative* echo rate is unaffected. The shape of the ionization curve will assume importance only if there is a rapid alteration of shape with meteor mass. There is indeed some evidence (Weiss 1960*b*) that short trails are associated with bright meteors, but the change in the length of the trail with meteor brightness is far too slow to affect relative echo rates measured over a comparatively small range of α_0.

(e) *The Distribution of Echo Durations*

The theory of the rate of detection of persistent echoes, originally formulated by Kaiser (1955*a*), has been extended to include the effect of removal of free electrons from the trail by attachment to neutral molecules. This severely limits the durations of the most persistent echoes. Only a brief summary of the results will be given here; full details will be found in Weiss (1961).

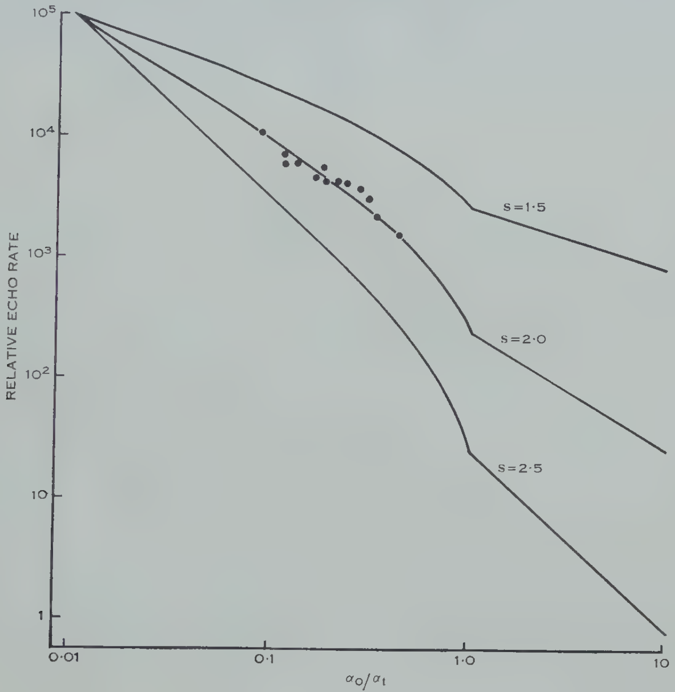

Fig. 2.—The relative echo rate as a function of the limiting line density α_0 and mass distribution parameter s. Full lines are the (normalized) theoretical distributions of equation (5). α_t is the line density corresponding to the point of transition from Lovell-Clegg to persistent scattering. Dots are observations of relative echo rates of sporadic meteors, fitted to the theoretical curve for $s=2\cdot0$.

The effects of attachment are introduced through a parameter $B=\beta_e n_m$. β_e is the attachment coefficient and n_m is the density of the ion-forming molecules. B is a function of height. It is convenient to introduce a specific value of B, namely B_0, the value of B at a datum height of 95 km.

From expression (3b) it is apparent that when $\alpha > 10^{13}$/cm, W varies very slowly with both α and s, and it is sufficient to put $W=\text{constant}=\overline{W}_T$. With this substitution, the rate of detection of echoes with durations exceeding T becomes, from (2),

$$N_T = hH\overline{W}_T I_T \alpha_T^{1-s}/(s-1), \tag{6}$$

where α_T is the maximum line density in the weakest trail capable of giving the duration T. The integral I_T is a slowly varying function of T. For the range of s-values and echo durations considered in this paper, $I_0/I_T \simeq \sqrt{2}$. For $\alpha_T \simeq 10^{13}$/cm, when the effects of attachment are small, $T \propto \alpha_T{}^{4/3} v^{-2}$ (v is the meteor velocity). For the most persistent echoes measured, $\alpha_T \simeq 10^{16}$/cm and $T \propto \alpha_T{}^{2/9} v^{2/3} B_0{}^{-2/3}$. The slight change in the mean height h with echo duration may be neglected. For uniform meteor velocity the integral distributions of echo durations, that is, the numbers of echoes N_T whose durations exceed T, in these two limiting cases are accordingly

$$N_T \propto T^{3(1-s)/4}, \tag{7}$$

and

$$N_T \propto T^{9(1-s)/2}. \tag{8}$$

For intermediate echo durations the relation between T and α_T, and hence the distributions of echo durations, are most easily found by numerical means (Weiss 1961).

Values of s may be obtained for shower meteors by direct comparison of the observed distributions of echo durations with these predicted distributions. But, because the dependence of echo duration on meteor velocity varies with the duration, the theoretical distributions for meteors with uniform velocity cannot be used immediately to derive s-values from observational data on the durations of sporadic meteor echoes. It is first necessary to average over all meteor velocities, from 15 to 75 km/s, according to the probabilities of detection. When this is done, it is found, to a good approximation, that the frequency distribution of the durations of sporadic meteor echoes corresponds to that for $v = 40$ km/s.

The errors in s-values derived through these theoretical distributions, arising from neglect of the dependence of I_T and W on T, are unlikely to exceed a few per cent. Further sources of error, of greater importance, are the violations of the basic assumptions that the meteor evaporates as a solid particle and that reflection is specular. Fragmentation and crumbling of the meteor particle, followed by evaporation of the fragments, gives a better description of the ablation process amongst bright meteors than simple evaporation. The failure of specular reflection is brought about by distortion and twisting of the initially straight trail, due to turbulent motion of the atmosphere. This causes an increase, which can be as large as a factor of 4 or 5, in the effective value of W for the more massive meteors. For the narrow-beam aerial system used here, however, the increase in W will not be as large as this.

Considering all sources of error, the uncertainty in values of s derived by comparing observed distributions of echo durations with the theoretical distributions should not exceed 20%. The term "theoretical distributions" is here to be understood to refer to the distributions (7) and (8) and those obtained numerically for values of T intermediate between these two limiting cases of small and large T.

IV. Distribution of Maximum Line Densities, Sporadic Meteors

During 1957 the relative rate of sporadic echoes was determined as a function of limiting line density α_0, by varying the receiver gain. The recordings were made by splitting the receiver video stage into two channels with unequal gains ; the sensitivity of one channel was held constant to provide a base rate at the highest sensitivity, and the gain of the other channel was systematically reduced. Relative values of α_0 were found by calibration of the receiver, assuming Lovell-Clegg scattering.

The observations are plotted in Figure 2, where they have been fitted to the theoretical curve for $s=2\cdot0$, which is the accepted value for sporadic meteors (Browne *et al.* 1956). In making this fit, both the echo rate and the value of α_0 at the highest sensitivity were considered as adjustable parameters. From this fit a value of $\alpha_0/\alpha_t=0\cdot09$ is deduced for the minimum detectable line density under normal operating conditions. There is some uncertainty in the value to be taken for α_t. According to the values of the reflection coefficient given in Figure 12 of Kaiser and Closs (1952), $\alpha_t\simeq8\times10^{11}$/cm, which is somewhat lower than the value of $\alpha_t\simeq2\cdot4\times10^{12}$/cm found from the condition that the incident wave should penetrate completely through the trail. Since the transition from Lovell-Clegg to persistent scattering will take place smoothly over a small range of α, rather than abruptly, we will adopt $\alpha_t=1\times10^{12}$/cm. With this value of α_t, $\alpha_0=9\times10^{10}$/cm, which agrees well with the previous determination of $\alpha_0=1\cdot3\times10^{11}$/cm described in Section II. These observations are thus consistent with a value of $s=2\cdot0$ for sporadic meteors in the range of line densities $10^{11}<\alpha_{\max.}<10^{12}$/cm.

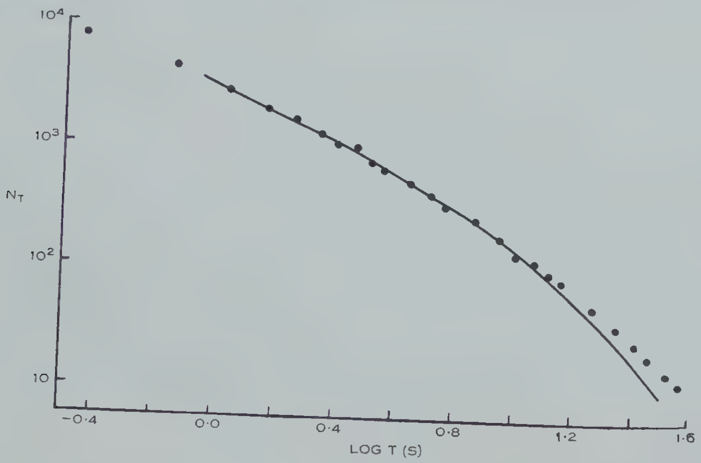

Fig. 3.—Distribution of echo durations at 67 Mc/s for sporadic meteors, 1957. The plot is double-logarithmic and shows the number of echoes N_T with durations $\geqslant T$ s. Observations are shown by dots, and the full line is the theoretical distribution for $s=2\cdot5$, $B_0=0\cdot015$/s.

The frequency distribution of echo durations leads to a larger value of s for $\alpha_{\max.}>10^{13}$/cm. The numbers of echoes whose durations exceed T s, obtained over an extended period during 1957, are plotted in Figure 3. By comparing these experimental data with theoretical distributions calculated after the manner described in Section III (*e*), we obtain for the conditions of best fit, $s=2\cdot5$, $B_0=0\cdot015/s$. This theoretical distribution is also shown in Figure 3. A value of $s=2\cdot5$ is little larger than the $s=2\cdot34$ found by Hawkins and Upton (1958) from the luminosity function for photographic meteors. The value of $B=0\cdot015/s$ at a height of 95 km is the same as that found by Davis, Greenhow, and Hall (1959) from the relation between echo duration and visual brightness of Perseid and Geminid meteors. However, the shape of the theoretical durations distribution is not particularly sensitive to B_0, and the value of this parameter cannot be stated more precisely than to within a factor of 2.

It may be concluded that the values of s for sporadic meteors deduced from the present observations are in agreement with determinations by other workers using different observational methods. The value of s increases from $s=2\cdot0$ for $10^{11}<\alpha_{\text{max.}}<10^{12}$/cm to $s=2\cdot5$ for $\alpha_{\text{max.}}>10^{13}$/cm. With the exception of distributions of echo durations, all observations on shower echo rates will be analysed by comparing them with similar data for sporadic meteors, taking for the latter the above values of s.

V. Distributions of Maximum Line Densities, Shower Meteors

(*a*) *Relative Echo Rates*, $10^{11}<\alpha_{\text{max.}}<10^{12}/cm$

Total numbers of echoes detected simultaneously at two different equipment sensitivities are listed in Table 1, for three showers. The numbers of echoes refer to totals summed over the dates shown and are not indicative of the relative strengths of the showers. The sporadic echo rates are totals summed over the same periods as the shower echoes. With the assumption $s=2\cdot0$, they provide information on the relative sensitivity of the equipment in the two operating conditions.

Table 1

SHOWER ECHO RATES AND s-VALUES FOR MAXIMUM LINE DENSITIES 10^{11}–10^{12} ELECTRONS/CM

Shower	Year	Dates of Observation	Sporadic Echo Rates		Shower Echo Rates		r	R	s_1
			n_0	n_1	N_0	N_1			
η-Aquarids	1960	May 4–9	2672	683	514	215	3·91	2·39	1·61
δ-Aquarids	1959	July 21–Aug. 9	3862	1334	5675	3199	2·90	1·77	1·54
Geminids	1957	Dec. 11–14	210	47	228	108	4·47	2·11	1·50

It will be seen that in no case is the sporadic rate sufficiently low that it may be neglected when estimating the shower echo counts. In fact, the η-Aquarid shower rates are a good deal lower than the sporadic rate and cannot be regarded as free from uncertainty.

If α_0 and α_t were accurately known, the s-values for the showers could be determined from graphs such as those illustrated in Figure 2. With $s=2\cdot0$

and α_0 known, the sporadic counts could be used to determine the limiting line density α_1 at the lower sensitivity, and the value of s for the shower could then be read off from the curve which best fitted the shower counts. But since α_0 is not accurately known (the 1959 and 1960 observations were made at 61 Mc/s and the calibrations discussed in Section IV do not apply to this equipment), an alternative procedure has been adopted.

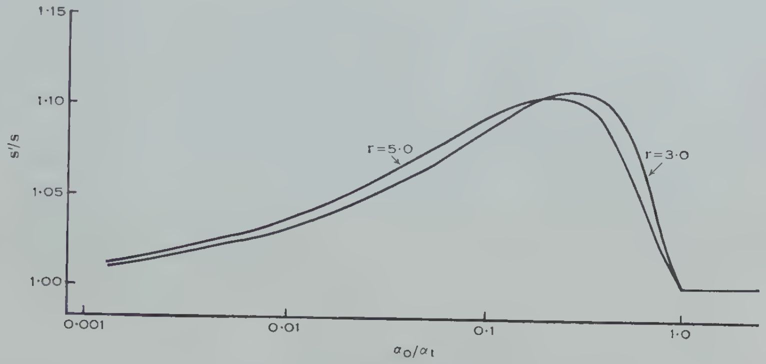

Fig. 4.—The error in the value of s derived from shower echo rates measured at two different equipment sensitivities, when it is improperly assumed that equation (10) is valid in the vicinity of the transition point α_t. s' is the value of s obtained using (10), and the curves are drawn for $s=1\cdot5$. α_0 is the limiting line density of the equipment at the higher sensitivity, r is the ratio of the sporadic meteor echo rates at higher and lower sensitivity.

It will be recalled from equation (5) that when either $\alpha_0 \ll \alpha_t$ or $\alpha_0 \gg \alpha_t$,

$$N \propto \alpha_0^{1-s}. \tag{9}$$

Denoting the counts at higher and lower sensitivity by the subscripts 0 and 1 respectively, and putting $R=N_0/N_1$ for showers and $r=n_0/n_1$ for sporadics, it follows that within the range of validity of (9) and with $s=2\cdot0$ for sporadics, the values of s for showers are given by

$$s=1+(\log R)/(\log r). \tag{10}$$

In view of the general similarity of the shapes of the curves of Figure 2 for different values of s, it is reasonable to expect that (10) will not be seriously in error even in the vicinity of the transition point α_t. Values of s found using (10) are listed in Table 1.

It remains to assess the errors introduced by the assumption that (10) holds over the range of line densities to which these determinations apply. This can be done in the following manner. Assume an r and an α_0/α_t. Calculate α_1/α_t from (5) with $s=2\cdot0$. Evaluate the ratio R corresponding to these values of α_0/α_t and α_1/α_t when $s\neq2\cdot0$. With this R and the given r, use (10) to find the value of s, which we call s', which results from the improper use of (10). Two sets of calculations, with $s=1\cdot5$ and $r=3\cdot0$ and $5\cdot0$, suffice to indicate the errors in the s-values given in Table 1. The results are plotted in Figure 4.

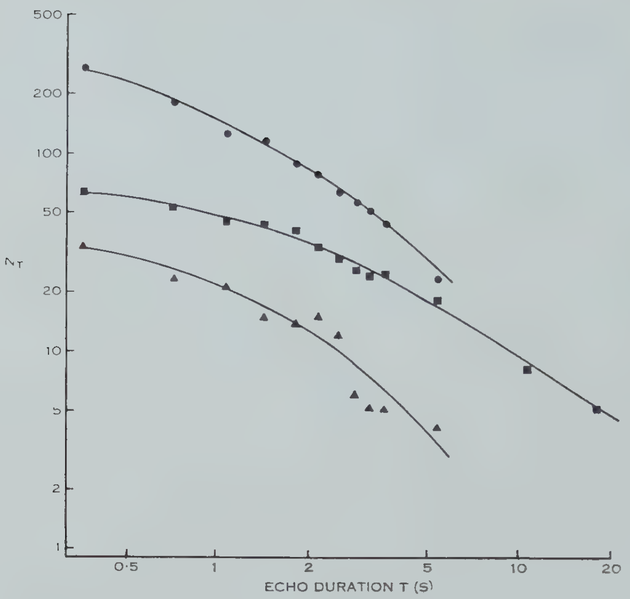

Fig. 5.—Distributions of shower echo durations at 67 Mc/s. The plot is double-logarithmic and shows the numbers of echoes N_T with durations $\geqslant T$ s. ■ η-Aquarids; ● δ-Aquarids; ▲ Geminids.

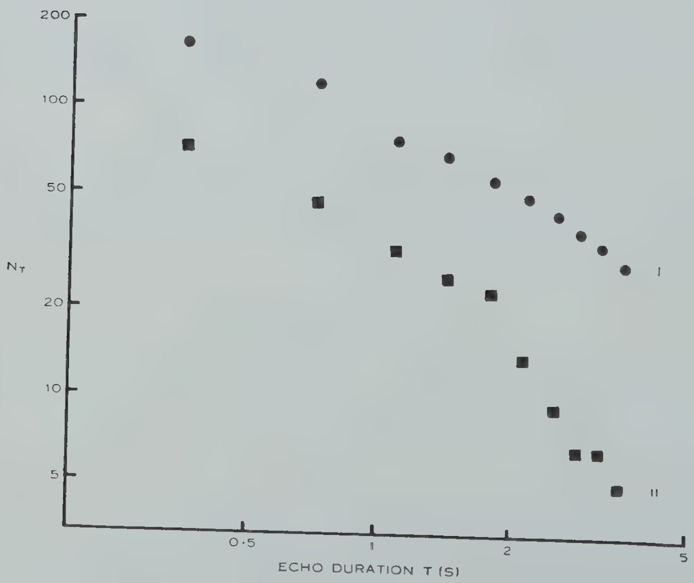

Fig. 6.—Double-logarithmic plot of numbers of echoes with durations $\geqslant T$ s, showing the increase in the relative number of bright δ-Aquarid meteors when the shower rate is a maximum. I: echoes observed over period of peak activity, July 28–31, 1957. II: July 27 and August 1–3, 1957.

It is seen that for the showers under consideration and with probable values of α_0 not much larger than $0 \cdot 1\alpha_t$, the values of s listed in Table 1 are not likely to be in error by more than 10%. They are also upper limits.

(*b*) *Durations Distributions*, $\alpha_{\max.} > 10^{13}/cm$

Distributions of echo durations are given for the three showers in Figure 5. They have been obtained by subtraction of the estimated sporadic components from the distributions for all echoes (shower plus sporadic) over the periods of activities of the showers. Unlike that for the sporadic meteors, these distributions cannot be fitted, over the whole range of durations from $\frac{1}{3}$ to 10 s, by theoretical curves with constant values of s, unless the attachment parameter B_0 takes on impossibly large values. The values of s have therefore been determined using the same value of B_0 as was found from sporadic meteors, namely, $B_0 = 0 \cdot 015/\text{s}$. They are listed in Table 2. The measurements for the η-Aquarids apply to slightly higher line densities than for the other two showers because of the higher velocity of the former meteors.

In each case there is a large increase in s as $\alpha_{\max.}$ increases from 10^{13} to 10^{14}/cm.

TABLE 2

s-VALUES FOR MAXIMUM LINE DENSITIES $>10^{13}$ ELECTRONS/CM FROM DISTRIBUTIONS OF ECHO DURATIONS, 1957

Shower	Dates of Observation	s_2	Limits of $\alpha_{\max.}$ (cm^{-1})	s_3	Limits of $\alpha_{\max.}$ (cm^{-1})
η-Aquarids	May 3–10	1·4	$2\text{–}6 \times 10^{13}$	2·0	$6 \times 10^{13}\text{–}5 \times 10^{14}$
δ-Aquarids	July 23–Aug. 7	1·9	$1\text{–}4 \times 10^{13}$	2·7	$4 \times 10^{13}\text{–}1 \times 10^{14}$
Geminids	Dec. 9–14	1·7	$1\text{–}4 \times 10^{13}$	2·7	$4 \times 10^{13}\text{–}1 \times 10^{14}$

(*c*) *Changes in* s *across the* δ-*Aquarid Stream*

The δ-Aquarid activity is sufficiently high that day-by-day changes in the distribution of maximum line densities can be traced, at least qualitatively, during the greater portion of the 1957 activity. In Figure 6 the distributions of echo durations for July 27 and August 1–3 are compared with those for July 28–31; the latter four days cover the period of peak activity. The two curves do more than merely indicate the average behaviour over the two periods; without exception, the distribution for each individual day conforms to the shape characteristic of the period to which it belongs. Figure 7 (*a*) gives the proportion of echoes with duration $\geqslant 0 \cdot 36$ s. These two diagrams taken together imply an increase in the number of bright meteors, relative to that of the fainter meteors, over the period of peak activity. This increase, which is most marked amongst the brightest meteors ($\alpha_{\max.} > 4 \times 10^{13}$/cm), extends down to meteors at least as faint as $\alpha_{\max.} = 10^{13}$/cm.

Values of s, determined for individual days in 1959 from comparison of echo rates at different equipment sensitivities, are plotted in Figure 7 (*b*); this applies to meteors with $\alpha_{\max.} < 10^{12}$/cm. Unlike the brighter meteors, there is here no evidence for a change in s at the time of peak activity. Although the relative echo rate and durations data apply to different years, this constancy of s amongst the fainter meteors is consistent with the above-noted decrease in s for the brighter meteors at the time of peak activity.

A similar concentration of bright meteors to the centre of the stream has been noted by Browne *et al.* for the Geminids. The Perseids, however, show a contrary behaviour, with a rise in the relative number of fainter meteors when the shower rate is a maximum.

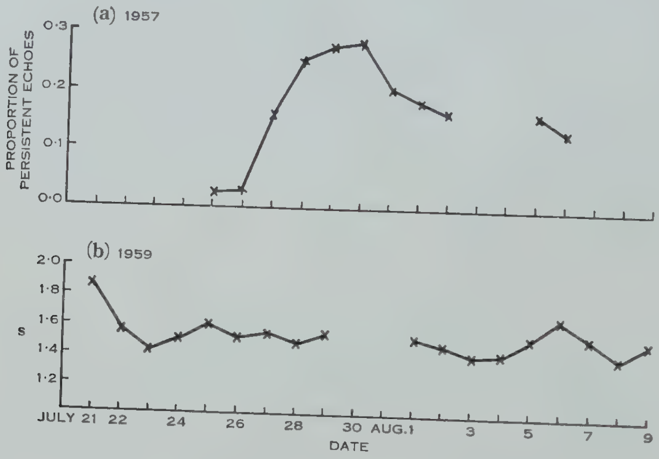

Fig. 7.—The increase in the proportion of bright meteors near maximum activity, δ-Aquarids. (*a*) Proportion of persistent echoes with durations $\geqslant 0\cdot36$ s, $\alpha_{\text{max.}} \geqslant 10^{13}$/cm ; (*b*) s-values from relative echo rates, using equation (10), $\alpha_{\text{max.}} < 10^{12}$/cm.

VI. The Rate of Persistent Echoes

The form (3b) for the aerial aperture function W when $\alpha_{\text{max.}} > \alpha_t$ has been used in interpreting relative echo rates, and also echo durations distributions. It will be recalled that this involves an extrapolation of the numerical evaluation illustrated in Figure 1, which is itself an empirical derivation. Experimental verification of the form adopted for the function W is therefore desirable. This will be achieved by *a posteriori* arguments if it can now be shown that the proportion of persistent to all echoes is consistent with the expressions (3) and the s-values which have been derived from them through (5a) and (6).

Echo counts giving the proportion which echoes with durations $\geqslant 0\cdot36$ s bear to the total numbers of echoes are listed in Table 3. Counts for the showers relate to the same dates as the data in Table 2. Sporadic counts were made in March, May, July, and December 1957.

As has already been pointed out in Section III (*e*), if expression (3b) holds then W is a slowly varying function of $\alpha_{\text{max.}}$ when $\alpha_0 \ll \alpha_t$ and $\alpha_{\text{max.}} > 10^{13}$/cm. This behaviour, arising as it does essentially from the weak dependence of echo amplitude upon line density amongst persistent echoes, is expected to be

TABLE 3

PROPORTIONS OF PERSISTENT TO TOTAL ECHOES

Source of Meteors	Total Echoes Detected	Persistent Echoes Detected	Proportion of Persistent Echoes	Effective Aerial Aperture Function $\overline{W}_T$
η-Aquarids	361	63	0·17	8·2
δ-Aquarids	1,177	269	0·23	11
Geminids	268	34	0·13	4·4
Sporadics	72,500	7,825	0·11	23

characteristic of any reasonable aerial polar diagram. It is therefore sufficient to put W=constant. This constant value of W, which has been denoted in (6) by $\overline{W}_T$, represents some average value of W for $\alpha_{\text{max.}} > 10^{13}$/cm. It may be calculated from the experimental data of Tables 1–3 in the following manner.

Let the theoretical number of echoes from meteors for which $\alpha_0 \leqslant \alpha_{\text{max.}} \leqslant \alpha_T$ be denoted by ν_1. Writing s_1 for the value of s for this range of $\alpha_{\text{max.}}$, and subtracting from (5a) the number of echoes from meteors with $\alpha_{\text{max.}} \geqslant \alpha_T$ when $s=s_1$, we obtain

$$\nu_1 = \frac{I_0 \alpha_0^{1-s_1}}{(s_1-1)^2}\left\{1-\frac{3}{4}\left(\frac{\alpha_0}{\alpha_t}\right)^{s_1-1}\right\} - \frac{W_1 I_0 \alpha_T^{1-s_1}}{s_1-1}, \tag{11}$$

where

$$W_1 = \ln(\alpha_t/\alpha_0) + \tfrac{1}{4}\ln(\alpha_T/\alpha_t) + 1/4(s_1-1). \tag{12}$$

Now let ν_2 be the theoretical number of echoes from meteors for which $\alpha_{\text{max.}} \geqslant \alpha_T$. In calculating ν_2 it is necessary to take into account the relative values of the ionization curve integrals I_0 and I_T, and also the changes in the s-values (Tables 1 and 2). For convenience it has been assumed that the changes in s take place discontinuously at α_T and α_2, which are the lower and upper limits of $\alpha_{\text{max.}}$ in the fourth column of Table 2. For $\alpha_T \leqslant \alpha_{\text{max.}} \leqslant \alpha_2$ we put $s=s_2$, and for $\alpha_{\text{max.}} \geqslant \alpha_2$, we put $s=s_3$. In order to ensure continuity in the differential distribution (1), the value of the constant c must be adjusted at each change in s-value. The fitting conditions are

$$c_1 \alpha_T^{-s_1} = c_2 \alpha_T^{-s_2},$$
$$c_2 \alpha_2^{-s_2} = c_3 \alpha_2^{-s_3},$$

and with $c_1=1$ these become

$$c_2 = \alpha_T^{s_2-s_1},$$
$$c_3 = c_2 \alpha_2^{s_3-s_2}.$$

Then

$$\nu_2 = \overline{W}_T I_T \alpha_T^{s_2-s_1}\left\{\frac{1}{s_2-1}(\alpha_T^{1-s_2}-\alpha_2^{1-s_2}) + \frac{1}{s_3-1}\alpha_2^{1-s_2}\right\}. \tag{13}$$

Denoting the observed proportion of persistent echoes by x, we have

$$\nu_1/\nu_2 = (1-x)/x. \tag{14}$$

$\overline{W}_T$ is the only unknown occurring on the right-hand side of (11) and (13). It can therefore be calculated from (14) using the values of s_1, s_2, s_3, and α_T, α_2 already given in Tables 1 and 2, and x from Table 3. Values of $\overline{W}_T$ obtained with $\alpha_0=10^{11}$/cm, $\alpha_t=10^{12}$/cm, and $I_0/I_T=\sqrt{2}$ are listed in the last column of Table 3.

These values of $\overline{W}_T$ are to be compared with the theoretical values, slightly larger than 3, which are obtained from (12) with s_1 replaced by s_2. For showers, $\overline{W}_T$ exceeds the theoretical value by factors of from 1·5 to 3·5. This is not unexpected. As already mentioned, the values of s_1 given in Table 1 are upper limits. Further, trail distortion and consequent detection of trails not formed in the specularly reflecting condition will result in an increase in the effective aerial aperture for persistent echoes. Thus even if W is correctly represented by expressions (3a), (3b), experimental values of $\overline{W}_T$ should still be too high. In addition, any misalignment of, or errors in phasing of, the elements of the aerial arrays will widen the main lobe of the aerial beam, particularly at the fringes, and so still further increase the relative aperture for persistent echoes.

In the case of sporadic echoes, however, the excess of $\overline{W}_T$ over the theoretical value is uncomfortably large. None of the factors mentioned in the previous paragraph as increasing $\overline{W}_T$ for showers should be more effective for sporadic meteors. The values of s_1 for showers were obtained by comparison of shower with sporadic echo rates, assuming $s_1=2\cdot 0$ for the latter. From the point of view adopted here, this value is exact (and well verified experimentally) and this source of error is eliminated. The incidence of trail distortion is identical amongst sporadic and shower meteors. The proportion of persistent echoes showing recognizable signs of amplitude or range disturbance is remarkably constant, being 0·35 for sporadics and δ-Aquarids, and 0·36 for Geminids and η-Aquarids. Finally, the aerial polar diagram is of course independent of the source of the meteors, and it is impossible that $\overline{W}_T$ should increase as s increases.

The only feasible explanation seems to be that persistent sporadic echoes are collected in minor aerial lobes which are not effective for shower echoes. Echo detection in minor lobes of low gain could markedly increase the proportion of persistent echoes without much affecting the total echo rate. Counts of persistent shower echoes were confined to intervals of time which extended little beyond the times of passage of the radiants through the main collecting areas of the equipments. Any minor lobes sufficiently removed in azimuth from the axis of the major lobe thus make no contribution to the persistent echo rates for showers, but are fully effective for sporadics where no time selection is involved. Collection in minor lobes in elevation is precluded by echo range discrimination. The theoretical polar diagram of the array predicts only two azimuthal minor lobes in which detection of persistent echoes could occur, but no measurements of the aerial polar diagram have been made at very low levels of gain. Examination of the diurnal pattern in the incidence of persistent echoes during the peak activity of the δ-Aquarid shower has established that there are no minor lobes comparable in gain with the main lobe, but this does not rule out the possibility that weaker minor lobes are present.

It is worth while pointing out that if, despite the arguments advanced above, it is assumed that (3b) gives the correct value of $\overline{W}_T$, the observed rate of persistent sporadic echoes implies a limiting line density for the equipment under normal operating conditions of $\alpha_0 \simeq 8 \times 10^{11}$/cm. This is quite incompatible with the $\alpha_0 \simeq 1 \times 10^{11}$/cm deduced from the calibrations already described.

The preceding discussion suggests that the experimental values of $\overline{W}_T$ are not excessively large. It follows that within the limits imposed by specular reflection, by neglect of trail distortion, and by an aerial pattern conforming to the theoretical polar diagram, the logarithmic form (3) is a satisfactory representation of the aerial aperture function. Amongst persistent echoes these restrictive conditions are relaxed and (3) undoubtedly understates the value of this function. Whilst this is of some consequence to the rate of persistent echoes, it exerts much less influence on the total echo rate if $\alpha_0 \ll \alpha_t$. The values of s given in Table 1 are therefore considered to be reliable.

VII. Discussion

It has been shown that, provided proper precautions are taken when interpreting rates of persistent echoes, relative echo rates measured at different equipment sensitivities can be used to obtain reliable determinations of the distribution of maximum electron line densities in meteor trails, and hence the mass distribution, over a wide range of brightness. The accuracy of these determinations depends on how well the aerial polar diagram is known. Results of acceptable accuracy are possible even if detailed knowledge of the aerial system is lacking.

Values of s for the Geminid shower agree well with determinations made over the same range of brightness by Browne *et al.* (1956) at Jodrell Bank, using different techniques. Sporadic meteors and the Geminid and δ-Aquarid showers all show increases in s as $\alpha_{\text{max.}}$ increases from 10^{11}/cm to 5×10^{13}/cm; the η-Aquarids show no increase in s over this range of $\alpha_{\text{max.}}$. For the first two showers the increase in s for $\alpha_{\text{max.}} > 5 \times 10^{13}$/cm is very steep indeed, so steep that it amounts effectively to a cut-off of meteors larger than the mass corresponding to $\alpha_{\text{max.}} \simeq 10^{14}$/cm. Sporadic meteors, on the other hand, do not appear to be subject to such a physical cut-off, and the value of $s = 2 \cdot 5$ still applies for $\alpha_{\text{max.}} > 10^{15}$/cm, which corresponds to a radio magnitude of -3, according to the definition given by Kaiser (1955*b*).

One attractive feature of the present method is that it is quite insensitive to the ionization curve of the meteor trails, and so is largely independent of the incidence of fragmentation amongst the meteors. The only other method of measuring s for fainter meteors which has received adequate theoretical treatment is the height distribution method (Kaiser 1954; Weiss 1959). This is at a disadvantage in measuring distributions of meteor masses, as it is sensitive to the shape of the ionization curve and the dependence of the height of the trails on maximum line density. The agreement between the s-values for fainter Geminid meteors found from echo rates (this paper) and from height distributions (Browne *et al.*), both of which were obtained by comparison with $s = 2 \cdot 0$ for sporadic meteors, can be taken to mean that Geminid meteors are subject to fragmentation to the same extent as sporadic meteors.

Similar comparisons of values of s derived for identical ranges of brightness from echo rates and from height distributions, for the same shower and preferably simultaneously, promise an easy means of estimating the incidence of fragmentation amongst shower meteors. Since the values of s are obtained by either method by comparison of shower data with similar data for sporadic meteors, it is the extent of the fragmentation relative to that for sporadic meteors which is really measured. Apart from the Geminids, s-values have been derived from echo rates for the δ-Aquarids and the η-Aquarids (this paper), and from height distributions for the Quadrantids, Perseids, and day-time Arietids (Browne *et al.* 1956). Measurements of s-values by the complementary methods for these five showers would complete the specification of the extent of the fragmentation amongst the fainter meteors of the more prominent permanent meteor showers. Owing to lack of contrast with the sporadic background it is doubtful whether useful results could be obtained for any of the remaining, weaker, permanent showers.

Of the six showers for which a value of s has been obtained, the day-time Arietids is the only one for which $s>2\cdot0$ for $\alpha_{\text{max.}}<10^{12}$/cm. According to Browne *et al.* (1956), for this shower $s=2\cdot7$ from the height distribution method. A possible interpretation of this result is that the distribution of maximum line densities is much the same as for the other showers, but that extreme fragmentation so narrows the height distribution that the anomalous s-value is found. The echo rate measurements needed to settle this point were attempted as part of the present programme, but were frustrated by low echo rates arising from the small elevation of the radiant at transit. It would be profitable to repeat these measurements in the northern hemisphere, where the radiant is much more favourably situated.

Another shower which would repay study is the periodic Giacobinid shower. The photographic measurements of Jacchia, Kopal, and Millman (1950) have shown that the brightest meteors (visual magnitudes $<+1$) belonging to this stream suffer an unusually large amount of fragmentation during their flight through the atmosphere. It would be interesting to ascertain whether such extreme fragmentation is also characteristic of the fainter meteors of this stream. Because of the high declination (+55°) of this radiant, the shower is invisible from Adelaide.

VIII. ACKNOWLEDGMENT

The author wishes to thank Mr. J. W. Smith for his great assistance in carrying out all the observations, and in reading and analysing the data on persistent echoes.

IX. REFERENCES

BROWNE, I. C., BULLOUGH, K., EVANS, S., and KAISER, T. R. (1956).—*Proc. Phys. Soc. Lond.* B **69**: 83.

DAVIS, J., GREENHOW, J. S., and HALL, J. E. (1959).—*Proc. Roy. Soc.* A **253**: 130.

HAWKINS, G. S., and UPTON, E. K. L. (1958).—*Astrophys. J.* **128**: 727.

JACCHIA, L. G., KOPAL, Z., and MILLMAN, P. M. (1950).—*Astrophys. J.* **111**: 104.

KAISER, T. R. (1953).—*Advanc. Phys.* **2**: 495.

KAISER, T. R. (1954).—*Mon. Not. R. Astr. Soc.* **114**: 39.

Kaiser, T. R. (1955*a*).—" Meteors." (Ed. T. R. Kaiser.) p. 119. (Pergamon Press : London.)
Kaiser, T. R. (1955*b*).—" Meteors." (Ed. T. R. Kaiser.) p. 55. (Pergamon Press : London.)
Kaiser, T. R., and Closs, R. L. (1952).—*Phil. Mag.* **43** : 1.
McKinley, D. W. R. (1951).—*Canad. J. Phys.* **29** : 403.
Weiss, A. A. (1955).—*Aust. J. Phys.* **8** : 148.
Weiss, A. A. (1959).—*Aust. J. Phys.* **12** : 54.
Weiss, A. A. (1960*a*).—*Mon. Not. R. Astr. Soc.* **120** : 388.
Weiss, A. A. (1960*b*).—*Aust. J. Phys.* **13** : 532.
Weiss, A. A. (1961).—C.S.I.R.O. Aust. Div. Radiophys. Rep. RPR 139.

THE SWEEP OF LONG WATER WAVES ACROSS THE PACIFIC OCEAN

By R. Green*

[*Manuscript received October* 4, 1960]

Summary

Seismic sea waves (tsunamis) are shallow water waves. The leading tsunami wave from the Chilean earthquake of May 22, 1960 at 19 hr 11 min 20 s G.M.T. arrived at Hobart in 12 hr. The tsunami was also recorded on tide gauges up the east coast of Australia and at Norfolk and Lord Howe Islands. The wave took 14 hr 04 min to reach Auckland, N.Z., but this is because of the low speed of the wave over the extensive submerged continental structure off the eastern coast of North Island. The tsunami was not recorded at Port Melbourne. From the travel-times the average depth of the Pacific Ocean between Tasmania and South America is 5500 m.

I. Introduction

Recently, Jaeger (1960) discussed many of the types of surface waves recorded by tide gauges. Subsequently, one special type of wave, the seismic sea wave or tsunami which was propagated all the way across the Pacific Ocean from Valdivia in Chili has been recorded in Australia and New Zealand. The wave on arriving at Hobart and Sydney caused unusual and spectacular ebbs and flows in the tides of these two harbours and the phenomenon attracted widespread public interest and press and radio comment.

The tsunami had its origin in a violent earthquake of magnitude $8\frac{1}{4}$ that occurred at Valdivia, Chili (lat. $39\frac{1}{2}$° S., long. 73° W.) in the afternoon of May 22 at 19 hr 11 min 20 s G.M.T. It is often presumed that geological faulting and sudden changes in the depth of the sea-bed cause a disturbance to the sea's surface and the disturbance is propagated as a seismic sea wave. On the other hand, Gutenberg (1939) noticed that invariably the first movement on a tide gauge is a recession of the sea and furthermore some earthquakes with epicentres on land have been associated with tsunamis and he suggests that the mechanism for the generation of tsunamis is the sudden movement of thick sedimentary deposits down the continental slope. The precise mechanism of the cause of the tsunami from Valdivia is not investigated in this paper.

The question of allocating an arrival time for the initial movement of a train of tsunami waves is difficult. The criterion which has been followed is to pick the first recognizable long period depression. This criterion appears to be decidedly satisfactory in that all the records show a similar character with long period oscillations preceding the more obvious shorter period oscillations. Reports of the wave have been received from many parts of the Pacific Ocean and this analysis for the Tasman Sea is based on the tide gauge records at Hobart, Mel-

---

* Geology Department, University of Tasmania, Hobart.

TABLE 1

THE FUNDAMENTAL DATA AS READ FROM THE TIDE GAUGE RECORDS AT TWELVE STATIONS IN AUSTRALIA AND NEW ZEALAND

Tide Gauge	Arrival Time May 23, 1960 E.S.T.= U.T.+10 hr		Travel-time				Arc Distance (degrees)	Average Speed (km/hr)	Average Depth of Ocean (m)
			Observed		Calculated				
	(hr	min)	(hr	min)	(hr	min)			
Hobart	17	10	12	00	13	30	89	824	5340
Camp Cove ..	18	45	13	34	14	55	95	779	4770
Fort Denison ..	18	45	13	34	14	55	95	779	4770
Newcastle ..	19	30	14	19	15	40	96	750	4410
Eden	19	00	13	49	14	50	93	746	4400
Norfolk Island ..	19	05	13	54	15	05	90	720	4090
Lord Howe I. ..	19	20	14	09	15	30	94	739	4300
Manukau (W) ..	19	15	14	04	15	40	81	641	3230
Waitemata (E)	19	15	14	04	15	05	81	641	3230
Melbourne ..	not recorded								
Pt. Lonsdale ..	indefinite								
Welshpool ..	indefinite								

bourne, Port Lonsdale, Port Welshpool, Eden, Norfolk Island, Lord Howe Island, Camp Cove and Fort Denison (Sydney), Newcastle, and Manukau and Waitemata (Auckland). The primary data taken from these records are given in Table 1.

II. WATER WAVES

For a uniform train of long crested waves of small amplitude (i.e. excluding capillary waves) Coulson (1952) gives the following expression for the velocity of the wave

$$C^2=(g\lambda/2\pi)\tanh 2\pi h/\lambda, \qquad (1)$$

where λ is the wavelength, C the speed of the wave, g the gravitational acceleration, and h the depth of water.

From Table 1 it can be seen that the average value for the speed of the waves is of the order of 700 km/hr and from the records of Hobart and Sydney tide gauges (see Figs. 3, 4, and 5), the period of waves is of the order of $\frac{1}{2}$ hr. Hence the wavelengths of the water waves in the open ocean are of the order of 300–400 km, in which case the waves in crossing the Pacific Ocean, where typical depths are 4–5 km, behave like shallow water waves. In such cases where $h \ll \lambda$, equation (1) can be simplified to

$$C^2=gh. \qquad (2)$$

The speed of the wave is not dependent upon wavelength and there is no dispersion. Hence the group velocity is the same as the phase velocity, and over water of uniform depth a pulse is propagated with unchanged shape. If the depth of water is different from place to place it can be seen from equation (2) that changes in speed and wavelength of the wave will result and the invariability of the pulse shape no longer holds.

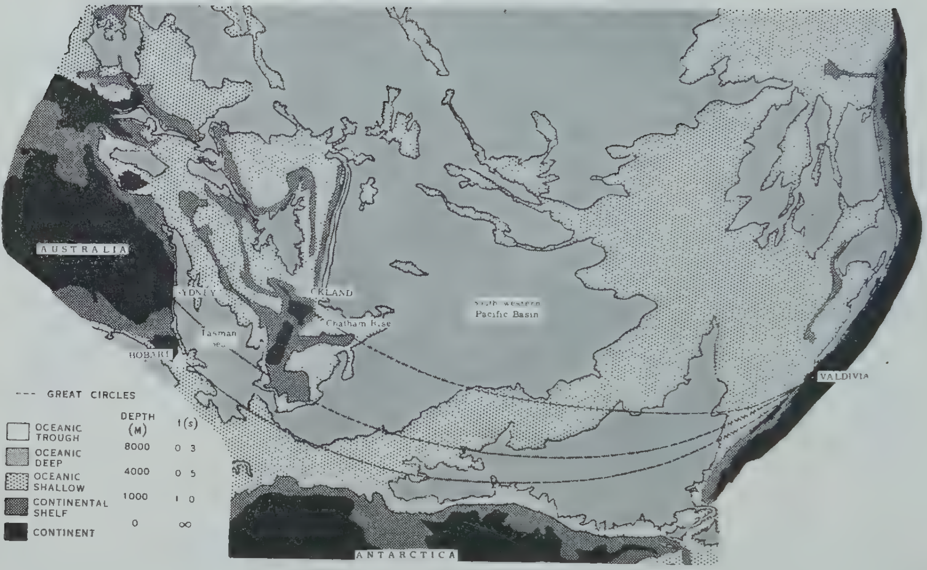

Fig. 1.—Map of the Pacific Ocean on Lambert's zenithal equal-area projection, 1 : 75,000,000. Contours are shown giving the depth of the water in terms of $f(s)$, which is the time taken for a tsunami to cover unit distance. The great circle arcs (shortest distances) between Valdivia and Hobart, Sydney, and Auckland are given. Notice that much of the path to Hobart is over deep water.

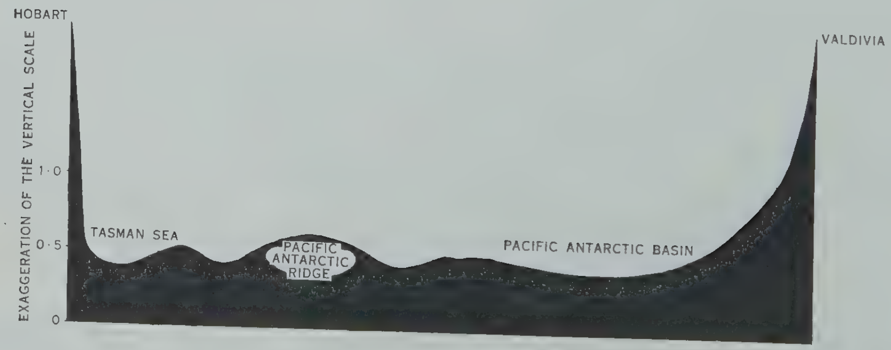

Fig. 2.—A profile of $f(s)$ along the direct path joining Valdivia to Hobart. The increased time for the tsunami to cross the South Eastern Pacific Plateau and the Pacific Antarctic Ridge is clearly indicated.

III. A New Method of Predicting Travel Times

In practice, the speed of these waves is very rarely measured directly; it is usual for the time of travel over a given variable-speed path length to be measured. For a given ray along a path of length S, the expected travel time τ is given by

$$\tau = \int_0^S \frac{dS}{C}, \tag{3}$$

and from (2) and (3)

$$\tau = \frac{1}{g^{\frac{1}{2}}} \int_0^S \frac{dS}{h^{\frac{1}{2}}}. \tag{4}$$

Numerical calculations of τ can be greatly simplified by means of the following transformation. Let

$$f(S) = 1/h^{\frac{1}{2}}, \tag{5}$$

in which case from (4) and (5)

$$\tau = 1/g^{\frac{1}{2}} \int_0^S f(S).dS. \tag{6}$$

The integral in (6) is conveniently the area under the curve $f(S)$. If the path length S is given in kilometres and the depth h is also in kilometres, the travel time τ in hours is given by

$$\tau = 1/356 \int_0^S f(S).dS. \tag{7}$$

Figure 1 shows not the depth of water in the Pacific Ocean but contours of equal values of $f(S)$ for use in (7). Figure 2 shows the profile of $f(S)$ along the direct path joining Valdivia to Hobart, and the computed time, which is 1/356 of the area under the profile of $f(S)$ between the two towns, is found to be 13 hr 30 min. It will be appreciated that it is much simpler and quicker and more accurate to draw a profile and to take the area under the curve than to determine and sum piecemealwise the travel times of successive portions of the entire path. The fact that the calculated time is slightly greater than the observed time may be because the Pacific is deeper than present-day contour maps show. On the other hand, as pointed out by Green (1946), when discussing the tsunami generated by the Alaskan earthquake of May 1, 1946, the sea wave is invariably more successful than the geophysicist in deciding the path of minimum time between two points.

IV. The Tide Gauge Records

Figure 3 shows the tide gauge records made at Hobart on May 23–24. The first arrival of the tsunami is indicated by a slight drop in sea level at 05 10 p.m. (Australian E.S.T.). Thereafter the frequency and amplitude of the oscillations build up reaching a maximum some 12 hr later.

Figure 4 is a tracing from the Camp Cove (N.S.W.) tide gauge. This instrument is more damped than the Hobart gauge and consequently wave action is less apparent. The arrival of the tsunami can be seen as a recession at 06 45 p.m. E.S.T.

Figure 5 is a tracing from the Fort Denison (N.S.W.) tide gauge. It is very similar to the Camp Cove record. On this record the first arrival time of the tsunami has been placed at 06 45 p.m. E.S.T.

Figure 6 is a tracing of the Newcastle record. Late in the night of May 23 large amplitude waves were set up in the harbour but the first arrival of the tsunami is indicated by a drop in sea-level at 07 30 p.m.

The Melbourne tide gauge reported that the tsunami was not detected. The Point Lonsdale and Port Welshpool tide gauges recorded small amplitude tsunami wave oscillations with an indefinite beginning. Mr. C. O'Malley, Port Officer for Victoria, reported in a personal communication that " The disturbances at Point Lonsdale were similar in magnitude to those at Port Welshpool, although the maximum occurred some seven hours later ". It would appear that the shallow, island-studded Bass Strait presents serious resistance to the progress of the tsunami. This is in marked contrast to the towns on the New South Wales coast which border the Tasman Sea.

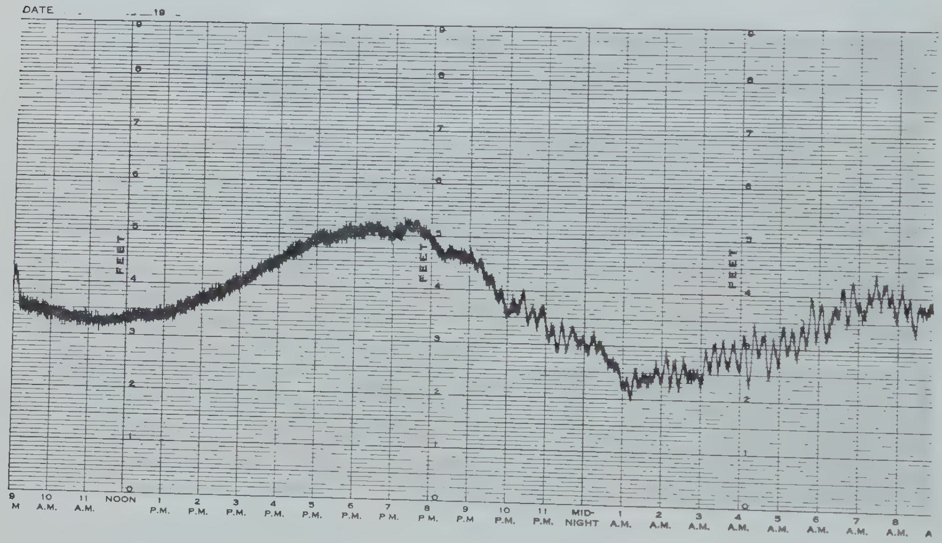

Fig. 3.—Tide gauge record made at Hobart on May 23–24. The first long depression is taken as the arrival of the tsunami.

Eden on the New South Wales coast recorded the first arrival at 07 00 p.m. E.S.T. and clear large amplitude waves built up from 10 30 p.m. E.S.T. Lord Howe Island recorded the first movement at 07 20 p.m. E.S.T. and large amplitude waves built up from 09 20 p.m.

The first arrival at Norfolk Island was placed at 07 00 p.m. E.S.T.

In New Zealand the tide gauges at Manukau (Auckland—Tasman Sea coast) and Waitemata (Auckland—Pacific Ocean coast) both recorded the effects of the tsunami. A tracing of the records is shown in Figure 7. Both of these gauges are over-damped for recording of tsunami waves. The first positive

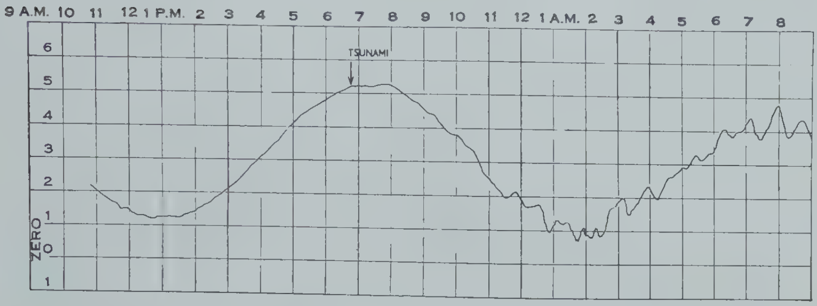

Fig. 4.—Tide gauge record made at Camp Cove, N.S.W., May 23–24.

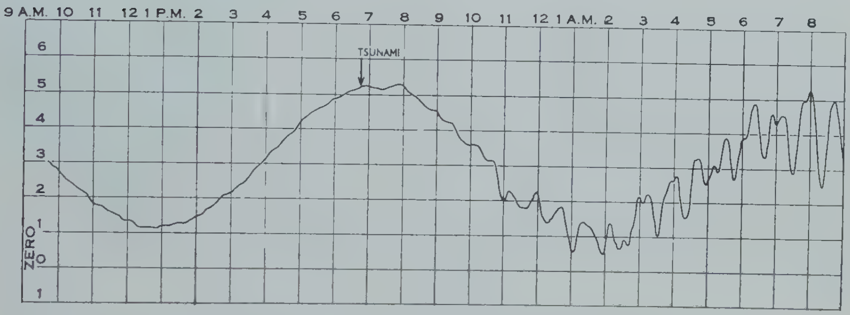

Fig. 5.—Tide gauge record made at Fort Denison, N.S.W., May 23–24. If Figure 4 is compared with Figure 5, a high order of correlation is found. This is probably due to seiches being set up in Port Jackson.

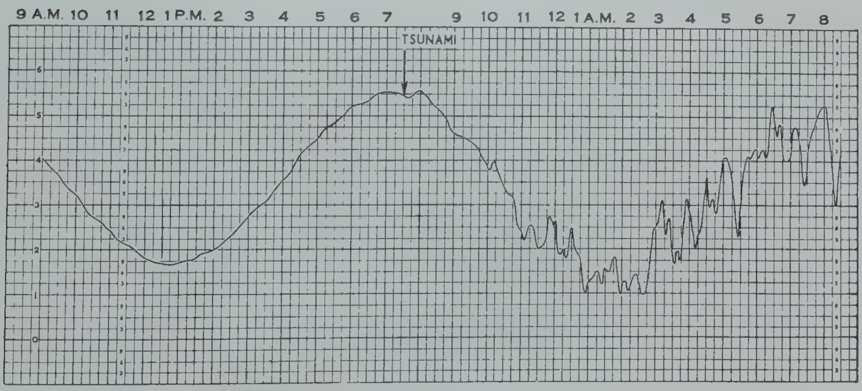

Fig. 6.—Tide gauge record made at Newcastle on May 23–24.

movement of the Waitemata gauge was at 07 15 p.m. Australian E.S.T. On the Manukau gauge the first arrival of the tsunami is most indefinite; using the criteria as set out in Section I for the identification of the initial tsunami wave, the arrival time is placed at 07 15 p.m. Australian E.S.T.

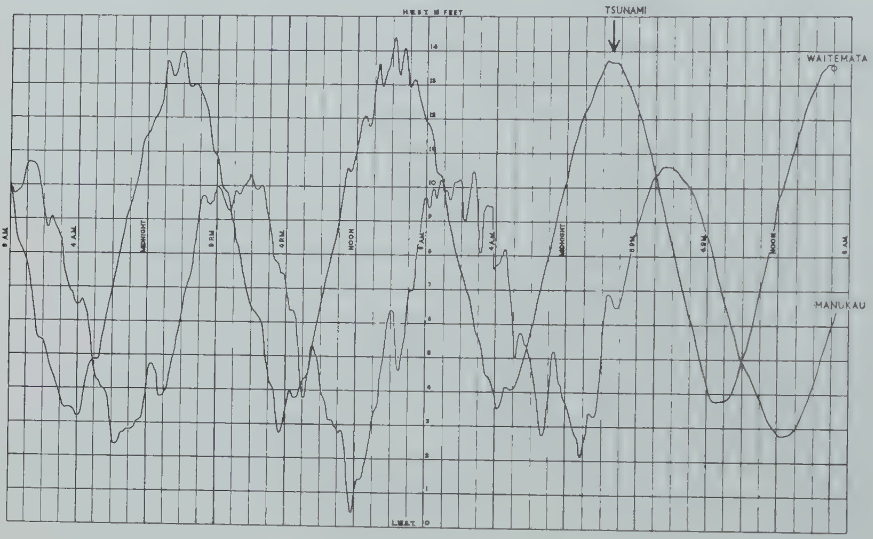

Fig. 7.—Tide gauge records made at Auckland in Manukau (Tasman Sea Coast) and Waitemata (Pacific Ocean Coast) harbours.

V. Comments on the Results

In Table 1 the calculated travel-times by the method given in Section III are compared with the observed times. The consistently greater value for the calculated travel-time compared with the observed travel-time suggests that the South Pacific Ocean is deeper than recent charts suggest (Bathymetric charts—Monaco Hydrographic Institute). Also listed in Table 1 are the average ocean depths between Valdivia and the Australasian recording stations. The average depth between Valdivia and Hobart along the path traversed by the tsunami is 5340 m. Proceeding up the Australian coast, the computed average depth decreases. A surprising result is the Eden record which shows the first wave arriving 15 min after Sydney's first arrival. The early arrivals at Sydney could be due to the influence of the Ulladulla trough off Sydney and Newcastle.

The New Zealand station gives a value of 3230 m. This calculated average depth is clearly too low, but it must be remembered that the 87° of arc which was used in the calculation as the great circle distance from Valdivia to Auckland is less than the actual path traversed by the wave. Part of the great circle between Auckland and Valdivia lies across the North Island of New Zealand. The seismic sea wave must have, in consequence, travelled over a longer path and even so, a large part of any path to Auckland is over submerged continental crust with water depths less than 1000 m where the speed of a shallow water wave will be less than 356 km/hr compared with an average speed of a wave to Hobart of 824 km/hr.

Tsunami waves are slowed down and quickly reduced in amplitude when they enter a shallow shelf-area which is studded with islands such as Bass Strait. Melbourne shows no trace of the tsunami and from the Point Lonsdale and Port Welshpool records very little can be gleaned.

VI. Conclusions

It can be expected that from earthquakes originating off-shore of South America the seismic sea wave will arrive first in Tasmania in 12 hr and then sweep up the eastern coast of Australia reaching Newcastle some 2 hr later. The forward crest of the wave would travel up the mid Tasman deep and towns on the Tasman Sea side of New Zealand would be affected by this wave at roughly the same time as towns on the eastern coast of Australia. It would be expected that the tsunami would arrive at towns in the South Island of New Zealand (see Fig. 1) considerably earlier than at Auckland.

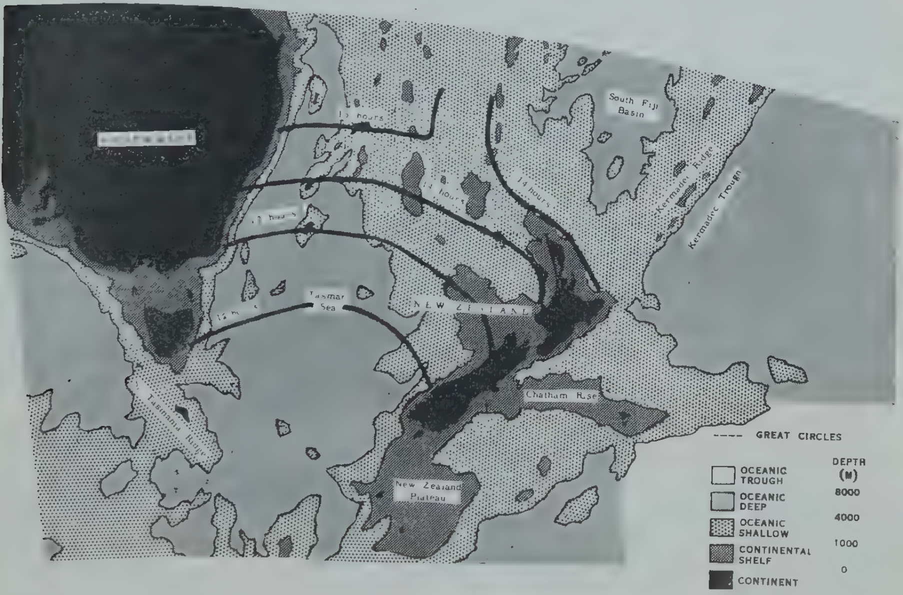

Fig. 8.—This shows the tsunami spreading over the Tasman Sea. The map in Bonnes projection 1 : 28,000,000. By means of the Antarctic Basin the wave quickly arrives in the South Tasman Sea. Notice the interference pattern obtained off the Queensland coast. Notice also the retarding effect of shallow water on the progress of the wave.

The spreading of the tsunami over the Tasman Sea is shown in Figure 8. This figure is based on calculations of the type in Section III for the form of the wave fronts, and on tide gauge observations for the numerical values of the isochronous fronts.

Much of the Queensland coast (see Fig. 1) is protected by a submerged continental shelf over which the speed of the wave would be greatly reduced similarly as in the approach to Auckland. It would be expected that the effect of the wave would be small on Queensland coastal towns. Also shown in Figure 8 is that the initial wave may arrive at places in the northern part of the Tasman Sea by two widely different paths ; one path via the Antarctic Basin—Tasman Sea and the other path more directly across the Pacific Basin and the South Fiji Basin. The wave front for the former case will be travelling northwards, whereas in the latter case it will be travelling westwards, and the two sets of waves will interfere with one another off the Queensland coast.

The phase relationships between the waves recorded by the Camp Cove and Fort Denison gauges are interesting. These two gauges in Sydney Harbour show very little difference in phase for the first few hours after the arrival of the tsunami but as time elapses the phase difference becomes large as Sydney Harbour is excited into a resonant seiche.

The seismic sea waves are often destructive in Japan and Hawaii but it is very unlikely that a " tidal wave " will inundate Australian towns because, as Figure 1 shows, nowhere in Australia is the coast flanked by a great ocean deep ($\simeq$9000 m). The Ulladulla deep is our nearest approach to this type of structure but even the Ulladulla deep is only of the order of 5000 m.

VII. Acknowledgments

I wish to thank the various harbour authorities and other organizations for copies of their records : The Hobart Marine Board, the Maritime Services Board of New South Wales, The Auckland Harbour Board, The Melbourne Harbour Trust Commissioners, The Department of Public Works (Victoria), The Division of Fisheries and Oceanography, C.S.I.R.O., and the Department of Geophysics, Australian National University.

VIII. References

Coulson, C. A. (1952).—" Waves." 6th Ed. (Oliver and Boyd : Edinburgh.)

Green, C. K. (1946).—Seismic sea waves of April 1, 1946, as recorded on tide gauges. *Trans. Amer. Geophys. Un.* **27** : 490.

Gutenberg, B. (1939).—Tsunamis and earthquakes. *Bull. Seism. Soc. Amer.* **29** : 517.

Jaeger, J. C. (1960).—Long ocean waves. *Aust. J. Sci.* **23** : 41.

ESTIMATION OF THE MAXIMUM TEMPERATURE IN A RADIALLY CONSTRICTED GAS DISCHARGE BETWEEN ELECTRODES

By P. W. Seymour*

[*Manuscript received November* 16, 1960]

Summary

A steady-state deuterium discharge between two electrodes is considered and the free boundary surface of the plasma is assumed thermally insulated when pinched away from the walls of the discharge tube. Cooling is therefore by heat conduction to the electrodes, compared to which bremsstrahlung loss is shown to be negligible if the discharge is not too long. The main question examined is how much the maximum temperature T_m can be raised by constricting the cross section of the discharge near the centre.

The analysis is confined to substantially ionized deuterium, and curves based on the Saha equation are provided to show the minimum gas temperatures required for various particle densities. With neglect of thermoelectric effects, there exists a median plane, normal to the longitudinal axis of the discharge, about which the distributions of temperature and voltage are symmetrical. The analysis is carried through both by specializing the current density and heat flux vectors, $\mathbf{j}$ and $\mathbf{q}$, to cater for an isotropic plasma, and for a plasma made anisotropic by a strong, external magnetic field. Prior to detailed mathematical analyses, however, a simple continuity argument yields the important relationship, $\mathbf{q}+V\mathbf{j}=0$, where V is the electric potential, provided that everywhere within the discharge $\mathbf{q}$ is parallel to $\mathbf{j}$. This type of flow, termed for convenience longitudinal flow, is the main concern of the paper.

The detailed axi-symmetric analyses for slightly and greatly constricted discharges show that $T^2+(\sigma_0/K_0)V^2=T_m^2$, where σ_0 and K_0 are related to Spitzer's formulae for the electrical and thermal conductivities of a highly ionized gas, and T_m is the temperature on the median plane, where $V=0$. Use of an electric stream function Ψ and the electric potential V as curvilinear coordinates simplifies the plasma energy equation. An analytic solution of this equation if the temperature T is a function of Ψ only, shows that the heat flow can be everywhere perpendicular to the flow of electricity only when the streamlines are straight and parallel to the longitudinal axis of symmetry. Analytic solutions if T is a function of V, representing the longitudinal flow, are given for (1) straight streamlines parallel to the longitudinal axis of symmetry, (2) hyperbolic streamlines to represent a discharge constricted at the median plane. A curve giving the variation of T with distance along the linear discharge is included.

Upper-limit expressions for the central temperature T_m are obtained in terms of the total current carried by the longitudinally stabilized discharge and its characteristic dimensions, and a curve gives the dependence on constriction of T_m and of the resistance R between the electrodes for constant total discharge current. If a large radial constriction at the median plane is achieved by use of a strong guiding magnetic field which makes the conductivities anisotropic, a tensorial analysis is required, but leads to the same results for longitudinal flow. Where the thermal insulation and neglect of bremsstrahlung approximations apply, the direction of heat flow is not expected to depart significantly anywhere from that of the flow of electricity, and so the above curve should provide a useful guide to the increase of T_m and R due to constriction. For an area constriction of 400 : 1, T_m and R are increased by a factor of about 4.

---

* Research School of Physical Sciences, Australian National University, Canberra.

Characteristics relating T and the magnetic field H, when $\omega_e\tau_e=1$ (ω_e is the electron gyrofrequency, τ_e the electron collision time) are given for various values of the total particle density. Hence it is possible to find where the vector ($\omega_e\tau_e\ll 1$) and tensor ($\omega_e\tau_e\gg 1$) solutions are applicable.

I. INTRODUCTION

In the following analysis the flows of heat and electricity in a steady non-equilibrium state gas discharge between a pair of electrodes are examined, with the principal object of determining theoretically the maximum plasma temperature T_m. For simplicity, the treatment is confined to discharges of highly ionized gases having low bremsstrahlung loss and free boundary surfaces perfectly insulated thermally by a high vacuum. Non-constricted and constricted discharges are treated.

II. APPLICATION OF THE SAHA EQUATION

The Saha equation (Saha 1920 ; Saha and Saha 1934 ; Allis 1956 ; Cobine 1958) applies to a gaseous system in thermal equilibrium, whereas we shall consider systems which depart from this condition by virtue of an excess of the electron temperature over the ion temperature, as discussed by Allis in the above reference, and treated in greater detail by Alfvén (1950). However, as Allis points out, the temperature can never become less than that given by the Saha equation, and accordingly we apply it here to obtain some idea of the minimum temperatures at which a gas may be regarded as substantially ionized as the particle density varies over an appropriate range. Thus, applying Cobine's form of the Saha equation to a plasma, having equal concentrations of singly ionized atoms and electrons ($n_e=n_i$) we obtain

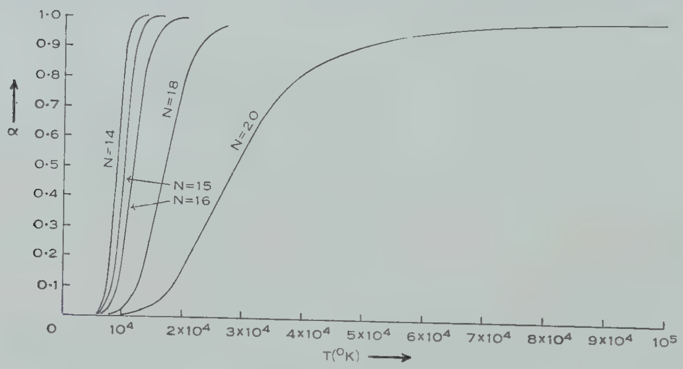

Fig. 1.—Saha curves for hydrogen. n_a atoms/cm³ ($n_a=10^N$) ; n_i singly ionized atoms/cm³ ; $\alpha=n_i/n_a$, degree of ionization ; T, gas temperature.

$$\log\{\alpha^2/(1-\alpha)\}=1\cdot 5\log T-(N-15\cdot 385)-5050V_i/T, \tag{2.1}$$

where, if n_a atoms/cm³ is the original concentration of the gas,

$\alpha=n_i/n_a$ is the degree of ionization,
T is the gas temperature in degrees Kelvin,
$N=\log n_a$,
V_i is the ionization potential of the gas in volts.

Here our main interest will be in the hydrogen isotope, deuterium, and so the temperature dependence of α for hydrogen has been calculated from equation (2.1) for N-values varying from 14 to 20, and presented in Figure 1.

For substantially ionized hydrogen gas ($\alpha \sim 0 \cdot 9$, say) the minimum temperature for a given value of N can now be readily obtained. It is of interest to note from each of these curves that this minimum temperature lies well below the temperature corresponding to the ionization potential of the gas concerned, particularly for the smaller values of N.

III. Preliminary Discussion of the Current Density and Heat Flux Vectors

In the absence of an external magnetic field $\mathbf{H}$, the flows of electricity and heat in a system mutually interfere, and, as Callen (1948) has pointed out, the thermoelectric effects of Peltier and Seebeck may be viewed as the result of this interference. Further, if an external magnetic field is impressed on the system, thermomagnetic and galvanomagnetic effects (Ettingshausen, Hall, Nernst, and Righi-Leduc effects) appear. To account for these effects, we shall now follow the procedure adopted by Marshall in his comprehensive report (1957) and, for a region made anisotropic by the presence of a magnetic field, write the conduction current density vector, $\mathbf{j}$, and the heat flux vector, $\mathbf{q}$, as

$$\mathbf{j} = \underbrace{\sigma^{\mathrm{I}}\mathbf{E}^{||} + \sigma^{\mathrm{II}}\mathbf{E}^{\perp}}_{\substack{\text{No special}\\ \text{name}}} + \underbrace{\sigma^{\mathrm{III}}\mathbf{h}\times\mathbf{E}^{\perp}}_{\text{Hall}} + \underbrace{\varphi^{\mathrm{I}}(\nabla T)^{||} + \varphi^{\mathrm{II}}(\nabla T)^{\perp}}_{\text{Seebeck}} + \underbrace{\varphi^{\mathrm{III}}\mathbf{h}\times(\nabla T)^{\perp}}_{\text{Nernst}}, \tag{3.1}$$

where $\mathbf{E}$ is the electric field,
$\mathbf{E}^{||}$ is the component of $\mathbf{E}$ parallel to $\mathbf{H}$,
$\mathbf{E}^{\perp}$ is the component of $\mathbf{E}$ perpendicular to $\mathbf{H}$,
$\mathbf{h} = \mathbf{H}/H$ is a unit vector in the direction of $\mathbf{H}$,
∇T is the temperature gradient,
$(\nabla T)^{||}$ is the component of ∇T parallel to $\mathbf{H}$,
$(\nabla T)^{\perp}$ is the component of ∇T perpendicular to $\mathbf{H}$,
σ^{I}, σ^{II}, and σ^{III} are coefficients of electrical conductivity,
φ^{I}, φ^{II}, and φ^{III} are thermal diffusion coefficients,

and

$$\mathbf{q} = -\lambda^{\mathrm{I}}(\nabla T)^{||} - \lambda^{\mathrm{II}}(\nabla T)^{\perp} - \lambda^{\mathrm{III}}\mathbf{h}\times(\nabla T)^{\perp} + \Psi^{\mathrm{I}}\mathbf{j}^{||} + \Psi^{\mathrm{II}}\mathbf{j}^{\perp} + \Psi^{\mathrm{III}}\mathbf{h}\times\mathbf{j}^{\perp}, \tag{3.2}$$

where $\mathbf{j}^{||}$ is the component of $\mathbf{j}$ parallel to $\mathbf{H}$,
$\mathbf{j}^{\perp}$ is the component of $\mathbf{j}$ perpendicular to $\mathbf{H}$,
λ^{I}, λ^{II}, and λ^{III} are thermal conductivity coefficients, Ψ^{I}, Ψ^{II}, and Ψ^{III} are coefficients giving the heat flux due to electric currents.

Using (3.1), (3.2) can be written

$$\mathbf{q} = \underbrace{-K^{\mathrm{I}}(\nabla T)^{||} - K^{\mathrm{II}}(\nabla T)^{\perp}}_{\text{No special name}} \underbrace{-K^{\mathrm{III}}\mathbf{h}\times(\nabla T)^{\perp}}_{\text{Righi-Leduc}} + \underbrace{\xi^{\mathrm{I}}\mathbf{E}^{||} + \xi^{\mathrm{II}}\mathbf{E}^{\perp}}_{\text{Peltier}} + \underbrace{\xi^{\mathrm{III}}\mathbf{h}\times\mathbf{E}^{\perp}}_{\text{Ettingshausen}}, \tag{3.3}$$

where K^{I}, K^{II}, and K^{III} are thermal conductivity coefficients when electric currents are allowed to flow, given by

$$\left.\begin{aligned} K^{\mathrm{I}}&=\lambda^{\mathrm{I}}-\Psi^{\mathrm{I}}\varphi^{\mathrm{I}},\\ K^{\mathrm{II}}&=\lambda^{\mathrm{II}}-\Psi^{\mathrm{II}}\varphi^{\mathrm{II}}+\Psi^{\mathrm{III}}\varphi^{\mathrm{III}},\\ K^{\mathrm{III}}&=\lambda^{\mathrm{III}}-\Psi^{\mathrm{II}}\varphi^{\mathrm{III}}-\Psi^{\mathrm{III}}\varphi^{\mathrm{II}}, \end{aligned}\right\} \tag{3.4}$$

and ξ^{I}, ξ^{II}, and ξ^{III} are coefficients accounting for the contribution to the heat flux from the electric field $\mathbf{E}$, given by

$$\left.\begin{aligned} \xi^{\mathrm{I}}&=\Psi^{\mathrm{I}}\sigma^{\mathrm{I}},\\ \xi^{\mathrm{II}}&=\Psi^{\mathrm{II}}\sigma^{\mathrm{II}}-\Psi^{\mathrm{III}}\sigma^{\mathrm{III}},\\ \xi^{\mathrm{III}}&=\Psi^{\mathrm{II}}\sigma^{\mathrm{III}}+\Psi^{\mathrm{III}}\sigma^{\mathrm{II}}. \end{aligned}\right\} \tag{3.5}$$

The results (3.4) and (3.5) are not given explicitly by Marshall; they can alternatively be obtained from results given in Part 3 of his report (pp. 28–9) by neglecting the electron mass m_e relative to the ion mass m_i, and by noting that the K's here correspond to Marshall's θ's.

Further information on the terms representing the effects discovered by Ettingshausen, Hall, Nernst, Peltier, Righi and Leduc, and Seebeck in the expressions (3.1) and (3.3) for $\mathbf{j}$ and $\mathbf{q}$ is provided by Chapman and Cowling (1953), Hix and Alley (1958), Linhart (1960), and the above article by Callen.

An attempt to base the following analysis on equations (3.1) and (3.3) encounters mathematical difficulties. However, realistic solutions can be obtained to the present problem by considering two special forms of $\mathbf{j}$ and $\mathbf{q}$:

(i)
$$\mathbf{j}=\sigma^{\mathrm{I}}\mathbf{E}^{\parallel}+\sigma^{\mathrm{II}}\mathbf{E}^{\perp}+\sigma^{\mathrm{III}}\mathbf{h}\times\mathbf{E}^{\perp} \tag{3.6}$$
and
$$\mathbf{q}=-K^{\mathrm{I}}(\nabla T)^{\parallel}-K^{\mathrm{II}}(\nabla T)^{\perp}-K^{\mathrm{III}}\mathbf{h}\times(\nabla T)^{\perp}, \tag{3.7}$$
(ii)
$$\mathbf{j}=\sigma^{\mathrm{I}}\mathbf{E}^{\parallel}+\sigma^{\mathrm{II}}\mathbf{E}^{\perp}+\varphi^{\mathrm{I}}(\nabla T)^{\parallel}+\varphi^{\mathrm{II}}(\nabla T)^{\perp} \tag{3.8}$$
and
$$\mathbf{q}=-K^{\mathrm{I}}(\nabla T)^{\parallel}-K^{\mathrm{II}}(\nabla T)^{\perp}+\xi^{\mathrm{I}}\mathbf{E}^{\parallel}+\xi^{\mathrm{II}}\mathbf{E}^{\perp}. \tag{3.9}$$

This analysis is based on (3.6) and (3.7), which amount to (3.1) and (3.3) with the terms multiplied by φ and ξ omitted; i.e. we neglect the effect of thermal diffusion on $\mathbf{j}$ and the contribution of the electric field to $\mathbf{q}$. Limiting forms of (3.6) and (3.7) are obtained in the next section, for insertion later into the plasma energy equation, which is established in Section V.

Equations (3.8) and (3.9), which include thermoelectric effects, exclude thermomagnetic and galvanomagnetic effects, but nevertheless apply if the magnetic field is parallel to $\mathbf{E}$ and ∇T, will be used in a subsequent paper.

IV. j AND q FOR CONDITIONS OF ISOTROPY AND EXTREME ANISOTROPY (HALL AND RIGHI-LEDUC EFFECTS ONLY INCLUDED)

By associating with the unit vector $\mathbf{h}$ further unit vectors $\mathbf{f}$ and $\mathbf{g}$, to produce an orthogonal right-handed set, we can write (3.6) and (3.7) as

$$\mathbf{j}=\mathbf{f}(\sigma^{\mathrm{II}}E_f-\sigma^{\mathrm{III}}E_g)+\mathbf{g}(\sigma^{\mathrm{II}}E_g+\sigma^{\mathrm{III}}E_f)+\mathbf{h}\sigma^{\mathrm{I}}E^{\parallel}, \tag{4.1}$$

where $E_f=\mathbf{f}\cdot\mathbf{E}^{\perp}$ and $E_g=\mathbf{g}\cdot\mathbf{E}^{\perp}$, and

$$\mathbf{q}=\mathbf{f}[-K^{\mathrm{II}}(\nabla T)_f+K^{\mathrm{III}}(\nabla T)_g]+\mathbf{g}[-K^{\mathrm{II}}(\nabla T)_g-K^{\mathrm{III}}(\nabla T)_f]-\mathbf{h}K^{\mathrm{I}}(\nabla T)^{\parallel}, \tag{4.2}$$

where $(\nabla T)_f=\mathbf{f}\cdot(\nabla T)^{\perp}$ and $(\nabla T)_g=\mathbf{g}\cdot(\nabla T)^{\perp}$.

The tensorial nature of the electrical and thermal conductivity coefficients is perhaps at this stage best displayed by writing (4.1) and (4.2) using matrix notation. Thus, for (4.1)

$$\begin{bmatrix} j_f \\ j_g \\ j_h \end{bmatrix} = \begin{bmatrix} \sigma^{\mathrm{II}} & -\sigma^{\mathrm{III}} & 0 \\ \sigma^{\mathrm{III}} & \sigma^{\mathrm{II}} & 0 \\ 0 & 0 & \sigma^{\mathrm{I}} \end{bmatrix} \begin{bmatrix} E_f \\ E_g \\ E^{\parallel} \end{bmatrix}, \tag{4.3}$$

so that in general the matrix form of the electrical conductivity tensor is

$$[\ \sigma\ ] = \begin{bmatrix} \sigma^{\mathrm{II}} & -\sigma^{\mathrm{III}} & 0 \\ \sigma^{\mathrm{III}} & \sigma^{\mathrm{II}} & 0 \\ 0 & 0 & \sigma^{\mathrm{I}} \end{bmatrix}. \tag{4.4}$$

However, as Pease (1957) mentions, in the discharges we shall discuss the Hall current cannot flow. We therefore seek the modification to (4.4) for a zero Hall current.

Suppose that the Hall current becomes zero because of the appearance of a cancelling electric field, $\mathbf{E}_c^{\perp}$, in the direction of $\mathbf{h}\times\mathbf{E}^{\perp}$. Then, with total perpendicular electric field $(\mathbf{E}^{\perp}+\mathbf{E}_c^{\perp})$ we have from (3.6)

$$\mathbf{j}=\sigma^{\mathrm{I}}\mathbf{E}^{\parallel}+(\sigma^{\mathrm{II}}\mathbf{E}^{\perp}+\sigma^{\mathrm{III}}\mathbf{h}\times\mathbf{E}_c^{\perp})+(\sigma^{\mathrm{II}}\mathbf{E}_c^{\perp}+\sigma^{\mathrm{III}}\mathbf{h}\times\mathbf{E}^{\perp}). \tag{4.5}$$

Putting the component of $\mathbf{j}$ parallel to $\mathbf{E}_c^{\perp}$ to zero gives

$$\mathbf{E}_c^{\perp}=-(\sigma^{\mathrm{III}}/\sigma^{\mathrm{II}})\mathbf{h}\times\mathbf{E}^{\perp}, \tag{4.6}$$

and so

$$\mathbf{j}=\mathbf{f}\sigma^{\perp}E_f+\mathbf{g}\sigma^{\perp}E_g+\mathbf{h}\sigma^{\mathrm{I}}E^{\parallel}, \tag{4.7}$$

where we have introduced the perpendicular conductivity

$$\sigma^{\perp}=\sigma^{\mathrm{II}}[1+(\sigma^{\mathrm{III}}/\sigma^{\mathrm{II}})^2]. \tag{4.8}$$

We see now that when the Hall current cannot flow, the matrix of the conductivity tensor varies from the form (4.4) to the diagonal form

$$[\ \sigma\ ] = \begin{bmatrix} \sigma^{\perp} & 0 & 0 \\ 0 & \sigma^{\perp} & 0 \\ 0 & 0 & \sigma^{\mathrm{I}} \end{bmatrix}. \tag{4.9}$$

For (4.2),

$$\begin{bmatrix} q_f \\ q_g \\ q_h \end{bmatrix} = - \begin{bmatrix} K^{\mathrm{II}} & -K^{\mathrm{III}} & 0 \\ K^{\mathrm{III}} & K^{\mathrm{II}} & 0 \\ 0 & 0 & K^{\mathrm{I}} \end{bmatrix} \begin{bmatrix} (\nabla T)_f \\ (\nabla T)_g \\ (\nabla T)^{\parallel} \end{bmatrix}, \tag{4.10}$$

giving the matrix form of the thermal conductivity tensor as

$$[\ K\ ] = \begin{bmatrix} K^{\mathrm{II}} & -K^{\mathrm{III}} & 0 \\ K^{\mathrm{III}} & K^{\mathrm{II}} & 0 \\ 0 & 0 & K^{\mathrm{I}} \end{bmatrix}. \tag{4.11}$$

To identify the forms of $[\sigma]$ and $[K]$ under isotropic conditions, and conditions of extreme anisotropy, we first use Marshall's report (pp. 66, 69) to construct Table 1, where, with the symbol $\simeq$ showing that the usual plasma approximations ($m_i \gg m_e$, $n_i \approx n_e \approx \frac{1}{2}n$, $e_e = -e_i = -e$) have been made, the electron gyrofrequency is

$$\omega_e \simeq eH/m_e c, \tag{4.12}$$

or

$$\omega_e \simeq 1\cdot758 \times 10^7 H \text{ s}^{-1} \text{ gauss}^{-1}, \tag{4.13}$$

and the electron collision time is

$$\tau_e \simeq \frac{3}{4\sqrt{(2\pi)}} \frac{m_e^{\frac{1}{2}} k^{3/2} T^{3/2}}{n_e e^4 \ln \lambda}, \tag{4.14}$$

or

$$\tau_e \simeq 0\cdot551 \frac{T^{3/2}}{n \ln \lambda} \text{ s cm}^{-3} \text{ deg}^{-3/2}, \tag{4.15}$$

with $\lambda = \overline{h/p_0}$, where $h = (kT/4\pi n_e e^2)^{1/2}$ is the Debye shielding distance, $p_0 = e^2/3kT$ an impact parameter defined by Spitzer (1956), and k is Boltzmann's constant.

Here we have written Marshall's τ in terms of Spitzer's $\ln \lambda$, using $\Psi \approx 2 \ln \lambda$. It is worth noting that Spitzer's t_c (p. 78) for electrons interacting with themselves is closely equal to Marshall's τ. Ln λ has a slow dependence on n_e and T, and a value in the region of 10 (values of $\ln \lambda$ are given by Spitzer in Table 5.1, and values of Ψ are given by Marshall, Appendix B).

Since $\omega_e \tau_e = (\frac{2}{3})^{1/2} \lambda_e / \rho_e$, where λ_e is the electron mean free path and ρ_e the electron gyroradius (Alfvén, p. 49), we see that for a relatively dense gas in the presence of negligible magnetic field,

$$\omega_e \tau_e \ll 1, \tag{4.16}$$

while for a tenuous gas in the presence of strong **H**,

$$\omega_e \tau_e \gg 1. \tag{4.17}$$

We now determine the forms of **j** and **q** for the conditions described by (4.16) and (4.17).

(*a*) **j** *and* **q** *for Isotropic Conditions* ($\omega_e \tau_e \ll 1$)

TABLE 1

COMPONENTS OF THE ELECTRICAL AND THERMAL CONDUCTIVITY TENSORS

Components of $[\sigma]$	Components of $[K]$
$\sigma^{\mathrm{I}} = 1\cdot931 \frac{n_e e^2 \tau_e}{m_e}$	$K^{\mathrm{I}} = 7\cdot18 \frac{n_e k^2 T \tau_e}{m_e}$
$\sigma^{\mathrm{II}} = \frac{n_e e^2 \tau_e}{m_e} \frac{\omega_e^2 \tau_e^2 + 1\cdot802}{\omega_e^4 \tau_e^4 + 6\cdot282 \omega_e^2 \tau_e^2 + 0\cdot933}$	$K^{\mathrm{II}} = \frac{2n_e k^2 T \tau_e}{m_e} \left\{ \frac{0\cdot458 \omega_e^2 \tau_e^2 + 3\cdot01}{\omega_e^4 \tau_e^4 + 6\cdot282 \omega_e^2 \tau_e^2 + 0\cdot933} + \frac{4\cdot458}{\omega_e^2 \tau_e^2 + 12\cdot716} \right\}$
$\sigma^{\mathrm{III}} = \frac{n_e e^2 \tau_e}{m_e} \frac{-\omega_e \tau_e (\omega_e^2 \tau_e^2 + 4\cdot382)}{\omega_e^4 \tau_e^4 + 6\cdot282 \omega_e^2 \tau_e^2 + 0\cdot933}$	$K^{\mathrm{III}} = \frac{2\cdot5 n_e k^2 T \tau_e}{m_e} \left\{ \frac{\omega_e \tau_e}{\omega_e^2 \tau_e^2 + 12\cdot716} - \frac{\omega_e \tau_e (\omega_e^2 \tau_e^2 + 6\cdot2)}{\omega_e^4 \tau_e^4 + 6\cdot282 \omega_e^2 \tau_e^2 + 0\cdot933} \right\}$

When $\omega_e\tau_e \ll 1$, Table 1 gives

$$\left.\begin{aligned} \sigma^{\mathrm{I}} &= 1{\cdot}931 n_e e^2 \tau_e / m_e, \\ \sigma^{\mathrm{II}} &\approx \sigma^{\mathrm{I}}, \\ \sigma^{\mathrm{III}} &\approx -\sigma^{\mathrm{I}}\, 2{\cdot}432\, \omega_e \tau_e \sim 0. \end{aligned}\right\} \tag{4.18}$$

Hence (4.8) gives $\sigma^{\perp} \approx \sigma^{\mathrm{I}}$, and (4.9) becomes

$$[\,\sigma\,] = \begin{bmatrix} \sigma^{\mathrm{I}} & 0 & 0 \\ 0 & \sigma^{\mathrm{I}} & 0 \\ 0 & 0 & \sigma^{\mathrm{I}} \end{bmatrix}. \tag{4.19}$$

The electrical conductivity is thus a scalar quantity, $\sigma = \sigma^{\mathrm{I}}$, when the magnetic field is negligible and the gas is sufficiently dense that collisions are dominant.

Similarly, from Table 1

$$\left.\begin{aligned} K^{\mathrm{I}} &= 7{\cdot}18 n_e k^2 T \tau_e / m_e, \\ K^{\mathrm{II}} &\approx K^{\mathrm{I}}, \\ K^{\mathrm{III}} &\approx -K^{\mathrm{I}}\, 2{\cdot}286\, \omega_e \tau_e \sim 0, \end{aligned}\right\} \tag{4.20}$$

and accordingly (4.11) may be written

$$[\,K\,] = \begin{bmatrix} K^{\mathrm{I}} & 0 & 0 \\ 0 & K^{\mathrm{I}} & 0 \\ 0 & 0 & K^{\mathrm{I}} \end{bmatrix}, \tag{4.21}$$

so that the thermal conductivity is a scalar, $K = K^{\mathrm{I}}$.

Using (4.19) and (4.21), and the notation of (3.6) and (3.7), equations (4.3) and (4.10) reduce to the isotropic forms

$$\mathbf{j} = \sigma \mathbf{E}, \tag{4.22}$$

the simple form of Ohm's law, and

$$\mathbf{q} = -K \nabla T, \tag{4.23}$$

which, referring to the definition of K following (3.3), is a form of Fourier's law (Weatherburn 1957).

(b) j *and* q *for Conditions of Extreme Anisotropy* ($\omega_e\tau_e \gg 1$)

When $\omega_e\tau_e \gg 1$, Table 1 gives

$$\left.\begin{aligned} \sigma^{\mathrm{I}} &= 1{\cdot}931 \frac{n_e e^2 \tau_e}{m_e}, \\ \sigma^{\mathrm{II}} &\approx \sigma^{\mathrm{I}} \frac{1}{1{\cdot}931\, \omega_e^2 \tau_e^2} \sim 0, \\ \sigma^{\mathrm{III}} &\approx -\sigma^{\mathrm{I}} \frac{1}{1{\cdot}931\, \omega_e \tau_e} \sim 0. \end{aligned}\right\} \tag{4.24}$$

From (4.8), $\sigma^{\perp} \approx \tfrac{1}{2}\sigma^{\mathrm{I}}$, and so (4.9) becomes

$$[\,\sigma\,] = \begin{bmatrix} \tfrac{1}{2}\sigma^{\mathrm{I}} & 0 & 0 \\ 0 & \tfrac{1}{2}\sigma^{\mathrm{I}} & 0 \\ 0 & 0 & \sigma^{\mathrm{I}} \end{bmatrix}. \tag{4.25}$$

The electrical conductivity is therefore a simple tensor when the magnetic field is strong and the gas tenuous.

Similarly, from Table 1

$$\left.\begin{aligned} K^{\mathrm{I}} &= 7\cdot18\frac{n_e k^2 T\tau_e}{m_e}, \\ K^{\mathrm{II}} &\approx K^{\mathrm{I}}\frac{1\cdot369}{\omega_e^2\tau_e^2}, \\ K^{\mathrm{III}} &\approx 0, \end{aligned}\right\} \tag{4.26}$$

and so (4.11) may be written

$$[\,K\,] = \begin{bmatrix} \varepsilon & 0 & 0 \\ 0 & \varepsilon & 0 \\ 0 & 0 & K^{\mathrm{I}} \end{bmatrix}, \tag{4.27}$$

with $\varepsilon = K^{\mathrm{I}}(1\cdot369/\omega_e^2\tau_e^2) \ll 1$; for the gyrotropic plasma considered here the thermal conductivity is thus a simple tensor.

Using (4.25) and (4.27), and the notation of (3.6) and (3.7), equations (4.3) and (4.10) reduce to

$$\mathbf{j} = \sigma\mathbf{E}^{||} + \tfrac{1}{2}\sigma\mathbf{E}^{\perp}, \tag{4.28}$$

and

$$\mathbf{q} = -K(\nabla T)^{||}. \tag{4.29}$$

Equations (4.28) and (4.29) represent **j** and **q** for extreme anisotropy, when the conduction is predominantly in the direction of **H**.

Clearly, the analysis that follows must fall into two main parts. The first, corresponding to (*a*) above, essentially employs vector methods; the second, corresponding to (*b*) above, will be of a simple tensorial nature. To summarize the principles on which the analyses will be based:

(i) Expressions for the thermal and electrical conductivities for fully ionized deuterium will be employed, and Figure 1 can be used to show the temperature and concentration conditions where this is permissible, and

(ii) The cases for $\omega_e\tau_e \ll 1$, $\omega_e\tau_e \gg 1$ will be examined separately, and Figure 2 has been included to show the dividing line, $\omega_e\tau_e = 1$, between them. This figure, which relates H and T for given $n = 2n_e$, and is based on $\omega_e\tau_e \approx 10^7(HT^{3/2}/n \ln \lambda)$ gauss^{-1} cm^{-3} deg$^{-3/2}$ obtained from (4.13) and (4.15), can be used to discover where the vector and tensor solutions are applicable within the indicated practical ranges of temperature and total concentration, which were chosen after consideration of Figure 1.

V. ESTABLISHMENT OF THE PLASMA ENERGY EQUATION

With reference to, say, Weatherburn (pp. 49–50) the energy equation in terms of **j** and **q** can here be written as

$$\operatorname{div}\mathbf{q} + P = \mathbf{j}\cdot\mathbf{E}, \tag{5.1}$$

where

$$P = 1\cdot42\times10^{-34} n_i^2 T^{1/2} \text{ W cm}^3 \text{ deg}^{-1/2} \tag{5.2}$$

is the loss due to bremsstrahlung for a fully ionized gas of atomic number $Z=1$ (Spitzer, p. 90).

We recall that for the steady-state condition

$$\mathbf{E}=-\text{grad } V, \tag{5.3}$$

where V is the electric potential.

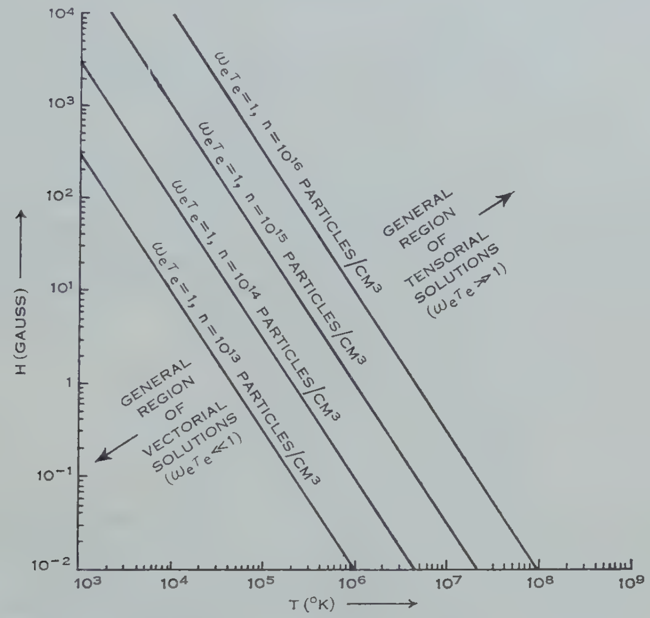

Fig. 2.—Relationship between magnetic field H and temperature T, with total concentration, $n=2n_e$, as parameter. In general, $\omega_e\tau_e \approx 10^7(HT^{3/2}/n \ln \lambda)$ gauss^{-1} cm^{-3} deg$^{-3/2}$. (Above lines for $\omega_e\tau_e=1$ are based on $\ln \lambda=10$.)

Similarly, for this condition, the electrical continuity equation reduces to

$$\text{div } \mathbf{j}=0. \tag{5.4}$$

For fully ionized deuterium, we can from Table 1 and equation (4.14) obtain expressions showing explicitly the temperature dependence of σ and K. However, it is of interest to compare σ and K for an actual gas with their values in a Lorentz gas, and so we choose to follow Spitzer and Härm (1953), by writing

$$\sigma=2\left(\frac{2}{\pi}\right)^{3/2}\frac{k^{3/2}T^{3/2}}{m_e^{1/2}e^2 \ln \lambda}\gamma_E, \tag{5.5}$$

and

$$K=20\left(\frac{2}{\pi}\right)^{3/2}\frac{k^{7/2}T^{5/2}}{m_e^{1/2}e^4 \ln \lambda}\delta_T, \tag{5.6}$$

where the charge on the electron, e, has been taken in e.s.u. Here σ and K for an actual gas have been expressed in terms of their values in a Lorentz gas by means of the transport coefficients γ_E and δ_T, given by Spitzer and Härm as

$\gamma_E=0\cdot5816$, $\delta_T=0\cdot2252$. (Spitzer and Härm's σ and K agree closely with those of Marshall.)

Writing (5.5) as

$$\sigma=\sigma_0(T^{3/2}/\ln\lambda), \tag{5.7}$$

and (5.6) as

$$K=K_0(T^{5/2}/\ln\lambda), \tag{5.8}$$

we obtain by inserting numerical values

$$\sigma_0=1\cdot53\times10^{-4}\ \text{ohm}^{-1}\ \text{cm}^{-1}\ \text{deg}^{-3/2}, \tag{5.9}$$

and

$$K_0=4\cdot396\times10^{-12}\ \text{joule s}^{-1}\ \text{cm}^{-1}\ \text{deg}^{-7/2}. \tag{5.10}$$

In general, expression (5.2) for the bremsstrahlung loss has a dependence on Z^3, so that the loss due to free-free transitions can assume significant proportions if the plasma becomes contaminated by high-Z elements; such contamination may well occur if the temperature at each electrode is allowed to become too high. However, if the length of the discharge is of order L, and the central temperature is T_m, then when $Z=1$ we find from (4.23) and (5.8)

$$\text{div}\,\mathbf{q}\sim-\frac{K_0}{L^2}\frac{T_m^{7/2}}{\ln\lambda}. \tag{5.11}$$

Hence, using (5.2) and (5.10),

$$\frac{|\,\text{div}\,\mathbf{q}\,|}{P}\sim3\times10^{21}\frac{T_m^3}{L^2n_i^2}\ \text{cm}^{-4}\ \text{deg}^{-3}. \tag{5.12}$$

For $T_m=10^5$ °K, $n_i=10^{15}$ ions/cm^3, $L=20$ cm, (5.12) gives $|\,\text{div}\,\mathbf{q}\,|/P\sim7\cdot5\times10^3$. We therefore conclude that for conditions of interest, neglect of the bremsstrahlung loss compared with the heat conduction loss to the electrodes in equation (5.1) does not appear to involve significant error provided the discharge is not too long. With the reasonable assumption that perfect thermal insulation exists at the plasma boundary surface when it is pinched away from the walls of the discharge tube during the containment period, we conclude that Joule heating of the plasma is balanced by heat conduction to the electrodes while the steady-state condition prevails: the plasma energy equation is now

$$\text{div}\,\mathbf{q}=\mathbf{j}\cdot\mathbf{E}. \tag{5.13}$$

Using equations (5.3) and (5.4), equation (5.13) can be written

$$\text{div}\,\mathbf{M}=0, \tag{5.14}$$

where

$$\mathbf{M}=\mathbf{q}+V\mathbf{j}. \tag{5.15}$$

VI. SOLUTIONS OF THE PLASMA ENERGY EQUATION

The analysis of a general, constricted discharge having symmetry about a median plane is conveniently carried through by introduction of an orthogonal curvilinear coordinate system, which can be specialized later to deal with the cases of non-constriction, and constriction corresponding to various practical conditions. However, before considering these cases, we can gain physical insight into the problem by considering a curved stream tube of a discharge constricted in the median plane and having smoothly increasing cross section towards the electrodes.

(a) *Curved Stream Tube of a Constricted Discharge*

Figure 3 shows a curved stream tube having symmetry about a median plane. Considering the semi-tube above the median plane, we see that on the median plane the total heat flux entering the tube at A is Q_0, and the total electric current entering at A is I. The electric potential on the median plane is assumed constant at V_0. Emerging from the tube at B is a total heat flux Q. Equation (5.4) and the definition of a stream tube (see, for example, Milne-Thomson 1955) ensure that the total electric current leaving the tube at B is I. The electric potential on the end of the tube at B is assumed constant at $V<V_0$.

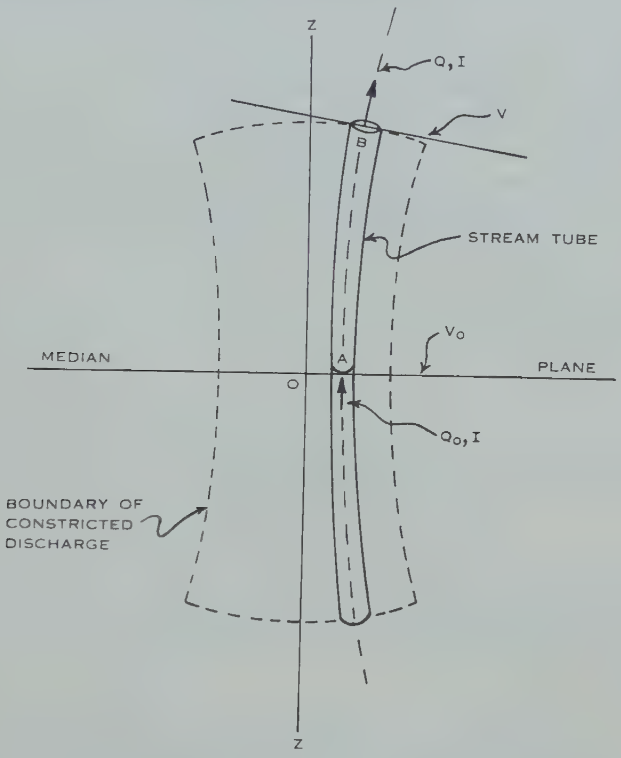

Fig. 3.—Curved stream tube of a constricted discharge.

For the steady-state condition the Joule heating, $(V_0-V)I$, must be balanced by the net heat outflow, $Q-Q_0$, and so

$$(V_0-V)I=Q-Q_0. \tag{6.1.1}$$

In the absence of thermoelectric effects it can be reasonably assumed that on the median plane $V_0=Q_0=0$, and (6.1.1) then reduces to

$$\mathbf{q}+V\mathbf{j}=0, \tag{6.1.2}$$

where we have returned to current and heat flux densities.

Formally, we can proceed as follows. Referring again to Figure 3, we can, in the absence of thermoelectric effects, assume a symmetry which leads to

$V_0=0$, $\partial T/\partial z=0$ on the median plane. Hence, if it is further assumed that on the median plane the temperature is everywhere constant, and equal to the maximum temperature T_m, then, with reference to equation (5.15), we see that **M** vanishes on the median plane. Thus, bearing in mind that the divergence of **M** is also zero (*vide* equation (5.14)), it follows that at every point within the tube, and within any similar tube contained by the constricted discharge, $\mathbf{M}=0$, or, using (5.15),

$$\mathbf{q}+V\mathbf{j}=0. \tag{6.1.3}$$

Clearly, this important result does not depend on the shape of the stream tubes, provided there is a median plane and that **q** and **j** at each point have the same direction, and since this type of heat and electricity flow is of main interest here, we give it the special name of longitudinal flow. Where the discharge has no external magnetic field acting upon it, and is non-constricted, the flow is expected to be approximately longitudinal owing to the assumed thermal insulation of the boundary surface mentioned in Section V. Where a strong external guiding magnetic field is used to constrict the discharge, both electric current and heat flow along the magnetic field lines, and this approximation holds even more closely.

Using (4.22) and (4.23) for **j** and **q** when $\omega_e\tau_e \ll 1$, together with (5.7) and (5.8), we obtain from (6.1.3)

$$T^2+(\sigma_0/K_0)V^2=T_m^2, \tag{6.1.4}$$

which shows that for longitudinal flow T is a function of V only. Inserting in (6.1.4) the values given by (5.9) and (5.10),

$$(T_m^2-T^2)^{1/2}=5899V \text{ deg V}^{-1}. \tag{6.1.5}$$

Similarly, for longitudinal flow the relationship between T and V when $\omega_e\tau_e \gg 1$ will be obtained in Section VI (*e*). As might be expected, it turns out to be the same as found here.

(*b*) *Use of the Stream Function* Ψ *and the Electric Potential* V *as Orthogonal Curvilinear Coordinates* ($\omega_e\tau_e \ll 1$)

It is mathematically convenient to concentrate first on axi-symmetric discharges for which $\omega_e\tau_e \ll 1$, accepting the fact that generally magnetic fields may not be very large.

In the case of steady axi-symmetric flow of an incompressible fluid, for which $\operatorname{div}\mathbf{v}=0$, where **v** is the velocity of a fluid particle, it is helpful to analyse in terms of a stream function (Stokes 1842).

Similarly, since from (5.4) the vector **j** is solenoidal, it is found advantageous here to introduce an electric stream function Ψ, such that

$$I(P)=2\pi\Psi(P), \tag{6.2.1}$$

where $I(P)$ is the total electric current through a surface generated by rotation of a line NP, not necessarily an equipotential, about the symmetry axis OZ

in Figure 4. If P moves along a line LQ such that $\Psi(P)=\text{const.}$, LQ is by definition a current stream line, everywhere tangent to **j**. Rotation of LQ about OZ results in a stream surface $\Psi(P)=(1/2\pi)I(P)=\text{const.}$ Clearly, the stream function vanishes on the axis of symmetry. By integration,

$$I(P)=2\pi\int_0^{s(P)} \rho j_n ds, \tag{6.2.2}$$

where, with reference to Figure 4, ρ is a cylindrical coordinate, s is arc length, measured along NP from the axis of symmetry, j_n is the component of **j** normal to ds.

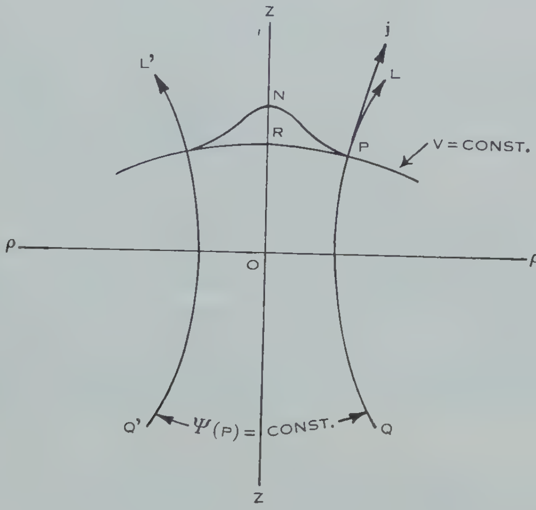

Fig. 4.—V and Ψ as orthogonal curvilinear coordinates (axi-symmetric flow).

From (6.2.1) and (6.2.2),

$$j_n=\frac{1}{\rho}\frac{\partial\Psi}{\partial s}, \tag{6.2.3}$$

which confirms that, when the electric stream function is constant and the element of arc lies along a stream line, there is no flow of electricity across the corresponding stream surface. If in (6.2.3) the element of arc is taken to lie along an equipotential line, such as RP in Figure 4, j_n becomes j, the magnitude of **j**, and

$$I(P)=2\pi\int_0^{s(P)} \rho j ds \quad (V=\text{const.}). \tag{6.2.4}$$

Since axi-symmetric flow is being examined, it is possible to write the energy equation (5.13) in a form which proves to be initially useful by introducing as curvilinear coordinates Ψ, φ, and V. Noting from (4.22) that **E** has the direction of **j**, we see from (5.3) that the equipotential surfaces $V=\text{const.}$, generated by rotation of lines such as RP through $\varphi=2\pi$ about OZ, are orthogonal to the streamlines and stream surfaces Ψ=const. With E as the magnitude of $\mathbf{E}$, we note from Figure 4 that the scale factors are

$$\left.\begin{aligned} h_1 &= \left|\frac{\partial s}{\partial \Psi}\right| = \frac{1}{\rho j}, \\ h_2 &= \left|\frac{\partial s}{\partial \varphi}\right| = \rho, \\ h_3 &= \left|\frac{\partial s}{\partial V}\right| = \frac{1}{E}, \end{aligned}\right\} \tag{6.2.5}$$

and so grad T has components

$$\operatorname{grad} T = \left(\rho j \frac{\partial T}{\partial \Psi},\ 0,\ E\frac{\partial T}{\partial V}\right). \tag{6.2.6}$$

Referring to Weatherburn (p. 16) and equations (4.22), (4.23), (5.7), (5.8), (6.2.5), and (6.2.6), we can write the plasma energy equation (5.13) in terms of Ψ and V (the physical variables are not dependent on φ because the flow is axi-symmetric) as follows :

$$\frac{1}{5}\,\frac{K_0\sigma_0}{(\ln\lambda)^2}\,\frac{\partial}{\partial\Psi}\left(\rho^2\frac{\partial(T^5)}{\partial\Psi}\right) + \frac{1}{2}\,\frac{K_0}{\sigma_0}\,\frac{\partial}{\partial V}\left(\frac{\partial(T^2)}{\partial V}\right) = -1. \tag{6.2.7}$$

Two families of analytic solutions of this non-linear equation have been found. One, in Section VI (*d*) on, completes the discussion for longitudinal flow ; the other, which for completeness is briefly presented in Section VI (*c*), represents flow with $\mathbf{q}$ perpendicular to $\mathbf{j}$. Otherwise, for given boundary conditions numerical solutions of (5.13), and hence (6.2.7), could be obtained.

(*c*) *Solution of the Energy Equation when the Heat Flow is everywhere Perpendicular to the Flow of Electricity* ($\omega_e\tau_e \ll 1$)

In this case T is a function of Ψ only, (6.2.6) becomes

$$\operatorname{grad} T = (\rho j \partial T/\partial\Psi,\ 0,\ 0),$$

and (6.2.7) reduces to

$$\frac{1}{5}\,\frac{K_0\sigma_0}{(\ln\lambda)^2}\,\frac{\partial}{\partial\Psi}\left(\rho^2\frac{\partial(T^5)}{\partial\Psi}\right) = -1. \tag{6.3.1}$$

Integration gives

$$T^5(\Psi) - T^5(0) = -5\frac{(\ln\lambda)^2}{K_0\sigma_0}\int_0^{\Psi}\frac{\Psi'}{\rho^2}\,d\Psi'. \tag{6.3.2}$$

In general ρ is a function of Ψ and V. However, inspection of (6.3.2) shows that ρ can only be a function of Ψ, otherwise the equation is inconsistent. Hence, by inversion

$$\Psi = \Psi(\rho). \tag{6.3.3}$$

The physical interpretation of (6.3.3) is simply that the current stream lines are straight, and parallel to OZ. The heat flow is perpendicular to the electric stream lines, and so is purely radial. This requires heat flow across the free boundary surface of the plasma. Since we are concerned with heat flow to the electrodes, this solution is not considered further in this paper. However, it is still possible to have purely radial temperature gradients if bremsstrahlung is included, and for this case Pease (1957) has obtained the stationary-state radial distribution functions and current-voltage characteristics of a bremsstrahlung-cooled, axially symmetric, pinched discharge generated in a long, straight tube, in which end effects can be neglected.

(*d*) *Solution of the Energy Equation for Longitudinal Flow* ($\omega_e\tau_e \ll 1$)

As was seen in Section VI (*a*), the flow for T a function of V only is longitudinal. For this important type of flow, (6.2.6) becomes grad $T=(0, 0, E\partial T/\partial V)$, and the energy equation (6.2.7) reduces to

$$\frac{1}{2}\frac{K_0}{\sigma_0}\frac{\partial}{\partial V}\left(\frac{\partial(T^2)}{\partial V}\right)=-1. \tag{6.4.1}$$

Integration gives

$$T^2+(\sigma_0/K_0)V^2=T_m^2, \tag{6.4.2}$$

in agreement with (6.1.4). Rearranging,

$$V=\pm(K_0/\sigma_0)^{1/2}(T_m^2-T^2)^{1/2}. \tag{6.4.3}$$

It is convenient to take $V>0$ for $z<0$, so that the flow of electric current is upward in Figure 4. Thus, in (6.4.3) and following equations the upper sign refers to $z<0$ and the lower sign to $z>0$.

Introducing now more general orthogonal curvilinear coordinates w, v, and u, we assume henceforth that V and T are functions of u only. It thus follows that the only non-zero component of **j** is j_u, and from equations (4.22), (5.3), (5.7), and (6.4.3),

$$j_u=\pm\frac{(K_0\sigma_0)^{1/2}}{\ln\lambda}\frac{T^{5/2}}{(T_m^2-T^2)^{1/2}}\frac{1}{h_3}\frac{\partial T}{\partial u}, \tag{6.4.4}$$

or

$$j_u=(1/h_3)g(u). \tag{6.4.5}$$

From the continuity equation (5.4), we obtain for axial symmetry

$$j_u=f(w)/h_1h_2. \qquad (6.4.6$$

Combination of (6.4.4) and (6.4.6) results in the useful equation

$$f(w)\int_0^u\frac{h_3}{h_1h_2}\mathrm{d}u'=\pm\frac{(K_0\sigma_0)^{1/2}}{\ln\lambda}\int_{T_m}^{T}\frac{T'^{5/2}\mathrm{d}T'}{(T_m^2-T'^2)^{1/2}}, \tag{6.4.7}$$

which yields an immediate solution if the variables in $h_3/(h_1h_2)$ are separable.

We shall now consider two axi-symmetric discharges having boundary surfaces of prescribed shape.

Case 1.—*Streamlines parallel to the Axis of Symmetry*

In this case we consider a discharge between parallel, circular electrodes of radius ρ_2, separated by a distance $2z_e$ ($z_e>0$). The plasma is contained within a cylindrical boundary surface $\rho=\rho_1$, $\rho_1<\rho_2$. The cross section in the ρ–z plane is shown in Figure 5 (*a*).

Using cylindrical coordinates, with $w=\rho$, $v=\varphi$, and $u=z$, we have $h_1=h_3=1$, $h_2=\rho$, and $V=V(z)$, $T=T(z)$, $\Psi=\Psi(\rho)$. In the ρ–z plane the streamlines are parallel to OZ and the equipotential lines are normal to OZ. Using the above scale factors, (6.4.5) and (6.4.6) yield

$$j_z=g(z)=f(\rho)/\rho=\text{const.} \tag{6.4.8}$$

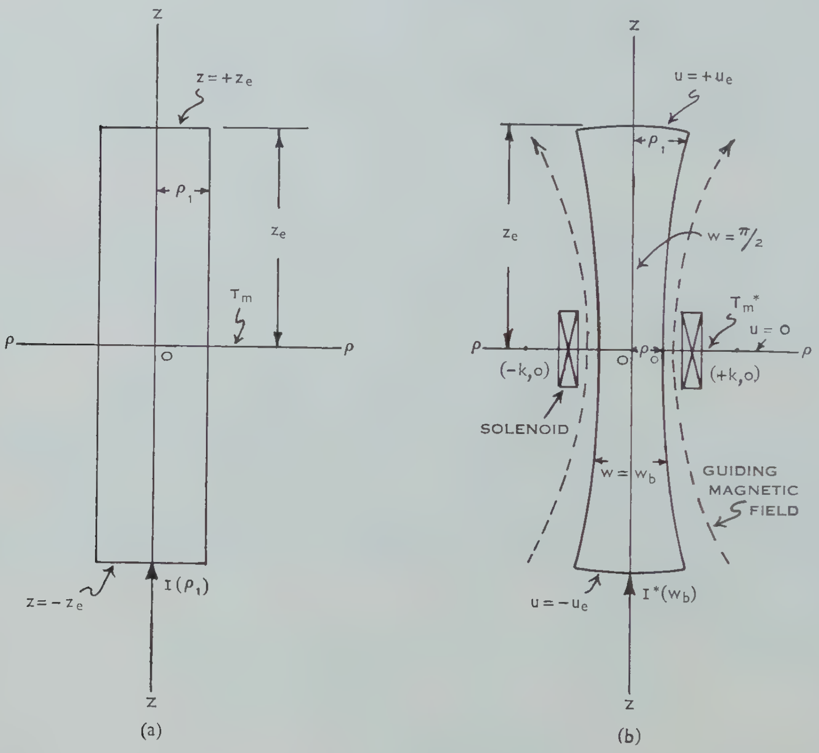

Fig. 5.—Discharge cross sections in the ρ-z plane. (*a*) Streamlines parallel to OZ; (*b*) streamlines curved.

Using this result, (6.2.4) gives

$$I(\rho)=\pi\rho^2 j_z, \tag{6.4.9}$$

and (6.2.1)

$$\Psi(\rho)=\frac{1}{2}\rho^2 j_z. \tag{6.4.10}$$

Introducing a variable $\theta=\cos^{-1}(T/T_m)$, and again using the above scale factors, together with the constant $j_z=f(\rho)/\rho$, (6.4.7) becomes in this case

$$z=\mp\frac{(K_0\sigma_0)^{1/2}}{\ln\lambda}\,\frac{T_m^{5/2}}{j_z}\int_0^{\theta}\cos^{5/2}\theta'd\theta'. \tag{6.4.11}$$

With $z_0>0$, let $2z_0$ be the length which the discharge of central temperature T_m would have if the electrodes were at zero temperature. Then, using Wallis's integral $W_{5/2}=\int_0^{\pi/2}\cos^{5/2}\theta d\theta=\frac{1}{2}\pi^{1/2}\frac{\Gamma(7/4)}{\Gamma(9/4)}\approx 0\cdot 72$ (Franklin 1944; Dwight 1957 for a table of the gamma function), (6.4.11) gives

$$\frac{z}{z_0}=\mp\frac{1}{0\cdot 72}\int_0^{\theta}\cos^{5/2}\theta' d\theta'. \tag{6.4.12}$$

Numerical integration of (6.4.12) results in Figure 6, which shows T/T_m plotted against z/z_0 for this discharge.

If the electrodes are at some finite temperature $T(\mp z_e)=T_e=T_m\cos\theta_e$, the corresponding ratio z_e/z_0 may be read off Figure 6, and so z_0 is determined in terms of the known electrode separation $2z_e$. Then Figure 6 gives the variation of temperature, normalized to T_m, with respect to distance along the discharge, normalized to z_0. Actually, z_e and z_0 differ by less than 5% if $T_e<\frac{1}{2}T_m$. Since the condition of interest is $T_e\ll T_m$, we can thus obtain some useful approximate results when the temperature of the electrodes is non-zero. The central temperature is derived from (6.4.11) as

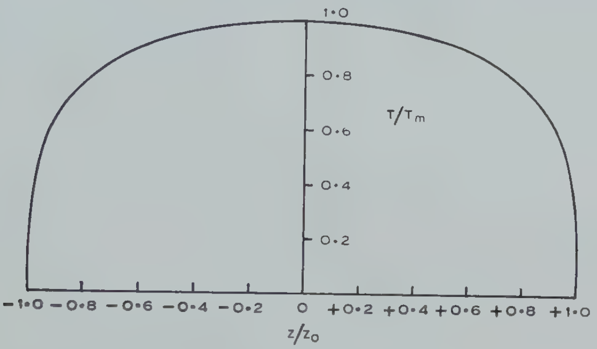

Fig. 6.—Temperature *v.* distance characteristic for non-constricted cylindrical discharge of circular cross section.

$$T_m=\left(\frac{z_e j_z \ln\lambda}{(K_0\sigma_0)^{1/2}\int_0^{\theta_e}\cos^{5/2}\theta d\theta}\right)^{2/5}\approx\left(\frac{z_e j_z\ln\lambda}{0\cdot 72(K_0\sigma_0)^{1/2}}\right)^{2/5}. \tag{6.4.13}$$

Inserting into this result the numerical values given by (5.9) and (5.10), and taking $\ln\lambda=10$,

$$T_m\approx 1962\left(\frac{z_e I(\rho_1)}{\rho_1^2}\right)^{2/5}\text{A}^{-2/5}\,\text{cm}^{2/5}\,\text{deg}, \tag{6.4.14}$$

where $I(\rho_1)=\pi\rho_1^2 j_z$, the total current carried by the discharge, has been introduced by means of (6.4.9).

Similarly, (6.4.3) gives

$$T_m\approx 5899 V_e\ \text{V}^{-1}\,\text{deg}, \tag{6.4.15}$$

and so, from (6.4.14) and (6.4.15),

$$V_e\approx 0\cdot 333\left(\frac{z_e I(\rho_1)}{\rho_1^2}\right)^{2/5}\text{A}^{-2/5}\,\text{cm}^{2/5}\,\text{V}, \tag{6.4.16}$$

where $V_e=V(-z_e)=-V(+z_e)$.

From (6.4.14) it is seen that for given z_e and $I(\rho_1)$, T_m increases as ρ_1 decreases, as would be physically expected.

This case has been studied by Kaufman and Furth (1958) and Haines (1960).

Case 2.—Streamlines Curved

Suppose that the "linear" discharge of Case 1 is modified by the effect of a magnetic field, produced, say, by a short solenoid with axis OZ, situated symmetrically about $z=0$. Here we assume the constriction to be produced by fields compatible with $\omega_e\tau_e \ll 1$, and expect the streamlines to be shaped as in Figure 5 (*b*). To obtain a solution which should reasonably represent the practical situation, let us approximate the current streamlines by hyperbolae. Mathematically we suppose that the coordinates u and w (with $V=V(u)$ and $\Psi=\Psi(w)$ as before) are related to ρ and z by the conformal transformation

$$\rho+iz=k\cosh(u+iw),\quad k \text{ defined below.} \tag{6.4.17}$$

Expansion gives

$$\rho=k\cosh u\cos w, \tag{6.4.18}$$

and

$$z=k\sinh u\sin w, \tag{6.4.19}$$

and so

$$\frac{\rho^2}{k^2\cosh^2 u}+\frac{z^2}{k^2\sinh^2 u}=1, \tag{6.4.20}$$

$$\frac{\rho^2}{k^2\cos^2 w}-\frac{z^2}{k^2\sin^2 w}=1. \tag{6.4.21}$$

In the ρ–z plane the curves $u=$const., $w=$const. form a family of confocal ellipses and hyperbolae, with common foci at $(\pm k, 0)$. Hence the equipotential surfaces $V(u)=$const. are ellipsoids, and the streamlines $\Psi(w)=$const. are hyperbolae. For this discharge the boundary surface is a hyperboloid of one sheet, where we take $w_b>0$, and $w=\frac{1}{2}\pi$ on the axis OZ. Since T and V are functions of u, the heat and electricity flow along the hyperbolic streamlines: the flow is longitudinal, as required.

For the conformal transformation (6.4.17) the scale factors are

$$h_1=h_3=k(\sinh^2 u+\sin^2 w)^{1/2}, \tag{6.4.22}$$

and

$$h_2=k\cosh u\cos w. \tag{6.4.23}$$

The total current through any surface of constant potential and temperature intersecting the free boundary surface of the discharge is obtained from (6.2.4) as

$$I^*(w_b)=2\pi\int_0^{s(b)} j_u h_2\,ds. \tag{6.4.24}$$†

Thus, using (6.4.6) and $ds=-h_1dw$, this becomes

$$I^*(w_b)=2\pi\int_{w_b}^{\frac{1}{2}\pi} f(w)\,dw. \tag{6.4.25}$$

---

† The star superscript is used when necessary to indicate a Case 2 quantity.

Combination of (6.4.5), (6.4.6), (6.4.22), and (6.4.23) leads to

$$g(u)\cosh u = f(w)/k\cos w = A = \text{const.}, \tag{6.4.26}$$

a result which permits integration of (6.4.25) to give

$$I^*(w_b) = 2\pi k A(1-\sin w_b). \tag{6.4.27}$$

Inspection of Figure 5 (*b*) gives, with the aid of (6.4.18) and (6.4.19),

$$\left.\begin{aligned} \rho_0 &= k\cos w_b, \\ \rho_1 &= k\cosh u_e \cos w_b, \\ z_e &= k\sinh u_e, \end{aligned}\right\} \tag{6.4.28}$$

where $u = \mp u_e$ gives the electrodes.

Equations (6.4.28) yield

$$\sinh u_e = [(\rho_1/\rho_0)^2 - 1]^{1/2}, \tag{6.4.29}$$

$$z_e = k[(\rho_1/\rho_0)^2 - 1]^{1/2}, \tag{6.4.30}$$

$$\sin w_b = [1-(\rho_1/z_e)^2(\rho_1/\rho_0)^{-2}\{(\rho_1/\rho_0)^2 - 1\}]^{1/2}. \tag{6.4.31}$$

In this case use of (6.4.7), (6.4.22), (6.4.23), and the variable $\theta = \cos^{-1}(T/T_m^*)$ gives

$$\int_0^u \frac{du'}{\cosh u'} = \frac{\mp (K_0\sigma_0)^{1/2} T_m^{*\,5/2}}{\ln \lambda\{f(w)/k\cos w\}} \int_0^\theta \cos^{5/2}\theta'\,d\theta'. \tag{6.4.32}$$

Integrating the left-hand side, and using (6.4.26) and (6.4.27)

$$\tan^{-1}(\sinh u) = \frac{\mp 2\pi k (K_0\sigma_0)^{1/2}(1-\sin w_b) T_m^{*\,5/2}}{\ln \lambda I^*(w_b)} \int_0^\theta \cos^{5/2}\theta'\,d\theta', \tag{6.4.33}$$

or

$$T_m^* = \left(\frac{\mp \ln \lambda I^*(w_b)\tan^{-1}(\sinh u)}{2\pi k (K_0\sigma_0)^{1/2}(1-\sin w_b)\int_0^\theta \cos^{5/2}\theta'\,d\theta'}\right)^{2/5}. \tag{6.4.34}$$

By considering $u = \mp u_e$ at the electrodes, where $T_e = T(\mp u_e) = T_m^* \cos\theta_e$, we can use (6.4.29) to (6.4.31) to write (6.4.34) in the form

$$T_m^* = \left(\frac{\ln \lambda I^*(w_b)(\nu^2-1)^{1/2}\tan^{-1}(\nu^2-1)^{1/2}}{2\pi z_e (K_0\sigma_0)^{1/2}\{1-[1-(\rho_1/z_e)^2\nu^{-2}(\nu^2-1)]^{1/2}\}\int_0^{\theta_e}\cos^{5/2}\theta\,d\theta}\right)^{2/5}, \tag{6.4.35}$$

where $\nu = \rho_1/\rho_0$ is defined as the radial compression ratio. As ν approaches unity, (6.4.35) reduces to the exact form of (6.4.13), Case 1. Again, for $T_e \ll T_m^*$,

$$T_m^* \approx \left(\frac{\ln \lambda\, I^*(w_b)(\nu^2-1)^{1/2}\tan^{-1}(\nu^2-1)^{1/2}}{(2)(0\cdot 72)\pi z_e (K_0\sigma_0)^{1/2}\{1-[1-(\rho_1/z_e)^2\nu^{-2}(\nu^2-1)]^{1/2}\}}\right)^{2/5}. \tag{6.4.36}$$

Again referring to (5.9) and (5.10), and taking $\ln \lambda = 10$, (6.4.36) becomes

$$T_m^* \approx 1487\left(\frac{z_e I^*(w_b)}{\rho_1^2}\right)^{2/5}\left(\frac{(\rho_1/z_e)^2(\nu^2-1)^{1/2}\tan^{-1}(\nu^2-1)^{1/2}}{1-[1-(\rho_1/z_e)^2\nu^{-2}(\nu^2-1)]^{1/2}}\right)^{2/5} \text{A}^{-2/5}\,\text{cm}^{2/5}\,\text{deg.} \tag{6.4.37}$$

This is a cumbersome expression, and it is fortunate that we can take advantage of the inequality $(\rho_1/z_e)^2 \lesssim 0 \cdot 04 \ll 1$, which is in accord with typical physical conditions, and which permits simplification of (6.4.37) to the form

$$T_m^* \approx 1962 \left(\frac{z_e I^*(w_b)}{\rho_1^2} \right)^{2/5} \left(\frac{\nu^2 \tan^{-1} (\nu^2 - 1)^{1/2}}{(\nu^2 - 1)^{1/2}} \right)^{2/5} \text{A}^{-2/5}\,\text{cm}^{2/5}\,\text{deg}. \tag{6.4.38}$$

In this case (5.9), (5.10), and (6.4.3) give

$$T_m^* \approx 5899\, V_e^* \ \text{V}^{-1}\,\text{deg}, \tag{6.4.39}$$

when $T_e \ll T_m^*$, and so, from (6.4.38) and (6.4.39),

$$V_e^* \approx 0 \cdot 333 \left(\frac{z_e I^*(w_b)}{\rho_1^2} \right)^{2/5} \left(\frac{\nu^2 \tan^{-1} (\nu^2 - 1)^{1/2}}{(\nu^2 - 1)^{1/2}} \right)^{2/5} \text{A}^{-2/5}\,\text{cm}^{2/5}\,\text{V}, \tag{6.4.40}$$

where $V_e^* = V(-u_e) = -V(+u_e)$.

However, it should be recalled at this stage that the above results apply when $\omega_e \tau_e \ll 1$ and the discharge constriction is not pronounced, so that ν is small. We now examine the case of a well-constricted discharge.

(e) *Solution of the Energy Equation for Longitudinal Flow* ($\omega_e \tau_e \gg 1$)

Here it is supposed that a strong external guiding magnetic field is used to produce a well-constricted discharge in which both electric current and heat flow along the magnetic field lines, so that the magnetic field lines generate flux tubes which coincide with the current stream tubes of the type shown in Figure 3, and the flow is longitudinal. With $\omega_e \tau_e \gg 1$, (5.15) can be written by means of (4.28) and (4.29) as

$$\mathbf{M} = -K(\nabla T)^{||} + (\sigma \mathbf{E}^{||} + \tfrac{1}{2}\sigma \mathbf{E}^{\perp}) V. \tag{6.5.1}$$

Using the formal analysis of Section VI (*a*) as a guide, we assume $\mathbf{M} = 0$ and see what this implies later. Then (6.5.1) gives

$$\mathbf{E}^{\perp} = 0, \quad (\sigma V \neq 0), \tag{6.5.2}$$

and

$$\sigma V \mathbf{E}^{||} = K(\nabla T)^{||}, \tag{6.5.3}$$

or, writing $\mathbf{E}^{||} = -(\nabla V)^{||}$, and using (5.7) and (5.8)

$$(\nabla [T^2 + (\sigma_0/K_0) V^2])^{||} = 0. \tag{6.5.4}$$

Integrating (6.5.4), and applying the result to the axis of the discharge, we obtain the familiar form,

$$T^2 + (\sigma_0/K_0) V^2 = T_m^2, \tag{6.5.5}$$

from the symmetry about the median plane.

The assumption $\mathbf{M} = 0$ here leads to $\mathbf{E} = \mathbf{E}^{||}$ (from (6.5.2)), but imposes no particular condition on $(\nabla T)^{\perp}$. Nevertheless, $(\nabla T)^{\perp}$ is likely to be zero in view of our original approximations of perfect thermal insulation at the free boundary surface, and neglect of bremsstrahlung loss from the plasma, so that $\nabla T = (\nabla T)^{||}$. Indeed, if the electron mean free path and gyroradius are not small compared with the average diameter of the discharge (and this may well be the case unless the gas is dense and the total confining magnetic field extremely strong), no mechanism exists that can give rise to a radial temperature gradient.

Since $\mathbf{E}=\mathbf{E}^{||}$, it follows that for this solution the total electric field must be shaped to follow the streamlines defined by the magnetic field. Then

$$\mathbf{j}=\sigma\mathbf{E}, \tag{6.5.6}$$

$$\mathbf{q}=-K\nabla T, \tag{6.5.7}$$

and the solution proceeds as in Section VI (*d*), Case 2, where $\omega_e\tau_e \ll 1$. In fact, for strictly longitudinal flow, with **q** and **j** parallel to **H** at every point, the results obtained in Section VI (*d*), such as (6.4.38) and (6.4.40), must hold for all values of $\omega_e\tau_e$ (that is, for all values of total H), and hence for all values of the radial compression ratio ν. However, it is to be noted that strictly longitudinal flow for intermediate values of $\omega_e\tau_e$ may be difficult to achieve in practice.

The case $\omega_e\tau_e \gg 1$ clearly can arise if the self-magnetic field of the discharge becomes large, but, remembering Teller's intuitively-based criterion for determining the stability of a plasma confined by a magnetic field (Bishop 1960), we see that this configuration is unstable, and hence of no interest to us.

However, when there is an external guiding magnetic field, large compared with the self-magnetic field of the discharge, so that the resultant magnetic field is predominantly in the direction of the external field, the case $\omega_e\tau_e \gg 1$ will arise, and Teller's criterion suggests a guiding magnetic field shaped as in Figure 5 (*b*) for a stable configuration. The ratio of external to self-magnetic field for stability of the discharge is at present being examined.

VII. Comparison of Maximum Temperatures and Discussion of Results

Since we have shown that bremsstrahlung loss from the plasma can be neglected for cases of interest (Section V), the expressions derived in Section VI (*d*) for T and T^* give upper limits for the central temperature.

Forming now the ratio T^*/T by means of (6.4.14) and (6.4.38), we obtain

$$\frac{T^*}{T}=\varepsilon=\left(\frac{\nu^2 \tan^{-1}(\nu^2-1)^{1/2}}{(\nu^2-1)^{1/2}}\right)^{2/5}, \tag{7.1}$$

if $I(\rho_1)=I^*(w_b)$, and the discharges have common ρ_1 and z_e, as in Figures 5 (*a*) and 5 (*b*). From the derivation of (6.4.38), it will be understood that (7.1) applies only when $(\rho_1/z_e)^2 \ll 1$.

The dependence of the temperature ratio ε on the compression ratio ν for practical cases of interest can therefore be obtained from (7.1), which is shown plotted in Figure 7 for $1<\nu<20$.

Further, if the discharge resistance between electrodes is R, then from (6.4.16) and (6.4.40) we see that for conditions as above,

$$\varepsilon=R^*/R. \tag{7.2}$$

This result should prove useful when experimental determinations of ε are attempted.

For $\nu=20$, which corresponds to a ratio of 400 for the cross-sectional areas in the median plane before and after constriction, we note from Figure 7 that

$\varepsilon \approx 4$. This low value of ε for large constriction of the discharge can be understood physically by referring to equations (5.7) and (5.8). The electrical conductivity σ increases as $T^{3/2}$; the thermal conductivity K as $T^{5/2}$. Since the Joule heating of the plasma, j^2/σ, is inversely proportional to σ, and the conduction of heat to the electrodes is proportional to K, the increase in central temperature that might be expected from severe constriction of a discharge is offset by the reduced efficiency of Joule heating and the increased efficiency of heat conduction to the electrodes, and the small values of ε given by Figure 7 result as a compromise.

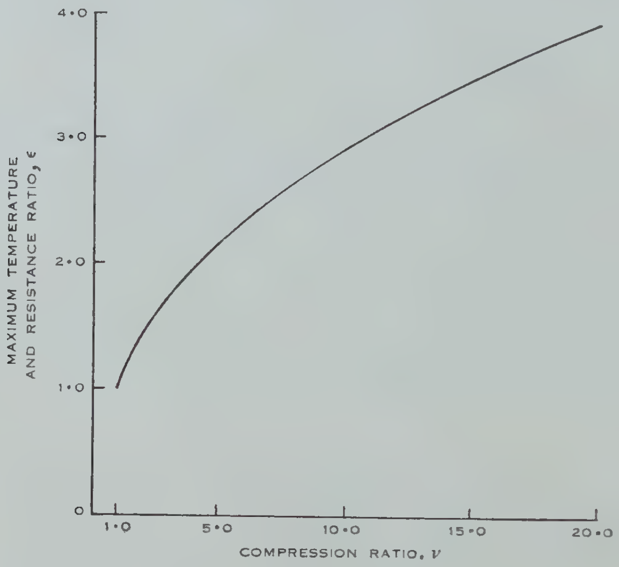

Fig. 7.—Maximum temperature and resistance ratio, ε, *v.* radial compression ratio, ν.

We have seen that for $\omega_e\tau_e \ll 1$, the plasma is isotropic, and that for $\omega_e\tau_e \gg 1$, the plasma possesses extreme anisotropy. For intermediate values of $\omega_e\tau_e$, the plasma will have a state lying between these extremes. Since, in a given case, the total central magnetic field, H_m, and central temperature can be determined, it follows that the numerical value of $\omega_e\tau_e$ (and thus an indication of the state of the plasma) can be obtained from Figure 2 if, in addition, the total concentration, n, is known. Using T^*_m, which reduces to T_m in the non-constricted case, an estimate of n can be obtained by assuming, for non-constricted and constricted discharges, that the kinetic pressure nkT^*_m of the plasma, is comparable to the magnetic pressure $H^2_m/8\pi$ of the total confining field. If here we take H_m in gauss and T^*_m in degrees Kelvin, this yields

$$n = 2\cdot 88 \times 10^{14} H^2_m/T^*_m \text{ particles cm}^{-3}, \tag{7.3}$$

which can then be used with the values of H_m and T^*_m to obtain an order of magnitude estimate of $\omega_e\tau_e$ from Figure 2.

VIII. ACKNOWLEDGMENTS

The author is indebted to Professor K. J. Le Couteur for suggesting this problem, and for his guidance and encouragement during the course of the work. He is also indebted to Dr. F. C. Barker for helpful discussions and suggestions on theoretical aspects of the analysis, particularly during an earlier period when the problem of the slightly constricted discharge was first solved using confocal ellipsoidal coordinates; and to Dr. A. H. Morton for useful discussions on the experimental applicability of the results obtained.

IX. REFERENCES

ALFVÉN, H. (1950).—" Cosmical Electrodynamics." pp. 43–7. (Clarendon Press: Oxford.)

ALLIS, W. P. (1956).—Series of lectures on physics of ionized gases. Part XA, pp. 9–10. Los Alamos Scientific Laboratory Report LA–2055.

BISHOP, A. S. (1960).—" Project Sherwood—The U.S. Program in Controlled Fusion." p. 87. (Doubleday and Co.: Garden City, New York.)

CALLEN, H. B. (1948).—The application of Onsager's reciprocal relations to thermoelectric, thermomagnetic, and galvanomagnetic effects. *Phys. Rev.* **73**: 1350.

CHAPMAN, S., and COWLING, T. G. (1953).—" The Mathematical Theory of Non-Uniform Gases." pp. 328–9. (Cambridge Univ. Press.)

COBINE, J. D. (1958).—" Gaseous Conductors." p. 92. (Dover Publications: New York.)

DWIGHT, H. B. (1957).—" Tables of Integrals and Other Mathematical Data." p. 212. (Macmillan: New York.)

FRANKLIN, P. (1944).—" Methods of Advanced Calculus." p. 261. (McGraw-Hill: New York.)

HAINES, M. G. (1960).—" Proceedings of the Fourth International Conference on Ionization Phenomena in Gases, Uppsala, Sweden." Heat losses to electrodes, pp. 901-3, Vol. 2. (North-Holland Publishing Co.: Amsterdam.)

HIX, C. F., and ALLEY, R. P. (1958).—" Physical Laws and Effects." pp. 86–90. (Wiley: New York.)

KAUFMAN, A. N., and FURTH, H. P. (1958).—Thermal equilibrium in a Joule-heated plasma. University of California Radiation Laboratory Report No. 5153.

LINHART, J. G. (1960).—" Plasma Physics." p. 184. (North-Holland Publishing Co.: Amsterdam.)

MARSHALL, W. (1957).—Kinetic theory of an ionized gas. Part 3. pp. 65, 67. Atomic Energy Research Establishment Report T/R 2419. (H.M. Stationery Office: London.)

MILNE-THOMSON, L. M. (1955).—" Theoretical Hydrodynamics." p. 6. (Macmillan: London.)

PEASE, R. S. (1957).—Equilibrium characteristics of a pinched gas discharge cooled by bremsstrahlung radiation. *Proc. Phys. Soc. Lond.* B **70**: 13.

SAHA, M. N. (1920).—Ionization in the solar chromosphere. *Phil. Mag.* **40**: 472–88.

SAHA, M. N., and SAHA, N. K. (1934).—" A Treatise on Modern Physics." p. 630. (Indian Press Ltd.: Allahabad and Calcutta.)

SPITZER, L., JR. (1956).—" Physics of Fully Ionized Gases." pp. 67, 72. (Interscience Publishers: New York.)

SPITZER, L., JR., and HÄRM, R. (1953).—Transport phenomena in a completely ionized gas. *Phys. Rev.* **89**: 977–81.

STOKES, G. G. (1842).—On the steady motion of incompressible fluids. *Trans. Camb. Phil. Soc.* **7**: 439–53.

WEATHERBURN, C. E. (1957).—" Advanced Vector Analysis." pp. 48–9. (Bell: London.)

AVERAGE FORCES IN ELECTROMAGNETIC SYSTEMS

By W. E. Smith*

[*Manuscript received September* 14, 1960]

Summary

The mechanical forces developed in electromagnetic systems are usually evaluated from surface integrals of the Maxwell stresses. For a large class of systems it is shown that the time average force can be expressed in terms of directly measurable circuit-theory parameters. The system must be linear and loss free, but there is no restriction on the frequency of excitation.

I. Introduction

We consider first a capacitor consisting of two parallel plates of separation x. When the capacitor is charged to a voltage V_0 there is an attractive force F_x between the plates. This attractive force may be obtained by finding the electrostatic field distribution and integrating the electric pressure on the plates. However, the force may also be obtained from energy conservation considerations giving

$$F_x=\tfrac{1}{2}V_0^2\partial C/\partial x, \tag{1}$$

where C is the electrical capacitance. F_x is now expressed in terms of the integral electrical parameter C.

For more complicated capacitors, equation (1) may still be used if x is taken as a generalized coordinate specifying the configuration of the capacitor. F_x is then interpreted as the generalized force corresponding to x by the procedure adopted in analytical mechanics.

If the capacitor is connected to an alternating voltage source, the instantaneous force may be calculated from equation (1). Of course, the frequency must be low so that the electric field is described adequately by the equations of electrostatics. The average force $(F_x)_{\mathrm{av}}$ is given by

$$(F_x)_{\mathrm{av}}=\tfrac{1}{2}(V_0)^2_{\mathrm{av}}\partial C/\partial x. \tag{2}$$

For sinusoidal voltages we may take,

$$V_0=\sqrt{2}.V_\omega\cos(\omega t+\varphi), \tag{3}$$

where V_ω is the r.m.s. voltage. We then have,

$$(F_x)_{\mathrm{av}}=\tfrac{1}{2}V_\omega^2\partial C/\partial x. \tag{4}$$

Equation (4) is also expressible in terms of the susceptance $B(\omega)$ or reactance $X(\omega)$ of the capacitor,

$$(F_x)_{\mathrm{av}}=\frac{1}{2\omega}\;V_\omega^2\;\frac{\partial B}{\partial x}, \tag{5}$$

$$(F_x)_{\mathrm{av}}=\frac{1}{2\omega}\;I_\omega^2\;\frac{\partial X}{\partial x}, \tag{6}$$

where I_ω is the r.m.s. current flowing to the capacitor.

---

* Applied Mathematics Department, University of New South Wales, Kensington, N.S.W.

A similar argument applies for the magnetic forces produced in an inductor L. The energy conservation equation corresponding to (1) is

$$F_x = \tfrac{1}{2} I_0^2 \partial L / \partial x, \tag{7}$$

where I_0 is the steady current flowing through the inductor. For low frequency alternating currents, the average force is easily shown to be given by equations (5) and (6).

Equations like (5) and (6) expressing $(F_x)_{\text{av}}$ in terms of gross electrical parameters may be obtained for very general electromagnetic systems. In Section II a general result is obtained which relates $(F_x)_{\text{av}}$ to field quantities on a mathematical surface enclosing the system. In practical situations this fundamental relation may be reduced to simple equations like (5) and (6). This reduction is carried out in Section III. For a two-terminal element or network, equations (5) and (6) remain true *but the restriction to low frequencies is removed.* The element may in fact have dimensions larger than the wavelength. For multiterminal-pair networks and multiport microwave circuits, generalizations of equations (5) and (6) are obtained. Some possible applications and extensions of the theory are discussed in Section IV.

II. A General Expression for the Average Force

The electromagnetic system is assumed to be linear, loss free, and reciprocal. A closed surface S is taken enclosing the system. The system is assumed to be excited by sinusoidal electric and magnetic fields from outside S. These electric and magnetic fields are not independent; a knowledge of either the electric or magnetic field over S being sufficient to specify the fields inside the system. We suppose that the position or orientation of conductors or of polarizable material within S depends upon a generalized coordinate x. We shall suppose that a small change δx is carried out adiabatically; i.e. sufficiently slowly that all Fourier components of the fields of the system lie close to a single frequency, and the Fourier components of δx are all close to zero frequency. The assumption of differentiability, where required, is also made.

Since the system is loss free and reciprocal the only "true" currents which flow within S are the surface currents of ideal conductors. It is true that non-reciprocal materials with asymmetric conductivity tensors may have non-vanishing current densities without causing energy loss, but we exclude these. The equation of conservation of electric charge, namely,

$$\operatorname{div} \mathbf{J} + \partial \rho / \partial t = 0, \tag{8}$$

then shows that the only "true" charges present are either surface charges on the conductors or static charges. We may suppose such static charges to be zero and take all field quantities with sinusoidal time dependence. Maxwell's equations are (in M.K.S. rationalized units):

$$\operatorname{curl} \mathbf{E}_\omega = -\mathrm{j}\omega \mathbf{B}_\omega, \tag{9}$$

$$\operatorname{curl} \mathbf{H}_\omega = \mathrm{j}\omega \mathbf{D}_\omega, \tag{10}$$

where $\mathbf{E}_\omega$, $\mathbf{H}_\omega$, $\mathbf{D}_\omega$, and $\mathbf{B}_\omega$ are complex field vectors and $\mathrm{j} = \sqrt{(-1)}$. For convenience r.m.s. amplitudes are taken for these fields; for example,

$$\mathrm{E}_\omega = \mathscr{R}.\mathscr{P}.(\sqrt{2}.\mathbf{E}_\omega e^{j(\omega t + \varphi)}). \tag{11}$$

In addition $\mathbf{D}_\omega$ and $\mathbf{E}_\omega$, $\mathbf{B}_\omega$ and $\mathbf{H}_\omega$ are related by

$$\mathbf{D}_\omega=[\varkappa_\omega].\mathbf{E}_\omega, \tag{12}$$

$$\mathbf{B}_\omega=[\mu_\omega].\mathbf{H}_\omega, \tag{13}$$

where $[\varkappa_\omega]$ and $[\mu_\omega]$ are the second rank tensors of permittivity and permeability. To preserve the linearity of the system, $[\varkappa_\omega]$ and $[\mu_\omega]$ are supposed independent of $\mathbf{E}_\omega$, $\mathbf{H}_\omega$. Further, to ensure that the system is loss free and reciprocal, they are taken real and symmetric.

The introduction of the tensors $[\varkappa_\omega]$ and $[\mu_\omega]$ rather than the more common scalars $\varkappa_\omega$ and μ_ω entails very little additional manipulation and establishes the theory for systems containing anisotropic materials.

Consider a surface integration of the complex Poynting vector $(\mathbf{E}_\omega\times\mathbf{H}_\omega^*)$ carried out over the surface S as the outer boundary, together with the surfaces S_1, S_2, . . . of any ideal conductors enclosed by S. In reckoning the total surface integrals consider the *inward* normal of S and the outward normals of S_1, S_2, . . . as positive, then

$$\int_{S,S_1,S_2\ldots}(\mathbf{E}_\omega\times\mathbf{H}_\omega^*).\mathrm{d}\mathbf{A}=-\int_v \operatorname{div}(\mathbf{E}_\omega\times\mathbf{H}_\omega^*)\mathrm{d}v, \tag{14}$$

where v is the volume over which the fields extend. Since $\mathbf{E}_\omega$ is normal at the conducting surfaces S_1, S_2, . . ., the only contribution remaining is from S,

$$\int_S(\mathbf{E}_\omega\times\mathbf{H}_\omega^*).\mathrm{d}\mathbf{A}=-\int_v \operatorname{div}(\mathbf{E}_\omega\times\mathbf{H}_\omega^*)\mathrm{d}v \tag{15}$$

$$=\int_v(\mathbf{E}_\omega.\operatorname{curl}\mathbf{H}_\omega^*-\mathbf{H}_\omega^*.\operatorname{curl}\mathbf{E}_\omega)\mathrm{d}v \tag{16}$$

$$=\mathrm{j}\omega\int_v(\mathbf{H}_\omega^*.\mathbf{B}_\omega-\mathbf{E}_\omega.\mathbf{D}_\omega^*)\mathrm{d}v \tag{17}$$

(by Maxwell's equations).

Now consider a variation of equation (17) generated by a change δx in the generalized coordinate x,

$$\delta\int_S(\mathbf{E}_\omega\times\mathbf{H}_\omega^*).\mathrm{d}\mathbf{A}=\mathrm{j}\omega\delta\int_v(\mathbf{H}_\omega^*.\mathbf{B}_\omega-\mathbf{E}_\omega.\mathbf{D}_\omega^*)\mathrm{d}v$$

$$=\mathrm{j}\omega\int_v\delta(\mathbf{H}_\omega^*.\mathbf{B}_\omega-\mathbf{E}_\omega.\mathbf{D}_\omega^*)\mathrm{d}v+\mathrm{j}\omega\int_{\delta v}(\mathbf{H}_\omega^*.\mathbf{B}_\omega-\mathbf{E}_\omega.\mathbf{D}_\omega^*)\mathrm{d}v. \tag{18}$$

The second integral in equation (18) takes account of any change of the conducting surfaces. For example a paddle may rotate or a sliding piston may shift. Further, $\frac{1}{2}(\mathbf{E}_\omega.\mathbf{D}_\omega^*-\mathbf{H}_\omega^*.\mathbf{B}_\omega)$ is the average pressure acting normally on the surfaces into the volume v. Thus the work $\delta W_\omega^{(S)}$ done by the field components of angular frequency ω on the conducting surfaces during an adiabatic displacement δx is given by

$$\delta W_\omega^{(S)}=\tfrac{1}{2}\int_{\delta v}(\mathbf{H}_\omega^*.\mathbf{B}_\omega-\mathbf{E}_\omega.\mathbf{D}_\omega^*)\mathrm{d}v, \tag{19}$$

and equation (18) becomes

$$\delta\int_S (\mathbf{E}_\omega\times\mathbf{H}^*_\omega).\mathrm{d}\mathbf{A}=2\mathrm{j}\omega\delta W^{(S)}_\omega+\mathrm{j}\omega\int_v \delta(\mathbf{H}^*_\omega.\mathbf{B}_\omega-\mathbf{E}_\omega.\mathbf{D}^*_\omega)\mathrm{d}v. \tag{20}$$

But from equations (12) and (13), together with the symmetry and reality of $[\varkappa_\omega]$ and $[\mu_\omega]$,

$$\begin{aligned}\delta(\mathbf{E}_\omega.\mathbf{D}^*_\omega)&=\delta\mathbf{E}_\omega.[\varkappa_\omega]^*.\mathbf{E}^*_\omega+\mathbf{E}_\omega.[\delta\varkappa_\omega]^*.\mathbf{E}^*_\omega+\mathbf{E}_\omega.[\varkappa_\omega]^*.\delta\mathbf{E}^*_\omega\\&=-\mathbf{E}_\omega.[\delta\varkappa_\omega].\mathbf{E}^*_\omega+\mathbf{E}^*_\omega.\delta\mathbf{D}_\omega+\mathbf{E}_\omega.\delta\mathbf{D}^*_\omega,\end{aligned} \tag{21}$$

and

$$\begin{aligned}\delta(\mathbf{H}^*_\omega.\mathbf{B}_\omega)&=\delta\mathbf{H}^*_\omega.[\mu_\omega].\mathbf{H}_\omega+\mathbf{H}^*_\omega.[\delta\mu_\omega].\mathbf{H}_\omega+\mathbf{H}^*_\omega.[\mu_\omega].\delta\mathbf{H}_\omega\\&=\mathbf{H}_\omega.[\delta\mu_\omega].\mathbf{H}^*_\omega+\delta\mathbf{H}^*_\omega.\mathbf{B}_\omega+\mathbf{B}^*_\omega.\delta\mathbf{H}_\omega.\end{aligned} \tag{22}$$

For mathematical convenience any surfaces of discontinuity on material boundaries are replaced by small regions of large, though finite, gradients of the material constants. This ensures the differentiability implied in the equations.

Equation (20) becomes

$$\begin{aligned}\delta\int_S (\mathbf{E}_\omega\times\mathbf{H}^*_\omega).\mathrm{d}\mathbf{A}=2\mathrm{j}\omega\delta W^{(S)}_\omega+\mathrm{j}\omega\int_v (\mathbf{E}_\omega.[\delta\varkappa_\omega].\mathbf{E}^*_\omega+\mathbf{H}_\omega.[\delta\mu_\omega].\mathbf{H}^*_\omega)\mathrm{d}v\\+\mathrm{j}\omega\int[(\delta\mathbf{H}^*_\omega.\mathbf{B}_\omega-\mathbf{E}_\omega.\delta\mathbf{D}^*_\omega)+(\mathbf{B}^*_\omega.\delta\mathbf{H}_\omega-\mathbf{E}^*_\omega.\delta\mathbf{D}_\omega)]\mathrm{d}v.\end{aligned} \tag{23}$$

But by Maxwell's equations the last integral in equation (23) is

$$\begin{aligned}&\int_v [(\mathbf{E}_\omega.\mathrm{curl}\,\delta\mathbf{H}^*_\omega-\delta\mathbf{H}^*_\omega.\mathrm{curl}\,\mathbf{E}_\omega)+(\delta\mathbf{H}_\omega.\mathrm{curl}\,\mathbf{E}^*_\omega-\mathbf{E}^*_\omega.\mathrm{curl}\,\delta\mathbf{H}_\omega)]\mathrm{d}v\\&\quad=-\int_v [\mathrm{div}\,(\mathbf{E}_\omega\times\delta\mathbf{H}^*_\omega)-\mathrm{div}\,(\mathbf{E}^*_\omega\times\delta\mathbf{H}_\omega)]\mathrm{d}v\\&\quad=\int_{S,S_1,S_2\ldots}[(\mathbf{E}_\omega\times\delta\mathbf{H}^*_\omega)-(\mathbf{E}^*_\omega\times\delta\mathbf{H}_\omega)].\mathrm{d}\mathbf{A}\\&\quad=\int_S [(\mathbf{E}_\omega\times\delta\mathbf{H}^*_\omega)-(\mathbf{E}^*_\omega\times\delta\mathbf{H}_\omega)].\mathrm{d}\mathbf{A},\end{aligned} \tag{24}$$

since elsewhere $\mathbf{E}_\omega$ is normal to the conducting surfaces.

Equation (24) may then be written

$$\int_S (\delta\mathbf{E}_\omega\times\mathbf{H}^*_\omega+\mathbf{E}^*_\omega\times\delta\mathbf{H}_\omega).\mathrm{d}\mathbf{A}=2\mathrm{j}\omega\delta W^{(S)}_\omega+\mathrm{j}\omega\int_v (\mathbf{E}_\omega.[\delta\varkappa_\omega].\mathbf{E}^*_\omega+\mathbf{H}_\omega.[\delta\mu_\omega].\mathbf{H}^*_\omega)\mathrm{d}v. \tag{25}$$

To deal with the final term in equation (25) we consider the Maxwell stress tensor T_{ij}. In terms of instantaneous field vectors,

$$T_{ij}=E_iD_j-\tfrac{1}{2}\delta_{ij}\mathbf{E}.\mathbf{D}+H_iB_j-\tfrac{1}{2}\delta_{ij}\mathbf{H}.\mathbf{B}. \tag{26}$$

This tensor gives a force density,

$$k_i=\sum_{j=1}^{3}\frac{\partial T_{ij}}{\partial r_j}. \tag{27}$$

For a region free of " true " currents and charges, this becomes

$$k_i=-\tfrac{1}{2}\mathbf{E}.\frac{\partial[\varkappa]}{\partial r_i}.\mathbf{E}-\tfrac{1}{2}\mathbf{H}.\frac{\partial[\mu]}{\partial r_i}.\mathbf{H}+\frac{\partial}{\partial t}(\mathbf{D}\times\mathbf{B}), \tag{28}$$

where the Maxwell equations and the symmetry of $[\varkappa]$ and $[\mu]$ have been used. For sinusoidal fields the average of the momentum reaction term $\partial(\mathbf{D}\times\mathbf{B})/\partial t$ is zero and

$$(k_i)_{\mathrm{av}} = -\tfrac{1}{2}\mathbf{E}_\omega.\frac{\partial[\varkappa_\omega]}{\partial r_i}.\mathbf{E}^*_\omega - \tfrac{1}{2}\mathbf{H}_\omega.\frac{\partial[\mu_\omega]}{\partial r_i}.\mathbf{H}^*_\omega. \tag{29}$$

Further, when the displacement δx is carried out adiabatically this average force may be used for computing the work done by the field as the material is moved.

In addition a torque density $\mathbf{G}$ results from the Maxwell tensor for anisotropic materials,

$$\mathbf{G} = \mathbf{D}\times\mathbf{E} + \mathbf{B}\times\mathbf{H}. \tag{30}$$

For sinusoidal fields,

$$(\mathbf{G})_{\mathrm{av}} = \mathscr{R}.\mathscr{P}.(\mathbf{D}_\omega\times\mathbf{E}^*_\omega + \mathbf{B}_\omega\times\mathbf{H}^*_\omega). \tag{31}$$

The total work done during an adiabatic displacement δx is

$$\delta W^{(P)}_\omega = \int_v (\mathbf{k})_{\mathrm{av}}.\delta\mathbf{r}\,\mathrm{d}v + \int_v (\mathbf{G})_{\mathrm{av}}.\delta\boldsymbol{\theta}\,\mathrm{d}v, \tag{32}$$

where $\delta\mathbf{r}$ and $\delta\boldsymbol{\theta}$ are the local displacements and rotations of polarizable material generated by δx.

Using (30) and (31) $\delta W^{(P)}_\omega$ may be written

$$\delta W^{(P}_\omega = \tfrac{1}{2}\int_v \mathbf{E}_\omega.[\delta\varkappa_\omega].\mathbf{E}^*_\omega\mathrm{d}v + \tfrac{1}{2}\int_v \mathbf{H}_\omega.[\delta\mu_\omega].\mathbf{H}^*_\omega\mathrm{d}v, \tag{33}$$

where $[\delta\varkappa_\omega]$ and $[\delta\mu_\omega]$ are changes at fixed points in the system due to both translation and rotation of polarizable material. Material movement is considered as the result of rigid body rotations and translations involving no strain. Under these conditions other proposed stress tensors such as that used by Livens (1929) lead to equation (33), and the choice of the Maxwell tensor is purely one of convenience.

Equation (25) then becomes

$$\int_S (\delta\mathbf{E}_\omega\times\mathbf{H}^*_\omega + \mathbf{E}^*_\omega\times\delta\mathbf{H}_\omega).\mathrm{d}A = 2\mathrm{j}\omega(\delta W^{(S)}_\omega + \delta W^{(P)}_\omega) \tag{34}$$

$$= 2\mathrm{j}\omega\delta W, \tag{35}$$

where δW is the total work done by the electromagnetic forces during the displacement δx.

δW may be equated to $(F_x)_{\mathrm{av}}\delta x$ where $(F_x)_{\mathrm{av}}$ is the average generalized force resulting from the electromagnetic fields giving,

$$2\mathrm{j}\omega(F_x)_{\mathrm{av}}\delta x = \int_S (\delta\mathbf{E}_\omega\times\mathbf{H}^*_\omega + \mathbf{E}^*_\omega\times\delta\mathbf{H}_\omega).\mathrm{d}\mathbf{A}, \tag{36}$$

which is the fundamental result.

III. REDUCTION OF THE SURFACE INTEGRAL

The electric and magnetic fields on S are not independent. A theorem of electromagnetism (Stratton 1941, Sec. 9.2) asserts that a knowledge of either $(\mathbf{E}_\omega\times\mathbf{n})$ or $(\mathbf{H}_\omega\times\mathbf{n})$ over S ($\mathbf{n}$ a unit normal) is sufficient to determine the fields of the whole system. In the surface integral of equation (36) only tangential components of $\mathbf{E}_\omega$ and $\mathbf{H}_\omega$ are involved. We may think of the system as being excited by fictitious surface currents and magnetic currents, and surface charges and magnetic charges (Stratton 1941, Sec. 8.14). By this device the variation δ may be performed with either $(\mathbf{E}_\omega \times \mathbf{n})$ or $(\mathbf{H}_\omega \times \mathbf{n})$ constant to obtain useful specializations of equation (36). The change $\delta \mathbf{H}_\omega$ or $\delta \mathbf{E}_\omega$ then results completely from changes within the system. We may write

$$(F_x)_{\mathrm{av}} = \frac{1}{2j\omega}\int_S \mathbf{E}^*_\omega \times \left(\frac{\partial \mathbf{H}_\omega}{\partial x}\right)_{(\mathbf{E}_\omega \times \mathbf{n})} .\mathrm{d}\mathbf{A}, \tag{37}$$

or

$$(F_x)_{\mathrm{av}} = \frac{1}{2j\omega}\int_S \left(\frac{\partial \mathbf{E}_\omega}{\partial x}\right)_{(\mathbf{H}_\omega \times \mathbf{n})} \times \mathbf{H}^*_\omega .\mathrm{d}\mathbf{A}, \tag{38}$$

where $\mathbf{H}_\omega$ is a linear functional of $(\mathbf{E}_\omega \times \mathbf{n})$ and $\mathbf{E}_\omega$ is a linear functional of $(\mathbf{H}_\omega \times \mathbf{n})$, over S. The functionals are determined by the details of the system and depend on x.

The results may also be expressed in terms of the complex power P_ω which is defined as the integral of the complex Poynting vector over the surface, i.e.

$$P_\omega = \int_S \mathbf{E}_\omega \times \mathbf{H}^*_\omega .\mathrm{d}\mathbf{A}, \tag{39}$$

yielding

$$(F_x)_{\mathrm{av}} = \frac{1}{2j\omega}\left(\frac{\partial P^*_\omega}{\partial x}\right)_{(\mathbf{E}_\omega \times \mathbf{n})}, \tag{40}$$

or

$$(F_x)_{\mathrm{av}} = \frac{1}{2j\omega}\left(\frac{\partial P_\omega}{\partial x}\right)_{(\mathbf{H}_\omega \times \mathbf{n})}. \tag{41}$$

For many practical systems equations (40) and (41) enable us to make a complete reduction to circuit theory parameters. First, consider a system for which ordinary a.c. circuit theory is applicable. We require that the fields on S are quasi-stationary and that the excitation is provided by n pairs of conductors. Let V_K be the complex r.m.s. voltage of angular frequency ω applied to the Kth terminal-pair and I_K the resulting complex r.m.s. current flowing to the system from this pair. The fields on S are the quasi-stationary fields resulting from the potential differences V_K and the currents I_K. By a well-known result for the flow of energy into the system,

$$P_\omega = \sum_{K=1}^{n} V_K I^*_K. \tag{42}$$

The electric field amplitude over S is maintained constant by

$$V_K = \text{constant}, \quad K = 1, \ldots, n,$$

and equation (40) becomes

$$(F_x)_{\mathrm{av}} = \frac{1}{2j\omega}\left(\frac{\partial P^*_\omega}{\partial x}\right)_{V_K}. \tag{43}$$

Similarly, the magnetic field condition in equation (41) is satisfied by

$$I_K=\text{constant}, \quad K=1, \ldots, n,$$

and equation (41) becomes

$$(F_x)_{\text{av}}=\frac{1}{2j\omega}\left(\frac{\partial P_\omega}{\partial x}\right)_{I_K}. \tag{44}$$

However, the V_K and I_K are related linearly by admittance and impedance matrices (Guillemin 1953) $Y_{KL}(\omega)$, $Z_{KL}(\omega)$,

$$I_K=\sum_{L=1}^{n} Y_{KL}V_L, \tag{45}$$

$$V_K=\sum_{L=1}^{n} Z_{KL}I_L. \tag{46}$$

For the loss-free reciprocal networks considered, Z_{KL}, Y_{KL} are purely imaginary and symmetrical.

Substitution into equations (43) and (44) yields

$$(F_x)_{\text{av}}=\frac{1}{2j\omega}\sum_{K=1}^{n}\sum_{M=1}^{n} V_K^*\frac{\partial Y_{KM}}{\partial x}V_M, \tag{47}$$

and

$$(F_x)_{\text{av}}=\frac{1}{2j\omega}\sum_{K=1}^{n}\sum_{M=1}^{n} I_K^*\frac{\partial Z_{KM}}{\partial x}I_M. \tag{48}$$

Equations (47) and (48) give the force in terms of derivatives of the admittance or impedance parameters of the system. They are generalizations of equations (5) and (6). For a two-terminal system equations (47) and (48) become

$$(F_x)_{\text{av}}=\frac{1}{2j\omega}VV^*\frac{\partial Y}{\partial x}=\frac{1}{2\omega}|V|^2\frac{\partial B}{\partial x}, \tag{49}$$

$$(F_x)_{\text{av}}=\frac{1}{2j\omega}II^*\frac{\partial Z}{\partial x}=\frac{1}{2\omega}|I|^2\frac{\partial X}{\partial x}, \tag{50}$$

which are just equations (5) and (6).

However, the fields within the two-terminal network need not be of low frequency and the network may have any degree of complexity. Equations (47) and (48) were obtained in an earlier paper (Smith 1960) in a restricted form, applicable to low frequency lumped-element circuits only.

The force may be expressed by equations (47) and (48) for another common practical system. A microwave circuit (Montgomery, Dicke, and Purcell 1948) with a number of entering waveguides may be described by "voltages" and "currents", V_K and I_K. The fields in the incoming waveguides are expanded in terms of normal mode fields. Each V_K is a coefficient of a normal mode electric field distribution in one of the guides and each I_K is a coefficient of a normal mode magnetic field distribution. The normal mode fields usually correspond to propagating modes but do not need to.

The V_K, I_K of the whole system are related linearly by admittance and impedance matrices as in equations (45) and (46). Further, the orthogonality of the modes and the choice of magnitudes enables the complex power P_ω to be written

$$P_\omega = \int_S (\mathbf{E}_\omega \times \mathbf{H}_\omega^*).\mathrm{d}\mathbf{A} = \sum_K V_K I_K^*, \tag{51}$$

the surface integration extending over the interiors of the waveguides. Equations (40) and (41) then lead to equations (43), (44) and (47), (48).

IV. Applications and Extensions

The results of Section III may be used as a foundation for the calibration of certain a.c. electrical measuring instruments. The results are relevant for instruments which are essentially loss free and dependent on the Maxwell stresses for providing an indicating force. The electrostatic voltmeter, quadrant electrometer, or current dynamometer are simple practical examples. A class of microwave power measuring instruments which rely on radiation pressures (e.g. Cullen and Stephenson 1952 ; Cullen, Rogal, and Okamura 1958) provides further examples. Equations (47) and (48) are applicable to these systems. A measurement of the admittance or impedance derivatives, together with the force produced in the instrument, provides a calibration of the instrument. If the derivatives are measured in terms of an absolute impedance or admittance standard, this calibration is absolute. The establishment of an impedance standard is a separate problem. In effect, it involves the calculation of a field distribution, but the standard is designed so that the calculations are simple. In the high frequency domain the characteristic impedance of an accurately constructed waveguide or transmission line usually constitutes the standard. In the low frequency region the standard is commonly derived from a calculable mutual inductance or capacitance.

The average force has been obtained for sinusoidally varying fields, but the extension to general time dependence follows immediately from a Fourier resolution of the exciting fields. The force is everywhere expressed as a quadratic function of field quantities. By Parseval's theory, the contributions to the average force from individual Fourier components are additive.

We have considered loss-free reciprocal systems only. The restriction to reciprocal systems is not of great importance in practice. However, the restriction to loss-free systems could be more serious. In some cases a means has been found for approximating the average force in lossy lumped-element systems (Smith 1960).

V. References

CULLEN, A. L., ROGAL, B., and OKAMURA, S. (1958).—*Trans. Inst. Radio Engrs.* **MTT-6** : 133.

CULLEN, A. L., and STEPHENSON, I. M. (1952).—*Proc. Instn. Elect. Engrs.* IV **99** : 294.

GUILLEMIN, E. A. (1953).—" Introductory Circuit Theory." (Wiley : New York.)

LIVENS, G. H. (1929).—" Theory of Electricity." (Cambridge Univ. Press.)

MONTGOMERY, C. G., DICKE, R. H., and PURCELL, E. M. (1948).—" Principles of Microwave Circuits." (McGraw-Hill : New York.)

SMITH, W. E. (1960).—A theory of steady forces in variable-parameter networks. Instn. Elect. Engrs. Monograph No. 366M. *Proc. Instn. Elect. Engrs.* C **107** : 228.

STRATTON, J. A. (1941).—" Electromagnetic Theory." (McGraw-Hill : New York.)

THE GRADATION AND INERTIA OF HURTER AND DRIFFIELD: A STUDY IN THEORY

By C. Candler*

[*Manuscript received May 5, 1960*]

Summary

In a deep emulsion the shape of the D–$\log E$ characteristic depends on two quantities, the photon number P, which is determined by the number of photons required to form a development centre, and the ratio K of the absorption cross sections of a silver halide crystal before and after development. The position of the curve on the exposure axis is determined by the mean reaction cross section s of the crystals. In a coating a fourth quantity enters, the " opacity before development " of Hurter and Driffield, here called the exposure ratio R of front to back surface.

If development changes K and only K, the Hurter and Driffield laws governing gradation and inertia automatically follow. Experiments have shown that P, s, and R are independent of development in one or two emulsions, but the extension of this to all emulsions depends on the general validity of the two laws which Hurter and Driffield themselves established.

In a Schumann plate the ratio D/D_s, where D_s is the saturation density, remains constant as development proceeds and the two laws are still valid.

I. Two Empirical Laws

May 31, 1960 is the seventieth anniversary of Hurter and Driffield's paper (1890), describing their *Photochemical Investigations on Photographic Plates*, a paper which still ranks as the most important ever written on the photographic process.

As the first scientists to investigate the photographic plate, Hurter and Driffield had to establish the experimental facts before they could attempt a theory. They always used white light and this handicapped them, for many important laws, which have emerged in recent years, and particularly the Kaiser transform (1948), are valid only in monochromatic light. The two laws, however, which are valid in white as well as monochromatic light, Hurter and Driffield discovered.

(*a*) *Gradation of Density*

When a plate is given two different exposures, and these produce densities D_1 and D_2, the " gradation " or density ratio D_1/D_2 is independent of the time of development, and of the developer too, provided the latter is " well balanced ". And in the sense here used, all commercial developers are " well balanced ", for Hurter and Driffield meant chiefly that the developer shall not contain excess bromide, or any other substance which will dissolve some of the silver halide (Ferguson 1920, p. 95; hereafter quoted as MV).

---

* South Australian Institute of Technology, Adelaide.

In support of this law Hurter and Driffield gave some measurements made on Ilford and Wratten plates (Table 1). They showed too that the law is valid after intensification (MV, p. 99), but not after reduction (MV, p. 100).

TABLE 1

SOME MEASUREMENTS BY HURTER AND DRIFFIELD (MV, p. 96) WHICH ILLUSTRATE THEIR GRADATION LAW

Plate	Exposure M.C.S.	Development		D_1/D_2
		4 min	12 min	
Ilford Red Label ..	10	0·77	1·26	1·63
	20	1·00	1·66	1·66
	40	1·18	1·96	1·66
	80	1·25	2·08	1·60
Wratten Drop Shutter..	10	1·17	1·74	1·50
	20	1·67	2·37	1·42
	40	2·06	2·91	1·41
	80	2·26	3·33	1·47

(b) *The Inertia*

When the so-called straight part of the characteristic is produced to cut the exposure axis, the point of intersection is written log i, and i is called the " inertia " of the plate. Experiment shows that when either the time of development or the composition of the developer is changed, the inertia remains the same. Thus a " Manchester Slow " plate was developed first in eikonogen and then in hydroquinone (Fig. 1), and the time of development was altered in each experiment, yet the inertia was practically the same in all four determinations.

II. HURTER'S THEORY

Hurter devoted much time to theory, but he failed to explain the two laws, and no later writer has been more successful. Yet the general line the argument should take is clear from a careful reading of Hurter's own work. For Hurter (MV, p. 108) showed that the exposure E_v reaching the virgin crystals is a fraction exp $(-Na_c)$ of the exposure E entering the surface of the emulsion,

$$E_v = E \exp(-Na_c). \tag{1}$$

Here N is the number of crystals already fertilized, or in Hurter's words (MV, p. 108) " the number of particles already changed ", while a_c is the absorption cross section of a halide crystal and the small volume of gelatine immediately surrounding it.

By implication Hurter also well understood that in the developed plate his " transparency ", a quantity identical with the " transmittance " of B.S. 1636 (British Standards Institution 1950), is

$$T = e^{-D} = \exp(-Na_g), \tag{2}$$

where the first equation defines the natural density **D**. True, the relationship between density and the absorption cross section of a silver grain

$$\mathbf{D}=Na_g \tag{3}$$

is generally attributed to Nutting (1913), who derived it from theory, and to Trivelli (1946), who verified it experimentally. True too, that the equation is not known to occur in any of Hurter's papers. But equation (1) does occur, expresses the same principle, and is much more recondite. Moreover, Hurter habitually used " weight of silver " and " density " as interchangable terms, even to the point where his editor felt bound to enter a caveat (MV, pp. 99, 100), so the reader can scarcely escape the conclusion that the Nutting equation was known to him.

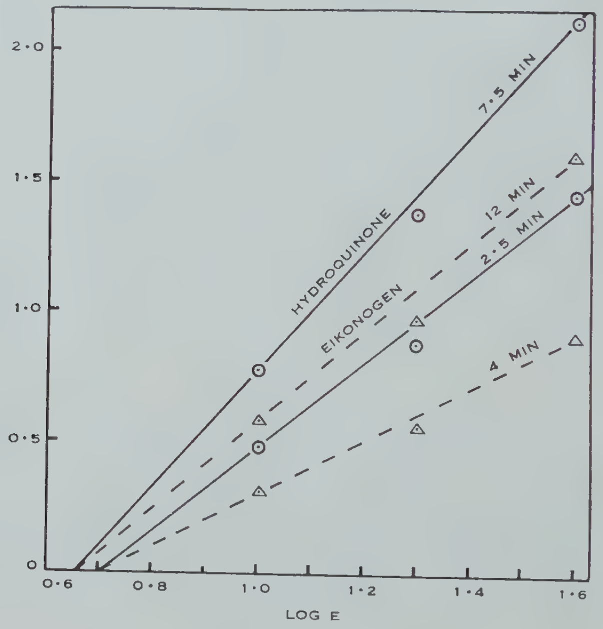

Fig. 1.—A Manchester Slow plate was given three different exposures and cut into four pieces. Two were developed in hydroquinone, one for 2½ and the other for 7½ min, and two in eikonogen for 4 and 12 min respectively. The densities are " exclusive of fog, which was very considerable ". In this figure Hurter and Driffield chose chords rather than tangents (MV, pp. 97, 120).

On combining the above equations, the exposure reaching the virgin crystals is seen to be

$$E_v=Ee^{-K\mathbf{D}}, \tag{4}$$

where K is the ratio of the absorption cross section of a halide crystal before and after development,

$$K=a_c/a_g. \tag{5}$$

This is possibly a more suggestive and significant way of stating Hurter's result than any he himself employed, but it can scarcely be said to advance his account of absorption one iota.

Yet these equations are very close to a solution of the problem Hurter was investigating. For during development K decreases as a_g increases; and if of the parameters which govern the form of the characteristic, all but K are determined at the instant of exposure and are unaffected by development, the density may be written

$$K\mathbf{D}=f(E), \tag{6}$$

where $f(E)$ is invariant during development. Given this equation, the laws of gradation and inertia are easily shown to follow.

Seeing how near Hurter himself came to a solution, the further history of the subject is curious. By 1920 (MV, p. 34) experiment had shown that Hurter's equation of the characteristic is erroneous, but analysis had failed to locate the error ; and this has remained true to the present day (Mees 1942, 1954).

After 1920 two lines of work can be distinguished. The Rochester school (Silberstein 1922, 1923 ; Silberstein and Trivelli 1930, 1938, 1945 ; Webb 1939, 1941, 1948) based their work on Silberstein's light dart hypothesis, and regarded as axiomatic the Poisson equation, which had already been shown to explain the characteristic produced by α-particles. True, Silberstein (1928) showed that the characteristic of a monolayer cannot be explained unless either the quantum theory or the Poisson equation is rejected. Although this conclusion was quite correct (Candler 1960), it was more than Silberstein himself was able to accept, and for another 20 years both quantum theory and Poisson law continued in general use.

Over the same period astronomers (Sampson 1923 ; Baker 1925, 1926, 1928 ; Wilson 1953) and spectrochemists (Kaiser 1941, 1948 ; Hughes and Murphy 1949 ; Morello 1955 ; Candler 1956 ; Arrak 1957) sought a transform linear in $\log E$. Generally, spectrochemists have been little interested in theory, but when Kaiser (1948) found a transform linear at all wavelengths, an exposure equation (Candler 1956) was immediately available, and analysis showed that the four parameters (Candler 1959) are precisely those selected by Hurter 70 years earlier.

Hurter's choice of the right parameters was a remarkable feat and reveals his intuitive grasp of a complex physical problem. For one might well expect with the Rochester school that grain size will alter the shape of the characteristic either directly or through its effect on the photon number.

In modern symbols Hurter's differential equation may be written

$$K\delta\mathbf{D}=(e^{-K\mathbf{D}}-R^{-1})\delta(sE). \tag{7}$$

This states that the number of fresh crystals fertilized by a small additional exposure δE is measured by the increase in density $\delta\mathbf{D}$, and is proportional to the fraction $e^{-K\mathbf{D}}$ of the additional exposure, which penetrates to the virgin crystals, less the fraction $1/R$ lost through the back surface, R being " the opacity of the unexposed plate " (MV, p. 110) or the exposure ratio of front to back surface. The sensitivity of the crystals is determined by their reaction cross section s, which is in effect the reciprocal of Hurter's ε " the energy required to change one particle of silver halide into the condition capable of development " (MV, p. 109).

Whether the energy lost through the back surface should be deducted is doubtful, but no decision is necessary for an emulsion so deep that no light is lost through the back surface is an easier problem than a coating. And, once the equation of a deep emulsion is known, the equation of a coating is easily derived (Candler 1959). So the term $1/R$ may be dropped.

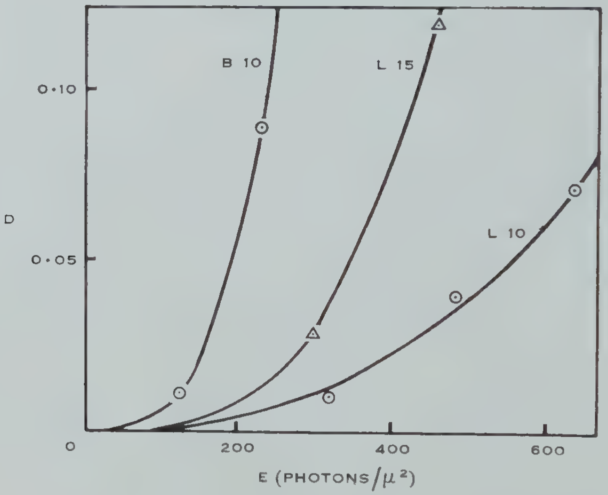

Fig. 2.—The density-exposure curves of three Kodak plates are all parabolic near the origin. These plates were exposed at 430 mμ and measured at Harrow in 1956.

For the rest, Hurter well understood that he had to know how the number of crystals fertilized varies with the exposure when the density is so low that absorption plays no part. Unfortunately, an unhappy extrapolation from high densities and an erroneous experiment (MV, p. 107) made him think that the number of crystals fertilized is proportional to the exposure, whereas later experiments (Fig. 2) have shown that the law is

$$D=kE^{P}, \tag{8}$$

where P is called the photon number, because it is most simply interpreted as the number of photons required to form a development centre. In most emulsions P lies between 1·5 and 3·0.

As Hurter believed P unity, he omitted it from his equation. When this error is corrected, his equation becomes

$$K\delta\mathbf{D}=e^{-PK\mathbf{D}}(sE)^{P-1}\delta(sE), \tag{9}$$

and on integration the exposure equation emerges

$$(sE)^{P}=e^{PK\mathbf{D}}-1. \tag{10}$$

At low densities this equation cannot be distinguished from the author's equation (Candler 1959) (Fig. 3), which may be written either as

$$(sE)^P = PK\mathbf{D}e^{PK\mathbf{D}} \tag{11}$$

or

$$A + \log E = PKD + \log D, \tag{12}$$

where **D** is the natural density ln $(1/T)$ and D the common density log $(1/T)$. At higher densities, however, differences occur, and a critical comparison is firmly in favour of the Hurter form. Nevertheless, Hurter's equation does possess one disadvantage ; it is much more difficult to fit to an experimental curve. As either equation will explain the two empirical laws, the author's form will be used for the rest of this paper.

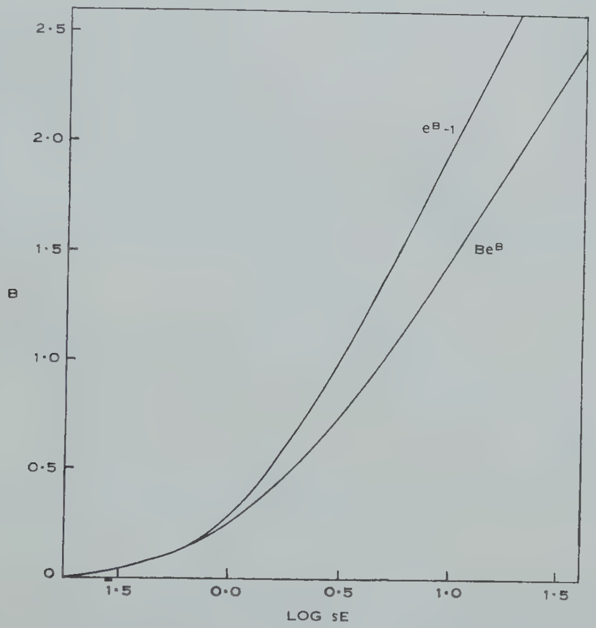

Fig. 3.—The Hurter characteristic of a deep emulsion is compared with one proposed by the author. B is an abbreviation for the product PKD. Both curves assume $P = 2$.

III. INVARIANCE OF THREE PARAMETERS

If theory is to be trusted, three parameters, the reaction cross sections, the photon number P, and the exposure ratio R of front to back surface, are all determined at the instant the development centres are formed, and only the fourth, the ratio K of the absorption cross sections, varies with development. This should remain true so long as the developer is one which neither aborts centres formed by the radiation nor develops grains which have not been fertilized by light.

Incidentally, this is a crucial test of theory. For, if the equation is really empirical and the theory illusory, all four parameters would surely vary.

Only one set of plates is known to have been developed for different times after being given the same exposure (Mees 1942, p. 409). The illuminant was white light, so one would not expect a monochromatic equation to apply. But Arrak (1957) noticed that a monochromatic equation is valid, presumably because the emulsion was panchromatic ; and with white light the effective wavelengths are limited to a narrow range where K happens to be constant.

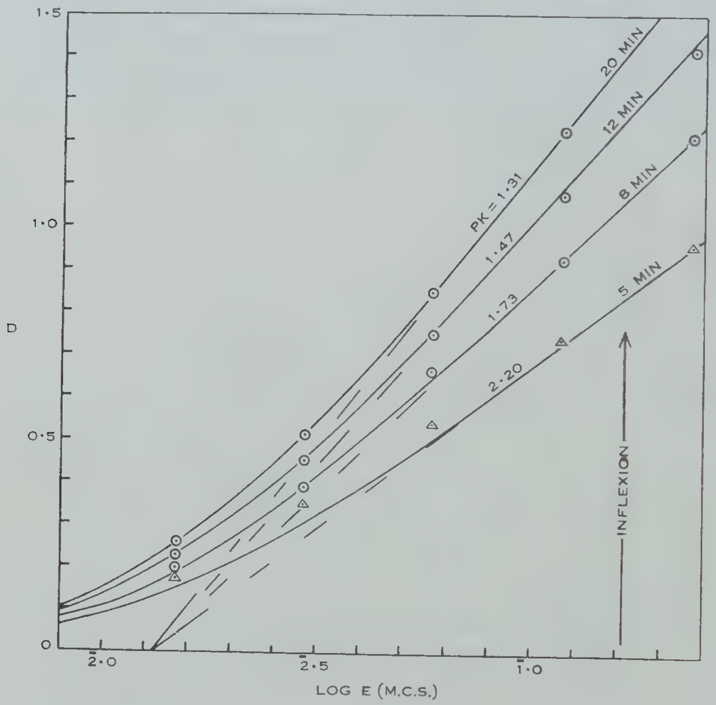

Fig. 4.—The characteristics of a panchromatic emulsion studied by Sheppard and Mees. The curves which follow theory, assume $P=2\cdot15$ and $\log(E_{\mathrm{MCS}}/sE_{\varphi})=\bar{2}\cdot07$; where the two exposures are in metre-candle-seconds and photons/μ^2 respectively. The circles are experimental. The development time and the value of PK are written beside each line.

The four characteristics can be fitted (Fig. 4) to an exposure equation with $P=2\cdot15$, and this confirms the invariance of P, which the author had noticed in a set of four B 10 plates developed, three in Ilford ID-2 of concentrations 33, 67, and 100%, and one in neat D.19b. In Sheppard's emulsion three curves of best fit have the same values of $A+\log PK$ (Table 2).

The development times were 8, 12, and 20 min, and a comparison of equations (11) and (12) shows that this establishes the invariance of the reaction cross section.

Hurter and Driffield's experiments were very extensive, and are still the substantial evidence that neither P nor s changes on development. In practice small changes in s do occur in many developers, because the developer is not perfectly balanced, so some development centres are aborted or some grains not fertilized by light develop.

TABLE 2

THE PARAMETERS A AND PK FOR THE CURVES OF BEST FIT IN THE PANCHROMATIC EMULSION STUDIED BY SHEPPARD AND MEES

The photon number is taken to be 2·15

Development Time (min)	PK	A	$A+\log PK$
5	2·20	3·68	4·02
8	1·73	3·56	3·80
12	1·47	3·62	3·79
20	1·31	3·66	3·78

IV. THE GENERALIZED DENSITY

The shape of the characteristic depends on both P and K, and this makes the discussion of any general property laborious; but, when the natural density $\mathbf{D}$ is replaced by the natural form of the generalized density $\mathbf{B}$ defined as

$$\mathbf{B}=PK\mathbf{D}, \tag{13}$$

the shape of the generalized characteristic, or B–log E curve, depends only on P, and discussion is simplified. Inserting this quantity in the exposure equation,

$$(s\mathbf{E})^P=\mathbf{B}e^{\mathbf{B}}. \tag{14}$$

Convenient as natural logarithms and natural densities are in theoretical work, common logarithms and common densities are preferred for computation. Fortunately, the values of P and K are unchanged, and the above equation may be written

$$P\log(s\mathbf{E})=B+\log(B/M), \tag{15}$$

where $M=0\cdot434$. Here s remains the reaction cross section provided $\mathbf{E}$ is measured in photons per unit area; but if E is measured in arbitrary units s becomes a mere constant without physical significance.

Interest is largely concentrated on the B–log E characteristic, whose slope (Fig. 5) is

$$\mathbf{B}'=\mathrm{d}\mathbf{B}/\mathrm{d}(\ln E)=P\mathbf{B}/(1+\mathbf{B}), \tag{16}$$

or

$$B'=\mathrm{d}B/\mathrm{d}(\log E)=PB/M+B), \tag{17}$$

and whose curvature (Fig. 6) is

$$\mathbf{B}''=\mathrm{d}^2\mathbf{B}/\mathrm{d}(\ln E)^2=P^2\mathbf{B}/(1+\mathbf{B})^3, \tag{18}$$

or

$$B''=\mathrm{d}^2B/\mathrm{d}(\log E)^2=MP^2B/(M+B)^3. \tag{19}$$

Incidentally, one may easily show that

$$B=M\mathbf{B},\quad B'=\mathbf{B}',\quad B''=\mathbf{B}''/M. \tag{20}$$

As B, B', and B'' are all functions of sE, the generalized slope and curvature can be plotted for any assumed value of P.

In a coating the shapes of the characteristic and its two derivatives depend on the photon number and the exposure ratio of front to back surface, two quantities that are independent of the development time and the composition of the developer. Thus in a coating the generalized density may be expressed as a difference between front and back surfaces,

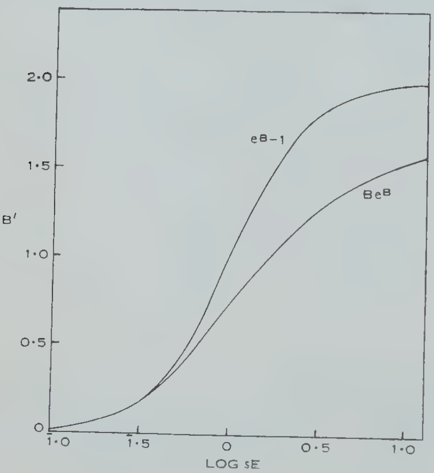

Fig. 5

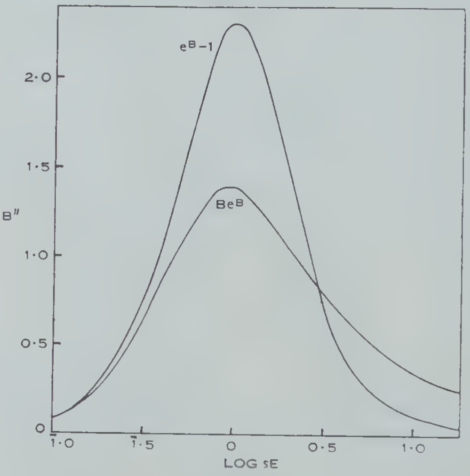

Fig. 6

Fig. 5.—The slope of the Hurter characteristic compared with an alternative proposed by the author.

Fig. 6.—The curvatures of the two characteristics similarly compared.

$$B_{ct}=B_f-B_b \tag{21}$$

This equation remains true when differentiated, so the slope and curvature of a coating may also be expressed as differences :

$$B'_{ct}=B'_f-B'_b, \tag{22}$$

$$B''_{ct}=B''_f-B''_b. \tag{23}$$

V. The Gradation of Density

When two plates are given the same exposure, the generalized density after development is the same even though the development is different. Accordingly, if the two plates are developed for times t_1 and t_2 and the resulting densities are D_1 and D_2,

$$B=PK_1D_1=PK_2D_2. \tag{24}$$

Hurter and Driffield's gradation law follows at once,

$$D_1/D_2=K_2/K_1, \tag{25}$$

for when the exposure is changed K_2/K_1 remains the same. Theory shows that in monochromatic light the gradation law is valid at all wavelengths, and this suggests a new method of verification. For if the effective exposures $s'E'$ at λ'

and $s''E''$ at λ'' are equal, the generalized densities will also be equal, since P is invariant in wavelength (Candler 1959),

$$D'/D''=K''/K'. \tag{26}$$

The size of the silver grains formed on development is independent of the wave length, so a_g' and a_g'' are equal, and

$$K''/K'=a_c''/a_c'. \tag{27}$$

In this form the gradation law can be verified experimentally only when the exposure is measured in absolute units, for only so can the effective exposures

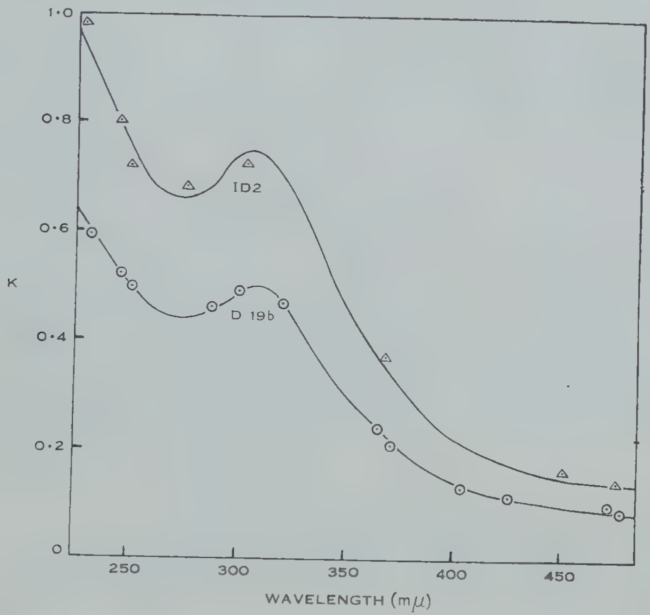

Fig. 7.—The variation of K with wavelength in two B 10 plates developed for 3 min, one in 33% ID-2 and the other in neat D.19b. In the empirical curves the density ratio varied from 1·3 to 1·6, but here the two curves have been adjusted until the ratio is 1·5 throughout.

$s'E'$ and $s''E''$ be made equal. But, if a change in the time of development or the composition of the developer changes the value of K at one wavelength from K_1' to K_2', and at another wavelength from K_1'' to K_2'',

$$K_1'/K_2'=K_1''/K_2''. \tag{28}$$

So the curves of K against wavelength should have ordinates in the same ratio when either the time of development or the composition of the developer is changed. This rule has been verified for a Kodak B 10 plate developed in Kodak D.19b and Ilford ID-2 (Fig. 7).

The gradation law remains valid after intensification (MV, p. 99) but not after reduction (MV, p. 100), and it is not valid if the developer contains excess bromide or any other agent which dissolves silver bromide. These observations are simply explained if the law is valid only when the number of development centres is unchanged during development. As the number of centres cannot be increased without producing fog or decreased without loss of speed, almost all commercial developers satisfy this condition. The only important exception is the fine grain developer, which does in fact entail some sacrifice of speed.

VI. THE INERTIA

If the " straight " part of the characteristic is extended to cut the exposure axis at log i, i is called the " inertia ". The straight part may be written

$$D=\gamma \log E/i, \tag{29}$$

where γ is the maximum slope.

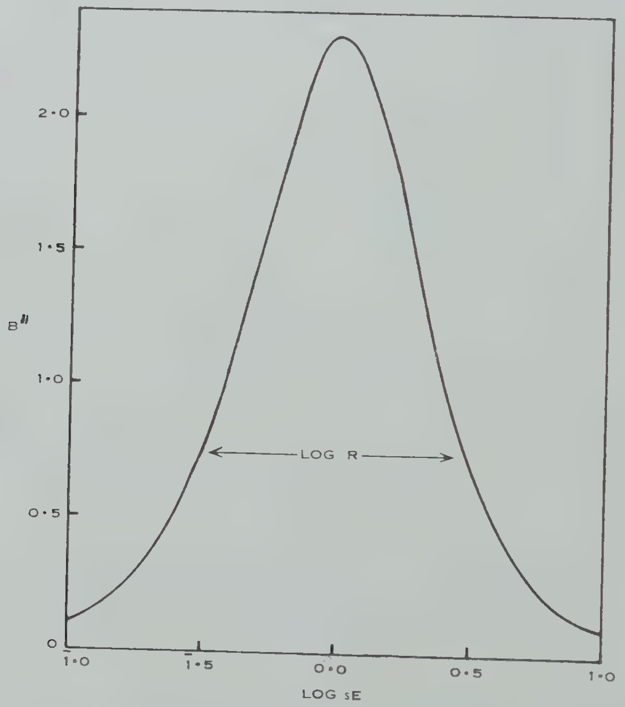

Fig. 8.—At the inflexion of the characteristic of the coating the curvatures introduced by the front and back surfaces must be equal and be a distance log R apart on the log E axis. Clearly there is only one exposure at the front surface which will satisfy both conditions.

When Hurter's theory (MV, p. 107) and Driffield's experiment (MV, p. 112) showed that no part of the characteristic is truly straight, Hurter identified the so-called straight part as the tangent at the point of inflexion X, or, in his own words, at " the point of double flexure " (MV, pp. 36, 222). In the notation of the present paper, the equation of this tangent is

$$D-{}_xD_{ct}={}_xD'_{ct} \log E/xE, \tag{30}$$

where ${}_xD_{ct}$, $\log {}_xE$ are the coordinates of the point of inflexion, and ${}_xD'_{ct}$ is the slope, commonly written γ. Accordingly, the intercept on the exposure axis is

$$\log i = \log {}_xE - {}_xD'_{ct}/{}_xD_{ct}. \tag{31}$$

This equation shows that the point of confluence lies on the exposure axis only if the exposure ${}_xE$ at inflexion and the ratio of slope to ordinate ${}_xD'_{ct}/{}_xD_{ct}$ are both independent of the time of development. These two conditions were recognized as necessary by Mees (1942, p. 409).

At inflexion the curvature of the coating is zero, so the curvatures due to the front and back surfaces are equal; and an examination of the B''–$\log E$ curve (Fig. 8) shows that for a given exposure ratio of front to back surface, this condition admits of only one solution. So at inflexion the exposure ${}_xE$ at the front surface, the generalized density of the coating, and its derivative ${}_xB'_{ct}$ are all uniquely determined. But by definition the generalized density is PKD, so at inflexion

$${}_xB'_{ct}/{}_xB_{ct} = {}_xD'_{ct}/{}_xD_{ct}. \tag{32}$$

Thus the two conditions, which Mees recognized as necessary and sufficient, derive directly from theory.

While the inertia is precisely determined by the parameters s, P, and R, it cannot easily be made explicit in these quantities. In particular, the inertia is not simply related to the reaction cross section, which is the best measure of the speed of an emulsion, although not of a coating. Theory therefore gives no grounds for accepting the inertia as a measure of the speed, and this confirms an opinion long since reached empirically.

VII. White Light Illumination

Hurter and Driffield verified the invariance of gradation and inertia with white light. The theoretical proof given above applies only to monochromatic light.

Logically the natural line is from monochromatic to dichromatic illumination, and then by generalizing the results to white light; but so far as is known, not a single dichromatic characteristic is on record with which to check any calculations.

A preliminary study suggests that no difficulty occurs in passing from monochromatic to dichromatic illumination of a monolayer, provided the intensities of both radiations are measured in absolute units. From monolayer to deep emulsion should require no more than integration in depth, a procedure surely possible by numerical methods, even if the integrals are intractable.

A direct attack on the dichromatic characteristic of a deep emulsion is difficult, because the two radiations penetrate to different depths. If this does not completely bar the road, it is certain that the best line of attack is still obscure.

VIII. The Schumann Plate

The characteristic of a Schumann Plate (Baker 1928; Candler 1960) has the same shape as that of a monolayer,

$$(sE)^P = D/(D_s - D), \tag{33}$$

where D_s is the saturation density. (Incidentally, this equation also describes the characteristics of five emulsions exposed to X-rays of wavelengths 0·23–0·63 Å by Tellez-Plasencia (1954).)

As development continues one may expect the ratio D/D_s to remain constant along with s and P, so that the gradation law will be satisfied.

The slope of the Schumann characteristic is

$$\mathrm{d}D/\mathrm{d}\,(\log E)=PD(D_s-D)/MD_s, \tag{34}$$

where $M=0\cdot434$. This is a maximum when $D=\frac{1}{2}D_s$, the slope being

$$\mathrm{d}D/\mathrm{d}\,(\log E)=PD_s/4M. \tag{35}$$

Thus the slope and ordinate at the point of inflexion increase together as development proceeds, and the inertia is constant, just as in a deep emulsion.

Note added in Proof

A dozen equations purporting to describe the characteristic have been published, but not one has claimed to describe the monolayer as well. In this Hurter's equation stands alone, for on differentiating (5) with respect to the depth, the equation of the monolayer (Candler 1960) emerges.

These two equations, monolayer and deep emulsion, describe the characteristic not only in the visible, ultraviolet, and X-ray regions of the spectrum, but also the characteristic of fast electrons, and the grain density along the track of an ionized particle. The evidence will be published shortly in the *Zeitschrift für wissenschaftliche Photographie.*

IX. References

Arrak, A. (1957).—*Appl. Spectros.* **11**: 38.

Baker, E. A. (1925).—*Proc. Roy. Soc. Edinb.* **45**: 166.

Baker, E. A. (1926).—*Proc. Roy. Soc. Edinb.* **47**: 34.

Baker, E. A. (1928).—*Proc. Roy. Soc. Edinb.* **48**: 106.

British Standards Institution (1950).—Terms used in spectrographic analysis. B.S. 1636.

Candler, C. (1956).—*Spectrochim. Acta* **8**: 256.

Candler, C. (1959).—*Appl. Spectros.* **13**: 97.

Candler, C. (1960).—*Aust. J. Phys.* **13**: 419.

Ferguson, W. B. (1920).—" A Memorial Volume to Hurter and Driffield." (Roy. Photogr. Soc.: London.)

Hughes, H. K., and Murphy, R. W. (1949).—*J. Opt. Soc. Amer.* **39**: 501.

Hurter, F., and Driffield, V. C. (1890).—*J. Soc. Chem. Ind.* **9**: 455.

Kaiser, H. (1941).—*Spectrochim. Acta* **2**: 4.

Kaiser, H. (1948).—*Spectrochim. Acta* **3**: 159.

Mees, C. E. K. (1942).—" The Theory of the Photographic Process." p. 409. (Macmillan: New York.

Mees, C. E. K. (1954).—Idem (later edition).

Morello, B. (1955).—*Mikrochim. Acta* **2**: 390.

Nutting, P. G. (1913).—*Phil. Mag.* **26**: 43.

Sampson, R. A. (1923).—*Mon. Not. R. Astr. Soc.* **83**: 174.

Sampson, R. A. (1925).—*Mon. Not. R. Astr. Soc.* **85**: 112.

Silberstein, L. (1922).—*Phil. Mag.* **44**: 256.

Silberstein, L. (1923).—*Phil. Mag.* **45**: 1062.

Silberstein, L. (1928).—*Phil. Mag.* **5**: 164.

SILBERSTEIN, L., and TRIVELLI, A. P. H. (1930).—*Phil. Mag.* **9** : 787.
SILBERSTEIN, L., and TRIVELLI, A. P. H. (1938).—*J. Opt. Soc. Amer.* **28** : 441.
SILBERSTEIN, L., and TRIVELLI, A. P. H. (1945).—*J. Opt. Soc. Amer.* **35** : 93.
TELLEZ-PLASENCIA, H. (1954).—*Sci. Ind. Phot.* **25** : 425.
TRIVELLI, A. P. H. (1946).—*J. Franklin Inst.* **240** : 1.
WEBB, J. H. (1939).—*J. Opt. Soc. Amer.* **29** : 309.
WEBB, J. H. (1941).—*J. Opt. Soc. Amer.* **31** : 559.
WEBB, J. H. (1948).—*J. Opt. Soc. Amer.* **38** : 27.
WILSON, R. (1953).—*Mon. Not. R. Astr. Soc.* **113** : 557.

RESOLUTION OF BREMSSTRAHLUNG EXPERIMENTS

By H. H. Thies*

[*Manuscript received June 7, 1960*]

Summary

This paper investigates how mathematical approximations and statistical errors are transmitted into computed cross sections in the analysis of experimental bremsstrahlung yield data. The resolution of bremsstrahlung experiments is defined in analogy with optical resolution and an expression for the practical evaluation of resolution is derived. Methods of cross-section computation, and smoothing and curve-fitting are discussed.

I. Error Inherent in the Yield Analysis

The bremsstrahlung experiment measures the yield of a photonuclear reaction. The corresponding cross section is derived by a transformation calculation. This investigation is concerned with how approximations in the transformation calculation and standard errors of the original discrete set of experimental yield ordinates are propagated into the computed cross section, and how well the computed cross section portrays the true (exact) cross section. It is assumed that the bremsstrahlung spectrum is known and that experimental yield ordinates contain no other than truly statistical errors.

Yield $y(E_{0k})$ and cross section $s(E)$ are related through the normalized bremsstrahlung distribution function $P(E,E_{0k})$ by the integral equation

$$y(E_{0k})=\int_{E_{th}}^{E_{0k}} P(E,E_{0k})s(E)\mathrm{d}E. \tag{1}$$

E_{0k} is the maximum energy of the spectrum, $E=h\nu$ the energy of a photon interacting with a nucleus, and E_{th} the reaction threshold.

Experimental yield data are invariably given as a discrete set of yield values only and not as a continuous function. Thus the knowledge about the yield function is restricted to that of a finite number of yield ordinates, and nothing is known *a priori* about the behaviour of the function between these ordinates. If $y(E_{01}), y(E_{02}), \ldots, y(E_{0k}), \ldots, y(E_{0p})$ are the yield values corresponding to energies $E_{01}, E_{02}, \ldots, E_{0k}, \ldots, E_{0p}$, then the equation

$$y(E_{0k})=\sum_{i=1}^{k} P(E_i,E_{0k})\bar{s}(E_i)\Delta E_i\,;\quad k=1,\ 2,\ldots,p, \tag{2}$$

must be substituted as an optimum approximation for (1). Here $\Delta E_i=E_{0i}-E_{0,i-1}$,

$$E_i=E_{0i}-\tfrac{1}{2}\Delta E_i,\ \text{and}\ \bar{s}(E_i)\,;\quad i=1,\ 2,\ldots,p$$

represents a discrete set of cross-section ordinates which are to approximate ordinates $s(E_i)$ of the exact cross section $s(E)$. Any approximation other than

---

* Department of Physics, University of Western Australia, Nedlands, W.A.

(2) would make assumptions about $y(E_{0k})$ and $s(E)$, i.e. about the "smoothness" of $y(E_{0k})$, which are not contained in the experimental data.

(2) represents a system of p linear equations in the p unknowns $\bar{s}(E_i)$; $i=1, 2, \ldots, p$, and thus in general has a unique solution and any exact method to solve (2) will give the same unique solution. Existing methods are the total spectrum method (Johns *et al.* 1950), the photon difference method (Katz and Cameron 1951), and the modified total spectrum method of Penfold and Leiss (1958). An iteration method is used by Carver and Lokan (1957).

It is convenient to choose a constant energy interval

$$\Delta E_i = \Delta E_A,$$

and write (2) in matrix form, namely,

$$\mathbf{y}_0 = \Delta E_A \mathbf{P} \cdot \bar{\mathbf{s}}. \tag{3}$$

Here

$$\mathbf{y}_0 = \begin{bmatrix} y_{01} \\ y_{02} \\ \cdot \\ \cdot \\ y_{0,p-1} \\ y_{0,p} \end{bmatrix}; \quad \mathbf{P} = \begin{bmatrix} P_{1,1} & 0 & 0 & \cdot & 0 & 0 \\ P_{2,1} & P_{2,2} & 0 & \cdot & 0 & 0 \\ \cdot & \cdot & \cdot & \cdot & \cdot & \cdot \\ \cdot & \cdot & \cdot & \cdot & 0 & 0 \\ P_{p-1,1} & P_{p-1,2} & \cdot & \cdot & P_{p-1,p-1} & 0 \\ P_{p,1} & P_{p,2} & \cdot & \cdot & P_{p,p-1} & P_{p,p} \end{bmatrix}; \quad \bar{\mathbf{s}} = \begin{bmatrix} \bar{s}_1 \\ \bar{s}_2 \\ \cdot \\ \cdot \\ \bar{s}_{p-1} \\ \bar{s}_p \end{bmatrix}$$

and the following abbreviations are used

$$y(E_{0k}) = y_{0k}, \quad P(E_i, E_{0k}) = P_{k,i}, \quad \bar{s}_i = \bar{s}(E_i).$$

Defining

$$\mathbf{P}^{-1} = \mathbf{C} = \begin{bmatrix} C_{1,1} & 0 & 0 & \cdot & 0 & 0 \\ C_{2,1} & C_{2,2} & 0 & \cdot & 0 & 0 \\ \cdot & \cdot & \cdot & \cdot & \cdot & \cdot \\ \cdot & \cdot & \cdot & \cdot & 0 & 0 \\ C_{p-1,1} & C_{p-1,2} & \cdot & \cdot & C_{p-1,p-1} & 0 \\ C_{p,1} & C_{p,2} & \cdot & \cdot & C_{p,p-1} & C_{p,p} \end{bmatrix}, \tag{4}$$

solve (3) for $\bar{\mathbf{s}}$, by premultiplying each side of (3) by $(1/\Delta E_A)\mathbf{C}$. Thus,

$$\bar{\mathbf{s}} = (1/\Delta E_A)\mathbf{C} \cdot \mathbf{y}_0, \tag{5}$$

which is equivalent to the p equations

$$\bar{\mathbf{s}}(E_i) = \frac{1}{\Delta E_A} \sum_{n=1}^{i} C_{i,n} y_{0n}; \quad i=1, 2, \ldots, p. \tag{6}$$

From (6) each ordinate $\bar{s}(E_i)$ can be evaluated directly, independently of other ordinates $\bar{s}(E_j)$, $j \neq i$. The coefficients $C_{i,n}$ are related to the coefficients $B_{i,n}$ of Penfold and Leiss (1958) by

$$C_{i,n} = E_i B_{i,n}. \tag{7}$$

Values of $B_{i,n}$ for several values of ΔE_A and for E_{0p} up to 1 BeV are tabulated by Penfold and Leiss (1958) for an integrated-over-angles Schiff spectrum (Schiff 1951).

If $y(E_{0k})$ is given as a continuous function and ΔE_A is chosen smaller than E_{th}, the summation (2) may be started at any energy value E_{00} between 0 and ΔE_A ($E_{00}=E_{01}-\Delta E_A$). Each corresponding set of ordinates $y(E_{0k})$ will define a set of ordinates $\bar{s}(E_i)$, and all the sets $y(E_{0k})$ will define a continuous function $\bar{s}(E)$, where $\bar{s}(E)$ approximates $s(E)$. Any discrete set $\bar{s}(E_i)$, $i=1, 2, 3, \ldots, p$ will lie on $\bar{s}(E)$ rather than on $s(E)$.

The difference $s(E)-\bar{s}(E)$, which is the error introduced by replacing the integration in (1) by the summation of finite difference of (2), will now be computed. It is assumed that $P(E,E_{0k})s(E)$ may be expanded by its Taylor series in any energy interval ΔE_A.

Using the notation

$$\frac{\partial}{\partial E}[P(E,E_{0k})s(E)]_{E=E_i}=[P_{k,i}s_i]',$$

and similarly for higher derivatives, the Taylor expansion of $[P(E,E_{0k})s(E)]$ for the energy interval

$$E_{0,i-1}<E<E_{0i}$$

becomes

$$P(E,E_{0k})s(E)=P_{k,i}s_i+\frac{1}{1!}[P_{k,i}s_i]'(E-E_i)+\frac{1}{2!}[P_{k,i}s_i]''(E-E_i)^2+\ldots \tag{8}$$

With (8) the p yield ordinates y_{0k}; $k=1, 2, \ldots, p$, may be expressed through the p equations

$$y_{0k}=\sum_{i=1}^{k}\left[\int_{E_i-\frac{1}{2}\Delta E_A}^{E_i+\frac{1}{2}\Delta E_A}\{[P_{k,i}s_i]+[P_{k,i}s_i]'(E-E_i)+\tfrac{1}{2}[P_{k,i}s_i]''(E-E_i)^2+\ldots\}\mathrm{d}E\right];$$
$$k=1, 2, \ldots, p. \tag{9}$$

Performing the integration, one obtains

$$y_{0k}=\sum_{i=1}^{k}\left\{[P_{k,i}s_i]\Delta E_A+[P_{k,i}s_i]''\frac{\Delta E_A^3}{24}+[P_{k,i}s_i]^{(N)}\frac{\Delta E_A^5}{1920}+\ldots\right\};\quad k=1, 2, \ldots, p,$$

where the nth term in the bracket is of order

$$\Delta E_A^{2n-1}/(2n-1)!\,2^{2n-2},$$

i.e. the series are strongly convergent, and a sufficiently good approximation is

$$y_{0k}\simeq\sum_{i=1}^{k}P_{k,i}s_i\Delta E_A+\sum_{i=1}^{k}[P_{k,i}s_i]''\frac{\Delta E_A^3}{24};\quad k=1, 2, \ldots, p. \tag{10}$$

Here

$$[P_{k,i}s_i]''=\left\{\frac{\partial^2 P(E,E_{0k})}{\partial^2 E}s(E)+\frac{\partial P(E,E_{0k})}{\partial E}\,\frac{\partial s(E)}{\partial E}+P(E,E_{0k})\,\frac{\partial^2 s(E)}{\partial E^2}\right\}_{E=E_i}.$$

Writing

$$\left.\frac{\partial P(E,E_{0k})}{\partial E}\right|_{E=E_i}=P'_{k,i};\quad \left.\frac{\partial s(E)}{\partial E}\right|_{E=E_i}=s'_i,$$

and defining the matrices

$$\mathbf{P}'=\begin{bmatrix} P'_{1,1} & 0 & 0 & \cdot & 0 & 0 \\ P'_{2,1} & P'_{2,2} & 0 & \cdot & 0 & 0 \\ \cdot & \cdot & \cdot & \cdot & \cdot & \cdot \\ \cdot & \cdot & \cdot & \cdot & 0 & 0 \\ P'_{p-1,1} & P'_{p-1,2} & \cdot & \cdot & P'_{p-1,p-1} & 0 \\ P'_{p,1} & P'_{p,2} & \cdot & \cdot & P'_{p,p-1} & P'_{p,p} \end{bmatrix}; \quad \mathbf{s}'=\begin{bmatrix} s'_1 \\ s'_2 \\ \cdot \\ \cdot \\ s'_{p-1} \\ s'_p \end{bmatrix},$$

and analogously for higher derivatives, and derivative matrices, the p equations (10) may be written as one matrix equation

$$\mathbf{y}_0 \simeq \Delta E_A \mathbf{P}.\mathbf{s}+(\Delta E_A^3/24)\{\mathbf{P}''.\mathbf{s}+2\mathbf{P}'.\mathbf{s}'+\mathbf{P}.\mathbf{s}''\}. \tag{11}$$

Premultiplying each side of (11) by $(1/\Delta E_A)\mathbf{C}$, one obtains with (4) and (5)

$$\mathbf{s}-\overline{\mathbf{s}}=-(\Delta E_A^2/24)\{\mathbf{C}.\mathbf{P}''.\mathbf{s}+2\mathbf{C}.\mathbf{P}'.\mathbf{s}'+\mathbf{s}''\}.$$

Numerical coefficients of the matrices $\mathbf{C}.\mathbf{P}''$ and $2\mathbf{C}.\mathbf{P}'$ were computed using the spectral distribution function of Penfold and Leiss (1958). It was found that in practical cases an error smaller than 20% in the values of elements of $\mathbf{s}-\overline{\mathbf{s}}$ is introduced if the further approximation

$$\mathbf{s}-\overline{\mathbf{s}} \simeq -(\Delta E_A^2/24)\mathbf{s}'' \tag{12}$$

is used. Equation (12) defines p ordinates $s(E_i)-\bar{s}(E_i)$; $i=1, 2, \ldots, p$, but as the summation (9) may be started at any energy E_{00} between 0 and ΔE_A, all the sets $s(E_i)-\bar{s}(E_i)$, corresponding to all the values E_{00} define a continuous function $s(E)-\bar{s}(E)$, where

$$s(E)-\bar{s}(E)=-\frac{\Delta E_A^2}{24}\,\frac{\partial^2 s(E)}{\partial E^2}. \tag{13}$$

Assume, for example, that $s(E)$ is a resonance of height S and half-width Γ, and has a Gaussian shape symmetric about E_M, i.e.

$$s(E)=S\exp\left[-4(\ln 2)\frac{(E-E_M)^2}{\Gamma^2}\right],$$

and then with (13)

$$\begin{aligned}\bar{s}(E)&=s(E)+\frac{\Delta E_A^2}{24}\,\frac{\mathrm{d}^2 s(E)}{\mathrm{d}E^2}\\ &=s(E)\left\{1-0{\cdot}230\frac{\Delta E_A^2}{\Gamma^2}+1{\cdot}281\frac{\Delta E_A^2}{\Gamma^2}\left(\frac{E-E_M}{\Gamma}\right)^2\right\}.\end{aligned}$$

$\bar{s}(E)$ has very nearly Gaussian shape, with height $\overline{S}$ and half-width $\overline{\Gamma}$, where

$$\overline{S}=S(1-0{\cdot}230\Delta E_A^2/\Gamma^2), \tag{14}$$

$$\overline{\Gamma}=\frac{\Gamma}{(1-0{\cdot}230\Delta E_A^2/\Gamma^2-0{\cdot}043\Delta E_A^4/\Gamma^4+\ldots)}. \tag{15}$$

Thus, if $\Gamma > \Delta E_A$, it is a very good approximation to write

$$S\Gamma=\overline{S}\overline{\Gamma}.$$

Equations (14) and (15) may be used to estimate the error in $\bar{s}(E)$ for the case of a non-symmetric resonance. If $\Gamma \sim \frac{1}{2}\Delta E_A$, the resonance is " smoothed out " in $\bar{s}(E)$. The " smoothing " effect due to the use of finite differences (with intervals ΔE_A) is demonstrated by an example in Figure 1.

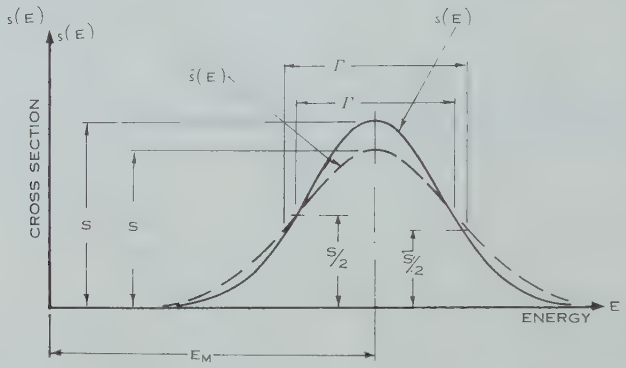

Fig. 1.—Smoothing effect due to the use of finite differences in the yield analysis of a Gaussian resonance. $(\Delta E_A = 0 \cdot 83\Gamma)$. $s(E) = S \exp[-4(\ln 2)(E-E_M)^2/\Gamma^2]$, $\bar{s}(E) = s(E) + (\Delta E_A^2/24)\{d^2s(E)/dE^2\}$.

It has been suggested (Cook 1957) that integrated cross sections be computed directly, and that cross sections be found by differentiation. If $\bar{I}_{0k}$ is the directly computed integrated cross section ordinate, corresponding to the exact ordinate $I(E_{0k})$, it is

$$\bar{\mathbf{I}}_0 = \begin{bmatrix} \bar{I}_{01} \\ \bar{I}_{02} \\ \cdot \\ \cdot \\ \bar{I}_{0,p-1} \\ \bar{I}_{0p} \end{bmatrix} = \Delta E_A \begin{bmatrix} 1 & 0 & 0 & \cdot\cdot & 0 & 0 \\ 1 & 1 & 0 & \cdot & 0 & 0 \\ \cdot & \cdot & \cdot & \cdot & \cdot & \cdot \\ \cdot & \cdot & \cdot & \cdot & 0 & \cdot \\ 1 & 1 & \cdot & \cdot & 1 & 0 \\ 1 & 1 & \cdot & \cdot & 1 & 1 \end{bmatrix} . \begin{bmatrix} \bar{s}_1 \\ \bar{s}_2 \\ \cdot \\ \cdot \\ \bar{s}_{p-1} \\ \bar{s}_p \end{bmatrix} = \Delta E_A \mathbf{D}.\bar{\mathbf{s}}$$

and with (5)

$$\bar{\mathbf{I}}_0 = \mathbf{D}.\mathbf{C}.\mathbf{y}_0 = \mathbf{F}.\mathbf{y}_0.$$

It is easily verified that, as long as (13) is valid, $\bar{I}_{0k} = I_{0k}$. However, as long as no *a priori* assumption is made about the smoothness of the exact continuous integrated cross section $I(E)$, the cross section derived from the discrete set of ordinates I_{0k} will be in error again by an amount as given by (13). Unless one is particularly interested in the integrated cross section itself, its computation is thus only an unnecessary complication in cross-section computations.

II. STATISTICAL ERRORS

In general the discrete set of exact yield ordinates $y(E_{0k})$, $k=1, 2, \ldots, p$ is not known. The experiment rather supplies a discrete set of yield ordinates

$$\mathfrak{y}(E_{0k}) \pm \text{st}\,[\mathfrak{y}(E_{0k})]\ ; \quad k=1, 2, \ldots p,$$

where st $[\mathfrak{y}(E_{0k})]$ denotes the standard error in $\mathfrak{y}(E_{0k})$. If the set of cross-section ordinates

$$\bar{\mathfrak{s}}(E_k) = \bar{\mathfrak{s}}_k\ ; \quad k=1, 2, \ldots, p,$$

is computed from (6), by using in place of ordinates y_{0k} the ordinates $\mathfrak{y}(E_{0k})=\mathfrak{y}_{0k}$, the standard error $\mathrm{st}[\bar{\mathfrak{s}}_k]$ can be computed from (6) by the law of propagation of errors, namely,

$$\mathrm{st}[\bar{\mathfrak{s}}_k]=\frac{1}{\Delta E_A}\left(\sum_{i=1}^{k} C_{k,i}^2\,\mathrm{st}[\mathfrak{y}_{0i}]^2\right)^{\frac{1}{2}}.$$

The coefficients $C_{k,i}$ decrease rapidly with decreasing i. Then if $\mathrm{st}[\mathfrak{y}_{0i}]$ does not vary much for neighbouring values of E_{0k}, a good approximation is

$$\mathrm{st}[\bar{\mathfrak{s}}_k]\simeq\frac{1}{\Delta E_A}\,\mathrm{st}[\mathfrak{y}_{0k}]\left(\sum_{i=1}^{k} C_{k,i}^2\right)^{\frac{1}{2}}. \tag{16}$$

The square root in (16) was computed for the energy interval

$$5\ \mathrm{MeV}<E_{0p}<25\ \mathrm{MeV}$$

for several values of ΔE_A. It was found that (16) may be approximated for this energy interval by

$$\mathrm{st}[\bar{\mathfrak{s}}_k]\simeq\Delta E_A^{-3/2}E_{0k}\,\mathrm{st}[\mathfrak{y}_{0k}]\cdot\mathrm{const.} \tag{17}$$

The error in $\mathrm{st}[\bar{\mathfrak{s}}_k]$ due to this approximation is smaller than 20%, even in extreme cases.

III. Experimental Resolution

Suppose a cross section $s(E)$ contains several maxima. If $s(E)$ were known, it would be possible in principle to calculate the probability that two particular maxima of $s(E)$ are resolved with statistical significance through a discrete set of experimental cross-section ordinates

$$\bar{\mathfrak{s}}_k\pm\mathrm{st}[\bar{\mathfrak{s}}_k]\ ;\quad k=1,\ 2,\ldots,p.$$

As $s(E)$ is unknown in practice, it is convenient to use a hypothetical function ${}_Rs(E)$ as a standard analytical function, which contains two maxima, and to investigate under which conditions for p, $\mathrm{st}[{}_R\mathfrak{y}_{0k}]$, and ΔE_A these maxima would be resolved through the corresponding discrete set of computed cross-section ordinates ${}_R\bar{\mathfrak{s}}_k\pm\mathrm{st}[{}_R\bar{\mathfrak{s}}_k]$. Then a quantitative criterion is obtained which indicates the minimum distance between two maxima in a standard function ${}_Rs(E)$, for which the information contained in the corresponding set ${}_R\bar{\mathfrak{s}}_k\pm\mathrm{st}[{}_R\bar{\mathfrak{s}}_k]$ is sufficient to resolve these maxima with statistical significance. This criterion will enable one to decide, at least with reasonable assurance, whether two maxima apparent from some set of experimental ordinates $\bar{\mathfrak{s}}_k\pm\mathrm{st}[\bar{\mathfrak{s}}_k]$ are real, or are only apparent owing to statistical fluctuations. The procedure is analogous to the definition of resolution in the optical case. Here one examines a standard image interference pattern as seen by the imperfect optical system with its finite resolution, and which corresponds to two image points of a perfect optical system, having infinite resolving power.

A function which is the superposition of two symmetric Gaussian resonances, each with height S and half-width Γ is chosen for the standard function ${}_Rs(E)$, that is,

$${}_Rs(E)=S\left\{\exp\left[-4(\ln 2)\left(\frac{E-E_{M1}}{\Gamma}\right)^2\right]+\exp\left[-4(\ln 2)\left(\frac{E-E_{M2}}{\Gamma}\right)^2\right]\right\}. \tag{18}$$

The two maxima at E_{M1} and E_{M2} shall be separated by (see Fig. 2)

$$d=E_{M2}-E_{M1}=1\cdot41165\Gamma\simeq\sqrt{2}.\Gamma.$$

The dip at $E=\frac{1}{2}(E_{M1}+E_{M2})$ is exactly $\frac{1}{2}S$. The corresponding function ${}_Rs(E)$ is computed, by making use of equation (13). For the interval

$$E_{M1}<E<E_{M2}, \tag{19}$$

equation (18) may be approximated by

$${}_Rs(E)\simeq\tfrac{3}{4}S+\tfrac{1}{4}S\cos\left[(2\pi/d)(E-E_{M1})\right],$$

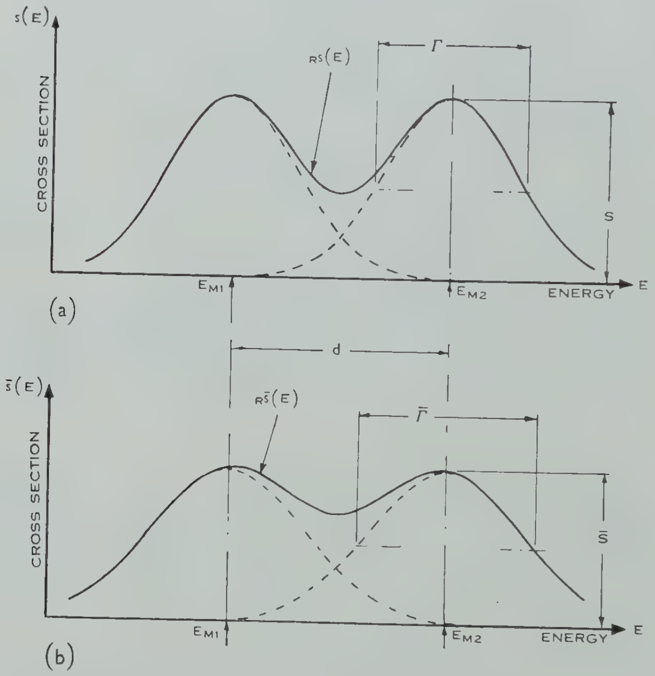

Fig. 2 (*a*).—Standard cross-section ${}_Rs(E)$. (Superposition of two Gaussian resonances.)
${}_Rs(E)=S\{\exp[-4(\ln 2)(E-E_{M1})^2/\Gamma^2]+\exp[-4(\ln 2)(E-E_{M2})^2/\Gamma^2]\}$.
Fig. 2 (*b*).—Smoothing effect due to the use of finite differences in the yield analysis on ${}_Rs(E)$ of Figure 2 (*a*). ($\Delta E_A=0\cdot83\Gamma$).
${}_R\bar{s}(E)={}_Rs(E)+(\Delta E_A^2/24)\{\mathrm{d}^2{}_Rs(E)/\mathrm{d}E^2\}$.

and with (13) the corresponding approximation for ${}_R\bar{s}(E)$ becomes

$${}_R\bar{s}(E)=\tfrac{3}{4}S+\tfrac{1}{4}S\left[1-\frac{\Delta E_A^2}{24}\,\frac{4\pi^2}{d^2}\right]\cos\left[\frac{2\pi}{d}(E-E_{M1})\right]. \tag{20}$$

In interval (19) the error due to this approximation is smaller than $0\cdot4\%$ for ${}_Rs(E)$ and smaller than $1\cdot5\%$ for ${}_R\bar{s}(E)$ for $\Delta E_A<\Gamma$. ${}_Rs(E)$ and ${}_R\bar{s}(E)$ for $\Gamma=1\cdot2\Delta E_A$ are shown on Figure 2. The dip in ${}_R\bar{s}(E)$ will disappear for $\Delta E_A>1\cdot1\Gamma$.

Suppose now from yield ordinates of a hypothetical experiment cross-section ordinates with standard errors

$$_R\bar{\bar{s}}_k \pm \mathrm{st}[_R\bar{\bar{s}}_k]\ ;\quad k=1,\ 2,\ .\ .\ .,\ p,$$

were computed, and that of the p ordinates, g ordinates

$$_R\bar{\bar{s}}_f \pm \mathrm{st}[_R\bar{\bar{s}}_f]\ ;\quad f=1,\ 2,\ .\ .\ .,\ g,$$

lie in the interval defined by (19). If $\Delta E_e = E_{f+1} - E_f$,

$$g \cdot \Delta E_e \simeq E_{M2} - E_{M1} = d. \tag{21}$$

ΔE_e need not be equal to ΔE_A, but ΔE_A has to be an integral multiple of ΔE_e. For example, E_{0k} may have values 8·00, 8·25, 8·50, 8·75, . . ., 18·00 MeV. Then one may split the corresponding yield ordinates into two groups, one at energies 8·00, 8·50, 9·00, . . ., 18·00 MeV (group I) and the second one at energies 8·25, 8·75, 9·25, . . ., 17·75 MeV (group II), and analyse group I and group II independently with $\Delta E_A = 0{\cdot}5$ MeV. (Here then $\Delta E_e = 0{\cdot}25$ MeV and $\Delta E_A = 2\Delta E_e$.)

It follows from (20) that $_R\bar{s}(E)$ has to be of the form

$$_R\bar{s}(E) = A_1 + A_2 \cos\left[(2\pi/d)(E - E_{M1})\right], \tag{22}$$

where A_1 and A_2 are constants. To reconstruct $_R\bar{s}(E)$ for the interval (19) from the set of ordinates $_R\bar{\bar{s}}_f \pm \mathrm{st}[_R\bar{\bar{s}}_f]$; $f=1,\ 2,\ .\ .\ .,\ g$, one has to fit by a Gaussian least square fit to $_R\bar{\bar{s}}_f$; $f=1,\ 2,\ .\ .\ .,\ g$, a function

$$_R\hat{\bar{\bar{s}}}(E) = \hat{A}_1 + \hat{A}_2 \cos\left[(2\pi/d)(E - E_{M1})\right]. \tag{23}$$

The fitting of a curve here is unambiguous, as the analytical form of $_R\bar{s}(E)$ is known. Then

$$\hat{A}_2 = \frac{2}{g} \sum_{f=1}^{g} {_R\bar{\bar{s}}_f} \cos\left[\frac{2\pi}{d}(E_f - E_{M1})\right],$$

and by the law of propagation of errors, the standard error $\mathrm{st}[\hat{A}_2]$ in $\hat{A}_2$ becomes

$$\mathrm{st}[\hat{A}_2] = (2/g)^{\frac{1}{2}} \mathrm{st}[_R\bar{\bar{s}}]. \tag{24}$$

In equation (24) it is assumed, for the sake of simplicity, that standard errors $\mathrm{st}[_R\bar{\bar{s}}_f]$ are approximately equal to $\mathrm{st}[_R\bar{\bar{s}}]$.

Only if $\hat{A}_2$ is positive will the dip be apparent from (23).

If

$$\gamma\, \mathrm{st}[\hat{A}_2] = A_2, \tag{25}$$

the chance that the dip is apparent from (23) is approximately 62% for $\gamma=1$, 86% for $\gamma=1{\cdot}5$, etc. With (20) and (22)

$$A_2 = \tfrac{1}{4} S\left[1 - \frac{\Delta E_A^2}{24}\, \frac{4\pi^2}{d^2}\right]. \tag{26}$$

Thus the condition that the dip is seen with a chance corresponding to γ is, with (24), (25), and (26),

$$\gamma \left(\frac{2}{g}\right)^{\frac{1}{2}} \mathrm{st}[_R\bar{\bar{s}}] = \tfrac{1}{4} S\left[1 - \frac{\Delta E_A^2}{24}\, \frac{4\pi^2}{d^2}\right]. \tag{27}$$

Reversing the argument, if $\mathrm{st}[{}_R\bar{\mathfrak{s}}]$, S, and ΔE_A are given, d of (27) is then the minimum separation of two maxima in a cross section of form (18) for which the dip is apparent with statistical significance form $\bar{\mathfrak{s}}_k \pm \mathrm{st}[\bar{\mathfrak{s}}_k]$; $k=1, 2, \ldots, p$. The resolution $r(\gamma, \Delta E_A)$ is then defined by

$$r(\gamma, \Delta E_A)=1/d. \tag{28}$$

Through (27), d and $r(\gamma, \Delta E_A)$ are given as function of γ, g, $\mathrm{st}[{}_R\bar{\mathfrak{s}}]$, and ΔE_A. From experimental data $\mathrm{st}[\bar{\mathfrak{s}}_k]=\mathrm{st}[\bar{\mathfrak{s}}]$ may be computed from (17), but is still a function of ΔE_A. It is convenient to express $\mathrm{st}[\bar{\mathfrak{s}}]$ in terms of a fixed reference value $\Delta E_{A,1}$ (e.g. $\Delta E_{A,1}=1$ MeV). Then with (17)

$$\mathrm{st}[\bar{\mathfrak{s}}]\Delta E_A^{3/2}=\mathrm{st}[\bar{\mathfrak{s}}]_1\Delta E_{A,1}^{3/2}, \tag{29}$$

where $\mathrm{st}[\bar{\mathfrak{s}}]_1$ is the standard error computed from experimental data with $\Delta E_{A,1}$. A parameter which is characteristic of the amount of information contained in a discrete set of experimental yield ordinates $\mathfrak{y}_{0k} \pm \mathrm{st}[\mathfrak{y}_{0k}]$ is then given by

$$\varepsilon_1=\gamma S^{-1}\,\mathrm{st}[\bar{\mathfrak{s}}]_1\Delta E_{A,1}^{3/2}(2\Delta E_e)^{\frac{1}{2}}. \tag{30}$$

Using (27) with (21), (28), (29), and (30) as an equation for $r(\gamma, \Delta E_A)$ in terms of ΔE_A, one obtains

$$r^2(\gamma, \Delta E_A)+\frac{24\varepsilon_1}{\pi^2\Delta E_A^{7/2}}\{r(\gamma, \Delta E_A)\}^{\frac{1}{2}}=\frac{24}{4\pi^2\Delta E_A^2}. \tag{31}$$

Equation (31) is a quartic equation in $\{r(\gamma, \Delta E_A)\}^{\frac{1}{2}}$, in which the parameter ε_1 is independent of ΔE_A. Solutions of d and $r(\gamma, \Delta E_A)$ as function of ΔE_A and ε_1 may be interpolated from Figure 3.

The resolution $r(\gamma, \Delta E_A)$ depends on the choice of ΔE_A in the following way. If ΔE_A is chosen large, the smoothing effect due to the replacement of integration by summation of finite differences (equation (2) replaces (1)) becomes large, and apparent statistical errors (equation (29)) are small. If ΔE_A is chosen small the smoothing effect becomes negligible, but apparent statistical errors become excessively large.

The condition that the resolution $r(\gamma, \Delta E_A)$ has a maximum ($r_{\mathrm{max.}}$), and d has a minimum ($d_{\mathrm{min.}}$) is

$$\frac{\partial r(\gamma, \Delta E_A)}{\partial(\Delta E_A)}=0\,; \quad \frac{\partial^2 r(\gamma, \Delta E_A)}{\partial(\Delta E_A)^2}<0.$$

From equation (31), the value $\Delta E_A=\Delta E_{\mathrm{opt.}}$, corresponding to $r_{\mathrm{max.}}$ and $d_{\mathrm{min.}}$, is given by

$$\left.\begin{aligned}\Delta E_{\mathrm{opt.}}&=2\cdot 236\varepsilon_1^{1/2},\\ r_{\mathrm{max.}}&=0\cdot 2282\varepsilon_1^{-1/2}=0\cdot 5104\Delta E_{\mathrm{opt.}}^{-1},\\ d_{\mathrm{min.}}&=1\cdot 959\Delta E_{\mathrm{opt.}}=4\cdot 472\varepsilon_1^{1/2}.\end{aligned}\right\} \tag{32}$$

If a cross section has exactly the shape of ${}_Rs(E)$ (Fig. 2), the choice of $\Delta E_A=\Delta E_{\mathrm{opt.}}$ would give maximum resolution, but, as in practice $s(E)$ may have a shape quite different from ${}_Rs(E)$, the use of $\Delta E_{\mathrm{opt.}}$ for the cross-section computation need not necessarily ascertain that the maximum amount of information contained in the set $\mathfrak{y}_{0k} \pm \mathrm{st}[\mathfrak{y}_{0k}]$ is expressed in the corresponding set $\bar{\mathfrak{s}}_k \pm \mathrm{st}[\bar{\mathfrak{s}}_k]$.

The choice of ΔE_A is limited to two or three values in any case if the tabulated values $B_{i,n}$ of Penfold and Leiss (1958) (equations (6) and (7)) are used for the yield analysis. It is recommended that cross sections be computed twice independently with the two available values ΔE_A nearest to $\Delta E_{\text{opt.}}$.

ΔE_e is inversely proportional to p, the number of yield ordinates $\mathfrak{y}_{0k}$. st$[\mathfrak{S}_k]$ is inversely proportional to the square root of the number of counts (events) taken, to measure one ordinate $\mathfrak{y}_{0k}$. Then with (30), ε_1 is inversely proportional to the total number of counts taken, to measure all ordinates $\mathfrak{y}_{0k}$, and hence with (32)

$$r_{\text{max.}}=1/d_{\text{min.}}\propto(\text{total number of counts})^{\frac{1}{4}}. \tag{32a}$$

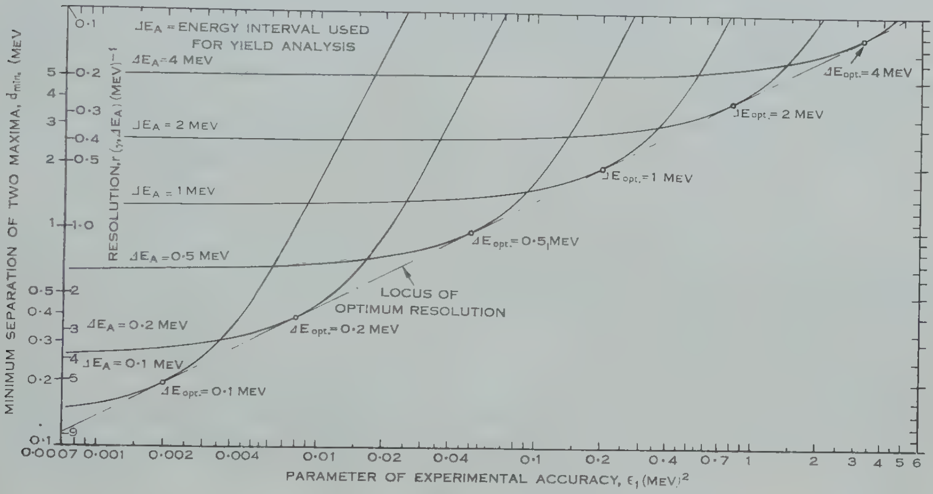

Fig. 3.—Experimental resolution of bremsstrahlung experiments $r(\gamma, \Delta E_A)$, equation (28), as function of experimental accuracy (parameter ε_1, equation (30)).

$$\varepsilon_1=\gamma\,\text{st}[\mathfrak{S}]_1\Delta E_{A,1}^{3/2}(2\Delta E_e)^{\frac{1}{2}}/S \quad (\text{MeV})^2.$$

Suppose, for example, in a bremsstrahlung experiment yield ordinates were measured at 0·25 MeV intervals ($\Delta E_e=0\cdot25$ MeV), and with $\Delta E_A=\Delta E_{\text{opt.}}=1$ MeV for the yield analysis the cross section showed evidence for two resonances, 2 MeV apart. If the experimental resolution here was [2 MeV]$^{-1}$, ($d=2$ MeV), one would have reasonable assurance that the two observed resonances are real and not due to statistical fluctuations. If in an improved experiment one wants to make certain that the resonances are real one may endeavour to double the experimental resolution. According to (32a), here the total number of counts of the improved experiment has to be 16 times that of the initial experiment. This may be achieved by again measuring yield ordinates at 0·25 MeV intervals, but increasing the number of counts taken to measure individual yield ordinates by a factor of 16. An equivalent alternative would be to measure yield ordinates at for example 0·1 MeV intervals ($\Delta E_e=0\cdot1$ MeV) and increase the number of counts of individual yield ordinates by a factor of 6·4. According to (30) and (32) the optimum value of ΔE_A to be chosen for the yield analysis would be the same in either case (here $\Delta E_A=\Delta E_{\text{opt.}}=0\cdot5$ MeV).

IV. Smoothing and Curve-fitting

When a physical interpretation is to be given to a discrete set of ordinates with their errors, one will fit subjectively a smooth curve to the set of ordinates. As a matter of fact this process may often consist merely in picturing where the smooth curve would lie without actually drawing the curve. This subjective type of interpolation is not unambiguous if proportional errors are large and the ordinates are spaced widely. The following simple procedure is then often employed. One draws " by eye " a smooth curve with minimum curvature such that the smooth curve cuts only approximately two-thirds of the error bars. This method " smooths out " statistical fluctuations, but may also smooth out a certain amount of information contained in the experimental data.

In the analysis of experimental data, " smoothing by eye " may be applied to yield ordinates, yield first-difference ordinates, integrated cross-section ordinates, or cross-section ordinates. Whichever method is used, finally a continuous " smooth " cross section $\hat{\hat{\mathfrak{s}}}(E)$ is obtained, but the statistical uncertainty in $\hat{\hat{\mathfrak{s}}}(E)$ is only known vaguely (and for this reason is usually not stated in the literature).

The fitting of a " smooth " continuous function may be done analytically, by making a Gaussian least square fit of a set of known functions to the discrete set of ordinates. The statistical uncertainty in the resulting continuous function can be computed in this case.

Suppose, for example, that a set of functions is to be fitted analytically to a discrete set of cross-section ordinates $\bar{\bar{\mathfrak{s}}}_k \pm \mathrm{st}[\bar{\bar{\mathfrak{s}}}_k]$; $k=1, 2, \ldots, p$. For the sake of simplicity it will be assumed that all standard errors are equal,* and that ${}^{r}f(E)$; $r=1, 2, \ldots$, the set of functions to be fitted, is orthonormal in the energy interval

$$E_1-\tfrac{1}{2}\Delta E_e<E<E_p+\tfrac{1}{2}\Delta E_e, \tag{33}$$

that is,

$$\sum_{k=1}^{p} {}^{r}f(E_k)\,{}^{s}f(E_k)\Delta E_e=\delta_{rs}\left.\begin{matrix}=1, & r=s\\ =0, & r\neq s\end{matrix}\right\}\text{(orthonormality condition)} \tag{34}$$

$$\sum_{r=1}^{p} {}^{r}f(E_j)\,{}^{r}f(E_k)\Delta E_e=\delta_{jk}\left.\begin{matrix}=1, & j=k\\ =0, & j\neq k\end{matrix}\right\}\text{(closure property)} \tag{35}$$

If the first q functions ${}^{r}f(E)$ are fitted by a Gaussian least square fit to the p ordinates $\bar{\bar{\mathfrak{s}}}_k$,

$${}_{q}\hat{\hat{\mathfrak{s}}}(E)=\sum_{r=1}^{q} {}^{r}\hat{a}\,{}^{r}f(E). \tag{36}$$

The constants ${}^{r}\hat{a}$, which are the same for all values q due to (34), are then found from

$${}^{r}\hat{a}=\sum_{k=1}^{p} \bar{\bar{\mathfrak{s}}}_k\,{}^{r}f(E_k)\Delta E_e, \tag{37}$$

---

* If $\mathrm{st}[\bar{\bar{\mathfrak{s}}}_k]$ varies smoothly (or approximately smoothly) with E_k, the case may be reduced to the above one, by forming the function

$$\bar{\bar{\mathfrak{z}}}_k \pm \mathrm{st}[\bar{\bar{\mathfrak{z}}}_k]=\bar{\bar{\mathfrak{s}}}_k/\mathrm{st}[\bar{\bar{\mathfrak{s}}}_k] \pm \mathrm{st}[\bar{\bar{\mathfrak{s}}}_k]/\mathrm{st}[\bar{\bar{\mathfrak{s}}}_k] ;$$

$k=1, 2, \ldots, p$, and treating $\bar{\bar{\mathfrak{z}}}_k$ as above.

and by the law of propagation of errors, the standard error $\mathrm{st}[{}^{r}\hat{a}]$ in ${}^{r}\hat{a}$ becomes, with (34) and (37),

$$\mathrm{st}[{}^{r}\hat{a}]=\mathrm{st}[\bar{\mathbf{s}}](\Delta E_{e})^{\frac{1}{2}}, \tag{38}$$

and, with (35), (36), and (38), the standard error $\mathrm{st}[{}^{q}\hat{\bar{\mathbf{s}}}]$ in each of the p ordinates ${}^{q}\hat{\bar{\mathbf{s}}}(E_{k})={}^{q}\hat{\bar{\mathbf{s}}}_{k}$ becomes

$$\mathrm{st}[{}^{q}\hat{\bar{\mathbf{s}}}]=\mathrm{st}[\bar{\mathbf{s}}](q/p)^{\frac{1}{2}}.$$

Then if $q=p$, the function ${}^{q}\hat{\bar{\mathbf{s}}}(E)={}^{p}\hat{\bar{\mathbf{s}}}(E)$ will pass exactly through ordinates $\bar{\mathbf{s}}_{k}$ and standard errors $\mathrm{st}[{}^{p}\hat{\bar{\mathbf{s}}}]$ are identical with $\mathrm{st}[\bar{\mathbf{s}}]$, the experimental standard errors. If $q<p$, ${}^{q}\hat{\bar{\mathbf{s}}}(E)$ is "smoother" than ${}^{p}\hat{\bar{\mathbf{s}}}(E)$, i.e. it contains less detail, but the standard errors in the p ordinates ${}^{q}\hat{\bar{\mathbf{s}}}_{k}$ are smaller by a factor of $(q/p)^{\frac{1}{2}}$ than the original standard error $\mathrm{st}[\bar{\mathbf{s}}]$. In the extreme case $q=1$, ${}^{1}\hat{\bar{\mathbf{s}}}(E)$ is just a straight line parallel to the E-axis, at average cross-section height, with $\mathrm{st}[{}^{1}\hat{\bar{\mathbf{s}}}]=p^{-\frac{1}{2}}\,\mathrm{st}[\bar{\mathbf{s}}]$.

One requires the highest value of q for which the fitted continuous curve ${}^{q}\hat{\bar{\mathbf{s}}}(E)$ does not show yet apparent detail which is due to statistical fluctuations, and not originally contained in $s(E)$. This value of q may be found rigorously by applying chi-square tests to sets of ${}^{q}\hat{\bar{\mathbf{s}}}_{k}$, $\mathrm{st}[{}^{q}\hat{\bar{\mathbf{s}}}_{k}]$, and $\bar{\mathbf{s}}_{k}$ for successive values of q. An adequate criterion is to ascertain that for none of the coefficients ${}^{r}\hat{a}$ used, $\mathrm{st}[{}^{r}\hat{a}]\geqslant{}^{r}\hat{a}$. A curve ${}^{q}\hat{\bar{\mathbf{s}}}(E)$ fitted analytically with the highest permissible q value ideally will extract the maximum amount of information contained in the original data, and will in general show more genuine detail than a curve fitted "by eye with minimum curvature". However, analytical curve fitting may not be used unless the permissible number of curves is sufficiently large (say greater than five), and it is ascertained that boundary conditions at the limits of interval (33) do not introduce systematic distortions. ${}^{q}\hat{\bar{\mathbf{s}}}(E)$ does not approximate $\bar{s}(E)$ but rather a function ${}^{q}\hat{\bar{s}}(E)$, which would be obtained by fitting q functions to the "exact" ordinates $\bar{s}_{k}$; $k=1, 2, \ldots, p$. For $q<p$ the function ${}^{q}\hat{\bar{s}}(E)$ will be smoother again, in general, than $\bar{s}(E)$. This smoothing effect is very similar to the smoothing introduced by using a large ΔE_{A} in the yield analysis (there $s(E)\rightarrow\bar{s}(E)$, see Fig. 2).

To indicate the statistical accuracy of a continuous function ${}^{q}\hat{\bar{\mathbf{s}}}(E)$, draw the smooth curves ${}^{q}\hat{\bar{\mathbf{s}}}(E)+\mathrm{st}[{}^{q}\hat{\bar{\mathbf{s}}}]$ and ${}^{q}\hat{\bar{\mathbf{s}}}(E)-\mathrm{st}[{}^{q}\hat{\bar{\mathbf{s}}}]$. These curves enclose what shall be defined as the "area of statistical variation" of ${}^{q}\hat{\bar{\mathbf{s}}}(E)$. The meaning of this area of statistical variation is the following.

Approximately 62% linearly independent points of ${}^{q}\hat{\bar{\mathbf{s}}}(E)$ should lie less than $\mathrm{st}[{}^{q}\hat{\bar{\mathbf{s}}}]$ above or below ${}^{q}\hat{\bar{s}}(E)$. In the energy interval (33), the number of linearly independent points of ${}^{q}\hat{\bar{\mathbf{s}}}(E)$ is q. This may be indicated, e.g. by drawing q error bars with $\mathrm{st}[{}^{q}\hat{\bar{\mathbf{s}}}]=\mathrm{st}[\bar{\mathbf{s}}](q/p)^{\frac{1}{2}}$ equidistant on ${}^{q}\hat{\bar{\mathbf{s}}}(E)$. Only such q points can vary independently within statistical limits, and all other points are linearly dependent. This means effectively that ${}_q\hat{\bar{\mathfrak{S}}}(E)$ has to remain smooth between the q points, and that ${}_q\hat{\bar{\mathfrak{S}}}(E)$ preserves the number of its maxima, minima, and turning points, as the set $\bar{\mathfrak{S}}_k$; $k=1, 2, \ldots, p$ is varied within statistical limits.

It is of interest to know which value of $(q/p)^{\frac{1}{2}}$ corresponds approximately to the amount of smoothing introduced in " smoothing by eye with minimum curvature ". It was found empirically from examples that this value is of order $\frac{1}{2}$ (see Fig. 4). It appears that the value $(q/p)^{\frac{1}{2}} \sim \frac{1}{2}$ is rather the same, whether " smoothing by eye with minimum curvature " was applied to yield ordinates or cross-section ordinates, and thus there seems to be no preference for either method. One may obtain an estimate of the statistical accuracy of earlier published cross-section data, if one estimates st$[\bar{\mathfrak{S}}_k]$ from standard errors of corresponding yield data, and draws an " approximate area of statistical variation " with $\frac{1}{2}$st$[\bar{\mathfrak{S}}_k]$ above and below the published cross-section curve.

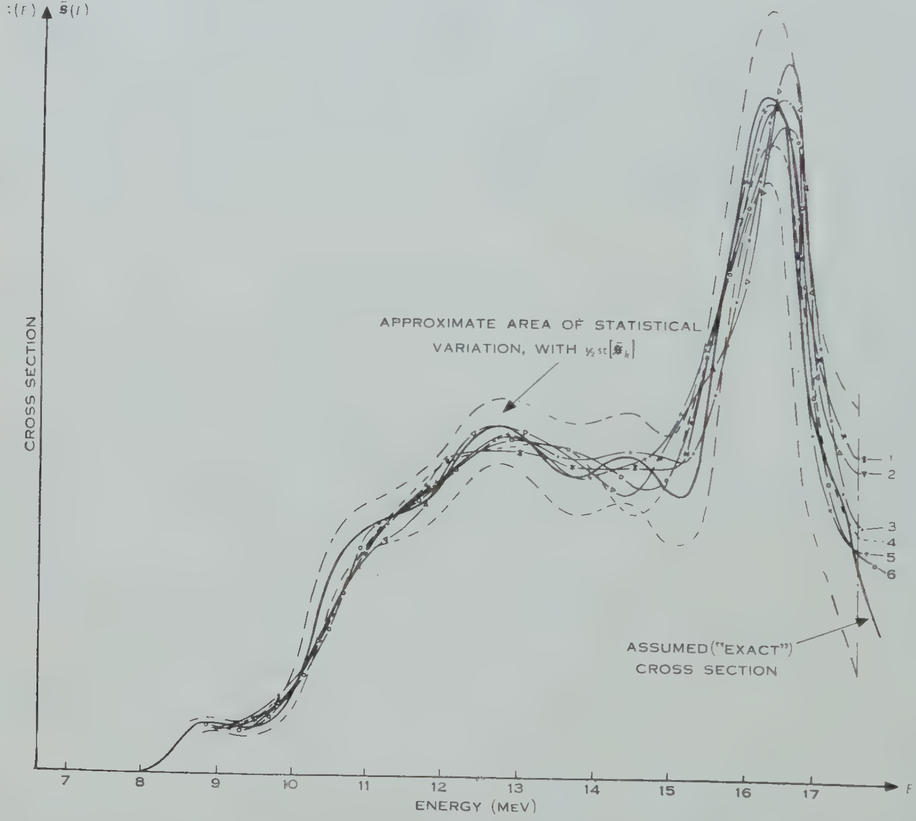

Fig. 4.—Empirical test of " smoothing by eye with minimum curvature " of yield ordinates. Six " experimental " sets of yield ordinates were produced from an assumed (" exact ") set of yield ordinates by a Monte Carlo process. Cross sections 1–6 were obtained by fitting " by eye with minimum curvature " smooth yield curves through the " experimental " yield ordinates and using for the yield analysis the Penfold-Leiss method.

V. Acknowledgments

The author wishes to thank Dr. B. M. Spicer for discussing the present investigation, and Imperial Chemical Industries of Australia and New Zealand for a research fellowship held during part of this work.

VI. References

Carver, J. H., and Lokan, K. H. (1957).—*Aust. J. Phys.* **10** : 312.

Cook, B. C. (1957).—*Phys. Rev.* **106** : 300.

Johns, A. E., Katz, L., Douglas, R. A., and Haslam, R. N. H. (1950).—*Phys. Rev.* **80** : 1062.

Katz, L., and Cameron, A. G. W. (1951).—*Canad. J. Phys.* **29** : 518.

Penfold, A. S., and Leiss, J. E. (1958).—Analysis of photo cross-sections. Physics Research Laboratory, University of Illinois, Champaign, Illinois.

Schiff, L. I. (1951).—*Phys. Rev.* **83** : 252.

ON THE EQUIVALENCE OF CURRENT LOOPS AND MAGNETIC SHELLS

By C. A. Hurst*

[*Manuscript received September 1, 1960*]

Summary

A paradox in the theory of the magnetic effects of stationary currents is discussed and is shown to arise from the neglect of a singular magnetic field which is required to complete the equivalence of magnetic shells and current loops.

I. Introduction

It appears paradoxical that whilst the force between two permanent magnets decreases when they are immersed in a medium with relative permeability greater than unity, the force between two current loops under the same circumstances increases. For the standard theory states that the magnetic effects due to a current loop are the same as those produced by a magnetic shell spanning the region bounded by the current loop. So the naive view would be that both magnets and current loops would behave similarly in a material medium. The usual explanation of this difference is to point out that the magnetic shell is only a fictitious shell, and the equivalence is only partial. For the field of a magnetic shell is conservative, and the potential single valued, whereas the field of a current loop is non-conservative and the potential multiple valued. But the precise way in which this lack of complete equivalence may be expressed mathematically, and the way in which it may lead to different consequences in the two cases, such as mentioned above, has not, to my knowledge, been shown. It appears that the proper way to distinguish between the two cases is given by an application of the mathematical theory of distributions, i.e. of the δ-function and its derivatives. For a magnetic shell correctly represents the field of the current loop *everywhere* except at the shell itself, and so, to distinguish between the two fields, a function which is zero everywhere except on a surface will be required.

As is well known, the potential at two points, close together but on opposite sides of the shell, differs by $4\pi M$, where M is the magnitude of the magnetic moment per unit area, and as the field of the shell is conservative, the potential must suffer a jump by $4\pi M$ on passing through the shell, in order to cancel this difference. This means that the magnetic field *on* the shell is highly singular, and it is just to cancel this singularity in the case of a current loop that an additional field is needed. But as a consequence the potential is continuous but not single valued.

When a current loop is fully immersed in a material medium, the additional magnetic field which distinguishes it from a magnetic shell, will produce an

---

* Department of Mathematical Physics, University of Adelaide.

additional polarization *over the surface of the shell only*, and this additional polarization will augment the equivalent magnetic moment from $\mu_0 IA$ to μIA where I is the current in the loop, and A is the area of the loop (assumed for the moment to be plane).

II. MATHEMATICAL THEORY OF THE CURRENT LOOP IN VACUO

From Maxwell's equations, we have

$$\mathbf{B} = \operatorname{curl} \mathbf{A}, \tag{1}$$

$$\nabla^2 \mathbf{A} = -\mu_0 \mathbf{I}, \tag{2}$$

where $\mathbf{I}$ is the current in a loop.

If the equation of the loop is parametrically given by

$$x = x_0(s),\ y = y_0(s),\ z = z_0(s)\ (0 \leqslant s \leqslant 1)$$

then

$$\mathbf{I}(x,y,z) = \mathbf{I} \int^1 \mathrm{d}s\, \delta(x - x_0(s))\delta(y - y_0(s))\delta(z - z_0(s)) \left(\mathbf{i}\frac{\mathrm{d}x_0}{\mathrm{d}s} + \mathbf{j}\frac{\mathrm{d}y_0}{\mathrm{d}s} + \mathbf{k}\frac{\mathrm{d}z_0}{\mathrm{d}s} \right), \tag{3}$$

and the solution of (2) is

$$\mathbf{A}(x,y,z) = \mu_0 \int\int\int \frac{\mathbf{I}(x',y',z')}{4\pi r} \mathrm{d}x' \mathrm{d}y' \mathrm{d}z' \text{ with } r = \sqrt{\{(x-x')^2 + (y-y')^2 + (z-z')^2\}}$$

$$= \frac{I\mu_0}{4\pi} \int \frac{\mathbf{t}}{r} \mathrm{d}s \text{ with } \mathbf{t} = \mathbf{i}\frac{\mathrm{d}x_0}{\mathrm{d}s} + \mathbf{j}\frac{\mathrm{d}y_0}{\mathrm{d}s} + \mathbf{k}\frac{\mathrm{d}z_0}{\mathrm{d}s}, \tag{4}$$

when (3) is substituted.

From (1), we get

$$\mathbf{H} = \frac{\mathbf{B}}{\mu_0} = \frac{I}{4\pi} \int_c (\mathbf{t} \times \nabla') \frac{1}{r} \mathrm{d}s. \tag{5}$$

A suitable generalization of Stokes' theorem gives, using tensor notation,

$$H_i = \frac{I}{4\pi} \int\int \mathrm{d}S \left(n_k \frac{\partial^2}{\partial x'_i \partial x'_k} - n_i \frac{\partial^2}{\partial x'^2_k} \right) \frac{1}{r},$$

or, in vector notation,

$$\mathbf{H} = \frac{I}{4\pi} \int\int_S \mathrm{d}S (\mathbf{n} \cdot \nabla' \nabla' - \mathbf{n} \nabla'^2) \frac{1}{r} \tag{5'}$$

$$= \mathbf{H}_m + \mathbf{H}_c.$$

The first term $\mathbf{H}_m$ is the field due to the equivalent magnetic shell, whereas the second term is a correction required to make $\mathbf{H}$ continuous through S. As $\nabla^2(1/r) = -\delta(r)/r^2$, where $\delta(r)$ is the Dirac δ-function, H_c describes a field which is zero everywhere except on S.

This is the term which is non-conservative, because

$$\int_{c'} \mathbf{H} \cdot \mathbf{t}' \mathrm{d}s = \int_{c'} \mathbf{H}_m \cdot \mathbf{t}' \mathrm{d}s + \int_{c'} \mathbf{H}_c \cdot \mathbf{t}' \mathrm{d}s' = \int_{c'} \mathbf{H}_c \cdot \mathbf{t}' \mathrm{d}s$$

for any closed circuit. If c' loops the circuit c, then

$$\int_{c'} \mathbf{H}_c \cdot \mathbf{t}' \mathrm{d}s = -\frac{I}{4\pi}\iiint_{Sc'} \mathrm{d}s\mathrm{d}S\mathbf{t}' \cdot \mathbf{n}\nabla^2\frac{1}{r} = \pm\frac{I}{4\pi}\iiint \mathrm{d}V\frac{\delta(r)}{r^2} \tag{6}$$
$$= \pm I,$$

with the sign determined by the relative sense of $\mathbf{t}'$ and $\mathbf{n}$. The "source" of such a field will be that which produces a "potential"

$$\Omega_{ik} = \frac{I}{4\pi}\iint_s \mathrm{d}Sn_i\frac{\partial}{\partial x_k'}\frac{1}{r}, \tag{7}$$

which is a tensor, and not a scalar, quantity. So the magnetic field of a current is the sum of a true magnetostatic field together with a pseudo-magnetostatic field produced by a distribution of "sources" over the surface of the shell. The combined effect of these sources will be to produce a field which is everywhere regular and non-conservative.

III. EXTENSION TO A PERMEABLE MEDIUM

When a current loop is placed in a medium, of permeability μ, a distributed magnetization is produced with a magnetic moment density given by $\mathbf{M} = \chi\mathbf{H}^R$ (in non-ferromagnetic materials), with $\mathbf{H}^R$ the resultant field in the medium. So $\mathbf{H}^R$ is determined by the integral equation

$$\mathbf{H}^R = \mathbf{H}_m + \mathbf{H}_c + \nabla\int_V \chi\mathbf{H}^R \cdot \nabla\left(\frac{1}{r}\right)\mathrm{d}V. \tag{8}$$

$\mathbf{H}^R$ is non-conservative, but the quantity $\mathbf{H}^R - \mathbf{H}_c$ satisfies the equation

$$\mathbf{H}^R - \mathbf{H}_c = \mathbf{H}_m + \nabla\int_V \chi\mathbf{H}_c \cdot \nabla\left(\frac{1}{r}\right)\mathrm{d}V + \nabla\int_V \chi(\mathbf{H}^R - \mathbf{H}_c) \cdot \nabla\left(\frac{1}{r}\right)\mathrm{d}V, \tag{8'}$$

in which no non-conservative terms appear. In fact the non-homogeneous term

$$\mathbf{H}_m + \nabla\int_V \chi\mathbf{H}_c \cdot \nabla\left(\frac{1}{r}\right)\mathrm{d}V$$

is the field due a magnetic shell of moment $\mu_0 I + \chi I = \mu I$ per unit area, i.e. the effective magnetic moment has been increased. Hence the mutual potential energy of two current loops, which *in vacuo* is proportional to $\mu_0 I_1 I_2$, becomes, in a medium of permeability μ, proportional to $\mu I_1 I_2$, which may be written as

$$(\mu I_1)(\mu I_2)/\mu = M_1 M_2/\mu, \tag{9}$$

where M_1, M_2 are the equivalent moments of the magnetic shells. So, unlike two magnetic sources, the force between the current sources in a medium increases (if $\mu > \mu_0$) because the strength of both sources increases and more than compensates the decrease in field produced by the shielding effect of the induced dipoles.

SHORT COMMUNICATIONS

THE OXIDATION OF POLYCRYSTALLINE BERYLLIUM IN CARBON DIOXIDE*

By W. J. van Peer†

The growth and structure of beryllium oxide on polycrystalline beryllium was studied, using weight gain versus time curves, electron diffraction, and X-ray diffraction.

The rates of oxidation varied widely for the different materials used and the ways in which the metal was produced.

Here the specimens were cut off from extruded bar of french flake powder, which was hot pressed and oxidized very rapidly in moist carbon dioxide at 700 °C in a furnace with a large constant temperature zone, at atmospheric pressure.

The electron diffraction camera used was an R.C.A. type E.M.C. electron microscope, converted into a diffraction camera by Dr. C. S. Lees at Harwell (1954) and modified by the author.

Working at a fixed voltage of 30 kV and a camera length of 25 cm, λL was of the order of $1 \cdot 7$Å cm. The central spot diameter varied between $0 \cdot 02$ and $0 \cdot 025$ cm.

The oxide grew with a preferred 001 orientation and an estimate of crystal sizes was made at regular intervals.

This was calculated from the ring breadths, using the formula $t \simeq \lambda L/B'$, where B' is the corrected half-breadth of the *hkl* ring and t is the effective mean thickness of the crystal in a direction normal to the *hkl* plane.

Scherrer's formula was applied for correction $B' = B - b$, where B is the observed half-breadth of the ring and b the instrumental broadening due to the diameter of the electron beam.

The ring chosen for measurement was the 100 reflection, giving an estimate of the thickness normal to the c axis.

Specimens examined before oxidation, being etched in a suitable solution to take off the work-hardened layers, showed beryllium oxide present on the surface with a crystal size of a few hundred Ångström units (Plate 1, Fig. 1).

The interplanar spacings from the patterns always corresponded to the A.S.T.M. X-ray data for crystalline hexagonal beryllium oxide.

In the electron diffraction case, however, the 002 diffraction arcs were very weak or missing. This must be due to the beryllium oxide crystals being plate shaped, with large smooth 001 faces, parallel to the beryllium substrate.

---

* Manuscript received October 11, 1960.

† Australian Atomic Energy Commission.

Diffractions such as 100 and 101 will then arise by transmission through the tips of flakes oriented with an edge projecting from the surface, while the 002 can arise only by a grazing Bragg reflection from 001 faces of flakes lying flat in the surface and will therefore suffer severe refraction and more broadening than the other diffractions. This causes the 002 diffraction to be very much diffused and weakened. It has been found by X-ray diffraction that the rod has a definite fibre texture with the orientation axis at right angles to the rod axis.

The next specimens were heated for 10 min at 700 °C in carbon dioxide at atmospheric pressure and show that a large number of very small beryllium oxide crystals appear in a mean preferred 001 orientation with a crystal size of 20–50 Å. (Plate 1, Fig. 2.)

After 1 hr at 700 °C the specimens show that beryllium oxide needles have grown, probably on dislocations with a crystal size of 100–200 Å.

After some hours the needles have grown into large beryllium oxide flakes. The rings become very spotty as Plate 1, Figure 3, shows, particularly the 100 and 110 reflections. The size of the flakes was estimated at 1000 Å.

Plate 1, Figure 4, shows a transmission pattern of a thin film of beryllium oxide taken from specimen 2.

No beryllium carbide rings appeared in the patterns, because the carbide formed on the surface readily hydrolysed to beryllium oxide in the moist carbon dioxide atmosphere. Its presence was made evident, particularly for the stronger reflections, in an X-ray diffractometer.

In the oxidation of beryllium with carbon dioxide the following thermodynamically possible reactions occur:

$$(1)\quad Be+CO_2 \rightarrow BeO+CO,$$

$$(2)\quad 2Be+CO_2 \rightarrow 2BEO+C.$$

The beryllium carbide which is formed in the oxide layer comes from the reaction

$$(3)\quad 2Be+C \rightarrow Be_2C.$$

An appreciable percentage of the deposited carbon in the specimens is present as beryllium carbide. The reaction between beryllium and graphite powders is known to start at about 600 °C.

Because of the water vapour in these experiments (2%) the beryllium carbide in the outer surface is converted into methane,

$$Be_2C+2H_2O \rightarrow 2BeO+CH_4.$$

THE OXIDATION OF POLYCRYSTALLINE BERYLLIUM IN CARBON DIOXIDE

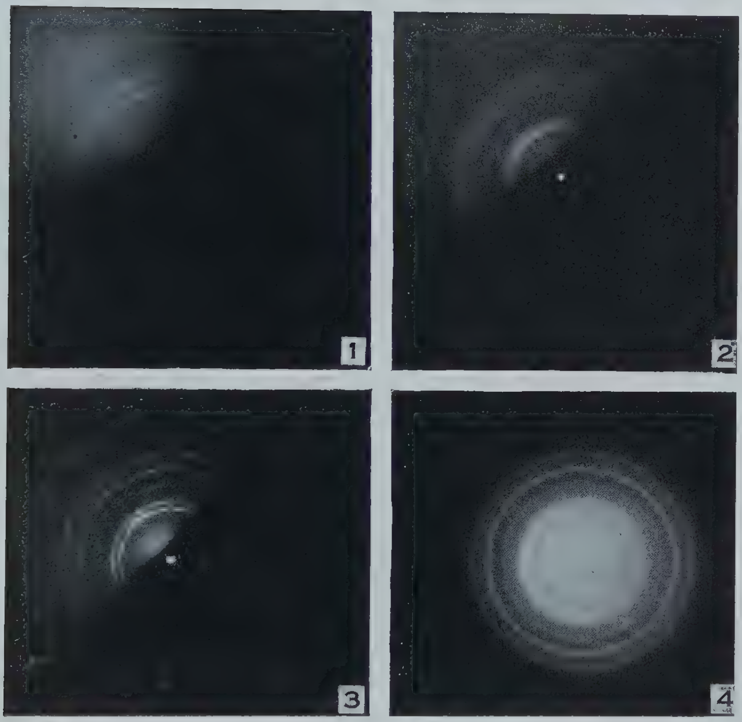

Electron diffraction patterns of beryllium oxide.

ORIENTATION OF POLAR AURORAS*

By J. V. Denholm† and F. R. Bond†

Weill (1958) has shown that the orientation of " homogeneous arc " auroras at Dumont d'Urville (see Fig. 1) exhibits definite diurnal variation, the arcs being aligned approximately on the azimuth of the Sun. Hatherton and Midwinter (1960), in considering morphology of the auroras near Scott Base and Hallett Station express the opinion that the Dumont d'Urville auroral behaviour seems unique. Observations presented below from Wilkes, Scott Base, and Hallett indicate, however, that diurnal variation of orientation, a main feature of Weill's paper, is not peculiar to the vicinity of Dumont d'Urville.

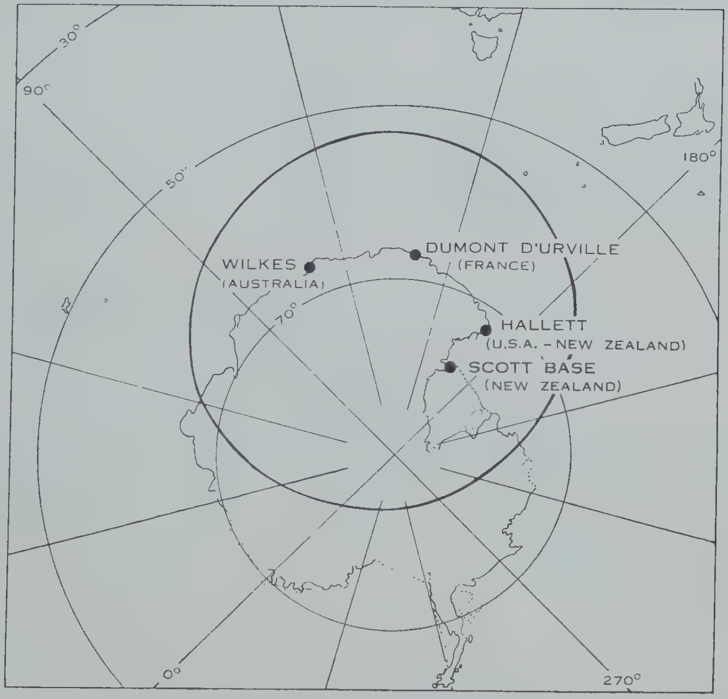

Fig. 1.—Station locations in relation to southern isoaurore of maximum frequency, after Bond and Jacka (1960).

Auroras observed from Scott Base and Hallett (using the visual observations examined by Hatherton and Midwinter), from Wilkes (using all-sky camera records obtained by the Australian National Antarctic Research Expedition in 1959), and from Dumont d'Urville (visual observations and all-sky camera records, July 1957–September 1958), have been plotted on synoptic maps, assuming the height of all auroral lower borders to be 105 km. The orientations of homogeneous arcs and simply shaped homogeneous bands near these stations have been examined, measurement being restricted to auroras within 3° of each station. Orientation was measured as the angle from geographic north to the tangent to the plan position of the aurora, clockwise being taken as positive.

---

* Manuscript received November 18, 1960.

† Antarctic Division, Department of External Affairs, Melbourne.

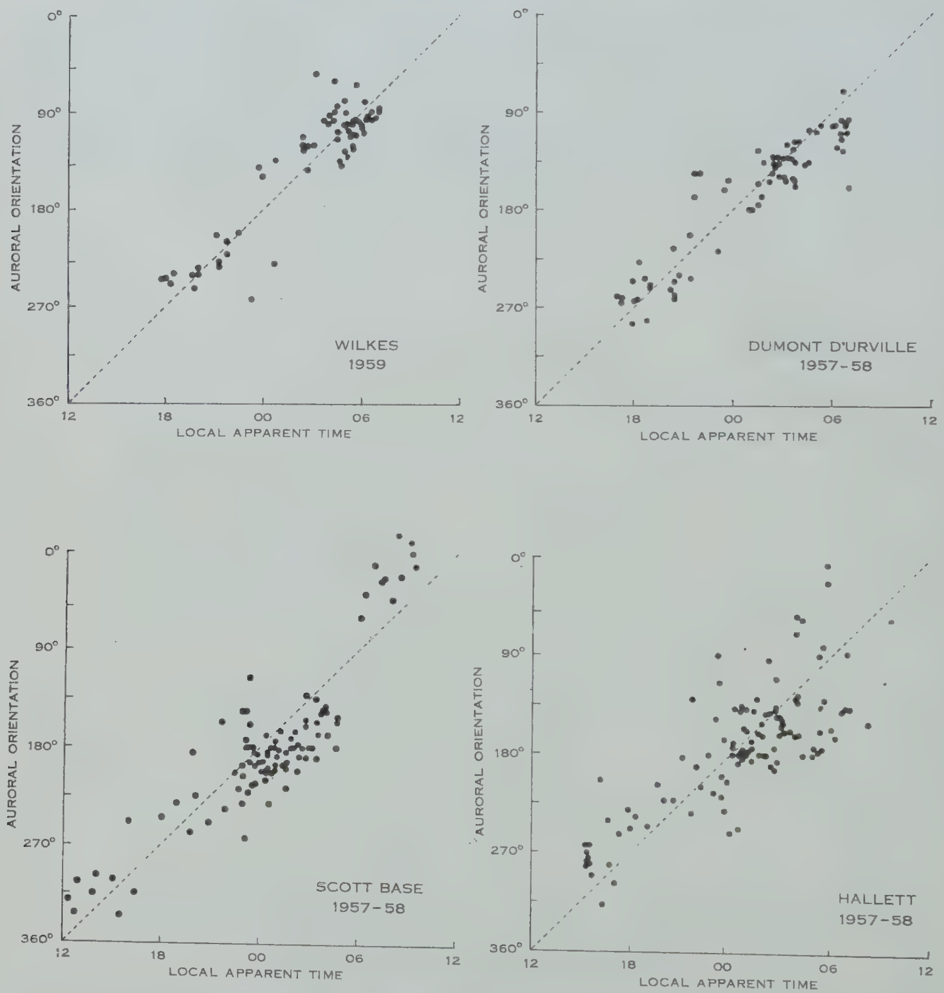

Fig. 2.—Auroral orientation versus local apparent time. Dotted lines represent annual mean azimuth of the Sun.

In Figure 2 orientations are plotted against local apparent time at the meridian at which orientation was measured. The plots from the other stations indicate a diurnal variation in orientation similar to that near Dumont d'Urville.

Wilkes, Dumont d'Urville, Hallett, and Scott Base are all well on the polewards side of the isoaurore of maximum frequency (Bond and Jacka 1960) reproduced in Figure 1. The data of Figure 2 suggest that rotation with the

Sun may be a general morphological feature of (homogeneous) auroras within the central polar region. This conclusion is supported also by Davis (1960) from a study of auroras over Resolute Bay, within the northern polar cap. (It is noted, however, that all auroras over Resolute Bay were rayed forms.)

Cole (1960) has suggested that auroral forms lie along the lines of flow of the geomagnetic disturbance current system. Davis's (1960) studies on and within the northern auroral zone strongly support Cole's suggestion.

Assuming a total current system of general form similar to that of the S_D current system derived from magnetic storm data by Vestine *et al.* (1947), with its intense electrojets along the maximum frequency isoaurore of Bond and Jacka, and with its lines of transpolar current flow approximately in the Sun-Earth direction (as in Chapman's (1956) idealized system), then the positions of Wilkes, Dumont d'Urville, Scott Base, and Hallett relative to the current system are such that the observed diurnal rotation is that to be expected from Cole's suggestion.

The writers are grateful to Geophysics Division, D.S.I.R., New Zealand, for permission to make use of data from the Hallett and Scott Base auroral logs and to G. Weill for permission to extract data from synoptic maps prepared by him from data of Dumont d'Urville. The all-sky camera at Wilkes is the property of the U.S. Air Force Cambridge Research Centre.

References

BOND, F. R., and JACKA, F. (1960).—*Aust. J. Phys.* **13**: 610.
CHAPMAN, S. (1956).—"Vistas in Astronomy." Vol. 2. p. 912. (Pergamon Press: London.)
COLE, K. D. (1960).—*Aust. J. Phys.* **13**: 484.
DAVIS, T. N. (1960).—*J. Geophys. Res.* **65**: 3497.
HATHERTON, T., and MIDWINTER, G. G. (1960).—*J. Geophys. Res.* **65**: 1401.
VESTINE, E. H., LANGE, I., LAPORTE, L., and SCOTT, W. E. (1947).—The geomagnetic field, its description and analysis. Carnegie Institute of Washington Publication No. 580.
WEILL, G. (1958).—*C.R. Acad. Sci., Paris* **246**: 2925.

ENERGY LEVELS IN ^{13}N†‡

By V. R. McKenna,§ A. M. Baxter,§ and G. G. Shute§

The latest tabulation of energy levels in ^{13}N (Ajzenberg-Selove and Lauritsen 1959) shows that there is a region from 8·08 to 22·7 MeV which previously has been inaccessible to thorough investigation. Since the mirror nucleus, ^{13}C, has been thoroughly investigated and shows a well-defined level scheme in this region, it was decided to make a search for similar levels of the ^{13}N nucleus in the excitation range 6·5–12·5 MeV in this laboratory by means of elastic scattering of protons from ^{12}C.

Protons with energies continuously variable from 5 to 11·5 MeV were available from the University of Melbourne Variable Energy Cyclotron (Caro, Martin, and Rouse 1955), the energy being determined by a 60° magnetic analyser which was nuclear-resonance controlled. Accurate energy calibration of this analyser at the high end of its range has not yet been completed, but its stability and resolution are known to be better than 0·1%.

After magnetic analysis the proton beam entered a large scattering chamber (16 in. radius), and was scattered from a thin (1 mg cm^{-2}) polythene target. Scattered protons were detected at angles between 10° and 170° by a rotatable scintillation counter using a thin CsI(Tl) crystal scintillator, the output pulses being fed into a 100-channel analyser. Unscattered beam was collected in a Faraday cup and measured by a vibrating reed type current integrator.

Angular distributions were taken at 100 keV steps throughout the machine energy range, at approximately 5° intervals from 25° to 170°. The absolute values of differential cross section thus obtained have been compared with data of other experimenters at machine energies of 5 MeV (Reich, Phillips, and Russell 1956), 7 MeV (Schneider 1956), 9·5 MeV (Greenlees, Kuo, and Petravic 1957), and 10 MeV (Fischer 1954). Agreement better than 5% is obtained at 5 and 7 MeV both as to absolute cross section and angular distribution. At the higher energies, while quite good agreement is obtained as to the absolute cross section values, the angular distributions differ somewhat at back angles from the curves published at 9·5 MeV (Greenlees, Kuo, and Petravic 1957) and 10 MeV (Fischer 1954). This is probably due to the critical dependence of cross section upon energy at back angles, which we have found to occur in the neighbourhood of the newly discovered resonances at these energies. Typical angular distributions over the energy range are shown in Figure 1. Figure 1 (*a*) shows a typical distribution at

---

† Supported in part by a grant from the Australian Atomic Energy Commission.

‡ Manuscript received December 2, 1960.

§ Physics Department, University of Melbourne.

5 MeV, which is in excellent agreement with the Houston results; Figure 1 (*b*) shows a distribution at 7·3 MeV just above the region of overlap with the Zürich experiment. Figure 1 (*c*) shows the rapid variation of cross section at backward angles as the 9·2 MeV resonance region is crossed, while Figure 1 (*d*) shows the typical angular distribution obtained above 11 MeV. A further check has been made by use of the hydrogen-proton scattering from the hydrogen content of the polythene target. Values of cross section obtained by this means agree with the published values from 5 to 7 MeV and at 10 MeV (Jarmie and Seagrave 1956) to better than 10%. The overall estimate of accuracy of the absolute cross section for ^{12}C(pp) is about ±7%, the main sources of uncertainty being

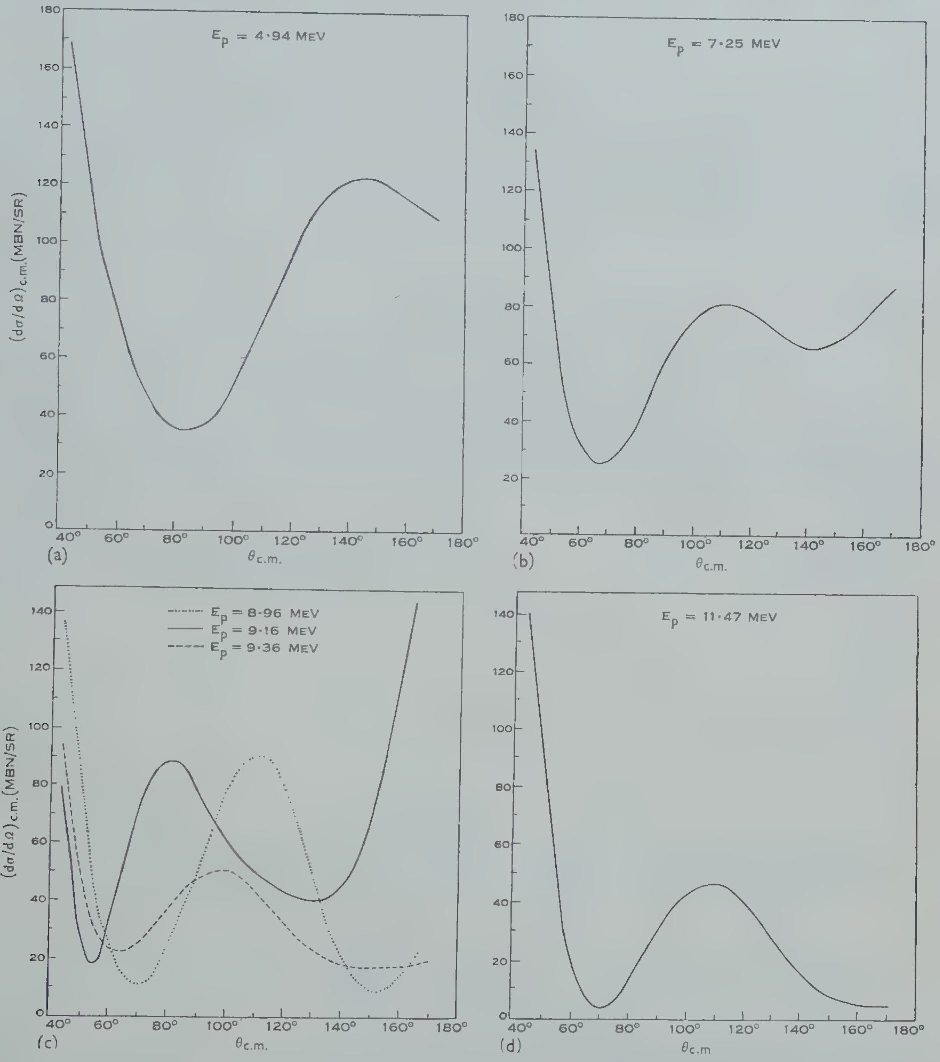

Fig. 1.—^{12}C(pp)^{12}C centre of mass differential cross sections *v.* centre of mass angle at bombarding energies near 5·0, 7·3, 9·2, and 11·5 MeV.

(*a*) target thickness variation over the area of bombardment, (*b*) possible inefficient collection of charge by the Faraday cup.

The spectrum display on the 100-channel analyser enables not only the elastic scattering peak but also the inelastic scattering to the 4·43 MeV level in ^{12}C to be measured, as well as, at forward angles, the H(*pp*)H scattering referred to above. The inelastic scattering data thus obtained are at present being processed and will be used to supplement the elastic scattering data in the analysis of the level properties in the resonance regions.

Energy distributions at the angles shown in Figure 2 show resonance structure at bombarding energies 5·4, 5·9, 6·65, 7·6, 8·2, 9·2, and 10·5 MeV. The first three of these correspond to levels previously reported (Reich, Phillips, and Russell 1956) and (Schneider 1956), whereas the remainder are previously unreported.

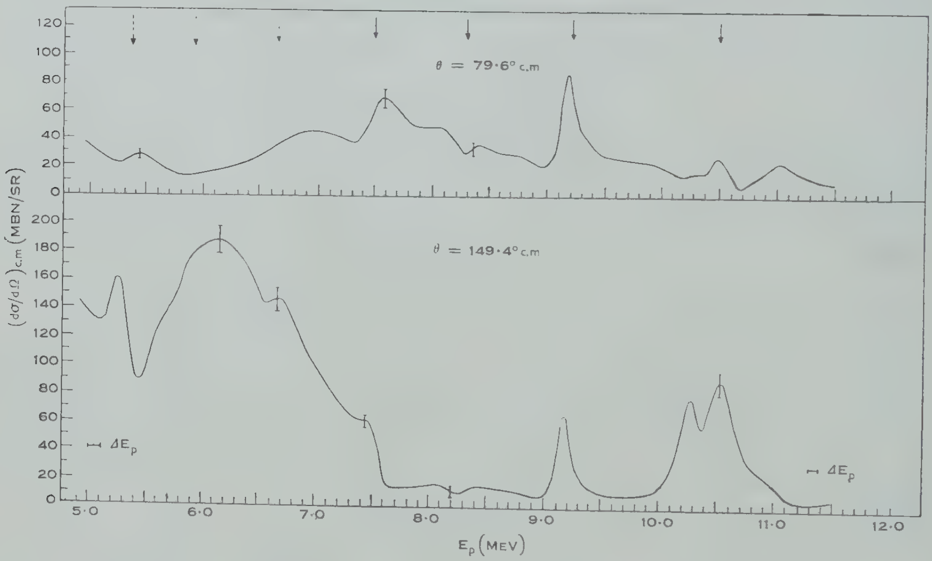

Fig. 2.—The ^{12}C(*pp*)^{12}C centre of mass differential cross section *v*. bombarding energy at two representative angles. Typical error bars for energy resolution and cross section are shown. Positions of known resonances in ^{13}N are indicated by dotted arrows; solid arrows indicate previously unreported resonances.

At present a Legendre polynomial least squares smoothing is being applied to the primary data in the region 5–7 MeV prior to a conventional phase shift analysis using 5 phases (Critchfield and Dodder 1949). However, at higher energies the (*pp*′) cross section starts to rise rapidly, becoming comparable to the elastic cross section at 9 MeV. In this region, therefore, the above-mentioned scattering theory will have to be modified to include the partial width of the competing inelastic process (Blatt and Biedenharn 1952).

The intention of this short communication is to announce the previously unreported levels in ^{13}N near the excitation energies 8·9, 9·5, 10·4, and 11·6 MeV, (the ^{12}C+*p* reaction leading to an excitation of 1·941 MeV in ^{13}N). Full analysis will be necessary to determine the exact energies of these resonances.

Note added in Proof

Brief reports of scattering experiments by A. B. Whitehead at Harwell and Y. Nagahara at Tokyo (Kingston Conference on Nuclear Structure), and by F. L. Bordell *et al.* at Florida (Illinois Meeting, *Bull. Amer. Phys. Soc.* 5), have been sighted since this communication was prepared, and confirm the above results.

The authors would like to acknowledge the most valuable assistance of Dr. D. E. Caro, Dr. J. L. Rouse, and other members of the Cyclotron team who assisted in the tedious running associated with the taking of the more than 80 angular distributions which were needed. Dr. Caro was responsible for the design of the beam current integrator used during the experiment. The authors would like to thank also Mrs. B. C. de Ladizesky for the plotting of some of the preliminary data.

REFERENCES

AJZENBERG-SELOVE, F., and LAURITSEN, T. (1959).—*Nuclear Phys.* **11** : 1.

BLATT, J. M., and BIEDENHARN, L. C. (1952).—*Rev. Mod. Phys.* **24** : 258.

CARO, D. E., MARTIN, L. H., and ROUSE, J. L. (1955).—*Aust. J. Phys.* **8** : 306.

CRITCHFIELD, C. L., and DODDER, D. C. (1949).—*Phys. Rev.* **76** : 602.

FISCHER, G. E. (1954).—*Phys. Rev.* **96** : 704.

GREENLEES, G. W., KUO, L. G., and PETRAVIC, M. (1957).—*Proc. Roy. Soc.* A **243** : 206.

JARMIE, N., and SEAGRAVE, J. D. (1956).—Charged particle cross sections. Los Alamos Report LA 2014.

REICH, C. W., PHILLIPS, G. C., and RUSSELL, J. L., JR. (1956).—*Phys. Rev.* **104** : 143.

SCHNEIDER, H. (1956).—*Helv. Phys. Acta* **29** : 55.

AUSTRALASIAN MEDICAL PUBLISHING CO. LTD.
SEAMER AND ARUNDEL STS., GLEBE, SYDNEY

A $\frac{1}{8}$ Å BIREFRINGENT FILTER FOR SOLAR RESEARCH

By W. H. Steel,* R. N. Smartt,* and R. G. Giovanelli*

[*Manuscript received December* 29, 1960]

Summary

A description is given of a wide-field birefringent filter having a bandwidth of $\frac{1}{8}$ Å at half-intensity, centred on Hα and tunable over ±16 Å. Constructional details are included.

I. Introduction

Monochromatic photographs of the Sun are complementary to spectra, in that the latter provide detailed information about physical conditions and their depth variations at highly localized positions on the Sun, while the former provide information on variations across the surface. Birefringent filters of the type developed by Öhman (1938) and Lyot (1944) have been widely used in monochromatic photography of the chromosphere (e.g. flare patrols), prominences, and the corona, being preferred to spectroheliographs for many purposes on the counts of cost, compactness, speed, and convenience. In no case, however, has the spectral resolution approached that of the large spectrographs, the narrowest bandwidth used hitherto being 0·5 Å at half-intensity.

In view of the advantages of filters for studying extended regions on the Sun, we have designed and constructed (with the assistance of many colleagues) a birefringent filter having a bandwidth of $\frac{1}{8}$ Å at half-intensity. Operating at 40 °C, it is centred on Hα and is tunable over a total spectral range of ±16 Å. It has a nominal total field angle of $2\frac{1}{4}°$ and a circular aperture of 35 mm. The particular bandwidth has been chosen so as to be small compared with that of the Sun's Hα line (rather more than 1 Å), and therefore suitable for a detailed study of chromospheric structure; but it is also comparable to the widths of normal Fraunhofer lines, one of which, the Fe line at 6569·2 Å with a central intensity of 0·48 (Allen 1934), falls conveniently within the tuning range. With the sizes of calcite crystal at present available, it seems unlikely that a much narrower bandwidth could be achieved in a birefringent filter of this type.

The design is described below, together with an account of the construction, which, we hope, will enable many of the difficulties to be avoided in other equivalent filters.

II. Design

The optical design is shown in Figure 1. It is a development from Lyot's original design and incorporates refinements due to Evans (1949). The detailed calculations of the filter characteristics have been computed by a method analogous to that of Jones (1941) and are described by Steel (1961).

---

* Division of Physics, C.S.I.R.O., University Grounds, Chippendale, N.S.W.

It may be recalled that, in its simplest form, the birefringent filter consists of a series of elements, each composed of a retardation plate of birefringent crystal (usually quartz or calcite) with axes parallel to the faces and lying between polarizers whose axes bisect those of the retardation plate (Fig. 2 (*a*)). The transmittance of the element is a sinusoidal function of wavelength, i.e. a channel spectrum. In each successive element, the spacing between spectral maxima is halved, the filter as a whole transmitting a set of narrow lines (principal maxima) whose widths are determined by the thickest elements and spacings by the thinnest.

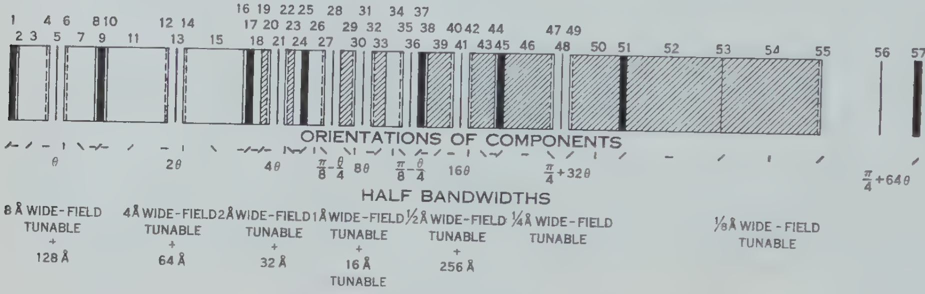

Fig. 1.—Optical design of $\frac{1}{8}$ Å filter. Scale drawing of the layout of the various optical components. For ready identification, calcite components are hatched and polarizers are drawn in black ; half- and quarter-wave plates are shown schematically, and windows before component 1 and after component 55 are omitted. Axis orientation in the surface is shown under each component, together with the relative orientations of the $\frac{1}{2}\lambda$ tuning plates. Details are as follows : 1, 9, 17, 25, 37, 45, 51, 57 : " Polaroid " polarizers, axes diagonal ; 4, 6, 12, 14, 20, 22, 30, 32, 40, 42 : compound quartz $\frac{1}{4}\lambda$ plates, axes parallel to edge ; 27, 35, 47, 49, 55 : compound quartz $\frac{1}{4}\lambda$ plates, axes diagonal ; 5, 13, 21, 28, 31, 36, 41, 48 : compound quartz $\frac{1}{2}\lambda$ plates, directions of axes immaterial ; 53 : compound quartz $\frac{1}{2}\lambda$ plate, axes diagonal ; 56 : mica $\frac{1}{2}\lambda$ plate, axis direction immaterial, mounted in cover glasses with 5′ angle between outer faces.

Tolerances on $\frac{1}{2}\lambda$ and $\frac{1}{4}\lambda$ plates : retardation $\pm 0\cdot 02\lambda$, axis direction $\pm 0\cdot 5°$.

Component	Material	Optic Axis* Orientation to Side	Axes to lie in Surface to within	Approx. Thickness (mm)	Retardation at Hα (λ)
2, 8	quartz	0°	1°	0·9	12¼
3, 7	quartz	45°	0·25°	14·0	192
10, 16	quartz	0°	0·5°	1·8	24½
11, 15	quartz	45°	0·1°	28·0	384
18, 24	quartz	0°	0·25°	3·5	48¼
26, 34	quartz	0°	0·05°	7·0	96
38, 44	quartz	0°	1°	0·45	6¼
19, 23	calcite	45°	0·05°	2·9	743
29	calcite	45°	0·025°	5·8	1 486¼
33	calcite	45°	0·025°	5·8	1 486
39, 43	calcite	45°	0·01°	11·6	2 972
46, 50	calcite	0°	0·005°	23·2	5 944
52, 54	calcite	0°	0·005°	46·4	11 888

* Tolerance on optic axis orientation : 0·5°.

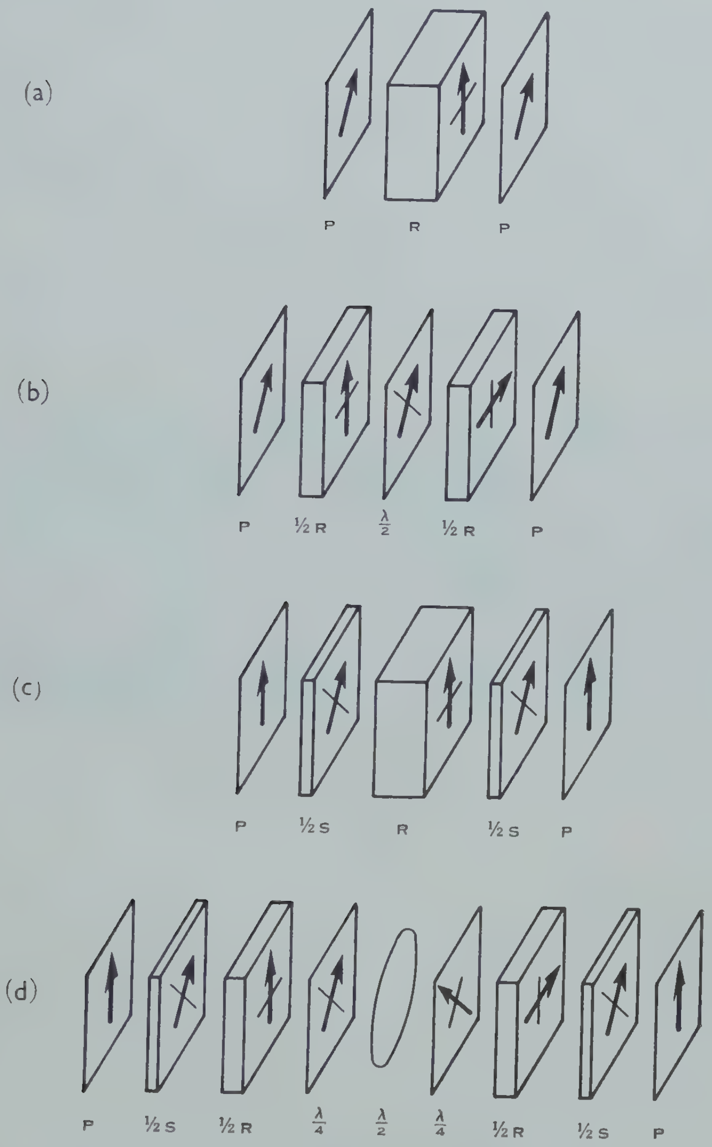

Fig. 2.—Basic types of birefringent filter element. (*a*) The simple element, with a retardation plate *R* between polarizers *P*. (*b*) Lyot's type I wide-field element. The retardation plate is split into halves, with axes crossed, and separated by a $\frac{1}{2}\lambda$ plate. (*c*) Evans's scheme of split elements. One retardation plate *R* lies between the halves of another retardation plate *S*. (*d*) Evans's scheme of split elements with tuning on the inner element. The inner retardation plate of (*c*) is split and separated by a pair of $\frac{1}{4}\lambda$ plates, between which lies a rotatable $\frac{1}{2}\lambda$ plate; retardation plate *R*, but not *S*, is tunable and of the wide-field form.

Axis orientations are shown by the arrows.

At a fixed temperature and wavelength, a simple element has transmittance $\cos^2 \varkappa\pi$, where $\varkappa$ is the retardation in wavelengths. The variation in $\varkappa$ with angle to the normal limits the angular field. If this variation is not to exceed 0·1, then for quartz and calcite retardation plates the semi-fields are both very nearly $40\varkappa^{-\frac{1}{2}}$ degrees; this amounts to about $\frac{1}{4}°$ for a $\frac{1}{8}$ Å simple element. Lyot described several methods of increasing the field; in his type I wide-field form, a retardation plate is split into two equal parts, with axes crossed, and separated by a $\frac{1}{2}\lambda$ plate with axes at 45° (Fig. 2 (*b*)). For quartz and calcite plates, the field is then increased by factors of 18·6 and 4·4 respectively.

Evans's scheme of split elements, used extensively in the $\frac{1}{8}$ Å filter, enables one retardation plate to be placed between the two halves of another, with polarizers outside the combination (Fig. 2 (*c*)). The total number of polarizers is then nearly halved, considerably reducing absorption losses if sheet polarizers are used. The inner plate and the outer half-plates can themselves be made in Lyot's type I wide-field form.

Elements may also incorporate "tuning systems", as described by Lyot and Evans. We have used a system consisting of two $\frac{1}{4}\lambda$ plates with axes crossed and separated by a $\frac{1}{2}\lambda$ plate whose rotation through an angle ψ changes the retardation of the element by $2\psi/\pi$ wavelengths. This system can replace the $\frac{1}{2}\lambda$ plate in a wide-field element (Fig. 2 (*d*)); or can follow a single plate, in which case the second $\frac{1}{4}\lambda$ plate may be omitted if it is followed immediately by a polarizer.

The filter (Fig. 1) contains basically 12 elements, the five pairs of split plates of highest retardation being of calcite, the remainder of quartz. The semi-field is limited to 1·13° by the thickest calcite element; all calcite elements and the two thickest quartz elements are of the wide-field type, the semi-field of the next thickest quartz element, 2·86°, having negligible influence on the field of the filter as a whole. Each of the five sections lying between consecutive polarizers starting from the left-hand side of Figure 1 is of Evans's split element type, and contains two elements, the central one being wide-field and tunable. The fourth section is modified so that the outer element is also tunable (but not wide-field). The last two sections of the filter contain single wide-field tunable elements.

Wavelength variations are achieved by rotating the various $\frac{1}{2}\lambda$ plates in the ratios shown. The whole filter assembly is immersed in oil at a temperature of 40 ± 0·01 °C.

The optical tolerances require strict attention. For wavelength uniformity across the filter aperture, a high degree of parallelism is needed in every plate; we have attempted to keep the retardation uniform to within 0·02λ. Similar tolerances apply to the retardations of untuned plates; these are all outer components of split elements, and the tolerances apply for each half separately as well as to the combination. Giovanelli and Jefferies (1954) have shown that errors of 0·5° in the alignment of crystal and polarizer axes about the filter axis are negligible; in practice, these errors can be reduced to nearer 0·1°. More stringent tolerances apply to the alignment of the crystal optic axis in the surfaces of wide-field elements, errors causing great asymmetry in the field; nominal tolerances are listed in Figure 1.

III. OPTICAL CONSTRUCTION

While quartz of fairly good homogeneity is available, high quality calcite in the sizes required is virtually unobtainable; and it has been a major task to make use of imperfect material.

The starting point has been to examine the optical homogeneity of the quartz and calcite interferometrically, the slabs being plane parallel, with the optic axes lying approximately in the surfaces. The thinner quartz plates have been selected from almost perfect material, but almost all the calcite, and to a lesser extent the thicker quartz slabs, though highly transparent and superficially of good appearance, showed serious optical defects of one form or another (Fig. 3). The calcite defects appear mainly in the extraordinary ray, the waveform for the ordinary ray being much the superior in all cases.

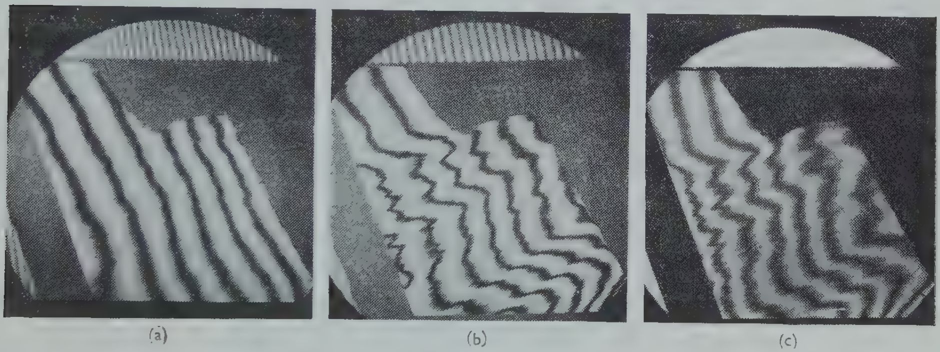

Fig. 3.—Optical quality of one of the calcite crystals with plane parallel faces. (*a*) Interference fringes, ordinary ray. (*b*) Interference fringes, extraordinary ray. (*c*) Birefringent fringes (see text).

After selection, the plates are polished flat* and parallel, slightly oversize, the optic axis being aligned in the surface by trial and error. The test for the latter is the centering of the isochromatic fringe system, checked by rotating the crystal in the plane of its surface; with sufficient care, the required accuracy can be obtained. With poor material, some prior figuring may be required, as described below, to obtain uniform retardation across the surface.

The optical inhomogeneities can be corrected only by first figuring to achieve uniform retardation; this results in equal distortions of both ordinary and extraordinary rays. These distortions are then corrected together, as described later. To test for uniformity of retardation, the plate is placed between polarizers and examined in collimated light. A Twyman interferometer was converted for the purpose by covering the comparison mirror (Fig. 4) and inserting a polarizer before the entrance pupil and one near the eye, both with axes at 45° to those of the plate under test. Fringes of equal retardation are then obtained (Fig. 3 (*c*)). This system has an advantage that light passes twice through the plate, thus doubling the sensitivity. The crystal is then figured to a uniform appearance. It is helpful at times to place a thin quartz wedge before the plate to provide, say, 5 fringes across the field, any deformations being due to the plate. As light source, a cadmium lamp with red filter has been used, giving a sharp line close to Hα; laboratory Hα sources yield lines too broad for satisfactory contrast on thick calcite plates. Figure 5 shows two of the components after figuring.

---

* A method of polishing blemish-free high quality optical surfaces on calcite is described by Smartt (1961).

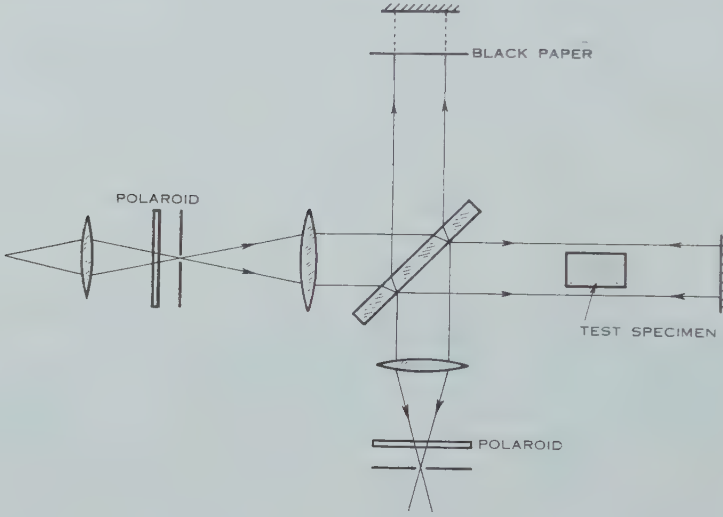

Fig. 4.—Twyman interferometer modified for viewing birefringent fringes. Polarizers are inserted before the entrance pupil and near the eye, with axes at 45° to those of the test specimen. The comparison mirror is covered with black paper.

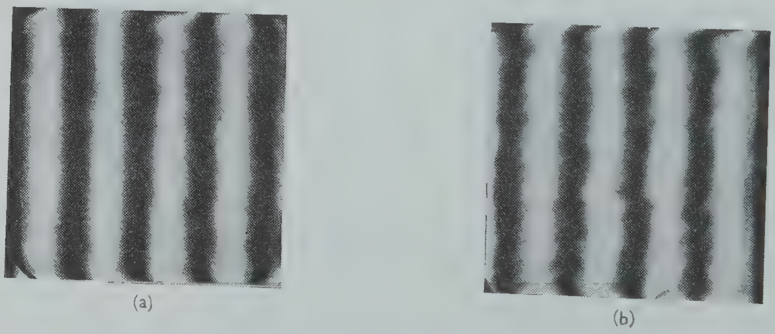
(a)
(b)

Fig. 5.—Birefringent fringes (double transmission) of each of the two thickest (46 mm) calcite components. A thin supplementary quartz wedge provides several fringes across the surface. The right-hand component is the worst in the whole filter.

In general, unfigured calcite showing a deformation of not more than one-half a birefringent fringe on double transmission, as described above, has proven to be quite satisfactory material, all but one of the 10 calcite components being of this quality or better. The remaining calcite component, one of the two thickest, showed a deformation of nearly two birefringent fringes; exceedingly difficult to figure, its residual errors dominate the wavelength non-uniformity of the filter as a whole.

Adjustment of thickness has been by polishing on the unfigured face. The thinnest elements were made to thicknesses computed from available refractive index data; this subsequently proved a cause of strong secondary spectral maxima, owing to imperfect birefringence data, though measurements by Smartt and Steel (1959) have now provided more accurate values. Elements of intermediate retardation were checked at 40 °C by visual spectroscopic intercomparison of the channel spectra. For the highest retardations, inadequate spectral resolution was available, and checking was made at 40 °C with a Babinet compensator. The latter has special advantages where components are made in pairs, as here; for when crossed their retardations should cancel, giving a central black fringe with collimated white light, while separately they should cancel the sum of the two thinner components. This technique is also valuable in the transition from the quartz to the calcite retardation plates; because of their differing dispersions, matching can be achieved only in a restricted spectral range, but the relevant " white light " fringe can still be identified using a suitable red filter. The accumulation of errors from plate to plate can be eliminated by ensuring an integral number of wavelengths retardation with an Hα source. The Babinet compensator is undoubtedly the simplest and best of the test instruments for adjusting retardation plates of all thicknesses.

The $\frac{1}{4}\lambda$ and $\frac{1}{2}\lambda$ plates were originally intended to be of mica, but we had great difficulty in splitting mica in parallel sheets without scratching. At one stage it was proposed to cement the mica plates between cover glasses using a mixture of Aroclor 4465 and Canada balsam, of refractive index intermediate to those of mica, to reduce scattered light; but this cement showed a tendency to become cloudy owing to crystallization. An alternative plan had been to immerse the filter as a whole in a fluid of this index. This scheme met with difficulty in the selection of immersion liquids which would attack neither the laminated polarizers nor the sealing gaskets. Mica plates were finally abandoned and replaced by pairs of quartz plates, differing in retardation by either $\frac{1}{4}\lambda$ or $\frac{1}{2}\lambda$ and mounted in opposition. These have the advantages of freedom from scratches, better transparency than mica, and, in the outer 3 mm, better optical performance than a cemented plate, which usually shows marked variations in optical path near the edge. The problem of producing scratch-free mica plates was ultimately solved, nevertheless, and will be described elsewhere by Smartt and Mugridge.

The transparency of the filter depends almost solely on that of the Polaroid polarizers used in it. Very high transparency Polaroid does not polarize completely, though Giovanelli and Jefferies (1954) showed that under some conditions advantage could even be taken of this to reduce parasitic light; it has been impossible to obtain Polaroid having such optimum properties near Hα and remaining satisfactory at longer wavelengths. We have used unlaminated Polaroid K sheet selected by Dr. Schurcliff of The Polaroid Corporation, with a transmittance of 0·89 at Hα for plane polarized incident light (neglecting surface reflections). The immersion fluid (Dow Corning silicone oil 702) has been chosen so that its refractive index (1·512) matches that of the Polaroid (1·50) fairly closely, thus eliminating optical defects due to surface ripples.

The final stage in optical construction is the correction for wave-front distortions introduced in figuring the retardation plates. We have already mentioned that the ordinary ray is scarcely affected by crystal inhomogeneities so that, in principle, the wave-front could be restored by the use of a liquid or cement matching the refractive index of the ordinary ray. No satisfactory liquids or cements of this high index have been found, though wave-front distortions are reduced considerably on immersion even in the lower index silicone oil. Three glass plates, refractive index 1·65, have been distributed through the filter, figured to correct for residual defects in neighbouring components.

IV. Assembly

The optical components are mounted in a cell, temperature controlled to $40 \pm 0 \cdot 01$ °C, containing suitable gearing for rotating the various $\frac{1}{2}\lambda$ plates for varying the wavelength. The four thickest calcite elements are tuned from the one shaft, the remaining tuned elements from another, and the two shafts can be rotated independently or together to give rapid or fine variation of wavelength over a range of 16 Å on either side of Hα.

The assembly has been monitored in detail by examining the spectrum of the light transmitted by the separate elements ; this has enabled the adjustments of the rotatable $\frac{1}{2}\lambda$ plates to be optimized individually. The ability to do this has an important bearing on the accuracy of retardation required for the quartz and calcite plates, for the transmittance of any tunable element can be maximized on Hα. Even so, it is necessary to control the element thickness to some extent, for parasitic light can otherwise become serious. A tolerance of $\pm\frac{1}{4}\lambda$ on the sum of the retardations of the two halves of each tunable element is adequate, ensuring a displacement of no more than $0 \cdot 02\lambda$ in the retardation at the next primary maxima ; for various reasons, manufacturing tolerances were kept much below this value. In practice, the major source of parasitic light has originated from small errors in the retardations of the thin untuned elements.

The large number of re-entrant parts in the filter cell has necessitated considerable care in the elimination of air bubbles, and deep channels have been needed in the cell to allow for ready penetration of the oil and escape of air. Provision has been made for thermal expansion of the oil by attaching a flexible Nylex tube, sealed at one end, to an outlet in the cell wall. Neoprene has been chosen, after considerable testing, as the most suitable material for the various seals around the end windows and control shafts.

V. Performance

Interferometer tests on the transmitted wave-front with an incident plane wave show deformations of a somewhat irregular nature amounting to nearly $\frac{1}{2}\lambda$ across the full aperture. These arise almost entirely from deformations of the end windows, particularly the one nearer the $\frac{1}{8}$ Å element. While they could undoubtedly be largely eliminated by reassembly, they are harmless in view of the particular way the filter is to be used, with only a narrow cross section to any image-forming cone of rays.

The spectrum shows a number of subsidiary maxima at multiples of 32 Å from Hα, arising from the untuned elements, and the next primary maximum near 6100 Å has a much poorer profile than that at Hα. On the long wavelength side of Hα, the subsidiary maxima become very strong, owing to the falling off in quality of the polarizers. An auxiliary narrow-band red interference filter, centred on Hα, is needed to remove this parasitic light ; the present filter has a half-width of about 180 Å (central transmission 89%), appreciably reducing though not completely eliminating the stray light.

Wavelength uniformity across the filter is difficult to test directly, and is probably easiest assessed from the residual retardation defects in the poorer of the thickest calcite components (Fig. 5). These are about $0 \cdot 1\lambda$, corresponding to wavelength fluctuations over a range of 1/80 Å.

The profile of the principal maximum near Hα has been examined with a Fabry-Perot interferometer constructed by Dr. C. F. Bruce for length-standard determinations. The detailed analysis needed for the wings and secondary maxima has not yet been undertaken, but over the main part of the principal maximum the profile is close to theoretical.

The transmittance maximum has been measured without the final polarizer ; it is 13%. With either a further Polaroid or a polarizing beam-splitter this would be reduced to 12%.

VI. SIMULTANEOUS OBSERVATIONS IN TWO WAVELENGTHS SPACED $\frac{1}{8}$ Å APART

For some purposes it is desirable to make observations in two wavelengths simultaneously, so that atmospheric distortions are identical on each. This can be done for wavelengths $\frac{1}{8}$ Å apart as follows.

If the final polarizer is replaced by a polarizing beam-splitter which separates two beams plane polarized at right angles to one another, the final element produces two sets of complementary channel spectra with maximum $\frac{1}{8}$ Å apart. These are each superimposed on the transmission spectrum of the remainder of the filter, which has a bandwidth of $\frac{1}{4}$ Å at half-intensity. On turning the final $\frac{1}{2}\lambda$ plate through $22\frac{1}{2}°$ from its normal position, the two beam-splitter images are centred $\pm\frac{1}{16}$ Å from the nominal wavelength.

The beam-splitter is shown in Figure 6. A layer of calcite is sandwiched between two glass prisms at such an angle that total internal reflection occurs for the extraordinary ray (R.I. 1.485) but not for the ordinary ray (R.I. 1.654), which passes through the calcite. The glass, Schott SF17 (R.I. 1.645), has been selected so as to avoid appreciable reflection of the ordinary ray. It was originally intended to oil the prism assembly together with a liquid of the same refractive index, but it has proven impracticable to secure a surface on the long thin calcite component sufficiently flat to avoid distortion of the reflected image. The calcite has therefore been contacted optically onto the flat face of the front prism, the remainder of the assembly being oiled together with Aroclor 1254 (R.I. 1.64).

VII. Discussion

In retrospect, we must admit that the design of the filter could have been improved in many ways. Some modifications could be incorporated if the filter cell were redesigned ; others are only possible in a completely new filter.

The most important modification would be to tune the quartz and calcite sections separately from outside. These sections could be adjusted independently at any temperature during assembly, and could subsequently be matched at any other convenient temperature ; in the present filter, the quartz and calcite elements match only at 40 °C. Also, as much of the light transmitted outside the central band is due to errors in retardation of the untuned elements, a completely tuned filter is worth consideration.

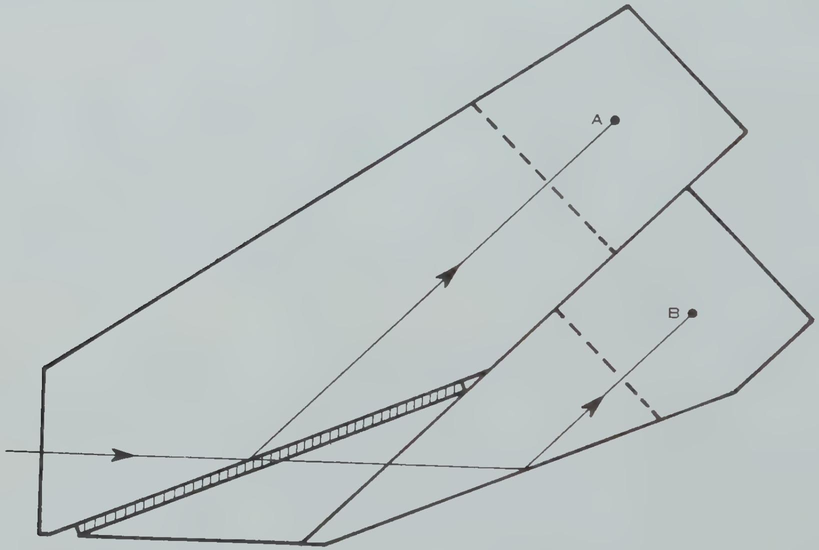

Fig. 6.—Polarizing beam-splitter. A plate of calcite (hatched), with its optic axis perpendicular to the plane of the diagram, is sandwiched between glass prisms, the extraordinary ray being reflected and the ordinary ray transmitted. Faces at 45° reflect the two rays upwards (perpendicular to the plane of the diagram) at *A* and *B*, the dimensions being such that the two images are in focus simultaneously on a plane parallel to that of the diagram.

A filter combining these two modifications could be tuned over a wide range of wavelengths, as the separate tuning would allow correction to be made for the differing dispersions of birefringence of quartz and calcite. The tuning range would be limited by the variation of retardation of the $\frac{1}{4}\lambda$ and $\frac{1}{2}\lambda$ plates with wavelengths, though these can be reduced by using " achromatic " combinations of plates as proposed by Pancharatnam (1955) and Koester (1959). Such composite wave plates could even be tuned themselves to ensure correct retardation at any wavelength ; the tuning would be very complex in practice, but in principle a filter could be made to tune to any wavelength.

In any future design of a narrow-band birefringent filter, the use of natural calcite should be avoided if possible. It seems likely that artificially grown crystals would have fewer imperfections. An obvious possibility is sodium nitrate with $1\frac{1}{2}$ times the birefringence of calcite, but further work is required on techniques for producing optical surfaces and controlling the thickness of a crystal of such high water solubility.

VIII. Acknowledgments

The construction of this filter has involved the closest cooperation of many colleagues who have made major contributions to its success. The optical assembly and most of the experiments on materials were undertaken by Mr. G. Norton and Mr. E. G. V. Mugridge. Mr. J. T. Jefferies assisted in various aspects of optical tolerancing and assembly. Mr. A. F. Young has supervised the various electronic controls involved in the final filter unit and in test equipment. The mechanical design of the filter cell is due to Mr. R. Riches, its mechanical construction to the Laboratory's workshop staff. Dr. R. G. Wylie made available a precision temperature controller and assisted materially in problems concerning thermal insulation. Dr. C. F. Bruce, of the Division of Metrology, kindly made a Fabry-Perot interferometer available for profile measurement.

IX. References

Allen, C. W. (1934).—*Mem. Commonw. Solar Obs. Aust.* **1** (5) : 65.
Evans, J. W. (1949).—*J. Opt. Soc. Amer.* **39** : 229.
Giovanelli, R. G., and Jefferies, J. T. (1954).—*Aust. J. Phys.* **7** : 254.
Jones, R. C. (1941).—*J. Opt. Soc. Amer.* **31** : 488.
Koester, C. J. (1959).—*J. Opt. Soc. Amer.* **49** : 405.
Lyot, B. (1944).—*Ann. Astrophys.* **7** : 31.
Öhman, Y. (1938).—*Nature* **141** : 157.
Pancharatnam, S. (1955).—*Proc. Indian Acad. Sci.* **41A** : 130, 137.
Smartt, R. N. (1961).—*J. Sci. Instrum.* **38** : 165.
Smartt, R. N., and Steel, W. H. (1959).—*J. Opt. Soc. Amer.* **49** : 710.
Steel, W. H. (1961).—C.S.I.R.O. Aust. Nat. Stand. Lab. Tech. Pap. No. 17.

VERTICAL VELOCITIES IN THE SOLAR CHROMOSPHERE

By R. G. Giovanelli* and J. T. Jefferies†

[*Manuscript received February 6, 1961*]

Summary

A $\frac{1}{8}$ Å birefringent filter has been used to photograph the chromosphere at various wavelengths across the Hα line. A process of photographic subtraction has then yielded photographs of velocity distributions. At all chromospheric depths, there is a close correlation between the intensity of the granules in Hα and the vertical velocity, the darker granules falling.

I. Introduction

In testing the $\frac{1}{8}$ Å birefringent filter (Steel, Smartt, and Giovanelli 1961), we have on several occasions obtained monochromatic photographs of parts of the Sun at various wavelengths across the Hα line. While the angular resolution is relatively poor, of the order of 5–10 sec of arc, these records enable us to study the broad features of the vertical velocity structure in the chromosphere.

The most comprehensive account of chromospheric granulation and velocities is probably that of de Jager (1957), who discussed (*a*) small granules (which he called " fine mottles "), diameters 4000 to 1700 km or less, seen in the core of the line, and (*b*) coarse granules (or " coarse mottles "), mean dimensions of the order of 45 000 km, visible mainly in the wings of Hα. In a later discussion, de Jager (1959) distinguished between

(i) fine mottles, diameter 10^3 km,
(ii) coarse mottles, diameter $5–8 \times 10^3$ km, consisting of clusters of fine mottles, and
(iii) the chromospheric network, diameter 5×10^4 km, composed of coarse mottles.

In the earlier paper, he pointed out that the greater contrast of the coarse granulation in the red as compared with the violet wing of Hα is due to a correlation between line width and vertical velocity such that the coarse bright and dark regions are moving upwards and downwards respectively with r.m.s. velocities of $\pm 1 \cdot 14$ km/s. He also gave arguments for thinking of the small *dark* granules as the bases of spicules, with mean vertical velocities of ± 18 km/s.

Previous studies of granule velocities have usually involved precise measurements of the wavelengths of spectral lines. By contrast, the present method is based on the well-known process of photographic differencing, which makes it easier to follow the velocity distribution over extended regions of the Sun's surface and with depth in the chromosphere.

---

* Division of Physics, C.S.I.R.O., University Grounds, Chippendale, N.S.W.

† Division of Physics, C.S.I.R.O., University Grounds, Chippendale, N.S.W. ; present address : National Bureau of Standards, Boulder, Colorado, U.S.A.

II. Process for Yielding Photographs of Velocity Distributions

Consider two photographs obtained at equal wavelength intervals $\pm\Delta\lambda$ from the centre of a Fraunhofer line ($H\alpha$). In the absence of vertical velocities the line profile should be symmetrical and the two photographs identical. Any vertical velocity causes a Doppler displacement of the line, the intensity increasing in one wing and decreasing in the other. Neither photograph alone is sufficient to demonstrate the presence of vertical velocities, because of the much greater intensity variations always present in the granulation; but a comparison of one photograph with another enables the Doppler displacements to be sorted out. This may be done most readily by making a unit contrast ($\gamma=1$) transparent print of one of the photographs. If this is precisely superimposed on its own negative, the pair have a uniform featureless appearance in transmitted light because higher densities in the negative are exactly compensated by lower densities in the print. But, if the print is superimposed on the photograph obtained in the opposite wing, the pair show density variations where the original photographs differed, i.e. where there were different Doppler displacements on the Sun.

The original photographs were obtained on Eastman 35 mm IV E film, processed in Kodak D.19 developer for 5 min at $20\pm0\cdot5$ °C to $\gamma\simeq3$. For convenience, these have been enlarged 2× on Ilford N.30 plates, with brush development in one part of Ilford ID2 to four parts of water for 4 min at $20\pm0\cdot5$ °C, yielding $\gamma\simeq2$. The unit gamma prints are obtained by brush development of Ilford N.30 plates in Kodak D.76 at $20\pm0\cdot05$ °C; $\frac{1}{4}$ gallon of developer is used per plate, the time being very closely controlled and lying in the range 5 min 35 s to 6 min 10 s, depending on the batch of developer. Prints of the superimposed plates are usually made on Ilford N.30 plates processed to $\gamma\simeq2$.

While we believe that Doppler displacements are the predominant physical cause of asymmetric $H\alpha$ profiles, the final photographs showing the apparent velocity distributions may suffer from various defects of instrumental or processing origin. For example, the central wavelength transmitted by the filter varies by about 0·01 Å across its surface, resulting in an apparent velocity variation across the final picture; though this is constant from picture to picture, and can be easily recognized or cancelled out if necessary. Again, it is difficult to make prints of precisely unit contrast; the control is such that usually $\gamma=1\pm0\cdot02$. Whether or not these limits are adequate depends on the intensity variations due to velocities as compared with normal variations across the granules; if necessary, a technique is available for a further stage of cancellation with an effective overall γ negligibly different from unity, though at the cost of additional photographic " noise ". The various checks used leave us confident that the final photographs represent chromospheric velocity distributions.

Plate 1 shows the chromosphere near the centre of the disk on August 11, 1960, the filter transmission maxima being respectively 0·2, 0·5, and 0·7 Å from the centre of $H\alpha$ on the successive rows of photographs. In each case, the left-hand picture shows the intensity distribution in the red wing, the right-hand picture shows the velocity distribution. Plate 2 shows corresponding intensity distributions at the line centre (*a*) and in the continuum (*b*). Plate 2 (*c*, *d*) shows intensity and velocity distributions at $\Delta\lambda = 0\cdot5$ Å on June 10, 1960. A careful comparison of the intensity and velocity distributions reveals a very close correlation, as found by de Jager for the coarse granulation, except that it now appears to hold for fine granulation also ; the bright granules are almost invariably moving upwards, the dark ones downwards.

III. Intensity and Velocity Structures in the Chromosphere

Apart from sunspots, whose velocities are shown incorrectly owing to the limited photometric range of the photographic emulsions, we may note filaments, general chromospheric granulation, and active (plage) regions on these plates. The main present significance of the filaments is in checking the photographic method of revealing velocities. For example, there is a filament on the left-hand side of Plate 2 (*c*), just above a small spot group. The velocity picture, 2 (*d*), shows that the right-hand end of the filament is rising, the left-hand end falling.

In considering the granulation, it is important to bear in mind the limited angular resolution, perhaps 5 sec of arc at best, despite which interesting comparisons can be made with de Jager's findings.

(*a*) *General Chromospheric Granulation*

Plates 1 (*a*, *c*, *e*) and 2 (*a*) clearly show the well-known differences in chromospheric structure at different wavelength settings. Though described often enough previously, it is important to reconsider them now that velocity distributions are available for comparison. In particular, it is to be remembered that the various features seen at the one wavelength arise from a more-or-less similar optical depth, but may differ radically in height above the photosphere. *With this reservation*, we can distinguish at least two major chromospheric levels :

(A) There is little change in the appearance of the granules from the line centre out to $\Delta\lambda = \pm0\cdot2$ or even $\pm0\cdot3$ Å. Near active regions, the granules are drawn out to lengths of several minutes of arc, but they are all narrow ; elsewhere they are more compact.

(B) By $\Delta\lambda = \pm0\cdot4$ Å, and more particularly $\Delta\lambda = \pm0\cdot5$ Å, and out to say $\Delta\lambda = \pm0\cdot7$ Å, the structure is on the whole much coarser and more contrasty, with broader bright regions separated by narrower dark channels ; these both have fine structures, the dark channels being subdivided into sequences of dark points and the bright regions crossed by faint dark markings. By $\Delta\lambda = \pm0\cdot7$ Å, the granulation is somewhat simpler, the structure having almost disappeared in the bright regions. By $\Delta\lambda = \pm1\cdot0$ Å, the dark points and channels are only just discernible.

There is little difficulty in identifying the coarse structure of level (B) with de Jager's coarse granulation or chromospheric network. In the core of the line ($\Delta\lambda \leqslant 0\cdot2$ Å) our resolution is inadequate to show de Jager's very fine granulation properly ; what we see corresponds almost certainly to what he described in 1959 as " coarse mottles ", consisting of clusters of very fine granules.

The features at levels (A) and (B) are by no means independent. Most of the dark points in the lower level (B) can be identified as dark points in the upper level (A) where, however, they are otherwise indistinguishable from other fine dark granules. Similarly, the faint structures in the bright granules of (B) coincide with granules in (A). We can find no evidence for de Jager's (1957) comment: " The coarse mottling " (i.e. granulation) " remains faintly visible even in the very centre of the line. It seems further that the coarse structure at $\Delta\lambda=0\cdot0$ Å is more or less a negative image of the coarse structure at $\Delta\lambda=0\cdot4$ Å. Bright patches in the line centre seem to be dark at $0\cdot4$ Å and vice-versa."

The velocity is closely correlated with intensity in both (A) and (B). At $\Delta\lambda=0\cdot7$ Å, the predominant features of the velocity pattern are a set of downward moving " points " (i.e. dark in Plate 1 (*f*)) which coincide with the dark points of Plate 1 (*e*). There is also a smaller number of upward moving " points " in Plate 1 (*f*); these occur in the broad, bright granules, but there seems to be very little on the intensity picture to distinguish them.

At $\Delta\lambda=0\cdot5$ Å, there is more detail than at $\Delta\lambda=0\cdot7$ Å, but the velocity distributions are still very similar. Almost every downward or upward moving point at $\Delta\lambda=0\cdot7$ Å lies immediately below a similar point at $\Delta\lambda=0\cdot5$ Å, but at the higher level a velocity structure is now obvious between the points, while the upward moving points are more pronounced. The correlation between the intensity and velocity patterns at $\Delta\lambda=0\cdot5$ Å is very strong.

As with the intensities, the differences between the velocity distributions at levels (A) and (B) are very considerable. Nevertheless, some connexion can be found. Most of the falling and rising points at $\Delta\lambda=0\cdot5$ Å can be detected as similar points at $\Delta\lambda=0\cdot2$ Å, though at the higher level the relative velocity variations differ considerably from those lower down. As before, there is a very close correlation between the intensity and velocity distributions at $\Delta\lambda=0\cdot2$ Å, the dark granules descending and the bright granules rising. In particular, the long-drawn-out granules near active regions appear to be rising or falling uniformly along their lengths.

(*b*) *Active Regions*

The plage regions are very different in their vertical structure. At the centre of Hα the most obvious features are the bright cord-like flocculi. These are very faint at $\Delta\lambda=0\cdot4$ Å, and have almost disappeared by $\Delta\lambda=0\cdot5$ Å. At the latter wavelength a broad dark region underlies and extends beyond the bright flocculi, which are still marked by a faint brightening. The dark region possesses a fine structure rather like that of the granulation in quiet regions, though darker; it appears to be almost identical with that of the overlying granulation seen in the core of the line where not obscured by bright flocculi, and persists quite clearly to $\Delta\lambda=0\cdot7$ Å. At $\Delta\lambda=0\cdot5$ Å, the well-known drawn-out structure of the granules near plages commences immediately beyond the dark region. The latter has disappeared by $\Delta\lambda=1\cdot0$ Å, where the plages appear bright once more, though much less obvious than at the line centre.

As before, the velocity and intensity distributions are closely related. The broad, dark region at $\Delta\lambda=0\cdot5$ Å is probably slowly sinking as a whole, though within it there is the familiar pattern of rising and falling granules. At $\Delta\lambda = 0\cdot 2$ Å, the velocity pattern is much less pronounced than elsewhere on the Sun. It has not been established as yet whether there are vertical motions in the bright flocculi.

IV. Discussion

The most striking aspect of these results is the almost universal association between granule intensity and velocity. However, any temptation to attribute this to buoyancy effects must be resisted, at least for the time being, because the intensity in Hα is far from a simple function of gas temperature. It will be an important future task to unravel the origin of the correlation.

The extraordinary general velocity pattern appears to be somewhat as shown schematically in Figure 1, with narrow columns rising or falling through the chromosphere.* These columns often occur in widely spaced arrays which, in the lower chromosphere, are separated by relatively undisturbed regions. In the higher chromosphere, the velocity pattern has a much finer structure.

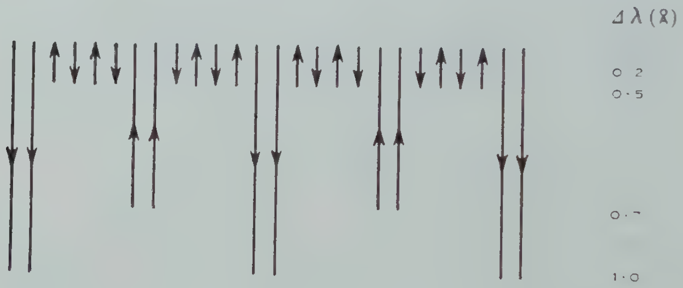

Fig. 1.—Schematic diagram of normal chromospheric velocity structure. Chromospheric heights are represented by the distance from the centre of Hα at which the features may be seen.

It will be of considerable interest, when higher angular resolution is available, to see whether the intensity-velocity correlation found here applies for the fine, dark granules observed by de Jager in the Hα core, and considered by him to represent the bases of spicules. Their height-time curves suggest that spicules rise to their maximum heights, after which they may fade or may descend back to the chromosphere, the upward and downward velocities being similar in magnitude. Rush and Roberts (1954) have pointed out that apparent *downward* velocities may be due to variations in excitation rather than actual downward motions. But if the very fine dark chromospheric granules all turn out to have downward motions, this will necessitate a reinterpretation of their relationship to spicules.

---

* In a personal communication, Dr. R. B. Leighton also has reported a distinct columnar structure in the Doppler field in the lower chromosphere.

VERTICAL VELOCITIES IN THE SOLAR CHROMOSPHERE

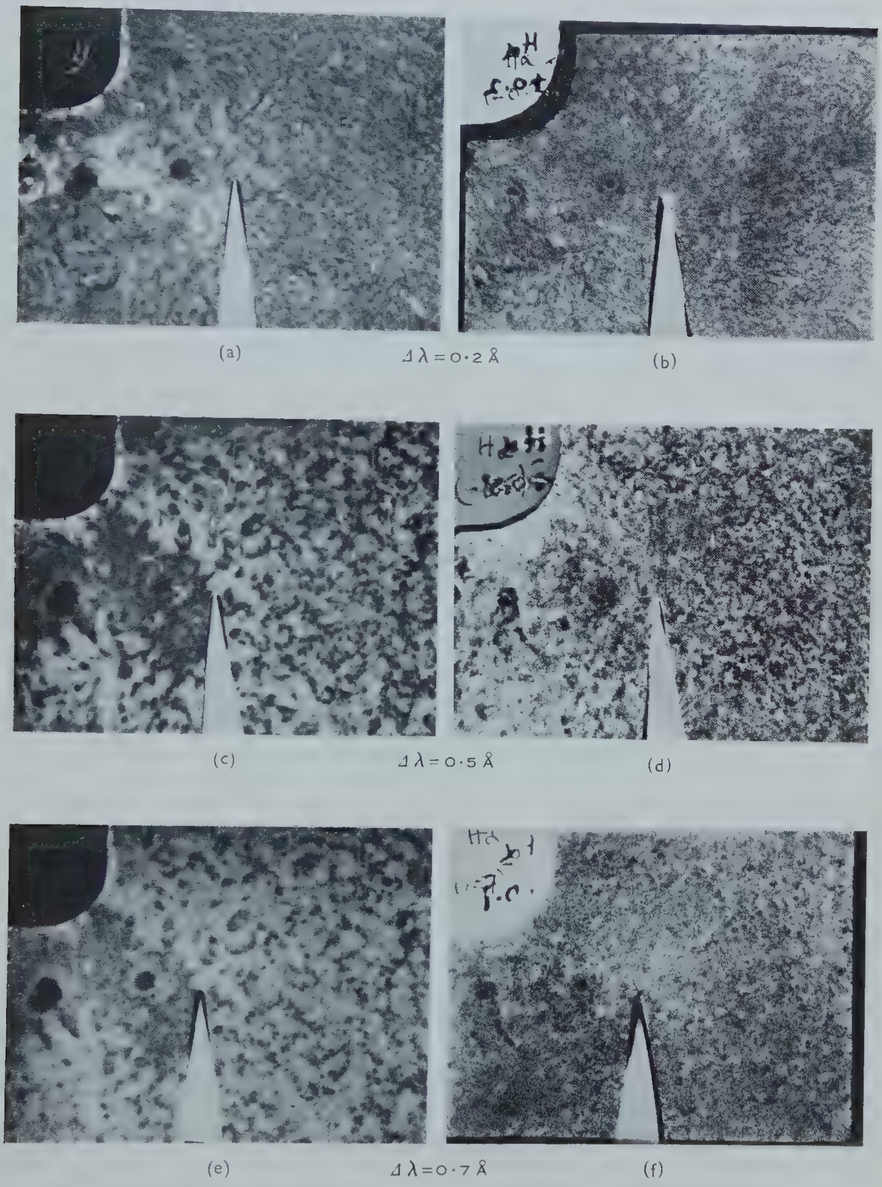

(a) $\Delta\lambda = 0{\cdot}2$ Å (b)

(c) $\Delta\lambda = 0{\cdot}5$ Å (d)

(e) $\Delta\lambda = 0{\cdot}7$ Å (f)

Solar chromosphere near centre of disk, August 11, 1960. The left-hand pictures (*a*), (*c*), and (*e*) are normal photographs obtained in the red wing of Hα. The right-hand pictures (*b*), (*d*), and (*f*) show the corresponding velocity distributions (see Section II); rising and descending regions appear bright and dark respectively, except in sunspots, where velocities are distorted. A dark vertical band on the right-hand side of (*b*) is spurious, being due to a slight wavelength variation across the filter.

VERTICAL VELOCITIES IN THE SOLAR CHROMOSPHERE

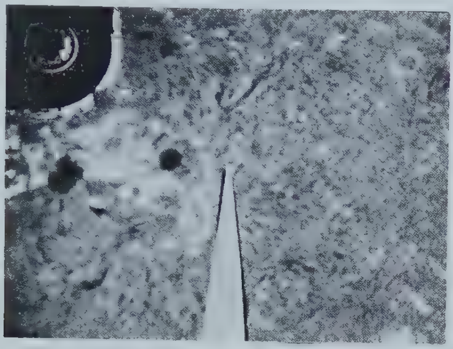

(a) $\Delta\lambda = 0 \cdot 0$ Å

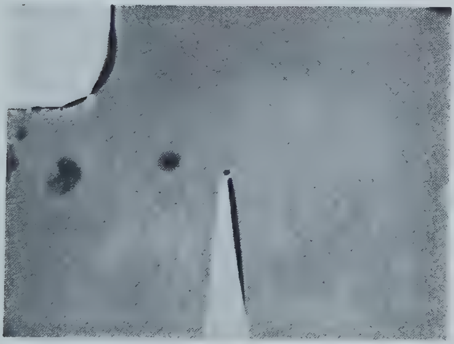

(b) $\Delta\lambda = 5$ Å

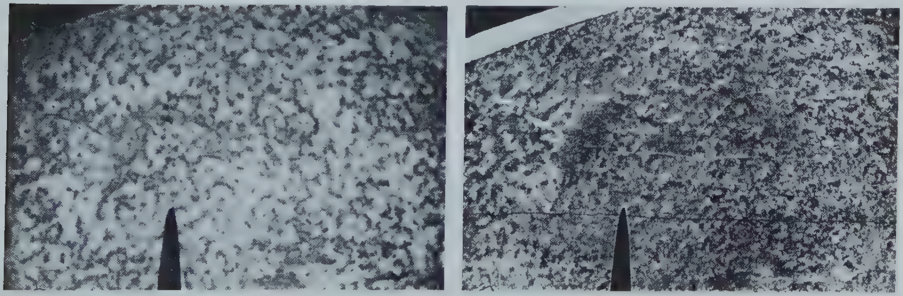

(c) $\Delta\lambda = 0 \cdot 5$ Å (d)

(*a*) and (*b*) are normal photographs of the region shown in Plate 1, obtained in the Hα line centre and in the continuum. (*c*) shows, on a smaller scale, a normal photograph $0 \cdot 5$ Å from the centre of Hα on June 10, 1960, (*d*) being the corresponding velocity distribution. The curved arc near the upper left-hand corner is due to a diaphragm; the upper right-hand corner is close to the Sun's limb.

V. Acknowledgments

It is a pleasure to acknowledge the assistance of Miss M. K. McCabe and Mr. H. R. Gillett, who have developed the reproducible methods of controlling photographic processes required for this work.

VI. References

de Jager, C. (1957).—*Bull. Astr. Insts. Netherlds.* **13** : 133.

de Jager, C. (1959).—"Paris Symposium on Radio Astronomy." p. 89. (Stanford Univ. Press.)

Rush, J. H., and Roberts, W. O. (1954).—*Aust. J. Phys.* **7** : 230.

Steel, W. H., Smartt, R. N., and Giovanelli, R. G. (1961).—*Aust. J. Phys.* **14** : 201.

A STUDY OF IONOSPHERICS AT MACQUARIE ISLAND

By B. A. McInnes*

[*Manuscript received January* 9, 1961]

Summary

Very low frequency radio emissions of natural origin, sometimes known as ionospherics, recorded at Macquarie Island have been examined and grouped into classes. The diurnal variations of all classes show a non-uniform distribution with a peak shortly before local midday. The ionospherics appeared to fall into three groups as regards dependence on magnetic K-index. Strong correlations were discovered between values of emission frequency and K-index, for several classes of ionospherics. The role of Čerenkov radiation in the generation of ionospherics is discussed. Suggested energy distributions are put forward to explain various classes of ionospherics. The magnetic associations and diurnal variation are explained on the basis of current geomagnetic disturbance theory. Ionospheric absorption is also considered to affect the diurnal variation. The phenomenon of " surf ", as reported by Campbell and Pope, is discussed.

I. Introduction

During the past few years there have been a number of reports on the occurrence of very low frequency natural radio emissions for which the U.R.S.I. (1960) has suggested the term " Ionospherics ". Several attempts have been made to explain the generation of ionospherics, such as the travelling-wave amplification model of Gallet (1959), the Čerenkov radiation model of Ellis (1959), and the Doppler-shifted gyrofrequency model of MacArthur (1959) and Murcray and Pope (1960). These all suffer from lack of generality.

The travelling-wave amplification model is based on the condition that the velocity of the ionized stream is equal to the phase velocity of electromagnetic radiation. From this, Gallet (1959) finds that two frequencies are simultaneously generated, and these are given by

$$f=\tfrac{1}{2}f_H\left[1\pm\left\{1-\left(\frac{f_p}{f_H}\,\frac{v}{\mathbf{c}}\right)^2\right\}^{\frac{1}{2}}\right],$$

where f is the wave frequency,

$f_p=(N_e\mathbf{e}^2/\varepsilon_0\mathbf{m})^{\frac{1}{2}}$=plasma frequency,

$f_H=\mu_0\mathbf{e}H/\mathbf{m}$=electron gyrofrequency,

N_e=electron density,

$\mathbf{e}$=electronic charge,

$\mathbf{m}$=electronic mass,

H=magnetic field,

ε_0=electrical permittivity of free space,

μ_0=magnetic permeability of free space,

v=velocity of ionized stream of particles,

$\mathbf{c}$=velocity of electromagnetic waves in free space.

---

* Physics Department, University of Queensland, Brisbane.

The lower frequency, which reduces to

$$f_1=\left(\frac{v}{\mathbf{c}}\right)^2\frac{f_p^2}{f_H},$$

explains such types of ionospherics as horizontal tones and hooks. When the inequality $(2f_p/f_H)(v/\mathbf{c})>1$ holds, no emission will take place.

The Čerenkov radiation model is based on the condition that the particle velocity is greater than the phase velocity of electromagnetic radiation in the surrounding dielectric. Ellis (1957) finds that Čerenkov radiation is possible for values of wave frequency close to the electron gyrofrequency.

In both these approaches the ionospherics are explained as arising from streams of charged particles trapped in the geomagnetic field. These particles are considered to have originally formed part of a solar corpuscular stream and to have undergone acceleration and subsequent trapping at the unstable boundary between the geomagnetic field and the solar stream (Parker 1958 ; Dessler and Parker 1959). This theory gives no guide as to the energy distribution among the particles, but it will be shown later that certain classes of ionospherics require for their explanation suitable energy distributions.

Dessler and Parker (1959) have shown that the main phase of a magnetic storm can be explained by the stresses exerted by these trapped particles from the solar plasma. Thus, on the one hand, we have a source of the corpuscular stream which may give rise to the ionospherics, and, on the other hand, an explanation for disturbances of the magnetic field. Dessler and Parker proceed to show that, just as the increase in the geomagnetic field is related to the energy of the solar plasma compressing the fields, so also the decrease in field caused by the stresses exerted by the trapped particles depends only on the total energy of the stream.

In the present paper, a systematic study of ionospherics recorded at one station is presented, together with an extension of the theory, on the Čerenkov model, for the generation of ionospherics.

II. Experimental Observations

(a) *Experimental Methods*

The recordings used in this work were obtained on Macquarie Island, latitude 54° 29′ S., longitude 158° 58′ E., geomagnetic latitude 60° S., using standard VLF recording equipment kindly lent by Stanford University. Recordings of 2 min duration were made at 35 min past each hour (U.T.). The records used in this analysis cover the period March 1958 to January 1959. Using a Kay “ Sonograph ”, graphical representations of frequency against time were made for all emissions of sufficient intensity other than atmospherics and whistlers. These representations are referred to as “ sonograms ”. Somewhat over 2400 sonograms were obtained and classified according to the method suggested by Gallet (1959), with minor additions. This classification is shown in Figure 1.

(b) *Relative Occurrence and Diurnal Variation*

An investigation of the diurnal variation of the various classes of ionospherics was carried out. Figure 2 shows the histograms obtained for the most common

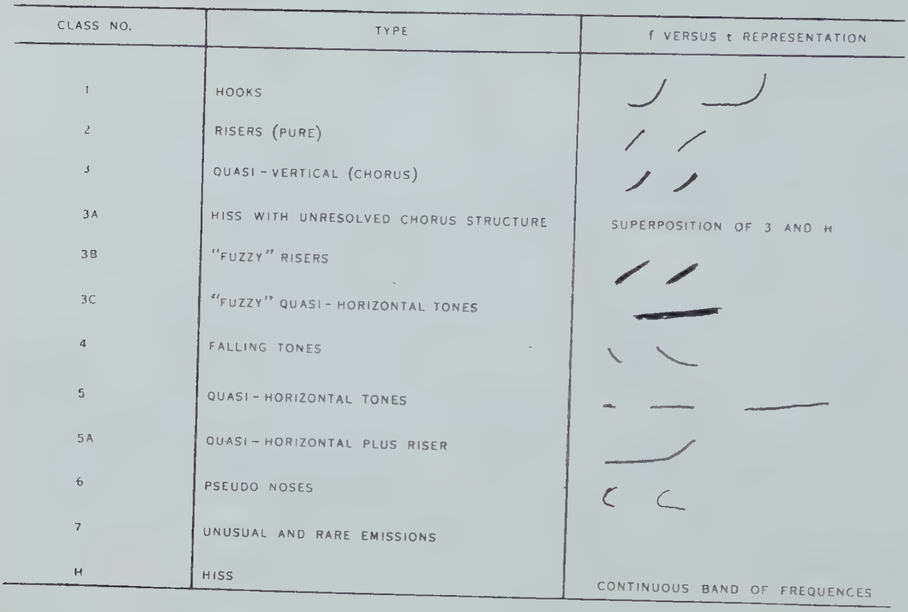

CLASS NO.	TYPE	f VERSUS t REPRESENTATION
1	HOOKS	
2	RISERS (PURE)	
3	QUASI - VERTICAL (CHORUS)	
3A	HISS WITH UNRESOLVED CHORUS STRUCTURE	SUPERPOSITION OF 3 AND H
3B	"FUZZY" RISERS	
3C	"FUZZY" QUASI - HORIZONTAL TONES	
4	FALLING TONES	
5	QUASI - HORIZONTAL TONES	
5A	QUASI - HORIZONTAL PLUS RISER	
6	PSEUDO NOSES	
7	UNUSUAL AND RARE EMISSIONS	
H	HISS	CONTINUOUS BAND OF FREQUENCES

Fig. 1.—Classification of ionospherics.

classes 3, 3A, 3B, 3C, 5, and H. Table 1 shows the mean time of occurrence and standard deviation from these means for the various classes. Table 1 also indicates the relative frequency of occurrence of the various classes.

TABLE 1

RELATIVE OCCURRENCE AND DIURNAL VARIATION OF IONOSPHERICS

Class	No. in Sample	Mean Local Time of Occurrence	Standard Deviation
1	15	10·9	5·6
2	103	8·6	3·4
3	403	8·4	2·7
3A	162	9·4	2·9
3B	75	9·0	2·8
3C	133	9·0	2·6
4	21	10·7	3·6
5	110	10·2	3·0
5A	31	10·3	2·9
6	7	9·4	2·0
H	153	10·2	3·5

(c) *Long-term Variation*

For each of the nine months, March 1958–December 1958 inclusive, the occurrence of each class, as a percentage of the total emission, was calculated and the subsequent results plotted as shown in Figure 3. There appear to be

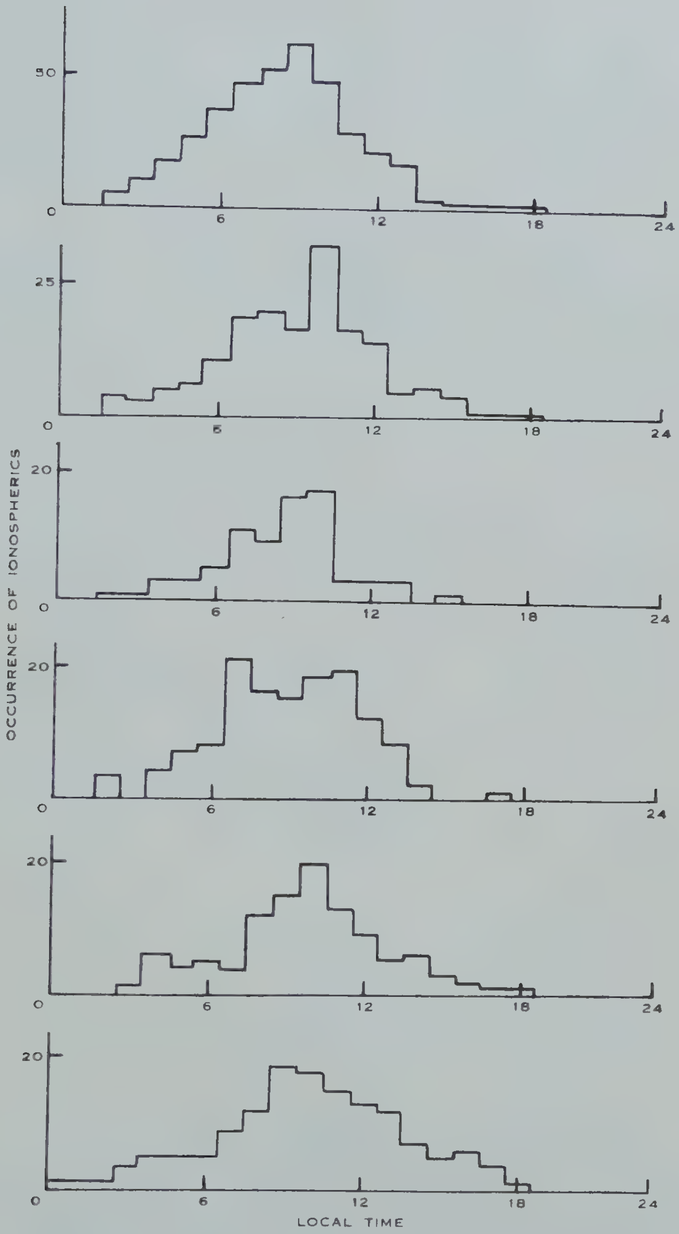

Fig. 2.—Diurnal variation of ionospherics. (*a*) Quasi-vertical emissions, (*b*) hiss with unresolved " chorus " structure, (*c*) " fuzzy " risers, (*d*) " fuzzy " quasi-horizontal tones, (*e*) quasi-horizontal tones, (*f*) hiss.

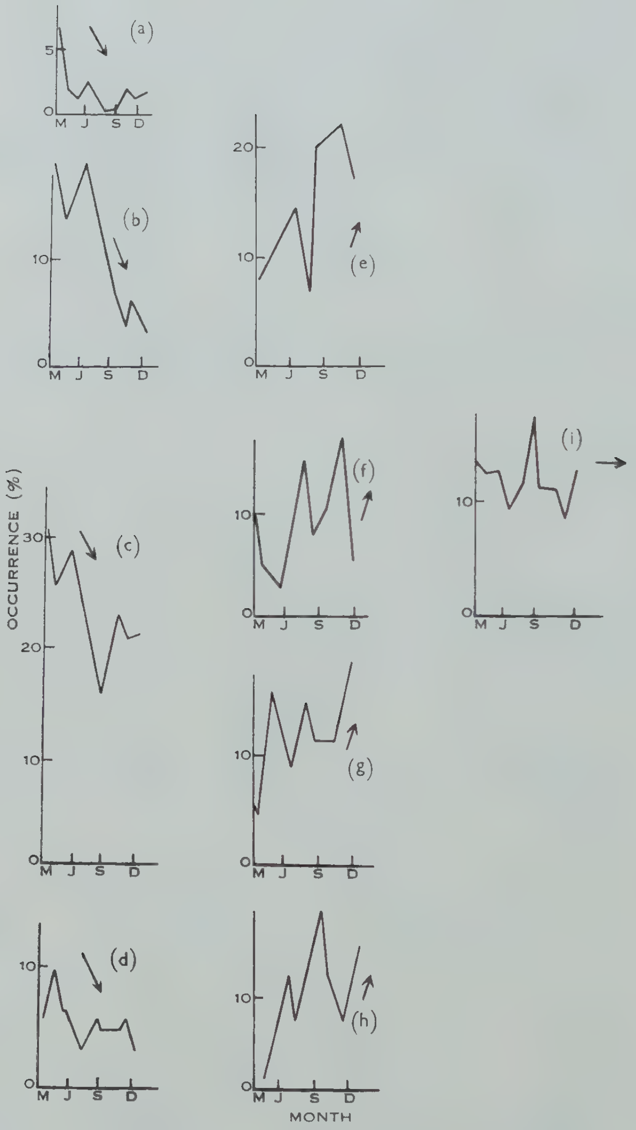

Fig. 3.—Percentage occurrence of various ionospherics over a 9-month period. (*a*) Hooks, (*b*) risers, (*c*) quasi-vertical, (*d*) quasi-horizontal plus riser, (*e*) hiss with unresolved "chorus", (*f*) "fuzzy" risers, (*g*) "fuzzy" quasi-horizontal, (*h*) hiss, (*i*) quasi-horizontal.

three general types of behaviour : (i) the " chorus " type shown by dawn chorus, risers, and hooks, the relative frequency of occurrence of which tended to decrease during the period investigated, (ii) the quasi-horizontal type, which tended to remain steady, (iii) the hiss type shown by pure hiss and ionospherics associated with hiss, namely, 3A, 3B, 3C, the relative frequency of occurrence of which tended to increase. We shall discuss later other phenomena in which a similar grouping is valid.

(*d*) *Frequency Range of Ionospherics*

The maximum and minimum frequencies indicated by a sonogram represent those frequencies where the intensity has fallen to about 30 dB below the maximum intensity in that particular ionospheric. The average maximum and minimum frequencies thus defined and their difference were determined for each month. These are shown in Figure 4. There are indications of a maximum in July and a minimum in December. Histograms have been plotted of the occurrence, in each class of ionospheric, and in the aggregate, of each particular frequency ($\pm 0 \cdot 25$ kc/s). These distributions are reproduced in Figure 5. Most ionospherics lie between 1 kc/s and $3 \cdot 5$ kc/s, but most hooks, some risers, and a little dawn chorus extend somewhat higher. The dawn chorus that is of a higher frequency than normal tends to be associated with hooks and/or high frequency risers. The hiss band covers 1–4 kc/s, the most commonly observed frequency being 2 kc/s. No recordings were found lower than 500 c/s.

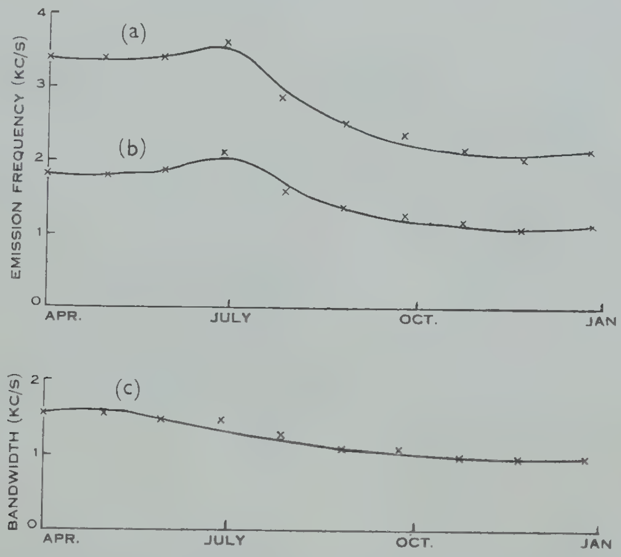

Fig. 4.—Variation of frequency parameters of ionospherics over a 9-month period. (*a*) Maximum frequency, (*b*) minimum frequency, (*c*) bandwidth.

(*e*) *Association with Magnetic Activity*

(i) An investigation of the relationship between the magnetic disturbance *K*-index and the occurrence of the various classes of ionospherics was carried out in the following manner. Using both the local *K*-index and the planetary *K*-index, the number of occasions emission occurred for each particular *K* value was found and the mean *K* value and the standard deviation from the mean were calculated for each of the various distributions. Table 2 shows the results obtained.

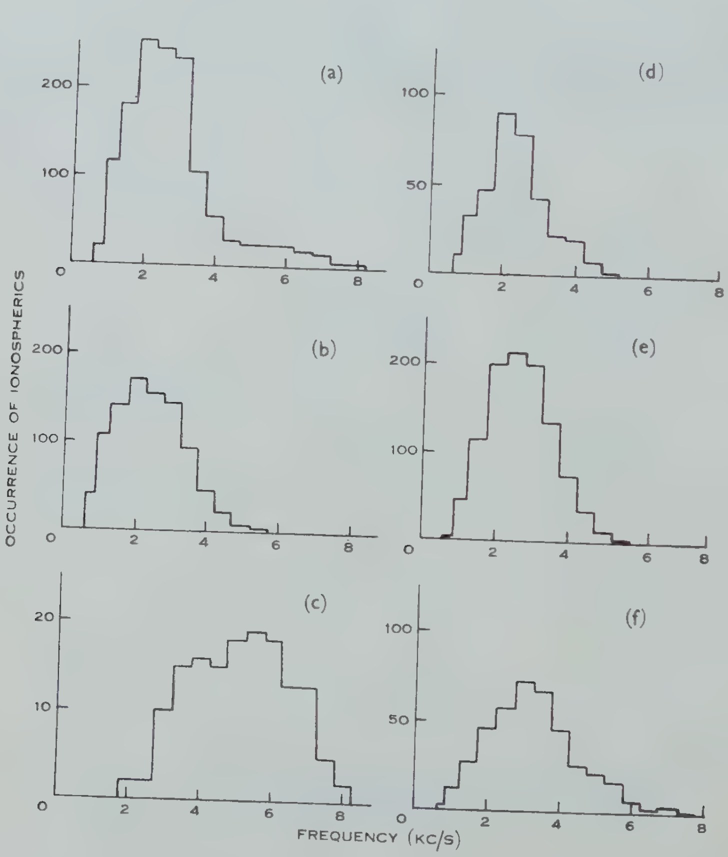

Fig. 5.—Emission frequency of ionospherics. (*a*) Aggregate, (*b*) hiss, (*c*) hooks, (*d*) horizontal tones, (*e*) quasi-vertical, (*f*) risers.

The grouping shown in Table 2 has been adopted on the basis of the statistical test of Welch and Aspin (Bennett and Franklin 1954) for determining whether a small difference in mean value (less than the variance), denotes a real difference in behaviour. The behaviour is unlikely to be similar within a particular confidence level α, if the value of their function t exceeds the corresponding value of the function $t_{\nu,\alpha}$, where ν is the number of degrees of freedom as defined by them. Table 3 gives a list of the t-values obtained and the corresponding values of $t_{\nu,\alpha}$, for $\alpha=5\%$ and 1%.

Apart from classes 3A and 3B, which appear in two groups, the test indicates a clear separation into three groups as shown in Table 2. This suggests that within a range of K values, which are themselves moderately low, horizontal tones tend to occur with low values of K, hiss type ionospherics with moderate values of K, and chorus type with high values of K.

(ii) The behaviour of certain frequency parameters, such as minimum frequency of dawn chorus, the frequency of discrete emissions and bandwidth of hiss, was investigated as a function of the magnetic K-index : Table 4 shows all results significant to a level better than 5%.

TABLE 2

ASSOCIATION BETWEEN OCCURRENCE OF IONOSPHERICS AND MAGNETIC DISTURBANCE

Group	Type	K_1		K_p	
		Mean	Standard Deviation	Mean	Standard Deviation
Chorus ..	3	3·1	0·7	3·4	1·2
	1	2·9	1·1	3·4	1·3
	2	2·9	1·5	3·6	1·3
	3A	2·9	1·6	3·2	1·5
	3B	2·8	1·3	3·2	1·5
Hiss	H	2·7	1·1	2·9	1·4
	3A	2·9	1·6	3·2	1·5
	3B	2·8	1·3	3·2	1·5
Horizontal ..	5	2·1	1·4	2·4	1·4
	3C	2·2	1·7	2·8	1·3

The significance of the test was calculated, eliminating any effect of non-normality by using the z-test (Fisher 1950). The extremely significant relationships between magnetic disturbance and certain emission frequencies (especially in the case of the quasi-horizontal tone where the measured frequency is independent of absorption) is discussed later in the paper.

(*f*) *Ionospheric Relationship*

Owing to the paucity of ionospheric records for 1958 for Macquarie Island it was difficult to investigate the association of changing ionospheric parameters and emission of ionospherics. It was found, however, that there was no tendency towards change in emission during periods of ionospheric black-out.

(*g*) *Association with Solar Flares*

For a group of 400 ionospherics, it was found that only on five occasions emissions occurred concurrently with solar flares. The emission which did occur concurrently did not tend to fall into any particular class, being divided between hiss, dawn chorus, and hiss with unresolved dawn chorus. The solar flares which occurred concurrently with ionospherics were all of importance 1, measured on a 1–3 scale. On no occasion did the flare appear to initiate the period of emission of ionospherics, but it occurred sometime after the commencement of the period.

TABLE 3

COMPARISON OF CLASSES OF IONOSPHERICS AS REGARDS OCCURRENCE WITH MAGNETIC DISTURBANCE

Classes Compared	ν	t	$t_{\nu,5}$	$t_{\nu,1}$	Same or Different Parent Population
H *v.* 3	126	2·61	1·98	2·61	Different
H *v.* 5	136	2·91	1·97	2·60	Different
5 *v.* 3	112	5·60	1·98	2·62	Different
1 *v.* 3	26	0·63	2·06	2·78	Same
2 *v.* 3	28	0·59	2·05	2·76	Same
3A *v.* H	58	0·63	2·00	2·67	Same
3A *v.* 3	43	0·66	2·02	2·70	Same
3A *v.* 5	75	2·40	2·00	2·65	Different
3C *v.* H	105	2·65	1·99	2·63	Different
3C *v.* 3	89	5·59	2·00	2·64	Different
3C *v.* 5	107	0·47	1·99	2·63	Same

TABLE 4

ASSOCIATION OF FREQUENCY PARAMETERS OF IONOSPHERICS AND MAGNETIC DISTURBANCE

Class	Correlation	Size of Sample	Correlation Coefficient	Significance Level (%)
3	$F_{\text{min.}}$ *v.* K_1	82	0·38	0·1
5	F *v.* K_1	75	0·49	0·01
H	*B.W.* *v.* K_1	70	0·23	5
	B.W. *v.* K_p	70	0·31	1
4	*B.W.* *v.* K_p	19	0·46	4
3B	$F_{\text{min.}}$ *v.* K_1	17	0·64	1

There thus seems to exist no positive evidence of a direct connection between solar flares and the occurrence of ionospherics through a non-corpuscular agent, such as X-rays, which would act immediately.

III. Discussion

(a) Čerenkov Radiation and Hiss

The refractive index of the ionosphere, for propagation in the whistler, or longitudinal extraordinary mode with the wave normal direction approximately the same as that of the Earth's magnetic field, as derived from magneto-ionic theory, is given by Gallet (1959),

$$n^2=1+\frac{f_p^2}{f(f_H-f)},$$

where all symbols are as previously described. In this expression the effect of collisions is neglected. Figure 6 shows a plot of n^2 against f. It will be noted that n goes to infinity at $f=0$ and $f=f_H$.

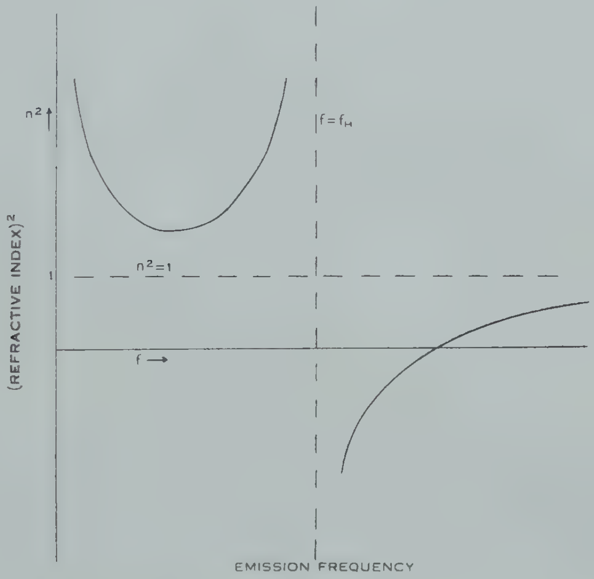

Fig. 6.—Plot of refractive index of ionosphere against frequency.

The relation between refractive index and particle velocity for emission of Čerenkov radiation is

$$vn>\mathbf{c},$$

or

$$n>1/\beta,$$

where $\beta=v/\mathbf{c}$. Figure 6 indicates that no matter how small the stream velocity, emission should always occur at the gyrofrequency and at zero frequency. As the stream velocity increases, the two bands of emission widen but the upper limit of the upper band remains at the gyrofrequency. The mathematical problem of finding the limits of the bands is identical with that used by Gallet (1959) in his treatment of the travelling-wave model and the expressions there obtained for discrete frequencies are the values for the limits of the bands.

It has previously been seen that in the travelling-wave model no emission takes place if $2f_p v/f_H \mathbf{c} > 1$, but in the Čerenkov model, since emission may occur if the stream velocity is greater than the phase velocity, rather than merely equal to it, this condition indicates that the two bands merge into one and emission occurs from zero frequency to the gyrofrequency.

The lower limit of the ionospherics as received may, however, not be zero. Budden (1959) in a theoretical analysis has shown that irregularities which have a total length small compared with the wavelength may prevent the propagation of very low frequency radio waves through the ionosphere. At the lowest frequencies there will be more irregularities which will come under the heading of "small compared with the wavelength" and hence greater attenuation. In any case, the flux density of Čerenkov radiation decreases with decreasing frequency. The actual cut-off frequency will depend on propagation conditions and the method of recording.

The higher emission band would normally be much more difficult to record because of the uncertainty of its frequency, which will depend on the gyrofrequency of its point of generation. In addition, as Helliwell (1958) has pointed out, attenuation is heavy for frequencies within 5% of the gyrofrequency, so unless the band is wider than this limit it will be of very low intensity. However, if the hiss is generated far out on a field line which intersects the Earth's surface at a high magnetic latitude, the electron gyrofrequency is small and the upper band will come within the scope of conventional whistler-ionospheric recorders. In this case a double band of hiss would be recorded, as has been found in fact by Martin, Helliwell, and Marks (1960) at Byrd Station, Antarctic, and by Aarons, Gustafsson, and Egeland (1960) at Kiruna, Sweden. If we consider a stream producing a double band of hiss, each of bandwidth 1·5 kc/s, as it moves from a location where the gyrofrequency is 3·5 kc/s to a location where the gyrofrequency is 5 kc/s, along a field line reaching the Earth at 65° N. geomagnetic, and remember that attenuation will affect both the lowest frequencies of the lower band and the highest frequencies of the upper band, we expect to record two bands of frequency 0·5–1·5 kc/s and 2–4·5 kc/s. This is what is actually recorded by Aarons, Gustafsson, and Egeland. Again, in accordance with their results we would not expect much variation in the emission frequencies of the lower band as compared with that of the upper band.

Dowden (1960), recording at Hobart, Australia, has observed noise simultaneously at one occasion on 4, 9, 70, and 230 kc/s, and again on 9 and 230 kc/s. In the latter case his equipment at 4 and 70 kc/s was out of action. The geomagnetic latitude at Hobart is 51° S., so the minimum gyrofrequency along the field line through Hobart will not be much less than 100 kc/s. This minimum gyrofrequency occurs at the top of the path. The lower frequency recordings obviously belong to the lower band but the origin of the higher frequencies is more doubtful. Depending on the position on the field line where they are generated, they may belong to the lower or to the upper band, or alternately, emission may be occurring at all frequencies below the gyrofrequency. Recordings made at a large number of frequencies would not necessarily clarify the situation, since, if there does exist an emission-free frequency region at one point along the field line, emission may still occur in that range at a different point along the line. The close correspondence of amplitude fluctuation at the different frequencies, which Dowden observed, is consistent with the simultaneous generation of a band of frequencies as suggested by the present theory.

(*b*) *Different Classes of Ionospherics*

The signal actually received at the Earth's surface will depend on the relative efficiency of the two mechanisms, the Čerenkov mechanism for the production of the band of noise and the travelling-wave mechanism for the amplification of the limiting frequency. Figure 7 shows a sonogram (of the class 3C) where we have a band of frequencies possibly produced by the Čerenkov mechanism, together with a much more intense line at the upper frequency limit, possibly caused by the travelling-wave mechanism. In this case, apparently the stream of particles was uniform in energy but sufficiently powerful to produce emission strong enough to be recorded using conventional antennae.

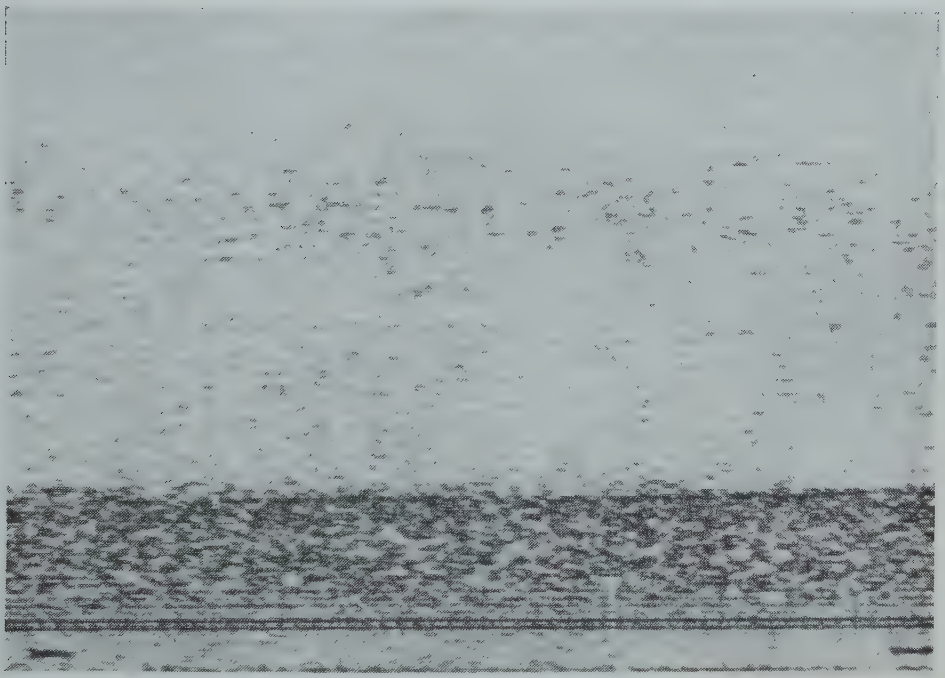

Fig. 7.—A sonogram of class 3C.

For a stream of particles of non-uniform energy Čerenkov radiation emission can occur over a wide range of energies of the particles, but the travelling-wave amplification at any one frequency will depend critically on the distribution of energy. If the particles do not differ greatly in energy, a large amplification by the travelling-wave mechanism could occur at the appropriate frequency, giving high emission. The quasi-horizontal and the fuzzy quasi-horizontal types could be accounted for in this way. In the case of the quasi-horizontal tones, the Čerenkov radiation is not intense enough to be recorded, whereas in the case of the fuzzy quasi-horizontal tones and the quasi-horizontal plus hiss mixture, the upper part of the Čerenkov radiation band appears as well as the limiting frequency.

In his explanation of various classes of ionospherics Gallet (1959) has assumed an electron density distribution of the outer ionosphere such that f_p^2/f_H is a constant. During a period of frequent emission, such as when dawn chorus is occurring, it is to be expected that there would be an increase in electron density because of many streams of particles being trapped in the geomagnetic field, and the correct model may tend to approach f_p/f_H constant. Thus a stream of particles travelling along a field line would be entering a region where the electron density would be greater than normally the case and the resultant ionospheric would show a quasi-vertical structure. Whether this structure will appear embedded in a hiss structure, as in class 3A, or whether merely the quasi-vertical structure, class 3, will be recorded will depend on the intensity of the original Čerenkov radiation.

The rising tone often found on the end of horizontal emissions and in hooks may be explained, following Gallet (1959), by a large increase in electron density, as in the F region of the ionosphere, leading to an increase in emission frequency. Since streams of spiralling particles are normally reflected in the Earth's magnetic field at points higher than the F region, one would expect to find relatively few of these types of emissions compared with quasi-horizontal tones, as is indeed the case (see Table 1). In addition, only high energy streams would penetrate to the F region, which agrees with the fact that hooks have a higher emission frequency than other classes of ionospherics (Fig. 5).

A broad uniform energy spectrum will result in poor travelling-wave amplification at any particular frequency, and so decrease the likelihood of recording discrete tones at the Earth's surface, but it will be no less effective than a peaked spectrum for generating Čerenkov radiation. Hence, in this situation only the hiss band is likely to be recorded at the Earth.

(c) *Correlation with Magnetic Activity*

As has been noted in the introduction, the total energy of the stream will control magnetic disturbance. It has also been noted that the energy of the individual particles determines the frequency of the ionospheric. Since, in the present investigation, ionospherics of roughly the same intensity have been considered, it is reasonable to expect that the energy per particle will control both magnetic disturbance and emission frequency. This fact fits in very well with the correlation between the index of magnetic disturbance K and the emission frequency, as observed in the Macquarie Island data.

Magnetic disturbances take the form of a series of increases and decreases which may be interpreted as the effect of plasma clouds impinging on the Earth's field and then penetrating the field and being trapped therein. This situation results in a stream of particles suitable for the generation of ionospherics being continually renewed. This explains the general increase of occurrence of ionospherics with rise in K-index (see, e.g. Crouchley and Brice 1960).

The slight association indicated in Section II (*b*) between the K-index and the ratios between the frequencies of occurrence of the three groups of types of ionospheric can be roughly interpreted as follows. Where the horizontal tones are predominant, the particles in the trapped plasma stream tend to be homogeneous in energy. They will thus tend to produce a steady rather than a wildly fluctuating field change and hence give a relatively low K-index. On the other hand, where hiss is predominant the particles tend to have a wide range of energies. They will thus be more likely to produce wildly fluctuating field changes and hence give a higher K-index.

(*d*) *Diurnal Variation*

If the emissions depend on the solar wind a maximum of occurrence would be expected where the plasma cloud meets the Earth and infiltrates the geomagnetic field. However, in addition to the direct stream from the Sun, which normally consists of roughly 100 atoms/cm^3 with a velocity of 500 km/s, (the quiet day stream postulated by Parker (1960)) there is a stream caused by the orbital motion of the Earth through the permanent interplanetary gas containing around 100 atoms/cm^3, the velocity being 30 km/s.

Thus, neglecting ionospheric absorption, the diurnal variation of ionospherics should show a maximum at noon, and a much smaller maximum at 0600. Appleton (1953) has noted that the diurnal maximum of absorption in the ionosphere is reached a short time, of the order of an hour, after noon, owing to the " sluggishness " of the ionosphere. Thus absorption could move the peak a little to the morning side of noon. The absence of a gap between the early morning and the midday distributions seems to indicate that the width of the two distributions is such that they run smoothly into one another. This accounts for the distribution found in Figure 2.

Crouchley and Brice (1960) found that the time of maximum occurrence is earlier for lower latitudes. This could be caused by the different behaviour of ionospheric absorption at different latitudes. The absorption increases more markedly after sunrise at lower latitudes. Therefore the displacement of the peak of the distribution will be greater at lower latitudes.

Figure 2 and Table 1 show that all classes of ionospherics have a non-uniform diurnal distribution. Contrary to this, Gallet (1959) at Boulder has noted an almost uniform distribution for risers and quasi-horizontal tones. It may well be that the Boulder data include emissions of lower intensity than those included in the Macquarie Island data. It is possible that strong emissions occurring at distant localities will be transmitted by ionosphere plus ground reflections and will be recorded as weak emissions at the receiving station. This would tend to eliminate non-uniformity in the diurnal distribution.

(*e*) *Recordings of " Surf "*

Pope and Campbell (1960) have reported an unusual emission which consists of a family of ionospherics with increasing central frequency and increasing rate of spread with time. Because of the resemblance of the sound of the emission to that of ocean breakers during a storm, they suggest the name of " surf " to describe this emission. It is suggested that surf may be explained in the following manner. A bunch of particles travelling along the magnetic field lines with velocity slightly larger than average—the average velocity particles being responsible for the generation of a hiss band, with a maximum frequency at 2 kc/s which is simultaneously recorded—generates surf by a combination of Čerenkov radiation and travelling-wave amplification. The emission frequency of surf of 3 kc/s suggests a stream velocity of 9×10^6 m/s and this in conjunction with the average period of recurrence of 6·3 s and a path length of 6×10^7 m suggests that conditions may be suitable for generation of the emission in a region located between the top of the field line and the point of magnetic mirroring. The increase in frequency may be explained as due to an increase in electron density resulting from increased ionization along the path of the stream. The gradual spreading of signal may be caused by a spreading of the velocities of the particles with time. The reason for the finite lifetime of the disturbance would be a decrease in the density of the stream on account of collisions, especially in the regions of higher electron density about the mirror points.

IV. Acknowledgments

Acknowledgments are due to the Australian National Committee of the International Geophysical Year, the University of Queensland, and the Electrical Engineering Department, Stanford University, for the provision of finance for the equipment, and to the Antarctic Division, Department of External Affairs, for the housing and operation of equipment. The recordings were made by Mr. J. Munro and the author whilst members of the Australian National Antarctic Research Expedition. Magnetograms were kindly supplied by the Bureau of Mineral Resources. The author wishes to thank the Commonwealth Education Office for the provision of an award under which part of this work was carried on. The work was supervised by Mr. J. Crouchley to whom many thanks are due. It is a pleasure to acknowledge the unfailing interest and assistance of Professor H. C. Webster.

V. References

Aarons, J., Gustafsson, G., and Egeland, A. (1960).—*Nature* **185** : 148.

Appleton, E. V. (1953).—*J. Atmos. Terr. Phys.* **3** : 282.

Bennett, C. A., and Franklin, N. L. (1954).—" Statistical Analysis." (Wiley : New York.)

Budden, K. G. (1959).—*J. Res. Nat. Bur. Stand.* **63D** : 135.

Crouchley, J., and Brice, N. M. (1960).—*Planet. Space Sci.* **2** : 238.

Dessler, A. J., and Parker, E. N. (1959).—*J. Geophys. Res.* **64** : 2239.

Dowden, R. L. (1960).—*Nature* **187** : 677.

Ellis, G. R. (1957).—*J. Atmos. Terr. Phys.* **10** : 302.

Fisher, R. A. (1950).—" Statistical Methods for Research Workers." (Oliver and Boyd : London.)

Gallet, R. M. (1959).—*Proc. Inst. Radio Engrs., N.Y.* **47** : 211.

Helliwell, R. A. (1958).—Low frequency propagation studies, Part I. A.S.T.I.A. Document No. AD110184.

MacArthur, J. W. (1959).—*Phys. Rev. Letters* **2** : 491.

Martin, L. H., Helliwell, R. A., and Marks, K. R. (1960).—*Nature* **187**: 751.

Murcray, W. B., and Pope, J. H. (1960).—*Phys. Rev. Letters* **4**: 5.

Parker, E. N. (1958).—*Phys. of Fluids.* **1**: 171.

Parker, E. N. (1960).—"Plasma Dynamics." (Addison-Wesley: Reading, Mass.)

Pope, J. H., and Campbell, W. H. (1960).—*J. Geophys. Res.* **65**: 2543.

U.R.S.I. (1960).—AG60/IU/1, Commission IV, Terrestrial Noise Terminology.

SLOW DRIFT SOLAR RADIO BURSTS: HARMONIC FREQUENCY RATIOS, SOLAR LONGITUDE DEPENDENCE, AND FREQUENCY DRIFT RATES

By Marion B. Wood*

[*Manuscript received January 9, 1961*]

Summary

Frequency ratios of second harmonic to fundamental bands are determined for 19 slow drift bursts. The ratios measured at the high frequency edges of the bands yield a mean value of 2·00, whereas the mean value of the low frequency edge ratios is significantly lower than 2.

No definite solar longitude dependence is observed in either the number of bursts occurring or in the second harmonic to fundamental frequency ratios; further, fundamental bands do not drop out for sources far from the centre of the disk.

Frequency drift rates are found to bear no definite relationship to the geomagnetic effectiveness of the bursts.

I. Introduction

One of the features of greatest interest appearing on solar radio noise records is the " slow drift burst ". This event, observed with dynamic spectrum equipment, is an extremely intense outburst which drifts from higher to lower frequencies over a typical frequency range of about 200 down to 50 Mc/s in about 5 to 15 minutes. Slow drift bursts are comparatively rare events associated with certain solar flares, and are typically observed to have fundamental and second harmonic bands.

Wild, Murray, and Rowe (1954) proposed a model in which slow drift bursts are produced by plasma oscillations in the solar corona, with fundamental bands centred around the local plasma frequency. These authors predicted that the frequency ratio of second harmonic to fundamental, measured at peak intensity points, should be slightly less than 2. This prediction was based on their picture of cut-off of the low frequency part of the fundamental band due to complete absorption below the plasma frequency. Observations by these authors and later by Roberts (1959) confirmed this suggestion. The prediction was also made that the frequency ratio should decrease with increasing source distance from the centre of the Sun, and that the fundamental band should drop out altogether for distances greater than about a half a solar radius. However, these latter predictions of centre-to-limb variations have not been borne out by the later observations of Roberts (1959) or of Maxwell, Thompson, and Garmire (1959). No definite variation with solar longitude in either frequency ratio or in number of bursts occurring was observed by these authors.

---

* National Bureau of Standards, Boulder Laboratories, Boulder, Colorado, U.S.A.

The present study extends these observations, using both the early and the recent data obtained at the Harvard Radio Astronomy Station, Ft. Davis, Texas. The first part of the paper will be concerned with harmonic frequency ratios and with solar longitude dependence; the second part will deal with frequency drift rates of the bursts and their relationship to geomagnetic activity.

II. SECOND HARMONIC TO FUNDAMENTAL FREQUENCY RATIOS; SOLAR LONGITUDE DEPENDENCE

In Figure 1 is shown a very idealized drawing of a slow drift burst with fundamental and second harmonic bands. Time increases from left to right in the horizontal direction; frequency increases from top to bottom in the vertical. The points are drawn on to show how harmonic to fundamental frequency ratios (f_2/f_1) are obtained on both the low frequency and the high frequency edges of the bands. According to the model of Wild, Murray, and Rowe (1954), in which loss of the low frequency part of the fundamental occurs, the low frequency edge values of f_1 should be raised in frequency, while f_1 at the high frequency edge should not be affected. We would thus expect low frequency edge values of f_2/f_1 to be less than 2, while those for the high frequency edges should approximate 2.

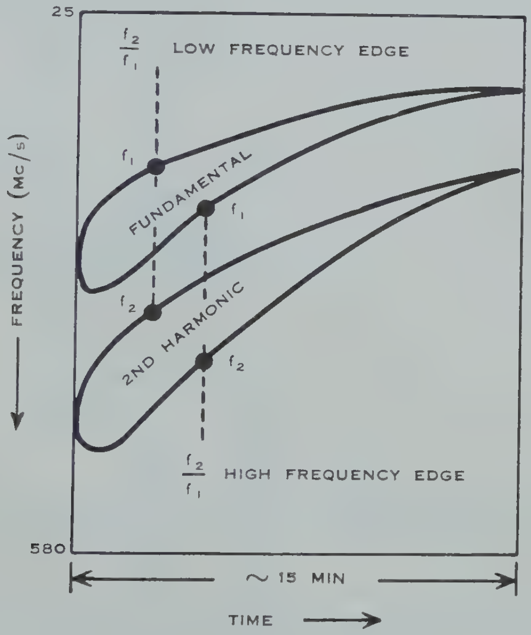

Fig. 1.—Idealized picture of harmonics in a slow drift burst.

To test this prediction, f_2/f_1 values were measured from the Ft. Davis films. From October 1956 to December 1958 the frequency range covered by this swept frequency equipment was 580 down to 100 Mc/s; since the beginning of 1959 the low frequency end of the observing range has been extended down to 25 Mc/s.

Frequency ratios were obtained for both low frequency and high frequency edges, and several measures were made whenever possible at different times on a single burst. Nineteen bursts entered this sample. For the 1959 data, with the low frequency extension, about 75% of the bursts showed second harmonic and fundamental bands, although frequency ratios were measured on only the more clear-cut examples. No case of a third harmonic was observed.

The results of the study confirm our prediction that low frequency edge ratios should be reduced in value because of absorption, while the high frequency ones should remain unchanged. Figure 2 (*b*) shows the low frequency edge ratios; here the mean value of f_2/f_1 is $1\cdot90\pm0\cdot06$ (p.e.). Figure 2 (*a*), the histogram for the high frequency edge ratios, yields the mean value $2\cdot00\pm0\cdot03$ (p.e.). The probability that this large a difference could occur by chance is about 10^{-4}. This value is obtained using the *t*-test for the difference between two sample means (cf. Crow, Davis, and Maxfield 1955).

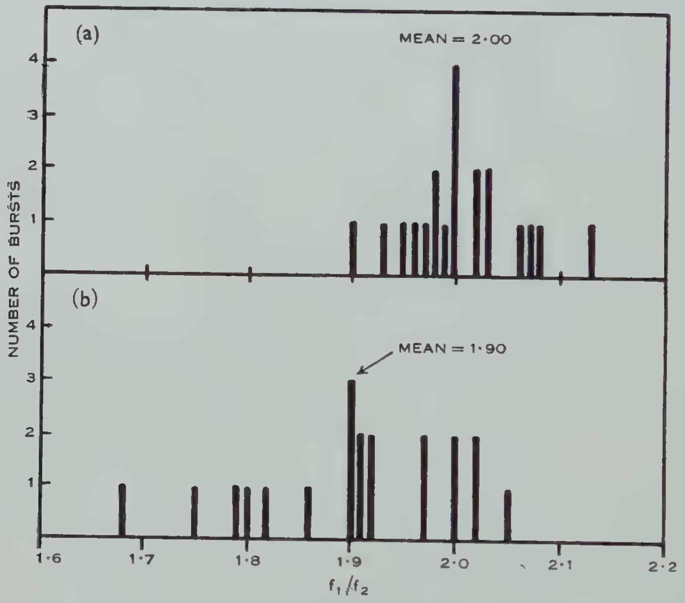

Fig. 2.—Harmonic frequency ratios: (*a*) at high frequency edges and (*b*) at low frequency edges.

In evaluating this probability figure, one must take into account the possibility of a systematic error which could arise from varying receiver sensitivity with frequency. However, care was taken to avoid measurements near insensitive bands, and it is felt that the results have not been basically affected. It is reassuring in this regard that when f_2/f_1 values are studied as a function of frequency of measurement, no definite variation in ratios occurs.

As the next step in the investigation, f_2/f_1 values are plotted in Figure 3 against solar longitude. Positions of the bursts are inferred from positions of time-associated flares. In agreement with the results of the authors previously mentioned, the ratios show no definite decrease in value toward the limb and, certainly, fundamental bands do not drop out for large central meridian distances.

In Figure 4, the frequency of occurrence of the bursts themselves, rather than f_2/f_1 values, is plotted against solar longitude. The upper histogram is for all bursts whose positions could be determined from time association with a solar flare; the lower graph is for the flare-matched bursts that showed a definite fundamental and second harmonic. Although there is a slight tendency for drop-off away from central longitudes, the effect is no greater for bursts with fundamental and harmonic than for the total sample. Thus again, in this analysis, fundamental bands are not lost toward the limb.

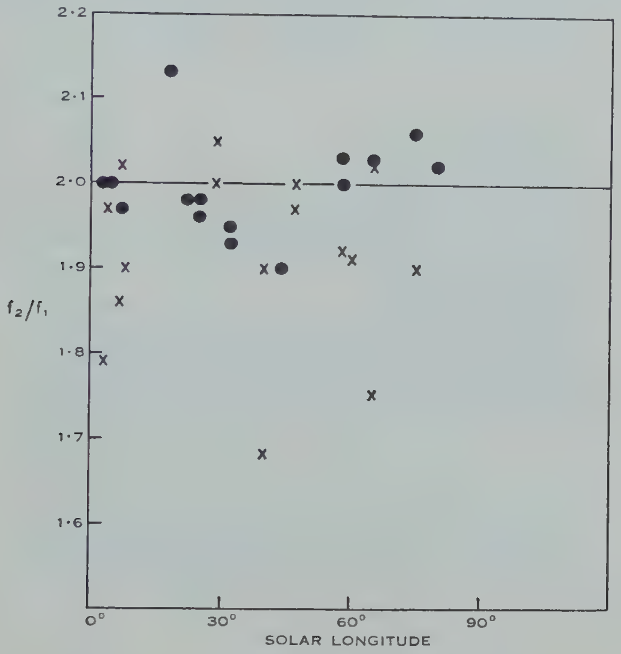

Fig. 3.—Harmonic frequency ratios as a function of solar longitude. ● High frequency edge, × low frequency edge.

In summary, the reduced mean f_2/f_1 value for low frequency edge measures, compared to the mean value 2·00 for the high frequency edges, strongly supports the model of Wild, Murray, and Rowe (1954). In this model, slow drift bursts are generated by plasma oscillations in the solar corona, with complete absorption taking place below the plasma frequency.

The solar longitude observations extend and confirm the results of Roberts (1959) and of Maxwell, Thompson, and Garmire (1959). The observed lack of significant dependence upon longitude in either f_2/f_1 or in numbers of bursts occurring is not consistent with a spherically symmetrical corona. Such symmetry imposes severe limitations on the escape directions of the fundamental band. With increasing solar longitude more and more of the fundamental is cut off from a Sun-Earth path until f_1 is eliminated entirely beyond about 30° longitude. A mechanism is therefore necessary which will produce more nearly isotropic radiation. Roberts (1959, personal communication 1960) proposes a picture in which local irregularities in density provide this mechanism. In invoking such a model, two possibilities arise: either the irregularities act as scattering centres, scattering the fundamental into a Sun-Earth path, or local density condensations act as noise sources themselves and emit more or less isotropically. The latter case is attractive because of the association of slow drift bursts with ejected streams of solar corpuscles, expelled at times of flares. Such streams would provide the necessary density irregularities for wide-cone emission and thus permit observation of fundamental bands from non-central sources.

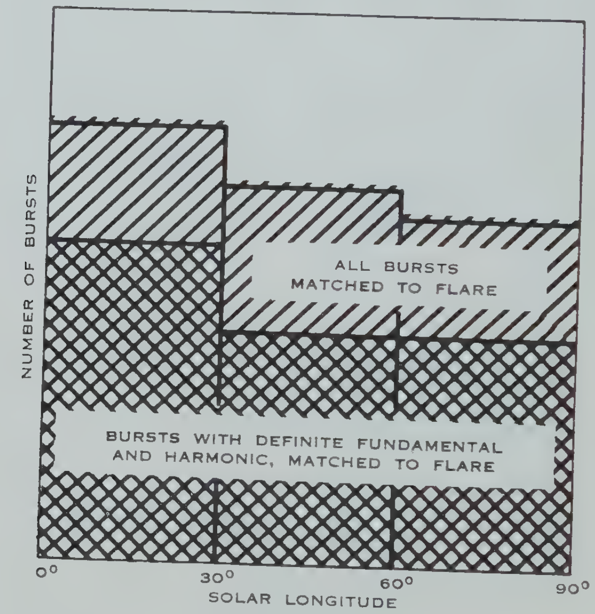

Fig. 4.—Centre-to-limb variation in burst occurrence.

III. Frequency Drift Rates of Slow Drift Bursts; Relation to Geomagnetic Disturbance

A priori, slow drift bursts would seem excellent candidates for association with geomagnetic storms: they are of great intensity; they are associated with flares of greater than average importance; and their velocities, inferred from frequency drift rates and assumed coronal model, are of the order of 1000 km/s, a value consistent with observed time intervals between flares and geomagnetic storms. However, when such bursts are related to magnetic disturbance level, the results are disappointing. Shown in Figure 5 (*a*) is a superposed epoch representation of mean geomagnetic index, *Ap*, on days before and after all slow drift bursts observed from October 1956 to September 1959 (88 cases). There is a tendency, although not marked, for an increase in geomagnetic activity on days 0–2 after the bursts. For comparison, in Figure 5 (*b*) is plotted the corresponding curve for geomagnetic disturbance level on days before and after outstanding continuum events which occurred during the same period (73 cases). In only seven cases were the continuum events and the slow drift bursts time associated within ±1 hr ; in only 20 cases were they as closely associated as ±1 day. Thus the two samples are effectively independent. We see that the degree of association with geomagnetic activity is greater for the continuum events than for the slow drift bursts. It should be remarked that the only requirements placed on the continuum events in order to enter the sample are that they be classified, in the Fort Davis published data (National Bureau of Standards, F-Series, Part B 1956–1959), as " continuum ", i.e. events with smoothly varying intensity, and that they be of importance $\geqslant 3$ and of duration $\geqslant 5$ min. Thus the majority are not the fairly rare, wide band, long duration events referred to as type IV continuum, which McLean (1959) found associated with geomagnetic disturbance. Other studies of burst and continuum relations to geomagnetic disturbance have also been made by Maxwell, Thompson, and Garmire (1959).

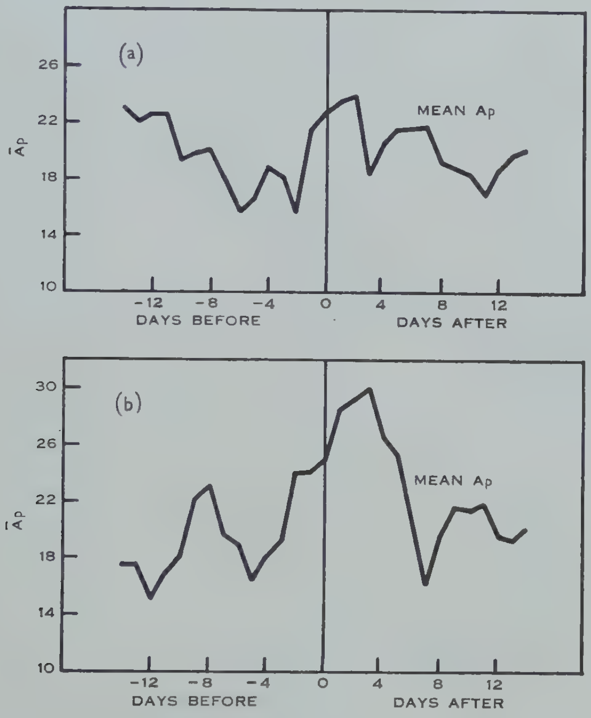

Fig. 5.—Geomagnetic disturbance level : (*a*) related to slow drift bursts and (*b*) to continuum events.

Although no striking geomagnetic relation occurs in the case of the bursts, there does appear a degree of association, and it is of interest to try to find some burst characteristic, varying from event to event, which might differentiate between the storm and the non-storm producers. In this regard, frequency drift rates of the bursts are promising. The drift rates vary appreciably from burst to burst, and those events with fast frequency drifts may be related to noise sources with high outward velocities through the solar corona. Thus one would expect that the faster the frequency drift the greater the chance of escape from the Sun of the particles in the noise source and, thus, the greater the chance for magnetic disturbance.

Figure 6 (*b*) shows drift rates *v.* frequency for bursts followed by storm, while Figure 6 (*a*) shows the corresponding rates for bursts with no storm. The events entering the samples in Figure 6 are all observed slow drift bursts, October 1956–1959, which had well-defined and measurable frequency drift rates. According to an earlier interpretation of Wood and Warwick (1959), based on the data going down only to 100 Mc/s, we should have expected the difference between storm and no storm drift rates to increase with decreasing frequency. However, the new lower frequency data do not bear out this expectation; rather, there appears to be no definite difference between rates at either low or high frequencies.

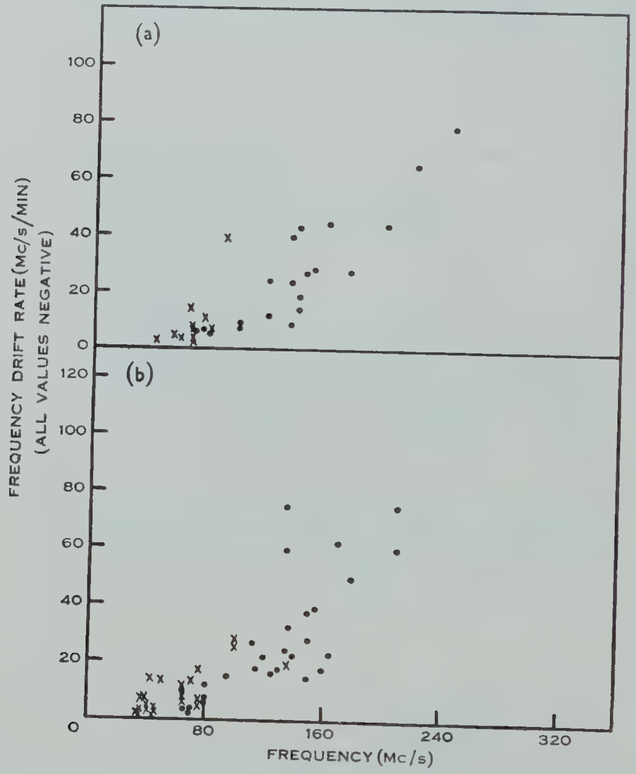

Fig. 6.—Frequency drift rates: (*a*) without storm, and (*b*) with storm. ● Harmonic, × fundamental.

In summary, the present results indicate that outstanding continuum events appear more strongly related to geomagnetic disturbance than do the slow drift bursts. Further, frequency drift rates of the bursts do not provide a means of distinguishing the storm-producing bursts from those not associated with geomagnetic disturbance.

IV. ACKNOWLEDGMENTS

I would like to thank Drs. Maxwell and Thompson of the Harvard Radio Astronomy Station at Ft. Davis for their hospitality and help, and for making their records available to me. Also, I would like to express my thanks to Dr. C. S. Warwick and Mr. R. S. Lawrence for their interest in the work and for their helpful suggestions.

V. REFERENCES

CROW, E. L., DAVIS, F. A., and MAXFIELD, M. W. (1955).—" Statistics Manual." (U.S. Naval Ordnance Test Station.)

MAXWELL, A., THOMPSON, A. R., and GARMIRE, G. (1959).—*Planet. Space Sci.* **1** : 325.

McLEAN, D. J. (1959).—*Aust. J. Phys.* **12** : 404.

NATIONAL BUREAU OF STANDARDS (1956–1959).—F-series, Part B.

ROBERTS, J. A. (1959).—IAU/URSI Symposium on Radio Astronomy. (Stanford Univ. Press.)

WILD, J. P., MURRAY, J. D., and ROWE, W. C. (1954).—*Aust. J. Phys.* **7** : 439.

WOOD, M. B., and WARWICK, C. S. (1959).—*Nature* **184** : 1471.

EXCITED STATES OF ^{64}Zn

By M. J. Kenny* and D. E. Caro*

[*Manuscript received January 5, 1961*]

Summary

The reaction ^{63}Cu$(p,n)^{63}$Zn has been studied at bombarding energies between 5 and $11 \cdot 5$ MeV using an activation technique with good energy resolution. Previously unknown levels in ^{64}Zn at excitation energies of approximately $13 \cdot 3_7$, $13 \cdot 7_5$, $14 \cdot 1_2$, $14 \cdot 3_1$, $14 \cdot 9_0$, $15 \cdot 1_8$, $15 \cdot 6_1$, and $15 \cdot 7_7$ MeV have been found. It is shown that six of these levels, and the observed absence of levels in some energy regions, can be accounted for in terms of Nilsson's calculations for the single-particle states of a deformed nucleus. If this interpretation is correct, the deformation of ^{64}Zn must be negative, at least in its highly excited states.

I. Introduction

In previous studies of the cross section for the reaction ^{63}Cu$(p,n)^{63}$Zn (Blaser *et al.* 1950 ; Ghoshal 1950 ; Howe 1958) the measurements have not been made with any high degree of precision. The principal limitations on accuracy have been due to the use of targets several hundred keV thick and the lack of a suitable source of variable-energy protons. In all the previous experiments the technique of stacked foils has been used. The results obtained have shown a smooth variation of cross section with bombarding energy above 5 MeV. As a result, it was concluded that the levels of ^{64}Zn are numerous and closely spaced, as suggested by compound nucleus theory.

In the present experiment, the yield curve for the reaction has been obtained with considerably increased resolution. The results show that discrete levels in ^{64}Zn are observable at excitation energies above 13 MeV.

II. Experimental Details

It is not convenient to study the reaction by means of neutron counting, since the presence of 30% of ^{65}Cu in natural copper results in neutrons from the reaction ^{65}Cu$(p,n)^{65}$Zn. The number of neutrons produced by this competing reaction is comparable to the number produced by the ^{63}Cu reaction. Both ^{63}Zn and ^{65}Zn are radioactive, decaying by positron emission to ^{63}Cu and ^{65}Cu. Since the half-life of ^{63}Zn is $38 \cdot 4$ min while that of ^{65}Zn is 256 days, the two decays can be easily separated. In consequence, a measurement of the activity of a copper foil after proton bombardment affords a convenient method for studying the ^{63}Cu$(p,n)^{63}$Zn reaction. This method has been used for the present experiment.

Twenty copper foils of thickness $2 \cdot 8$ mg cm^{-2} were used. These foils have a half-thickness of 60 keV at 5 MeV and 35 keV at $11 \cdot 5$ MeV. The relative thickness of the targets was accurately determined by bombarding them all with protons of the same energy. This calibration was repeated for several proton energies.

---

* Physics Department, University of Melbourne.

The extracted proton beam of the Melbourne University Variable Energy Cyclotron (MUVEC) was used for the experiment. Any energy between 5 and 11·5 MeV can be obtained. The proton energy was determined by means of a magnetic analyser stabilized by a proton nuclear resonance set. The energy reproducibility and resolution of this system are better than 0·1%. The absolute energy of the analyser has been determined by calibration with 5·3 MeV α-particles from polonium 210. Up to date no other points on the calibration curve have been obtained. Until a more complete analyser calibration is carried out, it is possible that energy estimates may be in error in the 11 MeV region. However, it is unlikely that the error could be as great as 2% at 11 MeV.

Measurements of the relative cross section for the reaction $^{63}\mathrm{Cu}(p,n)^{63}\mathrm{Zn}$ were made at intervals of 30 keV from 5·0 to 11·5 MeV proton energy. For each bombardment, the foils received a charge of 2 μC over a period of about 1 min. The charge was measured by a vibrating reed integrator having an accuracy of ±0·2%. The decay of the ^{63}Zn during bombardment was compensated for by using an appropriate leakage resistor across the integrating condenser.

Positrons from the decay of ^{63}Zn were counted by a Geiger tube connected to a scaler, the time for 30 000 counts being recorded. The geometry of the system was fixed, so that the relative values of cross section could easily be obtained. No attempt was made to evaluate the absolute cross section, owing to the uncertainty in determining the solid angle of the counter with respect to the source. The error due to counting statistics was ±0·6% and the overall reproducibility of the results was ±1%. The measurements were all repeated and any doubtful points were taken a third time.

III. Experimental Results

If the curve of cross section as a function of energy contains a resonance whose width is less than the energy loss of the protons in the target, the peak height will be reduced. If there are two or more peaks less than about 100 keV apart, these will not be resolved. Furthermore, a large number of close spaced peaks of equal size will be indistinguishable and will appear as a continuum. The initial data have been corrected for target thickness by considering each point as representing the mean cross section over an energy range corresponding to the thickness of the target to the particular energy of the incident protons. A histogram of all the points was then plotted and an appropriate smooth curve having the same area as the histogram was produced.

The experimental curve which was obtained for the relative cross section is shown in Figure 1. The energy scale is plotted in centre-of-mass coordinates. It can be seen that eight prominent peaks have been found at proton energies, in the centre-of-mass system, of $5\cdot 6_6$, $6\cdot 0_4$, $6\cdot 4_1$, $6\cdot 6_0$, $7\cdot 1_9$, $7\cdot 4_7$, $7\cdot 9_0$, and $8\cdot 0_6$ MeV. The addition of a proton to ^{63}Cu leads to an excitation of 7·71 MeV in ^{64}Zn. These peaks therefore correspond to excitations of $13\cdot 3_7$, $13\cdot 7_5$

$14 \cdot 1_2$, $14 \cdot 3_1$, $14 \cdot 9_0$, $15 \cdot 1_8$, $15 \cdot 6_1$, and $15 \cdot 7_7$ MeV in ^{64}Zn. For proton energies above 8·06 MeV, it was not possible to distinguish any peaks with certainty. When all the points in this energy region were plotted with their appropriate error bars, it was possible to draw a smooth curve through them. There may, however, be small peaks in this region. It must be pointed out that before an analysis for target thickness was applied, the peaks at 7·47 and 8·06 MeV were

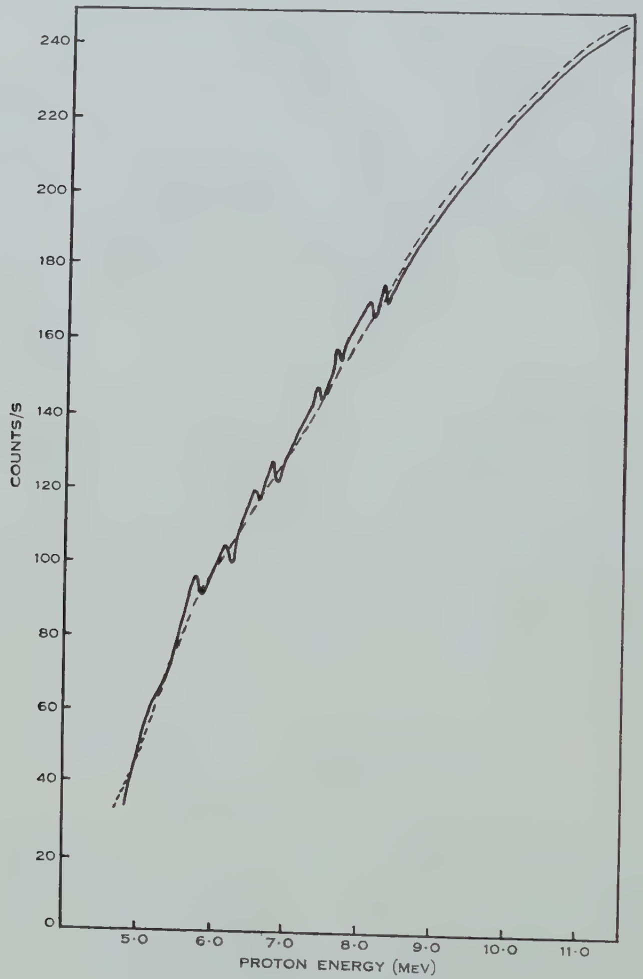

Fig. 1.—^{63}Cu$(p,n)^{63}$Zn relative cross section plotted in counts/s as a function of proton energy.

just barely distinguishable and in the analysis they were assumed to be genuine. A change of about $1\frac{1}{2}\%$ in two neighbouring points could have made these appear much more real or alternatively made them almost disappear. The fact that all the points were repeatable to an accuracy of 1% suggested that they were genuine. There was also some evidence for a peak at $5 \cdot 1_8$ MeV, however, it was not possible to establish its existence with certainty and so a smooth curve was drawn through this region.

In Figure 2 a smoothed out version of the results is compared with the absolute cross sections of Blaser, Ghoshal, and Howe. The results of this experiment were normalized to give best agreement with the curves of Blaser, Ghoshal, and Howe. The same normalization factor gives the agreement with the Shapiro theory indicated in Figure 1. The shape of the experimentally determined cross section is seen to agree well with the results obtained by previous workers.

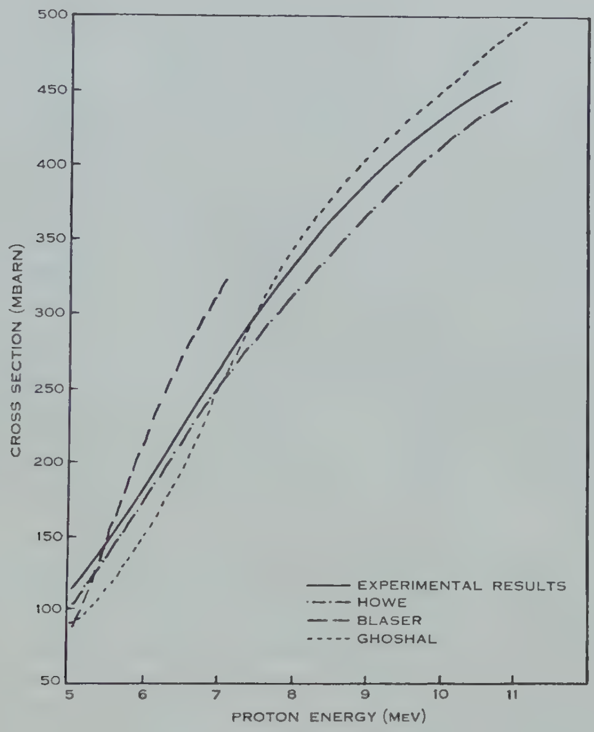

Fig. 2.—Comparison of experimental results with previous measurements. The cross section in millibarns is plotted as a function of centre-of-mass proton energy.

IV. Discussion of Results

Shapiro (1953) has calculated the expected cross section for a number of (p,n) reactions including ^{63}Cu$(p,n)^{63}$Zn. It is assumed that there are a large number of closely spaced levels and the theoretical cross section obtained is an average over many resonances. In consequence, the theory predicts a cross section which rises smoothly with increasing energy. The absolute magnitude of the theoretical cross section is somewhat arbitrary since to obtain agreement with experiment it is necessary to vary the value of the nuclear radius parameter from one nucleus to another. The theoretical cross section is sensitive to changes in the value of the nuclear radius parameter. For example, a change in its value from $1 \cdot 3$ to $1 \cdot 5$ fermi increases the theoretical cross section by 50%. Shapiro's theory has achieved a good deal of success in predicting the shape of the cross-section curve but the absolute value of the predicted cross section often differs from experimental values by a factor as large as two. The theory gives values for the total cross section which includes capture elastic and inelastic scattering as well as neutron emission. At bombarding energies above 5 MeV, the neutron emission process predominates, so that the curve of cross section versus energy as calculated by Shapiro might be expected to fit the experimental data for the (p,n) reaction.

The broken line in Figure 1 shows the theoretical cross section predicted by the Shapiro theory using a nuclear radius parameter of 1·3 fermi. The curve has been arbitrarily normalized to fit the experimental data. As is seen, the general trend of the cross section is in good agreement with the theory. However, the eight peaks appear as definite anomalies. Conventional ideas of compound nucleus formation suggest that, in the energy region involved in this experiment, the levels in ^{64}Zn would be only about 20 keV apart. Levels with this spacing would not be resolved in the present experiment and the resultant cross-section curve would be expected to resemble the theoretical curve due to Shapiro over the whole energy range. The presence of the eight peaks shows that the simple compound nucleus concept is not entirely adequate.

While it is possible to postulate that the observed peaks are due to a fortuitous grouping of a number of compound nucleus levels, a more plausible explanation of the structure may be obtained by considering a single-particle model. The addition of a proton to ^{63}Cu to form ^{64}Zn in an excited state may be considered to occur in either of two ways:

(i) by the addition of a proton to the ground state of ^{63}Cu so that the bombarding particle becomes the excited particle in ^{64}Zn, or
(ii) by the addition of a proton into the nucleus of ^{63}Cu followed by the excitation of one of the nucleons from the target nucleus.

The first process leads to a number of relatively widely spaced levels while the latter process leads to a large number of closely spaced levels. The single-particle picture therefore allows for the possibility of a number of widely spaced levels due to process (i) superimposed on a continuum due to all possible processes of type (ii). It is not impossible that type (ii) processes may also produce a limited number of resolvable levels.

While the single-particle picture gives a plausible qualitative explanation for the presence of resonances in the cross section obtained in the present experiment, it is necessary to show that the observed levels occur at the correct energies and to explain the absence of observed peaks at bombarding energies greater than 8·1 MeV.

Calculations of the binding states of individual nucleons in strongly deformed nuclei have been made by Nilsson (1955). The basis of the calculations was a model for the interaction of nucleons with a deformed nuclear field. Nilsson introduced a single-particle Hamiltonian containing a modified ellipsoidal oscillator and a spin-orbit term. From these calculations the single-particle states in ^{64}Zn may be found provided the nuclear deformation parameter η is known. Stelson and McGowan (1960) have obtained an experimental value for the deformation δ of ^{64}Zn by a Coulomb excitation technique. The value obtained is $\pm(0\cdot21\pm0\cdot03)$. The sign of the deformation cannot be determined by this technique.

The parameter δ, determined experimentally, and the parameter η, used in the Nilsson theory are linked by the relation

$$\delta=\varkappa\eta f(\delta).$$

The term $f(\delta)$ can be taken to be unity without affecting calculations by more than 1%. However, it is necessary to know the value of the constant $\varkappa$ before values of η and δ can be compared. Nilsson assigns a value of $0\cdot05$ to $\varkappa$. There is, however, some doubt as to its true value and it may well vary from nucleus to nucleus. It seems likely that in the region of ^{64}Zn, $\varkappa$ should be, if anything, larger than $0\cdot05$.

Using the scheme formulated by Nilsson, calculations have been made of the single-particle states of ^{64}Zn assuming values of η of $-3\cdot2$, $-3\cdot4$, $-3\cdot6$, $-3\cdot8$, $-4\cdot0$, $-4\cdot4$, and $+4\cdot0$. Of these values, $\eta=-3\cdot6$ and $\eta=-3\cdot8$ give good agreement with the experimental results. The remainder do not. It appears unlikely that any positive value of η will give good agreement. For $\eta=-3\cdot6$ and an energy step of $10\cdot0$ MeV per unit (Nilsson suggests $10\cdot25$ MeV for ^{64}Zn), it is found that the single-particle states of ^{64}Zn lie at excitations of $13\cdot00$, $13\cdot30$, $13\cdot50$, $15\cdot02$, $15\cdot19$, $15\cdot51$, $15\cdot73$, and $17\cdot23$ MeV. This is shown in Figure 3, where the parameter δ is computed on the assumption that $\varkappa=0\cdot05$. These results agree within 2% with the experimentally observed values of $13\cdot3_7$, $13\cdot7_5$, $14\cdot9_0$, $15\cdot1_8$, $15\cdot6_1$, and $15\cdot7_7$ MeV. They do not explain the presence of the peaks observed at $14\cdot1_2$ and $14\cdot3_1$ MeV. The Nilsson prediction of a peak at $13\cdot00$ MeV corresponds to a proton energy of $5\cdot30$ MeV. It was pointed out earlier that there was slight evidence for a peak at a proton energy of $5\cdot1_8$ MeV. It would thus seem possible that this was in actual fact a weak resonance. The predictions also suggest the existence of another single-particle state at a proton energy of about $5\cdot0$ MeV. It is probable that this was not found because the proton energy was not reduced sufficiently. Considering the inaccuracy involved in the assessment of the energy of a peak superimposed on a rising curve, the agreement between the Nilsson theory and the experimental data is very good. It is possible that the two observed peaks which are not explained by the Nilsson theory are due to processes of type (ii) referred to above.

Another interesting feature of the Nilsson theory is that it predicts the absence of peaks for $1\cdot5$ MeV above an excitation of $15\cdot7$ MeV. This also is in agreement with experiment. At excitation energies above $17\cdot23$ MeV, the Nilsson theory predicts a number of relatively close spaced levels which could not be resolved in this experiment.

To check whether the value of η (and consequently δ) required to fit the experimental data is sensitive to small errors in the experimentally determined energies of the peaks, calculations have been made assuming the cyclotron energy calibration to be correct at 5 MeV and to have a linearly increasing error up to 1% at 8 MeV. These calculations show no significant changes in η, and the unit energy necessary to predict the positions of the peaks.

If Nilsson's value of 0·05 for the constant $\varkappa$ is correct, this experiment gives a value for δ of about $-0 \cdot 18$ or $-0 \cdot 19$ for ^{64}Zn. The magnitude of this agrees reasonably well with the value of $\pm(0 \cdot 21 \pm 0 \cdot 03)$ obtained by Coulomb excitation. However, it is not possible to draw significant conclusions from the agreement, since the value of δ depends directly on the assumed value of $\varkappa$.

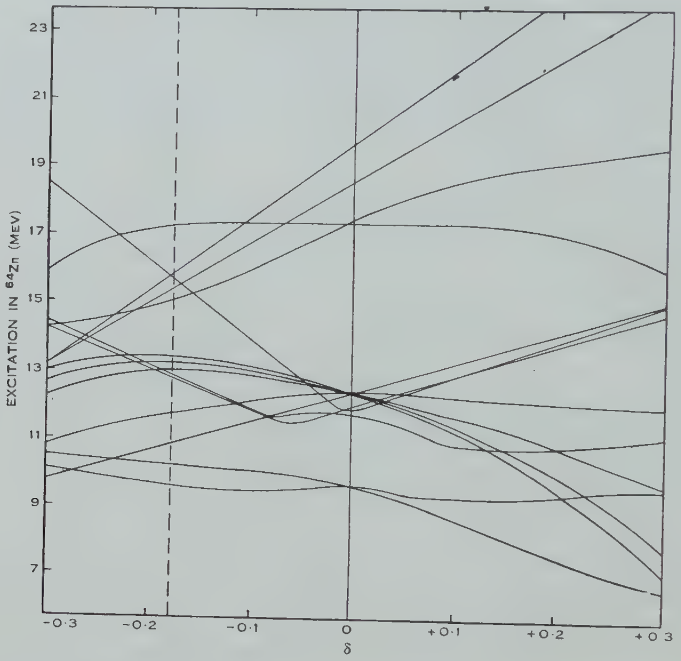

Fig. 3.—Nilsson scheme showing the locations of excited states in ^{64}Zn as a function of deformation parameter δ.

V. Conclusions

The agreement between the levels predicted by the Nilsson theory and those found experimentally appears to be quite good. This result indicates the probability of highly excited states of ^{64}Zn which are formed by the excitation of a single particle.

If this interpretation is correct, the deformation of ^{64}Zn must be negative, at least in its highly excited states, since no assumption of positive deformation leads to a fit with the experimental data.

VI. Acknowledgments

The authors wish to acknowledge the assistance of Dr. J. L. Rouse and members of the cyclotron team who assisted in the running of the cyclotron and the taking of data during this experiment. Our thanks are due to Dr. B. M. Spicer with whom we have had many helpful discussions concerning deformed nuclei. The cooperation of the C.S.I.R.O. Division of Tribophysics in providing the copper targets is gratefully acknowledged. One of us (M.J.K.) acknowledges the receipt of a University Research Grant during the time in which this experiment was carried out.

VII. REFERENCES

BLASER, J. P., BOEHM, F., MARMIER, P., and PEASLEE, D. (1950).—*Helv. Phys. Acta* **24** : 3.
GHOSHAL, S. N. (1950).—*Phys. Rev.* **80** : 939.
HOWE, H. A. (1958).—*Phys. Rev.* **109** : 2083.
NILSSON, S. (1955).—*Math.-fys. Medd.* **29**, Nr. 16.
SHAPIRO, M. (1953).—*Phys. Rev.* **90** : 172.
STELSON, P., and MCGOWAN, K. (1960).—O.R.N.L. 2910/UC34, February 12, 1960.

SUM–COINCIDENCE MEASUREMENTS ON ^{154}Eu

By A. W. Parker*

[*Manuscript received February 24, 1961*]

Summary

By examining γ-rays from the radioisotope ^{154}Eu with a fast-slow sum-coincidence spectrometer any β-transition to a possible $1 \cdot 82$ MeV level in ^{154}Gd has been shown to have an abundance less than 1% of that of the β-transition to the neighbouring $1 \cdot 72$ MeV level. The presence of a $1 \cdot 60$ MeV γ-ray from the $1 \cdot 72$ MeV level is confirmed; the intensity of this γ-ray was found to be $6 \cdot 4$% of that of the $1 \cdot 28$ MeV γ-ray.

I. Introduction

The current knowledge of the energy levels of ^{154}Gd has been obtained from a study of the radioisotopes ^{154}Eu and ^{154}Tb. The results of these experiments have been tabulated by Way *et al.* (1959), and Figure 1 shows the levels populated by the decay of ^{154}Eu.

A level at $1 \cdot 82$ MeV was suggested by Cork *et al.* (1957) because, in an investigation of the decay of ^{154}Eu, they found a β-transition with an end point of 150 keV. They estimated the abundances of β-transitions to the $1 \cdot 82$ and $1 \cdot 72$ MeV levels to be 12% and 28% of all β-transitions. However, Way *et al.* (1959) suggest that the 150 keV transition occurs in the decay of ^{155}Eu.

Cork *et al.* (1957) also suggested that the $1 \cdot 82$ MeV level de-excites by a 694 keV γ-transition. Toth and Rasmussen (1959) also detected a γ-ray of 692 keV in the decay of ^{154} Tb; and they recalculated the energy of an intense γ-transition, detected by Juliano and Stephens (1957), from fission-produced ^{154}Eu in which ^{152}Eu was absent. This they showed to be 692 keV. On the other hand, other workers (Gallagher and Thomas 1959; Nathan and Hultberg 1959; Sheline 1960; Marklund, Van Nooijen, and Grabowski 1960) have suggested that this γ-ray may result from the de-excitation of either a 692 keV level or a 815 keV level—via the 123 keV level—in ^{154}Gd.

Further evidence for the presence of a $1 \cdot 82$ MeV level is suggested by the measurements of Jha *et al.* (1959), who used a fast-slow sum-coincidence spectrometer to investigate the γ-rays of ^{154}Eu. However, their results were not conclusive because of poor statistics and because they did not completely consider the effects of triple coincidences.

No γ-ray from the $1 \cdot 29$ MeV level shown in Figure 1 to the ground state is known, and no 100 keV transition which might occur between the $1 \cdot 821$ and $1 \cdot 723$ MeV levels has been observed. Hence, by far the most probable mode of de-excitation of a 1·821 MeV level will be via the 0·692–1·006–0·123 MeV cascade. The present paper describes sum-coincidence measurements aimed at detecting this triple cascade and thus obtaining information on the existence of a 1·821 MeV level.

---

* Physics Department, University of Melbourne.

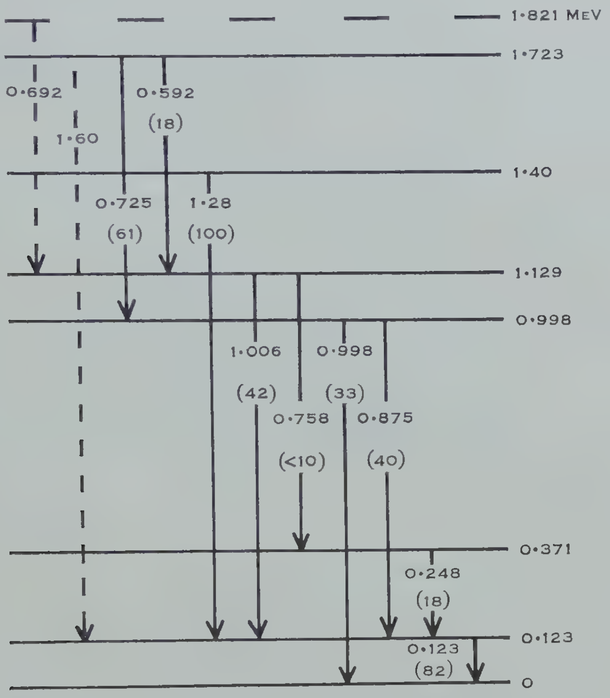

Fig. 1.—Energy levels of $^{154}_{64}$Gd as determined in the β-decay of $^{154}_{63}$Eu.

II. Method

The ^{154}Eu source used for these measurements was obtained from the Oak Ridge National Laboratory, and was prepared by the neutron capture of 99·4% enriched ^{153}Eu. γ-Rays from this source were detected by a fast-slow sum-coincidence spectrometer similar to that suggested by Hoogenboom (1958). Two 1·5 in. diameter by 1 in. thick Na(Tl) crystals were used, and β-rays were absorbed by the canning material which consisted of 0·7 mm of aluminium and 2·0 mm of magnesium oxide.

A block diagram of the apparatus is shown in Figure 2. Pulses from the two detectors are summed, and a narrow window includes only those pulses corresponding to the energy level of interest. If, for example, the level decays only by a simple double cascade, the coincidence spectrum will show two Gaussian peaks corresponding to the full energy peaks of the γ-rays. In this apparatus a fast-coincidence unit is used to reduce random coincidences, and so the coincidence spectrum does not show a full energy peak corresponding to both γ-rays being absorbed in one detector. Random-coincidence spectra were obtained by inserting a long delay at the input to one channel of the fast-coincidence unit.

Hoogenboom (1958) has shown that the half-width Γ_{S1} of a sum-coincidence peak is given by

$$\Gamma_{S1}=\Gamma_1(\Gamma_2^2+\Gamma_S^2)^{\frac{1}{2}}/(\Gamma_1^2+\Gamma_2^2+\Gamma_S^2)^{\frac{1}{2}},$$

where Γ_1 and Γ_2 are the half-widths of the two γ-ray peaks in the singles spectrum and Γ_S is the half-width of the sum channel. Further, the detection efficiency ε_{S1} of this peak is given by

$$\varepsilon_{S1}=2\{(\ln 2)/\pi\}^{\frac{1}{2}}\varepsilon_1\varepsilon_2\Gamma_S/(\Gamma_1^2+\Gamma_2^2+\Gamma_S^2)^{\frac{1}{2}},$$

where ε_1 and ε_2 are photo-peak efficiencies (including solid angle).*

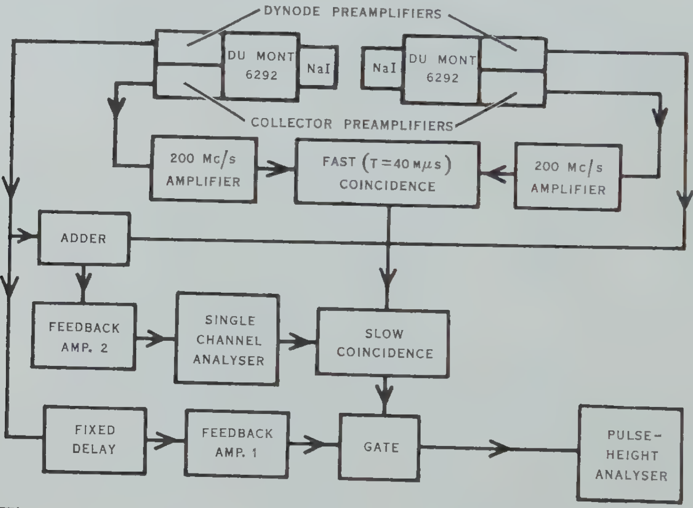

Fig. 2.—Block diagram of the fast-slow sum-coincidence spectrometer.

Triple cascades are detected by two γ-rays being absorbed in one detector whilst the third γ-ray is absorbed in the other, thus producing six peaks of energies E_1, E_2, E_3, E_1+E_3, E_2+E_3, and E_3+E_1 in the coincidence spectrum. Using assumptions similar to those of Hoogenboom (1958) it is easily shown that, while the sum peaks E_1+E_2 etc. are not strictly Gaussian, the half-width Γ_{S1} for the peak E_1 is given by

$$\Gamma_{S1}=\Gamma_1(\Gamma_2^2+\Gamma_3^2+\Gamma_S^2)^{\frac{1}{2}}/(\Gamma_1^2+\Gamma_2^2+\Gamma_3^2+\Gamma_S^2)^{\frac{1}{2}}.$$

However, the detection efficiencies of the peaks E_1 and E_2+E_3 are equal for matched detectors and

$$\varepsilon_{S1}=2\{(\ln 2)/\pi\}^{\frac{1}{2}}\varepsilon_1\varepsilon_2\varepsilon_3\Gamma_S/(\Gamma_1^2+\Gamma_2^2+\Gamma_3^2+\Gamma_S^2)^{\frac{1}{2}}.$$

In this experiment only the relative detection efficiencies for double and triple cascades are of interest and hence the factors involving half-widths may be neglected; but an additional factor is required when 123 keV transitions are involved because of internal conversion. Hence the double- and triple-coincidence rates C_D and C_T were estimated using the formulae

---

* Values of these efficiencies were taken from Mott and Sutton (1958).

$$C_D = N_D\varepsilon_1\varepsilon_2/(1+\alpha), \quad C_T = N_T\varepsilon_1\varepsilon_2\varepsilon_3/(1+\alpha), \tag{1}$$

where $\alpha = N_e/N_\gamma$ is the internal conversion coefficient of the 123 keV transition. Here N_D is the transition rate of the 1·60 MeV γ-ray leading directly to the 123 keV level and N_T is the transition rate leading to this level via a double cascade.

This sum-coincidence spectrometer was easily modified to display the summed output from the two detectors. The modification involved connecting amplifier 2 to the gate input and opening the gate with the fast-coincidence unit. Dead-time corrections to the kicksorter were avoided by inserting a scale-of-ten between the fast-coincidence unit and the gate. An energy calibration curve was obtained by removing one input to the adder so that pulses from one counter only were accepted when the scale-of-ten recorded a fast coincidence.

For a double cascade using this latter arrangement, the two photo-peaks sum to produce a peak E_1+E_2, and the coincidence rate is given by $2C_D$, where C_D is the rate calculated from equation (1); similarly, a triple cascade produces a peak $E_1+E_2+E_3$ and the coincidence rate is given by $6C_T$.

With either arrangement of this apparatus the ability to distinguish neighbouring energy levels is dependent on the energy resolution of the corresponding summed peaks. Thus reference to Figure 1 shows that any attempt to detect γ-rays from a possible 1·821 MeV level must allow for the overlapping of the summed peak associated with the 1·723 MeV level. This was done by using the first arrangement described above. In this case, the sum-coincidence spectrum displays the detailed composition of the sum peak presented to the window. A significant variation of this composition as the window height is increased above 1·723 MeV would then indicate the presence of the 1·821 MeV level. Since Figure 1 also indicates that the presence of a 1·6 MeV γ-ray from the 1·723 MeV level has not been definitely established, it is clear that the starting point of these measurements is the investigation of γ-rays associated with this level.

From this type of coincidence data it is also possible to calculate the relative abundance of β-transitions to these two levels. However, for this calculation the data were supplemented by measurements of the summed output of the detectors using the second arrangement, because this avoids uncertainties associated with the relatively wide window and its transmission characteristics.

III. RESULTS

Figure 3 shows the sum-coincidence spectrum with the window height set at 1·75 MeV and the window width set at 0·023 MeV. The three peaks* shown correspond to the cascades 0·725–0·998 and 1·60–0·123 MeV. Using equation

---

* The fourth expected peak at 123 keV was removed by the bias applied to the linear gate. Only that portion of the spectrum above about 0·3 MeV is shown because the gate occasionally passed large non-coincident pulses at a reduced level, and hence the spectrum in the first five channels of the kicksorter was unreliable.

(1) with $\alpha=1\cdot5$, together with the relative intensities of Figure 1, the corresponding intensity of the 1·60 MeV γ-ray was found to be $6\cdot4\pm0\cdot5$, the error shown being the statistical error in the present experiment. The distance of the source from the crystals was 4·5 cm and, with this geometry, triple cascades can contribute less than 3% of the peak counts, while the true-to-random ratio for the cascades was found to be 12 and 18 respectively.

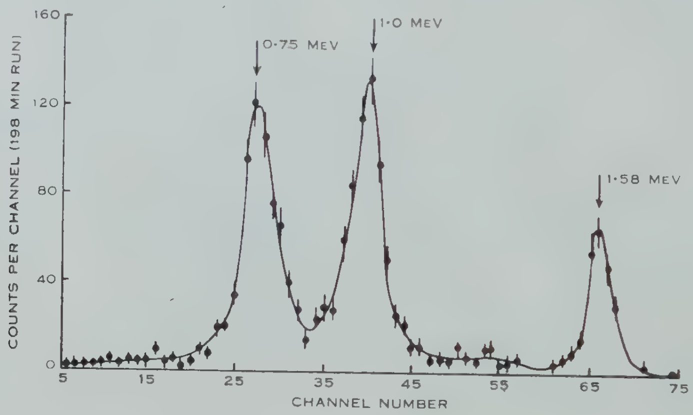

Fig. 3.—Sum-coincidence spectrum at 1·75 MeV with the source distance 4·5 cm.

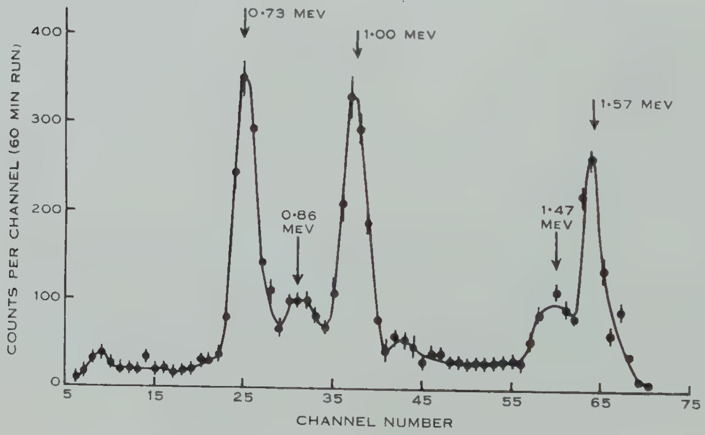

Fig. 4.—Sum-coincidence spectrum at 1·725 MeV with the source distance 0·5 cm.

Figure 4 shows the sum-coincidence spectrum with the window set at 1·725 MeV but with the crystals closer together and a weaker source placed 0·5 cm from each. With this geometry four cascades of 0·725–0·998, 1·60–0·123, 0·725–0·875–0·123, and 0·592–1·006–0·123 MeV should be detected. By use of the data from Figure 3 and the γ-ray intensities from Figure 1, the relative intensities of the peaks expected in this spectrum can be estimated. Table 1 shows these calculated intensities. These relative intensities are expected to be accurate to about 10%.

In the spectrum, the peaks at 0·725 and 0·715 MeV cannot be resolved. Hence it is expected that the peak at 1·60 MeV will have an intensity of 56/108=0·52 of that of the peak actually observed at 0·725 MeV. The experimental value of this ratio, calculated from the areas under the peaks, is 0·60±0·05, which is in reasonable agreement with this prediction. It is difficult to achieve any accuracy in the measurement of the intensities of the weaker peaks, but their intensities are certainly of the same order of magnitude as those predicted in Table 1, provided allowance is made for backscattering, which contributes to the peaks at 0·86 and 1·47 MeV.

Table 1

Expected intensities of the peaks in the spectrum of figure 4

Energy .. .. (MeV)	0·123 1·60	0·592 1·129	0·715 1·006	0·725 0·998	0·848 0·875
Relative intensity ..	56	8	8	100	15

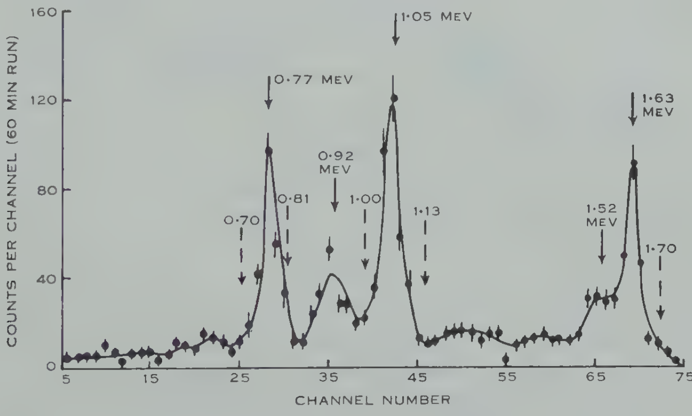

Fig. 5.—Sum-coincidence spectrum at 1·825 MeV with the source distance 0·5 cm.

Figure 5 shows the spectrum obtained with the window set at 1·825 MeV. This shift in the position of the window is less than the width of the sum peak at 1·723 MeV which is presented to the window. Hence it is expected that the peaks of the 1·723 MeV spectrum will still be present—although at lower intensities—but will be displaced in the direction of higher energies. This effect has been discussed by Hoogenboom (1959).

The 0·692–1·006–0·123 MeV cascade from the 1·821 MeV level, if present, should produce peaks at energies of 0·123, 0·69, 0·81, 1·01, 1·13, and 1·7 MeV and these peaks in the sum-coincidence spectrum should all have equal intensities. There is no evidence for any of these peaks in Figure 5.

The spectrum of summed pulses due to γ-rays from the 1·723 MeV level had a " tail " which would still be of appreciable intensity at a pulse height corresponding to 1·825 MeV, and might tend to mask any pulses in this region due to γ-rays from the 1·821 MeV level. With the window set somewhat above this pulse height, the reduction in the " tail " of the 1·723 MeV pulses should be considerably greater than that in the pulse-height distribution due to any genuine 1·821 MeV sum distribution. For this reason a spectrum was taken with the window set at 1·88 MeV, and the result is shown in Figure 6.

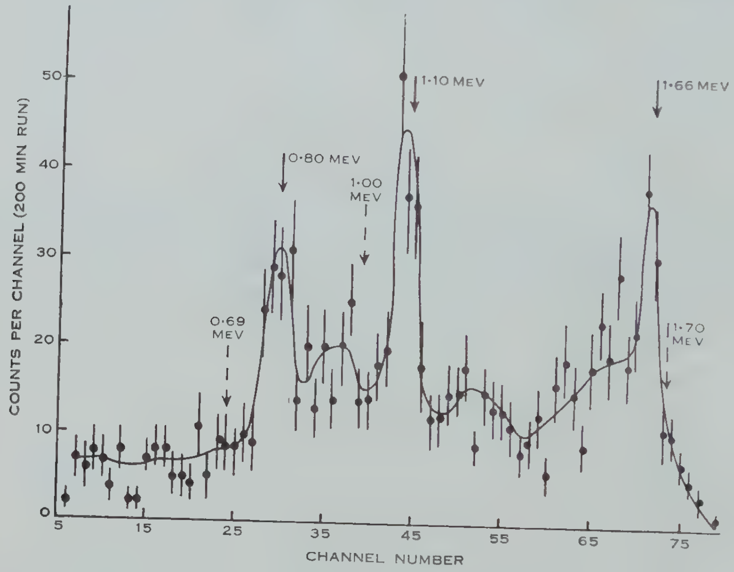

Fig. 6.—Sum-coincidence spectrum at 1·88 MeV with the source distance 0·5 cm.

Comparison of Figure 4 with Figures 5 and 6 strongly suggests that these latter are dominated by γ-rays from the 1·723 MeV level. This conclusion is reinforced by the following consideration. The ratio of the total area under the peaks at 0·725 and 1·006 MeV to that under the peak at 1·62 MeV in Figure 4 is 3·2 ±0·3. The same ratio has the values 2·9 ±0·5 and 2·8 ±0·5 for the spectra of Figures 5 and 6 respectively.

An estimate of an upper limit for the contribution to the spectrum of Figure 6 from γ-rays associated with the 1·821 MeV level may be made as follows. No definite peaks are apparent at energies of 0·69, 0·82, 1·0, 1·13, and 1·70 MeV, and, since these peaks would not all be completely obscured by the displaced peaks associated with the 1·723 MeV level, a visual inspection of Figure 6 shows that it is reasonable to associate not more than 20 counts with each of these possible peaks. Also Figure 4 may be suitably normalized and superposed on Figure 6. Again 20 counts is an absolute upper limit to the intensity of any one of these peaks. Hence a total of 100 counts may be associated with the

1·821 MeV level, and this may be compared with the total number of counts, 1060, in Figure 6. It is therefore certain that not more than 10% of the pulses which sum to 1·88 MeV are associated with γ-rays from any 1·821 MeV level.

Figure 7 shows the spectrum of the summed output of the two detectors, the energy calibration spectrum, and the random-coincidence spectrum. These support the previous conclusion that any level at 1·821 MeV is very weakly populated. The ratio of counts at 1·723 and 1·821 MeV is 24; but the previous sum-coincidence measurements show that less than 10% of the pulses in the "tail" of the 1·723 MeV peak can come from γ-rays associated with the 1·821 MeV level. Thus the lower limit on R_C, the ratio of the counts associated with the 1·723 MeV level to those associated with the 1·821 MeV level is increased from 24 to 240. Now, if the internal conversion of γ-rays from the 1·821 MeV level is negligible, the ratio R of the abundances of the β-transitions to these levels is simply the ratio of the total γ-ray transition rates from the two levels.

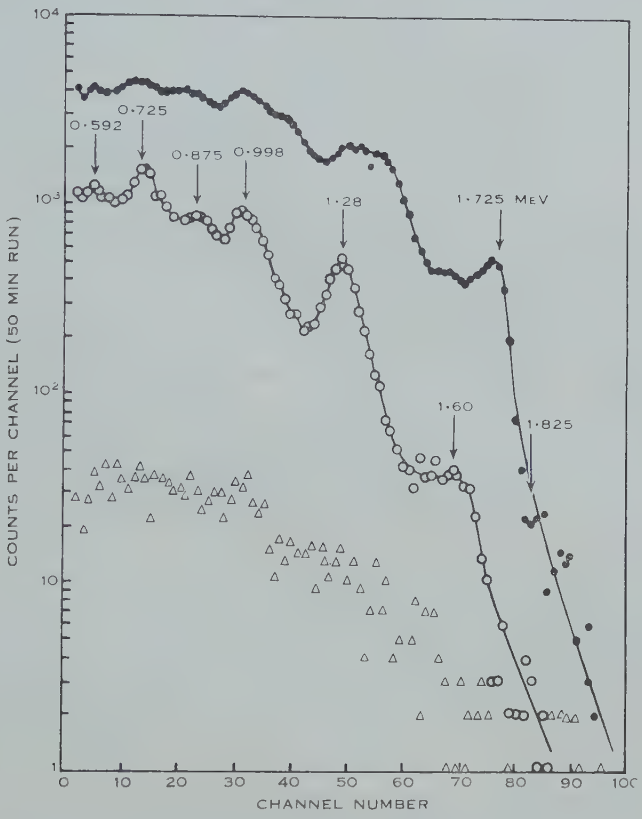

Fig. 7.—Summed spectrum (●), energy calibration spectrum (○) (15 min run), and random-coincidence spectrum (△) with the source distance 0·5 cm.

The relation between R and R_C may then be obtained as follows. The 1·723 MeV level de-excites by three γ-rays of known relative transition rates, Since the total transition rate is the sum of these separate rates, these separate rates may be expressed as fractions of the total transition rate. Also, the branching ratios of γ-rays from lower levels are known, and hence the coincidence rate due to a definite cascade may be expressed in terms of the total transition rate by using equations (1) as explained in Section II. By summing the coincidence rates due to different cascades, the total coincidence rate is thus expressed in terms of the total transition rate. Similarly, the total coincidence rate due to γ-rays associated with the 1·821 MeV level may be related to the total transition rate from that level; in this case the calculation is simplified because it is assumed that this level de-excites only by the 692–1006–123 keV cascade. The ratio of these two total coincidence rates then leads to the result that $R=0\cdot 50R_C$. Thus since $R_C>240$, $R>120$, i.e. any β-transition to a possible 1·821 MeV level has an abundance of less than 1% of that of the β-transition rate to the neighbouring 1·723 MeV level.

IV. Discussion

Measurements made by Juliano and Stephens (1957) and by Bhattacharjee, Raman, and Mitra (1958) using scintillation spectrometers indicated the possible presence of a 1·60 MeV γ-ray. The values of the intensity of this γ-ray found in these two experiments were 7·4 and 4 respectively, on the intensity scale shown in Figure 1. However, coincidence measurements made by them were inconclusive in that they failed to confirm the existence of this γ-ray.

The sum-coincidence measurements of Jha *et al.* (1959) showed a peak at 1·6 MeV, but the intensity of their peak is consistent with its being formed as a result of two triple cascades. Hence their results suggest the absence of a 1·6 MeV γ-ray.

The present experiment indicates the presence of this γ-ray, with an intensity, on the same scale mentioned above, of 6·4±0·5. However, the accuracy of this result depends on the assumed value of the internal conversion coefficient of the 123 keV γ-ray, and also on the relative intensities of the other γ-rays as found by other workers. Taking these factors into consideration increases the possible range of error to 20%, so that the final result for the intensity of this γ-ray is 6·4±1·3.

The present experiment also suggests that no level exists at 1·821 MeV in ^{154}Gd. If this is so, the query raised by Way *et al.* (1959) as to the interpretation of the angular correlation measurements of Hickman and Wiedenbeck (1958) no longer applies. Furthermore, this result removes one of the possibilities of fitting the 692 keV γ-transition into the level scheme of ^{154}Gd. Although this transition may come from the low-energy 0+ β-vibrational state predicted by Sheline (1960), the present experiment gives no direct information on the existence of low-energy states.

V. Acknowledgments

The author would like to thank Dr. J. A. McDonell for his interest and for many helpful discussions during the course of this work. The author also wishes to acknowledge the tenure of a Commonwealth Postgraduate Award.

VI. REFERENCES

BHATTARCHARJEE, S. K., RAMAN, S., and MITRA, S. K. (1958).—*Proc. Indian Acad. Sci.* **47A** : 295.

CORK, J. M., BRICE, M. K., HELMER, R. G., and SARASON, D. E. (1957).—*Phys. Rev.* **107** : 1621.

GALLAGHER, C. J., JR., and THOMAS, T. D. (1959).—*Nuclear Phys.* **14** : 18.

HICKMAN, G. D., and WIEDENBECK, M. L. (1958).—*Phys. Rev.* **111** : 539.

HOOGENBOOM, A. M. (1958).—*Nuclear Instruments* **3** : 57.

HOOGENBOOM, A. M. (1959).—In " Nuclear Electronics ", Vol. I. (International Atomic Energy Agency : Vienna.)

JHA, S., DEVARE, H. G., RAO, M. N., and PRAMILA, K. G. C. (1959).—*Proc. Indian Acad. Sci.* **50A** : 303.

JULIANO, J. O., and STEPHENS, F. S., JR. (1957).—*Phys. Rev.* **108** : 341.

MARKLUND, I., VAN NOOIJEN, B., and GRABOWSKI, Z. (1960).—*Nuclear Phys.* **46** : 533.

MOTT, W. E., and SUTTON, R. B. (1958).—In " Handbuch der Physik ", Vol. XLV. (Springer: Berlin.)

NATHAN, O., and HULTBERG, S. (1959).—*Nuclear Phys.* **10** : 118.

SHELINE, R. K. (1960).—*Rev. Mod. Phys.* **32** : 1.

TOTH, K. S., and RASMUSSEN, J. O. (1959).—*Phys. Rev.* **115** : 150.

WAY, K., *et al.* (1959).—" Nuclear Data Sheets." (National Research Council : Washington. D.C.)

A SKY SURVEY OF NEUTRAL HYDROGEN AT λ 21 CM

I. THE GENERAL DISTRIBUTION AND MOTIONS OF THE LOCAL GAS

By R. X. McGee* and J. D. Murray*

[*Manuscript received February 20, 1961*]

Summary

A survey for neutral hydrogen of the whole sky visible from Sydney has been carried out with a multichannel H-line receiver and a 2°·2 aerial beam. A sample of the profiles obtained has been analysed to present the disposition of local hydrogen in terms of three schematic diagrams : (1) the distribution of N_H, the number of hydrogen atoms in a line-of-sight column of 1 cm² section, (2) a diagram of representative line half-widths, and (3) the observed distribution of profile peak radial velocities.

Indications were found that the gas is stratified parallel to the galactic plane in general but with some regions of excess density. From the orientation of the N_H contours it is inferred that the local hydrogen may have some correlation with the local galactic magnetic field.

The line profiles away from the Milky Way were mostly single peaked and of half-widths 12–35 km/s, except in some large regions near the galactic poles where wide profiles of half-widths 36–140 km/s were observed. Large-scale grouping of profiles in the range from 12 to 20 km/s occurred, corresponding closely with some of the outstanding features in the N_H distribution.

The peak radial velocity distribution showed evidence of differential galactic rotation at middle and low latitudes and lack of data on distance prevented the complete removal of this effect. However, it was established that in the solar vicinity hydrogen is flowing outwards at a mean radial velocity of +6 km/s in these latitudes near the direction of the galactic centre and anticentre. It is flowing inwards from above and below in high galactic latitudes at a mean velocity of about −6 km/s.

I. INTRODUCTION

The whole sky visible from Murraybank (lat. −33°·75), near Sydney, has been observed with a multichannel 21-cm hydrogen line receiver and a wide-beam (2°·2 between half-power points) aerial. Because the hydrogen in the Galaxy is concentrated in a very thin layer, the bulk of these observations pertain to hydrogen close to the Sun, i.e. within a few layer thicknesses. In this paper, intended as the first of a series on the large-scale distribution of neutral hydrogen, the general disposition of gas in the local neighbourhood will be discussed.

Three previous surveys of hydrogen have been reported which include extensive observations away from the galactic plane. Christiansen and Hindman (1952) made pioneer observations to ±50° in galactic latitude. Erickson, Helfer, and Tatel (1959) at D.T.M., Washington, observed hydrogen in latitudes outside ±20°. Recently, Davies (1960) has covered the same region and extended observations to include the sky between ±20°.

---

* Division of Radiophysics, C.S.I.R.O., University Grounds, Chippendale, N.S.W.

In the present work the disposition of local neutral hydrogen is presented in terms of three schematic diagrams. One is the distribution of N_H, the number of hydrogen atoms in a line-of-sight column of 1 cm^2 section, the second is a diagram of sample line half-widths, the variations of which show some correlation with features in the N_H contours, and the third is the observed distribution of profile peak radial velocities.

II. Equipment and Observations

Although the equipment has been briefly described elsewhere (McGee and Murray 1959) a short account will be given here in view of recent improvements and modifications.

The receiver is of the conventional double-conversion superheterodyne type switched between the H-line frequency (1420·406 Mc/s) and a reference frequency 2·5 Mc/s above. The figure of merit as an excess noise temperature is about 800 °K. The later stages are split up into 50 channels, most of which are tuned at frequency intervals equivalent to 7 km/s in radial velocity. The outer two channels on each side of the reception band are used as zero line markers. The filters in these channels are 0·5 Mc/s between half-power points and are placed so as to completely fill the two frequency ranges between the first and last of the 7 km/s channels and frequencies $\pm 1\cdot 5$ Mc/s (equivalent to $\sim\pm 320$ km/s) from the central natural line frequency. A complete H-line profile is recorded every 2 min in sidereal time.

Changes to the primary feed of the aerial have improved the beamwidth to 2°·2 between half-power points.

A switched noise source at the vertex of the paraboloid provides a relative intensity calibration for the equipment. Deflections up to 200 °K aerial temperature are possible. It was found that the receiver sensitivity did not alter by more than a few per cent. over the entire survey.

Frequency monitoring depended on comparisons of harmonics of the crystal-controlled local oscillators with signals from WWV. Owing to various deficiencies in signal reception at the long range of WWV the accuracy in terms of radial velocity is restricted to 0·3 km/s. Recently, extensive tests made with a very accurate frequency counter indicate that both local oscillators have frequency stability better than one-tenth of this figure.

Sky observations were taken at meridian transit at intervals of 1° in declination from Dec. $-90°$ to Dec. $+42°$ over periods of 24 hr on each observing position. An H-line profile was evident at almost every point observed. The limit of sensitivity, governed by receiver noise plus inherent interchannel differences in zero level, was set by an r.m.s. fluctuation level of about 0·7 °K on a single profile. More than 95000 profiles were collected during the survey. The reproducibility of each profile selected for reduction was easily checked, in that two profiles in declination and a minimum of four in right ascension coordinates were recorded per aerial beamwidth. Instrumental resolution in both frequency and aerial beam size has produced a lower limit of about 12 km/s in the observed profile half-widths.

III. TREATMENT OF THE DATA

The diagrams in this paper are based on analysis of a sample from the mass of observations mentioned above. It is intended in succeeding papers to present data based on profiles at intervals of at least one degree in each coordinate. Work on this aspect of the project has been in progress on a large area around the galactic centre and in view of the large-scale features revealed in the intensity and particularly in the radial velocity contours it was decided to study first the gross distributions around the whole sphere. The sample consists of observations made at 2° intervals in galactic latitude along meridians of longitude 30° apart. It was found that all the essential features of the detailed charts remained while localized elements were conveniently eliminated. With the recent completion of preliminary detailed diagrams for the whole survey it has been possible to further check the sampling procedure and make some small corrections that were required in the regions near the galactic plane.

(a) *The H-line Profiles*

The profiles reduced could be divided into three classes. The first and most widely distributed over the sky were those obviously representing local gas: the half-widths were in the range from 12* to 35 km/s, in almost all cases they were single peaked and the values for the peak radial velocities did not exceed ±12 km/s. The maximum intensity of this class was ~50 °K.

Inside $b^{\mathrm{I}} = \pm 10°$ the galactic spiral structure was evident by the appearance of very wide and usually multi-peaked profiles of much greater intensity than elsewhere. The " local " gas was traced across this region by selecting a profile peak whose value was close to that of the single-peaked profiles immediately outside it. The " local " peak was unambiguous in some cases but in others the portion of profile selected as " local " probably contained contributions from more distant gas.

The third class of profile was obtained mainly in low intensity regions at high galactic latitudes. The half-widths ranged from 36 to 140 km/s. Some profiles exhibited two or three fairly definite peaks.

(b) *The H-line Intensities and Quantity of Neutral Hydrogen*

The quantity of local neutral hydrogen is indicated in terms of N_{H}, the number of hydrogen atoms in a 1 cm² line-of-sight column. Values of N_{H} were obtained in the following way. The observed H-line aerial temperatures were converted to brightness temperatures using a statistically established scale between Murraybank and Leiden temperatures. The optical depth of local gas appears to be quite low (profile maximum temperature rarely exceeded 60 °K) so that following from the calculations of Wild (1952) and others we may use the relation

$$N_{\mathrm{H}} = 1\cdot 84 \times 10^{18} \int_{-\infty}^{\infty} T(v)\mathrm{d}v,$$

---

* This value is limited by instrumental resolution.

where the numerical factor results from inserting the values for the atomic constants etc., T is the H-line brightness temperature in degrees Kelvin, and v is the radial velocity in kilometres per second. We assume that the integration extends over the local gas only.

A contour diagram of N_{H} is given in Figure 1 on an Aitoff projection using old galactic coordinates (Ohlsson).* The contour interval is $0 \cdot 2 \times 10^{21}$ H atoms cm^{-2}. In the region of the galactic plane indicated by the hatching N_{H} exceeds $2 \cdot 0 \times 10^{21}$ H atoms cm^{-2} and no data are given because of uncertainties in separating out local gas profiles.

(*c*) *The H-line Half-widths*

Figure 2 is an attempt to show how the shapes of the profiles vary over the sky. Sample profiles were selected to represent the gas in a latitude range of 10° along the 12 galactic longitudes. The half-width of a profile is indicated at its representative position by a whole number (km/s) and by the length of a rectangle drawn about the l^{I} meridian. The black portion to the left of a meridian indicates negative radial velocities and the white portion to the right positive velocities. The relative position of the profile peak is given by the arrowhead on top of each rectangle.

(*d*) *The Radial Velocity of the Gas*

Profile " peak " radial velocities, i.e. the velocities at the points of maximum brightness temperature on the H-line profiles, have been chosen to represent the velocity distribution of the gas. It will be noticed on inspection of the arrowhead positions in Figure 2 that peak and median values would be very close in the greater proportion of profiles. In any case we consider peak velocities a better indication of local gas velocity.

Observed peak values were read from the chart records to an accuracy of 1 km/s. They were corrected to allow for the Earth's orbital motion and the solar motion and are specified relative to the local standard of rest with the aid of Lund Observatory Tables.†

The large-scale distribution of radial velocities of local neutral hydrogen is presented in Figure 3. In the light grey shaded area velocities are positive, in the dark grey shaded areas negative, and in the white, zero. The contour interval is 3 km/s except in the range from $-1 \cdot 0$ to $+1 \cdot 0$ km/s which is classed as zero. The hatched areas along the Milky Way contain velocities exceeding ± 15 km/s. The uncertainty proviso (see Section III (*b*)) applies also to velocities in this region. Low intensity, wide profiles whose peak velocities differed widely between ± 30 km/s approximately were observed in the area north of the broken line XX.

---

* The symbols for galactic coordinates l and b are being written throughout as l^{I} and b^{I} following the convention to distinguish them from the new coordinates.

† Lund Observatory Tables for the conversion of galactic into equatorial coordinates and for the direction cosines in the equatorial system. Based on the Galactic Pole $12^{\mathrm{h}}\ 40^{\mathrm{m}}$; Decl. +28° (1900.0), corrected for precession to 1958.0. Table for the Reduction of velocities to the local standard of rest. D. A. MacRae and Gart Westerhout. Both published by The Observatory, Lund, Sweden, 1956.

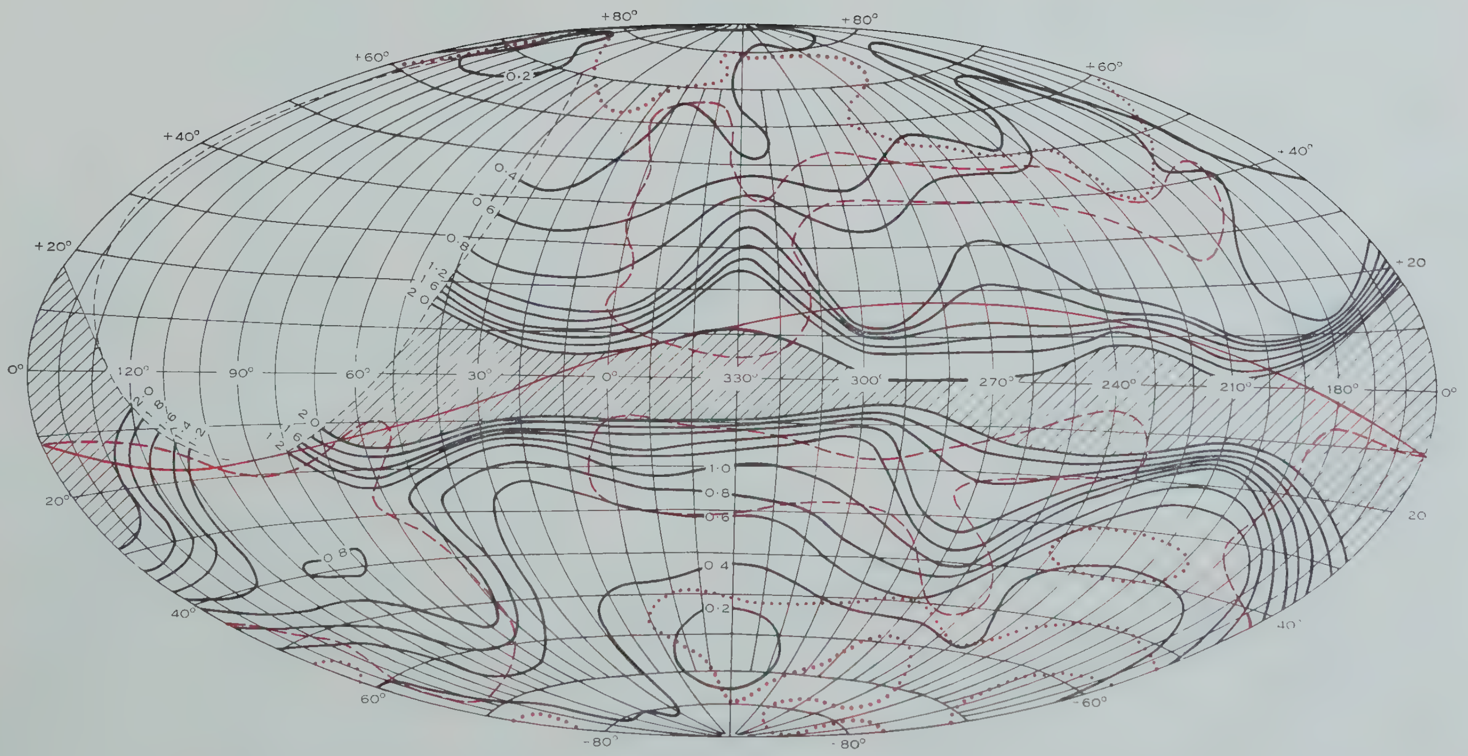

Fig. 1.—The local distribution in N_{H}, the number of hydrogen atoms/cm² in a line-of-sight column. The contour interval is $0 \cdot 2 \times 10^{21}$ H atoms cm⁻². Coordinates: old galactic system (Ohlsson). Projection: Aitoff. The red dashed lines enclose regions where profile half-widths are in the range 12–20 km/s (12 km/s is lower instrumental limit); the red dotted lines enclose regions of profiles exceeding 35 km/s. The unbroken red line is the equator corresponding to an axis parallel to the local galactic magnetic field as derived by Shaĭn.

The present survey information has been augmented by taking velocity values from the Leiden profiles (Muller and Westerhout 1957) in the region $b^{\mathrm{I}}=\pm10°$, $l^{\mathrm{I}}=45°$ to $l^{\mathrm{I}}=120°$, and by estimating several values from the D.T.M. survey at higher positive latitudes. These regions were not visible from Murraybank.

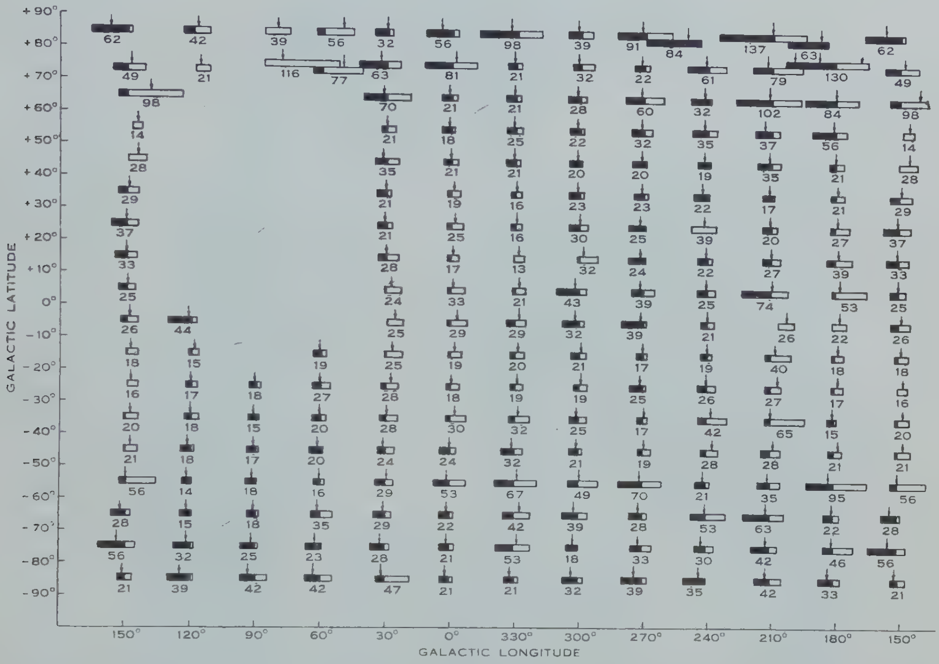

Fig. 2.—Hydrogen line half-widths. The length of each rectangle is proportional to the half-width in equivalent radial velocity; negative values are represented by the black portion to the left of the meridian line, positive values by the white on the right. The whole number beneath each rectangle is the half-width in km/s. The arrowheads denote the relative position of a profile peak.

IV. COMPARISON WITH OTHER LARGE-SCALE SURVEYS

The D.T.M. survey is based on profiles observed at intervals of 10° in both galactic longitude and latitude outside $|b^{\mathrm{I}}|=20°$; in the Jodrell Bank survey profiles were observed at 5° intervals.

A comparison of some of the amounts of neutral hydrogen recorded by the three surveys in the overlapping region has been made in Table 1. The D.T.M. data had to be taken from a rather small diagram and converted to N_{H} by an approximate factor quoted by the authors. In the table the D.T.M. values are consistently lower than the Murraybank N_{H} by an average $0 \cdot 2\times10^{21}$ units, the Jodrell Bank values show no systematic differences from ours except in the galactic plane region. The last two columns of Table 1 compare D.T.M. average radial velocities around parallels of latitude with corresponding Murraybank figures. In addition, individual radial velocities of the latter two surveys were compared. One hundred and fifteen pairs of values were available. The D.T.M.

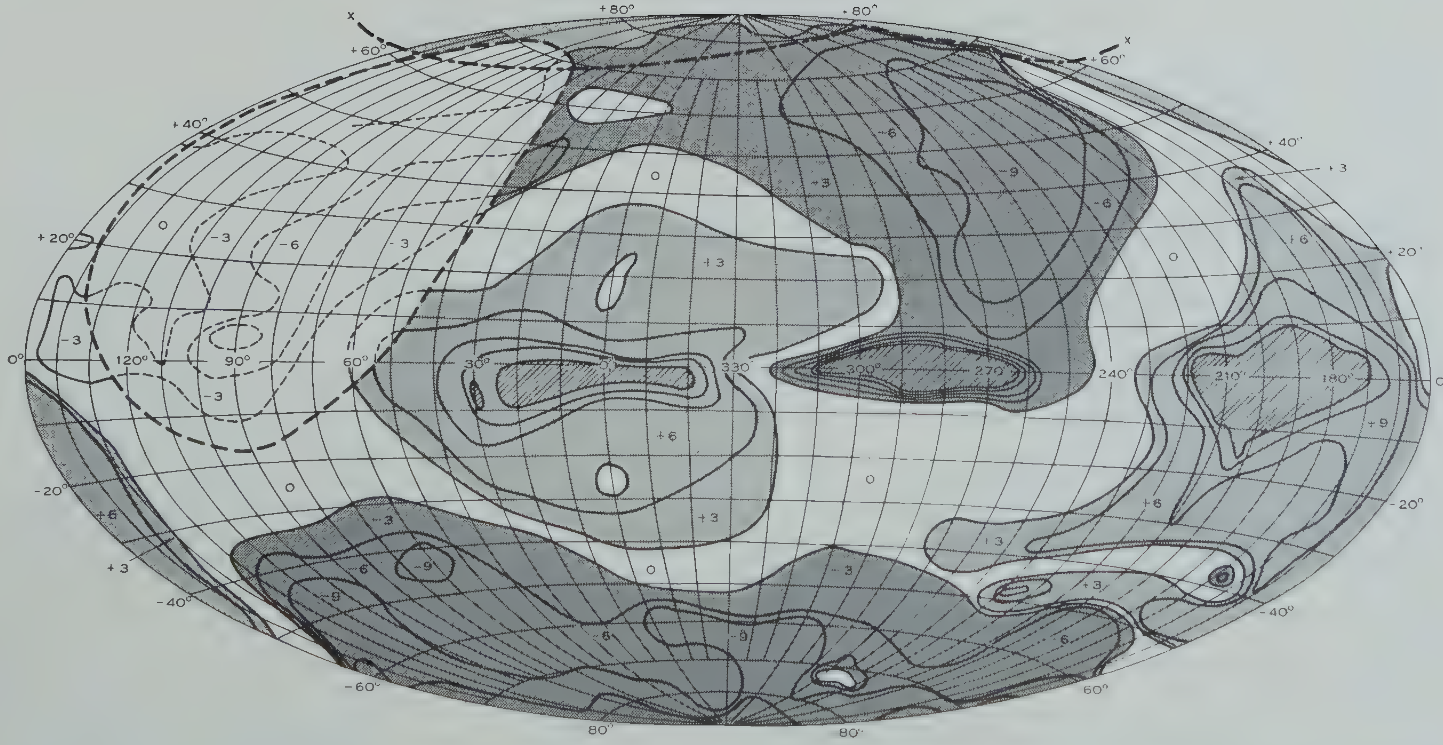

Fig. 3.—The distribution of H-line peak radial velocities. The contour interval is 3 km/s. Coordinates : old galactic system (Ohlsson). Projection : Aitoff. Light grey shading denotes regions of positive velocity, dark grey shading negative velocities, and white denotes zero velocity ($-1, 0, +1$ km/s).

value at a point was estimated from their radial velocity–galactic longitude diagrams. 30% of the pairs agree exactly, 31% had a | 1 | km/s difference, 18% a | 2 | km/s difference. The overall means were equal.

TABLE 1

SAMPLE COMPARISONS OF N_H AND AVERAGE RADIAL VELOCITIES OBTAINED BY D.T.M. (E), DAVIES (D), AND MURRAYBANK (M) SURVEYS

N_H (10^{21} H atoms cm^{-2})													Velocities Averaged Around Parallels of b (km/s)	
l^I	330°			30°			150°			210°				
b^I	E	D	M	E	D	M	E	D	M	E	D	M	E	M
+5	—	4·0	2·3	—	4·0	2·9	—	6·0	5·7	—	3·0	1·6	—	+0·0
+10	—	3·0	2·0	—	2·1	2·0	—	2·8	3·5	—	1·8	1·0	—	+0·3
+20	1·6	2·4	1·8	1·0	1·2	1·0	1·0	1·8	1·4	0·8	1·0	0·9	0·0	−0·6
+30	0·8	1·5	1·4	0·7	0·6	0·7	0·7	1·0	0·7	0·6	0·6	0·8	−2·2	−1·3
+40	0·6	1·0	1·0	0·2	0·5	0·5	0·2	0·7	0·5	0·6	0·6	0·9	−1·9	−2·4
+50	0·4	0·7	0·5	0·1	0·3	0·4	0·1	0·3	0·5	0·5	0·6	0·8	−4·0	−4·0
+60	0·3	0·6	0·4	0·1	—	0·3	—	—	0·5	0·3	0·6	0·9	−6·1	−2·2
+70	0·2	0·3	0·4	—	—	0·3	—	—	0·5	0·2	0·3	0·7	−3·0	−3·4
l^I	90°			30°			150°			210°				
−5	—	3·8	—	—	6·0	3·1	—	4·0	5·0	—	3·5	2·6	—	+3·3
−10	—	2·0	2·0	—	3·2	1·4	—	2·5	3·0	—	2·0	2·2	—	+2·6
−20	0·8	0·9	0·8	0·8	1·3	0·9	1·4	1·7	1·9	—	0·5	0·8	+3·8	+3·1
−30	0·3	0·9	0·5	0·6	0·6	0·9	1·0	1·6	1·9	—	0·6	0·5	+2·3	+3·1
−40	0·4	0·6	0·4	0·3	0·6	1·0	1·0	0·9	1·0	0·5	0·6	0·4	+0·6	−0·5
−50	0·4	0·6	0·5	0·6	0·6	0·9	0·4	0·8	0·6	0·5	0·3	0·3	−3·7	−3·0
−60	0·4	0·4	0·5	0·5	0·6	0·7	0·4	0·7	0·4	0·5	—	0·3	−6·0	−5·3
−70	0·3	0·3	0·4	0·4	0·4	0·3	0·5	0·3	0·4	0·3	—	0·3	−5·2	−6·0
−80	0·2	—	0·4	0·2	—	0·4	0·2	—	0·3	0·2	—	0·3	−6·8	−8·2

V. RESULTS AND DISCUSSION

(*a*) *The* N_H *Distribution*

(i) *Features.*—A number of large-scale features are prominent in the N_H contour diagram of Figure 1. In the northern galactic hemisphere two spurs dominate; one from the Scorpius-Ophiuchus region near the galactic plane to latitude +65° is spread over some 45° in longitude. The ridge is at first centred about l^I=327° but moves towards l^I=0° as latitude increases. References to Figure 2 will show that almost the whole spur is characterized by profiles in the half-width range 12–20 km/s. Areas containing profiles in this range have been indicated by the broken red lines in Figure 1. Such evidence would point to a compact complex of hydrogen clouds. Large dust clouds have been observed in the lower latitudes of this same region and, if association of dust and hydrogen is assumed, the region must be fairly close to the Sun—of the order of 150 parsecs distant.

The second spur develops from about $b^{\mathrm{I}}=+40°$ in Sextans and extends along $l^{\mathrm{I}}=210°$ to $b^{\mathrm{I}}=75°$. It is a region of broader profiles (>35 km/s half-widths which are found within areas indicated by the red dotted lines in Fig. 1). No optical feature seems to be associated with this spur.

In southern latitudes a weaker ridge begins from about $b^{\mathrm{I}}=-15°$, $l^{\mathrm{I}}=265°$ and shifts to $l^{\mathrm{I}}=240°$ as it reaches $b^{\mathrm{I}}=-60°$. An area some 20° wide about the centre line is one of the narrow width profiles (12–20 km/s).

The outstanding feature of the N_{H} diagram is in the Gemini-Taurus-Orion region with a continuation over a large area including Triangulum, Andromeda, and Pisces. The longitude range is approximately $l^{\mathrm{I}}=180°$ back to $l^{\mathrm{I}}=60°$ and the latitude $b^{\mathrm{I}}=+20°$ to $b^{\mathrm{I}}=-80°$. As the broken red line again shows, most of the region south of $b^{\mathrm{I}}=-10°$ exhibits profiles in the 12–20 km/s range. However, it could well be that here are two separate regions. The gradient of N_{H} contours in the $l^{\mathrm{I}}=130°$ vicinity is associated with a sudden change in radial velocities (see Fig. 3). This phenomenon was remarked in the earlier observations of the Taurus-Orion cloud.

The N_{H} contours fall to minima in both hemispheres at places away from the galactic poles. The northern minimum is centred on $l^{\mathrm{I}}=105°$, $b^{\mathrm{I}}=+72°$ with values below $0 \cdot 2\times10^{21}$ H atoms cm^{-2}, the southern minimum centre is approximately at $l^{\mathrm{I}}=335°$, $b^{\mathrm{I}}=-65°$, with similar N_{H} values. It is interesting to note that the mean longitudes of the major northern spur and the southern minimum and the northern minimum and the major southern spur are approximately the same.

Dr. W. C. Erickson has called the authors' attention to the fact that his estimated minimum (personal communication) of the D.T.M. survey and the northern minimum here agree exactly and that the position, $l^{\mathrm{I}}=105°$, $b^{\mathrm{I}}=+72°$, is the pole corresponding to the plane of the general magnetic field in the solar vicinity given by the late G. A. Shaǐn (1957). Noting systematic deviations of the position angles of the planes of preferential vibrations of stellar light, Shaǐn found that the local galactic magnetic field was inclined at an angle of 18° to the galactic plane. He had hoped to be able to compare the magnetic field plane with the distribution of local gas clouds. The plane is shown in red on Figure 1 cutting the galactic plane at $l^{\mathrm{I}}=15°$ and $l^{\mathrm{I}}=195°$. There does not seem to be sufficient evidence to come to any conclusions except that this plane fits the gas distribution very much better than the so-called Local System plane with its pole at $l^{\mathrm{I}}=170°$, $b^{\mathrm{I}}=+74°$.

(ii) *The Variation of* N_{H} *with* b.—The variation of N_{H} with galactic latitude was studied to provide information on the nature of the hydrogen distribution. If the gas is stratified parallel to the galactic plane the observed N_{H} should vary as the cosecant of the latitude.

N_{H} is plotted against b^{I} at each of 12 galactic longitudes in Figure 4. A reference value of $N_{\mathrm{H}}=0 \cdot 3\times10^{21}$ H atoms cm^{-2} was taken for $|b^{\mathrm{I}}|=90°$. A cosecant curve has been drawn from this point for comparison with each observed N_{H} curve. It can be seen that the N_{H} values tend to conform to the cosecant

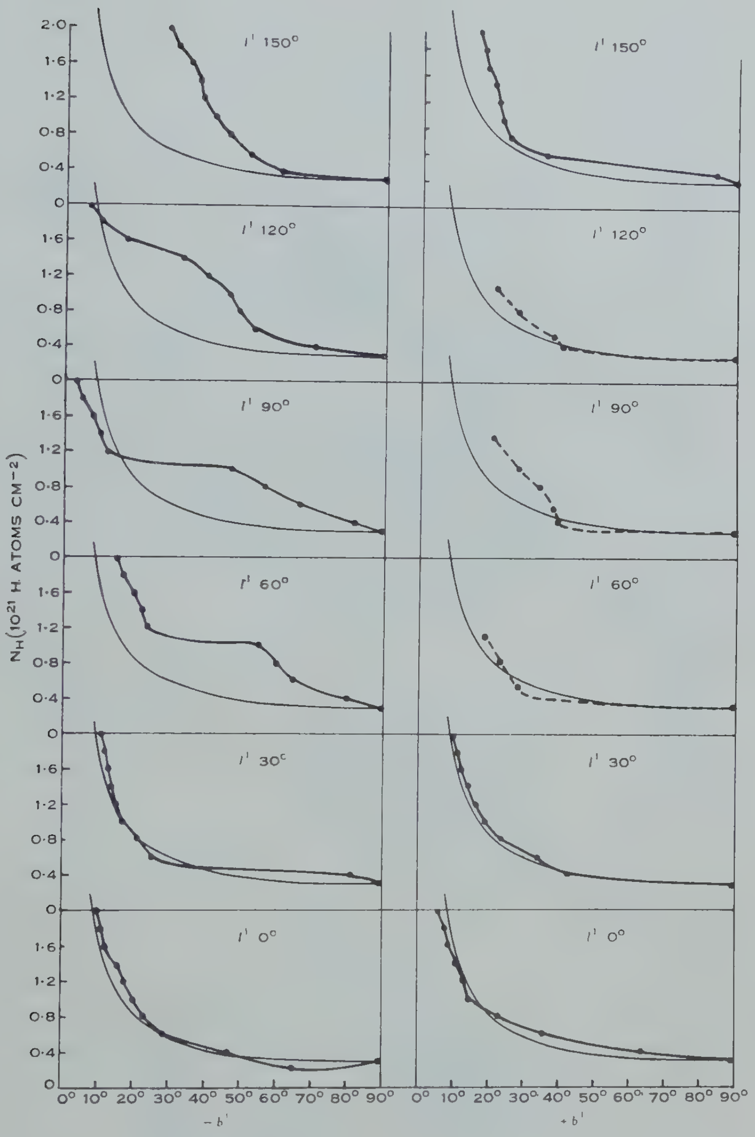

(a)

Fig. 4 (*a*).—The variation of N_H with galactic latitude at a number of galactic longitudes between 0° and 150°. The fine line curve in each is a cosecant curve ($N_H = | 0 \cdot 3 \times 10^{21} \operatorname{cosec} b^I |$).

distribution with some departures which are positive in most cases. We are led to the conclusion, then, that the local distribution is substantially horizontally stratified and that embedded in it is a number of concentrations of gas. The N_H values in the regions towards the north and south galactic poles appear normal in spite of the rather wider profiles observed in the high northern latitudes.

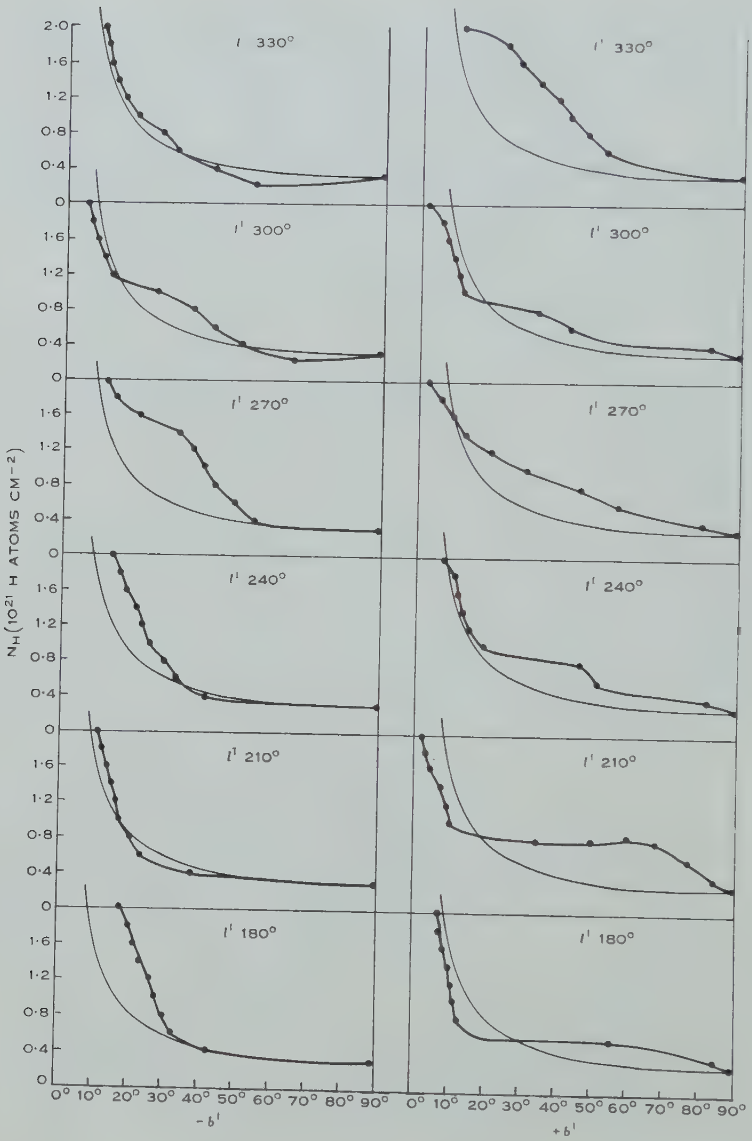

(b)

Fig. 4 (*b*).—The variation of N_H with galactic latitude at a number of galactic longitudes between 180° and 330°. The fine line curve is a cosecant curve ($N_H = | 0 \cdot 3 \times 10^{21} \operatorname{cosec} b^I |$).

The departures from horizontal stratification are illustrated in Figure 5 in which ΔN_H (the departure of the experimental N_H value from the cosecant distribution value) is plotted on a polar projection. The greater part of the local region is seen to be stratified, while features mentioned in earlier discussion emerge as areas of excess N_H. The region in Gemini-Taurus-Orion and the

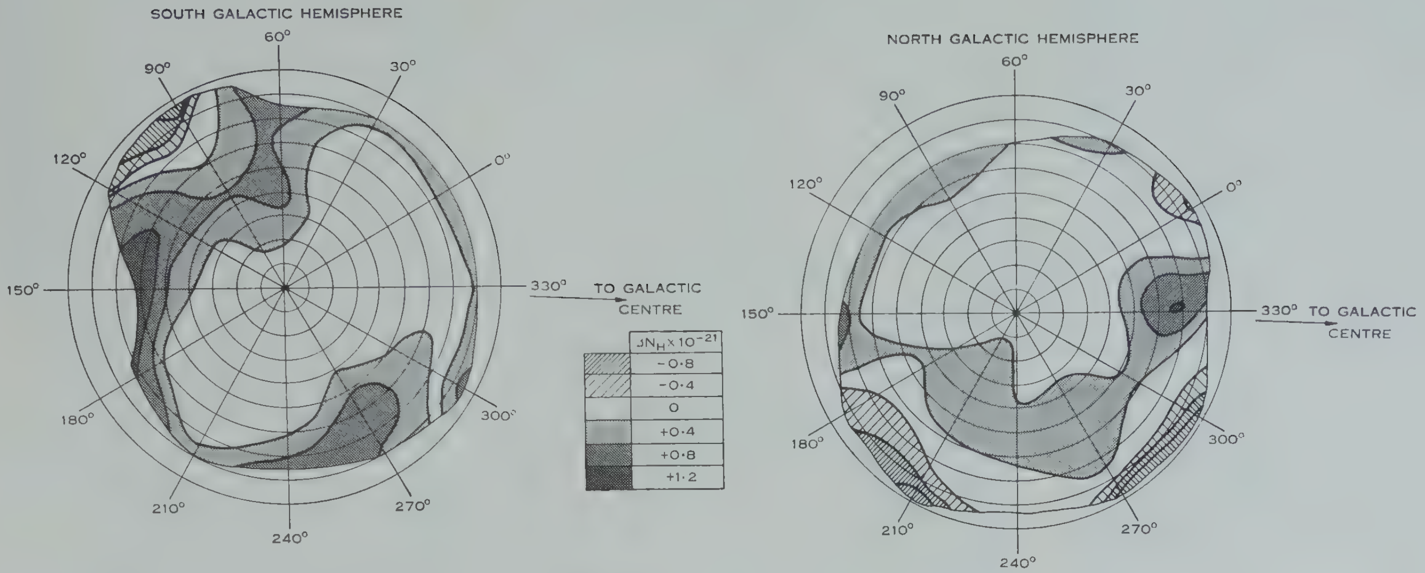

Fig. 5.—The distribution of ΔN_H, the departures of the observed N_H from a theoretical N_H cosecant b^I distribution. The hatched areas denote negative departures.

extension into Pisces are prominent, as is the Scorpius-Ophiuchus spur at the lower latitudes. The feature in south latitudes near $l^{\mathrm{I}}=270°$ is more accentuated in this representation. There are no obvious striations related in direction to the local spiral arm, which, if they had existed, would have been evident using this projection.

(iii) *Estimation of Gas Density in the Solar Vicinity.*—Our observations do not include an indication of distance and consequently cannot, without arbitrary assumptions as to distribution along the line-of-sight, yield density. However, Schmidt (1957), using the results of the extensive low latitude observations at Leiden, has derived a distribution of hydrogen in a direction perpendicular to the galactic plane. Assuming that our observations, including those at high latitudes, refer to the same distribution, we can use this model, together with our evidence of stratification and well-established values of N_{H}, to calculate the local gas density.

TABLE 2

MEAN VALUES OF N_{H} AROUND PARALLELS OF GALACTIC LATITUDE

b^{I}	$N_{\mathrm{H}}\times10^{-21}$ (H atoms cm^{-2})	$N_{\mathrm{H}}\sin b^{\mathrm{I}}$	b^{I}	$N_{\mathrm{H}}\times10^{-21}$ (H atoms cm^{-2})	$N_{\mathrm{H}}\sin b^{\mathrm{I}}$
+85°	0·37	0·370	−85°	0·33	0·330
+75°	0·40	0·386	−75°	0·33	0·318
+65°	0·50	0·454	−65°	0·36	0·326
+55°	0·55	0·450	−55°	0·46	0·376
+45°	0·62	0·439	−45°	0·64	0·450
+35°	0·81	0·465	−35°	0·85	0·488
+25°	0·93	0·393	−25°	1·10	0·465
+15°	1·24	0·322	−15°	1·62	0·420
+ 5°	2·68	0·233	− 5°	2·85	0·248
Means (excluding last entry)		0·41			0·40

Mean values of N_{H} around parallels of galactic latitude are given in Table 2. If the hydrogen were stratified horizontally the values of $N_{\mathrm{H}}\sin b$ would equal N_{H} for $b^{\mathrm{I}}=90°$ and would be constant for all values of b^{I}. We have therefore tabulated $N_{\mathrm{H}}\sin b^{\mathrm{I}}$ also, and, excluding the value at 5°, which is dubious for reasons given above, the values do not vary much. This is to be expected from the appearance of Figure 5 but the numerical evaluation gives a more representative value of N_{H} for a vertical column through the Galaxy. Thus, if we restrict attention to the regions within about 30° of the galactic poles, the values of N_{H} are about $0\cdot40\times10^{21}$ H atoms cm^{-2} to the north and $0\cdot33\times10^{21}$ H atoms to the south and imply that the Sun is a little to the south of the halfway position. If we extend consideration to 75° from the poles, thus including some of the clouds mentioned earlier, the values become $0\cdot40\times10^{21}$ H atoms cm^{-2} for both north and south.

Davies (1960) from his own observations found N_{H} values higher in the south than in the north and concluded that the Sun lay about 20 pc north of the galactic plane. The discrepancy seems due to averaging over different areas of sky: for example, we do not see the northern low intensity region near $l^{\mathrm{I}}=90°$, Davies does not see the southern low intensity region near $l^{\mathrm{I}}=300°$. We have tried including relevant values from the other two surveys, but results indicate that the Sun lies at the centre of the hydrogen layer within the observational uncertainty.

A mean value of N_{H} of $0\cdot35\times10^{21}$ H atoms cm^{-2} in the directions $b^{\mathrm{I}}=\pm90°$, in conjunction with Schmidt's shape for the distribution (determined unfortunately for other parts of the galactic disk) leads to a derived density near the Sun of $0\cdot46$ H atoms/cm^3. This may be compared with Westerhout's (1957) value for the mean density at the Sun's distance from the galactic centre of about $0\cdot5$ H atoms/cm^3.

(*b*) *Profile Shape*

The half-widths of the sample profiles in Figure 2 range from 12 to 140 km/s. The outstanding piece of information supplied by this diagram is the large-scale grouping of similar profiles. Profiles in the range 12–20 km/s were arbitrarily designated as " narrow ". Their deployment has been shown by the broken red lines superimposed on the N_{H} contours in Figure 1. It has already been remarked that the dominant features of the N_{H} distributions are regions of narrow profiles.

The red dotted lines in Figure 1 outline the regions of " wide " profiles—again arbitrarily chosen for half-widths greater than 35 km/s. The northern galactic polar cap has profiles of mean half-width 70 km/s and values up to 137 km/s. Some of these profiles have two and three peaks. In the south the mean half-width is 50 km/s with the maximum 95 km/s.

An interesting question has arisen concerning the value of these wide half-widths. Dr. Erickson (personal communication) has suggested that most of the local gas profiles are not in fact Gaussian in shape but are cusp-like, having broad wings with comparatively narrow, central sections. The broad wings may be due to some background of well-dispersed hydrogen—not necessarily in the galactic disk. Thus, when measuring half-widths for low intensity profiles where any " central sections " tend to be confused with noise, the value will be relatively much wider than for a profile whose maximum temperature is above, say, 10 °K.

A number of samples were chosen at random from the profiles used in the present results and divided into groups of half-width 12–35 km/s and 36–140 km/s. " Overall width ", meaning widths read between the estimated zero intensity points of the profiles, i.e. greater than about $0\cdot5$ °K, were measured and means taken for each group.

In the 12–35 km/s group the mean half-width was 24 km/s and the mean overall width 112 km/s. The ratio of half to overall width is $0\cdot22$. For the 36–140 km/s group the corresponding results are 80, 186 km/s, and $0\cdot44$. These figures would point to the existence of such an effect but it is not the whole story. More of this type of data are being collected to make a closer study of the broad low intensity contribution.

However, in spite of the above, there seems little doubt that the "wide" profiles are wider by at least a factor of two. The reason for their existence in a distribution of local gas remains unanswered at present. A number of possible explanations come to mind. Firstly, the areas of wide profiles may be simply large diffuse clouds, the north one fortuitously overlaying the galactic polar cap. If, in fact, some association exists between the local galactic magnetic field and the disposition of neutral gas in the spiral arm a reason exists for more diffusion in these areas. Against this, a gradation in profile widths with increasing latitude may be expected in such a case and none has been detected.

Again, it is known that clouds of gas may oscillate in the z-direction about an equilibrium position in the plane. Thus, a greater velocity spread might well be observed from high latitudes were the aerial to intercept radiation from a number of clouds in different phases of this motion.

The possibility that the wide profiles are due to hydrogen from the galactic corona, say, is not considered likely since the half-width increase is only of the order of three to one, the overall width three to two. A much greater dispersion is expected from the randomly moving and presumably highly dispersed gas clouds of the corona. Further, we should expect to see wide profiles even better at intermediate latitudes, where the longer, oblique paths should yield higher intensities.

(c) *The Radial Velocity Distribution*

(i) *The Observed Distribution.*—The striking feature of the observed distribution of peak radial velocities (Fig. 3) is the large-scale grouping of velocities of similar sign and magnitude. Two regions of positive velocity, one centred approximately on $l^{\mathrm{I}}=10°$ and the other on $l^{\mathrm{I}}=190°$, extend to galactic latitudes of $\pm 40°$ and over longitude ranges of more than 90° each. Regions of negative velocity lie between these at low latitudes. The high latitudes are characterized by negative velocities; the southern cap is completely occupied by approaching gas down to $b^{\mathrm{I}}=-40°$, the northern cap has approaching gas, together with a sector of diffuse gas of various velocities. Considerable regions between the four main features are occupied by gas at zero velocity. Some of the observed velocities in the hatched regions have magnitudes up to 34 km/s. The velocities of the purely local gas outside $|b^{\mathrm{I}}|=10°$ are restricted to about ± 12 km/s, except for the one "irregular" region centred on $l^{\mathrm{I}}=150°$ approximately and extending from $b^{\mathrm{I}}=+40°$ to $b^{\mathrm{I}}=+90°$. It has wide profiles and higher peak velocities (up to ± 30 km/s).

Some of the features of this distribution, e.g. the alternating positive and negative velocity regions along the galactic equator, are clearly associated with differential galactic rotation, but it would be of great interest if, in addition, a general flow pattern could be recognized. Here again, owing to the lack of a measure of the distance to the observed hydrogen we cannot assign a particular velocity to be expected in a given direction due to differential galactic rotation. We can make an estimate based on the current rotational model after assuming that the peak of the H-line profile should originate in a region not more than a given distance from the galactic plane.

The standard formula for the radial velocity due to differential galactic rotation of an object at a short distance r from the Sun is

$$v_g = rA \sin 2l' \cos b^{\mathrm{I}},$$

where v_g is the radial velocity in km/s; r is the distance from the Sun in kiloparsecs; A is Oort's constant, taken as 19·5 km/s/kpc; $l' = (l^{\mathrm{I}} - l_0^{\mathrm{I}})$, l^{I} is galactic longitude, $l_0^{\mathrm{I}} = 327°·5$, the l^{I} of the galactic centre; b^{I} is galactic latitude.

We assume a model in which the main concentration of local gas, giving rise to the profile maximum, is not more than 0·11 kpc from the galactic plane. This is the distance at which, according to Schmidt, the density has fallen to half its maximum value.

Curves of v_g against l^{I} at a number of galactic latitudes between ±4° and ±60° are sketched in grey in Figure 6. Observed radial velocity–galactic longitude curves have been superimposed in black at each latitude in the figure.

(ii) *Discussion of the Velocity Curves.*—Two quite definite results emerge from a study of Figure 6. The first comes from the fact that the amplitude of the model differential galactic rotation curve becomes less than 1 km/s at latitudes above $|b| \sim 50°$. This means that the values of the observed velocities in the high latitudes are effectively not influenced by differential rotation. The means of the negative velocities down to $|b^{\mathrm{I}}| \sim 40°$ (shown in dark grey in Fig. 3), are −5·6 km/s in the northern hemisphere and −6·1 km/s in the south.

In the second case, no matter how inaccurate the model may be, the differential rotational velocity must pass through zero at the longitudes of the galactic centre and anticentre ($l^{\mathrm{I}} = 327°·5$ and $147°·5$ respectively). Thus any observed departures at these points or differences in sign between the two curves cannot be due to differential rotation. In the direction near $l^{\mathrm{I}} = 327°·5$ positive velocities of mean value +4·5 km/s occur at all latitudes between $b^{\mathrm{I}} = \pm 30°$ and in $l^{\mathrm{I}} = 147°·5$ positive velocities of mean value +6 km/s at latitudes −4° to −50°. The mean velocity in the northern latitudes of $l^{\mathrm{I}} = 147°·5$ is approximately zero. These parts of the observed curves in Figure 6 are emphasized by thick segments.

We can conclude, then, that neutral hydrogen is flowing in towards the Sun from above and below in latitudes $|b^{\mathrm{I}}| = 90°$ to $|b^{\mathrm{I}}| \sim 40°$, at all longitudes, at approximately 6 km/s. The gas is flowing away from the solar vicinity in low and middle latitudes in directions centred on $l^{\mathrm{I}} = 327°·5$ and in southern latitudes on $l^{\mathrm{I}} = 147°·5$ at approximately the same speed.

Finally, the longitudes of the maximum velocities of the observed curves in Figure 6 have a tendency to be shifted with respect to the fixed longitudes of the stationary points of the model curves as galactic latitude increases. The $l^{\mathrm{I}} = 282°·5$ maximum (negative velocity) has moved from that value by some 30°, to a lower longitude, at latitudes ±32°. On inspection of the other maxima it is found that values initially at $l^{\mathrm{I}} = 102°·5$ in $\pm b^{\mathrm{I}}$, at $l^{\mathrm{I}} = 192°·5$ in $+b^{\mathrm{I}}$ decreased in l^{I}, at $l^{\mathrm{I}} = 12°·5$ in $-b^{\mathrm{I}}$ remained much the same, and at $l^{\mathrm{I}} = 192°·5$ in $-b^{\mathrm{I}}$ increased in l^{I} with increasing galactic latitude. This effect may be an indication of a shearing of the gas as distance from the galactic plane increases.

(iii) *Estimate of the Mass of Hydrogen Inflow.*—If $0\cdot46$ H atoms/cm^3 be accepted as a reasonable average density for the gas in the neighbourhood of the Sun responsible for the peaks in the profiles, the rate of inflow over the galactic polar caps at the mean velocity 6 km/s is $0\cdot7\times10^{-7}\,M_{\odot}$ per year per square parsec. This estimate is admittedly rather approximate but it shows that if such inflow is common over large areas of the galactic disk it would represent a highly significant item in the dynamics of the Galaxy.

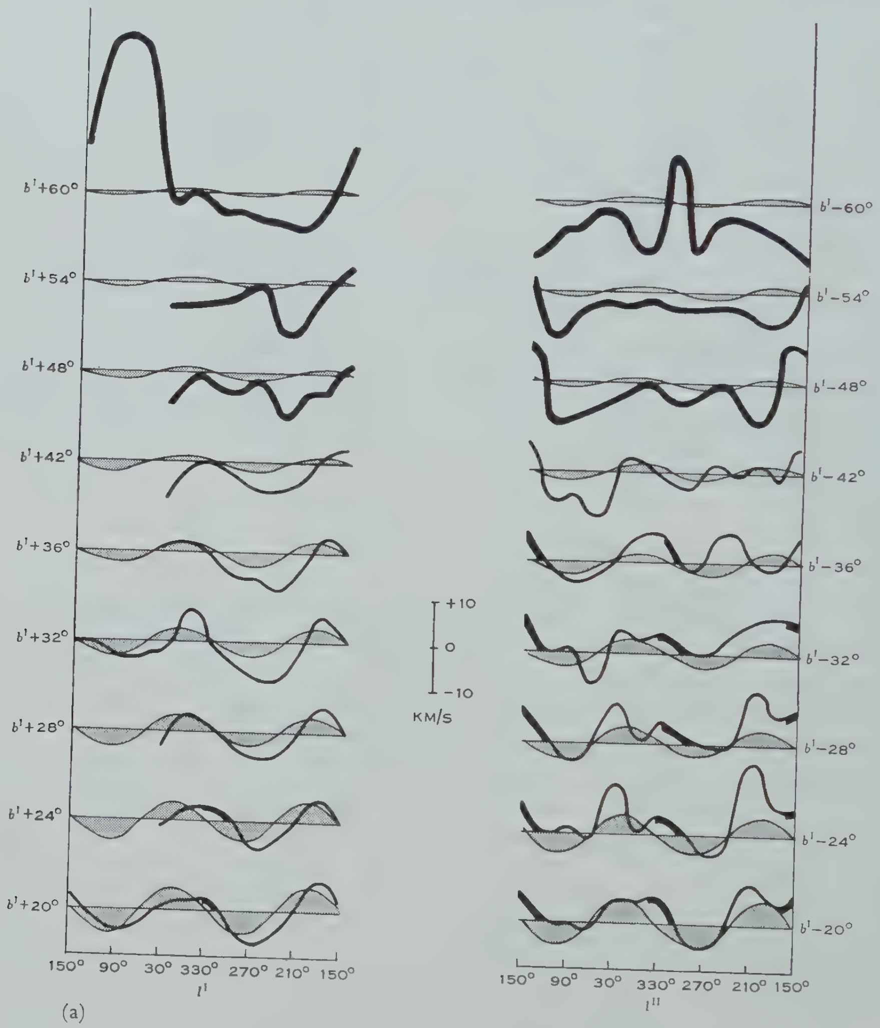

Fig. 6 (*a*).—Radial velocity as a function of galactic longitude. Observed velocities are the black curves; predicted velocities due to differential galactic rotation at points $0\cdot11$ kpc above and below the galactic plane ($v_g=0\cdot11\times19\cdot5\sin 2l'\cos b^{\mathrm{I}}\cot b^{\mathrm{I}}$) are shown in grey. Thick segments indicate definite discrepancies between observation and simple differential rotation.

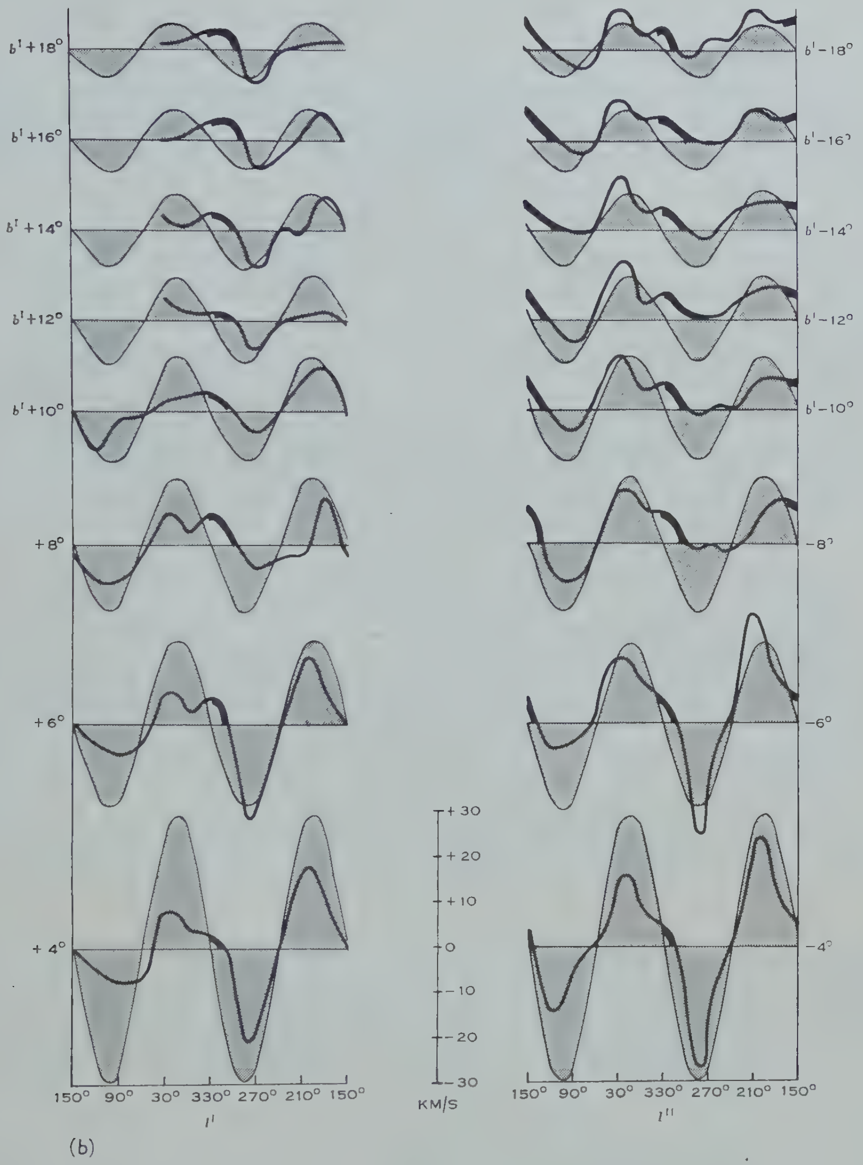

Fig. 6 (*b*).—For explanation see Figure 6 (*a*).

VI. CONCLUSION

Indications have been found that the local neutral hydrogen has a general horizontal stratification in which regions of excess density occur. The gas does not appear to be correlated closely with the so-called Local System, but the possibility exists that its disposition is in some way connected with the local galactic magnetic field.

The line profiles observed away from the Milky Way were generally single peaked with a range in half-width of 12–35 km/s. Wide profiles (36–140 km/s) were consistently observed in large regions near the galactic poles. Large-scale grouping of profiles into the comparatively narrow range 12–20 km/s occurred corresponding closely with outstanding features of the N_H distribution. This fact pointed to the compact nature of such large local complexes as the Scorpius-Ophiuchus spur and the Taurus-Orion region.

The peak radial velocity distribution was characterized by the simplicity of arrangement—two large regions of positive velocity in low and middle galactic latitudes were separated by negative velocity areas. The galactic polar caps down to $|b^{\mathrm{I}}|\sim 40°$ showed a great predominance of negative velocities. Part of this pattern is due to differential galactic rotation but two definite facts emerged from the observations : hydrogen is flowing away from the Sun at about 6 km/s in the directions of the galactic centre and anticentre in low and medium latitudes and is streaming in from above and below in latitudes $|b^{\mathrm{I}}|=90°$ to $|b^{\mathrm{I}}|\approx 40°$ at about 6 km/s. The maximum radial velocities involved in these motions are $\sim\pm 12$ km/s. The complete flow pattern could not be determined from the present investigations.

VII. Acknowledgments

The authors would like to express sincere appreciation of the very considerable help and encouragement received from Dr. J. L. Pawsey in the preparation of this paper. He has always been most enthusiastic about the advantages of a wide-beam aerial in a sky survey of this nature.

We have benefited from many discussions with colleagues from the Radiophysics Laboratory and Mt. Stromlo Observatory.

Finally, we gratefully acknowledge the major contribution made by Miss Janice Milton in the original reduction of the data.

VIII. References

Christiansen, W. N., and Hindman, J. V. (1952).—*Aust. J. Sci. Res.* A **5** : 437–55.
Davies, R. D. (1960).—*Mon. Not. R. Astr. Soc.* **120** : 483–97.
Erickson, W. C., Helfer, H. L., and Tatel, H. E. (1959).—Symp. I.A.U. (Paris) **9** : 390–7, 1958.
McGee, R. X., and Murray, J. D. (1959).—*Aust. J. Phys.* **12** : 127–33.
Muller, C. A., and Westerhout, G. (1957).—*Bull. Astr. Inst. Netherlds.* **13** : 151–95.
Schmidt, M. (1957).—*Bull. Astr. Inst. Netherlds.* **13** : 247–68.
Shaǐn, G. A. (1957).—*Soviet Astronomy A.J.* **1** : 1–8.
Westerhout, G. (1957).—*Bull. Astr. Inst. Netherlds.* **13** : 201–46.
Wild, J. P. (1952).—*Astrophys. J.* **115** : 206–21.

THE INFLUENCE OF THERMOELECTRIC EFFECTS ON THE MAXIMUM TEMPERATURE IN A RADIALLY CONSTRICTED GAS DISCHARGE BETWEEN ELECTRODES

By P. W. Seymour*

[*Manuscript received January* 9, 1961]

Summary

In an earlier paper the author provided a method for estimating the maximum temperature in a steady-state, centrally constricted, highly ionized deuterium discharge between electrodes. The analysis applied to discharges not too long, so that bremsstrahlung loss could be neglected compared to the main heat loss by conduction to the electrodes, and thermoelectric effects were not included.

Here the analysis is generalized to include thermoelectric effects, and carried through for strictly longitudinal flow, for which at every point within the discharge the heat flux vector $\mathbf{q}$ and the current density vector $\mathbf{j}$ are parallel to the magnetic field $\mathbf{H}$.

Again a simple continuity argument shows that $\mathbf{q}+V\mathbf{j}=0$, where V is the electric potential, but now the equipotential surface on which $\mathbf{q}=V=0$ is displaced from midway between the electrodes nearly to the cathode. In the linear case the maximum temperature is displaced somewhat from the midway position towards the anode. A similar remark applies to the constricted discharge. The important influence of inclusion of thermoelectric effects is that the maximum temperature is increased by approximately 14% for about the same applied voltage producing a given current in a particular discharge geometry. The characteristic relating the maximum temperature and resistance ratio ε and the radial compression ratio ν obtained in the earlier paper is not changed by thermoelectric effects. Comparison of voltage and also temperature versus distance characteristics for linear and constricted discharges without and with thermoelectric effects is given by means of graphs.

I. INTRODUCTION

In an earlier paper (Seymour 1961), referred to hereafter as S, a method was given for estimating the maximum temperature in a steady non-equilibrium state, centrally constricted, substantially ionized deuterium discharge between electrodes. The free boundary surface of the plasma was assumed thermally insulated when isolated from the walls of the discharge tube, and cooling was therefore by heat conduction to the electrodes, compared to which the bremsstrahlung loss was shown to be negligible if the discharge was not too long. Neglect of thermoelectric and other effects led to symmetry of the distributions of temperature and voltage about a median plane normal to the longitudinal axis of the discharge, on which the plasma temperature was assumed constant at its maximum value T_m.

With ω_e the electron gyrofrequency and τ_e the electron collision time, the estimation of maximum temperature in discharges having straight and hyperbolic

---

* Research School of Physical Sciences, Australian National University, Canberra.

current streamlines was made via a vector analysis for $\omega_e\tau_e \ll 1$, and a tensor analysis for $\omega_e\tau_e \gg 1$. For flow having **q** and **j** parallel to the magnetic field **H** at every point within the discharge (strictly longitudinal flow), it was seen that the results obtained for $\omega_e\tau_e \ll 1$ applied for all $\omega_e\tau_e$.

In this paper we examine the same cases as above, under the same approximations, except that we include thermoelectric effects by generalizing the previous analysis, which destroys the symmetry of the temperature and voltage distributions about the median plane. Since strictly longitudinal flow is considered, it is convenient and sufficient to employ a vector method only.

Initial consideration of the problem suggested that for simplicity thermoelectric effects should be excluded in the first attempt at solution, and included later if possible.

This solution procedure proved satisfactory, and showed that it was not desirable to combine the separate results obtained, hence the presentation of results in separate papers.

II. ISOTROPIC FORMS OF j AND q (SEEBECK AND PELTIER EFFECTS ONLY INCLUDED)

When the magnetic field **H** is negligible or parallel to the electric field **E** and the temperature gradient ∇T, the general equations for **j** and **q** include only the Seebeck and Peltier effects respectively, as in (3.8) and (3.9) of S. For $\omega_e\tau_e \ll 1$ these equations reduce to the isotropic forms

$$\mathbf{j} = \sigma\mathbf{E} + \alpha\nabla T, \tag{2.1}$$

and

$$\mathbf{q} = -K\nabla T - \beta\mathbf{E}, \tag{2.2}$$

where σ and K are the scalars obtained in Section IV (*a*) of S, and we have replaced Marshall's (1957) φ and ξ by Spitzer and Härm's (1953) α and $-\beta$ respectively, and used Table 1 (constructed from pp. 67 and 69 of Marshall's report) to show that $\alpha^{\mathrm{I}} = \alpha^{\mathrm{II}} = \alpha$, $\alpha^{\mathrm{III}} \sim 0$; $\beta^{\mathrm{I}} = \beta^{\mathrm{II}} = \beta$, $\beta^{\mathrm{III}} \sim 0$, when $\omega_e\tau_e \ll 1$.

TABLE 1

COMPONENTS OF THE THERMOELECTRIC TENSORS

Components of [α]	Components of [β]
$\alpha^{\mathrm{I}} = 1\cdot554\dfrac{kn_e e\tau_e}{m_e}$	$\beta^{\mathrm{I}} = 6\cdot38\dfrac{kn_e e\tau_e T}{m_e}$
$\alpha^{\mathrm{II}} = -1\cdot5\dfrac{kn_e e\tau_e}{m_e}\;\dfrac{\omega_e^2\tau_e^2 - 0\cdot966}{\omega_e^4\tau_e^4 + 6\cdot282\omega_e^2\tau_e^2 + 0\cdot933}$	$\beta^{\mathrm{II}} = 2\dfrac{kn_e e\tau_e T}{m_e}\;\dfrac{0\cdot5\omega_e^2\tau_e^2 + 2\cdot98}{\omega_e^4\tau_e^4 + 6\cdot282\omega_e^2\tau_e^2 + 0\cdot933}$
$\alpha^{\mathrm{III}} = -4\cdot3\dfrac{kn_e e\tau_e}{m_e}\;\dfrac{\omega_e\tau_e}{\omega_e^4\tau_e^4 + 6\cdot282\omega_e^2\tau_e^2 + 0\cdot933}$	$\beta^{\mathrm{III}} = -2\dfrac{kn_e e\tau_e T}{m_e}\omega_e\tau_e\left[\dfrac{1\cdot25\omega_e^2\tau_e^2 + 7\cdot627}{\omega_e^4\tau_e^4 + 6\cdot282\omega_e^2\tau_e^2 + 0\cdot933}\right]$

Comparing α and β with their values in a Lorentz gas, we find from Spitzer and Härm that when the atomic number $Z=1$,

$$\alpha=3\left(\frac{2}{\pi}\right)^{3/2}\frac{k^{5/2}T^{3/2}}{m_e^{1/2}e^3\ln\lambda}\gamma_T, \tag{2.3}$$

and

$$\beta=8\left(\frac{2}{\pi}\right)^{3/2}\frac{k^{5/2}T^{5/2}}{m_e^{1/2}e^3\ln\lambda}\delta_E, \tag{2.4}$$

where the electron charge e has been taken in e.s.u. Here α and β for an actual gas have been expressed in terms of their values in a Lorentz gas by means of the transport coefficients γ_T and δ_E, given by Spitzer and Härm as $\gamma_T=0\cdot2727$, $\delta_E=0\cdot4652$. Spitzer and Härm's α and β agree closely with those of Marshall, who, however, does not specifically relate actual and Lorentz gas values.

Writing (2.3) as

$$\alpha=\alpha_0T^{3/2}/\ln\lambda, \tag{2.5}$$

and (2.4) as

$$\beta=\beta_0T^{5/2}/\ln\lambda, \tag{2.6}$$

we obtain by inserting numerical values

$$\alpha_0=9\cdot285\times10^{-9}\ \mathrm{A\ cm^{-1}\ deg^{-5/2}}, \tag{2.7}$$

and

$$\beta_0=4\cdot223\times10^{-8}\ \mathrm{J\ V^{-1}\ cm^{-1}\ s^{-1}\ deg^{-5/2}}. \tag{2.8}$$

To complete these equations we recall from S, Section V, that

$$\sigma=\sigma_0T^{3/2}/\ln\lambda, \tag{2.9}$$

and

$$K=K_0T^{5/2}/\ln\lambda, \tag{2.10}$$

where

$$\sigma_0=1\cdot53\times10^{-4}\ \Omega^{-1}\ \mathrm{cm^{-1}\ deg^{-3/2}}, \tag{2.11}$$

and

$$K_0=4\cdot396\times10^{-12}\ \mathrm{J\ s^{-1}\ cm^{-1}\ deg^{-7/2}}. \tag{2.12}$$

III. Solution of the Plasma Energy Equation for Strictly Longitudinal Flow

Again, the analysis of a general, constricted discharge having geometric symmetry about a chosen plane is conveniently handled by introduction of an orthogonal curvilinear coordinate system, which can be specialized later to deal with linear discharges and those having hyperbolic streamlines. Before developing these solutions, however, the form of the differential equation for strictly longitudinal flow to be finally integrated can readily be obtained by a simple continuity argument.

(a) *Curved Stream Tube of a Constricted Discharge*

Figure 1 shows a curved current stream tube possessing geometric symmetry about a chosen plane. Suppose also that there exists an equipotential surface, normal to the curved axis of the tube, and nearer its lower end in Figure 1, on which $\mathbf{q}=0$ and on which it is convenient to take the constant electric potential as zero. Then, on that surface, with the notation of (5.15) of S, we have

$$\mathbf{M}=\mathbf{q}+V\mathbf{j}=0, \tag{3.1.1}$$

and since from (5.14) $\mathbf{M}$ is solenoidal, it follows that $\mathbf{M}$ vanishes identically at every point within the discharge, and the flow is longitudinal. Inserting (2.1) and (2.2) in (3.1.1), and using $\mathbf{E}=-\boldsymbol{\nabla}V$, together with (2.5), (2.6), (2.9), and (2.10) above, we obtain

$$\boldsymbol{\nabla}T/\boldsymbol{\nabla}V=(\beta_0T-\sigma_0V)/(K_0T-\alpha_0V). \tag{3.1.2}$$

From the mode of derivation we see that this equation is valid for all values of $\omega_e\tau_e$ if $\mathbf{q}$ and $\mathbf{j}$ are at every point parallel to $\mathbf{H}$, i.e. if the flow is strictly longitudinal.

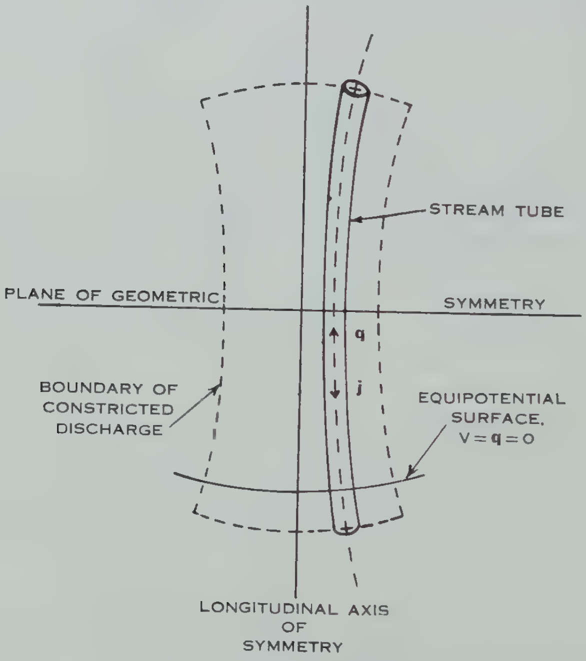
STREAM TUBE
PLANE OF GEOMETRIC
SYMMETRY
q
j
BOUNDARY OF CONSTRICTED DISCHARGE
EQUIPOTENTIAL SURFACE, V=q=0
LONGITUDINAL AXIS OF SYMMETRY

Fig. 1.—Curved stream tube of a constricted discharge.

(b) *Solution of a Simplified Form of the Plasma Energy Equation using Complex Variables*

For the detailed mathematical analyses of longitudinal flow the plasma energy equation, $\operatorname{div}\mathbf{q}=\mathbf{j}\cdot\mathbf{E}$, is again simplified initially by introduction of the orthogonal curvilinear coordinates, ψ (the current stream function), φ, and V; and by consideration of axi-symmetric flow, as in S, Section VI (*b*). Integration leads to

$$\partial T/\partial V=(\beta_0T-\sigma_0V)/(K_0T-\alpha_0V), \tag{3.2.1}$$

which is a convenient form of (3.1.2).

A method of integrating (3.2.1) runs as follows : first introduce a parameter p, such that

$$\partial T/\partial p=\beta_0 T-\sigma_0 V, \tag{3.2.2}$$

$$\partial V/\partial p=K_0 T-\alpha_0 V. \tag{3.2.3}$$

Assume now that the physical temperature and electric potential are the imaginary parts of complex quantities $\overline{T}$ and $\overline{V}$ respectively, so that, if Im is the imaginary part operator,

$$T=\mathrm{Im}\,\overline{T}, \tag{3.2.4}$$

and

$$V=\mathrm{Im}\,\overline{V}. \tag{3.2.5}$$

Further, assume that

$$\overline{T}=A\mathrm{e}^{mp}, \tag{3.2.6}$$

and

$$\overline{V}=B\mathrm{e}^{mp}, \tag{3.2.7}$$

where m is a complex quantity.

Then

$$mA=\beta_0 A-\sigma_0 B, \tag{3.2.8}$$

$$mB=K_0 A-\alpha_0 B. \tag{3.2.9}$$

Combination of (3.2.8) and (3.2.9) yields

$$A/B=-\sigma_0/(m-\beta_0)=(m+\alpha_0)/K_0, \tag{3.2.10}$$

and hence, from the right-hand side equation,

$$m=\tfrac{1}{2}(\beta_0-\alpha_0)+\tfrac{1}{2}\mathrm{i}\{4K_0\sigma_0-(\alpha_0+\beta_0)^2\}^{\frac{1}{2}}, \tag{3.2.11}$$

where $4K_0\sigma_0-(\alpha_0+\beta_0)^2>0$, and the positive square root has been chosen for convenience of solution.

Writing

$$a=(\beta_0-\alpha_0)/\{4K_0\sigma_0-(\alpha_0+\beta_0)^2\}^{\frac{1}{2}}, \tag{3.2.12}$$

(3.2.11) becomes

$$m=\tfrac{1}{2}\{4K_0\sigma_0-(\alpha_0+\beta_0)^2\}^{\frac{1}{2}}(a+\mathrm{i}). \tag{3.2.13}$$

We now define a variable θ in terms of p as

$$\theta=\tfrac{1}{2}\{4K_0\sigma_0-(\alpha_0+\beta_0)^2\}^{\frac{1}{2}}p, \tag{3.2.14}$$

and then, on the permissible assumption that B is a real constant, write (3.2.7) as

$$V=B\mathrm{e}^{a\theta}\mathrm{e}^{\mathrm{i}\theta}, \tag{3.2.15}$$

and, with the aid of (3.2.10), write (3.2.6) as

$$T=\{(m+\alpha_0)/K_0\}B\mathrm{e}^{a\theta}\mathrm{e}^{\mathrm{i}\theta}. \tag{3.2.16}$$

Using (3.2.11), it is a simple proposition to show that

$$m+\alpha_0=(K_0\sigma_0)^{\frac{1}{2}}e^{i\varepsilon}, \tag{3.2.17}$$

where

$$\varepsilon=\tan^{-1}\left[\frac{\{4K_0\sigma_0-(\alpha_0+\beta_0)^2\}^{\frac{1}{2}}}{\alpha_0+\beta_0}\right]. \tag{3.2.18}$$

Hence, using (3.2.17), we may write (3.2.16) in the form

$$\overline{T}=(\sigma_0/K_0)^{\frac{1}{2}}\cdot Be^{a\theta}e^{i(\theta+\varepsilon)}. \tag{3.2.19}$$

Application of the operator Im to the equations (3.2.15) and (3.2.19) yields the physical electric potential and temperature expressions

$$V=Be^{a\theta}\sin\theta, \tag{3.2.20}$$

and

$$T=(\sigma_0/K_0)^{\frac{1}{2}}Be^{a\theta}\sin(\theta+\varepsilon). \tag{3.2.21}$$

To determine the real constant B, we observe that when $\partial T/\partial\theta=0$, $T=T_m$, the maximum temperature, and $\theta=\theta_m$. From (3.2.21), $\partial T/\partial\theta=0$ gives

$$\tan(\theta_m+\varepsilon)=-1/a. \tag{3.2.22}$$

Since ε and a can be calculated from the available data, θ_m is determined by (3.2.22). B is therefore obtained from (3.2.21) as

$$B=\frac{(K_0/\sigma_0)^{\frac{1}{2}}T_m}{(\exp a\theta_m)\sin(\theta_m+\varepsilon)}. \tag{3.2.23}$$

Proceeding numerically, use of equations (2.7), (2.8), (2.11), and (2.12) in (3.2.12) and (3.2.18) gives

$$\left.\begin{aligned} a&=5\cdot446,\\ \varepsilon&=0\cdot1169 \text{ radians } (6\cdot7^\circ). \end{aligned}\right\} \tag{3.2.24}$$

Insertion of these results into (3.2.22) gives

$$\theta_m=2\cdot8431 \text{ radians } (162\cdot9^\circ), \tag{3.2.25}$$

and so, using (2.11), (2.12), (3.2.24), and (3.2.25), (3.2.23) gives

$$B=1\cdot7713\times10^{-10}T_m \text{ deg}^{-1}\text{ V}, \tag{3.2.26}$$

and the factor $(\sigma_0/K_0)^{\frac{1}{2}}B$ becomes

$$(\sigma_0/K_0)^{\frac{1}{2}}B=1\cdot045\times10^{-6}T_m. \tag{3.2.27}$$

Substitution of these results in (3.2.20) and (3.2.21) yields the numerical forms

$$V=1\cdot7713\times10^{-10}T_m e^{5\cdot4460}\sin\theta \text{ V deg}^{-1}, \tag{3.2.28}$$

and

$$T=1\cdot045\times10^{-6}T_m e^{5\cdot4460}\sin(\theta+0\cdot1169). \tag{3.2.29}$$

If the thermoelectric coefficients α_0 and β_0 are excluded from (3.2.12) and (3.2.18),

$$\left.\begin{aligned} a&=0, \\ \varepsilon&=\tfrac{1}{2}\pi, \end{aligned}\right\} \tag{3.2.30}$$

and hence, from (3.2.22),

$$\theta_m=0. \tag{3.2.31}$$

With these results the expression (3.2.23) for B becomes simply,

$$B=(K_0/\sigma_0)^{\frac{1}{2}}T_m,$$

and accordingly (3.2.20) and (3.2.21) reduce respectively to

$$V=(K_0/\sigma_0)^{\frac{1}{2}}T_m \sin\theta, \tag{3.2.32}$$

and

$$T=T_m \cos\theta, \tag{3.2.33}$$

which can be combined to give

$$T^2+(\sigma_0/K_0)V^2=T_m^2, \tag{3.2.34}$$

as obtained in S, Section VI (*a*).

To complete the detailed mathematical analyses of non-constricted and constricted axi-symmetric discharges, we follow the procedure adopted in Section VI (*d*) of S, and introduce a more general orthogonal curvilinear coordinate system, w, v, u, and assume henceforth that V and T are functions of u only. Again, the only non-zero component of j is j_u, which, from (2.1), (2.5), (2.9), (3.2.14), (3.2.2), and (3.2.3), is given in curvilinear form as

$$j_u=\frac{2(\alpha_0\beta_0-K_0\sigma_0)}{\{4K_0\sigma_0-(\alpha_0+\beta_0)^2\}^{\frac{1}{2}}}\,\frac{T^{5/2}}{(h_3\ln\lambda)}\,\frac{\partial\theta}{\partial u}, \tag{3.2.35}$$

or

$$j_u=G(u)/h_3, \tag{3.2.36}$$

where the notation adopted here is illustrated in Figure 2.

Integration of the steady-state form of the electrical equation of continuity, $\operatorname{div}\mathbf{j}=0$, gives, for axi-symmetric flow,

$$j_u=F(w)/h_1h_2. \tag{3.2.37}$$

Combination of (3.2.35) and (3.2.37) results in

$$F(w)\int_0^u \frac{h_3}{h_1h_2}\,du'=\frac{2(\alpha_0\beta_0-K_0\sigma_0)}{\{4K_0\sigma_0-(\alpha_0+\beta_0)^2\}^{\frac{1}{2}}}\,\frac{T_m^{5/2}}{\ln\lambda}\int_{\theta_1}^{\theta}\left(\frac{T}{T_m}\right)^{5/2}d\theta', \tag{3.2.38}$$

where we assume that the electrodes are held at $T=0$, so that from (3.2.21)

$$\left.\begin{aligned} &\theta_1 \text{ (at cathode)}=-0\cdot1169 \text{ radians } (-6\cdot7^\circ), \\ &\theta_2 \text{ (at anode)}\;\;\;=+3\cdot0246 \text{ radians } (+173\cdot3^\circ). \end{aligned}\right\} \tag{3.2.39}$$

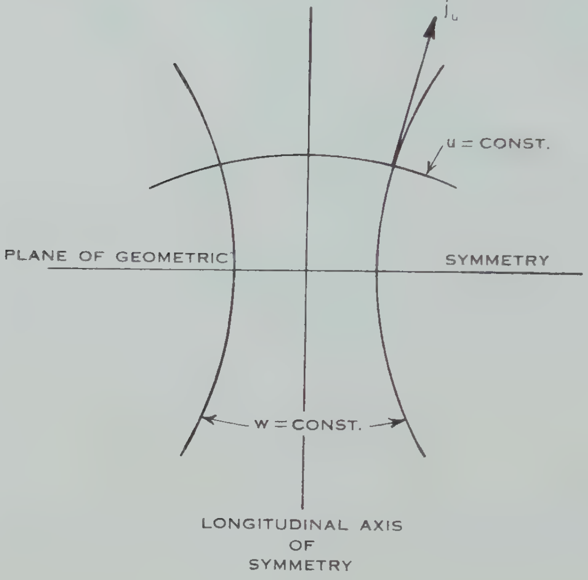

Fig. 2.—w and u as orthogonal curvilinear coordinates (axi-symmetric flow).

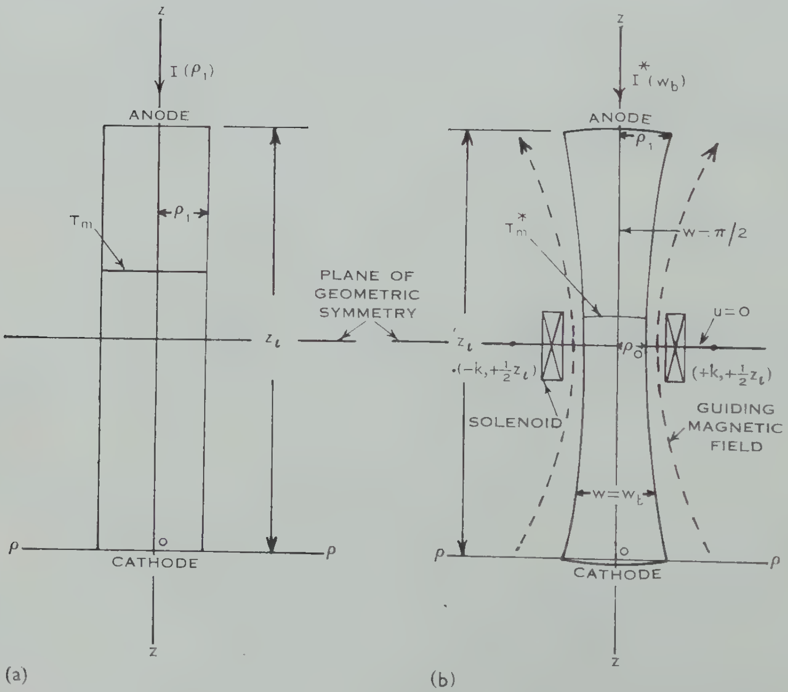

Fig. 3.—Discharge cross sections in the ρ-z plane. (a) Streamlines parallel to oz, (b) streamlines curved.

Equation (3.2.38) can be readily solved if the variables in $h_3/(h_1h_2)$ are separable. We now consider its application to (1) the linear, (2) the constricted discharge.

(c) *Specialization of Results for a Linear Discharge*

The cross section in the ρ-z plane for this case is shown in Figure 3 (*a*).

Using cylindrical coordinates, with $w=\rho$, $v=\varphi$, $u=z$, we have $h_1=h_3=1$, $h_2=\rho$, and $V=V(z)$, $T=T(z)$, $\psi=\psi(\rho)$. Thus, in Figure 3 (*a*) the streamlines are parallel to oz, and the equipotential lines are normal to oz. Using the above scale factors, (3.2.36) and (3.2.37) yield

$$j_z=G(z)=F(\rho)/\rho=\text{const.}, \tag{3.3.1}$$

and since (3.2.21) and (3.2.23) combine to give

$$\frac{T}{T_m}=\frac{(\exp a\theta)\sin(\theta+\varepsilon)}{(\exp a\theta_m)\sin(\theta_m+\varepsilon)},$$

use of the scale factors and these results in (3.2.38) gives

$$z=\frac{2(\alpha_0\beta_0-K_0\sigma_0)}{\{4K_0\sigma_0-(\alpha_0+\beta_0)^2\}^{\frac{1}{2}}}\,\frac{T_m^{5/2}}{j_z\ln\lambda}\int_{\theta_1}^{\theta}\left(\frac{(\exp a\theta')\sin(\theta'+\varepsilon)}{(\exp a\theta_m)\sin(\theta_m+\varepsilon)}\right)^{5/2}\mathrm{d}\theta', \tag{3.3.2}$$

or, using the earlier results for α_0, β_0, σ_0, K_0, and taking $\ln\lambda=10$,

$$z=-\frac{0\cdot9273}{10^8}\,\frac{T_m^{5/2}}{j_z}\int_{\theta_1}^{\theta}\left(\frac{(\exp a\theta')\sin(\theta'+\varepsilon)}{(\exp a\theta_m)\sin(\theta_m+\varepsilon)}\right)^{5/2}\mathrm{d}\theta'\ \text{A cm}^{-1}\,\text{deg}^{-5/2}. \tag{3.3.3}$$

The value of the integral in the right-hand side of (3.3.3) can be obtained for chosen values of θ in the range $\theta_1<\theta\leqslant\theta_2$ by numerical integration, since a, ε, and θ_m are known. In particular, the length of the discharge, $z_\iota>0$, corresponds to $\theta=\theta_2$, and (3.3.3) then leads to

$$\frac{z}{z_\iota}=\frac{1}{0\cdot293}\int_{\theta_1}^{\theta}\left(\frac{(\exp a\theta')\sin(\theta'+\varepsilon)}{(\exp a\theta_m)\sin(\theta_m+\varepsilon)}\right)^{5/2}\mathrm{d}\theta'. \tag{3.3.4}$$

Equation (3.3.4) gives the fraction z/z_ι for each value of θ chosen, and therefore, using (3.2.28) and (3.2.29), V/T_m and T/T_m can be plotted against z/z_ι, as in Figure 4 (*b*). With reference to S, Section VI (*d*), we also include for comparison Figure 4 (*a*), which shows V/T_m and T/T_m plotted against z/z_0 when thermoelectric effects are excluded.

Examination of (3.2.35) for this case suggests the form $j_z=-j$, where $j>0$. Using this result, the maximum temperature is derived from (3.3.3) as

$$T_m=2228\{\tfrac{1}{2}z_\iota I(\rho_1)/\rho_1^2\}^{2/5}\quad\text{A}^{-2/5}\,\text{cm}^{2/5}\,\text{deg}, \tag{3.3.5}$$

where $I(\rho_1)=\pi\rho_1^2 j$, and the semi-length, $\frac{1}{2}z_\iota$, has been introduced to facilitate comparison of the above result with S, (6.4.14).

From (3.2.28) and (3.2.29), we have at the anode of the discharge,

$$V_2=+2\cdot434\times10^{-4}T_m\ \text{V deg}^{-1}, \tag{3.3.6}$$

and at the cathode,

$$V_1=-1\cdot0933\times10^{-11}T_m\ \text{V deg}^{-1}. \tag{3.3.7}$$

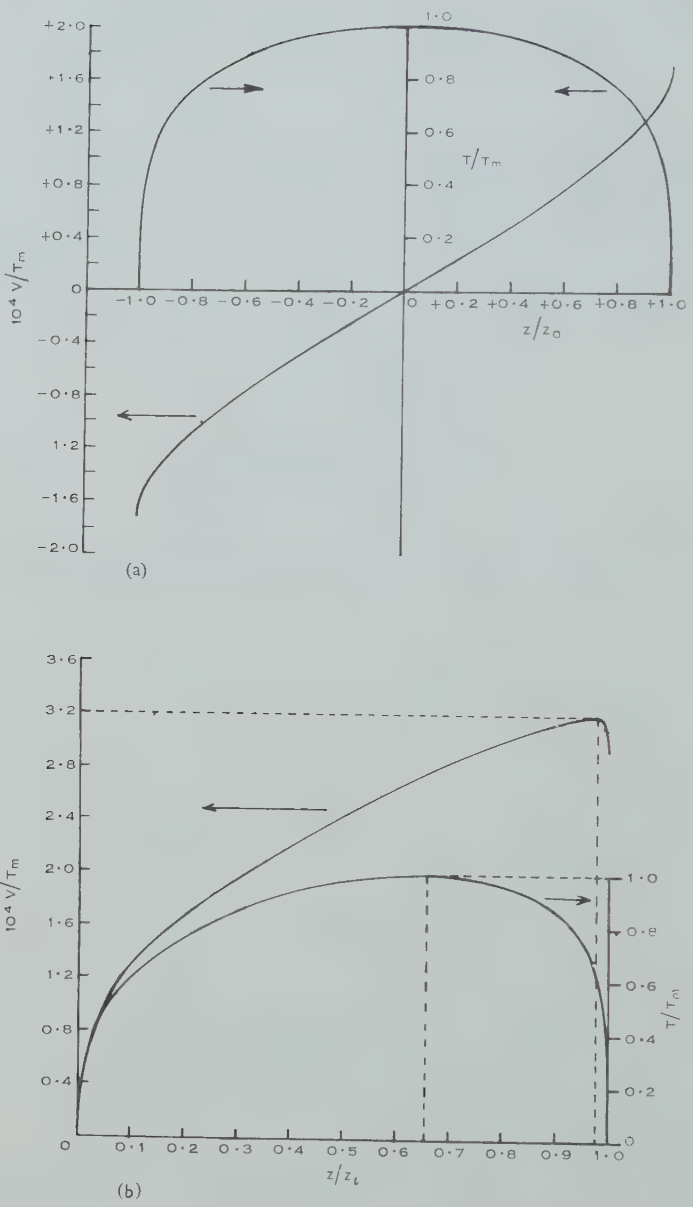

Fig. 4.—Temperature *v.* distance, voltage *v.* distance characteristics for linear discharge of circular cross section. (*a*) Thermoelectric effects excluded, (*b*) thermoelectric effects included.

The latter result shows that for values of T_m likely to be attained in practice, $V_1 \sim 0$, and accordingly the zero of potential may be conveniently considered located at the cathode. Then V_2 is the voltage across the discharge, and so, varying the subscript to ι,

$$T_m = 3397 V_\iota \text{ V}^{-1} \text{ deg.} \tag{3.3.8}$$

Combination of (3.3.5) and (3.3.8) results in

$$V_\iota = 0\cdot 656\left(\frac{\frac{1}{2}z_\iota I(\rho_1)}{\rho_1^2}\right)^{2/5} \text{A}^{-2/5}\ \text{cm}^{2/5}\ \text{V}. \tag{3.3.9}$$

(*d*) *Specialization of Results for a Discharge having Hyperbolic Streamlines*

The cross section in the ρ-z plane for this case is shown in Figure 3 (*b*). The short solenoid producing the constricting, or guiding, magnetic field has axis oz, and is assumed centrally located between anode and cathode of the discharge. With $V=V(u)$, $\psi=\psi(w)$, we can again approximate the current streamlines by hyperbolae to represent the practical situation. Mathematically, we relate u and w to ρ and z by the conformal transformation

$$\rho+\mathrm{i}(z-\tfrac{1}{2}z_\iota)=k\cosh(u+\mathrm{i}w),\ k\ \text{defined below}, \tag{3.4.1}$$

which expands to give

$$\rho=k\cosh u\cos w, \tag{3.4.2}$$

and

$$z-\tfrac{1}{2}z_\iota=k\sinh u\sin w. \tag{3.4.3}$$

Then

$$\rho^2/k^2\cosh^2 u+(z-\tfrac{1}{2}z_\iota)^2/k^2\sinh^2 u=1, \tag{3.4.4}$$

and

$$\rho^2/k^2\cos^2 w-(z-\tfrac{1}{2}z_\iota)^2/k^2\sin^2 w=1. \tag{3.4.5}$$

As in S, Section VI (*d*), Case 2, we see that in the ρ-z plane the curves $u=$const., $w=$const. form a family of confocal ellipses and hyperbolae, here with common foci at $(\pm k, +\frac{1}{2}z_\iota)$. Again, for the scale factors we have

$$h_1=h_3, \tag{3.4.6}$$

and

$$h_2=k\cosh u\cos w, \tag{3.4.7}$$

and accordingly, from (3.2.36), (3.2.37), and the above two equations

$$G(u)\cosh u=F(w)/k\cos w=\text{const.}=A. \tag{3.4.8}$$

Following the procedure of S, Section VI (*d*), we can establish

$$-I^*(w_b)=2\pi kA(1-\sin w_b). \tag{3.4.9}$$†

From Figure 3 (*b*) and equations (3.4.2), (3.4.3)

$$\left.\begin{aligned}\rho_0&=k\cos w_b,\\ \rho_1&=k\cosh u_e\cos w_b,\\ \tfrac{1}{2}z_\iota&=k\sinh u_e,\end{aligned}\right\} \tag{3.4.10}$$

where $u=\pm u_e$ gives the electrodes.

---

† The star superscript is used when necessary to indicate a Section III (*d*) quantity.

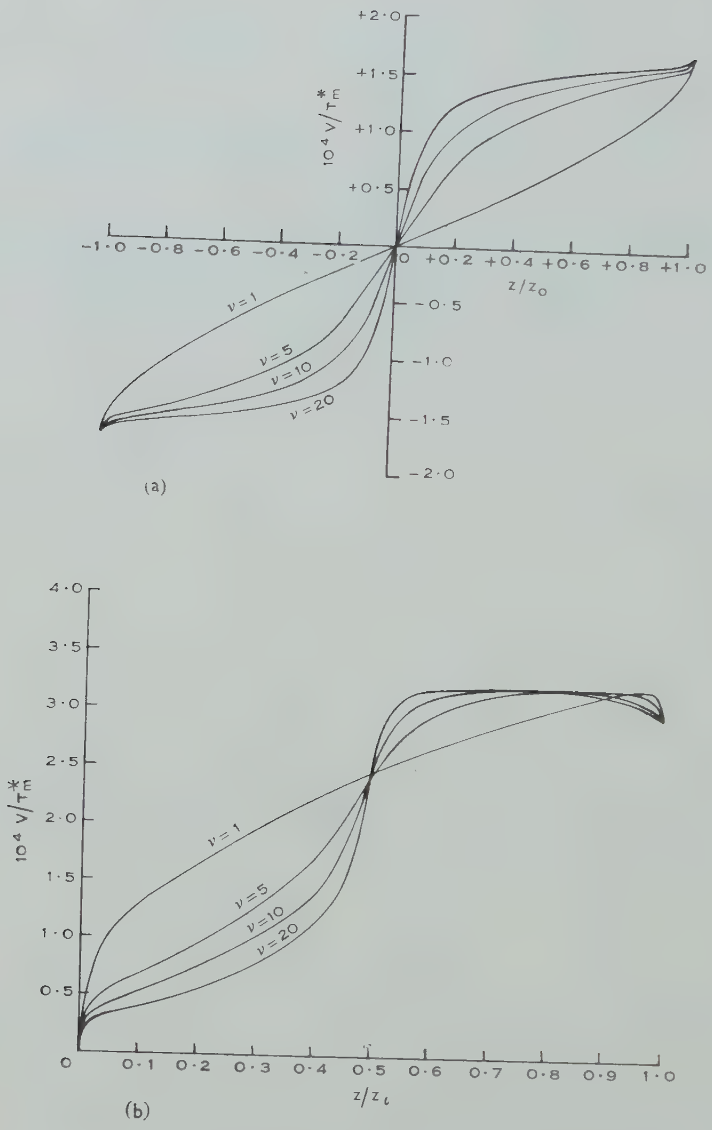

Fig. 5.—Voltage versus distance characteristics with radial compression ratio ν as parameter. (*a*) Thermoelectric effects excluded, (*b*) thermoelectric effects included.

By proper choice of the left-hand side integral limits in (3.2.38), and use of (3.2.21), (3.2.23), and (3.4.6) to (3.4.9), is obtained

$$\tan^{-1}(\sinh u)+\tan^{-1}(\sinh u_e)=$$

$$\frac{4\pi k(K_0\sigma_0-\alpha_0\beta_0)(1-\sin w_b)T_m^{*5/2}}{\ln \lambda I^*(w_b)\{4K_0\sigma_0-(\alpha_0+\beta_0)^2\}^{\frac{1}{2}}}\int_{\theta_1}^{\theta}\left(\frac{(\exp a\theta')\sin(\theta'+\varepsilon)}{(\exp a\theta_m)\sin(\theta_m+\varepsilon)}\right)^{5/2}d\theta'. \tag{3.4.11}$$

With $u=+u_e$ corresponding to $\theta=\theta_2$, application to (3.4.11) of the steps that led to (3.3.4) yields

$$\frac{\tan^{-1}(\sinh u)+\tan^{-1}(\sinh u_e)}{2\tan^{-1}(\sinh u_e)}=\frac{1}{0\cdot 293}\int_{\theta_1}^{\theta}\left(\frac{(\exp a\theta')\sin(\theta'+\varepsilon)}{(\exp a\theta_m)\sin(\theta_m+\varepsilon)}\right)^{5/2}\mathrm{d}\theta'=R \text{ say.} \tag{3.4.12}$$

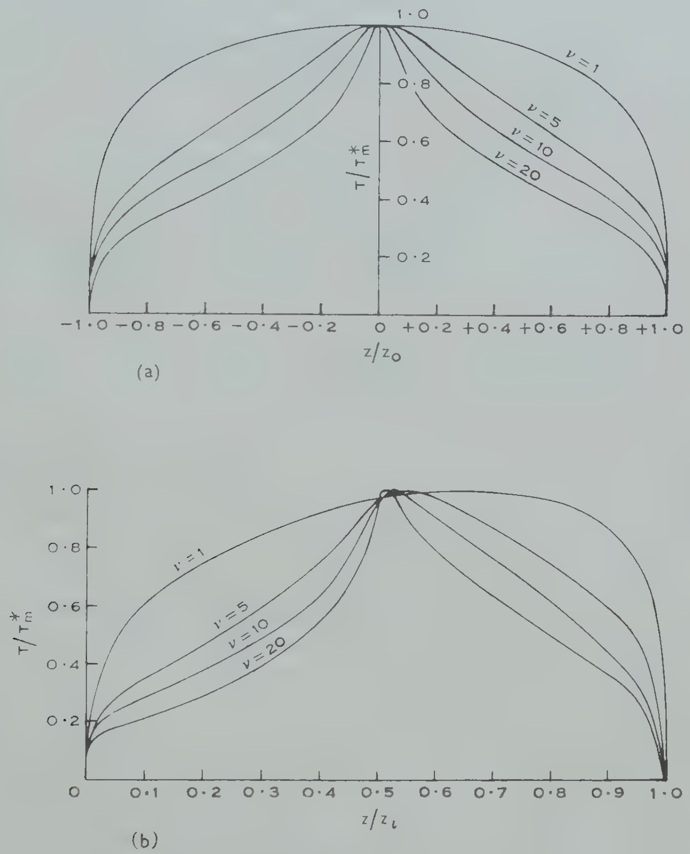

Fig. 6.—Temperature versus distance characteristics with radial compression ratio ν as parameter. (*a*) Thermoelectric effects excluded, (*b*) thermoelectric effects included.

When $w=\frac{1}{2}\pi$ we see from (3.4.2) and (3.4.3) that, as u varies, the point defined by the coordinates ρ and z moves along the symmetry axis oz in Figure 3 (*b*). Then, rearranging (3.4.12) and using (3.4.3) and the last equation of (3.4.10), we obtain

$$z/z_{\iota}=\tfrac{1}{2}[1+\{1/(\nu^2-1)^{\frac{1}{2}}\}\tan\{(2R-1)\tan^{-1}(\nu^2-1)^{\frac{1}{2}}\}], \tag{3.4.13}$$

where $\nu=\rho_1/\rho_0$ is the radial compression ratio. Clearly, $\nu=1$ reduces this equation to (3.3.4) as required.

Using appropriate numerical techniques we can obtain from (3.4.13) the fraction z/z_ι for each value of θ chosen, with ν as a parameter, and hence, with the further aid of (3.2.28) and (3.2.29), V/T_m^* and T/T_m^* can be plotted versus z/z_ι for suitable values of ν, as in Figures 5 (*b*) and 6 (*b*) respectively. Similarly, with reference to S, (6.4.33), and the associated expressions $T=T_m^* \cos\theta$, $V=(K_0/\sigma_0)^{\frac{1}{2}}T_m^* \sin\theta$, $-\frac{1}{2}\pi \leqslant \theta \leqslant +\frac{1}{2}\pi$, we can calculate for comparison the characteristics of Figures 5 (*a*) and 6 (*a*), which show respectively V/T_m^* and T/T_m^* versus z/z_0 when thermoelectric effects are excluded.

Using the corresponding values $u=+u_e$ and $\theta=\theta_2$, the maximum temperature is derived from (3.4.11) as

$$T_m^*=\left(\frac{\ln \lambda I^*(w_b)\{4K_0\sigma_0-(\alpha_0+\beta_0)^2\}^{\frac{1}{2}} \tan^{-1} (\sinh u_e)}{(0\cdot 293)2\pi k(1-\sin w_b)(K_0\sigma_0-\alpha_0\beta_0)}\right)^{2/5}. \qquad (3.4.14)$$

The results (3.4.10) can be interpreted geometrically with the aid of Figure 3 (*b*) as in S, Section VI (*d*), and (3.4.14) accordingly becomes

$$T_m^*=\left(\frac{\ln \lambda I^*(w_b)\{4K_0\sigma_0-(\alpha_0+\beta_0)^2\}^{\frac{1}{2}}(\nu^2-1)^{\frac{1}{2}} \tan^{-1} (\nu^2-1)^{\frac{1}{2}}}{(0\cdot 293)2\pi(\frac{1}{2}z_\iota)(K_0\sigma_0-\alpha_0\beta_0)[1-\{1-(\rho_1/\frac{1}{2}z_\iota)^2\nu^{-2}(\nu^2-1)\}^{\frac{1}{2}}]}\right)^{2/5}. \qquad (3.4.15)$$

Again referring to (2.7), (2.8), (2.11), (2.12); taking $\ln\lambda=10$, and from physical considerations, $(\rho_1/\frac{1}{2}z_\iota)^2 \ll 1$, (3.4.15) reduces to the more attractive form

$$T_m^*=2228\left\{\frac{\frac{1}{2}z_\iota I^*(w_b)}{\rho_1^2}\right\}^{2/5}\left\{\frac{\nu^2 \tan^{-1} (\nu^2-1)^{\frac{1}{2}}}{(\nu^2-1)^{\frac{1}{2}}}\right\}^{2/5} \mathrm{A}^{-2/5}\,\mathrm{cm}^{2/5}\,\mathrm{deg}. \qquad (3.4.16)$$

Combining (3.4.16) with (3.3.8), which is also applicable here,

$$V_\iota^*=0\cdot 656\left\{\frac{\frac{1}{2}z_\iota I^*(w_b)}{\rho_1^2}\right\}^{2/5}\left\{\frac{\nu^2 \tan^{-1} (\nu^2-1)^{\frac{1}{2}}}{(\nu^2-1)^{\frac{1}{2}}}\right\}^{2/5} \mathrm{A}^{-2/5}\,\mathrm{cm}^{2/5}\,\mathrm{V}. \qquad (3.4.17)$$

IV. DISCUSSION OF RESULTS

To estimate the influence of thermoelectric effects, we first take from S the results (6.4.38) and (6.4.40), and combine them with (3.4.16) and (3.4.17) above to obtain for a given discharge the ratios

$$\widetilde{T}_m^*/T_m^*=1\cdot 136, \qquad (4.1)†$$

and

$$\widetilde{V}_\iota^*/2V_e^*=0\cdot 985. \qquad (4.2)$$

Comparing Figures 4 (*a*) and 4 (*b*), we observe that, for the linear discharge, inclusion of thermoelectric effects results in a displacement of the zero of the heat flux vector and electric potential from midway between the electrodes virtually to the cathode. Also, in Figure 4 (*b*) it is evident that the slope of the electric potential characteristic changes sign near the anode, and so, from (2.1), we see that in this region the constant current density $\mathbf{j}$ of the linear discharge is maintained by the term $\alpha\nabla T$ acting against $\sigma\mathbf{E}$. By forming the scalar product $\mathbf{j}\cdot\mathbf{E}$, we see that the Joule heating per unit volume in this region is made up of a cooling term, $\alpha\mathbf{E}\cdot\nabla T$, and a smaller heating term, σE^2. Considering the nature of the Seebeck and Peltier effects included in the basic equations (2.1) and (2.2) for **j** and **q**, this is perhaps not a surprising result.

---

† The curly bar is used when necessary to indicate a thermoelectric case quantity.

Since, for the linear discharge, $q_z+Vj_z=0$, where the current density $j_z=-j, j>0$, is a constant, it is of interest to note that the voltage characteristics of Figures 4 (*a*) and 4 (*b*) also represent the heat flux characteristics $q_z/(jT_m)$ plotted against z/z_0 and z/z_ι respectively.

Further comparison of Figures 4 (*a*) and 4 (*b*) shows that thermoelectric effects displace the temperature maximum from midway between the electrodes towards the anode, but here the displacement is not marked.

When the discharge is constricted at the plane of geometric symmetry and thermoelectric effects are excluded, the shape of the temperature versus distance characteristic varies with increase of radial compression ratio, as shown in Figure 6 (*a*). Since the central constriction produces an increase of plasma temperature at and near the plane of symmetry, the narrowing of the peaks of the characteristics in Figure 6 (*a*) with increase of radial compression ratio can be readily understood physically.

Figure 6 (*b*) gives corresponding characteristics when thermoelectric effects are included. Broadly, the above remark on Figure 6 (*a*) applies here, and, as would also be expected from physical reasoning, the displaced temperature maximum of the linear discharge tends to return towards the plane of geometric symmetry as the radial compression ratio assumes values greater than unity.

As can be verified by means of (3.2.36), (3.4.8), and S, (6.4.22), when the discharge is centrally constricted the current density is no longer constant, but becomes a function of w and u. This remark also applies when thermoelectric effects are excluded, as can be seen from S, (6.4.5), (6.4.22), and (6.4.26). These and other facts complicate the possibility of obtaining a simple physical explanation of the trend of the voltage against distance characteristics of Figures 5 (*a*) and 5 (*b*) as radial compression increases.

The important conclusion that can be drawn from equation (4.1) is that the maximum temperature $\widetilde{T}_m^*$ is raised above T_m^* by some 14% due to thermoelectric effects. However, by forming the temperature ratio, $\widetilde{T}_m^*/\widetilde{T}_m$, from (3.4.16) and (3.3.5); and the resistance ratio, $\widetilde{R}^*/\widetilde{R}$, from (3.4.17) and (3.3.9) for conditions outlined in S, Section VII, it is immediately evident that the characteristic of Figure 7 of that paper is also applicable when thermoelectric effects are included.

Equation (4.2) shows that the total voltage required to produce a given current in a particular geometry of discharge is about the same without and with thermoelectric effects.

V. ACKNOWLEDGMENT

Progress in the attempt to include thermoelectric effects in the analysis of the steady-state deuterium discharge cooled by heat flow to the electrodes was aided by discussions with Professor K. J. Le Couteur, and the author gratefully acknowledges the guidance and helpful suggestions received at these discussions.

VI. REFERENCES

MARSHALL, W. (1957).—Kinetic theory of an ionized gas. Part 3, p. 91. Atomic Energy Research Establishment Report T/R 2419. (H.M. Stationery Office: London.)

SEYMOUR, P. W. (1961).—Estimation of the maximum temperature in a radially constricted gas discharge between electrodes. *Aust. J. Phys.* **14**: 129–51.

SPITZER, L., JR., and HÄRM, R. (1953).—Transport phenomena in a completely ionized gas. *Phys. Rev.* **89**: 977–81.

COUNTS OF EXTRAGALACTIC RADIO SOURCES

By R. Van der Borght*

[*Manuscript received January* 20, 1961]

Summary

In this paper a formula is derived giving the cumulative totals of class II radio sources, to successive limits of flux density, when changes in the space-density and in the radiative properties of these sources are taken into account.

The formula is then compared with the observations and it is shown that it embodies the various attempts which have been made so far to explain the $-3/2$ power law.

I. Introduction

The number of radio sources in the space-time

$$\mathrm{d}s^2=\mathrm{d}t^2-\frac{R^2(t)}{c^2}\left\{\frac{\mathrm{d}r^2+r^2\mathrm{d}\theta^2+r^2\sin^2\theta\mathrm{d}\varphi^2}{(1+\frac{1}{4}\alpha r^2)^2}\right\}, \tag{1}$$

lying within $0\rightarrow r$, is given by the formula (McVittie 1956)

$$N=\frac{4\pi}{R_0^3}\int_0^{\zeta}\frac{R^3(t)\nu(t)\zeta^2\mathrm{d}\zeta}{(1+\zeta^2/a^2)^3}, \tag{2}$$

where

$$\zeta=R_0r,\quad a^2=4R_0^2/\alpha, \tag{3}$$

and $\nu(t)$ is the number of radio sources per unit volume at time t.

In relativistic cosmology, it is usually assumed that the space density parameter

$$\varepsilon=R^3(t)\nu(t) \tag{4}$$

is constant.

In order to account for the observed distribution of extragalactic radio sources (Mills, Slee, and Hill 1958) one has been led to one of the following alternatives :

1. All class II radio sources are assumed to be of equal power and to be at rest and scattered at random with constant space density in the Euclidian space. But, as pointed out by McVittie (1959), there are serious objections to this interpretation.

2. The space density parameter ε in formula (4) is assumed to be constant, but it is assumed that secular changes in the radiative properties of the sources are taking place (McVittie 1957).

---

* Australian National University, Canberra.

3. One assumes that all radio sources have equal power but that these sources are colliding galaxies, i.e. one abandons the assumption of constant space density parameter (Priester 1958 ; Davidson 1959).

It is the purpose of the present paper to derive a formula connecting the cumulative number N of radio sources to successive limits of flux density S, allowing for secular changes both in the radiative properties and in the space density of these sources.

II. Number of Radio Sources and Luminosity Distance

Using the expansion

$$(1+\zeta^2/a^2)^{-3}=1-3\zeta^2/a^2,$$

formula (2) may be written

$$N=\frac{4\pi}{R_0^3}\int_0^\zeta R^3(t)\nu(t)\left[\zeta^2-3\frac{\zeta^4}{a^2}\right]\mathrm{d}\zeta. \tag{5}$$

But (McVittie 1956)

$$R=R_0(1-x+gx^2), \tag{6}$$

where

$$x=h_1D/c, \tag{7}$$

and

$$g=(3h_1^2+h_2)/2h_1^2, \tag{8}$$

D being the luminosity distance, h_1 the Hubble constant $\dot{R}_0/R_0$, and $h_2=\ddot{R}_0/R_0$. Also

$$\zeta=(cx/h_1)(1-x+bx^2), \tag{9}$$

where

$$b=3/2+\tfrac{1}{2}h_2/h_1^2+c^2/h_1^2a^2. \tag{10}$$

Substituting (6) and (9) in (5) we have

$$N=4\pi\int_0^x \nu(x)(1-x+gx^2)^3\left\{\frac{c^2x^2}{h_1^2}(1-x+bx^2)^2\right.$$
$$\left.-\frac{3}{a^2}\left(\frac{cx}{h_1}\right)^4(1-x+bx^2)^4\right\}\frac{c}{h_1}(1-2x+3bx^2)\mathrm{d}x. \tag{11}$$

We now consider the space density as a function of the luminosity distance, given by the following expansion to the second order in x,

$$\nu=\nu_0+\nu_1x+\nu_2x^2. \tag{12}$$

Substituting (12) in (11), working out the various expansions and integrating we have

$$N=\frac{4\pi c^3x^3}{h_1^3}\left[\tfrac{1}{3}\nu_0+\tfrac{1}{4}(\nu_1-7\nu_0)x+\left\{\nu_2-7\nu_1+\nu_0\left(3g+19+5b+1-\frac{3c^2}{a^2h_1^2}\right)\right\}\frac{x^2}{5}\right]. \tag{13}$$

It is easily seen that

$$\varepsilon=\nu R^3=\nu_0+(\nu_1-3\nu_0)x+[\nu_2-3\nu_1+3\nu_0(g+1)]x^2, \tag{14}$$

and that for constancy of the space density parameter, that is,

$$\varepsilon = \nu_0,$$

we should have

$$\nu_1 = 3\nu_0, \tag{15}$$

and

$$\nu_2 = 3\nu_0(2-g). \tag{16}$$

Substituting these values of ν_1 and ν_2 in (13) we have, using (10),

$$N = (4\pi/3)\nu_0 D[1-3x+3\{2+(h_1^2+h_2)/2h_1^2+2c^2/5a^2h_1^2\}x^2], \tag{17}$$

which is the formula commonly used in relativistic cosmology (McVittie 1956).

Substituting the values for g and b from (8) and (10) in formula (13) we have

$$N = \frac{4\pi c^3x^3}{h_1^3} \cdot \frac{\nu_0}{3}\left\{1+\tfrac{3}{4}\left(\frac{\nu_1}{\nu_0}-7\right)x+3\left(\frac{\nu_2}{\nu_0}-7\frac{\nu_1}{\nu_0}+32+\frac{4h_2}{h_1^2}+\frac{2c^2}{a^2h_1^2}\right)\frac{x^2}{5}\right\}. \tag{18}$$

III. Number of Radio Sources and Flux Density

The flux density in watts/m² measured by the observer in the range $\lambda_1 \rightarrow \lambda_2$ of observed wavelength is

$$L = \frac{A}{4\pi D^2} \cdot \frac{1}{1+\delta}\int_{\lambda_1}^{\lambda_2} \sigma(\lambda)B\left(t, \frac{\lambda}{1+\delta}\right)\mathrm{d}\lambda, \tag{19}$$

where A is the total emitting area of the source,

$B(t, \lambda)\mathrm{d}\lambda$ is the energy emitted by the source at the time t in the range $\mathrm{d}\lambda$ in watts/m².

$\sigma(\lambda)$ is an empirical function depending on the atmospheric extinction and the response of the apparatus.

In this paper, in order to simplify the analysis, we assume that the function $B(t,\lambda)$ is the same for all sources, i.e. we assume that all sources have equal power. In fact this can only be a first approximation since recent observations (Mills 1960) seem to indicate a marked dispersion in the radiative power of the sources. The function $B(t,\lambda)$ should here be regarded as a mean value.

If L_0 is the flux density for a nearby standard source at distance d ($\delta=0$) we have

$$L_0 = \frac{A}{4\pi d^2}\int_{\lambda_1}^{\lambda_2} \sigma(\lambda)B(t_0, \lambda)\mathrm{d}\lambda. \tag{20}$$

Then

$$\frac{L}{L_0} = \frac{d^2}{D^2} \cdot \frac{1}{1+\delta} \cdot \frac{I}{I_0} \cdot \frac{1}{I} \cdot \int_{\lambda_1}^{\lambda_2} \sigma(\lambda)B\left(t, \frac{\lambda}{1+\delta}\right)\mathrm{d}\lambda, \tag{21}$$

where

$$I = \int_{\lambda_1}^{\lambda_2} \sigma(\lambda)B(t, \lambda)\mathrm{d}\lambda, \tag{22}$$

$$I_0 = \int_{\lambda_1}^{\lambda_2} \sigma(\lambda)B(t_0, \lambda)\mathrm{d}\lambda. \tag{23}$$

But, if S is the flux density in watts m^{-2} (c/s)$^{-1}$, we have

$$S=\frac{L}{|\nu_1-\nu_2|}=\frac{L\lambda_1\lambda_2}{c(\lambda_2-\lambda_1)},$$

and

$$S/S_0=L/L_0. \tag{24}$$

We take

1. for the correction due to secular changes in the radiative properties of the sources,

$$I/I_0=1+W_1x+W_2x^2, \tag{25}$$

2. for the K-correction,

$$\frac{1}{(1+\delta)I}\int_{\lambda_1}^{\lambda_2}\sigma(\lambda)B\left(t,\ \frac{\lambda}{1+\delta}\right)d\lambda=1+C_1x+C_2x^2. \tag{26}$$

Substituting (24), (25), (26) in (21) we get, to the second order in x,

$$S/S_0=(d^2h_1^2/c^2x^2)(1+\beta x+\alpha x^2), \tag{27}$$

where

$$\beta=C_1+W_1, \tag{28}$$

and

$$\alpha=W_1C_1+(W_2+C_2), \tag{29}$$

or

$$x[1+\beta x+\alpha x^2]^{-\frac{1}{2}}=y, \tag{30}$$

where

$$y=(dh_1/c)(S_0/S)^{\frac{1}{2}}. \tag{31}$$

It follows easily from (30) that

$$x=y+\tfrac{1}{2}\beta x^2+(\tfrac{1}{2}\alpha-\tfrac{3}{8}\beta^2)x^3. \tag{32}$$

It then follows from (32) that

$$\left.\begin{aligned}&x=y,\\&x=y+\tfrac{1}{2}\beta y^2,\\&x=y+\tfrac{1}{2}\beta y^2+(\tfrac{1}{2}\alpha+\tfrac{1}{8}\beta^2)y^3,\end{aligned}\right\} \tag{33}$$

are the first, second, and third approximations of x as a power series in y.

Substituting (33) in (18) we have, after a few reductions,

$$N=\frac{4\pi c^3\nu_0}{3h_1^3}y^3[1+(3B_1+A_1)y+(3B_2+3B_1^2+4A_1B_1+A_2)y^2], \tag{34}$$

where

$$\begin{aligned}A_1&=\tfrac{3}{4}(\nu_1/\nu_0-7),\\A_2&=\tfrac{3}{5}[\nu_2/\nu_0-7\nu_1/\nu_0+32+4h_2/h_1^2+2c^2/a^2h_1^2],\\B_1&=\tfrac{1}{2}(C_1+W_1),\\B_2&=\tfrac{1}{2}[W_1C_1+(W_2+C_2)+\tfrac{1}{4}(C_1+W_1)^2].\end{aligned}$$

IV. Comparison with Observations

Equation (34) to the first order in y could be written

$$N=\frac{4\pi\nu_0}{3}d^3\frac{S_0^{3/2}}{S^{3/2}}\left[1+(3B_1+A_1)\frac{dh_1}{c}\,\frac{S_0^{\frac{1}{2}}}{S^{\frac{1}{2}}}\right], \tag{35}$$

and in order to satisfy the experimental law, we should have

$$(3B_1+A_1)\frac{dh_1}{c}\cdot\frac{S_0^{\frac{1}{2}}}{S^{\frac{1}{2}}}=0. \tag{36}$$

This could be satisfied in a variety of ways.

We could take $h_1=0$, i.e. assume that the sources do not participate in the general expansion, and this would correspond to the hypothesis 1 of the introduction where the sources are supposed to be at rest and scattered at random with constant number density.

As shown by McVittie (1959) there are serious difficulties to this interpretation. Moreover, quite a few radio sources have now been identified with galaxies or pairs of galaxies (Mills 1960).

For small distances

$$d=(c/h_1)\delta_0, \tag{37}$$

and substituting this in (36) we would have the condition

$$(3B_1+A_1)\delta_0 S_0^{\frac{1}{2}}/S^{\frac{1}{2}}=0. \tag{38}$$

This could be satisfied if we assume that

$$3B_1+A_1=0,$$

that is,

$$2C_1+2W_1+\nu_1/\nu_0-7=0. \tag{39}$$

(a) *Space Density Parameter ε assumed Constant*

If we assume that the space density parameter ε is constant, i.e. that

$$\nu_1=3\nu_0,$$

then condition (39) reduces to

$$W_1+C_1=2, \tag{40}$$

and, since $C_1=-0\cdot2$ (see Appendix), we have

$$W_1=2\cdot2, \tag{41}$$

and from (25)

$$I/I_0=1+2\cdot2\delta. \tag{42}$$

A secular change of this order of magnitude was found by McVittie (1957) using the standard sources:

NGC 1275 (IAU 03N4A) with $S_0=240\times10^{-26}$ W m^{-2} (c/s)$^{-1}$,

$$\delta_0=0\cdot018,$$

and Cygnus A (IAU 19N4A) with $S_0=19{,}000\times10^{-26}$ W m^{-2} (c/s)$^{-1}$,

$$\delta_0=0\cdot056.$$

McVittie also found that in the case of NGC 1275 it was possible to get a good fit to the $-3/2$ power law, without the assumption of a secular change in the radiative power, but not if Cygnus A were taken as standard source.

This is due to the fact that (35) would reproduce the observed law fairly well if

$$|(3B_1+A_1)\delta_0 S_0^{\frac{1}{2}}/S^{\frac{1}{2}}|<1 \tag{43}$$

for all observed S. The best fit would be for the large values of the observed flux density.

If we do not assume secular changes in density and luminosity, we have

$$W_1=\nu_1=0,$$

and then (43) reduces to

$$\left|\left(3\frac{C_1}{2}-3\times\frac{7}{4}\right)\frac{\delta_0 S_0^{\frac{1}{2}}}{S_m^{\frac{1}{2}}}\right|<1, \tag{44}$$

where $C_1=-0\cdot 2$ and

S_m=the smallest observed value of the flux density
$=7\times 10^{-26}$ W m^{-2} (c/s)$^{-1}$.

Then (44) reduces to

$$\delta_0 S_0^{\frac{1}{2}}<0\cdot 48\times 10^{-13}. \tag{45}$$

For NGC 1275

$$\delta_0 S_0^{\frac{1}{2}}=0\cdot 28\times 10^{-13},$$

and therefore condition (45) is satisfied.

For Cygnus A

$$\delta_0 S_0^{\frac{1}{2}}=7\cdot 7168\times 10^{-13},$$

and then the agreement is very bad indeed.

It follows then from this analysis that the $-3/2$ power law can be approximately satisfied, without further assumptions, if the standard source is taken as being a nearby faint one.

(*b*) *Space Density Parameter not Constant*

We can also assume that the space density parameter is no longer constant. This is the case, if we assume that the majority of extragalactic radio sources are colliding galaxies.

Then, in the absence of changes in the radiative power, $W_1=0$ and formula (39) reduces to

$$\nu_1=\nu_0[7-2C_1],$$

or

$$\nu_1=7\cdot 4\nu_0,$$

that is,

$$\nu=\nu_0[1+7\cdot 4\delta]. \tag{46}$$

Priester (1958) and Davidson (1959) take for the number density of colliding galaxies

$$\nu(t)=\beta n^2(t), \tag{47}$$

where

$$n(t)=n_0R_0^3/R^3(t),$$

that is,

$$\nu(t)=k/R^3(t), \tag{48}$$

k being a constant.

But, in first approximation,

$$R=R_0(1-\delta),$$

therefore

$$\nu=(k/R_0^6)(1-\delta)^{-6},$$

or

$$\nu=(k/R_0^6)(1+6\delta). \tag{49}$$

A comparison of formulae (49) and (46) shows why the collision hypothesis cannot account exactly for the $-3/2$ power law, a fact already pointed out by McVittie (1959) in a different way.

Of course, one should keep in mind that the counts need correction at low flux densities because of effects of random noise and finite aerial resolution (Mills and Slee 1957). In addition, there is a recently discovered effect (Mills, Slee, and Hill 1960) which gives a systematic tendency to over-estimate the flux density of a source when the signal-to-noise ratio is low.

The $-3/2$ power law does not seem to be established with sufficient certainty yet, and it is to be expected that the various possibilities discussed in this paper might not be the only ones.

V. References

Davidson, W. (1959).—*Mon. Not. R. Astr. Soc.* **119**: 665.

McVittie, G. C. (1956).—" General Relativity and Cosmology." (Chapman & Hall: London.)

McVittie, G. C. (1957).—*Aust. J. Phys.* **10**: 331.

McVittie, G. C. (1959).—Cosmology and the interpretation of astronomical data. Symposium on " Les theories relativistes de la gravitation ", Royaumont, June 21–27, 1959.

Mills, B. Y. (1960).—*Aust. J. Phys.* **13**: 550.

Mills, B. Y., and Slee, O. B. (1957).—*Aust. J. Phys.* **10**: 162.

Mills, B. Y., Slee, O. B., and Hill, E. R. (1958).—*Aust. J. Phys.* **11**: 360.

Mills, B. Y., Slee, O. B., and Hill, E. R. (1960).—*Aust. J. Phys.* **13**: 676.

Priester, W. (1958).—*Z. Astrophys.* **46**: 179.

Whitfield, G. K. (1957).—*Mon. Not. R. Astr. Soc.* **117**: 680.

APPENDIX

The K-correction is given by the formula

$$K=K_1\delta+K_2\delta^2,$$

where

$$K_1=(2\cdot5/E)(1+J_0/I_0),$$

with

$$E=\ln 10=2\cdot303,$$

$$J_0=\int_0^\infty \sigma(\lambda)\lambda\frac{\partial B(t_0,\lambda)}{\partial\lambda}\mathrm{d}\lambda,$$

$$I_0=\int_0^\infty \sigma(\lambda)B(t_0,\lambda)\mathrm{d}\lambda.$$

For a narrow wave-band dλ in the neighbourhood of wavelength λ, with $\sigma(\lambda)=0$ outside this wave band,

$$K_1=\frac{2\cdot5}{E}\left(1+\frac{\lambda\frac{\partial}{\partial\lambda}B(t_0,\lambda)}{B(t_0,\lambda)}\right), \tag{50}$$

t_0 being the present epoch of observation.

But (Whitfield 1957)

$$B(t_0,\lambda)=\lambda^{-0\cdot8}.$$

It follows then that

$$\frac{\lambda\frac{\partial}{\partial\lambda}B(t_0,\lambda)}{B(t_0,\lambda)}=-0\cdot8.$$

and (50) can be written

$$K_1=\frac{2\cdot5}{2\cdot303}(1-0\cdot8),$$

or

$$K_1=0\cdot218. \tag{51}$$

But (McVittie 1956)

$$K=-2\cdot5\log_{10}\left\{\frac{1}{I(1+\delta)}\int_0^\infty \sigma(\lambda)B\left(t,\frac{\lambda}{1+\delta}\right)\mathrm{d}\lambda\right\}, \tag{52}$$

where

$$I=\int_0^\infty \sigma(\lambda)B(t,\lambda)\mathrm{d}\lambda.$$

Using (26)

$$\begin{aligned}K&=-2\cdot5\log_{10}\{1+c_1x+c_2x^2\}\\&=-(2\cdot5/2\cdot303)\ln\{1+c_1\delta+.\ .\ .\},\end{aligned}$$

and using

$$\ln(1+x)=x-\tfrac{1}{2}x^2,$$

we have

$$K=-(2\cdot 5/2\cdot 303)C_1\delta.$$

Comparing this to

$$K=K_1\delta+K_2\delta^2,$$

and using the value of K_1 given by (51) we have

$$C_1=-0\cdot 2. \tag{53}$$

The exponent $-0\cdot 8$ in formula (51) does not seem to be generally accepted by radio astronomers. A different value of the exponent would result in a different value of K_1 with a corresponding change in the value of C_1.

SHORT COMMUNICATIONS

THE 5577 Å OI EMISSION LINE OF THE AIRGLOW AT BRISBANE*

By I. J. Danziger†

During the four-month period from April to July 1960, a two-colour airglow photometer of the Huruhata type (Huruhata, Nakamura, and Tanabe 1957), recorded intensities of the night-sky emission at 5577 and 5300 Å at Brisbane (geographic latitude 27° 30′ S., longitude 153° 06′ E., and geomagnetic latitude 35° 06′ S.). A total of 156 hr of recording during 19 nights was obtained. A complete sky survey was made each 16 min. The corrections for van Rhijn variation and atmospheric extinction were applied in the analysis.

A 2–16 Mc/s ionosonde and a magnetometer measuring variations in the north-south horizontal component were operating on the same site.

Diurnal Variation

An analysis of individual diurnal variations revealed a wide range of behaviour. No systematic diurnal variation is indicated, in contrast with results obtained at Boulder by Roach (1955).

Intensity Distributions

The histogram of intensities of the green line showed the characteristic shape obtained at most other stations. This distribution is one with positive skewness. It has been pointed out by Roach, McCaulley, and Marovich (1959) that, if the Chapman reaction

$$\begin{gathered} \mathrm{O}+\mathrm{O}+\mathrm{O}\rightarrow\mathrm{O}_2+\mathrm{O}'\ (1S), \\ \mathrm{O}'\ (1S)\rightarrow 0'\ (1D)+h\nu\ (5577) \end{gathered}$$

is responsible for green line emission, then

$$I(5577)\propto N^3,$$

where $I(5577)$ is the green line intensity and N = number of oxygen atoms present. Thus

$$N\propto I^{\frac{1}{3}}.$$

If a normal distribution of oxygen atoms exists at this level one would expect a normal distribution in the values of $I^{\frac{1}{3}}$. The assumption of a normal distribution does not seem unreasonable if one keeps in mind De Moivre's theorem of large numbers, and the large number of independent factors influencing its presence, e.g. solar ultraviolet, recombination effects, and possibly turbulence.

---

* Manuscript received January 9, 1961.

† Physics Department, University of Queensland; present address: Mt. Stromlo Observatory, Australian National University, Canberra.

This was tested with the available data and the normal curve of best fit was applied to the histogram obtained (Fig. 1). The goodness of fit was tested with the χ^2 test, which yielded a value for χ^2 of 13·3. Under the hypothesis that the $I^{\frac{1}{3}}$ values are normally distributed, 27% of similar observations would be expected to show a worse agreement than the current one.

Background Continuum

Although it is known that some of the 5300 Å background intensity must come from starlight, it is of interest to determine whether there is any correlation between the atmospheric component and the green line. Therefore a comparison was made between the variations of the 5300 and 5577 Å intensities for some individual nights. The intensities in the direction of the Celestial South Pole were chosen, to avoid changes in the contribution from the Galaxy. Results showed that the two intensities were covariant.

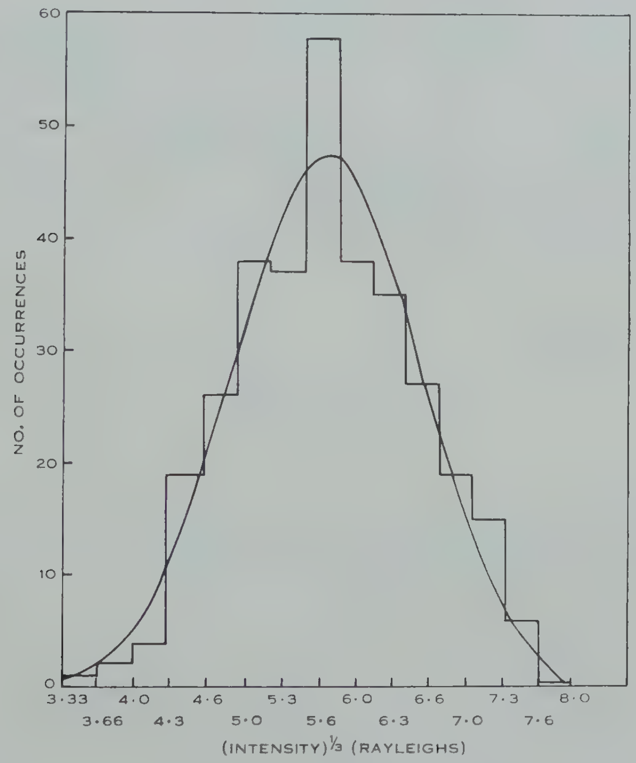

Fig. 1

Average values of 5300 Å intensity for all suitable nights were plotted against the corresponding average values of 5577 Å and a good linear relationship was obtained (Fig. 2). These results agree with those obtained by Barbier (1956) and Tohmatsu (1958). The van Rhijn variation of 5300 Å intensity is further evidence for its atmospheric origin and one can only conjecture with the available evidence that the covariancy of the two emissions is due to a linkage through either the mechanism of excitation or the possibility that 5300 Å emission is part of a broad molecular emission of molecular oxygen which at times becomes the atomic oxygen responsible for 5577 Å emission.

Velocity of Drift

From the isophote diagrams drift patterns in the green line emission layer were determined. The frequency of scan, i.e. one every 16 min, was sufficient for unambiguous results to be obtained in many cases. The amount of data analysed was not great enough to be of statistical value but values of velocity of drift between 120 and 150 m/s were obtained.

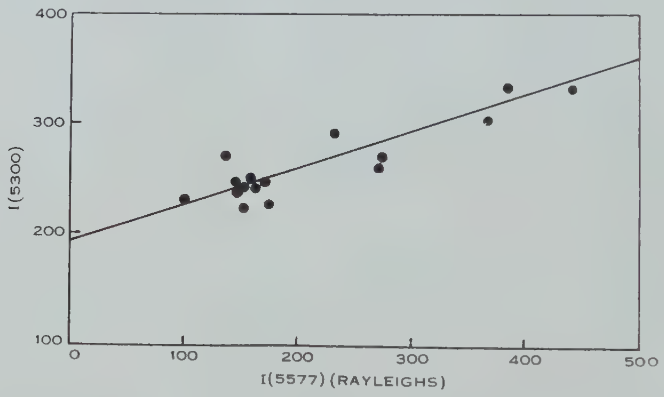

Fig. 2

Magnetic Control

No general correlation was found between the local K indices and green line intensity. However, a magnetic storm with K index 6, occurred on April 28, 1960, and in the same period the green line intensity exceeded 500 rayleighs as against the average green line intensity of approximately 250 rayleighs. It seems likely that the green line enhancement and the magnetic storm were associated. The more sensitive parameter ΔH, the variation in the Earth's horizontal field, was used to examine whether a magnetic control existed during magnetically quiet periods. The magnetometer did not measure the absolute field strength, so an arbitrary zero was set on the magnetometer records for the periods under investigation, the solar Sq variation being eliminated. ΔH was plotted against green line intensity for individual nights. The best straight-line fit was found and the slopes of the lines for the various nights compared. The results showed a general coherence, in so far as the slope was found to be always negative. Results were obtained for nine nights and slopes ranged between 0 and $-0 \cdot 2$/rayleigh with an average of $-0 \cdot 07$/rayleigh. This finding is consistent with that of McCaulley and Roach (1960).

Comments

The intensity distribution results still leave open the possibility of the Chapman reaction, which probably derives its energy from the solar ultraviolet.

The magnetic control results point to a magnetic influence and hence if this effect is analogous to auroral magnetic effects then the energy source would be the solar corpuscles either directly from the Sun or from the radiation belts surrounding the Earth. Evidence for the magnetic control seems to be increasing.

Grateful acknowledgement is made to Professor H. C. Webster and Dr. J. A. Thomas for advice and guidance during the course of this investigation. Thanks are due also to Professor M. Huruhata, who arranged the supply of the photometer and advised on its operation.

References

Barbier, D. (1956).—" The Air-Glow and Aurorae." (E. B. Armstrong and A. Dalgarno, Eds.) (Pergamon : London.)

Huruhata, M., Nakamura, T., and Tanabe, H. (1957).—Tokyo Astr. Bull. Second Series, No. 94.

McCaulley, J. W., and Roach, F. E. (1960).—*J. Geophys. Res.* **65** : 1499.

Roach, F. E. (1955).—*Ann. Géophys.* **11** : 214.

Roach, F. E., McCaulley, J. W., and Marovich, E. (1959).—*J. Res. Nat. Bur. Stand.* **63D** : 15.

Tohmatsu, T. (1958).—*Rep. Ionosph. Res. Japan* **12** : 169.

CONSTRUCTION OF THE EQUIVALENT ELECTRIC CIRCUIT FROM A FORCE CIRCUIT DIAGRAM BY A SIMPLE GRAPHICAL METHOD*

By N. W. Tschoegl†

It has been shown elsewhere (Tschoegl 1961) that mechanical problems may be formulated by constructing a force (or torque) circuit diagram setting forth the essential characteristics of the mechanical system by a set of conventional symbols. The mechanical problem may then be solved directly by the operational methods used in electric circuit analysis. Similarly, rheological problems may be formulated and solved by the aid of analogous stress circuit diagrams. The solution of mechanical and rheological problems via the equivalent electric circuit is thus completely by-passed. However, the equivalent circuit may still be needed for purposes of simulation. It is the aim of this communication to show how the equivalent electric circuit may be derived from a given force, torque, or stress circuit diagram by a simple graphical method. This is also the simplest way of setting up an equivalent circuit for a given mechanical problem since the force or torque circuit diagram is readily found by inspection.

---

* Manuscript received January 9, 1961.

† Bread Research Institute of Australia, North Ryde, N.S.W.

Consider the damped vibration absorber (Churchill 1958) represented in Figure 1. By inspection, simply tracing the actual connection of the elements and bearing in mind that force and mass are represented by 2-terminal symbols and that one terminal of the latter must always be referred to ground (Tschoegl 1961), we find the force circuit diagram as shown in Figure 2, disregarding the dotted lines. $f(s)$ and $v(s)$ are the Laplace transforms of force and velocity, while Is, F, E/s, etc. are the mechanical impedance operators. The symbols are the usual representation of the inertance I by a mass, the frictance (mechanical, or viscous, resistance) F by a dashpot, and the elastance E (the reciprocal of the compliance J) by a spring. The circle represents applied force and the small full circles velocity nodes. The ground or reference node is indicated by the base line. The nodes shown therefore actually represent node-pairs. From the force circuit diagram we obtain by "node-pair analysis" the Laplace transformations of the equations of motion (for zero initial conditions) as follows:

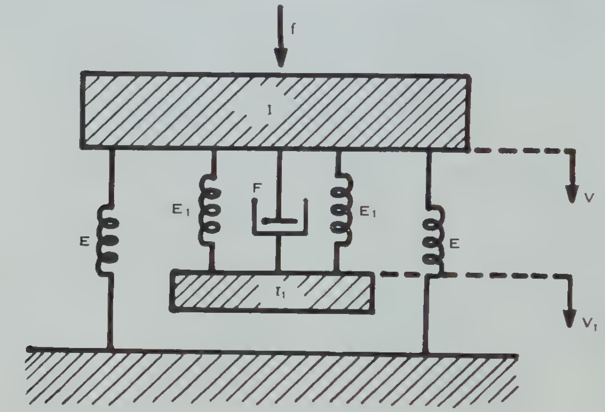

Fig. 1.—Damped vibration absorber.

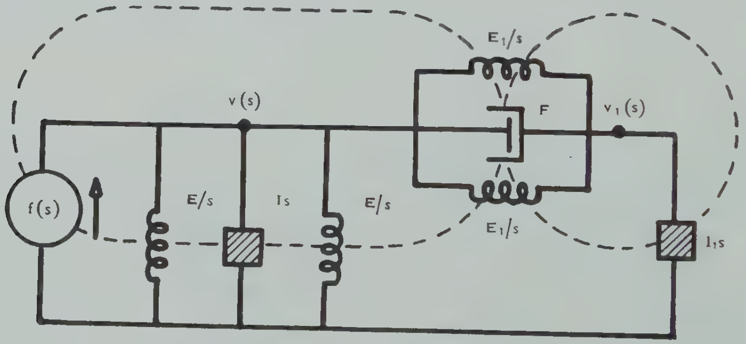

Fig. 2.—Force circuit diagram for damped vibration absorber.

$$[Is+2E/s+F+2E_1/s]v(s)-[F+2E_1/s]v_1(s)=f(s),$$
$$[I_1s+F+2E_1/s]v_1(s)-[F+2E_1/s]v(s)=0.$$

We now draw circles, as shown by the dotted lines in Figure 2, around each node shown, connecting all circuit elements attached to that node. Each circle represents a mesh of the equivalent electric circuit. Elements through which two circles pass are common to two meshes. The equivalent electric circuit can now be redrawn (Fig. 3) making the following substitutions :

Force Circuit	*Equivalent Electrical Circuit*
Inertance I	Inductance L
Frictance F	Resistance R
Elastance E	Reciprocal Capacitance $1/C$
Force f	Voltage V
Velocity v	Current i

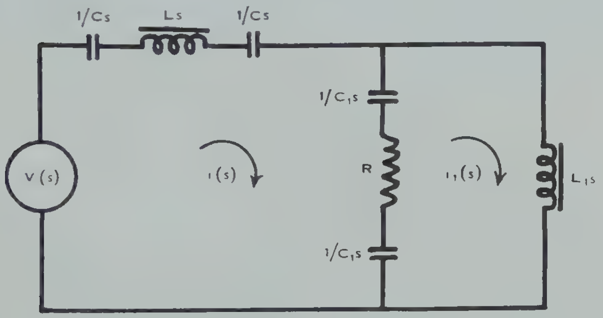

Fig. 3.—Equivalent electric circuit for damped vibration absorber.

From Figure 3 we find by the ordinary methods of " mesh-analysis " :

$$[Ls+2/Cs+R+2/C_1s]i(s)-[R+2/C_1s]i_1(s)=V(s),$$
$$[L_1s+R2/C_1s]i_1(s)-[R+2/C_1s]i(s)=0.$$

The method just outlined is related to the method for the graphical construction of the dual of an electric circuit (Bloch 1945 ; Gardner and Barnes 1953), originally proposed by Cauer (1934). In Cauer's method a dot is placed inside each mesh, another is placed outside the circuit, and the dots are connected by lines passing through the circuit elements. The dots represent the nodes of the dual circuit, the outside dot being the reference or ground node. Although it is formally possible to derive the original from the dual (and similarly the equivalent circuit from the force circuit diagram) by the same procedure, the method proposed here is the correct topological dual of Cauer's method.

References

Bloch, A. (1945).—*J. Instn. Elect. Engrs.* **92** : 157–69.
Cauer, W. (1934).—*Z. angew. Math. Mech.* **14** : 349–50.
Churchill, R. V. (1958).—" Operational Mathematics." (McGraw-Hill : New York.)
Gardner, M. F., and Barnes, J. L. (1953).—" Transients in Linear Systems." (Wiley : New York.)
Tschoegl, N. W. (1961).—*Kolloid Z.* **174** : 113–23.

CHARGED PARTICLE TRAJECTORIES IN STATIC ELECTRIC AND MAGNETIC FIELDS*

By K. J. Ausburn†

A trajectory passing through a given point in a given direction is completely determined if its curvature and torsion are known functions of its arc length. Relativistic expressions for the curvature and torsion in terms of the electric and magnetic field distributions are derived below. Besides their intrinsic interest these expressions may be useful in the analytical solution of some simple trajectory problems. In more complicated problems the trajectories may be extrapolated from their origin by means of the canonical equations, see, for example, Weatherburn (1955),

$$\left.\begin{aligned} x&=s-\varkappa_0^2s^3/6+\ldots,\\ y&=\varkappa_0s^2/2+\varkappa_0's^3/6+\ldots,\\ z&=\varkappa_0\tau_0s^3/6+\ldots,\end{aligned}\right\}\tag{1}$$

where $\varkappa_0$ and τ_0 are the curvature and torsion at the point O on the trajectory; $\varkappa_0'$ is the rate of change of curvature with regard to arc length evaluated at O; x, y, z are the rectangular Cartesian coordinates of the point at a distance s along the trajectory from O referred to the coordinate axes OX, OY, OZ which correspond respectively with the directions of the tangent, normal, and binormal to the trajectory at O.

Trajectory plotting by means of the equations (1) terminated at terms of the second degree in s has been done automatically by Gabor (1937) and Langmuir (1937) for purely electrostatic fields and low particle velocities. In this case only the curvature need be known and is $\varkappa=-E_n/2V$ where V is the potential at the point in question and E_n is the component of the electric field normal to the trajectory. The electrolytic tank analogue was used for the direct measurement of both V and E_n. If other than plane trajectories are to be plotted terms to at least the third degree in s must be used. Thus $\varkappa$, τ, and $\varkappa'$ must be known in terms of the field distributions. Relativistic formulas for these three quantities are derived below by the methods of differential geometry using vector notation. Unit vectors in the directions of the tangent, normal, and binormal to the charged particle trajectory are denoted by **t**, **n**, and **b** respectively. Derivatives with regard to arc length are denoted by a superscript dash.

Derivation of the Curvature

The trajectory of a charged particle of charge q, mass m, and speed v in an electric field **E** and magnetic field **B** is described by

$$v\mathrm{d}(mv\mathbf{t})/\mathrm{d}s=q(\mathbf{E}+v\mathbf{t}\times\mathbf{B}).\tag{2}$$

---

* Manuscript received January 13, 1961.

† School of Physics, Newcastle University College, Tighe's Hill, N.S.W.

In order to carry out the differentiation a convenient expression for m is sought. We have

$$mc^2-m_0c^2+qV=\text{constant} \tag{3}$$

as the energy equation. If we assume the particle, of charge q, had zero initial velocity in the region of zero potential, then the constant of (3) is zero. Note that for positive kinetic energy the product qV is negative. In what follows q and V will be treated as pure algebraic symbols so that both q and V may be of either sign but the product qV must be a negative quantity.

Equation (3) may be written as

$$m=m_0(1-V/V_0), \tag{4}$$

where $V_0=m_0c^2/q$ has the dimensions of electric potential. This " natural unit " of potential is approximately $+930\times10^6$ volts for a proton and $-0\cdot5\times10^6$ volts for an electron. Writing $\beta=(1-V/V_0)$ equation (2) becomes

$$m_0\beta v^2\varkappa\mathbf{n}+m_0\beta' v^2\mathbf{t}+m_0\beta vv'\mathbf{t}=q(\mathbf{E}+v\mathbf{t}\times\mathbf{B}), \tag{5}$$

where we have used $\mathbf{t}'=\varkappa\mathbf{n}$.

The normal component of (5) is

$$\begin{aligned} m_0\beta v^2\varkappa &= q(E_n+v\mathbf{t}\times\mathbf{B}\cdot\mathbf{n}) \\ &= q(E_n-vB_b), \end{aligned} \tag{6}$$

and the tangential component is

$$m_0\beta' v^2+m_0\beta vv'=qE_t, \tag{7}$$

where E_t, E_n, and E_b are the tangential, normal, and binormal components of $\mathbf{E}$ etc. (7) is the energy equation while (6) is a trajectory equation.

Making the following substitutions in (6)

$$\left.\begin{aligned} \beta &= (1-V/V_0)=(1-\delta), \\ v^2 &= c^2\delta(-2+\delta)/(1-\delta)^2, \\ v &= -c\delta^{\frac{1}{2}}(-2+\delta)^{\frac{1}{2}}/(1-\delta), \end{aligned}\right\} \tag{8}$$

gives for the curvature

$$\varkappa=\{E_n(1-\delta)+B_bc\delta^{\frac{1}{2}}(-2+\delta)^{\frac{1}{2}}\}/V(-2+\delta). \tag{9}$$

Note that δ is negative for positive kinetic energies. Thus $c\delta^{\frac{1}{2}}$ is imaginary and $\varkappa$ is real.

For low energies $\delta\to0$ and (9) reduces to

$$\varkappa=-\tfrac{1}{2}\left\{E_n-\left(\frac{|\,2qV\,|}{m_0}\right)^{\frac{1}{2}}B_b\right\}/V. \tag{10}$$

Arc Rate of Change of Curvature

To find $\varkappa'$, the rate of change of curvature with trajectory arc length, differentiate (5) with regard to s. This gives

$$\begin{aligned} (m_0\beta v^2\varkappa)'\mathbf{n}+(m_0\beta v^2\varkappa)\mathbf{n}'+(m_0\beta' v^2)\mathbf{t}'+(m_0\beta' v^2)'\mathbf{t}+(m_0\beta vv')'\mathbf{t}+(m_0\beta vv')\mathbf{t}' \\ =q\{\mathbf{E}'+v'\mathbf{t}\times\mathbf{B}+v(\mathbf{t}'\times\mathbf{B}+\mathbf{t}\times\mathbf{B}')\}. \end{aligned}$$

The normal component of this is

$$\begin{aligned}(m_0\beta v^2\varkappa)'+(m_0\beta' v^2)\varkappa+(m_0\beta v v')\varkappa&=q\{(\mathbf{E}')_n+v'\mathbf{t}\times\mathbf{B}\cdot\mathbf{n}+v\mathbf{t}\times\mathbf{B}'\cdot\mathbf{n}\}\\ &=q\{(\mathbf{E}')_n-v'B_b-v(\mathbf{B}')_b\}.\end{aligned}$$

Whence

$$\varkappa'=\frac{q}{m_0\beta v^2}\{(\mathbf{E}')_n-v'B_b-v(\mathbf{B}')_b\}-\varkappa\left\{\frac{2\beta'}{\beta}+\frac{3v'}{v}\right\}. \tag{11}$$

Using the relations (8), together with

$$\left.\begin{aligned}&\beta'=E_t/V_0,\\ &v'=-E_t c\delta^{\frac{1}{2}}/\{V(1-\delta)^2(-2+\delta)^{\frac{1}{2}}\},\end{aligned}\right\} \tag{12}$$

in (11) gives

$$\begin{aligned}\varkappa'=\frac{(\mathbf{E}')_n(1-\delta)}{V(-2+\delta)}+\frac{(\mathbf{B}')_b c\delta^{\frac{1}{2}}}{V(-2+\delta)^{\frac{1}{2}}}-\frac{2E_tB_bc\delta^{\frac{1}{2}}}{V(1-\delta)(-2+\delta)^{\frac{1}{2}}}\left\{\frac{1}{V_0}+\frac{1}{V(-2+\delta)}\right\}\\ -\frac{E_tE_n}{V(-2+\delta)}\left\{\frac{2}{V_0}+\frac{3}{V(-2+\delta)}\right\}.\end{aligned} \tag{13}$$

Substituting $c\delta^{\frac{1}{2}}=(qV/m_0)^{\frac{1}{2}}$ and allowing $\delta\to 0$ in (13) we have for low energies

$$\varkappa'=\frac{1}{2V}\left\{\left(\frac{|2qV|}{m_0}\right)^{\frac{1}{2}}(\mathbf{B}')_b-(\mathbf{E}')_n\right\}+\frac{E_t}{2V^2}\left\{\left(\frac{|2qV|}{m_0}\right)^{\frac{1}{2}}B_b-\frac{3E_n}{2}\right\}. \tag{14}$$

Torsion

To find an expression for the torsion τ, take the vector product of (5) with $\mathbf{t}$, whence

$$\begin{aligned}-m_0\beta v^2\varkappa\mathbf{b}&=q\{\mathbf{E}\times\mathbf{t}+v(\mathbf{t}\times\mathbf{B})\times\mathbf{t}\}\\ &=q\{\mathbf{E}\times\mathbf{t}+v\mathbf{B}-vB_t\mathbf{t}\}.\end{aligned} \tag{15}$$

Differentiating with regard to s gives

$$(-m_0\beta v^2\varkappa)'\mathbf{b}+m_0\beta v^2\varkappa\tau\mathbf{n}=q\{\mathbf{E}'\times\mathbf{t}+\mathbf{E}\times\mathbf{n}\varkappa+v'\mathbf{B}+v\mathbf{B}'-(vB_t)'\mathbf{t}-vB_t\varkappa\mathbf{n}\}.$$

The normal component of this is

$$\begin{aligned}m_0\beta v^2\varkappa\tau&=q\{\mathbf{E}'\times\mathbf{t}\cdot\mathbf{n}+\varkappa\mathbf{E}\times\mathbf{n}\cdot\mathbf{n}+v'B_n+v(\mathbf{B}')_n-vB_t\varkappa\}\\ &=q\{(\mathbf{E}')_b+v'B_n+v(\mathbf{B}')_n-vB_t\varkappa\}.\end{aligned}$$

Thus either $v^2\varkappa=0$ or

$$\begin{aligned}\tau&=\frac{q}{m_0}\left\{\frac{(\mathbf{E}')_b}{\beta v^2\varkappa}+\frac{v'B_n}{\beta v^2\varkappa}+\frac{(\mathbf{B}')_n}{\beta v\varkappa}-\frac{B_t}{\beta v}\right\}\\ &=\frac{q}{m_0\beta v\varkappa}\left\{\frac{(\mathbf{E}')_b}{v}+\frac{v'B_n}{v}+(\mathbf{B}')_n\right\}-\frac{qB_t}{m_0\beta v}.\end{aligned} \tag{16}$$

Substituting from (8) and (12) in (16) gives

$$\tau=\frac{(\mathbf{E}')_b(1-\delta)-E_tB_nc\delta^{\frac{1}{2}}/\{V(1-\delta)(-2+\delta)^{\frac{1}{2}}\}-(\mathbf{B}')_nc\delta^{\frac{1}{2}}(-2+\delta)^{\frac{1}{2}}}{E_n(1-\delta)+B_bc\delta^{\frac{1}{2}}(-2+\delta)^{\frac{1}{2}}}+\frac{B_tc\delta^{\frac{1}{2}}}{V(-2+\delta)^{\frac{1}{2}}}. \tag{17}$$

For low energies, $\delta \to 0$, we have either

$$\tau = \frac{(\mathbf{E}')_b - \dfrac{E_t B_n}{2V}\left(\dfrac{|2qV|}{m_0}\right)^{\frac{1}{2}} + (\mathbf{B}')_n\left(\dfrac{|2qV|}{m_0}\right)^{\frac{1}{2}}}{E_n - B_b\left(\dfrac{|2qV|}{m_0}\right)^{\frac{1}{2}}} + \frac{B_t}{2V}\left(\frac{|2qV|}{m_0}\right)^{\frac{1}{2}} \tag{18}$$

or $\varkappa = 0$.

Conclusion

In the absence of magnetic fields and for low energies

$$\left.\begin{aligned} \varkappa &= -E_n/2V, \\ \varkappa' &= -(\mathbf{E}')_n/2V - 3E_nE_t/(4V^2), \\ \tau &= (\mathbf{E}')_b/E_n. \end{aligned}\right\} \tag{19}$$

Note that in all the above expressions for $\varkappa$, $\varkappa'$, and τ the potential V is positive or negative according to whether q is negative or positive.

References

GABOR, D. (1937).—*Nature* **139**: 373.
LANGMUIR, D. B. (1937).—*Nature* **139**: 1067.
WEATHERBURN, C. E. (1955).—"Differential Geometry of Three Dimensions." Vol. 1. p. 18. (Cambridge Univ. Press.)

A PHENOMENOLOGICAL MODEL FOR HYPERNUCLEAR BINDING ENERGIES*

By J. W. OLLEY†‡

The form of the dependence of the binding energy of the Λ-particle in hypernuclei on the mass number A is of interest in obtaining empirical information about the hyperon-nucleon interaction. As an introductory calculation we considered the simple model in which the total Λ-nucleon interaction is replaced by a potential well $V(r)$ in which the Λ moves and in which the only effect of varying A is to vary the radius but not the depth of the well. The binding energy of the Λ, B_Λ, is then given by the ground state energy of a particle in this well. The aim of our calculations was to determine whether the present experimental values of B_Λ defined a unique well shape.

---

* Manuscript received January 18, 1961.

† The Daily Telegraph Theoretical Department, School of Physics, University of Sydney.

‡ Also supported by the Nuclear Research Foundation within the University of Sydney.

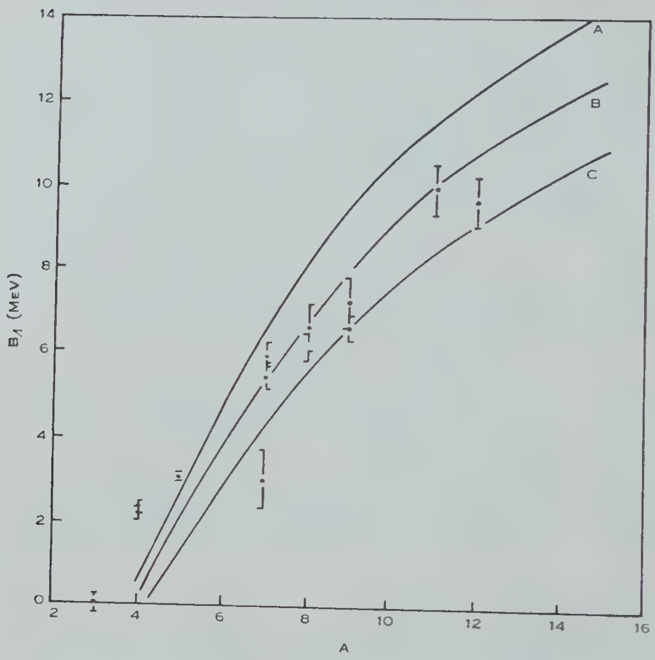

Fig. 1.—Square well, $r_0=1\cdot1$ fermi. Curve A: $V_0=29$ MeV; curve B: $V_0=27$ MeV; curve C: $V_0=25$ MeV.

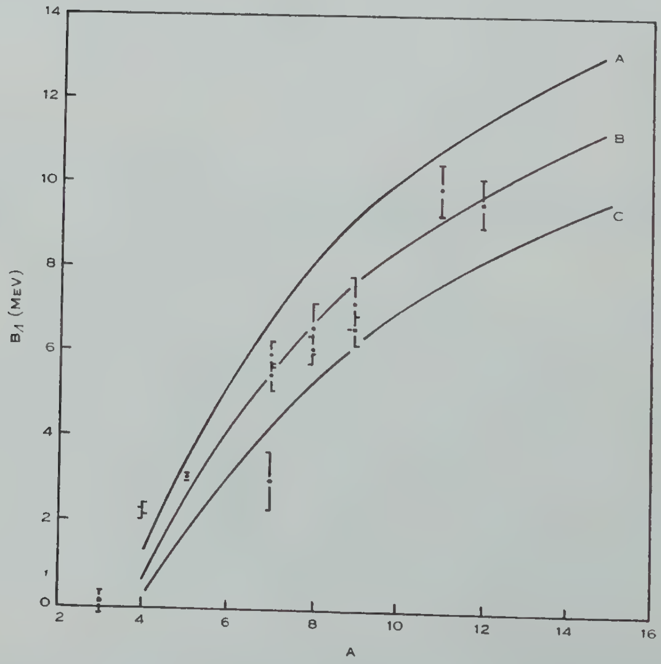

Fig. 2.—Square well, $r_0=1\cdot3$ fermi. Curve A: $V_0=24$ MeV; curve B: $V_0=22$ MeV; curve C: $V_0=20$ MeV.

Various authors, for example, Ivanenko and Kolesnikov (1956) and Walecka (1960) have considered this model taking

$$\begin{aligned} V(r) &= -V_0 \quad \text{for } r<R=r_0(A-1)^{\frac{1}{3}}, \\ &= \quad 0 \quad \text{for } r>R, \end{aligned}$$

where r_0 is a radius parameter. We shall refer to this as well (*a*). We considered this well and also the well (well (*b*)) given by

$$\begin{aligned} V(r) &= -V_0 & \text{for } r<R, \\ V(r) &= -V_0 \exp\{-(r-R)/0\cdot7\} & \text{for } r>R, \end{aligned}$$

where we measure r, R in units of 1 fermi$=10^{-13}$ cm.

For well (*a*) we may find $B_\Lambda(V_0, A)$ by solving (e.g. Walecka 1960)

$$s=\frac{1}{\sqrt{(1-x)}}\cot^{-1}\left(-\sqrt{\frac{x}{1-x}}\right), \tag{1}$$

where

$$\begin{aligned} s&=(A-1)^{\frac{1}{3}}\left(\frac{1}{1+1\cdot18/(A-1)}\right)^{\frac{1}{2}} r_0^2\left(\frac{2mV_0}{\hbar^2}\right)^{\frac{1}{2}}, \\ x&=B_\Lambda(V_0, A)/V_0. \end{aligned}$$

In passing it may be noted that the solution is found directly from tables if we rewrite (1) as

$$\frac{\sin\{s\sqrt{(1-x)}\}}{s\sqrt{(1-x)}}=\frac{1}{s}.$$

While well (*b*) is a more realistic well than well (*a*), $B_\Lambda(V_0, A)$ can only be found by numerical integration of the Schroedinger equation. This was done using the computer SILLIAC.

The results are plotted in Figures 1–4 and are presented here for general interest as a comparison and extension of Walecka's results. The experimental values are those of Ammar *et al.* (1960), which are approximately 0·36 MeV higher than those used by Walecka, due to a different value of Q_Λ, the energy release in the π^--decay mode of the free Λ, and which are much more accurate than those of Ivanenko and Kolesnikov. Evans, Jones, and Zakrzewski (1959) have also reported a ${}_\Lambda B^{11}$ with $B_\Lambda=11\cdot7\pm0\cdot8$ MeV, where to obtain this value the same Q_Λ as in Ammar *et al.* (1960) is used.

It is seen that the curve of best fit, Figure 4, is not oversensitive to variations in r_0 or to a change in the shape of the well. The situation would be improved if there were some experimental values of B_Λ with $A>12$, but some general, though tentative, observations can still be made.

The best fit to the experimental points is obtained with

$$\begin{aligned} \text{well } (a):\ & V_0=27 \text{ MeV} \ (r_0=1\cdot1 \text{ fermi}), \\ & V_0=22 \text{ MeV} \ (r_0=1\cdot3 \text{ fermi});^* \\ \text{well } (b):\ & V_0=21 \text{ MeV} \ (r_0=1\cdot1 \text{ fermi}). \end{aligned}$$

---

* Walecka obtains $V_0=21\cdot7$ MeV with $r_0=1\cdot3$ fermi, but this uses different experimental values and is equivalent to our $V_0=22$ MeV.

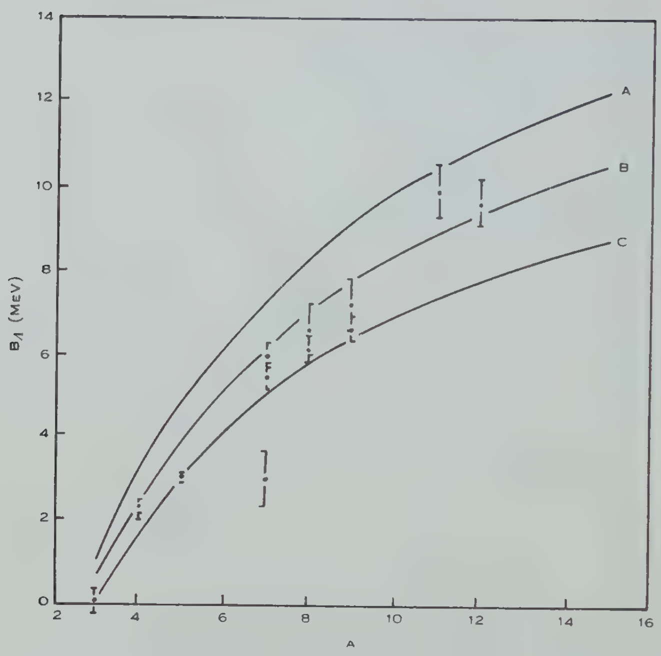

Fig. 3.—" Square " well with exponential sides, $r_0=1\cdot 1$ fermi. Curve A : $V_0=23$ MeV ; curve B : $V_0=21$ MeV ; curve C : $V_0=19$ MeV.

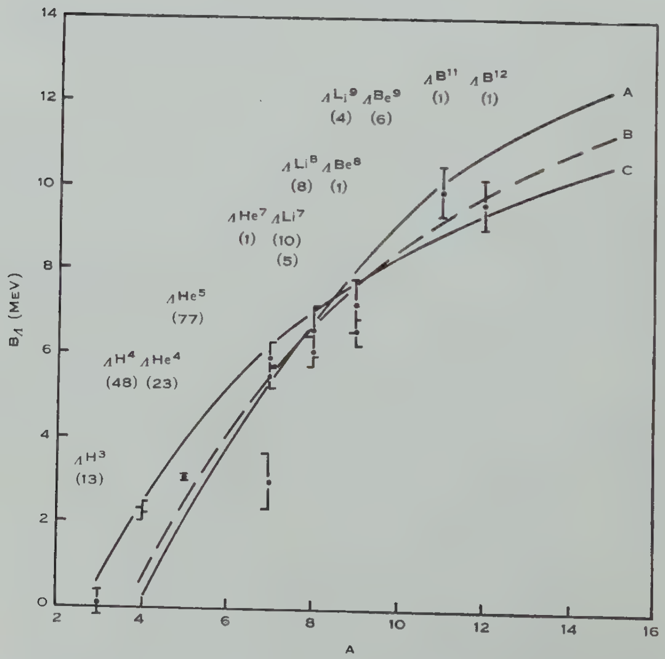

Fig. 4.—Comparison of curves of best fit. Curve A : square well, $r_0=1\cdot 1$ fermi, $V_0=27$ MeV ; curve B : square well, $r_0=1\cdot 3$ fermi, $V_0=22$ MeV : curve C : " square " well with exponential sides, $r_0=1\cdot 1$ fermi, $V_0=21$ MeV. The number of events for each hyperfragment is shown.

It is seen that saturation is reached very slowly, e.g. for the square well with $r_0=1\cdot 3$ fermi, $V_0=22$ MeV, $B_\Lambda=16\cdot 6$ MeV for $A=50$ and $18\cdot 5$ MeV for $A=100$.

In reality V_0 would be expected to decrease with decreasing A but to be almost constant for $A>7$, hence B_Λ will have been overestimated for small A, i.e. for small A the experimental values should lie below the curve. This indeed is the case for well (*b*), although here the predicted values for $A=11$, 12 may be too low. For well (*a*) no curve which gives a reasonable fit for higher A passes above the experimental points for small A. This is to be expected, since well (*a*) is a poor approximation to $V(r)$ for small A. It is also known that for nuclei of small A the radius parameter is approximately $1\cdot 5$ fermi (cf. our values $1\cdot 1$ and $1\cdot 3$ fermi).

It would appear that the best fit is given by a well like well (*b*) but with a less gradual tail, although, as mentioned earlier, this depends on further experimental results. It can be seen that this model gives a surprisingly accurate agreement with all B_Λ except the exceptional case of ${}_\Lambda He^7$.

I would like to thank Professor S. T. Butler for suggesting this problem and for his continued assistance, and Professor H. Messel for making available excellent research facilities. I would also like to thank the Australian Atomic Energy Commission for the award of a studentship.

References

AMMAR, R., LEVI SETTI, R., SLATER, W. E., LIMENTANI, S., SCHLEIN, P. E., and STEINBERG, P. H. (1960).—*Nuovo Cim.* **15**: 181.

EVANS, D., JONES, B. D., and ZAKRZEWSKI, J. (1959).—*Phil. Mag.* **4**: 1255.

IVANENKO, D., and KOLESNIKOV, N. (1956).—*J. Expt. Theor. Phys.* **30**: 800; *Soviet Physics, JETP* **3**: 955.

WALECKA, J. D. (1960).—*Nuovo Cim.* **16**: 342.

AN EXACT SOLUTION TO A PROBLEM IN HEAT TRANSFER*

By C. H. J. JOHNSON†

In order to determine the complete temperature history in problems concerning the transfer of heat from a moving fluid to a solid body one is obliged, in general, to solve both the flow and heat transport equations for the fluid and the heat conduction equation for the solid. Analytical solutions to this problem cannot in general be given owing to the (non-linear) way in which the flow and heat transport equations for the fluid are coupled.

However, there is a class of problems of this kind for which an exact unsteady-state solution can be given. These problems involve a symmetry which is such

---

* Manuscript received February 3, 1961.

† Chemical Engineering Section, Chemical Research Laboratories, C.S.I.R.O., Melbourne.

that in the equation for the fluid the convection terms vanish identically. The result is that these equations are uncoupled in the sense that the flow velocity is independent of the temperature distribution and the temperature depends on the flow only through the viscous dissipation function. Under these conditions the problem reduces to solving the heat conduction problem for a composite body with heat generation in one body, the fluid.

The problem we solve here concerns the parallel flow of fluid over a heat conducting half space, the motion being started impulsively. Other problems such as flow between parallel walls and flow round cylinders could be considered but not in the same way as the present problem.

The statement of problem is as follows: The region $z>0$ is occupied by a viscous heat-conducting incompressible constant property fluid. The region $z<0$ is occupied by a heat-conducting solid. The initial temperature of the fluid is T_0, while that of the solid is zero. To determine the temperature distribution in the system subsequent to the uniform impulsive motion of the fluid in a direction parallel to the plane $z=0$.

In the fluid, the pressure gradients being zero, we have

$$\partial u/\partial t-\nu\partial^2 u/\partial z^2=0, \qquad z>0,\ t>0, \tag{1}$$

$$\rho_1 c_1 \partial T_1/\partial t-k_1\partial^2 T_1/\partial z^2=\mu\left(\frac{\partial u}{\partial z}\right)^2, \quad z>0,\ t>0, \tag{2}$$

and in the solid,

$$\rho_2 c_2 \partial T_2/\partial t-k_2\cdot\partial^2 T_2/\partial z^2=0, \qquad z<0,\ t>0, \tag{3}$$

with

$$u=0, \qquad z=0,\ t>0, \tag{4}$$

$$u=U, \qquad z>0,\ t=0, \tag{5}$$

$$T_1=T_2, \qquad z=0,\ t>0, \tag{6}$$

$$k_1\partial T_1/\partial z=k_2\partial T_2/\partial z, \quad z=0,\ t>0, \tag{7}$$

$$T_1=T_0, \qquad z>0,\ t=0, \tag{8}$$

$$T_2=0, \qquad z<0,\ t=0, \tag{9}$$

with T_1, T_2, and u everywhere bounded.

The subscript "1" refers to the fluid and the subscript "2" to the solid. The remaining symbols have their usual meanings.

Introducing the dimensionless variable ξ, $\xi=z\,.\,(4\nu_1 t)^{-\frac{1}{2}}$, the solution to equation (1) with (4) and (5) is

$$u=\operatorname{erf}\xi. \tag{10}$$

Writing $v_1=T_1/T_0$ and using (10), equation (2) becomes

$$\mathrm{d}^2 v_1/\mathrm{d}\xi^2+2P.\xi.\mathrm{d}v_1/\mathrm{d}\xi=-b\,.\,\exp\left(-2\xi^2\right), \tag{11}$$

where $P=\nu/k_1$ is the Prandtl number and $b=(4/\pi)PE$, where the Eckert number E is given by $E=U^2/(c_1T_0)$.

Integrating equation (11) twice we find

$$v_1(\xi)=-d\int_{\eta=\xi}^{\infty}\exp(-P\eta^2)\,.\,\mathrm{erfc}\,\{\eta(2-P)^{\frac{1}{2}}\}\mathrm{d}\eta-A\,.\,\tfrac{1}{2}(\pi/P)^{\frac{1}{2}}\,.\,\mathrm{erfc}\,(\xi P^{\frac{1}{2}})+B, \quad (12)$$

where $d=\frac{1}{2}\,.\,b\,.\,(\pi/(2-P))^{\frac{1}{2}}$ and A and B are constants of integration. In order to satisfy equation (8) we must have $B=1$.

If $v_2=T_2/T_0$ we have from equation (3)

$$v_2(\xi)=C\,.\,\mathrm{erfc}\,\{-\xi(\nu/k_2)^{\frac{1}{2}}\},\quad \xi<0, \quad (13)$$

where C is a constant to be determined.

The constants A and C are to be determined from the two conditions (6) and (7), which in terms of the variable ξ become

$$\left.\begin{aligned} v_1&=v_2, & \xi&=0,\\ k_1\frac{\mathrm{d}v_1}{\mathrm{d}\xi}&=k_2\frac{\mathrm{d}v_2}{\mathrm{d}\xi}, & \xi&=0. \end{aligned}\right\} \quad (14)$$

Substituting (12) and (13) in (14) and solving for A and C we find

$$A=\frac{1-d\,.\,I(0,P)-d\varepsilon^{-1}}{\frac{1}{2}(\pi/P)^{\frac{1}{2}}+\varepsilon^{-1}}, \quad (15)$$

$$C=\frac{1+d[\frac{1}{2}(\pi/P)^{\frac{1}{2}}-I(0,P)]}{1+\varepsilon\,.\,\frac{1}{2}(\pi/P)^{\frac{1}{2}}}, \quad (16)$$

where

$$\varepsilon=\frac{2}{\pi^{\frac{1}{2}}}\cdot\frac{k_2}{k_1}\cdot\left(\frac{K_1}{K_2}\right)^{\frac{1}{2}}\cdot P^{\frac{1}{2}},$$

and

$$I(\xi,P)=\int_{\eta=\xi}^{\infty}\exp(-P\eta^2)\,.\,\mathrm{erfc}\,\{\eta(2-P)^{\frac{1}{2}}\}\mathrm{d}\eta. \quad (17)$$

We thus have

$$v_1(\xi)=1-A\,.\,\tfrac{1}{2}\,.\,(\pi/P)^{\frac{1}{2}}\,\mathrm{erfc}\,(\xi P^{\frac{1}{2}})-d\,.\,I(\xi,P). \quad (18)$$

The wall temperature is given by

$$v_1(0)=\frac{1+d[\frac{1}{2}(\pi/P)^{\frac{1}{2}}-I(0,P)]}{1+\varepsilon\,.\,\frac{1}{2}(\pi/P)^{\frac{1}{2}}}, \quad (19)$$

which is a constant.

The integral defining $I(\xi, P)$ cannot be evaluated in terms of elementary functions but the integral for $I(0, P)$ can be so evaluated. We find

$$I(0,P)=\left(\frac{1}{\pi P}\right)^{\frac{1}{2}}\left[\tfrac{1}{2}\pi-\tan^{-1}\left(\frac{2-P}{P}\right)^{\frac{1}{2}}\right], \quad (20)$$

whence

$$v_1(0)=\frac{1+d\,.\,(1/\pi P)^{\frac{1}{2}}\,.\,\tan^{-1}\{(2-P)/P\}^{\frac{1}{2}}}{1+\varepsilon\,.\,\frac{1}{2}(\pi/P)^{\frac{1}{2}}}. \quad (21)$$

On differentiating (18) it can be seen that the flux $Q(t)$ across the boundary $z=0$ is proportional to $t^{-\frac{1}{2}}$.

The parameter ε expresses the interaction between the solid and the fluid. Generally k_2/k_1 is large compared to unity and so ε will be large ($10^3 \sim 10^4$). The large value of k_2/k_1 implies that when a given quantity of heat crosses the boundary its effect after a given time is felt in the gas at a greater distance from the boundary than in the solid. The parameter d is usually much less than unity.

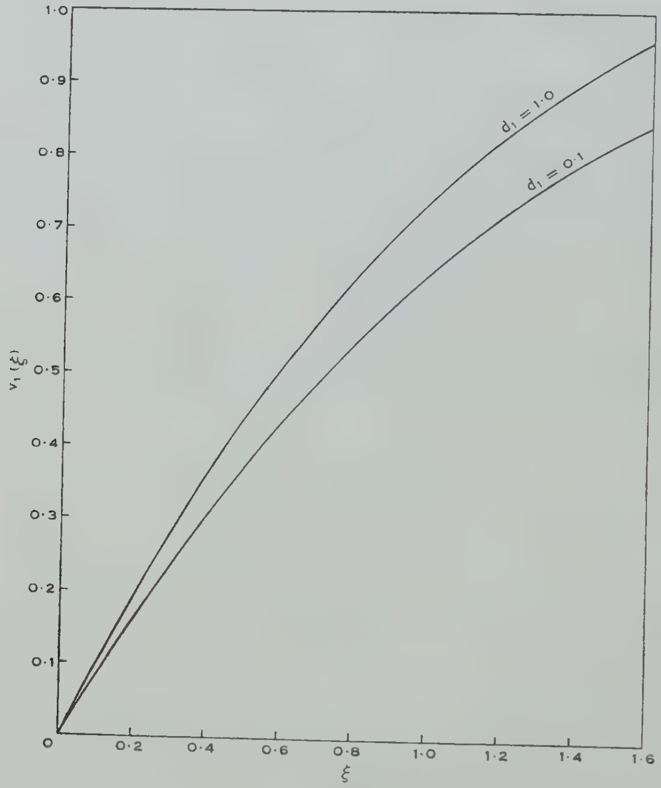

Fig. 1.—Graph of $v_1(\xi)$ as a function of ξ for $P=0\cdot 7$.

Neglecting terms involving ε^{-1} we have for

$$v_1(\xi)=1-[1-d\,.\,I(0,P)]\ \mathrm{erfc}\,(\xi P^{\frac{1}{2}})-d\,.\,I(\xi,P), \tag{22}$$

where $I(\xi, P)$ is given by (17). In Figure 1 we give curves for $v_1(\xi)$ for $P=0\cdot 7$, for large ε, and for two values of d.

The author is indebted to the referee for pointing out an error in the original manuscript.

AUSTRALASIAN MEDICAL PUBLISHING CO. LTD.
SEAMER AND ARUNDEL STS., GLEBE, SYDNEY

A STABILITY CRITERION FOR A RADIALLY CONSTRICTED GAS DISCHARGE BETWEEN ELECTRODES

By P. W. Seymour*

[*Manuscript received May 4, 1961*]

Summary

The stability of a centrally constricted, highly ionized deuterium discharge between electrodes is considered. Initially, the normal mode and energy principles for the examination of plasma stability are reviewed and the results contrasted. Teller's powerful stability criterion is next obtained in a useful integral form by means of a thermodynamic analysis of interchange instability. This general geometrical result is then applied to the centrally constricted plasma between electrodes, and a sufficient stability criterion derived. For this type of system, initially stabilized by a strong, external guiding magnetic field, it is found that the onset of instability occurs for a discharge current $I_0^*(w_b)\sim 1\cdot 6\varphi_E/z_e$, where φ_E from the external solenoid is the total flux through any discharge equipotential surface, z_e is the discharge semi-length, and practical simplifying assumptions of high radial compression ratio ν and maximum discharge radius $\rho_1 \lesssim \frac{1}{5} z_e$ have been made.

It is suggested that experimental confirmation of the above result would justify a more detailed stability analysis.

I. Introduction

By taking an appropriate moment of the Boltzmann transport equation for ionized gas particles, an equation of momentum transfer is obtained. Specialization of this result for ions and electrons gives a pair of equations often termed the two-fluid equations of a plasma. If the pressure tensor can be approximated by a scalar pressure, addition of these equations of motion for the ion and electron fluids leads to the linearized single-fluid equation of motion (Spitzer 1956; Linhart 1960) for a plasma in a magnetic field,

$$\rho\partial\mathbf{v}/\partial t=\mathbf{j}\times\mathbf{H}-\nabla p, \tag{1.1}$$

where ρ is the mean mass density,
$\mathbf{v}$ is the mean mass velocity,
$\mathbf{j}$ is the mean current density,
$\mathbf{H}$ is the magnetic field,
p is the scalar kinetic pressure,
and we have neglected gravitational effects.

As Artsimovich (1958) has indicated, equation (1.1) includes two extreme cases. If the gas pressure gradient is small, the body force $\mathbf{j}\times\mathbf{H}$ is balanced by the inertial force term $\rho\partial\mathbf{v}/\partial t$, and the plasma acquires a directed velocity. This magnetohydrodynamic phase is characterized by its short-duration transient nature; it serves to permit the conversion of kinetic energy of motion into heat by a suitably selected process.

---

* Research School of Physical Sciences, Australian National University, Canberra.

If, however, the plasma has negligible acceleration, the inertial term may be dropped from equation (1.1), and the body force is then balanced by the gradient of the scalar pressure,

$$\nabla p = \mathbf{j} \times \mathbf{H}, \tag{1.2}$$

independent of the time.

Early experimental work in the plasma physics field unfortunately showed that the stable plasma configurations that might profitably be associated with the steady-state equation (1.2) could not, in practice, be realized. Instabilities of various types were found to develop before significant plasma containment time had been achieved, and the desirable stable plasma configurations were destroyed. A major theoretical task thus became that of predicting the stability requirements of chosen plasma geometries. Mainly, cylindrical gaseous conductors received consideration, and further reference to this theoretical work will be made in Section II.

In earlier papers (Seymour 1961*a*, 1961*b*) methods were provided for estimating the distribution of temperature with axial distance along a steady-state centrally constricted, highly ionized deuterium discharge between electrodes, first neglecting thermoelectric effects, and then including them. The boundary surface of this discharge was conveniently approximated mathematically by a hyperboloid of one sheet. In the present paper we take up the problem of the stability of this particular plasma configuration against small-amplitude perturbations, and develop in Section IV a simple, sufficient stability criterion.

II. Stability Analyses of Cylindrical Gaseous Conductors: Teller's Stability Criterion

At present two main methods exist for the examination of stability. In the normal mode method an attempt is made to solve the linearized equations of motion for small-amplitude perturbations about an equilibrium state. If any perturbation grows in time the system is unstable; stability corresponds to bounded perturbation oscillation about an equilibrium state. The normal mode method encounters mathematical difficulties unless the plasma geometry is reasonably simple, and so, where specific knowledge of perturbation growth rates and frequencies is not required, an energy principle, based on the work of Lundquist (1951, 1952), has been developed by Bernstein *et al.* (1958) for determination of the stability of more complicated systems. This method depends on the fact that, if any realizable perturbation of a steady-state plasma equilibrium tends to reduce the potential energy of the system, the corresponding increase in kinetic energy can feed the perturbation so that its amplitude continues to grow with time. Mathematically, stability exists if the second-order variation of system potential energy due to perturbation of the plasma is positive definite.

(*a*) *Examples of Normal Mode Analysis*

As a first example of the method of small oscillations, we refer to the paper by Kruskal and Schwarzschild (1954). Mainly, these authors considered the stability of a plasma supported against gravity by the pressure of a horizontal magnetic field; and the stability of a cylindrical gaseous conductor radially pinched under the action of its self-magnetic field (see equation (1.2)). In each of these cases the electrical conductivity was assumed infinite, and suitable surface distributions of current and charge were chosen. The analyses showed both equilibria to be unstable, the first in close analogy to the Rayleigh-Taylor instability of a heavy fluid supported in a uniform gravitational field by a weightless fluid (Lamb 1945), and the second against lateral distortions.

Using the latter case to illustrate the method, the solution of the linearized equations for the perturbed plasma is effected by assuming that the disturbance has been analysed into its normal modes, and that the dependence on the cylindrical coordinates θ, z, and the time t of the perturbed quantities is given by $\exp\{i(m\theta+kz)+\omega t\}$, where m is an integer, k a wave number, and $e^{\omega t}$ represents the rate of growth of the instability. The solution gives ω as a function of m and k. If a choice of m and k results in ω being real and positive, perturbations of growing amplitude are obtained, and the system is unstable. Conversely, for purely imaginary ω, bounded oscillations of the perturbations about their means occur, and the system is stable. The phenomenon of overstability (oscillations of growing amplitude), corresponding to complex ω with positive real part, will not occur for static, conservative plasma equilibria (Bernstein *et al.* 1958, p. 22).

For this second case of self-magnetic field confinement, Kruskal and Schwarzschild limited their analysis to the condition $m=1$. In general this gives a corkscrew type of perturbation, for which the axis of the pinched gaseous conductor assumes helical form. To obtain lateral or kink type distortion of the plasma boundary surface, these authors superpose perturbation quantities having helices of opposite twist. This results in a lateral sinusoidal perturbation.

In correspondence to Kruskal and Schwarzschild's analysis of a plasma cylinder in a toroidal magnetic field, Tayler (1957*a*) has obtained results for a volume, rather than a surface, current, with m arbitrary. Particularly, Tayler shows that the infinite rate of growth for vanishingly small perturbation wavelength found by Kruskal and Schwarzschild is removed for a volume current distributed according to a power law.

Recalling that for infinite conductivity the magnetic lines of force appear to be frozen-in to the plasma (Spitzer 1956, pp. 36–37 ; Cowling 1957 ; Linhart 1960, p. 127), and that magnetic lines of force behave like elastic strings with a longitudinal tension $H^2/4\pi$ (Lundquist 1950 ; Cowling 1957, p. 9), physical reasoning suggests that the addition of an axial magnetic field to the interior of the type of plasma configuration discussed by Kruskal and Schwarzschild should produce stabilizing forces to compete with the destabilizing forces. An axial magnetic field external to the plasma would combine with the circular lines of force of the discharge self-magnetic field which exists in the vacuum region (the self-magnetic field vanishes within the plasma for an assumed surface current) to produce a helical resultant magnetic field. Again reasoning physically, for a helical perturbation of the same pitch as this resultant field, the lines of force can be moved into new positions with little bending, and hence with little effort. The magnetic field thus does little to suppress this interchange, and instability results. Interchange instability is considered in detail in Section III.

Using the linear theory, the instability of a pinched conducting fluid in the presence of a longitudinal magnetic field has been treated mathematically by a number of investigators, notably Kruskal and Tuck (1953, 1958), Rosenbluth (1957), Shafranov (1957), and Tayler (1957*b*). Broadly, the above physical considerations are supported by the analyses.

To summarize, when the longitudinal magnetic field is everywhere zero, the $m=0$ (sausage) instabilities, and the $m=1$ (corkscrew, kink) instabilities develop most readily. Particularly, theory predicts that the growth rate of the short-wavelength sausage mode, a purely radial perturbation, exceeds that of all others, and so increase in the pinch containment time should depend initially on suppression of this $m=0$ instability. Appropriate simple distribution of the axial magnetic field inside and outside the plasma theoretically results in suppression of the sausage instability.

Assessment of the effect of an axial field on the $m=1$ mode involves examination of two cases. First, if the helical perturbation twists in the opposite direction to the helical resultant magnetic field, theory shows that the presence of axial magnetic field stabilizes the corkscrew perturbation ; secondly, if the perturbation and resultant magnetic field helices twist in the same direction, it is shown that some corkscrew perturbations of long wavelength continue to grow in amplitude however strong the axial magnetic field. Since analysis also shows that the proximity of a coaxial conducting shell external to the discharge should have a suppressing effect on long wavelength instabilities (Bostick *et al.* 1953), it would appear that a properly chosen combination of axial magnetic field and external conducting shell should lead to complete stability. Conventional hydromagnetic surface current analyses tend to support this hypothesis, with the proviso that axial magnetic field must be minimized outside the plasma : also Chandrasekhar, Kaufman, and Watson (1958) have obtained very similar stability criteria, using a method in which the Boltzmann equation is taken as a starting point, and collisions between the gas constituents are ignored. However, an analysis by Tayler (1957*b*, pp. 1057–61) for uniform current through the discharge, and experience to date give contrary results !

(*b*) *Examples of Energy Principle Analysis*

First we consider the paper by Suydam (1958). Using the Bernstein energy principle, Suydam considers the stability of a linear pinch having a trapped longitudinal magnetic field. The plasma undergoes a displacement ξ, and the variational principle is used to obtain the resultant change in system potential energy. If any ξ can produce a reduction of potential energy, the system is unstable : if every displacement increases the potential energy, this will require external work, and the system is stable. The theorem obtained by Suydam states :

> " A *necessary* condition that $m\neq 0$ modes of a linear pinch be stable is that
>
> $$\frac{H_z^2}{8\pi}\,\frac{r}{4}\left[\frac{\mathrm{d}}{\mathrm{d}r}\left(\ln\frac{H_\theta}{rH_z}\right)\right]^2+\frac{\mathrm{d}p}{\mathrm{d}r}\geqslant 0 \tag{2.1}$$
>
> at every point in the plasma."

Here r, θ, z are cylindrical coordinates, H is the magnetic field, and p the kinetic pressure.

For plasma material at rest, Cowling (p. 4) derives a diffusion equation,

$$\frac{\partial \mathbf{H}}{\partial t}=\frac{1}{4\pi\mu\sigma}\nabla^2\mathbf{H}, \tag{2.2}$$

which suggests that the magnetic field leaks through the plasma with a characteristic time of decay,

$$\tau_d=4\pi\mu\sigma L^2, \tag{2.3}$$

where μ is the permeability, σ the electrical conductivity, and L a length comparable with the dimensions of the system.

Although it may be possible to establish initially a discharge having well-separated axial and azimuthal fields, this decay concept suggests that after a time of order τ_d these fields will diffuse and mix to such an extent that helical resultant magnetic fields will exist both inside and outside the plasma. This is the situation considered by Suydam. The trapped axial field tends to stabilize the plasma by twisting the magnetic lines of force so that a displacement will bend some of them. After a time diffusion will result in a reduction of the torsion of the lines of force, and a particular perturbation may produce a displacement with a minimum of field line bending, so leading to instability. Suydam emphasizes particularly the dangers of these fluted interchanges, whilst Spitzer (1959) discusses the use of " shear " magnetic fields for stabilization purposes. Such fields possess a resultant which changes direction with increase of radial distance from the discharge axis of symmetry, so that interchange of lines of force requires significant bending, and plasma stability should be improved.

The necessary stability criterion (2.1) is satisfied if the term involving H_θ and H_z can be made large near the plasma boundary ; this can be achieved if the sign of H_z is changed in that region. Using normal mode analysis, Rosenbluth (1958) has shown that a reversed axial magnetic field, applied externally to a plasma, pinched and containing the trapped, original axial field, can satisfy necessary and sufficient, or marginal, conditions. However, this procedure poses a practical problem because application of the reversed field must be suitably timed, and this requires extremely rapid establishment of its maximum value.

A second application of the energy principle (Bernstein *et al.* 1958, p. 31) is an examination of the stability of a plasma, confined by an external magnetic field but with no internal magnetic field. The result obtained may be stated as follows :

> " Calling **R** the vector from the centre of curvature of a magnetic line of force to a point on the line, then if **R** everywhere points away from the plasma the system is unstable : if **R** everywhere points towards the plasma, the system is stable."

Hereafter we shall refer to this result as Teller's criterion, because it was originally proposed on intuitive grounds by E. Teller at a Sherwood conference at Princeton, U.S.A., in 1954 (Bishop 1960). Teller's criterion is illustrated in Figure 1.

To conclude this section we observe that the detailed normal mode analyses yield results on instability frequencies and growth rates for various m, and provide either marginal or sufficiency conditions for stability. These conditions appear as rather simple relationships between parameters such as m, k, ω. Use of the energy principle leads to a necessary condition for stability, and confirmation of Teller's powerful criterion.

In the following section we give a thermodynamic treatment which provides useful insight into the phenomenon of interchange instability in a plasma having internal magnetic field. The approach follows broadly those of Rosenbluth and Longmire (1957) and Chandrasekhar and Trehan (1960), but unlike the latter authors, who discuss a curving, axially symmetric confining magnetic field, we give Teller's criterion in a useful mathematical form applicable to more general magnetic field configurations, and apply it in Section IV to the centrally constricted discharge described at the end of Section I.

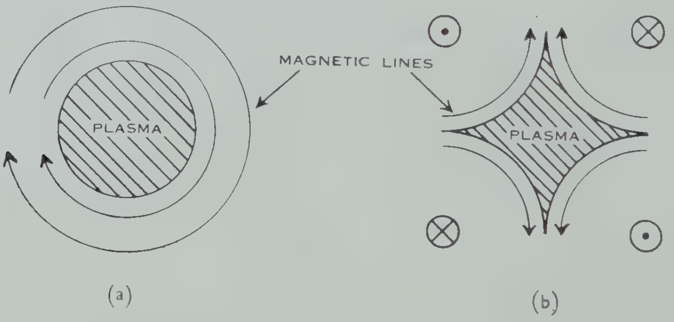

Fig. 1.—Illustration of Teller's criterion. (*a*) Unstable; (*b*) stable.

III. Thermodynamic Derivation of Teller's Stability Criterion

The following derivation gives a useful integral form of Teller's criterion. We consider a general region in which static plasma and magnetic lines of force are embedded in each other, and choose a pair of associated tubes generated by the flux lines. Remembering that the potential energy of this system is the sum of the magnetic and internal energies of the plasma, we first obtain expressions for the change in magnetic energy, δW, and the change in gas energy, δU, resulting from an interchange of the magnetic flux and plasma in tube 1 of volume V_1, with that in tube 2 of volume V_2.

(*a*) *Calculation of* δW

If l is distance along a flux tube n, having cross sectional area $A(l)$ and volume element $\mathrm{d}V=A(l)\mathrm{d}l$, the total magnetic energy within the tube n is

$$W_n=\int_n \frac{H^2}{8\pi}A\mathrm{d}l, \tag{3.1}$$

where the subscript n signifies that the integral is for the complete tube n.

Since div $\mathbf{H}=0$, the total flux $\varphi=HA$ is constant along a flux tube. Accordingly, (3.1) becomes

$$W_n=\frac{\varphi_n^2}{8\pi}\int_n \frac{dl}{A}. \tag{3.2}$$

Using (3.2), we obtain

$$\delta W=\frac{1}{8\pi}\left[\left(\varphi_2^2\int_1 \frac{dl}{A}+\varphi_1^2\int_2 \frac{dl}{A}\right)-\left(\varphi_2^2\int_2 \frac{dl}{A}+\varphi_1^2\int_1 \frac{dl}{A}\right)\right]$$

or

$$\delta W=\frac{\varphi_2^2-\varphi_1^2}{8\pi}\left[\int_1 \frac{dl}{A}-\int_2 \frac{dl}{A}\right]. \tag{3.3}$$

(*b*) *Calculation of* δU

On the reasonable assumption that the interchange between the associated flux tubes 1 and 2 is locally adiabatic (i.e. heat gain by Joule heating and heat loss by conduction does not occur), the first law of thermodynamics becomes

$$0=dU+p\,dV. \tag{3.4}$$

Using the adiabatic equation of state

$$pV^\gamma=\text{const.}, \tag{3.5}$$

equation (3.4) integrates to the form

$$U=pV/(\gamma-1), \tag{3.6}$$

where U is the internal energy of the plasma per unit mass, p the kinetic pressure, V the specific volume, and γ the ratio of the specific heat at constant pressure to that at constant volume. Since the steady-state equation (1.2) implies that the pressure p is constant along a line of force, the change in gas energy resulting from the interchange between flux tubes 1 and 2 can now be written

$$\delta U=\frac{1}{\gamma-1}[(p_2'V_1+p_1'V_2)-(p_1V_1+p_2V_2)], \tag{3.7}$$

where p_2', the pressure in tube 1 after the interchange, and p_1', the pressure in tube 2 after the interchange are, from (3.5), given by

$$p_2'=(V_2/V_1)^\gamma p_2,\quad p_1'=(V_1/V_2)^\gamma p_1. \tag{3.8}$$

Elimination of p_2' and p_1' from (3.7) by means of (3.8) gives

$$\delta U=-\frac{1}{\gamma-1}[(p_2V_2^\gamma-p_1V_1^\gamma)(V_2^{1-\gamma}-V_1^{1-\gamma})]. \tag{3.9}$$

If the flux tubes are in close proximity,

$$p_2=p_1+\delta p,\qquad V_2=V_1+\delta V, \tag{3.10}$$

and it is then evident that (3.9) becomes

$$\delta U=-\frac{1}{\gamma-1}\delta(pV^\gamma)\delta(V^{1-\gamma}),$$

or

$$\delta U=p(\delta p/p+\gamma\delta V/V)\delta V. \tag{3.11}$$

(c) The Flute Instability and Teller's Criterion

Consider a magnetic field **H** in a region R, produced by given currents outside the region. Then in R, div $\mathbf{H}$=curl $\mathbf{H}=0$, and there exist magnetic vector and scalar potentials. Call the magnetic scalar potential Ψ, so that $\mathbf{H}=\text{grad}\,\Psi$. Further, consider within R a sub-region r, of volume V_r bounded by a surface S_r, and let a displacement of the matter in V_r vary **H** to $\mathbf{H}+\mathbf{h}$, where the perturbation **h** vanishes on and outside S_r. Then div $(\mathbf{H}+\mathbf{h})=0$, so that **h** is also solenoidal. The flux tubes generated by **h** are therefore closed, and confined within the volume V_r. The change in magnetic energy here is

$$\delta W'=\frac{1}{8\pi}\int_{V_r}(\mathbf{H}+\mathbf{h})\cdot(\mathbf{H}+\mathbf{h})\mathrm{d}V-\frac{1}{8\pi}\int_{V_r}H^2\mathrm{d}V$$

or

$$\delta W'=\frac{1}{4\pi}\int_{V_r}\text{grad}\,\Psi\cdot\mathbf{h}\mathrm{d}V+\frac{1}{8\pi}\int_{V_r}h^2\mathrm{d}V. \tag{3.12}$$

With div $\mathbf{h}=0$, application of Green's theorem to the first integral on the right-hand side of (3.12) yields

$$\Omega=\frac{1}{4\pi}\int_{S_r}(\Psi\mathbf{h})\cdot\mathrm{d}\mathbf{S}. \tag{3.13}$$

Since **h** vanishes on S_r, $\Omega=0$, and (3.12) reduces to

$$\delta W'=\frac{1}{8\pi}\int_{V_r}h^2\mathrm{d}V>0, \tag{3.14}$$

thus confirming that an irrotational magnetic field **H** is stable against a finite perturbation **h**. The proof given is similar to that by Lundquist (1952, p. 308).

We now apply the results (3.3), (3.11), and (3.14) to the diffuse boundary of a plasma in a magnetic field, considering particularly the type of interchange instability which flutes the plasma surface along the magnetic lines. More specifically, we take the magnetic field near the plasma boundary, where the gas is very tenuous and the kinetic pressure vanishingly small, to be closely irrotational. Then, if the interchange attempts to bend lines of force, (3.14) shows that the magnetic energy must be increased. Hence, near the plasma boundary the only type of interchange that may lead to instability is that which leaves the magnetic field unchanged. By locating flux tubes 1 and 2 close to the boundary, we can satisfy this condition by making $\varphi_1=\varphi_2$, whereupon (3.3) gives

$$\delta W=0. \tag{3.15}$$

The flute interchange is illustrated in Figure 2. The condition for stability now assumes the simple form

$$\delta U>0. \tag{3.16}$$

On the realistic assumption that p vanishes smoothly with radial approach to the boundary, we have the conditions

$$\left.\begin{aligned}p&>0,\\ \delta p/p&<0,\\ |\delta p/p|&>|\gamma\delta V/V|.\end{aligned}\right\} \tag{3.17}$$

Hence (3.11) shows that the stability condition (3.16) becomes

$$\delta V<0. \tag{3.18}$$

Since for a flux tube, $V=\varphi\int \mathrm{d}l/H$, we have for the interchange considered the general result for stability

$$\delta\int \mathrm{d}l/H<0, \tag{3.19}$$

because $\varphi>0$.

The inequality (3.19) can be usefully transformed as follows. From the flute illustration, Figure 2, we have for the non-coplanar magnetic lines 1 and 2, separated at distance l by perpendicular distance $a(l)$,

$$\int_2 H\mathrm{d}l=\int_1 H\mathrm{d}l, \tag{3.20}$$

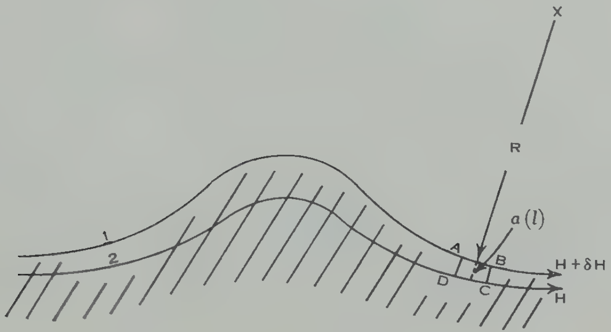

Fig. 2.—Flute instability at plasma boundary.

since the points connected by $a(l)$ are at the same magnetic scalar potential. The assumed condition curl $\mathbf{H}\sim 0$ in this region implies the vanishing of the line integral taken round the small rectangle *ABCD* in Figure 2, which gives

$$\delta H/H=a/R. \tag{3.21}$$

Forming now

$$\delta\int\frac{\mathrm{d}l}{H}=\int_2\frac{\mathrm{d}l}{H}-\int_1\frac{\mathrm{d}l}{H},$$

we obtain by means of (3.20)

$$\begin{aligned}\delta\int\frac{\mathrm{d}l}{H}&=\int\left(\frac{1}{H_2^2}-\frac{1}{H_1^2}\right)H\mathrm{d}l\\&=\int\delta\left(\frac{1}{H^2}\right)H\mathrm{d}l.\end{aligned} \tag{3.22}$$

Expanding under the integral sign, and eliminating $\delta H/H$ by means of (3.21),

$$\delta\int\frac{\mathrm{d}l}{H}=-2\int\frac{a\mathrm{d}l}{RH}. \tag{3.23}$$

The stability condition (3.19) can now be written in the important general form

$$\int \frac{a\mathrm{d}l}{RH} > 0, \tag{3.24}$$

where $a > 0$, $H > 0$, and the derivation has been based on the magnetohydrodynamic approximation of a scalar pressure, with $p \sim 0$ at the plasma boundary.

With the usual convention that the concavity of the magnetic lines of force in Figure 2 is upwards for $R > 0$ and downwards for $R < 0$, equation (3.24) gives a compact integral form of Teller's criterion. Applied to the flute interchange of Figure 2, it predicts instability because, in the middle region where $R < 0$, the magnetic field is least, and the net result is that the destabilizing forces exceed the stabilizing forces.

IV. Application of Teller's Criterion to a Radially Constricted Gas Discharge

Consistently with the findings of Section II, the result (3.24) supports the remark that the curvature of the magnetic lines of force is clearly in the unstable direction for any helical or azimuthal field (Berkowitz, Grad, and Rubin 1958).

In earlier papers by the present author (1961*a*, 1961*b*) the boundary surface of the discharge studied was represented by a hyperboloid of revolution of one sheet. Such a surface can be produced by rotation of a generating line about the axis of symmetry. The cross section of this discharge in the ρ-z plane is shown in Figure 3 (*a*), using the notation adopted earlier; a generator is also shown, and is to be imagined raised a vertical distance ρ_0 from the ρ-z plane. It is also helpful in the following discussions to imagine the discharge curved semi-surface above the ρ-z plane, produced by motion of this generator. Figure 3 (*b*) serves to define parameters associated with a generator.

Defining the azimuthal field due to $I^*(w_b)$ as H_φ, and the external guiding field due to the solenoid as H_E, we can at the discharge surface define an angle of inclination θ, of the resultant magnetic field to the direction of the axis of symmetry by the equation

$$\tan\theta \approx H_\varphi / H_E. \tag{4.1}$$

If we now regard the appropriately shaped H_E field as initially established at its full value, so that $\tan\theta$ can be increased by increasing H_φ (i.e. by increasing $I^*(w_b)$ from a threshold value corresponding to initiation of the discharge), the magnetic field resultant at a point on the generator in Figure 3 (*a*) can be made to swing from approximately the axial direction towards the direction of the generator. Further increase of H_φ leads to the magnetic field resultant crossing to the right of the generator. To permit a simple estimate of stability, it is assumed that the inclination θ_g of the generator to the axial direction is independent of $I^*(w_b)$ when central constriction is large, and, because of conservation of flux, that at the discharge surface H_E is approximately proportional to ρ^{-2}, where ρ is the radial distance from the symmetry axis; H_φ varies as ρ^{-1}. Then, when the magnetic field resultant is to the left of the generator, where $R > 0$, equation (3.24) shows that stabilizing forces act. However, to the right of the

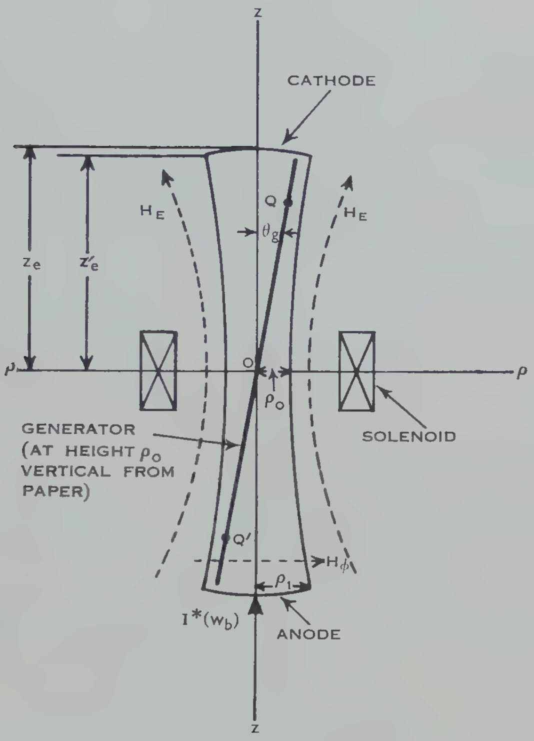

Fig. 3 (*a*).—Discharge cross section in the ρ-*z* plane.

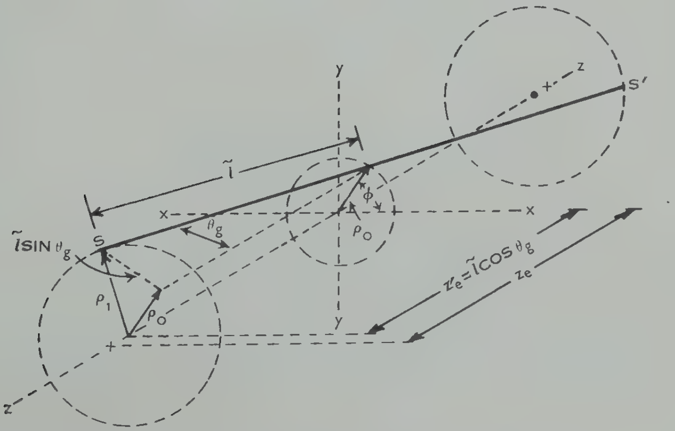

Fig. 3 (*b*).—Parameters associated with a generator *S*–*S*′.

generator, where $R<0$, the combined H_E and H_φ field forms a type of helix, and destabilizing forces contribute. Since $H_\varphi \propto \rho^{-1}$, $H_E \propto \rho^{-2}$, it follows from (4.1) that $\tan\theta \propto \rho$, and so from Figure 3 (*a*) we note that θ has a minimum at $z=0$ and equal maxima at the electrodes. Hence if θ of the field resultant matches θ_g at some point Q on a generator (Fig. 3 (*a*)), then these angles will again match at an image point Q', so that between Q and Q' stabilizing forces contribute, whilst between Q and the cathode and between Q' and the anode destabilizing forces act. Assessment of the net effect of these competing forces for chosen Q, Q' involves evaluation of the integral in (3.24). To overcome this difficulty and obtain a sufficient condition for stability, we set Q and Q' at the electrodes, so that stabilizing forces only contribute.

The current $I_0^*(w_b)$ which satisfies this sufficient stability condition can be estimated as follows. From Figure 3 (*b*), $z_e'=\tilde{l}\cos\theta_g$ and $(\rho_1^2-\rho_0^2)^{\frac{1}{2}}=\tilde{l}\sin\theta_g$, giving

$$\tan\theta_g=\frac{\rho_1}{z_e'\nu}(\nu^2-1)^{\frac{1}{2}}, \tag{4.2}$$

where $\nu=\rho_1/\rho_0$ is the radial compression ratio.

From equations (6.4.19), (6.4.28), and (6.4.31) (Seymour 1961*a*),

$$z_e'=z_e[1-(\rho_1/z_e)^2(1-1/\nu^2)]^{\frac{1}{2}},$$

where z_e is the discharge semi-length. Thus, eliminating z_e' from (4.2),

$$\tan\theta_g=\left(\frac{(\rho_1/z_e)^2(\nu^2-1)}{\nu^2-(\rho_1/z_e)^2(\nu^2-1)}\right)^{\frac{1}{2}}. \tag{4.3}$$

For the assumed ρ-dependences of H_φ and H_E, equation (4.1) gives at the electrodes

$$\tan\theta\approx\frac{\pi}{5}\,\frac{I^*(w_b)}{\varphi_E}\rho_1, \tag{4.4}$$

where the current unit is the ampere, and φ_E is the total flux from the solenoid through any equipotential surface terminating at the boundary surface of the discharge.

Setting $\theta=\theta_g$ in (4.4) and combining the result with (4.3),

$$I_0^*(w_b)\approx\frac{5\varphi_E}{\pi\rho_1}\left(\frac{(\rho_1/z_e)^2(\nu^2-1)}{\nu^2-(\rho_1/z_e)^2(\nu^2-1)}\right)^{\frac{1}{2}}. \tag{4.5}$$

V. Discussion of Results

For the type of discharge studied here, theory suggests that a stable plasma configuration can be obtained if the external field H_E, shaped to give the required centrally constricted boundary surface without too much assistance from the self-field H_φ, is initially strong enough.

Then, as $I^*(w_b)$ is increased, the destabilizing effect of the azimuthal H_φ becomes greater until, for a current of order $I_0^*(w_b)$ given by (4.5), the stable plasma configuration is destroyed. Since $(\rho_1/z_e)^2 \ll 1$ is a likely practical condition, and we desire $\nu^2 \gg 1$, equation (4.5) gives this current simply as

$$I_0^*(w_b) \sim 1 \cdot 6 \varphi_E / z_e. \tag{5.1}$$

In practice it may be more convenient to work in terms of $H_E(0)$ on the discharge median plane. Equation (5.1) then assumes the form

$$I_0^*(w_b) \sim 5 H_E(0) \rho_0^2 / z_e. \tag{5.2}$$

It is important to observe that the above conclusions are based on an assumed infinite electrical conductivity, so that τ_d of equation (2.3) is also infinite. In practice we must contend with finite τ_d, which, from (2.3) and Seymour (1961*a*, equation (5.7)), may be written in terms of the temperature T as

$$\tau_d \sim 2 \times 10^{-13} L^2 T^{3/2} \text{ cm}^{-2} \text{ deg}^{-3/2} \text{ s}, \tag{5.3}$$

when $\ln \lambda = 10$, a result which is consistent with Spitzer's result (1956, p. 38). For practical values of L and T, τ_d is in the region of milliseconds, and so the " steady state " is of short duration !

However, it is thought that the procedure outlined in Section IV could form the basis of an interesting laboratory experiment for the observation of transition from stability to instability in a constricted gas discharge between electrodes. Then, if the practical results obtained from such an experiment were to support the theory reasonably, there would be a case for a more detailed theoretical stability study of this type of discharge.

VI. Acknowledgments

The problem examined here is the last of a short series suggested by Professor K. J. Le Couteur. The author is indebted to Professor Le Couteur for recent stimulating discussions on the topic of plasma stability, and to Mr. G. F. Cawsey for earlier helpful discussions and interest in this work. He is also grateful to Dr. A. H. Morton, leader of the Experimental Plasma Physics Group at the Australian National University, who read this paper in manuscript form and gave the opinion that the proposed laboratory experiment is feasible.

VII. References

Artsimovich, L. A. (1958).—" Proceedings of the Second United Nations International Conference on the Peaceful Uses of Atomic Energy." Vol. 31. pp. 6–7. (United Nations Publication : Geneva.)

Berkowitz, J., Grad, H., and Rubin, H. (1958).—" Proceedings of the Second United Nations International Conference on the Peaceful Uses of Atomic Energy." Vol. 31. p. 183. (United Nations Publication : Geneva.)

Bernstein, I. B., Frieman, E. A., Kruskal, M. D., and Kulsrud, R. M. (1958).—An energy principle for hydromagnetic stability problems. *Proc. Roy. Soc.* A **244** : 17–40.

Bishop, A. S. (1960).—" Project Sherwood—The U.S. Program in Controlled Fusion." pp. 86–8. (Anchor Books, Doubleday and Co. : New York.)

Bostick, W. H., Levine, M. A., Combs, L. S., and Moncius, I. (1953).—Tufts College Laboratory Report No. 14.

Chandrasekhar, S., Kaufman, A. N., and Watson, K. M. (1958).—The stability of the pinch. *Proc. Roy. Soc.* A **245** : 435–55.

Chandrasekhar, S., and Trehan, S. K. (1960).—" Plasma Physics." pp. 87–91. (Univ. Chicago Press.)

Cowling, T. G. (1957).—" Magnetohydrodynamics." pp. 5–6. (Interscience Publishers : New York and London.)

Kruskal, M., and Schwarzschild, M. (1954).—Some instabilities of a completely ionized plasma. *Proc. Roy. Soc.* A **223** : 348–60.

Kruskal, M., and Tuck, J. L. (1958).—The instability of a pinched fluid with a longitudinal magnetic field. *Proc. Roy. Soc.* A **245** : 222–37. (*Originally* Los Alamos Report No. 1716, 1953.)

Lamb, H. (1945).—" Hydrodynamics." pp. 370–1. (Dover Publications : New York.)

Linhart, J. G. (1960).—" Plasma Physics." pp. 73–6, 169–72. (North-Holland Publishing Company : Amsterdam.)

Lundquist, S. (1950).—Magneto-hydrostatic fields. *Ark. Fys.* **2** (35) : 364–5.

Lundquist, S. (1951).—On the stability of magneto-hydrostatic fields. *Phys. Rev.* **83** : 307–11.

Lundquist, S. (1952).—Studies in magneto-hydrodynamics. *Ark. Fys.* **5** (15) : 297–347.

Rosenbluth, M. N. (1957).—Stability of the pinch. Los Alamos Report No. 2030 and Third International Conference on Ionization Phenomena in Gases, Venice.

Rosenbluth, M. N. (1958).—" Proceedings of the Second United Nations International Conference on the Peaceful Uses of Atomic Energy." Vol. 31. pp. 85–9. (United Nations Publication : Geneva.)

Rosenbluth, M. N., and Longmire, C. L. (1957).—Stability of plasmas confined by magnetic fields. *Ann. Phys., Lpz.* **1** : 129–33.

Seymour, P. W. (1961*a*).—Estimation of the maximum temperature in a radially constricted gas discharge between electrodes. *Aust. J. Phys.* **14** : 129.

Seymour, P. W. (1961*b*).—The influence of thermoelectric effects on the maximum temperature in a radially constricted gas discharge between electrodes. *Aust. J. Phys.* **14** : 279.

Shafranov, V. D. (1957).—On the stability of a cylindrical gaseous conductor in a magnetic field. *J. Nucl. Energy* **5** : 86–91.

Spitzer, L., Jr. (1956).—" Physics of Fully Ionized Gases." p. 21. (Interscience Publishers : New York and London.)

Spitzer, L., Jr. (1959).—The Stellarator program. " Plasma Physics and Thermonuclear Research." Vol. 1. p. 117. (Eds. C. Longmire, J. L. Tuck, and W. B. Thompson.) (Pergamon Press : London.)

Suydam, B. R. (1958).—" Proceedings of the Second United Nations International Conference on the Peaceful Uses of Atomic Energy." Vol. 31. pp. 157–9. (United Nations Publication : Geneva.)

Tayler, R. J. (1957*a*).—Hydromagnetic instabilities of an ideally conducting fluid. *Proc. Phys. Soc.* B **70** : 31–48.

Tayler, R. J. (1957*b*).—The influence of an axial magnetic field on the stability of a constricted gas discharge. *Proc. Phys. Soc.* B **70** : 1049–63.

GAMMA RAYS FROM THE ^{27}Al(p,γ) REACTION

By S. BASHKIN* and T. R. OPHEL†

[*Manuscript received April* 11, 1961]

Summary

Gamma-ray spectra and angular distributions have been measured at the 759, 766, 773, and 993 keV resonances of the ^{27}Al(p,γ) reaction.

The results obtained at the lower resonance are in agreement with previous work. At the 993 keV resonance a transition to the 7·80 MeV level of ^{28}Si has been observed.

Tentative J^{π} assignments to the resonance levels of 2^-(759 keV), 4^-(766 keV), 1^+(773 keV), and 3^+(993 keV) are discussed.

I. INTRODUCTION

The present investigation was commenced in order to establish the predominant gamma-ray transitions occurring at resonances of the ^{27}Al(p,γ)^{28}Si reaction for E_p=750–1000 keV as a preliminary to a study of the resonance levels and intermediate levels of ^{28}Si by means of angular correlation measurements. Many resonances of this reaction which occur at proton energies below 750 keV have been previously studied (Casson 1953; Rutherglen *et al.* 1954; Endt and Heyligers 1960; Okano 1960) but, of the resonances reported at proton energies between 750 and 1000 keV, namely, 759, 766, 773, 884, 922, 936, and 993 keV (Broström, Huus, and Tangen 1947; Andersen *et al.*, 1959) measurements of the gamma-ray spectra have been made only at 773 and 993 keV (Gove, Litherland, and Paul, unpublished data 1957; Smith and Endt 1958; Brenner 1959). It was intended to supplement measurements at these resonances and to examine the remainder.

II. EXPERIMENTAL PROCEDURE

A proton beam of up to 10 μA at the target was obtained from the Canberra 1·2 MeV Cockcroft-Walton accelerator after 90° magnetic analysis and electrostatic focusing through two tantalum defining apertures, $\frac{1}{8}$ in. in diameter, placed 2 ft apart (Fig. 1). Good energy stability and homogeneity of the beam was required to resolve the closely spaced resonances, and modifications to the accelerator input generator and the 90° magnet power supply were found to be necessary. The full width of the resonance at 773 keV, comprising target thickness, energy inhomogeneity, and the natural resonance width (less than 160 eV, Andersen *et al.* 1959), was typically 3 keV for the targets used, and measurements of the variations from maximum yield at this resonance as a function of time indicated that the energy stability was better than ±1·5 keV.

---

* Fulbright Research Scholar, Australian National University; present address: State University of Iowa, Iowa City, Iowa, U.S.A.

† Department of Nuclear Physics, Australian National University, Canberra.

Targets were prepared by evaporation of pure aluminium onto copper backings 0·030 in. thick which were mounted on a water-cooled holder. The target chamber (Fig. 1) was constructed of " Lucite " to minimize scattering in the vicinity of the target. Carbon deposition on the target was almost completely avoided by surrounding the target with a 0·015 in. thick copper cylinder which was maintained at liquid air temperature. For a typical run of five hours' duration, no drift of the resonance energy due to carbon build-up could be detected. The observed background from the $^{12}C(p,\gamma)$ reaction was attributed to carbon contamination during target preparation since there was no increase of the background with time.

The gamma rays were detected with a 5 in. diameter by 4 in. thick sodium iodide crystal optically coupled to a 3 in. DuMont 6363 phototube. The crystal-phototube assembly, housed in a lead shielding at least 4 in. thick in any direction, was mounted on a rotating table. Gamma rays entered the crystal through a conical defining aperture, 2 in. in diameter at the crystal and tapered so that the target was situated within the cone defined by the taper. Spectra were recorded on a Sunvic 100-channel pulse-height analyser. At each resonance, two spectra were recorded with the same overall gain but different analyser base-line values. In this way, the spectrum for gamma-ray energies between 1·5 and 13 MeV was contained in approximately 170 channels. The crystal response function, from which the line shape of a gamma ray of any energy between 1·5 and 13 MeV could be constructed, and energy calibrations were obtained from measurements of the gamma-ray spectra from the $^{11}B(p,\gamma)$, $^{19}F(p,\alpha\gamma)$, and $^{13}C(p,\gamma)$ reactions and ThC″ and ^{22}Na sources (Fig. 2).

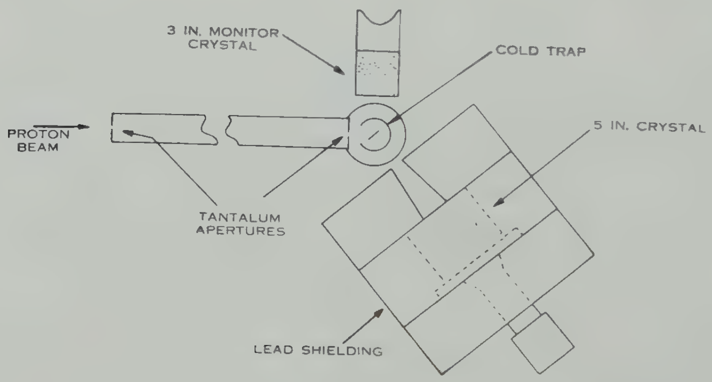

Fig. 1.—Schematic view of experimental arrangement.

An unshielded 3 in. by 3 in. sodium iodide crystal, mounted at 90° to the beam, was used for coincidence measurements and as a monitor. The output of this counter was fed to three scalers with discriminators set to count pulses corresponding to an energy loss in the crystal greater than 1·6, 4·0, and 8·0 MeV respectively. The ratios of counts thus obtained were very sensitive to the particular resonance being observed and therefore served to indicate any possible contribution from nearby resonances due to target deterioration or energy instability during the course of the measurement. For coincidence measurements, portions of the 3 in. counter output were selected with a single-channel analyser and fed to a coincidence circuit with a resolving time of $2\tau=1\cdot0$ μs. Coincidence measurements were made at the 773 and 993 keV resonances to determine the decay schemes, and, for these measurements, the front shielding of the large crystal was removed and the counter moved nearer to the target.

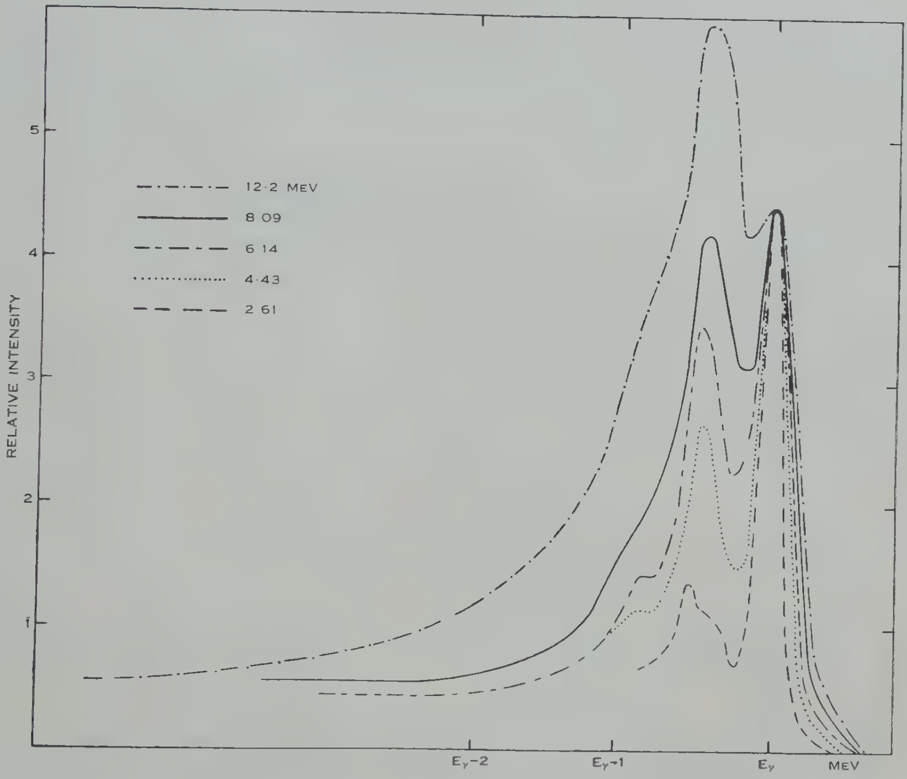

Fig. 2.—Line shapes obtained with the 5 in. by 4 in. crystal for the indicated gamma-ray energies.

A singles spectrum was recorded at each resonance at 90° to the beam and angular distributions were measured at six equal intervals of $\cos^2\theta$ between $\theta=0°$ and $\theta=90°$.

III. Results

The excitation functions obtained in the regions of $E_p=755$–775 keV and $E_p=990$–1010 keV are given in Figure 3. The excitation functions were recorded by applying a 20 keV sawtooth voltage to the target. The output of a gamma-ray detector triggered a pulse proportional to the instantaneous applied voltage so that the excitation function could be recorded directly on a pulse-height analyser (Carver and Waugh 1961).

(a) *759 keV Resonance* (*^{28}Si excitation—12·320 MeV*)

The spectrum obtained at $E_p = 761$ keV is shown in Figure 4. The resonance level decays almost entirely (approximately 90%) by a transition to the first excited state of ^{28}Si at 1·78 MeV, the ground state transition being very weak ($\leqslant$3%). The angular distribution of the 10·5 MeV gamma ray was isotropic to within 5%.

(b) *766 keV Resonance* (*12·327 MeV*)

The spectrum is shown in Figure 4. Gamma rays of energies 7·70, 2·84, and 1·78 MeV are observed, corresponding to a transition to the second excited state at 4·62 MeV followed by a cascade through the 1·78 MeV level. This mode of decay accounts for about 75% of the gamma-ray yield. Weak gamma rays at 6·8 MeV and in the vicinity of 4 MeV are apparent in the spectrum but they were not further investigated. Endt and Heyligers (1960) have identified these gamma rays as transitions through levels at 6·28, 8·41, and 8·59 MeV.

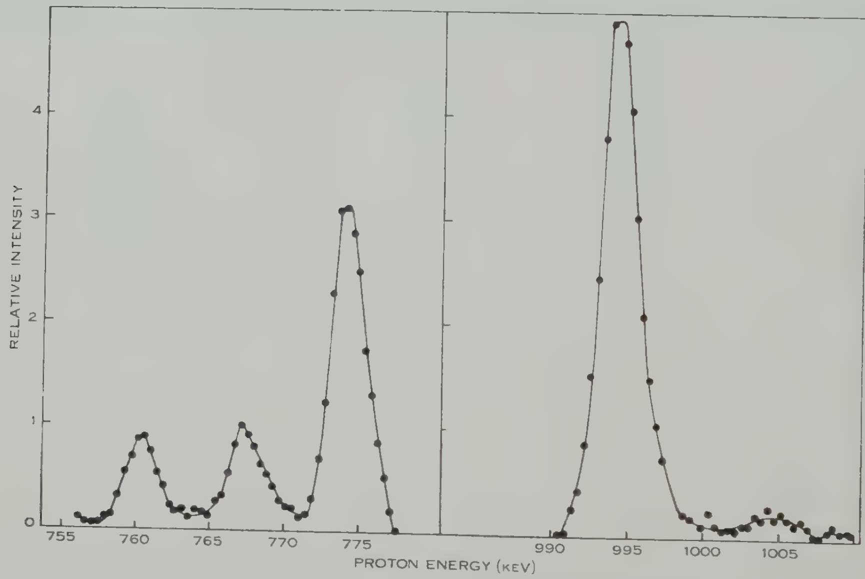

Fig. 3.—Excitation function of the ^{27}Al(p,γ) reaction in the regions of the resonances studied. The ordinate scales for the two sections of the excitation function are not related.

The angular distribution of the 7·7 MeV gamma ray was found to be $W(\theta) \sim 1 + (0\cdot25 \pm 0\cdot04) \cos^2 \theta$. Small monitoring corrections, based on the monitor scaler ratios, were necessary for the angular distribution measurement to account for contamination from adjacent resonances.

(c) *773 keV Resonance* (*12·333 MeV*)

This is the most intense of the three resonances and, as noted previously by Gove, Litherland, and Paul (unpublished data 1957) and Smith and Endt (1958), is characterized by a strong ground state transition (Fig. 4). Other gamma rays

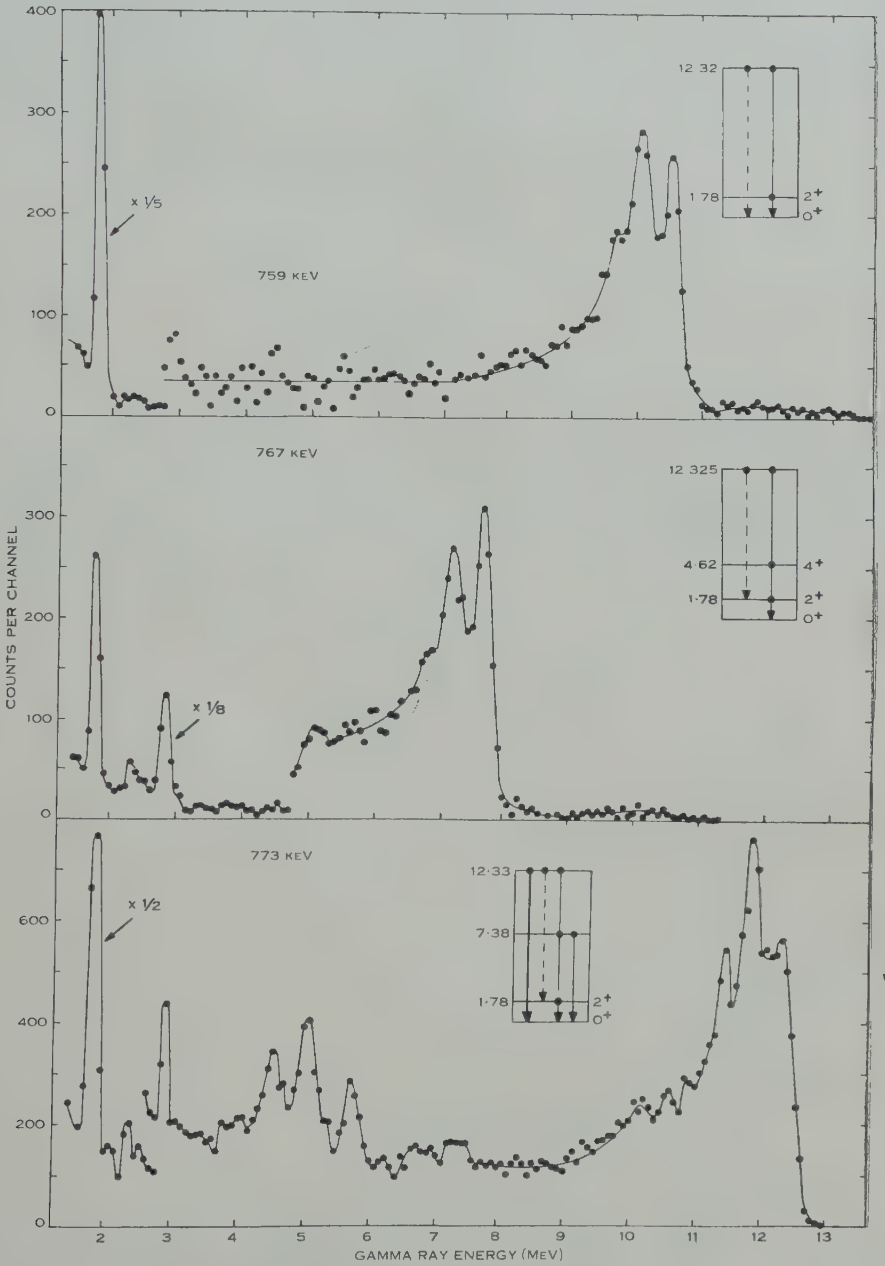

Fig. 4.—Gamma-ray spectra (measured at 90° to the beam) obtained at the 759, 766, and 773 keV resonances. Weak transitions (see text) are shown as broken lines.

are evident at 10·5, 7·4, 5·60, 5·0, 4·5, 2·85, and 1·78 MeV. The 10·5 MeV is identified as the transition to the first excited state. The 7·4 and 5·0 MeV gamma rays could result from a transition through the 4·96 MeV level or alternatively from a transition through the 7·38 MeV level. The former cascade is inconsistent with a recent assignment of 0^+ to the 4·96 MeV level of ^{28}Si (Gove, personal communication). Coincidence measurements, obtained by gating on various portions of the 3 in. crystal spectrum (summarized in Table 1), showed that the 5·0 MeV gamma ray was in coincidence with 7·4, 5·6, and 1·78 MeV gamma rays. Thus it can be concluded that the 5·0 MeV gamma ray is the result of a transition to the 7·38 MeV level, which decays either directly to the ground state or by a cascade through the first excited state with the emission of a 5·6 MeV gamma ray. The other weaker gamma rays were not investigated.

TABLE 1

GAMMA RAYS IN COINCIDENCE WITH SELECTED GAMMA RAYS AT THE 773 keV RESONANCE

Gate	Gamma Rays Observed in Coincidence
1·78 MeV	(10·5), 5·6, 5·0, 2·85 MeV
4–5 MeV	7·4, 5·6, 1·78 MeV
5–6 MeV	5·0, 2·85, 1·78 MeV

TABLE 2

SUMMARY OF RESULTS OBTAINED AT THE 993 keV RESONANCE

Gamma-ray Energy (MeV)	Intensity	Coincidence with 1·78 MeV Gamma Ray	Brenner	
10·76	100	yes	10·8	100
8·98±0·15	⩽3	—		
7·95±0·05	8	yes (partially)	8·04	17
7·40±0·10	⩽2	—	7·2	
6·3 ±0·10	⩽3	—		
6·04±0·05	10	yes	6·07	20
5·12±0·10	⩽2	—		
4·78±0·075	13	yes	}4·66	21
4·52±0·10	10	no		
3·12±0·10	⩽5	—		
2·84±0·05	10	yes	2·86	6*
1·78	124	—	1·80	100*

* Separate measurement which is not related to other intensities.

The angular distribution of the 12·4 MeV ground state transition was measured as $W(\theta)\sim 1-(0\cdot 18\pm 0\cdot 03)\cos^2\theta$ in good agreement with the results obtained by Gove *et al.* (1954).

(*d*) *884, 922, and 936 keV Resonances*

Strong resonances in the ^{19}F($p,\alpha\gamma$) reaction in the neighbourhood of each of these resonances were the source of a very troublesome background. No measurements were made at the 884 and 936 keV resonances, although a strong transition to the 1·78 MeV level was observed at the 884 keV resonance. The spectrum of the 922 keV resonance (not shown) closely resembled the result obtained at the 759 keV resonance in that the resonance level decayed almost entirely by a transition to the 1·78 MeV level.

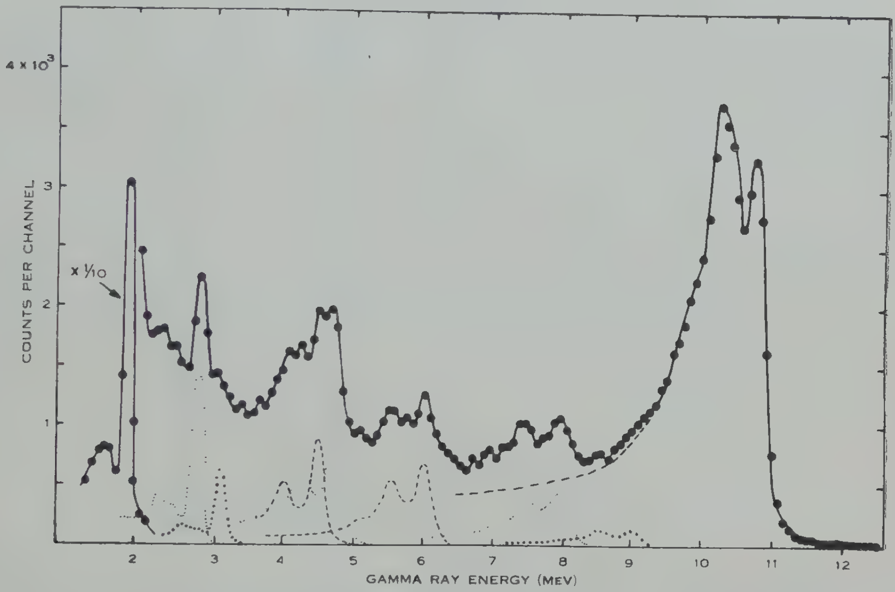

Fig. 5.—Gamma-ray spectrum of the 993 keV resonance (at 90°). The individual gamma rays, into which the spectrum was decomposed, are indicated.

(*e*) *993 keV Resonance* (*12·547 MeV*)

The spectrum obtained at this intense resonance is given in Figure 5 and the gamma rays identified and their relative intensities (at 90°) are listed in Table 2.

There is reasonable agreement with Brenner (1959) so far as the energies of the most intense gamma rays are concerned, although a considerable difference of the relative intensities of the 7·95 and 6·04 MeV gamma rays is to be noted. It is perhaps significant that possible contaminant reactions ^{13}C(p,γ) and ^{19}F($p,\alpha\gamma$) yield gamma rays of approximately these energies.

The present spectrum is better resolved than that obtained by Brenner and shows an important difference in that two gamma rays are resolved in the vicinity of 4·6 MeV, whereas Brenner identified only one gamma ray at 4·66 MeV. The decay scheme proposed (Fig. 6) is consistent with the observed energies and intensities and the present coincidence measurements as well as with the 8 and 4·6 MeV cascade observed by Gove, Litherland, and Paul (unpublished data 1957).

De-excitation of the various levels involved is in agreement with the scheme proposed by Endt and Heyligers (1960), although they did not observe the excitation of the level at 7·80 MeV at any of the resonances between $E_p=500$ and 800 keV. A transition to this level, followed by a cascade through the 1·78 MeV level, would result in gamma rays of energies 4·74 and 6·02 MeV as compared to the observed energies of 4·78 and 6·04 MeV. The only other level which could account for gamma rays of approximately these energies is the 7·93 MeV level. However, the energy discrepancy is in excess of 0·1 MeV for each gamma ray and, since 80% of the de-excitation of the 7·93 MeV level proceeds directly to the ground state (Endt and Heyligers 1960), an excess intensity of the 6·04 MeV gamma ray is observed. The intensity difficulty could arise from the angular distributions of the gamma rays but the energy discrepancy is considered to be too large, since the 4·78 MeV gamma ray was further calibrated by means of comparison with the spectrum obtained at 773 keV. The energy assigned to the 4·52 MeV gamma ray is less accurate since it is more dependent on analysis of the spectrum.

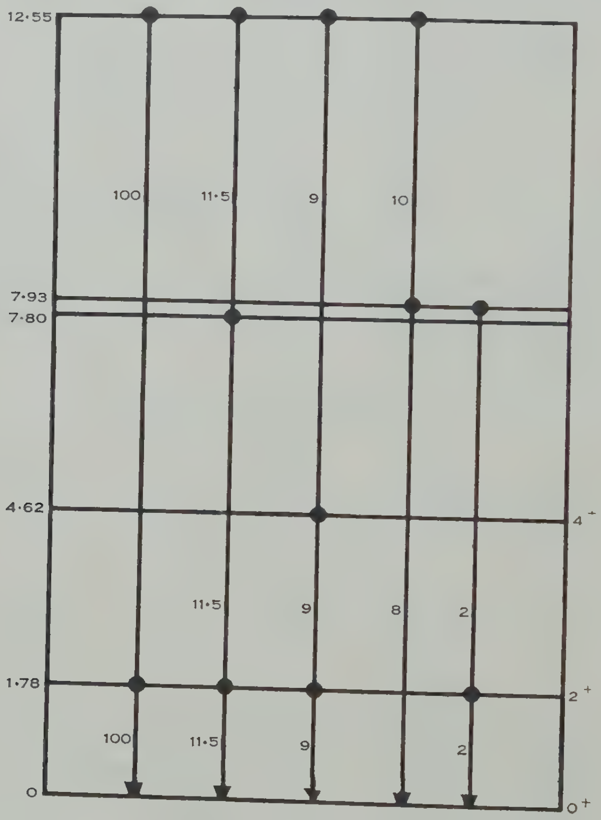

Fig. 6.—Proposed decay scheme of the 993 keV resonance level showing relative intensities of the gamma-ray transitions.

The 8·98 MeV gamma ray could result from excitation of either the 10·71 or 8·91 MeV levels.

The angular distribution of the 10·76 MeV gamma ray was measured as $W(\theta)\sim 1+(0\cdot 10\pm 0\cdot 03)\cos^2\theta$ as compared to the other measurements of $\sim 1+0\cdot 16\cos^2\theta$ (Brenner 1959) and $\sim 1+0\cdot 076\cos^2\theta$ (Gove *et al.* 1954). The 1·78 MeV gamma ray was found to be isotropic to within 2% and the triple correlation of these two gamma rays (10·76 MeV variable) was $\sim 1+(0\cdot 20\pm 0\cdot 03)\cos^2\theta$.

IV. DISCUSSION

During the course of the experiment, it was found that Endt and Heyligers (1960), as a means of establishing the energy levels of ^{28}Si, had already determined the gamma-ray scheme in detail at each resonance in the region E_p=500–800 keV. As has been indicated in Section III, the present results for the 759, 766, and 773 keV resonances are in agreement with the measurements of Endt and Heyligers.

Assignment of J^π values to the resonance levels by means of correlation measurements is complicated, since the ground state spin of the target nucleus is $5/2^+$. Considering *s*,*p*, and *d*-wave proton capture, the possible resonance states are as follows:

l_p	Channel Spin $s=2$	Channel Spin $s=3$
$l=0$	2^+	3^+
$l=1$	1^-, 2^-, 3^-	2^-, 3^-, 4^-
$l=2$	0^+, 1^+, 2^+, 3^+, 4^+	1^+, 2^+, 3^+, 4^+, 5^+

Even with the restriction of l_p, the angular correlations for most possible J^π values involve parameters for either or both channel spin mixing (t) and orbital angular momentum mixing (δ and a relative phase factor $\cos\varphi$) as well as a multipole mixing parameter (x) of the gamma-ray transition.

The reaction ^{27}Al(p,α)^{24}Mg does not provide any definite simplification of the possible spins since the alpha-particle yield (to the ground state of ^{24}Mg) is non-resonant at each of the four resonances under study (Shoemaker *et al.* 1951; Kuperus and Smith 1960). Non-emission of alpha particles implies that the spins of the resonance levels are in the sequence 1^+, 2^-, 3^+, 4^-, etc., but such an interpretation is not rigorous, since alpha-particle emission may be forbidden by isotopic spin selection rules.

In the following discussion, the observed correlations are compared with the theoretical predictions (Sharp *et al.* 1954; Ferguson and Rutledge 1957) with the assumptions that (i) the gamma-ray transitions are pure multipole of the lowest allowed order except that mixing is considered for possible ($M1$, $E2$) transitions (it is to be noted that $E1$ transitions may be inhibited since ^{28}Si is a self-conjugate nucleus) and (ii) proton capture is restricted to *s*, *p*, and *d*-wave capture. The inhibition of electric dipole radiation will depend on isotopic spin being a good quantum number at the excitations in question. Smulder, Smith, and Endt (personal communication 1961) have demonstrated, by examination of a number of resonances of the ^{24}Mg(α,γ)^{28}Si reaction, that isotopic spin is a good quantum number at excitation energies of 12 MeV.

(a) 759 keV (^{28}Si excitation—12·320 MeV)

The presence of a ground state transition indicates that $J \leqslant 2$ and eliminates $J=0\pm$. The assignment of 1^+ or 1^- is not consistent with the relative intensity of the ground state transition. The observed distribution of the transition to the first excited state, $W(\theta) \sim 1+(0\cdot 0 \pm 0\cdot 05)\cos^2\theta$ could result from either a spin of 2^+, which would be produced predominantly by s-capture, or a spin of 2^- with channel spin mixing $(s=3)/(s=2)$ in the range $2 \leqslant t \leqslant 8$. Non-emission of alpha particles from the level favours a 2^- assignment.

The properties of this resonance are very similar to those of the 226 keV resonance which de-excites almost entirely via the 1·78 MeV level, and the angular distribution of the transition is very nearly isotropic (Okano 1960).

(b) 766 keV (12·327 MeV)

At this resonance, no ground state transition is observed and the transition to the first excited state is very weak compared to the transition to the second excited state. Thus the spin is most probably $\geqslant 3$. The assignment of either 3^+ or 3^- is unlikely since, for 3^+, the transitions to both levels would be ($M1$, $E2$) and, for 3^-, both ($E1$, $M2$). In each case, the higher energy transition to the first excited state would be expected to be the more intense. The observed anisotropy is a further argument against a spin of 3^+ which would result predominately from s-wave capture.

The theoretical distribution for the transition $4^-(E1)4^+(l=1,\ s=3)$ is $\sim 1+0\cdot 46\cos^2\theta$, whereas the predicted distribution for the transition $4^+(M1\ E2)4^+(l=2,\ s=2,\ 3)$ can be fitted to the observed distribution for the ranges $0 \leqslant t \leqslant 8\cdot 1$ and $-0\cdot 23 \leqslant x \leqslant 1\cdot 66$ (where x is the $E2/M1$ ratio). Thus the level is almost certainly 4^+ and consequently a $T=1$ state since it is not an alpha-emitting level $(2Jr+1)\Gamma\alpha\Gamma p/\Gamma < 0\cdot 38$ eV. Some confirmation of the assignment can be found in a comparison of the resonance with the 326 and 405 keV resonances to which 4^- assignments have been made (Okano 1960).

The three resonances are similar in that the predominant transition is to the second excited state but the lower resonances show a fairly strong transition to one of the levels of the 6·88 MeV doublet. The absence of this transition at the 766 keV resonance is consistent with a spin assignment of 2^- to the 6·88 MeV level so that the transition would be $M2$ at the 766 keV resonance (and therefore weak) but $E2$ at the lower resonances.

(c) 773 keV (12·333 MeV)

This resonance has been discussed previously by Smith and Endt (1958). The strong ground state transition indicates that $J \leqslant 2$. A spin of 2^- is unlikely because of the weak transition to the first excited state and the observed anisotropy, $W(\theta) \sim 1-(0\cdot 18 \pm 0\cdot 03)\cos^2\theta$ rules out 2^+ which would result mainly from s-wave capture. The theoretical distribution for the transition

$1^+(M1)0^+(s=3, l=2)$ is $\sim 1-0\cdot 20 \cos^2\theta$, in good agreement with the observed distribution. However, the transition $1^-(E1)0^+(s=2, l=1)$ is by no means precluded since the predicted distribution is then $\sim 1-0\cdot 14 \cos^2\theta$.

(*d*) *993 keV (12·547 MeV)*

The spin of the 993 keV resonance level is likely to be $\geqslant 3$, since no ground state transition is observed and a triple correlation of the 8 and 4·66 MeV gamma rays measured at this resonance (Gove *et al.*, unpublished data 1957) is consistent with the sequence $3^+(M1)2^+(E2)0^+$. Previous measurements (Brenner 1959) do not exclude the possibility of 2^- and consequently the present three correlations have been analysed considering possible compound state spins of 2^-, 3^+, and 3^-.

The results for spins 2^- and 3^- are summarized in Table 3.

TABLE 3

CORRELATION COEFFICIENTS OF P_2 (cos θ) FOR GAMMA RAYS AT THE 993 keV RESONANCE

Sequence	First Gamma Ray	Second Gamma Ray	Triple Correlation
	$(a_2)_{\text{obs}}=0\cdot 065\pm 0\cdot 025$	$(a_2)_{\text{obs}}=0\pm 0\cdot 02$	$(a_2)_{\text{obs}}=0\cdot 12\pm 0\cdot 02$
$2^-(E1)2^+(E2)0^+$ $s=2, 3$ $l=1$	Yes $3\cdot 74\leqslant t\leqslant 3\cdot 95$	Yes $0\cdot 61\leqslant t\leqslant 1\cdot 24$	No $a_2<0$ for $0\leqslant t\leqslant \infty$
$3^-(E1)2^+(E2)0^+$ $s=2, 3$ $l=1$	Yes $1\cdot 05\leqslant t\leqslant 1\cdot 52$	Yes $0\cdot 72\leqslant t\leqslant 0\cdot 89$	Yes $1\cdot 35\leqslant t\leqslant 2\cdot 13$

The analysis of the $3^+(M1\ E2)2^+(E2)0^+$ sequence is complicated, since the small anisotropy of the first gamma ray indicates that some *d*-wave capture must be taken into account. The data were analysed graphically for the possible values of the mixing parameters assuming the amount of *d*-wave admixture to be small, i.e. $0<\delta\leqslant 1$. The measurements were found to be consistent with the predicted correlations for wide overlapping ranges of the parameters. Thus, the assignment 3^+ can be made with fair certainty since 2^- is eliminated and the various values of channel spin mixing required to fit the data for 3^- do not overlap. Some uncertainty concerning a spin of 3^- remains, since approximately 20% of the second gamma-ray intensity arises from other cascades.

V. ACKNOWLEDGMENTS

One of us (Stanley Bashkin) wishes to thank Professors M. L. Oliphant and E. W. Titterton for their hospitality during his stay at the Australian National University.

VI. REFERENCES

ANDERSEN, S. L., BÖ, H., LÖNSJO, O., and TANGEN, R. (1959).—*Nuclear Phys.* **9** : 509.

BRENNER, M. (1959).—*Soc. Sci. Fenn, Comm. Phys. Math.* **XXIII** (5) : 1.

BROSTRÖM, K. J., HUUS, T., and TANGEN, R. (1947).—*Phys. Rev.* **71** : 661.

Carver, J. H., and Waugh, J. B. (1961).—Australian National University Rep. P/230.

Casson, H. (1953).—*Phys. Rev.* **89** : 809.

Endt, P. M., and Heyligers, A. (1960).—*Physica* **26** : 230.

Ferguson, A. J., and Rutledge, A. R. (1957).—A.E.C.L. No. 420.

Gove, H. E., Paul, E. B., Bartholomew, G. A., and Litherland, A. E. (1954).—*Phys. Rev.* **94** : 749.

Kuperus, J., and Smith, P. B. (1960).—*Physica* **26** : 954.

Okano, K. (1960).—*J. Phys. Soc. Japan* **15** : 28.

Rutherglen, J. G., Grant, P. J., Flack, F. C., and Deuchars, W. M. (1954).—*Proc. Phys. Soc. Lond.* A **67** : 101.

Sharp, W. T., Kennedy, J. M., Sears, B. J., and Hoyle, M. G. (1954).—A.E.C.L. No. 97.

Shoemaker, F. C., Faulkner, J. E., Bouricius, G. M. B., Kaufmann, S. G., and Mooring, F. P. (1951).—*Phys. Rev.* **83** : 1011.

Smith, P. B., and Endt, P. M. (1958).—*Phys. Rev.* **110** : 397.

PHENOMENA ACCOMPANYING THE BIRTH OF SUNSPOT PORES

By R. E. Loughhead* and R. J. Bray*

[*Manuscript received April* 4, 1961]

Summary

Disturbances in the photospheric granulation accompanying the birth and development of some sunspot pores are illustrated (Plate 1) and described. The disturbances last for about 3 hr and take the form of a number of dark lanes lying between two groups of pores whose location with respect to the rest of the spot group suggests that they are of opposite magnetic polarities.

The detailed process of the birth and development of one of the pores is also illustrated (Plate 2). The pore starts as a dark area no larger than a single photospheric granule; subsequently it becomes darker and larger and coalesces with a pre-existing pore. Significant changes in shape and area take place within periods of half an hour.

The phenomena described are interpreted as evidence of the existence of a rising loop of magnetic flux. The nature of the interaction between the rising field and the solar material is discussed with reference both to the present observations and to observations of the umbral granulation.

I. Introduction

It is now generally accepted that the many diverse and often spectacular phenomena associated with active regions on the Sun owe their origin to the presence of magnetic fields which have risen from the solar interior and pushed their way through the photospheric layers into the chromosphere and corona above. Little is known about the three-dimensional configuration of the field in an active region; however, it can be pictured in an idealized way as a system of gigantic loops of magnetic flux whose ends are " anchored " to sunspot umbrae of opposite polarities (see, for example, Babcock and Babcock 1958).

The actual penetration of the visible layers by the loop of magnetic flux joining two sunspots of opposite polarities presumably takes place during the birth and initial development of the spots. At the ends of the loop, where the field is large and predominantly vertical, the photosphere is radically altered by the field—as is shown by the appearance of spots at these points. Between the spots, on the other hand, the field in the rising flux loop must be predominantly horizontal. Does the field in this region produce any effect on the photospheric granulation?

The observations described below show that disturbances in the neighbouring granulation do indeed accompany the birth and development of new sunspot pores. The disturbances take the form of dark lanes lying between two groups of pores whose location with respect to the rest of the spot group indicates that they are of opposite magnetic polarities (Section II). The detailed process of

---

* Division of Physics, C.S.I.R.O., University Grounds, Chippendale, N.S.W.

the birth and development of one of the pores is described in Section III. Finally, in Section IV the nature of the interaction between the rising field and the solar material is discussed with reference both to the present observations and to observations of the granulation in sunspot umbrae.

II. Disturbances in the Granulation between Growing Pores

In general the presence of a sunspot has no marked effect on the appearance of the surrounding photospheric granulation, although sometimes a slight increase in brightness is observed, particularly at shorter wavelengths (Waldmeier 1939; Das and Ramanathan 1953). Rösch (1959) and Miller (1960*b*) investigated the packing of the granules near and away from sunspots, but found no significant difference in the number per unit area. (Macris (1953) found a small difference in their mean diameters, but his result does not appear to be statistically significant.) In films of some 50 different spot groups obtained by the authors with the Sydney photoheliograph, a difference in the appearance of the granulation around a spot has been noticed on only one occasion: in this case the larger ($\sim 2''$ of arc) granules of the normal pattern were noticeably absent around portion of the periphery of the spot.

These results have been derived mainly from observations of the granulation in the neighbourhood of quiescent spots. In this paper, on the other hand, observations are described of the granulation in the neighbourhood of new and developing sunspot pores. In this case a marked disturbance in the granulation is found to occur.

The region of interest is indicated by the white rectangle in the lowest photograph of Plate 1; it lies between the leader and follower components of a typical bipolar sunspot group, which was photographed with the Sydney 5-in. photoheliograph (cf. Loughhead and Burgess 1958) for a period of 6 hr on February 4, 1958. During the period covered by the sequence of photographs shown in Plate 1, a pore is born on the upper right-hand side of the region and subsequently coalesces with a pre-existing pore; this event is described in detail in Section III. At the same time, similar events occur near the left-hand side of the region. The location of the region strongly suggests that the left- and right-hand pores are areas of opposite magnetic polarities (magnetic data are not available).

At $9^{\mathrm{h}}\,36^{\mathrm{m}}$ E.A.S.T. (Plate 1) the granulation between the two groups of pores appears to be more or less normal. However, a number of dark lanes are visible at $10^{\mathrm{h}}\,03^{\mathrm{m}}$, when the birth of the new pore on the right-hand side has already begun, at the point indicated by the arrows. The lanes appear to be somewhat darker than the ordinary intergranular material. Between the lanes individual photospheric granules can still be distinguished, but they now lie along lines parallel to the lanes. The direction of the lanes is roughly parallel to a line joining the two groups of pores. They are even more evident on the third photograph ($10^{\mathrm{h}}\,32^{\mathrm{m}}$); on this photograph they exhibit a decided curvature. They are most prominent at $11^{\mathrm{h}}\,03^{\mathrm{m}}$, by which time the two pores on the right-hand side have coalesced. By $12^{\mathrm{h}}\,42^{\mathrm{m}}$ the period of activity of the pores has come to an end; at the same time the disturbance in the granulation has died

PHENOMENA ACCOMPANYING THE BIRTH OF SUNSPOT PORES

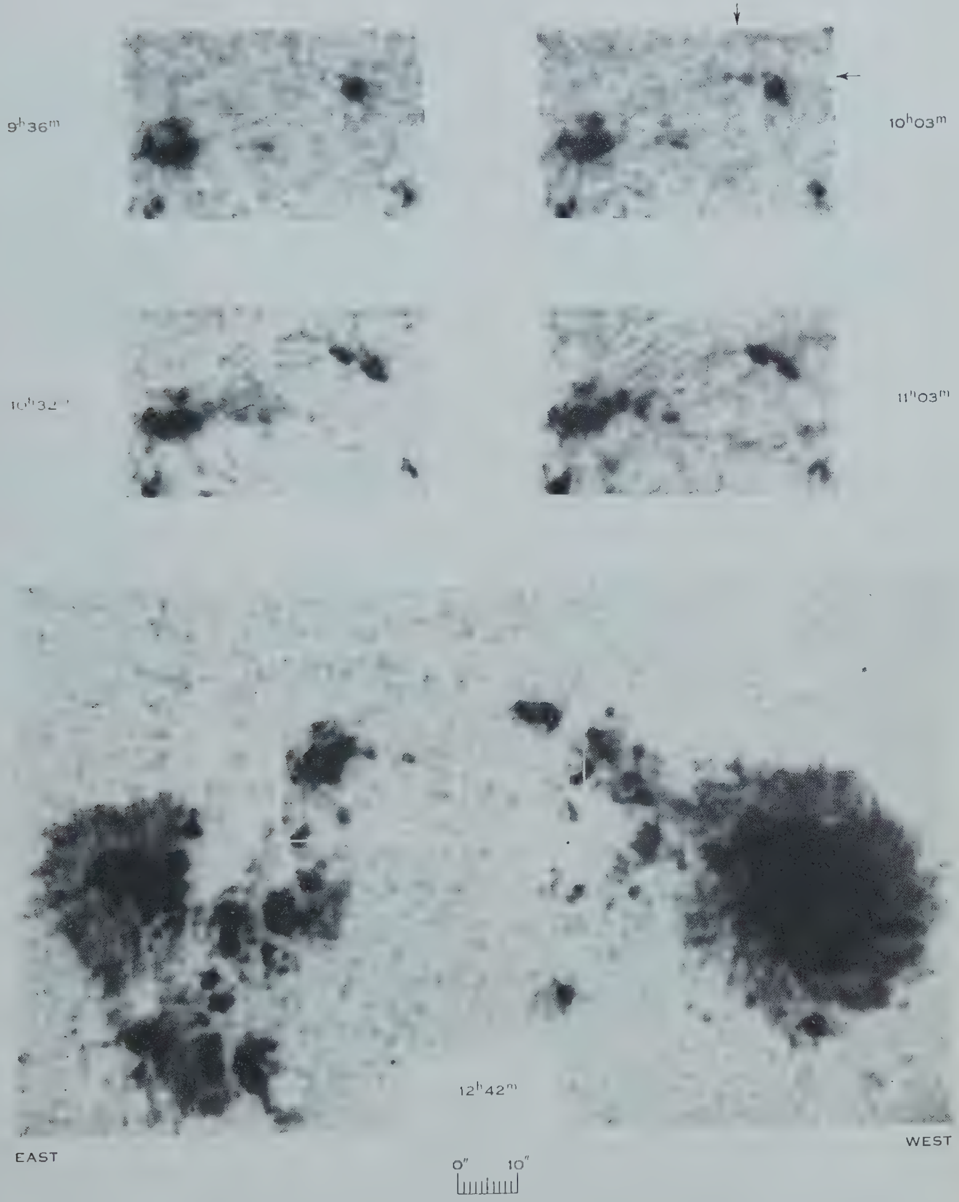

Dark lanes in the photospheric granulation between two groups of developing sunspot pores photographed on February 4, 1958. The lanes are prominent between $10^{\text{h}}\ 03^{\text{m}}$ and $11^{\text{h}}\ 03^{\text{m}}$ but have disappeared by $12^{\text{h}}\ 42^{\text{m}}$. Note the curvature of the lanes at $10^{\text{h}}\ 32^{\text{m}}$. The location of the two groups of pores with respect to the rest of the spot group (cf. $12^{\text{h}}\ 42^{\text{m}}$) indicates that they have opposite magnetic polarities. The arrows at $10^{\text{h}}\ 03^{\text{m}}$ point to a new pore which grows during the course of the sequence, ultimately coalescing with a pre-existing pore just to the right of it ; this event is shown in more detail in Plate 2.

PHENOMENA ACCOMPANYING THE BIRTH OF SUNSPOT PORES

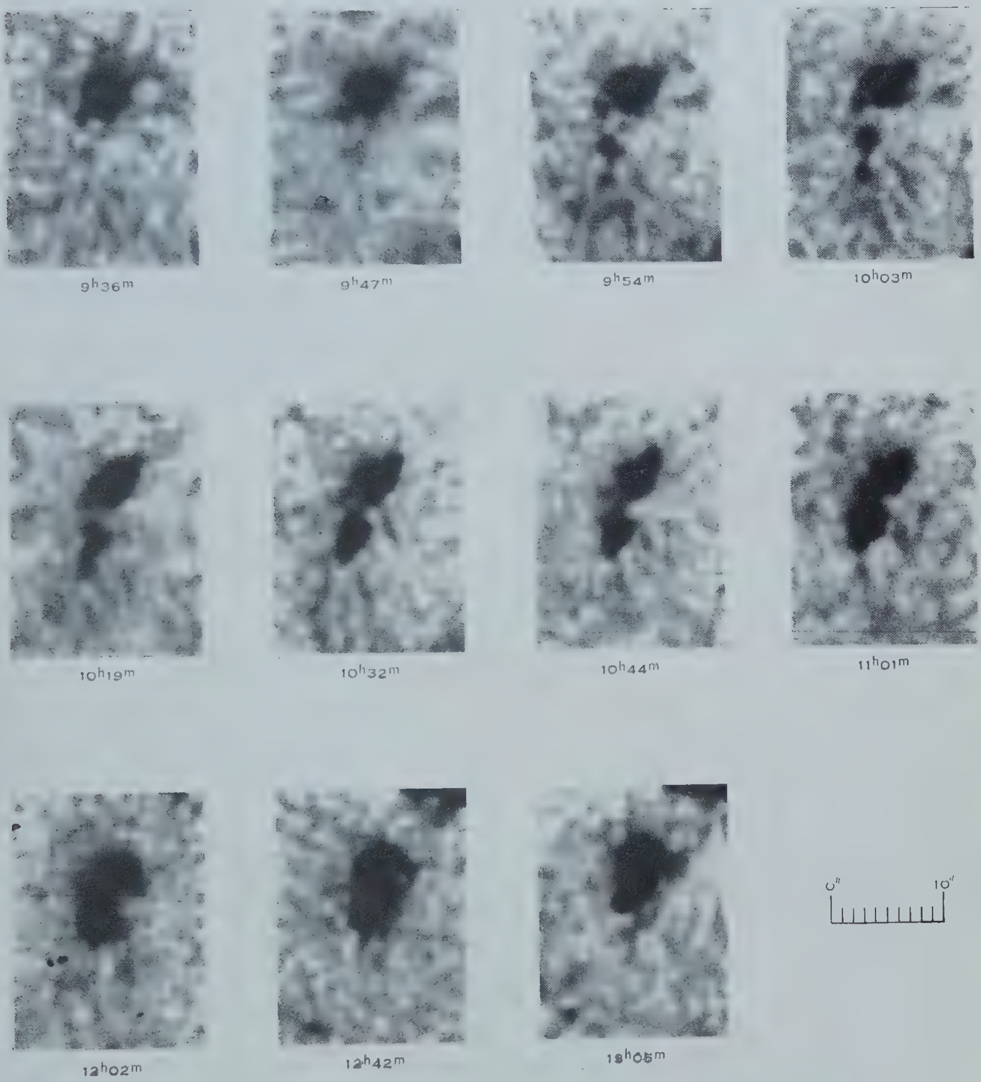
$9^{h}36^{m}$ $9^{h}47^{m}$ $9^{h}54^{m}$ $10^{h}03^{m}$

$10^{h}19^{m}$ $10^{h}32^{m}$ $10^{h}44^{m}$ $11^{h}01^{m}$

$12^{h}02^{m}$ $12^{h}42^{m}$ $13^{h}05^{m}$

Birth and development of a sunspot pore photographed on February 4, 1958. The new pore starts as a small dark area, only about 1″ of arc in diameter, in the photosphere a few seconds below a pre-existing pore (9^{h} 36^{m}). For a detailed description of its subsequent growth and development, see text. The photographs in Plate 2 are orientated at right angles with respect to those in Plate 1.

PHENOMENA ACCOMPANYING THE BIRTH OF SUNSPOT PORES

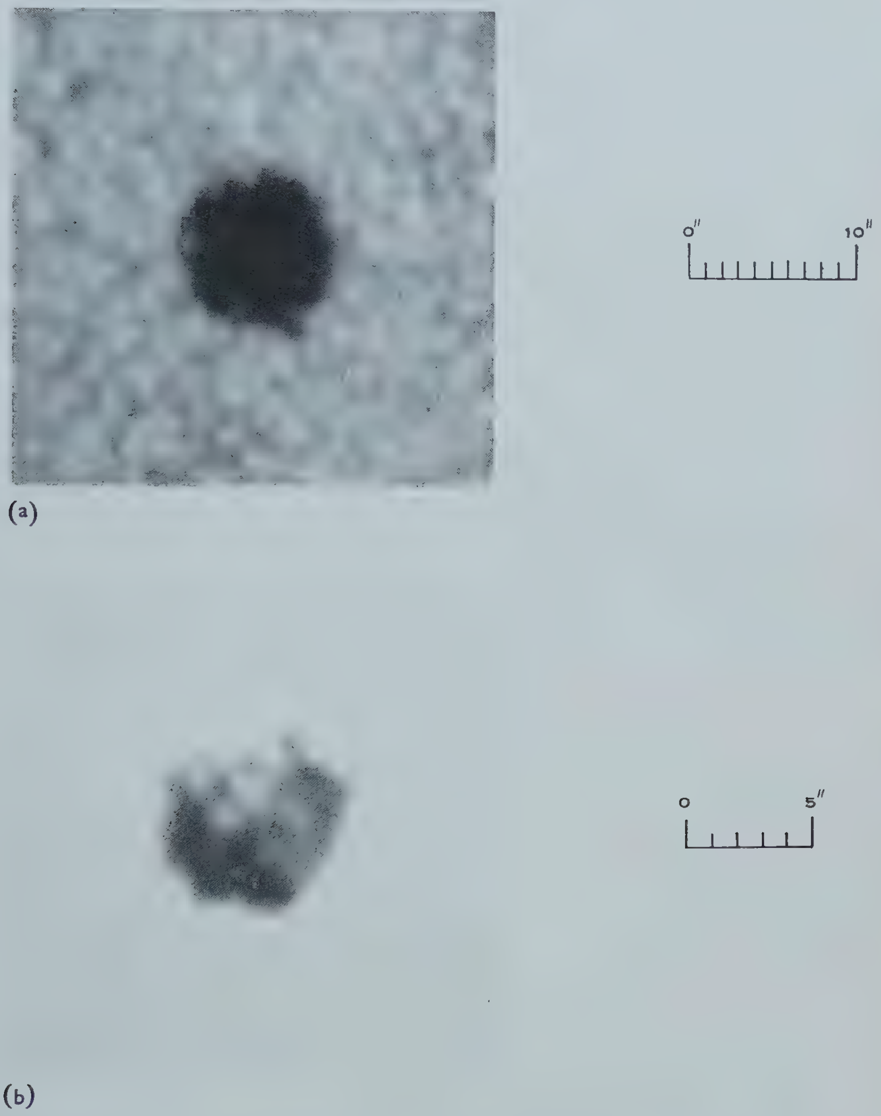

(*a*) Sunspot pore photographed at $13^h\ 59^m$ on August 27, 1958. Note the sharpness of the boundary and the normal appearance of the photospheric granules just outside.

(*b*) The same pore some 42 min later, shown with enhanced exposure and greater magnification. Although the right-hand side is somewhat smeared by mediocre seeing, several umbral granules are clearly visible. On the original negative one faint umbral granule can be seen in the lower left-hand side, which is darker than the rest; however, it fails to appear in the reproduction. Umbral granulation is a characteristic feature of sunspot pores and the umbrae of fully developed sunspots (see text).

away, the pattern reverting to normal. No further disturbance was observed between $12^h\ 42^m$ and the close of observations at $15^h\ 28^m$. The total time interval between the appearance and disappearance of the dark lanes is about 3 hr.

The possibility that the disturbances illustrated in Plate 1 might be due to poor seeing has been excluded by an examination of many other good-quality photographs taken during the same period. The persistence of the dark lanes from photograph to photograph leaves no doubt that the phenomenon is real.

III. Birth and Development of a Sunspot Pore

The birth and development of a new pore near the right-hand side of the region illustrated in Plate 1 are shown in more detail in Plate 2. (Note: the photographs in Plate 2 are orientated at right angles with respect to those in Plate 1.)

The first sign of the advent of the new pore is the appearance of a small dark region, only about 1″ of arc in diameter, in the photosphere a few seconds below the pre-existing pore. At first ($9^h\ 36^m$) this dark region is not distinguished in any way from normal intergranular material. However, it soon becomes darker and larger and, by $9^h\ 54^m$, a second such region has appeared, about 3″ below the first. At $9^h\ 54^m$ and $10^h\ 03^m$ the two small dark regions are seen to be joined together by a narrow lane of dark material. By $10^h\ 19^m$, the two regions have completely merged to form a typical sunspot pore of irregular shape, some 5″ long and 2″ wide at its narrowest point. The whole process of formation of the new pore from a region of hitherto normal photosphere is completed in a period of some 45 min.

The new pore now enters into the second phase of its development. Initially ($10^h\ 03^m$) it is separated from the upper pre-existing pore by a narrow strip of photospheric granulation. However, the granules in this region gradually disappear until, finally, only a single chain of granules separates the two pores ($10^h\ 32^m$). This chain is soon broken ($10^h\ 44^m$) and the pores merge into a single pore with a narrow waist; the amalgamation of the two pores takes place in about 25 min. Finally ($11^h\ 01^m$–$13^h\ 05^m$), the granules in the neighbourhood of the waist gradually disappear and the composite pore loses its dumbbell appearance.*

These observations show that significant changes in the shape and area of pores during their birth and development take place within periods of half an hour or so. A similar time scale was derived by Secchi (1875) from visual observations of changes during the *dissolution* of a pore. (Secchi recorded no observations of the birth of a pore.) This time scale is short compared with the total lifetime: even the smallest pores persist for at least several hours and, in fact, in most cases a single day's observations are not adequate to determine their lifetimes.

---

* The dark material visible in the top right-hand corners of the last two photographs of Plate 2 is portion of an elongated region of spot debris trailing the leader spot of the group (cf. Plate 1: $12^h\ 42^m$). During the day the distance between this debris and the pore illustrated in Plate 2 steadily decreased.

IV. Discussion

In our opinion the phenomena described in Sections II and III are to be interpreted as evidence of the existence of a rising loop of magnetic flux. This raises the question of the nature of the interaction between the rising field and the solar material.

Let us first consider the interaction in regions where the field is strong and predominantly vertical, i.e. sunspot pores or the umbrae of fully developed sunspots. Umbral granulation is invariably present in these regions (Bray and Loughhead 1959; Loughhead and Bray 1960). The umbral granules (apart from their smaller brightness) resemble the ordinary photospheric granules outside sunspots in appearance, but have substantially longer lifetimes and are more closely packed. If the umbral granules, like the photospheric granules, represent convection currents, then it is evident that even the strong magnetic fields present in the umbrae of large spots fail to suppress the convective motions. However, the interaction between the field and the convection currents is presumably responsible for the difference in properties between the umbral and photospheric granules. The observed sharpness of the boundaries of sunspot pores (cf. Plate 3 (*a*)) shows that the field can affect one granule but leave a neighbouring granule unaltered.

Secondly, in the region between the growing pores the magnetic field in the rising flux loop must be predominantly horizontal. In this case, as shown by the observations described in Section II, the field merely tends to align the granules in a preferred direction without affecting their brightness, although the material between the granules becomes somewhat darker than normal. The alignment lasts only while the magnetic loop is presumably pushing through the photospheric layers—a period of about 3 hr in the case of the present observations.

The difference in properties between the umbral and photospheric granules supplies direct evidence of an interaction between the field and the convection currents. This raises the question of the way in which the convection currents themselves influence the field. For example, do they assist the internal field to penetrate the visible surface layers? The answer to this question must await the development of an adequate theory of convection in the presence of a magnetic field under solar conditions.*

Miller (1960*a*) has published a photograph showing a number of curved dark lanes lying between regions of spot debris whose location with respect to the associated spot group is very similar to that of the pores illustrated in Plate 1. According to magnetic observations made at Mt. Wilson these areas of spot debris were probably of opposite polarities. The resolution of Miller's photograph is insufficient to show the granulation, and other supporting photographs are not available. Nevertheless, the similarity of the dark lanes photographed by Miller to those illustrated in Plate 1 (in particular the photograph at $10^h\ 32^m$)

---

* The question of explaining theoretically some of the more general properties of sunspots and sunspot groups by means of a rising magnetic flux loop has been considered by Parker (1955). According to Parker, the field of a sunspot group is derived from an internal toroidal field, part of which is raised to the surface by "magnetic buoyancy".

leaves little doubt that the phenomenon described by Miller is identical to that described in Section II. Miller suggests that the dark lanes follow lines of magnetic force.

Finally, Kiepenheuer (1960) has published good quality photographs of sunspots showing some of the small bright regions typical of the various types of bright structures commonly found in sunspot penumbrae (cf. Bray and Loughhead 1957). Although Kiepenheuer identifies these features with flux tubes of a deep-seated field which have penetrated the visible layers, they appear to be unrelated to the phenomenon described in Section II.

V. ACKNOWLEDGMENTS

The authors wish to thank Mr. H. Gillett for processing the film and making the enlargements.

VI. REFERENCES

BABCOCK, H. W., and BABCOCK, H. D. (1958).—" Electromagnetic Phenomena in Cosmical Physics." (Ed. B. Lehnert.) p. 239. (Cambridge Univ. Press.)
BRAY, R. J., and LOUGHHEAD, R. E. (1957).—*Observatory* **77** : 201.
BRAY, R. J., and LOUGHHEAD, R. E. (1959).—*Aust. J. Phys.* **12** : 320.
DAS, A. K., and RAMANATHAN, A. S. (1953).—*Z. Astrophys.* **32** : 91.
KIEPENHEUER, K. O. (1960).—*Z. Astrophys.* **49** : 73.
LOUGHHEAD, R. E., and BRAY, R. J. (1960).—*Aust. J. Phys.* **13** : 139.
LOUGHHEAD, R. E., and BURGESS, V. R. (1958).—*Aust. J. Phys.* **11** : 35.
MACRIS, C. (1953).—*Ann. Astrophys.* **16** : 19.
MILLER, R. A. (1960*a*).—*J. Brit. Astr. Ass.* **70** : 100.
MILLER, R. A. (1960*b*).—*J. Brit. Astr. Ass.* **70** : 146.
PARKER, E. N. (1955).—*Astrophys. J.* **121** : 491.
RÖSCH, J. (1959).—*Ann. Astrophys.* **22** : 584.
SECCHI, A. (1875).—" Le Soleil." 2nd Ed. Vol. I, p. 56. (Gauthier-Villars : Paris.)
WALDMEIER, M. (1939).—*Astr. Mitt., Zürich* **1939** (138) : 439.

DEVIATIONS FROM MATTHIESSEN'S RULE FOR PLATINUM*

By P. G. KLEMENS† and G. C. LOWENTHAL‡

[*Manuscript received March* 14, 1961]

Summary

An analysis of the resistivity-temperature relationship down to liquid helium temperatures of 17 platinum resistors as determined in various laboratories shows that deviations from Matthiessen's rule can be classed roughly into three groups. One of them follows the pattern predicted by Sondheimer and Wilson's theory. The other two cannot be fully explained in this way, and may be due to the sensitivity of the electronic band structure of transition metals to small concentrations of impurities. The behaviour of a resistor thus depends on the nature as well as the total amount of impurities and imperfections. In low temperature platinum resistance thermometry the resistors should be selected with regard to the type of residual impurity as well as total impurity content.

I. INTRODUCTION

The electrical resistivity of metals arises from disturbances of the regular periodicity of the crystal lattice by thermal vibrations and static imperfections (impurities and physical defects). The thermal vibrations cause the " ideal " resistivity ρ_i if the lattice is otherwise perfect, the imperfections cause the " residual " resistivity $\rho(0)$ at $T=0$. Matthiessen's rule states that the electrical resistivity at any temperature T is given by

$$\rho(T)=\rho(0)+\rho_i(T), \qquad (1)$$

where $\rho_i(T)\to 0$ as $T\to 0$ and $\rho(0)$ is independent of T.

Matthiessen's rule, if strictly valid, would greatly facilitate resistance thermometry, for given the resistance-temperature curve of one resistor, that of another resistor could be deduced by calibration at two temperatures only. A number of calibration procedures were suggested which are essentially based on Matthiessen's rule, and these proved reasonably reliable down to liquid air temperatures, but failed at lower temperatures. For a review of platinum resistance thermometry at low temperatures see Barber (1960).

It has become clear (e.g. Grüneisen 1933) that the resistivity shows deviations from equation (1) such that

$$\rho(T)=\rho_i(T)+\rho(0)+\Delta(T), \qquad (2)$$

where $\Delta(T)$ is a function of T and $\rho(0)$, but also depends on the nature of the imperfections causing $\rho(0)$ (Mott and Jones 1936, p. 289).

---

* This work was carried out while the authors were working at the Division of Physics, Commonwealth Scientific and Industrial Research Organization, Sydney, where one of us (G.C.L.) was in receipt of a research grant from the C.S.I.R.O.

† Westinghouse Research Laboratories, Pittsburgh, Pa., U.S.A.

‡ University of New South Wales, Sydney.

Matthiessen's rule is based on the proportionality of electrical resistance to the scattering probability of the conduction electrons, and positive deviations $\Delta(T)$ occur whenever two or more groups of electrons contribute to the conductivity, provided they are affected differently by the two scattering mechanisms. Specific theories of the deviation were advanced by Sondheimer and Wilson (1947), and by Sondheimer (1950). Sondheimer and Wilson's treatment is based on a two-band model, both bands contributing to the conductivity. For such a model $\Delta(T)$ must be positive for all values of T. The term $\Delta(T)$ can be approximated by

$$\Delta T=\rho_i\cdot\rho(0)/[a\rho_i+b\rho(0)], \tag{3}$$

where a, b are positive quantities of order unity (Wilson 1953, p. 312). It follows from (3) that $\Delta(T)\rightarrow 0$ as $\rho_i\rightarrow 0$ and, therefore, as $T\rightarrow 0$, and also as $\rho(0)\rightarrow 0$. At higher temperatures (above about 30 °K) where $\rho_i\gg\rho(0)$, $\Delta(T)$ approaches the constant value of $\rho(0)/a$ and (1) appears to be satisfied, so explaining the fair degree of success achieved with the use of Matthiessen's rule in resistance thermometry above about 60 °K.

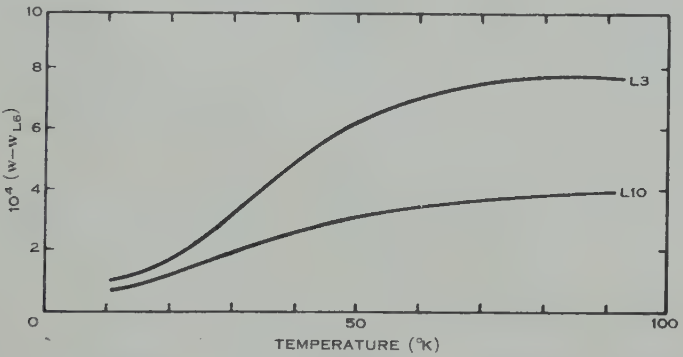

Fig. 1.—Difference in $w(T)$ between L6 and two other resistors according to Hoge and Brickwedde (1939).

The relative simplicity of (3) encouraged further attempts to use regularities in the deviations from Matthiessen's rule for the purposes of low temperature precision resistance thermometry. Van Dijk (1952, 1958) derived a number of expressions for the calculations of temperature from platinum resistance which were based partly on the results of Van der Leeden (1941) and Los and Morrison (1951) (see also White and Woods 1957) and implicitly on an expected regularity of the relation of $\Delta(T)$ with certain measurable characteristics of resistors such as their $\rho(0)$ values (obtainable by extrapolation from measurements at liquid helium temperatures) and also their α values, where α is defined by $(R_{373}-R_{273})/100\mathrm{R}_{273}$, R being the resistance. This coefficient is the greater the purer the platinum and has long been accepted as a measure of the purity of platinum resistors; for, although $\rho(0)$ is a more direct measure of purity than α, the former is measurable only in laboratories equipped for low temperature work.

Hoge and Brickwedde (1939) reported accurate measurements of the resistance-temperature relationship of six pure platinum resistors. Some of their results are given in Figure 1. The relative resistance $w(T)$ is defined as $R(T)/R(273)$, their purest resistor was L6, so that if it is assumed that $\Delta_{L6}(T)$ is very small then $w-w_{L6}$ is a measure of the deviation of the other five resistors from Matthiessen's rule. It was pointed out by Schultz (1957) that this behaviour is in conformity with Sondheimer and Wilson's expression (3) for $\Delta(T)$.

The apparent regularity of $\Delta(T)$ found by Van Dijk and Schultz is, however, not a general property of pure platinum resistors, but a consequence of the fact that in each case attention was focused on a group of resistors from the same source, and thus having impurities of similar nature. More recent measurements on a wider group of resistors, many of even greater purity, fail to yield similar regularities, and it is clear that the deviations from Matthiessen's rule depend not only on the residual resistivity but also on the nature of the principal impurities. This will now be discussed in detail.

II. Observed Deviations

Equation (2) cannot be tested directly in the absence of an accepted procedure for the determination of ρ_i. In addition, the geometrical factor relating resistivity and measured resistance is different for each resistor and somewhat uncertain. The last-named difficulty can be overcome by using the relative resistances $w(T)$. Thus using (2) and forming the difference between two resistors having relative resistances $w(T)$ and $w'(T)$,

$$w(T)-w'(T)=\frac{\rho_i(T)+\rho(0)+\Delta(T)}{\rho_i(273)+\rho(0)+\Delta(273)}-\frac{\rho_i(T)+\rho'(0)+\Delta'(T)}{\rho_i(273)+\rho'(0)+\Delta'(273)}. \tag{4}$$

Omitting terms involving the squares of very small quantities, this difference becomes

$$w(T)-w'(T)\approx\{w(0)-w'(0)\}\{1-w_i(T)\}+z(T)-z'(T)-w_i(T)\{z(273)-z'(273)\}, \tag{5}$$

where $w_i(T)=\rho_i(T)/\rho_i(273)\approx\rho_i(T)/\rho(273)$, and

$$z(T)=\frac{\Delta(T)}{\rho_i(273)}\approx\frac{\Delta(T)}{\rho(273)}.$$

The terms in $w_i(T)$ on the right-hand side of (5) arise because of the difference between $\rho(273)$ and $\rho'(273)$. They cannot be neglected unless $w_i(T)\ll 1$, i.e. $T\leqslant 20$ °K, or unless $w(0)\sim w'(0)$.

Equation (5) can be used to test relative deviations, though it must always be remembered that the significance of the results of such tests must depend greatly on the characteristics of the reference resistor.

The resistors here considered are listed in Table 1. It will be seen from an inspection of their $w(0)$ values that compared with more recently made resistors even the purest (L6) of those used by Hoge and Brickwedde (1939) is now relatively impure. The resistor T4 measured by Los and Morrison (1951) has one of the lowest residual resistivities, and it is reasonable to suppose that its values of $\Delta(T)$

are also lower than those of resistors of substantially higher $w(0)$.* This suggested the use of T4 as the standard of " quasi-ideal " resistor. Accordingly,

$$w(T)-w_{T4}(T)+w_i(T)\{w(0)-w_{T4}(0)\}$$

has been plotted in Figure 2 as a function of T for most of the resistors listed in Table 1. The deviations of these curves from horizontal straight lines indicate the extent to which Matthiessen's rule is not obeyed, being a measure of the quantity

$$z(T)-z_{T4}(T)-w_i(T)\{z(273)-z_{T4}(273)\}. \tag{6}$$

TABLE 1

VALUES OF $w(0)$, α, AND THE SONDHEIMER-WILSON PARAMETER $1/a$ CALCULATED FROM EQUATION (7) FOR A NUMBER OF RESISTORS

Designation	Reference*	$10^4 w(0)$	$10^6 \alpha$	Sondheimer-Wilson Parameter $1/a$ as a Function of Temperature		
				50 °K	70 °K	90 °K
T4	(1)	4·1	3926	—	—	—
G3	(2)	4·2	3927	—	small	—
Ch6	(3)	4·8†	3925‡	—	small	—
RS	(2)	9·8	3924	0·1	0·1	0·1
L6	(4)	24·0†	3917‡	0·2	0·2	0·2
L10	(4)	24·8†	3914	0·3	0·4	0·4
CT15	(5)	6·0	3926	—0·4	—0·3	+0·4
CT16	(5)	6·1	3926	—0·4	—0·3	+0·5
CT18	(5)	8·5	3924	0·3	0·3	0·7
L3	(4)	25·2†	3912	0·5	0·6	0·7
G2	(2)	4·4	3925	3	4	6
718157	(2)	5·1	3925	0·5	0·9	1·7
PS	(2)	5·9	3915	5·6	7·1	8·6
A1	(2)	7·5	3923	0·9	1·0	1·2
S1	(2)	8·9	3921	1·0	1·2	1·4
S2	(2)	8·9	3921	1·1	1·4	1·5
R10	(5)	15·7	3911	1·5	1·8	2·3

* References : (1) Los and Morrison (1951) ; (2) Barber (1958) ; (3) Chambre Centrale (1954) ; (4) Hoge and Brickwedde (1939) ; (5) Lowenthal, Kemp, and Harper (1958).

† Obtained by extrapolation from 10 °K.

‡ Estimated.

The most striking feature of these curves is their variety in shape, giving a clear indication that the deviations do not arise from a single cause. Certainly, the two-band model of Sondheimer and Wilson cannot account by itself for these variations. More particularly, the fact that CT15 and to a lesser extent G3 have negative values for (6) suggests that factors not considered by Sondheimer and Wilson must be operative, since the two-band mechanism does not admit of negative values of $\Delta(T)$. Of course, a negative value of (6) does not necessarily imply that either $z(T)$ or $z_{T4}(T)$ are negative anywhere. Firstly, it might merely be a reflection of a peculiarity in T4; but this is unlikely because a curve of CT15 versus G3 would also gives negative values. Secondly, however, is the objection that (6) may become negative because the last term might become larger in magnitude than $z(T)-z_{T4}(T)$. This would be so if the ratio $z(T)/z(273)$ was smaller than $w_i(T)$ at low temperatures, but increased faster with T than $w_i(T)$ above about 70 °K, for at 273 °K both quantities are equal. It is readily shown, however, that with $\Delta(T)$ due entirely to the two-band model (equation (3)), expression (6) would never be negative.

---

* It will be noted, though, that resistor G2 has nearly the same $\rho(0)$ value as T4 but obviously very different $\Delta(T)$ values.

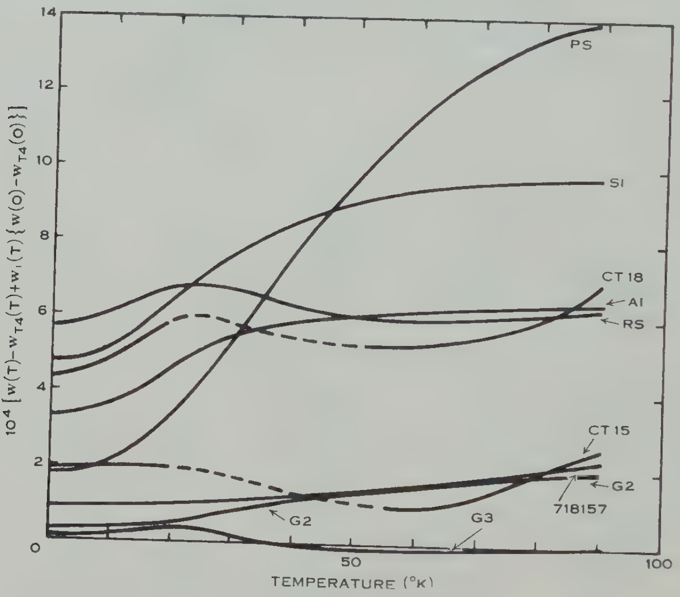

Fig. 2.—Deviations from Matthiessen's rule relative to T4 as shown by the temperature variation of $w(T)-W_{T4}(T)+w_i(T)\{w(0)-w_{T4}(0)\}$. Designation of resistors as in Table 1. Curves have been omitted for Ch6 (close to T4 and G3), CT16 (close to CT15), S2 (close to S1), and R10 (beyond range of graph).

III. Classification of Deviations

To get more direct information about the extent to which the Sondheimer-Wilson theory applies to the resistors listed in Table 1, one can assume that $\Delta(T)$ is given by (3), so that for $T \lesssim 30$ °K, where $\rho_i \gg \rho(0)$, one obtains $\Delta(T) \approx \rho(0)/a$ and therefore $z(T)=z(273)\approx w(0)/a$. Substituting this result into (5) leads to

$$w(T)-w_{T4}(T)=\{w(0)-w_{T4}(0)\}\{1-w_i(T)\}(1+1/a), \tag{7}$$

and if $\Delta(T)$ is indeed given by (3) than $1/a$ as calculated from (7) would be constant. It will be seen that this is generally not so. Instead, the resistors fall into three more or less distinct groups which are separated in Table 1 by horizontal lines. Resistors in group 1 have $1/a$ both small and constant, for those in group 2 it is still small but increases with temperature, while those in group 3 have $1/a$ values up to ten times greater than those in group 1 and increasing rather strongly with temperature. The divisions are, of course, somewhat arbitrary, not least because the magnitudes of $1/a$ depend on the characteristics of the resistor chosen as standard. Besides, some resistors are clearly borderline cases: L3 and CT18 could have been classed into group 1 while A1 and possibly S1 and S2 could have been classed into group 2.

Clearly, the behaviour of $\Delta(T)$ or $z(T)$ depends not only on $\rho(0)$ or on α. It is seen from Table 1 that L6 and L10, which are in group 1, have a much greater residual resistivity than each member of group 3. The α values of L6 and L10, on the other hand, are higher than those of R10 and PS but lower than those of the other members of group 3. But within each group the resistors have similar deviations, and if resistors belonging to one particular group, say group 1, could be identified in a convenient way, a relatively simple formula would serve to predict their characteristics with accuracy over a wide range of temperatures. Such a formula was discussed by Schultz (1957) and an even simpler procedure was used by Lowenthal, Kemp, and Harper (1958) (see also Lowenthal and Harper 1960).

The manner in which the groups of Table 1 have been obtained here is, of course, much too cumbersome to effect identification for purposes of resistance thermometry. It is not difficult, however, to derive practical selection criteria of the type which have long been familiar in thermometry and which are now an integral part of the International Practical Temperature Scale. One such criterion has been described elsewhere (Lowenthal, Kemp, and Harper 1958).

IV. Reasons for Deviations

The origin of these various deviations from Matthiessen's rule is a rather complex problem and no single completely satisfactory explanation appears to exist. It is believed, though, that variations in ρ_i due to variations in electron concentration are at least partly responsible for this effect. One would expect transition metals to be particularly sensitive to small changes in electron concentrations. This would cause $\Delta(T)$ to be proportional to T at high temperatures, while the two-band mechanism and its various modifications predict that at high temperatures $\Delta(T)$ becomes constant. In terms of the relative resistivities $w(T)$, both explanations lead to qualitatively the same behaviour. To distinguish with certainty between them would require the absolute measurement of $\Delta(T)$ and, therefore, accurate measurements of the specimen geometry. This, however is very difficult to do.

V. Conclusion

The two-band model and its modification as proposed by Sondheimer and Wilson are not adequate by themselves to account for the three more or less distinct types of deviations from Matthiessen's rule found for "thermo-pure" platinum resistors, though it does account satisfactorily for one of these types (group 1). It would appear that the sensitivity of the electronic band structure of transition metals to small concentrations of impurities is a further mechanism producing significant deviations.

To effect precision low temperature resistance thermometry without extensive calibrations it would then be necessary to control not so much the amount of the residual resistivity but rather the nature of the impurities and imperfections which give rise to $\rho(0)$. As a probably more practicable alternative a suitable selection procedure should be used to exclude all resistors with deviations from Matthiessen's rule differing from an agreed type of deviation such as for example from group 1 of Table 1. If this is done, it is readily shown (e.g. Lowenthal, Kemp, and Harper 1958) that all resistors satisfying such a requirement have similar resistivity-temperature relationships which, therefore, are predictable over a wide range of temperatures.

VI. References

Barber, C. R. (1958).—*P.V. Com. Int. Poids Més.* **26**: T52.

Barber, C. R. (1960).—Resistance thermometers for low temperatures. *In* "Progress in Cryogenics." Vol. 2. (Heywood and Co.: London.)

Chambre Centrale des Mésures et Instruments de Mésure, URSS (1954).—Memorandum, *P.V. Com. Int. Poids Més.* **24**: T141.

Grüneisen, E. (1933).—*Ann. Phys., Lpz.* (5) **16**: 530.

Hoge, J. H., and Brickwedde, F. G. (1939).—*J. Res. Nat. Bur. Stand.* **22**: 351.

Los, J. M., and Morrison, J. A. (1951).—*Canad. J. Phys.* **29**: 152.

Lowenthal, G. C., and Harper, A. F. A. (1960).—*Brit. J. Appl. Phys.* **11**: 205.

Lowenthal, G. C., Kemp, W. R. G., and Harper, A. F. A. (1958).—*Bull. Int. Inst. Refrig. Annexe* **1**: 107.

Mott, N. F., and Jones, H. (1936).—"The Theory of the Properties of Metals and Alloys." (Clarendon Press: Oxford.)

Schultz, H. (1957).—*Z. angew. Phys.* **9**: 465.

Sondheimer, E. H. (1950).—*Proc. Roy. Soc.* A **203**: 75.

Sondheimer, E. H., and Wilson, A. H. (1947).—*Proc. Roy. Soc.* A **190**: 435.

Van der Leeden, P. (1941).—Doctoral Thesis, Leiden University.

Van Dijk, H. (1952).—*P.V. Com. Int. Poids Més.* **23B**: T48.

Van Dijk, H. (1958).—*Bull. Int. Inst. Refrig. Annexe* **1**: 101.

White, G. K., and Woods, S. B. (1957).—*Rev. Sci. Instrum.* **28**: 638.

Wilson, A. H. (1953).—"The Theory of Metals." 2nd Ed. (Cambridge Univ. Press.)

THE ANOMALOUS THERMAL EXPANSION OF CHROMIUM

By G. K. White*

[*Manuscript received April* 19, 1961]

Summary

Experimental data on the linear thermal expansion between 20 and 50 °C of specimens of high-purity chromium confirm the existence of an anomaly centred at 38 °C. The exact shape of this expansion anomaly between about 37 and 39 °C varies markedly from sample to sample, but outside this narrow temperature interval the behaviour is more regular and seemingly related to antiferromagnetic ordering. Data on expansion are compared with other recent observations on heat capacity, magnetic susceptibility, and electrical resistivity of high-purity chromium. It is suggested that an electronic term in the expansion coefficient, observed below 20 °K to be negative, is sensitive to band structure and may be partly responsible for the change in expansion coefficient.

I. Introduction

The physical properties of chromium between 30 and 40 °C have long been rather puzzling. Sully (1954) has summarized most of the data obtained up to about 1953, usually for samples of rather high impurity content. These data indicated a marked minimum in the expansion coefficient α and in the Young's modulus and a sharp peak in the internal friction at or near 38 °C. A knee-shaped anomaly was observed in the electrical resistivity and Bridgman showed that increase in pressure could reduce the temperature at which this knee occurred by 50 degC or more. No definite anomaly was established in the heat capacity or magnetic susceptibility nor was any change in the body-centred cubic structure of chromium observed.

Due largely to the efforts of Greenaway and others at the Aeronautics Research Laboratory (A.R.L.), Melbourne, quantities of ductile chromium became increasingly available for research investigations after about 1954, and experimental data gathered in the period 1954 to 1959 have been summarized in the review of Edwards, Nish, and Wain (1959). This ductile chromium produced by electrodeposition from suitable solutions has a nitrogen content generally below 0·001 wt.-% (0·003 at.-%) and an oxygen content of 0·04 wt.-% or less. However, the observations on high-purity material have still revealed anomalies in resistivity (for example, Harper *et al.* 1957; de Vries and Rathenau 1957) and elastic moduli (de Vries and Rathenau 1957; Pursey 1958). In addition, Lingelbach (1958) observed a small knee-shaped anomaly in the magnetic

---

* Division of Physics, C.S.I.R.O., University Grounds, Chippendale, N.S.W.

susceptibility of a ductile chromium sample (from A.R.L.) near 37 °C and Straumanis and Weng (1955) reported a marked change in slope of the expansivity curve from X-ray observations of a sample containing less than 0·02% nitrogen. The latter workers expressed their results in terms of a linear expansion coefficient of $7 \cdot 47 \times 10^{-6}$/degC above 32·5 °C and $4 \cdot 4 \times 10^{-6}$ below 32·5 °C (see Fig. 3), although their lattice spacings obtained between 10 and 40 °C might equally indicate a gradual change in coefficient rather than an abrupt change at 32·5 °C. There was no line broadening suggestive of any alteration in the b.c.c. structure.

Further interest and difficulty arose when the first neutron diffraction observations, made on powdered chromium by Shull and Wilkinson (1953), indicated that antiferromagnetic ordering set in below about 175 °C, a temperature well above that at which these other anomalies appear.

Since the review by Edwards, Nish, and Wain was written, some major developments have been as follows.

(*a*) Neutron diffraction studies by Bykov *et al.* (1959), Corliss, Hastings, and Weiss (1959), Bacon (1960), and Wilkinson, Wollan, and Koehler (1960) on both single crystals and polycrystals have indicated a Néel point near 39 °C.

(*b*) Beaumont, Chihara, and Morrison (1960) have observed a small lambda-shaped anomaly in the specific heat of A.R.L. chromium at about 38 °C.

(*c*) Newmann and Stevens (1959) have reported on the magnetic susceptibilities, electrical resistivities, and expansion of alloys of chromium with small quantities of iron.

(*d*) Collings, Hedgcock, and Siddiqi (1961) have made further observations on the magnetic susceptibility of A.R.L. chromium, confirming the appearance of a bump at 38·5 °C. They have also studied electron spin resonance in this chromium and in chromium to which chromic oxide has been added; they conclude, like Newmann and Stevens, that the magnetic anomaly is characteristic of pure chromium and is not merely associated with the presence of oxide.

(*e*) X-ray observations of lattice spacing by Straumanis and co-workers (personal communication 1960) on samples with very low nitrogen content have led them to believe that an anomaly in the lattice parameter-temperature curve near 33 °C (Straumanis and Weng 1955, and Fig. 3 below) only appears when nitrogen is added to the sample. Apropos of the role which may be played by nitrogen impurity, thermoelectric power measurements of Edwards (personal communication 1960) have continued to show an anomaly when the nitrogen content fell below 0·0004 wt.-%.

The present paper reports some rather sensitive observations of linear thermal expansion of A.R.L. chromium which suggest that an anomaly persists with the purest samples, although the detailed form of the change in expansion coefficient very close to 38 °C may be very sensitive to impurity content or to metallurgical condition.

II. Experimental Details

A detailed description of the apparatus used for measuring linear thermal expansion has been given recently (White 1961*a*). Briefly, it depends on the comparison of three-terminal capacitors in a bridge with transformer ratio arms (Thompson 1958). A sample, 2 in. long with flat parallel end-faces of $\frac{7}{8}$ in. diameter, is mounted in an Invar cell (Mark I) or a copper cell (Mark II) to form a three-terminal capacitance. The well-defined capacitance between one end-face and the cell is about 5 pF and is determined to an ultimate limit of $\pm 1 \times 10^{-6}$ pF. This allows the change in length of the chromium sample to be determined relative to the change in length of cell. The cell is mounted in a cryostat specifically designed for use from near 100 °K down to 1 °K, where relative changes of 10^{-8} cm may be detected. For the purposes of obtaining data near room temperature on chromium, the cryostat was surrounded by a well-stirred oil bath, the temperature of which was controlled to a constancy of about 0·001 degC, using an electronic controller (Wylie 1948). This controller heats the oil bath electrically in response to a signal from an a.c. Wheatstone bridge, one arm of which is a sensitive copper resistance thermometer mounted in the bath. The actual temperature of the bath was measured by a platinum resistance thermometer.

In order to convert relative length changes of chromium with respect to the expansion cell into absolute values for chromium, the following figures have been used for the expansion coefficient of Invar and of copper between room temperature and 50 °C: $1 \cdot 2 \times 10^{-6}$/degC for Invar and $16 \cdot 7 \times 10^{-6}$/degC for copper. The former value for Invar was obtained by calibrating the cell Mark I with a copper specimen, and the value for copper was obtained from published data (Nix and MacNair 1941; Rubin, Altman, and Johnston 1954).

The chromium samples used were kindly supplied by Dr. H. L. Wain, of the Aeronautics Research Laboratory, Melbourne, and were machined and analysed in that laboratory. In the cases of Cr 1, Cr 2, and Cr 3a, samples were annealed by us at 800 °C for about 4 hr, each being sealed off *in vacuo* in a silica tube. Before measurements were made, the end faces were also lapped to flatness and parallelism of about 10^{-5} in.

Analyses and metallurgical history are as follows:

Cr 1: machined from extruded bar, 0·0008 wt.-% N_2, 0·03 wt.-% O_2.
Cr 2: machined from extruded bar, 0·0008 wt.-% N_2, 0·03 wt.-% O_2.
Cr 3: machined from arc-cast slab which had been press forged at 1050 °C, 0·0004 wt.-% N_2, 0·03 wt.-% O_2.
Cr 3a: Cr 3 after annealing at 800 °C and relapping.

In the case of Cr 1, which shows the most marked expansion anomaly near 38 °C, and was somewhat discoloured by annealing, re-analysis after completion of measurements showed no *observable* change in impurity content. It should be noted that nitrogen analyses may be in error by ±0·0004 wt.-%.

The results shown below are compared with measurements of heat capacity C_p (Beaumont, Chihara, and Morrison 1960), magnetic susceptibility (Collings, Hedgcock, and Siddiqi 1961), electrical resistivity ρ (Harper *et al.* 1957), all made on A.R.L. chromium samples: the heat capacity sample showed 0·001% N_2

and 0·04% O_2; one magnetic susceptibility sample showed 0·0004 wt.-% N_2 and probable O_2 content of 0·01–0·04%, and is identical with sample Cr 5 used by Harper *et al.* (see resistivity curve in Fig. 3). A second susceptibility sample of more recent origin is probably of slightly higher purity but gave values lying on the same curve (see Fig. 3).

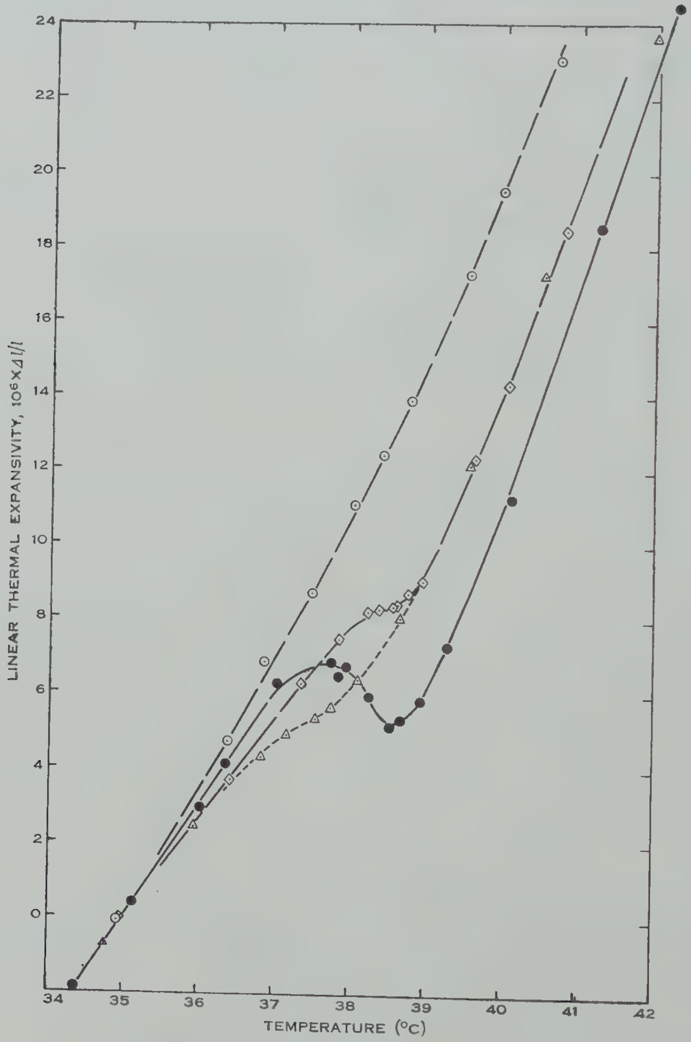

Fig. 1.—Linear thermal expansivity, $\Delta l/l$, of chromium (normalized to zero at 35 °C). ● Cr 1, ◇ Cr 2, ⊙ Cr 3, △ Cr 3a.

III. Results

In Figure 1 values are plotted of linear thermal expansivity (expansion per unit length) between 34 and 42 °C of the four specimens. Values for Cr 1 were obtained relative to Invar and corrected for the expansion of the Invar, and those for the other three samples were obtained relative to copper and corrected.

For purposes of comparison over this narrow temperature interval, values have been reduced to a common zero at 35 °C.

The slope at each point in Figure 1 represents the coefficient of linear expansion; it can be seen that for each sample the slopes are very similar except in the interval between 36 and 39 °C (see also Fig. 3). Only for Cr 1 is there a minimum in expansivity and hence a negative expansion coefficient. In Figure 2 a full curve is drawn showing the coefficient of expansion α for Cr 1 and Cr 3, determined from the slopes of the expansivity curves in Figure 1. The dashed curve of α below 293 °K (20 °C) is an extrapolation based on length changes observed over the temperature intervals 293–273°, 273–193°, 193–90°, 90–80°, and 80–70 °K. From 25° down to 1 °K, detailed observations on Cr 2, Cr 3, and Cr 3a have been made and these have yielded a linear expansion coefficient $\alpha = -(35 \pm 4) \times 10^{-10} T$ per degC (White 1961*b*), which presumably is electronic in origin and, at these low temperatures, much larger than the coefficient arising from the vibrational energy of the lattice, which is expected to vary as T^3. The dashed line, α_e, represents an extrapolation of this electronic term and indicates that near room temperature the free electrons may contribute a negative term of magnitude about -1×10^{-6} per degC to the linear expansion coefficient.

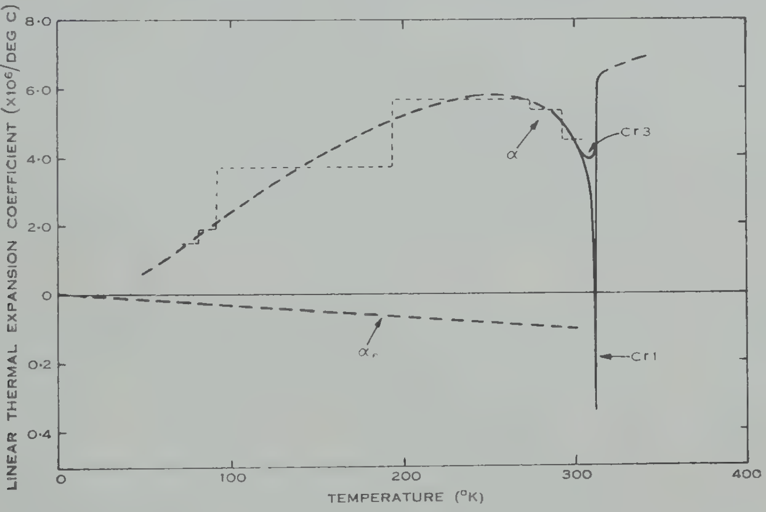

Fig. 2.—Linear thermal expansion coefficient α of chromium. The electronic component α_e is extrapolated from data obtained below 20 °K (White 1961*b*). The dotted "steps" represent the average expansion coefficients determined over temperature intervals 70–80 °K, 80–90 °K, etc.

Our present *relative* expansion cells, either of Invar or of copper, are rather unsuitable for precise studies on chromium between 30 °K and room temperature. It is hoped that soon a new *absolute* expansion cell will be completed and that, if a suitably shaped chromium specimen can be obtained, its expansion coefficient can be measured directly in this temperature range. In the case of Cr 1, some data were obtained for the expansivity between 140 and 170 °K in the Invar cell, to determine whether any anomaly was obvious in this region, as suggested by the neutron diffraction observations of Bykov *et al.* (1959) which showed that antiferromagnetic ordering disappeared below about 158 °K. We observed nothing unusual in the expansivity curve.

IV. Discussion

Comparison of the expansivity curves in Figure 1 with earlier data on rather impure chromium summarized by Sully (1954) and with that of Newmann and Stevens (1959) on chromium alloys containing small percentages of iron, shows that the form of anomaly—whether in expansivity or in expansion coefficient—is strongly impurity-dependent. Although chemical and gas analyses show no definite difference in purity between our Cr 1 and Cr 2, the former sample exhibited definite discoloration due to annealing, and has a marked minimum in expansivity curve between 38 and 39 °C. It seems probable to the author that the rather smooth curve of Cr 3 is most representative of pure chromium ; it is not inconceivable that differences in grain size or preferred orientation contribute to the differences shown in Figure 1, but it seems unlikely. Except in the very narrow temperature region between about 34 and 39 °C, our specimens give rather similar curves of expansion coefficient (Fig. 2), and these in turn are quite similar to that observed by Fine, Greiner, and Ellis (1951 ; see also Sully, loc. cit. p. 80).

Turning to the nature of the anomaly, there is no evidence to suggest the occurrence of any change in crystal structure or lattice rearrangement. Therefore, presumably it is electronic in origin and related to the anomalies occurring in other physical properties at the same temperature, anomalies which are in turn related to the onset of antiferromagnetism. It is tempting to suggest that part of the change in expansion coefficient stems from a change in the magnitude or even sign of the electronic component α_e. It has been shown (for example, Mott and Stevens 1957 ; Goodenough 1960 ; Shimizu and Takahashi 1960) that the Fermi energy ε_F in chromium probably lies close to a minimum in the density-of-states curve, the minimum being produced by the narrow overlap of two energy bands. Shimizu and Takahashi suggest that ε_F lies very slightly above the minimum on a steeply rising part of the density-of-states curve. Following Varley's (1956) theoretical treatment of electronic thermal expansion, the rather large positive value of $\partial n(\varepsilon_F)/\partial \varepsilon_F$ which would result from this could lead to a negative value for the electronic expansion term. Then a small change in the band shape or position of ε_F consequent upon the change in magnetic ordering near 38 °C might cause α_e to change appreciably. This need not imply any dramatic change in the actual density of states $n(\varepsilon_F)$ at the Fermi surface, which presumably would raise or lower the heat capacity curve.

Alternatively, an explanation may be sought based on Zener's views (1955) on the exchange interaction between the unfilled electron shells. Chandrasekhar (1958) has applied this concept of repulsive interaction between unfilled shells with parallel spins and attractive interaction between shells with antiparallel spins to explain the expansion anomalies (" knees " in the expansivity curve rather like Cr 1 in Fig. 1 or Fig. 3) observed in the rare earths gadolinium, terbium, and dysprosium (Barson, Legvold, and Spedding 1957; also Birss 1960 for Gd). This explanation may be satisfactory in the case of Curie points in Gd and Tb but seems less satisfactory for Néel points in Dy and Cr 1.

Figure 3 provides an interesting comparison of the anomalous behaviour in physical properties of chromium. Excepting the curve $\Delta a/a$ (taken from Fig. 2—lattice constant for sintered electrolytic chromium—of Straumanis and Weng 1955), the data were all obtained on samples of A.R.L. chromium of comparable purity. The resistivity anomaly is of rather the same knee-shape as that observed in some rare earth elements (e.g. Hall, Legvold, and Spedding 1960) and in α-manganese (White and Woods 1957). Coles (1958) has attributed the resistivity anomaly to change in scattering of the conduction electrons by the magnetic spins, the small maximum arising perhaps from increased scattering when only small local regions of spins are ordered. Certainly the neutron diffraction evidence in Cr and Mn indicates that the onset of antiferromagnetism (Néel point) occurs in the vicinity of the shallow minimum rather than at the maximum.

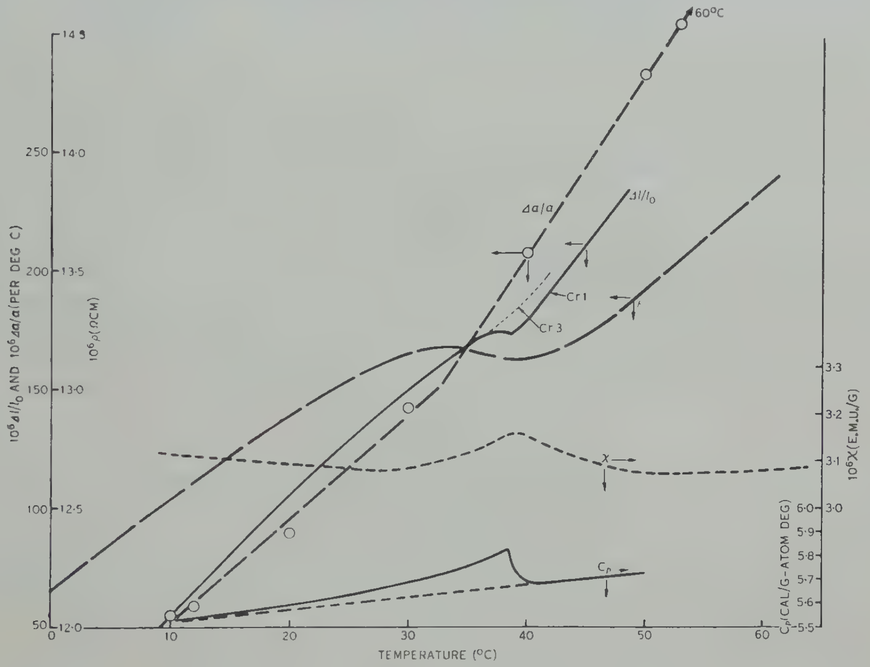

Fig. 3.—Some experimental data for high-purity chromium. $\Delta a/a$: linear expansivity from X-rays (Straumanis and Weng 1955), $\Delta l/l$: linear expansivity of Cr 1 and Cr 3, ρ: electrical resistivity (Harper *et al.* 1957), χ: magnetic susceptibility (Collings, Hedgcock, and Siddiqi 1961), C_p: heat capacity (Beaumont, Chihara, and Morrison 1960).

V. Conclusions

Most recent theoretical speculation on the electronic structure of chromium has been concerned with the evidence afforded by neutron diffraction experiments and studies of the magnetic susceptibility of chromium and its dilute alloys. Possible patterns for the behaviour of the magnetic spins have been discussed by Corliss, Hastings, and Weiss (1959), Kaplan (1959), Newmann and Stevens (1959), Cooper (1960), Lomer (1960), and Overhauser and Arrott (1960). The evidence presented here for the expansivity of high purity samples supplements the other recent evidence on heat capacity, susceptibility, and thermoelectric power in clarifying the experimental picture. It suggests that very small traces of impurity do influence the expansion anomaly (or " transition ") over a very narrow temperature region near the Néel point ; but that, disregarding this narrow interval, a genuine change in expansion coefficient occurs which is characteristic of pure chromium and related to the process of antiferromagnetic ordering.

VI. ACKNOWLEDGMENTS

I am most grateful to my colleagues Messrs. W. R. G. Kemp and A. M. Thompson for their advice ; to Mr. S. N. Howes and Mrs. P. C. Zeleny, who each helped with measurements and computations ; and to Dr. H. L. Wain of the Aeronautics Research Laboratory, Melbourne, who supplied and analysed the various chromium samples. Also, I should like to thank the following for giving me results prior to publication and for interesting correspondence : Drs. G. E. Bacon, B. S. Chandrasekhar, A. R. Edwards, F. T. Hedgcock, W. M. Lomer, J. A. Morrison, K. W. H. Stevens, and M. E. Straumanis.

VII. REFERENCES

BACON, G. E. (1960).—*Bull. Amer. Phys. Soc.* II **5** : 455.

BARSON, F., LEGVOLD, S., and SPEDDING, F. H. (1957).—*Phys. Rev.* **105** : 418.

BEAUMONT, R. H., CHIHARA, H., and MORRISON, J. A. (1960).—*Phil. Mag.* **5** : 188.

BIRSS, R. R. (1960).—*Proc. Roy. Soc.* A **255** : 398.

BYKOV, V. N., GOLOVKIN, V. S., AGEEV, N. V., LEVDIK, V. A., and VINOGRADOV, S. I. (1959).—*C.R. Acad. Sci. U.R.S.S.* **128** : 1153 ; *Transl. Soviet Physics—Doklady* (1960) **4** : 1070.

CHANDRASEKHAR, B. S. (1958).—*Acta Met.* **6** : 212.

COLES, B. R. (1958).—*Phil. Mag. Suppl.* **7** : 40.

COLLINGS, E. W., HEDGCOCK, F. T., and SIDDIQI, A. (1961).—*Phil. Mag.* **6** : 155.

COOPER, B. R. (1960).—*Phys. Rev.* **118** : 135.

CORLISS, L. M., HASTINGS, J. M., and WEISS, R. J. (1959).—*Phys. Rev. Letters* **3** : 211.

EDWARDS, A. R., NISH, J. I., and WAIN, H. L. (1959).—*Metall. Reviews* **4** : 403.

FINE, M. E., GREINER, E. S., and ELLIS, W. C. (1951).—*J. Metals* **3** : 56.

GOODENOUGH, J. B. (1960).—*Phys. Rev.* **120** : 67.

HALL, P. M., LEGVOLD, S., and SPEDDING, F. H. (1960).—*Phys. Rev.* **117** : 971.

HARPER, A. F. A., KEMP, W. R. G., KLEMENS, P. G., TAINSH, R. J., and WHITE, G. K. (1957).—*Phil. Mag.* **2** : 577.

KAPLAN, T. A. (1959).—*Phys. Rev.* **116** : 888.

LINGELBACH, R. (1958).—*Z. Phys. Chem.* **14** : 1.

LOMER, W. M. (1960).—*Aust. J. Phys.* **13** : 451.

MOTT, N. F., and STEVENS, K. W. H. (1957).—*Phil. Mag.* **2** : 1364.

NEWMANN, M. M., and STEVENS, K. W. H. (1959).—*Proc. Phys. Soc.* **74** : 290.

NIX, F. C., and MACNAIR, D. (1941).—*Phys. Rev.* **60** : 597.

OVERHAUSER, A. W., and ARROTT, A. (1960).—*Phys. Rev. Letters* **4** : 226.

PURSEY, H. (1958).—*J. Inst. Met.* **86** : 362.

RUBIN, T., ALTMAN, H. W., and JOHNSTON, H. L. (1954).—*J. Amer. Chem. Soc.* **76** : 5289.

SHIMIZU, M., and TAKAHASHI, T. (1960).—*J. Phys. Soc. Japan* **15** : 2236.

SHULL, C. G., and WILKINSON, M. K. (1953).—*Rev. Mod. Phys.* **25** : 100.

STRAUMANIS, M. E., and WENG, C. C. (1955).—*Acta Cryst.* **8** : 367.
SULLY, A. H. (1954).—" Chromium." (Butterworths : London.)
THOMPSON, A. M. (1958).—*I.R.E. Trans. Instrum.* I **7** : 245.
VARLEY, J. H. O. (1956).—*Proc. Roy. Soc.* A **237** : 413.
DE VRIES, G., and RATHENAU, G. W. (1957).—*J. Phys. Chem. Solids* **2** : 339.
WHITE, G. K., and WOODS, S. B. (1957).—*Canad. J. Phys.* **35** : 346.
WHITE, G. K. (1961*a*).—*Cryogenics* **1** : 151.
WHITE, G. K. (1961*b*).—*Phil. Mag.* (In press.)
WILKINSON, M. K., WOLLAN, E. O., and KOEHLER, W. C. (1960).—*Bull. Amer. Phys. Soc.* II **5** : 456.
WYLIE, R. G. (1948).—C.S.I.R.O. Aust. Div. Phys. Rep. PA–2.
ZENER, C. (1955).—*Trans. Amer. Inst. Min. (Metall.) Engrs.* **203** : 619.

LUMINESCENCE IN KI:Tl

By J. E. Alderson* and S. E. Williams*

[*Manuscript received February* 28, 1961]

Summary

Freshly cleaved single crystals of KI:Tl containing various concentrations of Tl have been irradiated in a vacuum monochromator in the 2800–1100 Å region at temperatures between —140 and 45 °C. The relative luminescence efficiencies in the Tl absorption bands and the host crystal fundamental absorption show that energy is transferred from host crystal to impurity centre to produce luminescence at room temperatures. To the high energy side of a threshold, which appears to depend on activator concentration, the luminescence efficiency is superlinear above about 15 °C for KI:Tl (0·0005%). Luminescence production shows a slow build-up which has been analysed in detail for irradiation at 1608 and 1216 Å. The build-up curve is found to have the form

$$L_t = L_s\{A(1-e^{-yt}) + B(1-e^{-zt})\},$$

where L_s is the saturation luminescence, L_t the luminescence t seconds after illumination starts, and A, B, y, and z are parameters associated with two processes for luminescence production involving recombination and the attainment of equilibrium in the filling of traps. The efficiency of the first process is superlinear and of the second approximately linear. As in the case of AgBr-AgI examined by Moser and Urbach, there is no observable phosphorescent decay. Thermal escape from traps followed by radiationless de-excitation has been observed by investigating the changes of the instantaneous component of luminescence production with varying intervals of darkness. An explanation is proposed in terms of the migration of holes from shallower to deeper traps near luminescence centres followed by recombination with free electrons.

I. Introduction

Studies of the luminescence in activated alkali halides fall roughly into three classes. Luminescence produced by absorption in the impurity bands of the activator has been interpreted as involving a simple monomolecular process occurring entirely within the impurity centre (Williams and Johnson 1959) although this has been questioned by others (Ewles and Joshi 1960). Luminescence produced by, or following X-ray or γ-ray excitation (Bonanomi and Rossel 1951 ; Smaller and Avery 1953) involves heterogeneous excitation energies as well as the production of lattice defects, which makes analysis of the luminescence mechanisms very complex. Finally, the luminescence resulting from irradiation of the crystal by photons whose energies lie within the fundamental absorption band of the host crystal has been examined by Teegarden (1957), by Lushchik and his collaborators (Lushchik *et al.* 1960), and by Ueta and Ishii (1959) and Tomura and Kaifu (1960). The upper limit of photon energy in these cases has been about 7·5 eV, which includes the exciton bands and part of

---

* Department of Physics, University of Western Australia, Nedlands, W.A.

the ionization region. The latter studies have provided evidence that energy transfer from host crystal to luminescence centre is an important factor in luminescence production.

The work described below involved the excitation of single crystals of KI:Tl by photons of energy up to 11 eV at temperatures between −140 and 45 °C. There was no visible evidence for the formation of colour centres even after several days' exposure to the highest intensities used. The luminescence phenomena observed at room temperatures closely resemble those recorded by Moser and Urbach (1957) for mixed crystals of AgI-AgBr at liquid air temperatures. They are similarly explainable on the assumption that free electrons and holes are produced and trapped even though attempts to observe photoconductivity in the alkali halides (Taylor and Hartmann 1959 ; Ewles and Joshi 1960 ; Meharry, personal communication) have been unsuccessful. While there are indications that similar processes persist into the exciton absorption band, the irradiation intensities at present available have not allowed a decisive investigation of this region.

II. Instrumental

The vacuum monochromator has previously been described (Bolton and Williams 1953). Modifications include external focusing adjustments and means of controlling the specimen temperature. The normal vacuum is about 2×10^{-5} mm and with the hydrogen arc operating about 10^{-3} mm. The pass band is about 2 Å. Growth and decay of luminescence were recorded either photographically using a galvanometer of period 0·1 s and film speed 1 cm/s or by a recording milliameter and a.c. amplifier. The a.c. signal was obtained by chopping the photomultiplier first dynode with a 270 c.p.s. square signal. No correction has been made for scattered light, which was approximately constant between 500 Å and the long wavelength limit of observation. The error introduced by this neglect is a maximum in the region between 1800 and 2000 Å, where the intensity of the arc is low and a wide exit slit is necessary to maintain constant intensity (for example in the luminescence efficiency observations of Fig. 1) and also in regions such as the exciton band, where the luminescence efficiency is low. For the maximum slit width used in these regions, scattered light, as measured at 500 Å, produced a maximum error of 5% in the luminescence efficiency. A KCl window was used when needed to eliminate second-order effects in the region above 2000 Å. Early observations on the growth of luminescence showed a lack of consistency which was eventually traced to contamination of the crystal face by oil from the backing pump. This was eliminated by inserting a liquid air trap in the backing line.

The KI:Tl specimens and a sodium salicylate monitor were mounted on a movable arm enabling either to be placed in the light beam. The KI:Tl crystals could be cooled to about 130 °K by conduction to a liquid air reservoir, but the monitor was always used at room temperature, since its efficiency is temperature dependent. Since high absorption restricts luminescence production to a thin surface layer, freshly cleaved single crystals were used, of a size 10 by 2 mm by 1·5 mm thick.

III. Luminescence Efficiency

The curves shown in Figure 1 indicate luminescence efficiency variation with wavelength at about 26 °C. They were obtained by a point-to-point survey comparing the saturation luminescence efficiency from KI:Tl with the intensity from the monitor. Because there is a non-linear dependence of saturation luminescence intensity on excitation intensity over certain regions of the spectral range, it was necessary to adjust the excitation intensity to a constant value by using the monitor before each measurement. A time of the order of 1 min was needed for the luminescence to attain saturation. The figure shows also an approximation to the transmission of KI in this region (Schneider and O'Bryan 1937 ; Eby, Teegarden, and Dutton 1959), because the simple assumption that luminescence is produced by absorption of radiation at Tl centres implies that the luminescence efficiency should be proportional to the mean free path of the photons in the host crystal.

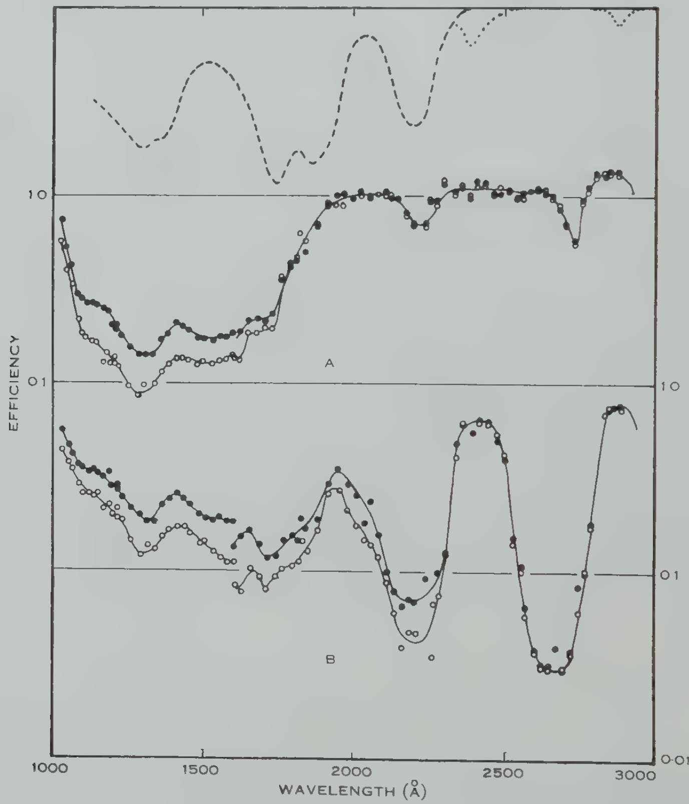

Fig. 1.—Variation of luminescence efficiency with irradiating wavelength. (*A*) KI:Tl (5%) ; (*B*) KI:Tl (0·0005%). ●●● Intensity 200. ○○○ Intensity 50. Broken line shows approximate variation of transmission of pure KI.

In the case of the 0·0005% Tl sample (curve *B*) the onset of KI fundamental absorption at 2300 Å divides the observations into two distinct regions. To the long wavelength side of this edge, absorption takes place only at the Tl impurity centres, producing luminescent emission in a band centred at about 4000 Å (von Meyeren 1929). (Transmitted light is not detected since its wavelength is below the transmission limit of the photomultiplier window at 3000 Å.) Luminescence efficiency then follows the absorption of the activated crystal.

Below 2300 Å the luminescence efficiency shows a tendency to follow the main features of the KI transmission. This is most clearly apparent at the exciton peak at 2200 Å and at the absorption peak at 1290 Å. However, the two peaks at 1730 and 1870 Å are not resolved and there is a marked divergence between 1750 and 1350 Å, where the efficiency fails to rise with the transmission. The long wavelength limit of this region corresponds to the threshold for external photoemission and the short wavelength limit to the saturation emission of electrons (Taylor and Hartmann 1959). (The discontinuity at 1600 Å marks a division between two runs of observations.) This correlation of luminescence efficiency and transmission agrees with the results of Teegarden (1957) and Ueta and Ishii (1959) over the range of energies to 8·2 eV.

The 5% Tl sample (curve A) shows very similar variations between 1750 Å and the short wavelength limit. The peaks of high efficiency corresponding to impurity absorption at 2870 and 2380 Å are very much broadened without any apparent increase in efficiency as compared with the low impurity concentration samples. The drop in efficiency at the exciton peak is much less for this sample.

IV. Superlinearity

Figure 1 shows that in some regions the luminescence efficiencies are not constant for different exciting intensities. All samples show this departure from a linear relationship between excitation and luminescence intensity in the spectral range through which they show similar efficiency variations, i.e. below about 1750 Å, but for the low impurity sample the departure extends through longer wavelengths to about 2280 Å.

If the saturation value of the luminescent output, L_s, of the phosphor is related to the exciting intensity I_e, by the equation $L_s = c.I_e^x$, where c is a constant, the phosphor is superlinear if x exceeds unity. Through the range of wavelengths indicated in Figure 1, x varies between unity and 1·5 at room temperature. However, except at wavelengths of high intensity, namely, 1216 and 1608 Å, the accuracy with which x can be measured is too low to give more than an indication of its manner of variation with wavelength.

Both the luminescence efficiency and the linearity (x) vary rapidly with temperature in the 0–50 °C range. The luminescence efficiency decreases by half as the temperature rises from 8 to 30 °C and by a further quarter between 30 and 45 °C. At 1608 Å, with an incident intensity range of 20 : 1, x is 1·23 at 28 °C, 1·06 at 18 °C, and 0·94 at −15 °C. The fall in luminescence efficiency at high temperatures makes accurate determination of the maximum value of x difficult, but up to 45 °C it is about 1·5. While the observation at −15 °C could have been affected by condensation of oil or water vapour on the crystal, subsequent measurements at a pressure 5×10^{-5} mm with a liquid air trap on the pumping line show that the KI:Tl becomes linear at about 15 °C.

V. Growth and Decay of Luminescence in KI:Tl (0·0005%)

When irradiated by wavelengths below about 2250 Å the low impurity concentration crystal does not immediately produce its maximum luminescence intensity. There is a slow build-up of luminescence which is analysed below in detail. The threshold wavelength for slow build-up for a crystal of KI:Tl containing 0·05% Tl was 2100 Å. In this case a KCl absorber was used to exclude second-order effects. Reasonable assumptions regarding the relative intensities of the scattered, first- and second-order light falling on the crystal with 0·0005% Tl do not explain the longer wavelength of the threshold and, since the threshold for KI:Tl (5%) is at 1750 Å, some effect of activator concentration on threshold seems to be indicated.

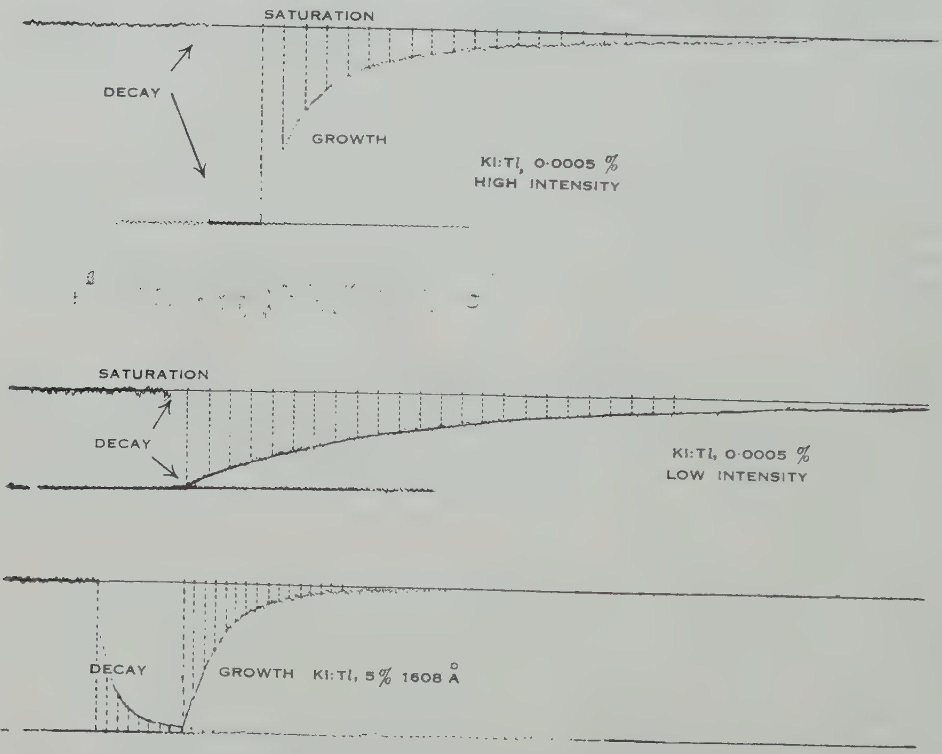

Fig. 2.—Photographically recorded growth and decay of luminescence in KI:Tl. Vertical broken lines are at 1 s intervals for KI:Tl (0·0005%) and at 0·5 s intervals for KI:Tl (5%).

Figure 2 shows typical records of the growth and decay of luminescence for low and high exciting intensities at 1608 Å for the 0·0005% Tl crystal compared with the 5% Tl crystal. It is clear that the decay is very fast relative to the growth and also that the time variation of the growth is intensity dependent. Neither of these characteristics is consistent with the assumption that the mechanism involved is the monomolecular process assumed by Williams and Johnson (1959) to be responsible for the production of luminescence in KCl:Tl irradiated in the impurity absorption bands.

The slow build-up of luminescence has been observed by Randall and Wilkins (1945), by Levialdi and Luzatti (1947), by Hoogenstraten (1953), and by Hoogenstraten and Klasens (1953) for luminophors which showed also a slow phosphorescent decay. Except for the present case of KI:Tl, slow build-up together with very fast decay has only been observed for mixed AgI-AgBr by Moser and Urbach (1957).

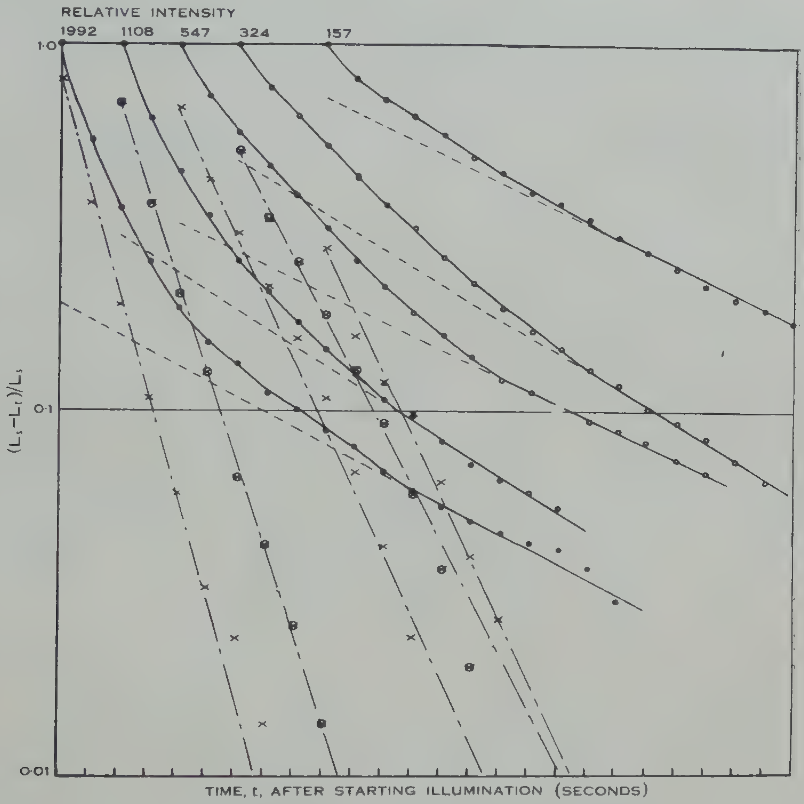

Fig. 3.—Growth of luminescence in KI:Tl (0·0005%) for various intensities of irradiation by 1216 Å. Growth curves for different intensities of irradiation have been separated along the time axis. Dissection of the curves shown by the broken lines is described in the text.

The growth curves have been analysed by a simpler method than that used by Schön (1954), although, as in his case, it has been assumed that the slow build-up is associated with the trapping of electrons and holes. An analysis of the curves is possible at 1216 and 1608 Å because of the high intensities available for excitation at these wavelengths. In Figures 3 and 4 the full lines show the difference between the saturation luminescence intensity L_s and the luminescence L_t, at time t after starting illumination at constant intensity. The curves have been displaced, for clarity, along the time axis. It is seen that with increasing intensity the growth curve departs from the simple exponential form. The broken lines show how the curves have been dissected. The straight part of the curve for large t has been extrapolated to zero time and subtracted from the full curve to give the second component. At both 1216 and 1608 Å the growth curves are then found to separate into two exponential components, so that the full curve can be represented by the formula

$$L_t=L_s\{A(1-e^{-yt})+B(1-e^{-zt})\},\ \text{where } A+B=1.$$

That the growth curves for luminescent SiO_2Cd could be represented as the sum of two exponentials, was recognized by Levialdi and Luzzati (1947). The numerical values are listed in Table 1.

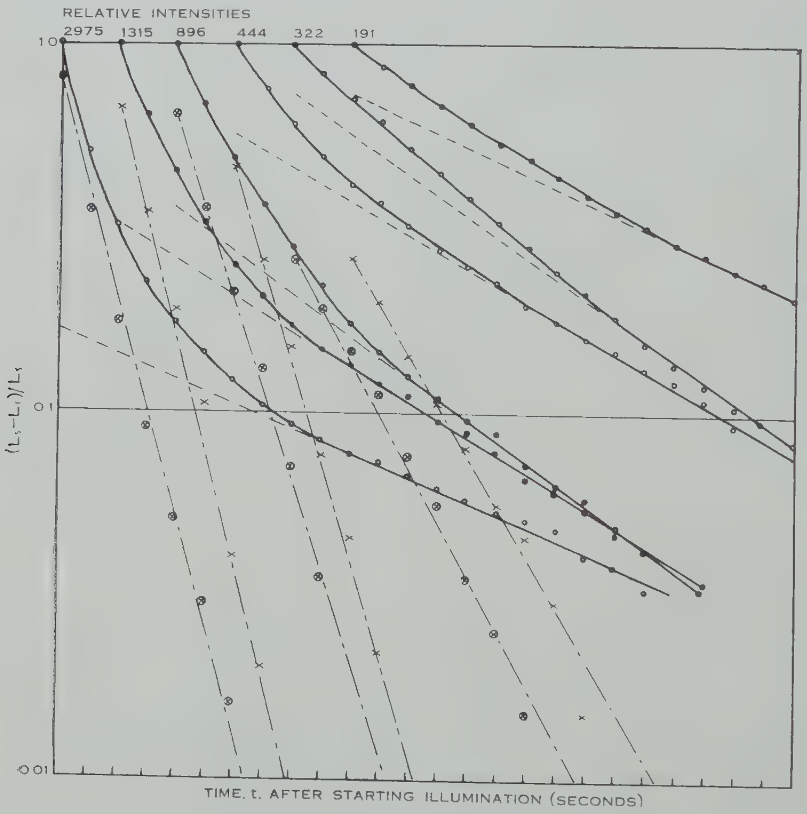

Fig. 4.—Growth of luminescence in KI:Tl (0·0005%) for various intensities of irradiation by 1608 Å.

It appears from this analysis that the intensity dependence of the growth curves results from a change in the relative importance of two processes for producing luminescence, designated by the parameters A and y, and B and z. The former increases in importance with increasing excitation intensity, the latter consequently decreases. Since A and B are the fractions of L_s produced by each of the two processes, then $A.L_s/I_e$ and $B.L_s/I_e$ are the respective luminescence efficiencies. The table shows that, while the efficiency for the first process increases rapidly, in fact about as $I_e^{1\cdot 5}$, the efficiency for the second process is approximately constant, showing a small decrease at the highest intensities. The original superlinearity, then, arises from the superlinear character of the first process. Further discussion is included below.

The available excitation intensity would not allow such a detailed examination of the intensity dependence of the luminescence growth at other wavelengths, but a slow build-up has been observed to extend into the exciton band region to the thresholds mentioned above.

Table 1

ANALYSIS OF GROWTH CURVES

Incident Intensity, I_e (from Monitor)	Saturation Luminescence Intensity, L_s	A	y	$A.L_s/I_e$	B	z	$B.L_s/I_e$
(*a*) At 1216 Å (Fig. 3)							
1992	530	0·81	0·67	0·21	0·19	0·10	0·05
1188	296	0·70	0·55	0·17	0·30	0·12	0·07
547	121	0·68	0·37	0·15	0·32	0·09	0·07
324	65	0·52	0·34	0·11	0·48	0·11	0·09
157	26	0·28	0·34	0·05	0·72	0·09	0·12
(*b*) At 1608 Å (Fig. 4)							
2975	1258	0·82	0·74	0·35	0·18	0·075	0·075
1315	468	0·67	0·74	0·24	0·33	0·10	0·12
896	296	0·63	0·59	0·18	0·37	0·12	0·12
444	109	0·46	0·53	0·11	0·54	0·10	0·13
322	69	0·26	0·33	0·06	0·74	0·12	0·16
191	34	0·26	0·31	0·05	0·74	0·08	0·13

VI. Instantaneous Components of Luminescence Growth

An instantaneous component can be observed at wavelengths lower than 1700 Å by illuminating the sample after a relatively short time in darkness following a previous illumination to saturation at the same intensity. Similar observations were made by Moser and Urbach (1957). The dependence of the magnitude of this instantaneous component relative to the saturation luminescence on the time since the crystal was previously illuminated is shown in Figure 5. The rate of decay is the same at 26 °C at both 1216 and 1608 Å, but it is greatly reduced by a decrease in the crystal temperature, as the curve for 1608 Å excitation at 15 °C shows.

When the temperature is lowered to, say, −100 °C the growth curve associated with the first illumination has a form determined by the time interval since the previous illumination and the start of cooling and the temperature during that interval. However, subsequent illuminations at the same intensity after periods up to 15 min in darkness at low temperature show a completely instantaneous rise in luminescence.

In an experiment in which the sample was allowed to warm up gradually as it was alternately irradiated to saturation and left in the dark, it was found that, following irradiation at −15 °C and 12 min in darkness while the temperature rose to 3 °C, the diminution of the instantaneous component was negligible. After irradiation to saturation at 3 °C followed by 13 min in darkness, during which time the temperature rose to 18 °C, the instantaneous component had completely disappeared when the sample was next irradiated. It appears that the process responsible for decay of the instantaneous component becomes much less probable when the temperature falls below about 10 °C. The decay curves of Figure 6 can be expressed as the sum of two exponentials, namely,

$$L_{\text{inst.}}=L_s(0\cdot58e^{-0\cdot1t}+0\cdot42e^{-0\cdot002t})\ \text{at 26 °C},$$

and

$$L_{\text{inst.}}=L_s(0\cdot36e^{-0\cdot06t}+0\cdot64e^{-0\cdot008t})\ \text{at 15 °C},$$

where t is the time in the dark.

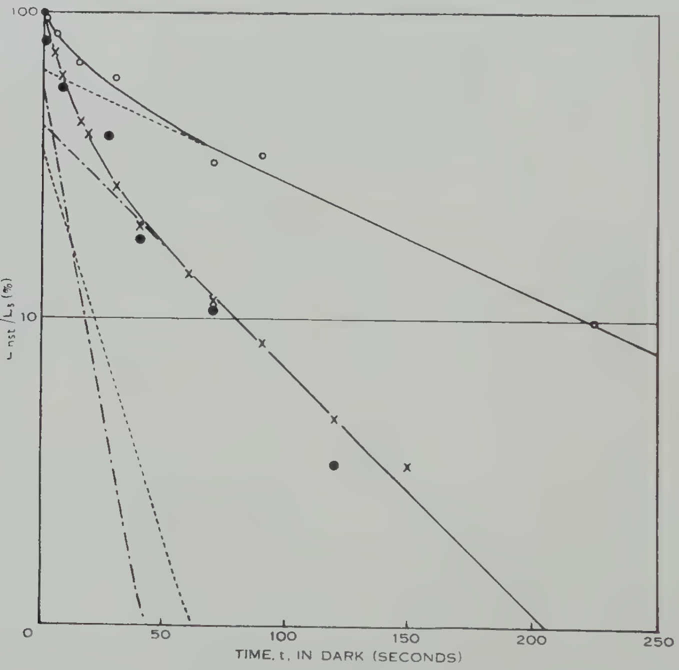

Fig. 5.—Decay of the instantaneous component of luminescence in KI:Tl (0·0005%) with time in darkness. ●●●● Irradiated by 1216 Å at 26 °C, ×××× irradiated by 1608 Å at 26 °C, ○○○○ irradiated by 1608 Å at 15 °C. Dissection of the curves by the broken lines is described in the text.

VII. Growth and Decay of Luminescence in KI:Tl (5%)

Some observations were made on the growth and decay of luminescence in the high impurity concentration crystal at about 26 °C. The most significant feature was the appearance of a phosphorescent decay whose half-life was shorter than the corresponding growth "half-life". A typical curve for excitation by 1608 Å radiation is shown in Figure 2, and Figure 6 shows typical growth and decay curves. The form of the decay does not change very much when the exciting intensity is increased by 25 times. The corresponding growth curves show some change with intensity, but the growth is so rapid (about 5 times faster) that it was not possible with the available equipment to observe the growth accurately enough to justify an analysis similar to that of Figures 3 and 4. Nor could it be determined whether any instantaneous component exists after short periods in darkness.

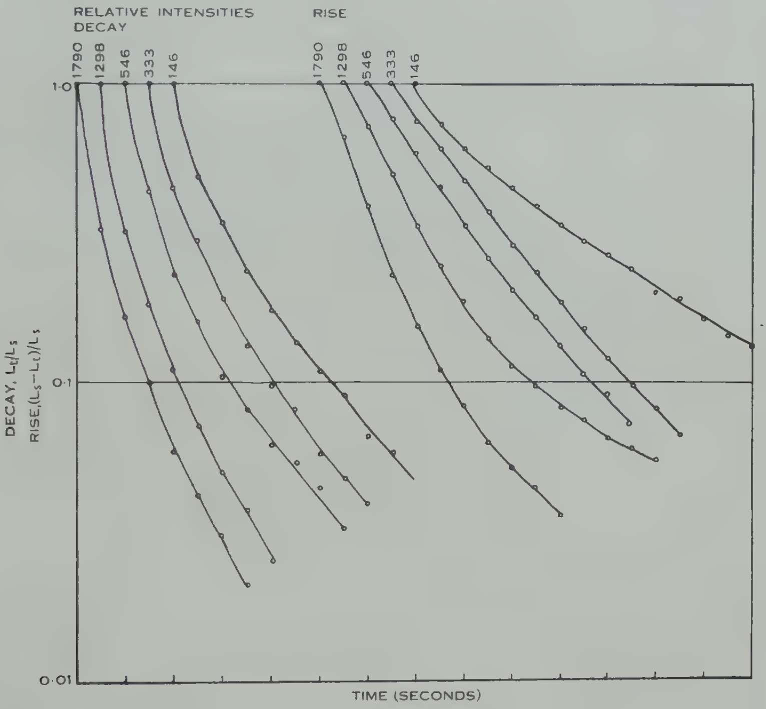

Fig. 6.—Curve of growth and decay of luminescence in KI:Tl (5%) irradiated by various intensities at 1608 Å. Curves displaced along time axis for clarity.

The probability for Tl ions to occupy adjacent cation sites in the lattice is much greater for the 5% Tl crystal. Adjacent Tl centres will introduce additional traps and at the same time, on the assumptions of the discussion below, the chance for radiationless de-excitation will be decreased in favour of phosphorescent emission.

VIII. Discussion

If the luminescence resulting from excitation energies falling within the fundamental absorption band of the host crystal were solely the result of direct absorption at Tl centres, the intensity of the luminescence would be expected to show a considerable decrease compared with that for excitation in the impurity peaks where the host crystal is transparent. The luminescence efficiency could be expected to follow the transmission of the sample in a general way.

The high luminescence efficiency observed within the fundamental absorption band throws doubt on this simple assumption even when superlinearity, slow growth, and very fast decay are neglected. The number of impurity centres directly accessible to radiation of wavelengths in the fundamental absorption band should be decreased compared with the number accessible to radiation of wavelengths in the impurity bands by a factor approximately equal to the ratio of the absorption coefficients, provided the crystal is thick enough to absorb completely in both regions. The absorption coefficient in the fundamental band is of the order of 10^5/cm (Schneider and O'Bryan 1937; Eby, Teegarden, and Dutton 1959). The absorption coefficient in the impurity bands depends on the impurity concentration. The observed value for the 2870 Å band for the 0·0005% Tl sample was about 100 cm^{-1}. At 2400 Å it was of this order but could not be measured accurately for the thinnest specimens which could be cleaved (0·02 cm). (Proximity to the tail of the fundamental absorption band also tends to mask the impurity absorption in this region.) A similar difficulty existed for the 5% sample. However, it is clear that the ratio of the absorption coefficients is at least of the order of 1 : 500 while the observed ratio of the corresponding luminescence efficiencies is of the order of 10 : 1.

This discrepancy could be the result of one or more of three causes. Firstly, there may be an increase in the cross section of the Tl centre for direct excitation by photons of energies within the fundamental absorption band, though any such increase would probably not be considerable over more than a very restricted energy range. Secondly, a luminescent process for de-excitation of the host crystal following irradiation in the absorption band may exist. It is reported, however, that KI in the pure form does not normally show luminescence at room temperature (Teegarden 1957). If such luminescence were promoted by the presence of the Tl activator, new emission bands of high intensity compared with the Tl emission bands should be observed on illumination within the fundamental absorption edge, unless their wavelength was coincident with the 4000 Å bands of Tl. No evidence has been reported for the existence of such bands, although Chatterjee (1950) and Smaller and Avery (1953), who used X-ray and γ-ray excitation, should have observed them if they existed. The remaining possibility is that the high luminescence efficiency results from the transfer of energy from the host crystal to the Tl ion responsible for luminescence emission. Such a transfer of energy is assumed to occur only in regions of the host crystal in the immediate neighbourhood of an impurity ion. To account for the increased luminescence efficiency, such regions must have a radius of the order of 5 lattice spacings.

Similar conclusions have been reached by other investigators. Tomura and Kaifu (1960) have concluded that at liquid air temperatures excitons produced in KI:Tl can transfer energy to the Tl ions to produce luminescence, though as the temperature rises the luminescence efficiency falls rapidly. Ewles and Joshi (1960) from a study of KCl:Tl concluded that, even for excitation in the impurity bands, transition between energy levels of a Tl ion cannot explain the characteristics of luminescence production. Johnson and Williams (1950) calculated from measurements of the variation of luminescence efficiency with

Tl concentration that the influence of the impurity extended over several lattice spacings. Lushchik and Pliavin (1959) have also proposed the occurrence of energy transport from host lattice to impurity centres.

In what follows, therefore, the details of luminescence production by a Tl ion have been ignored. The presence of an impurity ion in the lattice is assumed to cause the formation of a region in its vicinity containing trapping sites for electrons and holes additional to and probably deeper than those normally present in the remainder of the lattice. The analytical form of the growth curves, namely,

$$L=L_s\{A(1-e^{-yt})+B(1-e^{-zt})\}$$

indicates that luminescence production depends on the processes involving the attainment of equilibrium in the filling of traps. The probability of emptying of traps by recombination or by thermal escape is then measured by the coefficients y and z, and saturation luminescence production is attained when the number of occupied traps in the vicinity of a luminescence centre is a maximum.

Moser and Urbach assumed that free electrons recombined with trapped holes to produce luminescence in AgI-AgBr. A similar assumption has been made by Lushchik (Lushchik *et al.* 1960), in regard to activated alkali halides irradiated by photons of energy up to 7 eV. From the present work it cannot be decided whether the two terms in the expression for L_t represent the recombination of free electrons with trapped holes and the recombination of free holes with trapped electrons, or involve a further trapping process such as would result from a secondary generation of *F*-centres. However, following the abovementioned authors it is assumed that the first term, namely, $A(1-e^{-yt})$ represents the luminescence resulting from recombination of free electrons with trapped holes within a few lattice spacings from a Tl ion so that energy transfer to the Tl ion can occur. This process is superlinear, the efficiency AL_s/I_e varying at room temperature approximately as $I_e^{3/2}$. The second term also represents a recombination process involving traps and energy transfer to Tl centres, but this process is approximately linear.

Thermal release from the traps will produce free holes or electrons, but the absence of phosphorescence indicates that these holes and electrons do not recombine in the vicinity of Tl centres to transfer energy to the Tl, but tend to leave the region in which energy transfer can take place to recombine by a radiationless process elsewhere. In the 5% Tl crystal, because of the smaller distance between Tl centres, the possibility for this is less than in the 0·0005% Tl crystal and phosphorescence should be produced. The observation of phosphorescence in these high impurity content crystals with a decay curve whose form is independent of exciting intensity supports this assumption.

The thermal emptying of traps produces the decay of the instantaneous coefficient of luminescence on the one hand and a fall in luminescence efficiency with rising temperature on the other. Since the saturation luminescence intensity is inversely proportional to the probability of a trap being emptied, both y and z should be temperature dependent. At constant intensity y should be the sum of the probability of recombination of a free electron with a trapped hole and a temperature-dependent probability for thermal release which is observable as the exponential decay of the instantaneous component. Observations in the temperature range 18–45 °C tend to confirm this assumption, though the accuracy with which the growth and decay curves can be analysed is less than could be desired.

The observed superlinearity results from an increase in the efficiency $A.L_s/I_e$ of the relevant luminescence process, which makes $A.L_s$ increase approximately as $I_e^{1\cdot 5}$. $A.L_s$, the saturation luminescence intensity for this process, is proportionate to the equilibrium concentration of trapped holes near a Tl centre. At constant temperature, in the absence of any additional intensity-dependent influence, the concentration should be proportional to the incident intensity. Therefore to account for the observed superlinearity an additional intensity-dependent factor is required to raise the concentration of trapped holes suitably in the vicinity of Tl centres. The intensity-dependence of this factor is observed to increase from zero at about 10 °C, the threshold for superlinearity, to $I_e^{\frac{1}{2}}$ at room temperature and above. Since a rise in temperature will facilitate the migration of holes toward the deeper traps closest to Tl centres it is suggested that the intensity-dependent factor is to be associated with the process of hole migration.

IX. Acknowledgments

For samples of activated KI we are indebted to Dr. P. D. Johnson, G.E.C. Laboratories, Schenectady, N.Y., Dr. W. Ehrenburg, Birkbeck College, London, and Dr. J. Thewlis, A.E.R.E., Harwell. The work was supported by the University of Western Australia Research Fund. It is a pleasure to acknowledge the continued interest of Professor C. J. B. Clews in this work.

X. References

Bolton, J. H., and Williams, S. E. (1953).—*Brit. J. Appl. Phys.* **4** : 6.

Bonanomi, J., and Rossel, J. (1951).—*Helv. Phys. Acta* **25** : 725.

Chatterjee, A. (1950).—*Indian J. Phys.* **24** : 331.

Eby, J., Teegarden, K. J., and Dutton, D. B. (1959).—*Phys. Rev.* **116** : 1099.

Ewles, J., and Joshi, R. V. (1960).—*Proc. Roy. Soc.* A **254** : 358.

Hoogenstraten, W. (1953).—*J. Electrochem. Soc.* **100** : 356.

Hoogenstraten, W., and Klasens, H. A. (1953).—*J. Electrochem. Soc.* **100** : 366.

Johnson, P. D., and Williams, F. E. (1950).—*J. Chem. Phys.* **18** : 1477.

Levialdi, A., and Luzzati, V. (1947).—*J. Phys. Radium* **8** : 306, 341.

Lushchik, Ch. B., Liid'ya, G. C., Yaek, I. V., and Tiisler, E. S. (1960).—*Optika i Spektrosk.* **9** : 77.

Lushchik, Ch. B., and Pliavin, I. K. (1959).—*Optika i Spektrosk.* **7** : 41.

von Meyeren, W. (1929).—*Z. Phys.* **61** : 321.

Moser, F., and Urbach, F. (1957).—*Phys. Rev.* **106** : 852.

Randall, J. T., and Wilkins, M. H. F. (1945).—*Proc. Roy. Soc.* A **184** : 366.

Schneider, E. G., and O'Bryan, H. M. (1937).—*Phys. Rev.* **51** : 293.

Schön, M. (1954).—*Physica* **20** : 930.

Smaller, B., and Avery, E. (1953).—*Phys. Rev.* **92** : 233.

Taylor, J. W., and Hartmann, P. L. (1959).—*Phys. Rev.* **113** : 1421.

Teegarden, K. J. (1957).—*Phys. Rev.* **105** : 1222.

Tomura, M., and Kaifu, Y. (1960).—*J. Phys. Soc. Japan* **15** : 314.

Ueta, M., and Ishii, T. (1959).—*J. Phys. Soc. Japan* **14** : 857.

Williams, F. E., and Johnson, P. D. (1959).—*Phys. Rev.* **113** : 97.

CROSS-RELAXATION EFFECTS IN A RUBY *L*-BAND (1440 Mc/s) MASER AT LOW MAGNETIC FIELDS

By G. S. Bogle* and F. F. Gardner†

[*Manuscript received February* 28, 1961]

Summary

The reversals of maser behaviour which occur in ruby at low fields on cooling from 80° to 4 °K are explained in terms of cross-relaxation transitions (resonant interchanges of energy between neighbouring paramagnetic ions). For an angle of 29° between the magnetic field and the crystal axis a cross-relaxation process has been demonstrated which involves groups of three ions and has a transition probability of 700 ± 100 per second in $0 \cdot 013\%$ ruby. The profile of the cross-relaxation resonance has a half-width of 190 ± 30 Mc/s at half-intensity, and has an approximately Gaussian shape. It should be possible to obtain useful low-field *L*-band maser action at 4 °K by pumping ν_{41} with the magnetic field nearly perpendicular to the crystal axis, and also at 80 °K using a concentration ten times higher, i.e. $0 \cdot 13\%$

I. Introduction

Since Bloembergen's (1956) original proposal of the three-level solid-state maser a variety of phenomena have been discovered which have clearly demonstrated that processes other than spin-lattice relaxations play a part in determining populations of different states at low temperatures. For example, Autler and McAvoy (1958) found that a maser would not work if the concentration of the active spins was raised above a certain value.

Recently Bloembergen *et al.* (1959) have described a cross-relaxation mechanism which is capable of explaining some of the effects and have applied it in detail to maser action in potassium chromicyanide. The essence of the cross-relaxation process is that two or more neighbouring paramagnetic ions (hereinafter called spins) make simultaneous transitions owing to their mutual interaction. The quantum-mechanical treatment of Bloembergen *et al.* shows that the process has highest probability when the total energy of the participating spins is unchanged by their simultaneous transitions.

The probability of the cross-relaxation process depends only on the distances between neighbours and on their quantum-mechanical states and so is nearly independent of temperature. On the other hand the spin-lattice relaxation probabilities are sharply temperature dependent, and it can happen that at 4 °K cross-relaxations occur at a much higher rate than spin-lattice relaxations and will in a maser system radically influence the level populations. In this way, as

---

* Division of Physics, C.S.I.R.O., University Grounds, Chippendale, N.S.W.

† Division of Radiophysics, C.S.I.R.O., University Grounds, Chippendale, N.S.W.

Shapiro and Bloembergen (1959) have explained, L-band maser action in dilute potassium chromicyanide is destroyed when, by adjustment of magnetic field and orientation, two energy gaps are made equal so that double spin-flips may occur without change of total energy.

In this paper we report experiments on an L-band (1440 Mc/s) ruby maser. We shall show that cross relaxations involving triple spin-flips are capable of explaining how, under some conditions, maser action which is present at 80 °K deteriorates on cooling and is reversed at 4 °K. Effects of double spin-flips will also be described and discussed.

Mimms and McGee (1960) have also observed triple spin-flips in ruby, using a monitoring frequency of 7170 Mc/s. They have shown that two distinct relaxation times (cross-relaxation and spin-lattice) are exhibited by the spin system when it returns to equilibrium after having been disturbed. On the other hand we have studied, under steady-state conditions, the combined effect of the two kinds of relaxation. By varying temperature (i.e. by changing the spin-lattice relaxation rate) we have been able to distinguish the cross-relaxation processes and measure their rate.

II. ENERGY LEVELS OF Cr^{3+} IN RUBY AT LOW FIELDS

Ruby consists of corundum, α-Al_2O_3, with a small proportion of the diamagnetic Al^{3+} ions replaced by paramagnetic Cr^{3+}. In most maser work the atomic concentration of chromium is between $0 \cdot 01$ and $0 \cdot 1\%$.

The energy levels of Cr^{3+} in ruby are the eigenvalues of an operator called the spin Hamiltonian (see, for example, Bowers and Owen 1955), which is of the form

$$\mathscr{H}=D(S_z^2-5/4)+g\beta B.S,$$

where D is a constant, g is the spectroscopic splitting factor (analogous to the Landé g factor of optical spectroscopy), β is the Bohr magneton, S the spin operator, and B the applied magnetic flux density. S has the value 3/2, and there are four distinct energy levels except at zero magnetic field, when they consist of two degenerate doublets separated by $2D$. One doublet, at energy D, corresponds to the eigenstates with $S_z=\pm 3/2$, z being the axis of symmetry of the ruby crystal structure, and the other doublet, at $-D$, to $S_z=\pm 1/2$. In ruby, D is negative, so that the $\pm 1/2$ doublet lies higher in energy; the zero-field splitting frequency $2\,|\,D\,|/h$ is $11 \cdot 47$ Gc/s at low temperatures (Kikuchi *et al.* 1959).

At low magnetic fields, i.e. fields such that $g\beta B$ is small compared with $|\,D\,|$, the energies may be calculated by perturbation theory as a function of magnetic field strength (B) and its inclination (θ) to the crystalline axis:

$$\begin{aligned} E_{1,\,2}&=-|\,D\,|\mp\tfrac{3}{2}g\beta B\cos\theta-\tfrac{3}{8}(g\beta B\sin\theta)^2/|\,D\,|,\\ E_{3,\,4}&=|\,D\,|\mp\tfrac{1}{2}g\beta B(1+3\sin^2\theta)^{\frac{1}{2}}+\tfrac{3}{8}(g\beta B\sin\theta)^2/|\,D\,|. \end{aligned} \tag{1}$$

The errors in the above equations are of order $(g\beta B)^3/D^2$. The levels are shown for several values of θ in Figure 1. From a consideration of radiation-induced transition probabilities (see, for example, Howarth 1958 or Weber 1959), it is found that the transition between levels 4 and 3 is the one most suited for amplification in an L-band maser at low fields. To achieve amplification (see below) it is necessary to irradiate the ruby strongly at the frequency $\nu_{42}=(E_4-E_2)/h$ or ν_{41}, a process called " pumping at ν_{42} or ν_{41} ".

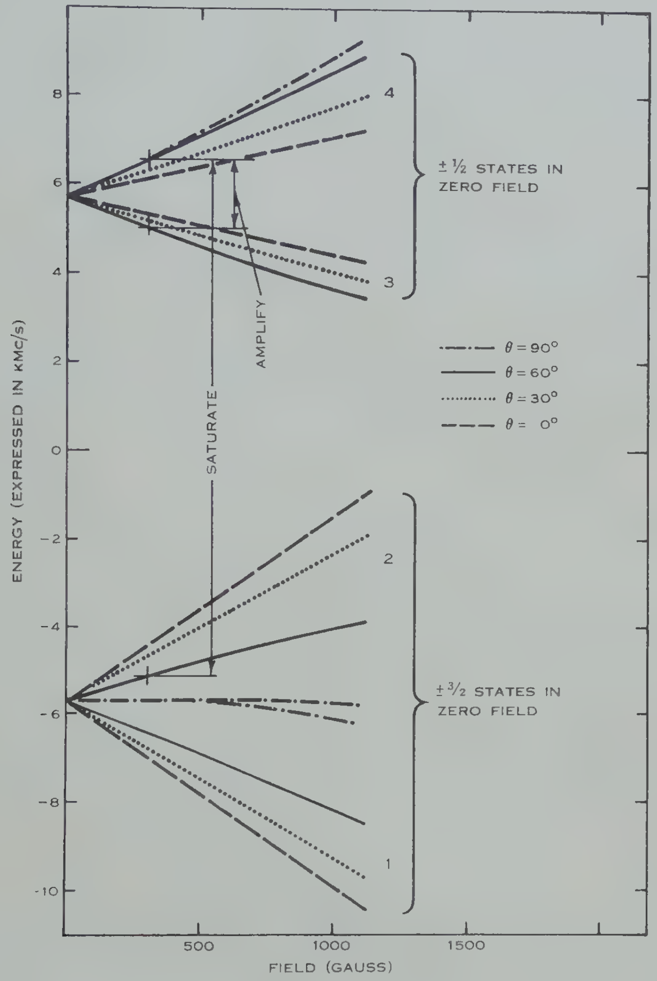

Fig. 1.—Ruby energy levels in low fields for several values of θ, the angle between the magnetic field and the crystalline axis. (For 90°, level 3 is not drawn separately because it is practically the same as for 60°.)

The most natural situation in maser experiments is that ν_{43} is fixed by the dimensions of a cavity resonator, but that a variety of angles, fields, and pumping frequencies are used. Figure 2 shows the values of ν_{41}, ν_{42}, ν_{31}, and B as a function of θ when B is always adjusted to keep the amplifying frequency ν_{43} at 1440 Mc/s ; these have been calculated from equation (1). The figure also shows the variation of ν_{21}, which is relevant to the cross-relaxation processes.

In the discussion of cross-relaxation processes which is given below it will be shown that particular interest attaches to the angles at which ν_{21}/ν_{43}, i.e. $3\cos\theta/(1+3\sin^2\theta)^{\frac{1}{2}}$, is an integer.

(i) For $\nu_{21}/\nu_{43}=2$, $\theta=29\cdot2°$. At this angle the total energy of three spins is unchanged by a cross-relaxation process in which two spins jump from levels 4 to 3 and one jumps from 1 to 2.

(ii) For $\nu_{21}/\nu_{43}=1$, $\theta=54\cdot7°$. At this angle the total energy of two spins is unchanged by one spin jumping from 4 to 3 and the other from 1 to 2.

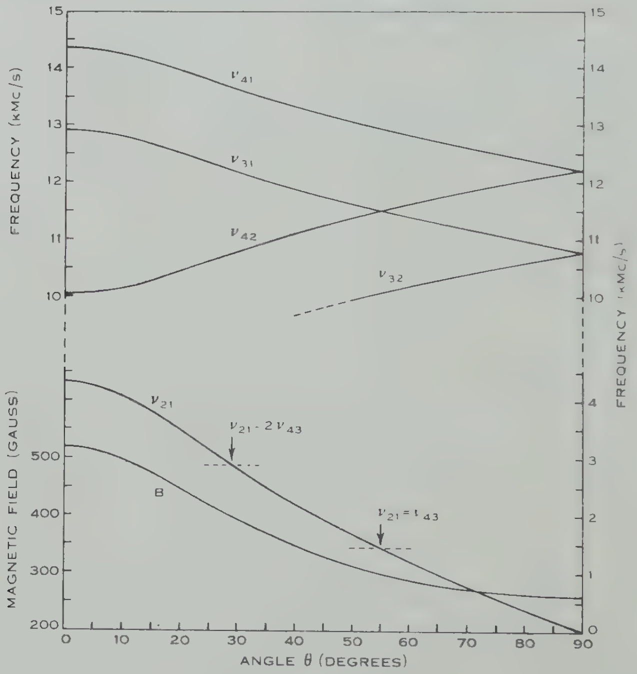

Fig. 2.—Variation of magnetic field and resonant frequencies with angle θ when ν_{43} is maintained at 1440 Mc/s.

III. Maser Behaviour without Cross Relaxation

We shall give here a brief recapitulation of Bloembergen's (1956) theory of the three-level paramagnetic maser, before going on to allow for the effect of cross relaxations.

(a) *System in Thermal Equilibrium*

For the sake of definiteness we consider a Cr^{3+} ion with four energy levels of which the populations are n_1, n_2, n_3, and n_4, totalling N. In thermodynamic equilibrium $n_j/n_i=\exp(-E_{ji}/kT)$ where $E_{ji}=E_j-E_i$ and k is Boltzmann's constant. Owing to the presence of lattice vibrations, spins continually jump from level to level with a transition probability w_{ij}, w_{ji}, etc. These jumps are called spin-lattice relaxations, and w_{ij} is a spin-lattice relaxation rate. In view of the principle of detailed balancing $n_iw_{ij}=n_jw_{ji}$, whence $w_{ij}=w_{ji}\exp(-E_{ji}/kT)$. The spin-lattice relaxations constitute the mechanism by which the spin system, when undisturbed, takes up the same temperature as the lattice. In ruby, typical values of w_{ij} are 10^4 and 10 s^{-1} at liquid air and liquid helium temperatures respectively.

(b) *System with Microwave Radiation*

When the microwave frequency is at or near a resonant frequency of the system, namely, $\nu_{ji}=(E_j-E_i)/h$, radiation-induced transitions occur from the level i to j, and vice versa, with the common transition probability W_{ij}. (For the moment, we suppose that $E_j>E_i$). W_{ij} is proportional to the incident power P, and the absorption of power is described by the equation

$$-\mathrm{d}P=(n_i-n_j)h\nu_{ji}W_{ij}. \tag{2}$$

The absorption coefficient is thus proportional to n_i-n_j, and this fact is used to monitor changes of n_i-n_j which may occur when the system is disturbed as in a maser.

For large power such that $W_{ij}\gg w_{ij}$, w_{kl}, etc., the power absorbed no longer increases in proportion to incident power but reaches a limit imposed by the spin-lattice relaxation rates. Thus the absorption coefficient and the population difference n_i-n_j both tend to zero. This is the phenomenon of " saturation of the resonance line " well known in microwave spectroscopy.

To operate a maser of the Bloembergen type, a system of energy levels, such as is shown in Figure 1, is used. The amplification frequency is chosen to correspond to one of the smaller energy splittings such as E_4-E_3, and strong microwave power is applied at one of the high frequencies such as ν_{42} in order to saturate the resonance. When the pumping power is applied the population difference, in this case n_3-n_4, becomes reversed in sign so that, according to equation (2), power applied at ν_{43} is amplified instead of being absorbed.

This population change may be calculated by the method of Bloembergen, and we quote the results below ; but it may also be understood by means of a simple geometric treatment which is modelled on that of Geusic *et al.* (1959).

(c) *Qualitative Treatment of Maser Action*

Let the populations n_i, which are proportional to exp $(-E_i/kT)$, be plotted as ordinate with energy as abscissa (Fig. 3 (*a*)). In the " high temperature approximation " always made in maser calculations, all energies are assumed small compared to kT, so that for all levels exp $(-E_i/kT)\simeq 1-E_i/kT$ and the populations are given by $n_i\simeq\frac{1}{4}N[1-(E_i-E_m)/kT]$, where E_m is the mean energy. This is a fairly good approximation in the present case where the highest frequency involved is about 15 kMc/s, since 4° K, the lowest temperature used, is equivalent to about 100 kMc/s. In this approximation a straight line with slope $-N/(4kT)$ may be drawn through the points n_1 to n_4 of Figure 3 (*a*).

Figure 3 (*b*) represents the effect of pumping at ν_{42}. The populations n_2 and n_4 have each been replaced by $n_4'=n_2'=\frac{1}{2}(n_2+n_4)$. It may be seen by inspection of the figure that if $\nu_{42}\gg\nu_{43}$ the population of the upper level E_4 exceeds that of E_3, so that maser action is possible at the frequency ν_{43}. Indeed, a simple calculation from the figure shows that the population excess is $(Nh/4kT)(\frac{1}{2}\nu_{42}-\nu_{43})$.

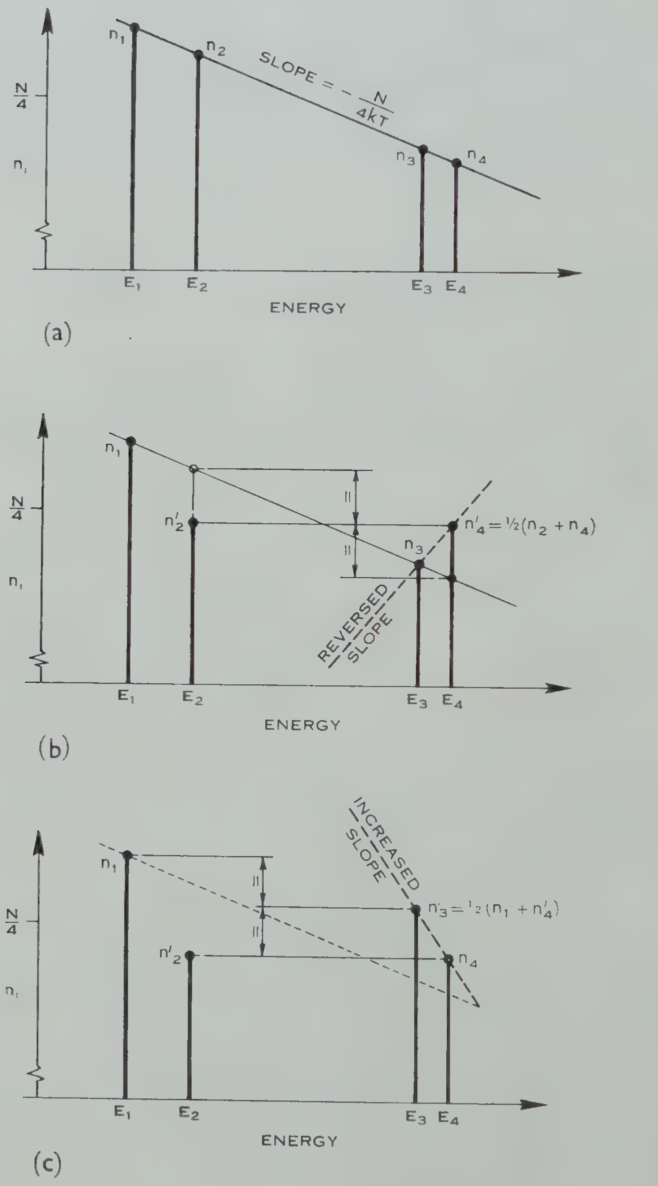

Fig. 3.—Level populations (*a*) in thermal equilibrium, (*b*) when ν_{42} is saturated, equalizing n_2 and n_4, and (*c*) when in addition a cross-relaxation process is present which makes n_3 equal to the mean of n_1 and n_4.

The natural quantity to measure in experiments is the ratio, with and without pumping, of the strengths of the resonance line at ν_{43} (treating an emission line as a negative absorption line). This, in turn, is equal to the ratio of the corresponding population differences, which we call Δn_{34} and $\Delta_0 n_{34}$ with and without pumping. Thus the maser equation is most conveniently written in terms of the ratio $\Delta n_{34}/\Delta_0 n_{34}$, and in the present case becomes

$$\Delta n_{34}/\Delta_0 n_{34} = 1 - \tfrac{1}{2}\nu_{42}/\nu_{43}. \tag{3}$$

(*d*) *Results of the Quantitative Theory of Maser Action*

The solution for a system of three levels has been given by Bloembergen (1956) and that for four levels, which is not different in principle, has been given, for example, by Bogle and Symmons (1959). Adapting level labels to the present case we obtain

$$\frac{\Delta n_{34}}{\Delta_0 n_{34}} = 1 - \frac{\nu_{42}}{\nu_{43}} \cdot \frac{w_1 w_{23} + w_{13} w_{12}}{w_1(w_{23}+w_{34}) + w_{13}(w_{12}+w_{14})}, \tag{4a}$$

where $w_1 = w_{12} + w_{13} + w_{14}$. (Owing to the nature of the approximations made there is no need to distinguish between w_{ij} and w_{ji}.) Some justification for the " geometric " calculation based on Figure 3 (*b*) is afforded by the fact that equation (4a) reduces to (3) when all the w_{ij} are the same.

Equation (4a) may be adapted for pumping ν_{41} instead of ν_{42} simply by interchanging the suffices 1 and 2, yielding

$$\frac{\Delta n_{34}}{\Delta_0 n_{34}} = 1 - \frac{\nu_{41}}{\nu_{43}} \cdot \frac{w_2 w_{31} + w_{23} w_{21}}{w_2(w_{31}+w_{34}) + w_{23}(w_{21}+w_{24})}. \tag{4b}$$

The expected value of $\Delta n_{34}/\Delta_0 n_{34}$ for a 1400 Mc/s maser, assuming equal w_{ij}'s, is about -3 at all angles whether ν_{42} or ν_{41} is pumped. We shall call this " a maser effect of 3 ".

If the pumping frequency is changed to ν_{31} it is easy to see, from a diagram like that of Figure 3 (*b*), that Δn_{34} is larger than $\Delta_0 n_{34}$, so that the absorption coefficient is increased. We call this " an antimaser effect ". The corresponding equation may easily be derived from (4a) by changing level labels and remembering that the ν_{ij} are signed quantities (i.e. that $\nu_{ij} = -\nu_{ji}$). The result is

$$\frac{\Delta n_{34}}{\Delta_0 n_{34}} = 1 + \frac{\nu_{31}}{\nu_{43}} \cdot \frac{w_2 w_{14} + w_{24} w_{12}}{w_2(w_{14}+w_{34}) + w_{24}(w_{12}+w_{23})}, \tag{5}$$

where $w_2 = w_{21} + w_{23} + w_{24}$. A similar equation holds for pumping at ν_{32}, and for either ν_{31} or ν_{32} the antimaser effect should be about 5, with only slight dependence on angle.

When $\theta = 90°$, levels 1 and 2 nearly coincide : their separation is only a few megacycles per second, whereas their widths are about 60 Mc/s. Thus pumping at ν_{42} inevitably implies pumping at ν_{41}, and, similarly, pumping at ν_{31} and ν_{32} are inseparable. This produces stronger maser and antimaser effects. For pumping at ν_{42} and ν_{41} ($=\nu_p$) the equation becomes

$$\frac{\Delta n_{34}}{\Delta_0 n_{34}} = 1 - \frac{\nu_p}{\nu_{43}} \cdot \frac{w_{13} + w_{23}}{w_{13} + w_{23} + w_{43}}, \tag{6}$$

and, for pumping ν_{31} and ν_{32} $(=\nu_p)$,

$$\frac{\Delta n_{34}}{\Delta_0 n_{34}}=1+\frac{\nu_p}{\nu_{43}}\cdot\frac{w_{14}+w_{24}}{w_{14}+w_{24}+w_{34}}. \tag{7}$$

The important conclusion from the above equations is that if the system is pumped at ν_{42} or ν_{41} the result can *only* be a maser effect (except in the unlikely event that at least two w's, e.g. w_{23} and w_{12} in equation (4a), are zero); and if pumped at ν_{31} or ν_{32} the result can only be an antimaser effect (unless two w's such as w_{14} and w_{12} in equation (5) are zero). In fact, at liquid helium temperatures, the opposite is observed: this shows that the picture of maser action presented above is not complete.

IV. Effect of Cross Relaxation on the Level Populations

The existence of cross-relaxation processes was first recognized by Bloembergen *et al.* (1959). They showed by a quantum-mechanical treatment that a group of neighbouring spins could execute simultaneous transitions under the influence of their mutual interaction. Figure 4 (*a*) shows a possible group of three closely neighbouring chromium ions α, β, and γ in a randomly distributed array. The probability of the simultaneous transition is greatest when the total energy of the participants is unchanged: that is, the cross-relaxation process is a type of resonance phenomenon. The conservation of energy need not be exact; there is a " line width " which is expected to be a few times greater than that of the levels themselves, and the latter is about 60 Mc/s in the ruby generally used in masers.

In ruby, with the magnetic field applied at the angle $\theta=29\cdot2°$ to the c-axis, it has been shown above that $2(E_4-E_3)=E_2-E_1$. Thus a cross-relaxation process is " on resonance " in which one spin jumps from E_2 to E_1, while two neighbours jump from E_3 to E_4. This process is illustrated in Figure 4 (*b*). The process of Figure 4 (*c*) is, of course, also on resonance and has the same effect on the level populations. We do not believe the two processes can be distinguished, and in what follows we shall, for clarity, speak in terms of the process of Figure 4 (*b*).

It is shown in the Appendix that the complete rate equation for, say, level 3 is now

$$\frac{dn_3}{dt}=\sum_{j\neq3}w_{j3}\left(n_j-n_3+\frac{Nh\nu_{j3}}{4kT}\right)+\sum_{j\neq3}W_{j3}(n_j-n_3)+2c^2w_c(n_1n_4^2-n_2n_3^2)/N^2. \tag{8}$$

The first term on the R.H.S. gives the contribution of the spin-lattice relaxations, the second that of the radiation-induced transitions, and the third that of the cross-relaxation processes. The cross-relaxation coefficient w_c depends on the quantum states of the Cr^{3+} ion and on the lattice spacings, and c is the ionic concentration of Cr^{3+} relative to Al^{3+}. In the steady state, of course, $dn_3/dt=0$.

Equation (8) and its companions may now be solved generally by the method of Shapiro and Bloembergen (1959). (In their notation c^2w_c would be called w_{124343}.) However, useful qualitative conclusions from equation (8) may readily be drawn. Let the pumping frequency be ν_{42}: then W_{42} is large but all W_{j3} are zero, so that the R.H.S. of equation (8) consists of only two terms. Since

$dn_3/dt=0$, and the first term on the R.H.S. is at most of order $w_{ij}N$, w_{ij} meaning a typical spin-lattice relaxation rate, it follows that

$$|(n_1n_4^2-n_2n_3^2)/N^3|\simeq w_{ij}/(c^2w_c).$$

If $c^2w_c\gg w_{ij}$, as we believe to be the case in our experiments at liquid helium temperatures (see below), the fractional difference between $n_1n_4^2$ and $n_2n_3^2$ must be very small. One may then treat the cross relaxations as imposing the restraint that $n_1n_4^2=n_2n_3^2$.

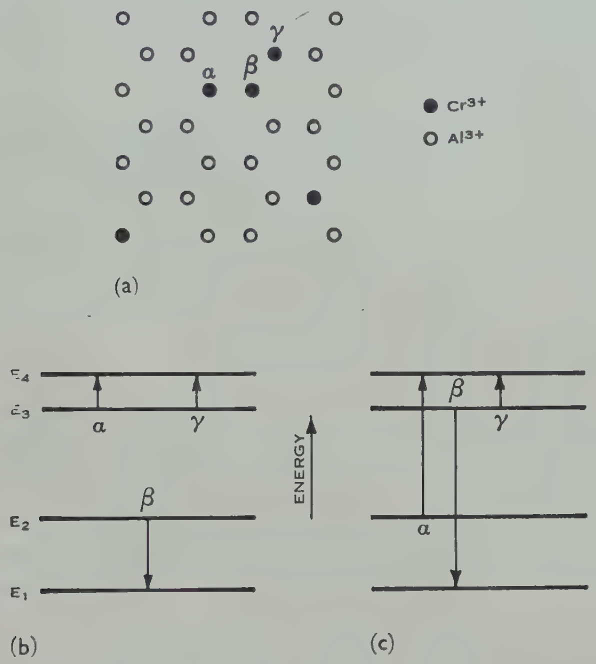

Fig. 4.—(*a*) Sketch of a small region of ruby crystal showing one of the occasional close groups of paramagnetic ions; (*b*) and (*c*) the cross-relaxation processes executed by a group when $E_2-E_1=2(E_4-E_3)$ as in ruby at $\theta=29°$.

Consider now the effect of cross relaxations when pumping at ν_{42}. Figure 3 (*a*) shows the system in equilibrium, Figure 3 (*b*) shows the effect of the constraint $n_2=n_4$ which is imposed by pumping at ν_{42}. Because $n_2=n_4$, the cross-relaxation constraint simplifies to $n_1n_4=n_3^2$. In other words, n_3 becomes the geometric mean of n_1 and n_4, or approximately the arithmetic mean, since all n's are supposed equal to within about $Nh\nu/4kT$. The cross relaxations, then, impose the restraint that $n_3=\frac{1}{2}(n_1+n_4)$. The effect of this last constraint is shown in Figure 3 (*c*). The final population difference $n_3'-n_4'$ is seen to be larger than in thermal equilibrium: in other words, there is an antimaser effect. (Strictly speaking, after n_3 is raised to n_3' all the populations in Figure 3 (*c*) should be reduced slightly to conserve total population; but this would have no effect on the argument, which is, in any case, only qualitative.)

The above discussion gives a physical picture of the way cross-relaxation processes can, near $\theta=29°$, reverse the maser effect which was expected on the basis of the old maser equations. We shall now give the results of the analytical treatment of the above situation and of others which are important for an understanding of our experiments.

(a) *Cross-relaxation Effects near* $\theta=29°$

At $\theta=29\cdot2°$, $\nu_{21}=2\nu_{43}$; the associated cross-relaxation process has been described immediately above.

(i) *Pumping at* ν_{42}.—For the general case, the solution of the set of equations like (8) leads to the result

$$\frac{\Delta n_{34}}{\Delta_0 n_{34}}=1-\frac{\nu_{42}}{\nu_{43}}\cdot\frac{w_1w_{23}+w_{13}w_{12}+(c^2w_c/16)(w_{23}-w_{13}-2w_{14})}{w_1(w_{23}+w_{34})+w_{13}(w_{12}+w_{14})+(c^2w/16)(w_3+4w_{12}+4w_{14})}. \qquad (9)$$

The reason why $c^2w_c/16$, rather than c^2w_c, enters the above equation is that, as shown in the Appendix, $c^2w_c/16$ is the quantity which has the same kind of significance as w_{ij}; that is, $c^2w_c/16$ is the rate per ion at which cross relaxations occur.

Three special cases of (9) are of interest.

(1) $c^2w_c/16\ll w_{ij}$'s.

This simply gives the familiar 4-level maser equation of equation (4*a*).

(2) $c^2w_c/16\gg w_{ij}$'s.

This is the case which has been qualitatively described above by means of Figure 3 (*c*). The equation is

$$\frac{\Delta n_{34}}{\Delta_0 n_{34}}=1+\frac{\nu_{42}}{\nu_{43}}\cdot\frac{2w_{14}+w_{13}-w_{23}}{w_3+4w_{12}+4w_{14}}, \qquad (10)$$

which bears out the conclusion of the "geometrical" method of Figure 3 that there is an antimaser effect (except in the unlikely event that $w_{23}>2w_{14}+w_{13}$).

(3) $c^2w_c/16=2w_{ij}$.

In this case, provided all the w_{ij} are equal, $\Delta n_{34}/\Delta_0 n_{34}=1$: that is, the application of pumping power leaves the absorption coefficient at ν_{43} unaffected. If the w_{ij}'s are not equal, the statement holds for some weighted average of the w_{ij}'s which could be computed from equation (9); but this refinement is hardly warranted in the present state of knowledge of the w_{ij}'s.

The variation of the maser effect for other ratios of w_{ij} to $c^2w_c/16$ is shown in Figure 5, again assuming equal w_{ij}'s.

(ii) *Pumping at* ν_{41}.—Proceeding as for equation (9), but with the simplification that $c^2w_c/16\gg w_{ij}$'s, we obtain

$$\frac{\Delta n_{34}}{\Delta_0 n_{34}}=1-\frac{\nu_{41}}{\nu_{43}}\cdot\frac{3w_{23}+2w_{24}+w_{13}}{4w_2+4w_{23}+w_3}, \qquad (11)$$

from which the important conclusion is that a maser effect is produced, just as in the absence of cross relaxations.

(iii) *Pumping at* ν_{31}.—With $c^2w_c/16 \gg w_{ij}$ as before, we obtain

$$\frac{\Delta n_{34}}{\Delta_0 n_{34}} = 1 - \frac{\nu_{31}}{\nu_{43}} \cdot \frac{2w_{23}+w_{24}-w_{14}}{w_4+4w_{12}+4w_{23}}. \tag{12}$$

This shows that, except in the unlikely event that $w_{14} > 2w_{23}+w_{24}$, there is a maser effect, contrary to the effect in the absence of cross relaxations.

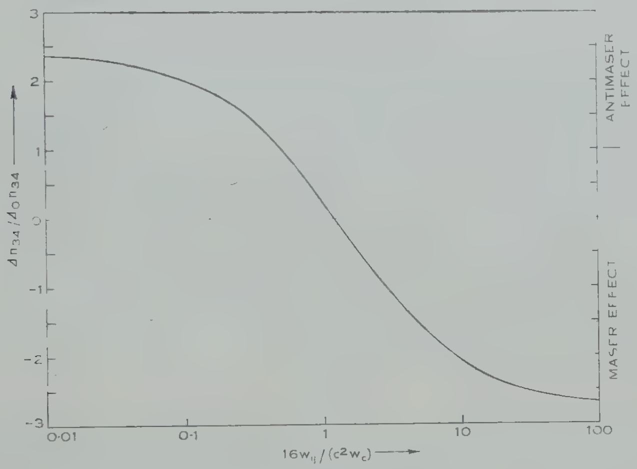

Fig. 5.—Variation of $\Delta n_{34}/\Delta_0 n_{34}$ as a function of the ratio of the spin-lattice relaxation rate w_{ij} to the cross-relaxation rate $c^2w_c/16$. The right-hand side of the diagram corresponds to higher temperature.

(*b*) *Cross-relaxation Effects near* $\theta = 55°$

At this angle $E_4 - E_3 = E_2 - E_1$, and the cross-relaxation process consists in an ion jumping from E_4 to E_3 while a neighbour jumps from E_1 to E_2. The quantity which must now be added to the rate equation for, say, level 3 is now readily shown to be $cw_c'(n_1n_4 - n_2n_3)/N$, where w_c' is quite distinct from the w_c which has been used for the $\theta = 29°$ case.

By the same kind of argument as before it is seen that the cross relaxations tend to equalize n_1n_4 and n_2n_3. The analysis in this case is very similar to that used by Shapiro and Bloembergen (1959); in their notation cw_c' would be called $w_{12,\,43}$.

The expressions given below have all been derived for the case $cw_c' \gg w_{ij}$.

(i) *Pumping at* ν_{42}.—

$$\frac{\Delta n_{34}}{\Delta_0 n_{34}} = 1 + \frac{\nu_{42}}{\nu_{43}} \cdot \frac{w_{14}-w_{23}}{w_{34}+w_{12}+w_{32}+w_{14}}. \tag{13}$$

(ii) *Pumping at* ν_{41}.—

$$\frac{\Delta n_{34}}{\Delta_0 n_{34}} = 1 - \frac{\nu_{41}}{\nu_{43}} \cdot \frac{2w_{23}+w_{24}+w_{31}}{2w_{23}+w_2+w_3}. \tag{14}$$

(iii) *Pumping at* ν_{31}.—The result is identical with (13) except that ν_{42} in that equation must be changed to ν_{31}. This identity is easy to understand physically: if the pumping makes $n_2=n_4$, the cross relaxations make $n_1=n_3$, and vice versa. At $\theta=55°$, of course, $\nu_{42}=\nu_{31}$ (Fig. 2).

The equality of ν_{42} and ν_{31} at 55° has another consequence: even if cross relaxations are negligible, pumping at ν_{42} or ν_{31} inevitably makes $n_2=n_4$ and $n_1=n_3$. The resulting equation for $\Delta n_{34}/\Delta_0 n_{34}$ is the same as equation (13). Thus, near 55°, it is difficult experimentally to distinguish whether cross-relaxation processes are dominant or not, when pumping at ν_{42} or ν_{31}.

V. SPIN-LATTICE RELAXATION RATES

The most complete set of measurements of the several w_{ij}'s which has been made appears to be that of Pace, Sampson, and Thorp (1960*a*, 1960*b*). (These authors quote values of the relaxation time T_1, but in the present discussion they have been converted to the corresponding relaxation rates $w=1/(2T_1)$.) At liquid air temperature it was found that the w_{ij}'s were nearly equal to each other while at liquid helium temperatures those transitions which had relatively low magnetic dipole moments were also found to have relatively low w's. The measurements were taken at much higher fields than in our experiments; but evidence was quoted that the relaxation rates were not strongly field dependent.

TABLE 1

ASSUMED VALUES OF THE w_{ij}'S AT 4° K ACCORDING TO THE "MAGNETIC DIPOLE MODEL" WITH FIELD ADJUSTED TO KEEP ν_{43} AT 1440 Mc/s (ARBITRARY UNITS)

θ	0°	30°	60°	90°
w_{34}	2·0	1·6	1·3	1·2
w_{23}	0·0	0·3	0·6	0·8
w_{12}	0·0	0·0	0·0	2·2
w_{24}	1·5	1·2	0·8	0·7
w_{13}	1·5	1·3	1·0	0·8
w_{14}	0·0	0·3	0·4	0·7

At the present state of knowledge it seems to us that the best course is to assume that at liquid helium temperatures the w_{ij}'s are proportional to the corresponding magnetic dipole transition probabilities, which are given, for example, by Howarth (1958) and Weber (1959). As an added refinement we have averaged the probabilities with regard to direction. The resulting spin-lattice relaxation rates, in arbitrary units, are given for several values of θ in Table 1. The field has been adjusted at each angle to maintain ν_{43} at 1440 Mc/s. We shall call this the "magnetic dipole model" of spin-lattice relaxation rates.

We also require the temperature variation of the spin-lattice relaxation rates. We have made measurements at several temperatures in the liquid oxygen and liquid helium ranges, by measuring the decay of the maser effect when the pumping power is switched off. The results are shown in Figure 6, together with those of Pace, Sampson, and Thorp (1960*a*, 1960*b*). The two curves taken together strongly confirm the conclusion of those authors that there is only slight dependence of relaxation rate on microwave frequency, in contrast to the theoretically predicted variation as ν^2 or ν^4 (Van Vleck 1940). The transition concerned in our relaxation measurements was that between the levels 3 and 4

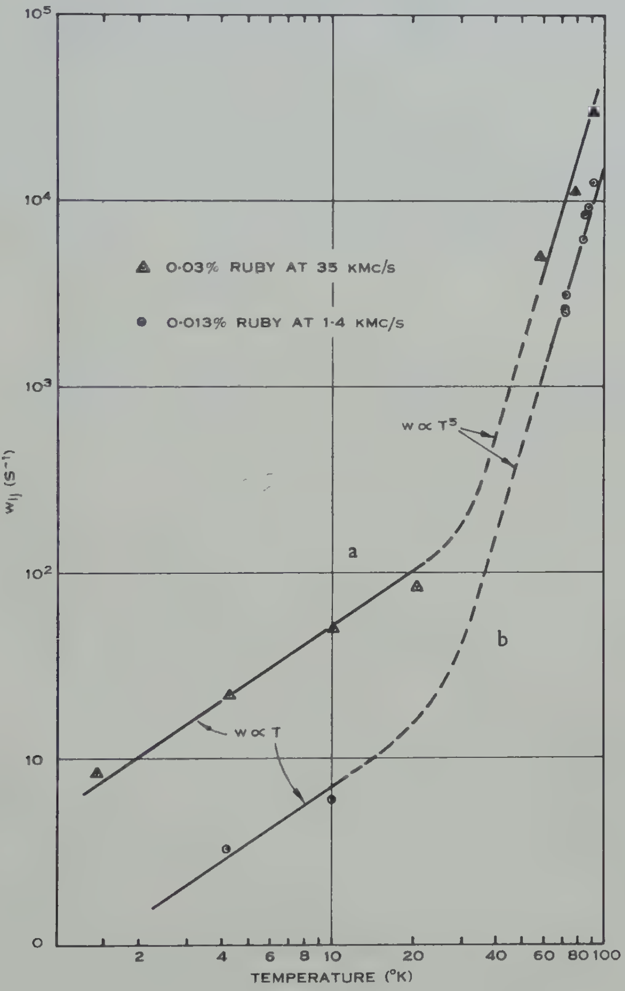

Fig. 6.—Measured and interpolated temperature-variation of the spin-lattice relaxation rate in ruby (*a*) at 35 kMc/s with 0·03% concentration (Pace, Sampson, and Thorp 1960*a*, 1960*b*); (*b*) at 1·4 kMc/s with 0·013% concentration (present work).

(i.e. between the ±1/2 states) and θ was 35° at liquid air temperatures (because this angle happened to favour strong pumping) and 90° at liquid helium temperatures (chosen in order to minimize cross-relaxation effects). It is true that the T^5 and T variations shown in the figure are not conclusively established by our own measurements but they are strongly suggested when the latter are taken together with the results of Pace, Sampson, and Thorp. Moreover, it will be seen below that this temperature variation is consistent with the observations of the change of the maser effect with temperature.

VI. EXPERIMENTAL BEHAVIOUR OF THE LOW-FIELD MODES

(*a*) *Experimental Procedure*

The experiments were carried out at temperatures between 4° and 90 °K with an X-band waveguide cavity containing an L-band quarter-wave strip-line resonator. The L-band frequency was fixed at 1440 Mc/s but a multiplicity of cavity resonances permitted a number of X-band pumping frequencies between 10 and 14 kMc/s to be used. (Strictly speaking, the frequencies from 12·4 to 14 kMc/s do not belong to X-band, but we shall use the term " X-band " for all our pumping frequencies.) Using a 50 c/s magnetic sweep, the L and X paramagnetic resonance lines could be displayed together on a double-beam oscilloscope. With the magnitude and orientation of the d.c. magnetic field adjusted so that the resonances coincided in field, the ratio of strengths of the 1440 Mc/s resonance with and without X-band pumping was noted. This ratio is equal to $\Delta n_{34}/\Delta_0 n_{34}$. Figure 7 shows examples

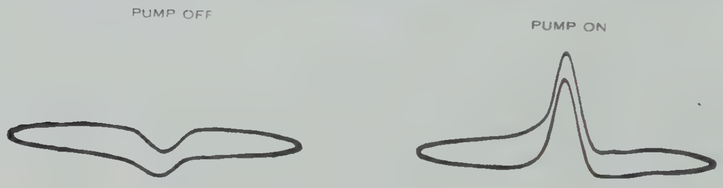

(a) PUMPING ν_{42} AT $\theta = 35$

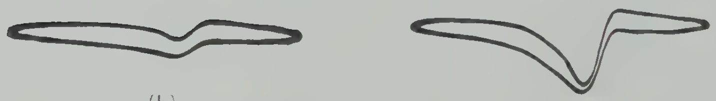

(b) PUMPING ν_{31} AT $\theta = 80$

Fig. 7.—Examples of (*a*) maser and (*b*) antimaser effects at 80 °K, pumping at 10·9 kMc/s. The magnetic sweep is 140 gauss peak-to-peak at 50 c/s and a downward dip corresponds to absorption. (The separation between the forward and backward traces is due to 50 c/s pick-up, and the asymmetry in (*b*) is due to a slight detuning of the L-band oscillator from the cavity resonant frequency).

(*a*) of stimulated emission or maser effect where $\Delta n_{34}/\Delta_0 n_{34}$ is negative, and

(*b*) of enhanced absorption or antimaser effect where $\Delta n_{34}/\Delta_0 n_{34}$ is positive and greater than unity.

The concentration of Cr^{3+} in the ruby used was found by comparing its paramagnetic resonance intensity with that of a weighed sample of $CuSO_4.5H_2O$. The atomic concentration of Cr^{3+} relative to Al^{3+} was estimated to be $0{\cdot}013 \pm 0{\cdot}003\%$.

Temperatures were measured with both a carbon resistor and a copper-constantan thermocouple, and the various temperatures between 4 and 60 °K were obtained sometimes by siphoning limited amounts of liquid helium into the cryostat and sometimes by following the slow warm-up of the cryostat after the evaporation of a charge of liquid helium. The temperature measurements in the above range are considered accurate to about ± 3 °K.

Because of the cut of the ruby used the angles θ available were limited to the range 20°–90°.

(*b*) *Behaviour at Liquid Air Temperature*

Maser effects are observed at all angles when pumping with ν_{41} or ν_{42}. With ν_{42}, the values of $\Delta n_{34}/\Delta_0 n_{34}$ are about -3, which is in agreement with the prediction of equation (4*a*). When ν_{31} is pumped, antimaser effects are observed with a magnitude typically of $+4$, in reasonable agreement with equation (5), which predicts $+5$.

(*c*) *Observations at Liquid Helium Temperatures*

There are now considerable variations with angle and we present the results in Figure 8 (pumping ν_{42} and ν_{41}) and Figure 9 (ν_{31}).

The essential features predicted by the cross-relaxation theory are exhibited. Near $\theta=29°$ both the ν_{42} and ν_{31} curves show the reversals which are predicted in equations (10) and (12). Near $\theta=55°$ they both show absence of any strong effect as predicted by equation (13), though (as discussed already in Section IV (*b*) (iii)) this is not definite evidence for a 55° cross-relaxation process. The curve for ν_{41} shows no maser reversal, which is in accordance with equations (11) and (14). The singularity in this curve at $\theta=55°$ is good evidence of the influence of the 55° cross-relaxation process.

The intensification of all effects at $\theta=90°$, which is expected from equations (6) and (7), is also clearly apparent. This is a consequence not of cross relaxation but, as has already been shown in Section III (*d*), of double pumping.

However, the quantitative predictions of the theory are not borne out by experiment. In Table 2 we compare the measured values of $\Delta n_{34}/\Delta_0 n_{34}$ with the predictions of the theory using both the magnetic dipole model of spin-lattice relaxation rates and the " homogeneous model " in which they are all equal.

The table shows that the actual effects are all smaller than expected from the theory. A possible explanation is that the w_{ij}'s are very different from those of either model. If, for example, at $\theta=29°$ the w_{ij}'s had the values given in Table 1 except that $w_{34}+4w_{12}=15$, then the theoretical ratios $\Delta n_{34}/\Delta_0 n_{34}$ would become $1\cdot 7$, $-0\cdot 8$, and $0\cdot 3$ for pumping at ν_{42}, ν_{41}, and ν_{31} respectively (experiment: $1\cdot 6$, $-0\cdot 6$, $0\cdot 0$). However, we believe that the true explanation is that at 4 °K a variety of other cross-relaxation processes, although not " on resonance ", have nevertheless attained an influence comparable to that of the spin-lattice relaxations. This situation has also been inferred by Mimms and McGee (1960), who have called it " general cross relaxation ". If the temperature were lowered further still (or the concentration raised) the situation would approach that discussed by Shapiro and Bloembergen (1959). They have shown that when the concentration is high enough the spin system as a whole warms up if any resonance is pumped: that is, $\Delta n_{34}/\Delta_0 n_{34}$ tends to zero, and maser action is impossible. Our case is less extreme; but it may be seen from Figure 8 that the effects are indeed diminishing as temperature is lowered. It appears that at about 20 °K the behaviour of 0·013% ruby would exemplify much better the theory presented in this paper. For example, near 20 °K and at $\theta=29°$ the observed effect when pumping ν_{42} is $+2\cdot3$ (theory, $+2\cdot4$); and at $\theta=55°$ pumping ν_{41} the effect is $-2\cdot4$ (theory, $-3\cdot5$).

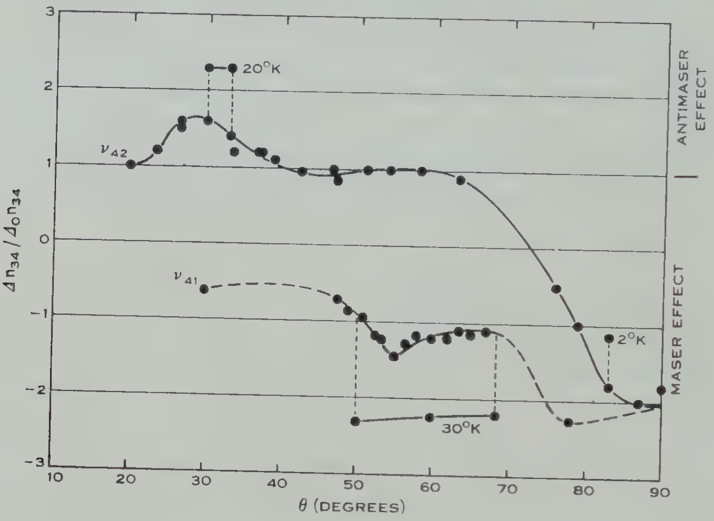

Fig. 8.—Maser and antimaser effects as a function of orientation when pumping at ν_{42} and ν_{41}. The temperature is 4 °K except where otherwise noted.

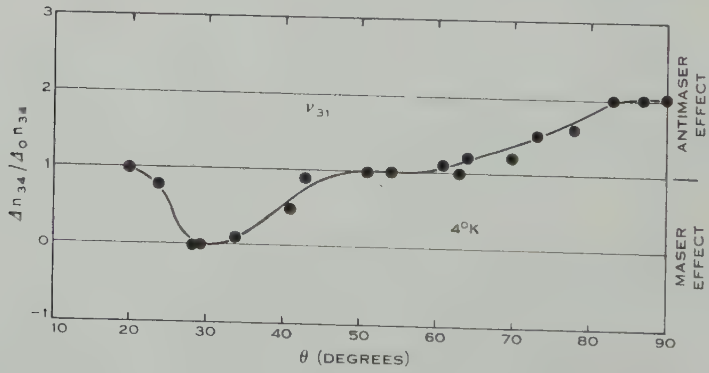

Fig. 9.—Variation of $\Delta n_{34}/\Delta_0 n_{34}$ with angle when ν_{31} is pumped at 4 °K.

(d) *Temperature Dependence of the Maser Effect*

It has been seen above that when the pumping frequency is ν_{42} and the angle θ is near 29° the maser effect reverses on cooling from liquid air to liquid helium temperatures. In Figure 10 we give tracings from oscilloscope photographs which show this change for $\theta=33°$. (These were taken in the early stages of the experiments when the *L*-band detector was a travelling-wave amplifier which was unduly susceptible to microphonic disturbances: the majority of our results have been obtained with a superheterodyne receiver which was much superior in this respect, as comparison of Figures 10 and 7 shows.)

During the course of the experiments a number of observations were made of the ratio $\Delta n_{34}/\Delta_0 n_{34}$ at various angles θ near 29° and various temperatures between 4 and 80 °K. Many of these are plotted as points in Figure 11. The points plotted as full circles are for θ close to its resonance value of 29°; and those as open circles and triangles for θ off-resonance by the amounts labelled. The curves have been calculated, choosing the value of $c^2 w_c/16$ which gives the best fit, by combining the information given by Figures 5 and 6. It may be seen that the on-resonance points are in good agreement with the theory with $c^2 w_c/16=700$/s and the 4° off-points with $c^2 w_c/16=180$/s. This statement is true of the change-over temperature region where the maser reversal is most rapid, and this fact increases our confidence in the assumptions underlying Figures 5 and 6 and in the values of $c^2 w_c/16$ deduced above. At helium temperatures the agreement is worse than appears from Figure 11 because the use of the magnetic dipole model of the w_{ij}'s, which should be a better approximation than the homogeneous model used for Figures 5 and 11, predicts an antimaser effect of nearly 4 as against the observed 1·6. We have already discussed how this effect is probably due to the participation of other cross-relaxation processes not on resonance (" general cross relaxation ").

TABLE 2

VALUES OF $\Delta n_{34}/\Delta_0 n_{34}$ AT 4 °K

Angle	$\Delta n_{34}/\Delta_0 n_{34}$		
	From Dipole Model	from Homogeneous Model	Experiment
	Pumping ν_{42}		
29	+3·7	+2·4	+1·6
55	+0·5	+1·0	+1·0
90	−3·8	−4·7	−2·0
	Pumping ν_{41}		
29	−3·3	−2·0	−0·6
55	−3·8	−3·5	−1·5
90	−3·8	−4·7	−2·0
	Pumping ν_{31}		
29	−3·0	−0·5	0·0
55	+0·5	+1·0	+1·0
90	+5·0	+6·0	+2·0

(e) *Profile of the 29° Cross-relaxation Process*

In the last section we have shown that the cross-relaxation rate $c^2 w_c/16$ falls from 700 to 180/s when θ is taken off-resonance by ±4°. Now it can easily be shown that between θ=20 and 40° the change of $2\nu_{43}-\nu_{21}$ is practically linear with angle, the slope being 63 Mc/s per degree, under the conditions of the

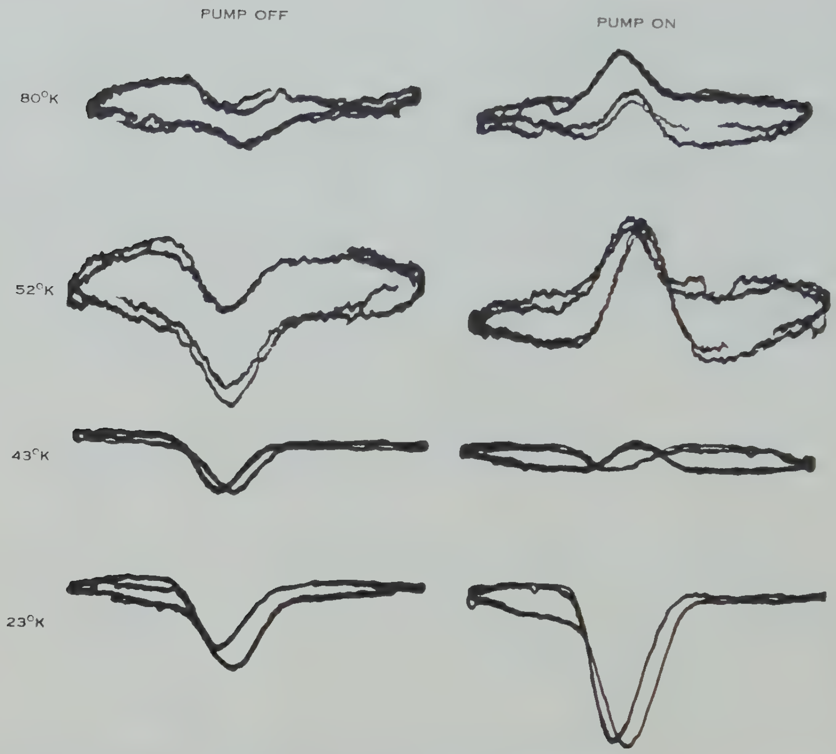

Fig. 10.—Maser reversal on cooling. The pumping frequency is ν_{42} and the angle 33°, and the method of display is the same as for Figure 7.

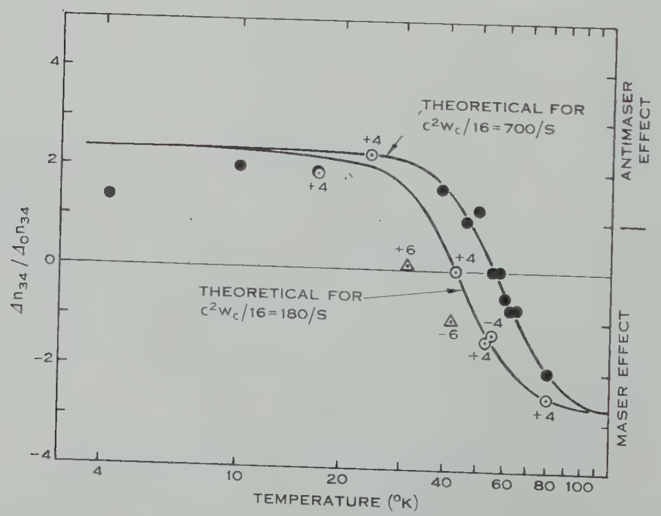

Fig. 11.—Maser reversal on cooling: values of $\Delta n_{34}/\Delta_0 n_{34}$ for pumping at ν_{42} with θ near 29°. The points are labelled with the values of $\theta - 29$ where this difference is greater than one degree.

experiment. Thus a plot of the cross-relaxation rate against angle is effectively a plot of the profile of the cross-relaxation resonance process. In Figure 12 we show the experimental points so plotted. The process of deducing $c^2w_c/16$ for a point is as follows: first the ratio of w_{ij}/c^2w_c is deduced from Figure 5 using the measured value of $\Delta n_{34}/\Delta_0 n_{34}$; then Figure 6 and the temperature of the measurement are used to derive w_{ij}, whence c^2w_c is known. The points in Figure 12 are labelled with the temperature of observation. Because of the strong temperature dependence of the spin-lattice relaxation rate we have been able to measure the cross-relaxation rate over the remarkably wide range of 100 : 1. To take advantage of this the rates are shown on a logarithmic scale. The points for 4 °K are rather uncertain because the theory underlying Figure 5 has obviously broken down at low temperatures, as discussed in relation to Figure 11. The points for temperatures other than 4 °K may be approximately fitted either by a Gaussian profile (full curve) with a half-width at half-intensity of 3·0° (190 Mc/s) or by a Lorentzian with a half-width of 2·0° (130 Mc/s). By taking into account the 4 °K points we conclude that the profile is more nearly Gaussian than Lorentzian, with maximum intensity 700 ± 100 s^{-1} and half-width 190 ± 30 Mc/s. In comparison, the half-widths of the paramagnetic resonance lines themselves are only about 30 Mc/s. We believe that this is the first measurement of a cross-relaxation profile in an electronic spin system.

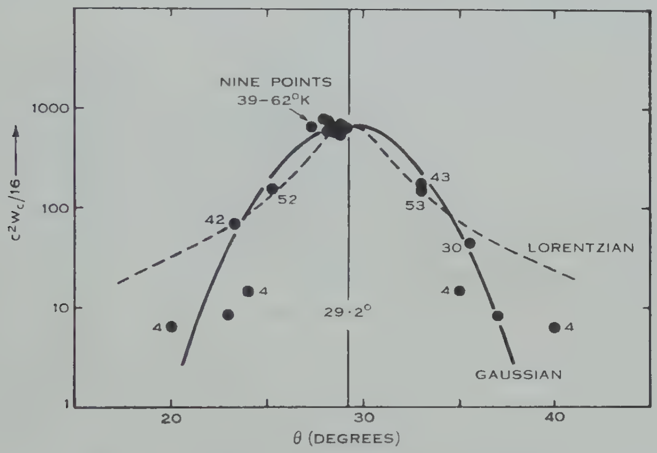

Fig. 12.—Profile of the θ = 29° cross-relaxation rate $c^2w_c/16$. Varying the angle from 29·2° takes the cross-relaxation process off resonance at the rate of 63 Mc/s per degree. The points are labelled with the temperature at which the measurement was made. Gaussian and Lorentzian curves are shown which give the best fit apart from the 4 °K points.

VII. Conclusions

(i) All the " anomalous " effects which we have observed in ruby are capable of explanation in terms of cross-relaxation processes. The effects at 4 °K are less extreme than predicted, probably owing to the influence of other " off-resonance " cross-relaxation processes; but it is suggested that at liquid hydrogen temperatures the individual 29° and 55° cross-relaxation effects would be manifested as strongly as predicted. For the $\theta=29°$ process the cross-relaxation term $c^2w_c/16$, which enters equation (9), has been found to have the value 700 s^{-1} in ruby with 0·013% chromium ion concentration. If the concentration were increased tenfold (to 0·13%) the cross-relaxation rate $c^2w_c/16$ would increase to 7×10^4 s^{-1}, and it may be seen using Figures 5 and 6 that strong anomalous maser effects would be observed at liquid air temperatures.

(ii) A method has been demonstrated for measuring the profile of the cross-relaxation process at $\theta=29°$. This could be developed to give much greater precision by constructing equipment in which the pumping frequency could be varied continuously and the temperature maintained at steady values between liquid air and liquid helium temperatures.

(iii) As regards the operation of low-field ruby maser; the best conditions appear (cf. Fig. 8) to be at $\theta\approx80°$ with pumping at ν_{41}, i.e. at about 12·4 Gc/s in the case of an *L*-band maser. The concentration of 0·013% is not necessarily the best for 4 °K operation. It appears that the low-field *L*-band maser has been hitherto unjustly neglected, for the inversion ratio is nearly half as great as in the more developed 2000 gauss type (Arams and Okwit 1959), and the amplifying transition is of comparable intensity and is more nearly circularly polarized. Useful maser action should also be obtainable at liquid air temperature, for the loss of performance associated with the twentyfold increase of temperature could be largely offset by a tenfold increase of chromium concentration.

(iv) The cross-relaxation measurements have an important bearing on the phenomenon of "clustering". Strandberg (1960, pp. 1319 and 1320) has suggested that the fact that the paramagnetic line widths in dilute ruby are greater than expected is due to a tendency of the chromium ions to cluster in groups instead of being randomly distributed. For a given average concentration c, any clustering must increase the average of c^2 and of c^2w_c. Thus, a measurement of the temperature variation of the maser effect at $\theta=29°$, which, as we have shown, effectively measures c^2w_c, would provide valuable contributory evidence of clustering and of its variation with annealing and other processes.

VIII. Acknowledgments

We are indebted to Mr. D. K. Milne for the construction of equipment and for assistance in the performance of the measurements, and to Professor N. Bloembergen who first suggested to us that our experiments could be explained in terms of cross relaxation.

IX. References

Arams, F. R., and Okwit, S. (1959).—*Proc. Inst. Radio Engrs., N.Y.* **47**: 992.
Autler, S. H., and McAvoy, N. (1958).—*Phys. Rev.* **110**: 280.
Bloembergen, N. (1956).—*Phys. Rev.* **104**: 324.
Bloembergen, N., Shapiro, S., Pershan, P. S., and Artman, J. O. (1959).—*Phys. Rev.* **114**: 445.
Bogle, G. S., and Symmons, H. F. (1959).—*Aust. J. Phys.* **12**: 1.
Bowers, K. D., and Owen, J. (1955).—*Rep. Progr. Phys.* **18**: 304.
Geusic, J. E., Schulz-Du Bois, E. O., DeGrasse, R. W., and Scovil, H. E. D. (1959).—*J. Appl. Phys.* **30**: 1113.

Howarth, D. J. (1958).—Royal Radar Establishment Memo. No. 1525.
Kikuchi, C., Lambe, J., Makhov, G., and Terhune, R. W. (1959).—*J. Appl. Phys.* **30** : 1061.
Mimms, W. B., and McGee, J. D. (1960).—*Phys. Rev.* **119** : 1233.
Pace, J. H., Sampson, D. F., and Thorp, J. S. (1960*a*).—*Phys. Rev. Letters* **4** : 18.
Pace, J. H., Sampson, D. F., and Thorp, J. S. (1960*b*).—Royal Radar Establishment Memo. No. 1693.
Shapiro, S., and Bloembergen, N. (1959).—*Phys. Rev.* **116** : 1453.
Strandberg, M. W. P. (1960).—*Proc. Inst. Radio Engrs., N.Y.* **48** : 1307.
Van Vleck, J. H. (1940).—*Phys. Rev.* **57** : 426.
Weber, J. (1959).—*Rev. Mod. Phys.* **31** : 681.

APPENDIX

Derivation of the Rate Equation in the Presence of Cross-relaxation Processes

It has been shown by Bloembergen (1956) that the rate equation for, say, level 3 is, disregarding cross relaxation,

$$\frac{\mathrm{d}n_3}{\mathrm{d}t}=\sum_{j\neq 3} w_{j3}\left(n_j-n_3+\frac{Nh\nu_{j3}}{4kT}\right)+\sum_{j\neq 3} W_{j3}(n_j-n_3), \tag{A1}$$

where the w's and W's are respectively spin-lattice relaxation rates and radiation-induced rates.

The contribution from cross-relaxation processes will now be derived. We shall confine ourselves to the situation in which $2(E_4-E_3)=E_2-E_1$, which is the case in ruby at low fields when $\theta=29°$. The following argument is intended to be read with the help of Figure 4 in the text.

If an ion is in level 3 and is at the lattice site α (Fig. 4 (*a*)), let us ask what is the probability of the cross-relaxation process shown diagrammatically in Figure 4 (*b*). (We disregard the inverse process for the meantime.) The process can occur only if sites β and γ (Fig. 4 (*a*)) are each filled with paramagnetic ions, and the chance of this is c^2, where c is the concentration of paramagnetic ions in the crystal. If β is filled, the chance that it is correctly filled with an ion in state 2 is n_2/N (for $N=n_1+n_2+n_3+n_4$) ; and similarly the chance that γ is correctly filled is n_3/N. Thus $c^2n_2n_3/N^2$ is the probability that the appropriate situation exists. Let the probability per second of a cross-relaxation transition under these circumstances be $w_{\alpha\beta\gamma}$; $w_{\alpha\beta\gamma}$ depends on quantum-mechanical variables and on the displacements of β and γ from α. The transition probability associated with these particular sites is then $w_{\alpha\beta\gamma}c^2n_2n_3/N^2$, and to dispose of the contribution of site α we must sum over all sites β and γ by replacing $w_{\alpha\beta\gamma}$ by

$$w_\alpha=\Sigma_{\beta\gamma}w_{\alpha\beta\gamma}.$$

As w_α is not necessarily the same for all sites α, let w_c be its average over unit cell of the crystal lattice ; then the total number of transitions in the crystal becomes

$$n_3\cdot w_c c^2n_2n_3/N^2.$$

Remembering now the inverse transitions, the net number of transitions is seen to be $c^2w_c(n_2n_3^2-n_1n_4^2)/N^2$. The effect of these transitions may now be added to equation (A1), noting that each transition takes one ion from level 2 to 1 but two ions from 3 to 4. Thus the rate equation for level 3 is

$$\frac{\mathrm{d}n_3}{\mathrm{d}t}=\sum_{j\neq 3} w_{j3}\left(n_j-n_3+\frac{Nh\nu_{j3}}{4kT}\right)+\sum_{j\neq 3} W_{j3}(n_j-n_3)+2c^2w_c(n_1n_4^2-n_2n_3^2)/N^2.$$

The above treatment shows that $c^2w_c/16$ is the quantity which has the same kind of significance as w_{ij}. For just as w_{ij} is the number of spin-lattice processes in one direction per ion per second, so is $c^2w_cn_2n_3/N^2$ the number of cross-relaxation processes in one direction per ion per second, and $n_2n_3/N^2\simeq 1/16$.

THE RADIO BRIGHTNESS DISTRIBUTION ON THE SUN AT 21 CM FROM COMBINED ECLIPSE AND PENCIL-BEAM OBSERVATIONS

By T. Krishnan* and N. R. Labrum*

[*Manuscript received March* 8, 1961]

Summary

A study of the brightness distribution on the Sun at 21-cm wavelength on April 8, 1959, is described. High resolution observations were made of the partial eclipse on that day with a simple radiometer of high sensitivity. The brightness distribution of the uneclipsed Sun at the same wavelength was obtained using a cross-grating interferometer, which enabled the bright regions to be located accurately.

Considerable similarity is shown to exist between the sizes, shapes, and relative intensities of radio bright regions and optical plages faculaires. The radio plages appear to overlie the plage faculaire at a height of about 70 000 km and have temperatures compatible with normal coronal temperatures at that height. The hypothesis that the enhanced radio emission originates thermally from coronal condensations would appear to be upheld. No significant radiation from small sources, which would be visible with the higher resolution, was detected.

The quiet-Sun distribution for this period of sunspot maximum appears to be similar to that derived by Labrum (1960), i.e. there is limb brightening at the equator but not at the poles, the temperatures being twice the sunspot minimum values. The higher resolution appears to reveal a higher peak temperature and gradient for the limb brightening, which is theoretically to be expected, but which has previously not been observed, probably owing to the smoothing effect of aerials of lower resolution.

I. Introduction

Early observations of the emission of radiation from the Sun at decimetre wavelengths showed that the radiation was normally steady over short periods but varied with periods comparable to the period of rotation of the Sun. These observations were made with aerials whose beamwidths to half-power points were much greater than the angular size of the Sun. For convenience, we shall refer to such low resolution devices, when used for observation of the Sun, as " radiometers ".

Covington (1947) observed a partial eclipse of the Sun with a radiometer at 10·7 cm wavelength. He found that there was a sharp decrease in the flux density simultaneous with the occultation of a large visible sunspot group, suggesting the presence of a localized radio source associated with the sunspot group. This was confirmed by statistical studies of the day-to-day variation in radio emission from the whole Sun at various decimetric wavelengths (Pawsey and Yabsley 1949 ; Denisse 1949). It was found that there was always a close correlation between the radio flux at a particular wavelength and the projected sunspot area and that by fitting a line of regression it was possible to distinguish

---

* Division of Radiophysics, C.S.I.R.O., University Grounds, Chippendale, N.S.W.

clearly between two main components of the solar radiation. The extrapolated value of flux corresponding to an unspotted disk was named the " quiet-Sun component " ; the variable part of the radiation, which was proportional to sunspot area, was named the " slowly varying component ".

The quiet-Sun component could be understood as being due to thermal radiation from the whole of the Sun. However, the association between the slowly varying component and sunspot area was less obvious. Since radio emission at decimetre wavelengths originates at levels many thousands of kilometres above the photosphere, the visible sunspots cannot themselves be the sources of the slowly varying component. This was confirmed by eclipse observations due to Christiansen, Yabsley, and Mills (1949), who showed that in some cases radio sources were present over the sites of old sunspot groups which were no longer visible. A search for solar features, associated with sunspot groups, longer-lived, and high enough above them to allow emission of radio waves, seemed desirable. Waldmeier and Müller (1950) suggested that coronal condensations might be the source of the slowly varying component.

The development of aerial arrays with higher resolving power than that of the simple radiometer made a systematic study of the brightness distribution on the Sun at decimetre wavelengths possible. At decimetre wavelengths these arrays took the form of the grating interferometer due to Christiansen and Warburton (1953) which was later developed into the crossed grating interferometer (Christiansen *et al.* 1961), the former having a fan-shaped beam and the latter a pencil beam. The beamwidths of these instruments was 2′ to 3′ of arc.

From a detailed study at 21 cm of bright regions with the grating interferometer, Christiansen, Warburton, and Davies (1957) were able to show that they had sizes from 3′ to 10′, that they lay in the solar atmosphere at an average height of about 25 000 km, and that they had peak temperatures of the order of 2×10^6 °K. These results were confirmed by two-dimensional observations with the crossed grating interferometer (Christiansen and Mathewson 1958).

An interesting discovery made by Christiansen, Warburton, and Davies was that the radio sources appeared to be always associated with plages faculaires and appeared when resolved to have the same size as the associated plages. Christiansen and Mathewson (1958) confirmed that there is a close correlation between plage areas and the sizes of the radio sources.

Christiansen *et al.* (1960) have described the results of combined optical and radio observations made on an international scale. The radio observations were at wavelengths of 7·5, 21, 88, and 176 cm. The results support the hypothesis that the slowly varying component is thermal in origin, having its source in dense regions which are at about normal coronal temperatures ; these regions invariably overlie plages faculaires and extend radially outward. They have also shown that for a wavelength of 21 cm the size and shape of a radio bright region or " radio plage " correspond to those of the associated chromospheric plage. The correspondence in shape is very striking in the illustration they have given (Fig. 14 of their paper). In the same paper Figure 20 shows the good correlation that exists between the peak brightness of plages faculaires seen in the *K* line of calcium and the peak brightness of the associated radio regions.

High resolution studies of the quiet-Sun component have been made at sunspot minimum and maximum. Christiansen and Warburton (1955) found that the distribution of brightness of the quiet Sun at a wavelength of 21 cm showed quadrant rather than circular symmetry, i.e. there was limb brightening at the equator but not at the poles. The peak temperature at the limbs on the equator was $6 \cdot 8 \times 10^5$ °K, while the temperature at the centre of the Sun's disk was $4 \cdot 6 \times 10^5$ °K.

Observations of the distribution at the same wavelength have been repeated in this laboratory in 1958, close to sunspot maximum, using fan and pencil-beam scanning of the Sun (Labrum 1960). While a detailed distribution could not be derived because of the very great intensity of the slowly varying component, it was shown that there is limb darkening at the poles and that the distribution does not appear to have changed in shape between minimum and maximum of the current sunspot cycle. The temperatures, however, are nearly twice the values obtained at minimum.

Eclipse observations can provide much greater resolution than any of the interferometers that have so far been used. Theoretically, the resolution is limited only by diffraction at the edge of the Moon. This limit at a wavelength of 21 cm is of the order of $\frac{1}{10}'$ of arc. In practice, the limit is set by the ability of the radiometer to measure small changes in the received power. It was of interest, therefore, to make observations of the partial eclipse of April 8, 1959, with the greatest available sensitivity and see whether the higher resolution produced a distribution that was in agreement with the results previously obtained from arrays.

We were interested in particular in finding out more of the detail of the structure of radio plages to see whether the hypothesis of thermal origin in condensations was still tenable. Intense and small bright regions that might be smoothed out by larger aerial beams leading to lower estimates of temperature would be revealed by the high resolution obtained at the eclipse.

The higher resolution was also expected to yield more information on the distribution of the quiet-Sun component than has so far been available. In observations of the distribution of the quiet-Sun component the effects of incomplete resolution have been noticed. In the distribution derived for sunspot minimum by Christiansen and Warburton (1955) the brightening at the solar equator, often called the " ear component ", appears much broader than is to be expected theoretically and this has been attributed by Smerd and Wild (1957) to aerial smoothing. It was hoped that observations made during the eclipse would reveal the presence of any limb brightening and show up its detail.

An eclipse observation with a single radiometer, though it has higher resolution than that given by most arrays, does not allow location of bright regions unambiguously. We have been able to overcome this difficulty by obtaining the brightness distribution on the uneclipsed Sun nearly simultaneously using a crossed grating interferometer with a resolution of 4′ of arc.

II. The Circumstances of the Eclipse

The eclipse of April 8, 1959 was annular along a path running across the continent of Australia. At Sydney it was visible as a partial eclipse. First contact optically was at 1159 hr Eastern Australian Standard Time and last contact at 1505 hr E.A.S.T. Maximum phase of the eclipse occurred at 1337 hr.

The circumstances of the eclipse at the point of observation near Sydney are shown in Figure 1. The circumstances were particularly favourable for radio observations. The whole of the northern hemisphere of the Sun was eclipsed. The solar elevation above the horizon was greater than 35° throughout the eclipse period so that no difficulties due to ground reflection were experienced.

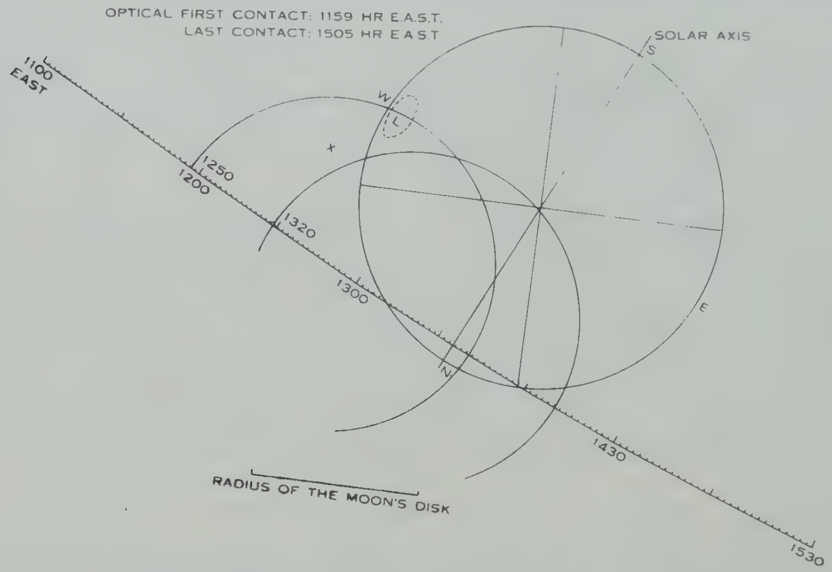
OPTICAL FIRST CONTACT: 1159 HR E.A.S.T.
LAST CONTACT: 1505 HR E.A.S.T
SOLAR AXIS
S
1100
EAST
W
L
x
1250
1200
1320
1300
E
N
1430
1530
RADIUS OF THE MOON'S DISK

Fig. 1.—The circumstances of the eclipse of April 8, 1959, as seen from the point of observation. The positions of the moon's disk for 1250 and 1320 relate to the discussion in Section IV (*b*).

III. Equipment

The main observations consisted of a record of the total flux density of radiation at 1423 Mc/s (21 cm wavelength) from the Sun using a total power radiometer. In addition, the crossed grating interferometer at Fleurs was used on the morning of the eclipse at 1000 hr E.A.S.T. to obtain a contour map (Fig. 2) of the brightness distribution on the solar disk.

The 1423 Mc/s radio isophotes in Figure 2 were measured with a beamwidth of 4′ of arc, i.e. with much lower resolution than that to be anticipated from the eclipse observations. However, the map gives the locations of the main bright regions and thus eliminates the ambiguities that otherwise would inevitably have occurred in interpreting an eclipse record from a single radiometer.

The total power radiometer used was at Pott's Hill, some 12 miles west of Sydney. The aerial was that used for routine observations of the flux of solar radiation. It is a section of a parabola about 18 ft square and has a beamwidth to half-power points of 2°·3 at our frequency of 1423 Mc/s. In the interest of obtaining high stability the aerial was driven automatically and manually corrected at frequent intervals so that it followed the Sun within 5′ of arc.

The receiver was a conventional superheterodyne receiver preceded by a Dicke switch. The noise factor was nine and the bandwidth 500 kc/s. In order to minimize the effect of receiver gain fluctuations, noise power from a good commercial noise generator was injected through the compariosn arm of the switch, the level being adjusted in the course of the eclipse by means of precision attenuators. The difference between input noise temperatures in the two positions of the switch was never greater than 400 °K.

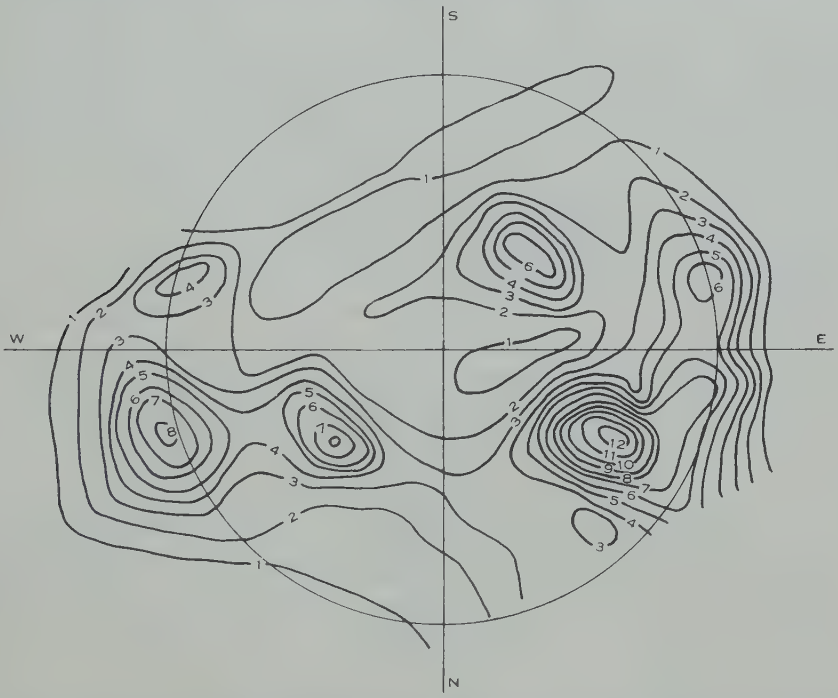

Fig. 2.—The brightness distribution on the solar disk on April 8, 1959, derived with the crossed grating interferometer (beamwidth 4′ of arc) is shown. The unit is 10 000 °K.

Trials made with the whole system on a number of days before the eclipse showed that the output was consistently steady. In the absence of solar activity, the output meter did not show a single excursion greater than 1% of the power received from the Sun. We have therefore concluded that the record obtained during the eclipse is good to $\pm\frac{1}{2}$%.

IV. The Derivation of the Brightness Distribution

The data obtained from the radiometer observations during the eclipse are plotted in Figure 3, which shows the flux visible as a percentage of the flux from the uneclipsed Sun against time. Values of the flux were taken from the record at intervals of 1 min of time so that the curve shown is smoothed to that extent. The temperature of the input of the receiver due to the uneclipsed Sun was 2900 °K, the corresponding aerial temperature being 5800 °K.

The rate of motion of the Moon's disk across the Sun is approximately 1′ of arc in 4 min of time ; this is the fastest rate of eclipsing at any point on the lunar limb. Therefore, any region on the Sun of size greater than $\frac{1}{4}'$ and having more than 1% of the total flux would be resolved in Figure 3.

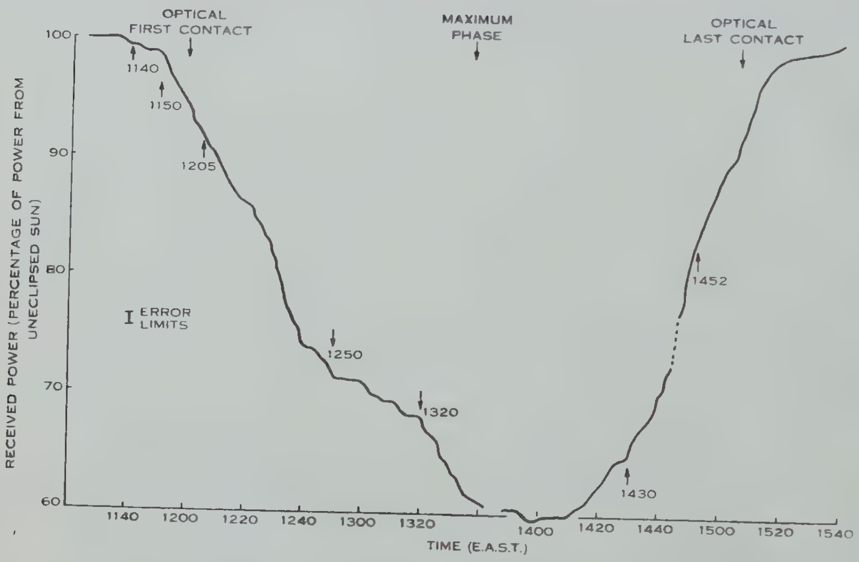

Fig. 3.—The power received by the radiometer from the Sun during the eclipse is shown. The curve was obtained by taking values at intervals of 1 min from the output record of the radiometer. The dashed region corresponds to an interval of 2 min when calibrations were made. The arrows show the various times of interest in Section IV.

The most obvious first step was to compare these results with the contour map (Fig. 2) obtained by the cross. The contour map was therefore eclipsed and the resulting curve compared with the one shown in Figure 3. While the overall shapes were similar, the two curves did not show agreement in detail, probably owing to the difference in resolution.

It therefore seemed desirable to interpret the eclipse curve obtained from the radiometer observation independently of the contour map, using the latter merely as a guide to the location of the main radio plages.

In order to do this it is necessary to separate the quiet-Sun and the slowly varying component in some way. External data that will allow identification of one component has to be induced and then the distribution of the other deduced. In principle, we cannot obtain a unique and unambiguous distribution of either component. In practice, however, the eclipse curve itself indicates the quiet-Sun model to be used and there is a striking similarity between radio plages and plages faculaires, so that it is possible to arrive at a pair of distributions that are more plausible than any other.

(*a*) *The Similarity between Optical and Radio Plages*

We felt that in trying to obtain information about the radio plages eclipsed in our observation, it would be instructive to study the distribution of plages faculaires seen in the K line of calcium. As a calcium spectroheliogram was not locally available we took for our study one provided for us by Mrs. Helen Dodson-Prince of the McMath Hulbert Observatory. This spectroheliogram on 35 mm film was taken 10 hr earlier and a print of it is shown in Plate 1.

As the photometer at our disposal had a comparatively large aperture and it was necessary to obtain a picture with resolution equivalent to that of the eclipse observation, an enlarged negative transparency was made on a glass plate. On this plate the diameter of the solar image was 5 cm and the slit of the photometer corresponded to a size of $\frac{1}{4}'$ of arc. The intensity of the image was plotted as a contour map, and the background Sun subtracted by inspection of the lower envelope of each scan. The bright areas were then represented by contours with intervals which were multiples of the background intensity, as measured from our enlargement. The contour which represented $1\cdot5$ times the background intensity was taken as the one defining the outer boundary of the plages.

The intensity scale we have used depends on the contrast introduced by the several photographic processes, but from a re-examination of the original 35 mm film with a microphotometer, and using calibration strips provided for the original 35 mm film we were able to assure ourselves that there had been no significant distortion of the intensity scale for our purpose. In our analysis the units of intensity are quite arbitrary and it is only necessary that the gradients of intensity taken along any line on the enlarged image should be proportional to the gradients of intensity taken along the same line on the original film.

As we have pointed out, Plate 1 represents the plages on the Sun 10 hr before the eclipse observation, and it seemed desirable to make an initial comparison between the optical and radio plages before correcting the distribution for this discrepancy. For the comparison the region marked "E" on the plate was chosen, as it was the only region which was sufficiently isolated to avoid complications due to the difference in heights of optical and radio plages.

We obtained the slope of the eclipsing of the optical region E in arbitrary units and compared it, after normalizing, with the slope of the eclipse curve for the corresponding radio region. The slopes were used for the comparison because it is the slope of the eclipse curve that represents the distribution of brightness temperature across the region. Figure 4 shows the two slopes arranged so that the peaks coincide in time. In normalizing the optical curve to fit the radio curve we assumed that the minimum slope immediately preceding the peak of the radio curve represented the gradient of quiet-Sun eclipsing.

The similarity between the two curves in Figure 4 is very striking, and leads us to hope that the resemblance might persist for all the plages on the disk.

(b) *The Quiet-Sun Model to be Assumed*

The curve of eclipsing shown in Figure 3 gives some indication of the distribution of the quiet-Sun component.

Firstly, it will be noticed that the radio eclipse begins much sooner than the optical. This indicates that the radio Sun extends beyond the photosphere.

Secondly, the eclipse curve is very flat between 1250 and 1320 hr, despite the fact that in the latter half of this period the bright radio region corresponding to the optical plage marked '*a*' in Plate 1 is being eclipsed. To obtain such a flat curve a bright source must be emerging somewhere on the opposite limb of the Moon.

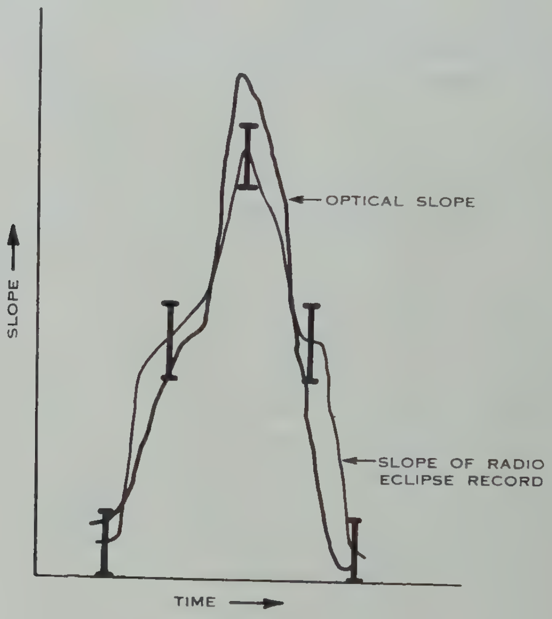

Fig. 4.—A comparison of the slope of the eclipse curve with the slope of the artificial eclipsing of region *E* (marked on Plate 1) as observed in the *K* line of calcium. The two curves are approximately normalized.

In Figure 1 we have drawn the positions of the lunar limb at 1250 hr and 1320 hr. The source being unobscured must lie between these two positions.

If a source were to be postulated in the solar atmosphere which was of the same nature as a radio plage we would expect it to lie in the same latitude belt as that of most of the plages observed optically, and given the limiting boundaries drawn it would have to be at a height above the photosphere of 100 000 km at least, with its centre somewhere near the spot marked *X* in Figure 1. Such a source would have to possess about 60% of the flux associated with the region marked *a* in Plate 1. The flux, associated with region *a*, which is unobscured between 1430 and 1452 hr, is of the order of 18·5% of the total solar flux, so

RADIO BRIGHTNESS DISTRIBUTION ON THE SUN

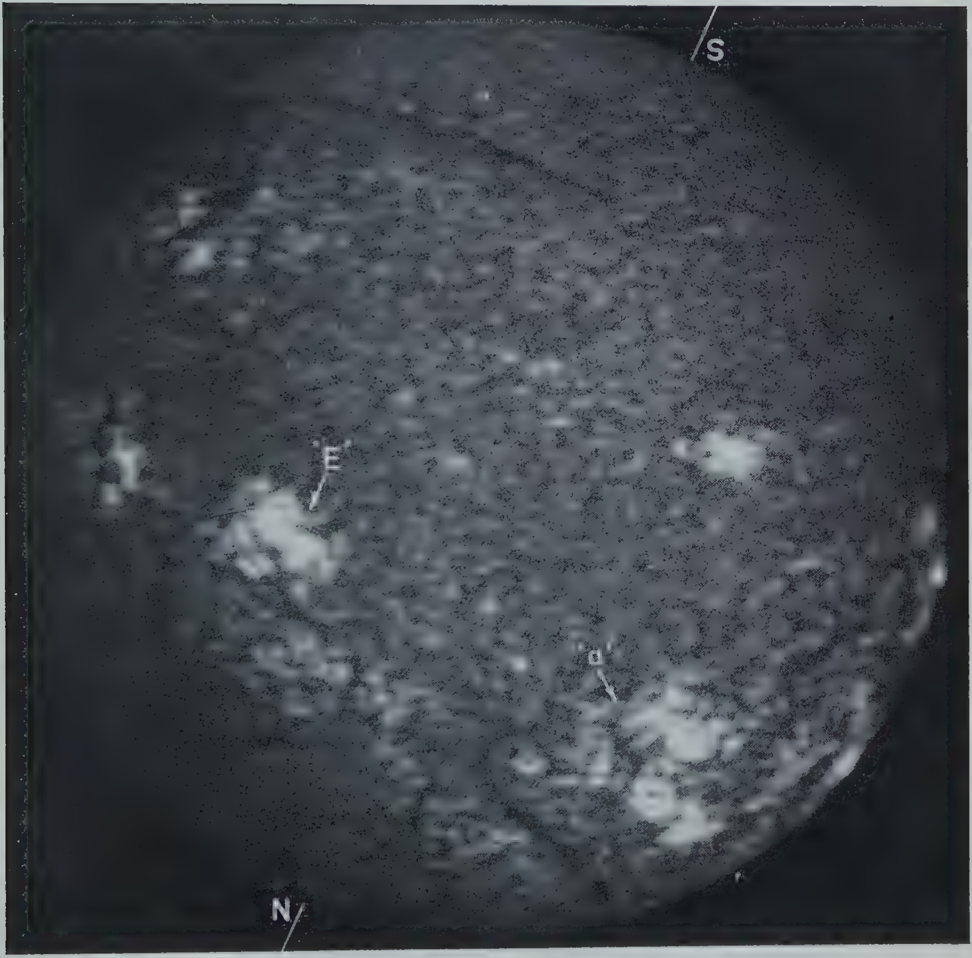

The picture of the Sun taken in the *K* line of calcium 10 hr before the eclipse that was used for the analysis (by courtesy of the McMath-Hulbert Observatory). The region marked "*E*" was used for the comparison of slopes of eclipsing in Figure 4; that marked "*a*" is discussed in Section IV (*b*).

that the region centred at X would have a flux of the order of 11%. Since the region at X would be eclipsed between 1140 and 1205 we should expect a decrease in flux of this order between these two times, while the observed decrease is no greater than 7%.

It can be seen that such a source seems implausible. In addition to the disparity we have pointed out there is also the problem of the large size of the order of 5′ which would have to be attributed to it. A source of this nature, at the limb, would be considerably foreshortened, and would therefore have been very large at meridian transit ; radio maps obtained by the cross in the previous fortnight do not show any such large radio region on the face of the Sun.

All these problems may be overcome by assuming that the source is on the solar equator near the region marked L in Figure 1. Here, the lunar limb obscures and unobscures small areas of the Sun in comparatively long periods of time. Such a source is available in the form of the ear component of the quiet-Sun distribution obtained by Christiansen and Warburton (1955). Alternatively, a model of the quiet Sun consisting of a uniform disk with a bright circular ring around it might suffice. We shall show in the next section how the results lead to some discrimination between plausible quiet-Sun models.

(*c*) *The Brightness Distribution on the Sun*

In subsection (*a*) we concluded with the hope that the close resemblance between the one pair of optical and radio plages would extend to all the bright regions on the Sun. In order to test this it is necessary to take into account the solar rotation which would have taken place between the taking of the calcium spectroheliogram and the time of the eclipse. The angle of rotation was 5° for the latitude belt where most of the plages were situated. The spectroheliogram contour diagram was suitably compensated for this rotation. In order to save laborious corrections, the shapes of the regions in the middle of the disk were retained : a more detailed point-by-point adjustment was, however, made for the regions at the limbs of the Sun. Figure 5 shows the distribution obtained for the northern half of the Sun, which alone was eclipsed by the moon ; the contours are expressed in the units we have explained in subsection (*a*).

In order to check whether the resemblance between optical and radio plages persists for all bright regions on the Sun it is necessary to subtract all quiet Sun effects from the radio eclipse curve. The optical plage picture that has been obtained does not contain any information on the background distribution at K line wavelength, and even if this distribution were available there would be no reason to expect any similarity between it and the radio quiet-Sun distribution.

Our measurements using arrays (Labrum 1960) suggest that near sunspot maximum the appropriate distribution is that of Christiansen and Warburton (1955) scaled up in temperature by a factor of 2. These measurements give a quiet-Sun flux density of $6 \cdot 2 \times 10^{-21}$ Wm^{-2} (c/s)$^{-1}$. This value was based on the use of daily total flux data, provided by the Heinrich Hertz Institute at Berlin, corrected to our frequency by assuming a linear relationship between flux density and frequency over the range 1420–1500 Mc/s. In order to be consistent, we have obtained the value of the total flux on the day of the eclipse by the same procedure. This value, corresponding to 100% in Figure 3, is $15 \cdot 6 \times 10^{-21}$ $\mathrm{Wm}^{-2}\ (\mathrm{c/s})^{-1}$.

The model of the quiet Sun that we have used to subtract quiet-Sun effects is the one indicated by our array observations (Labrum 1960). It has the flux shown above and in structure is identical to the one derived for sunspot minimum by Christiansen and Warburton (1955).

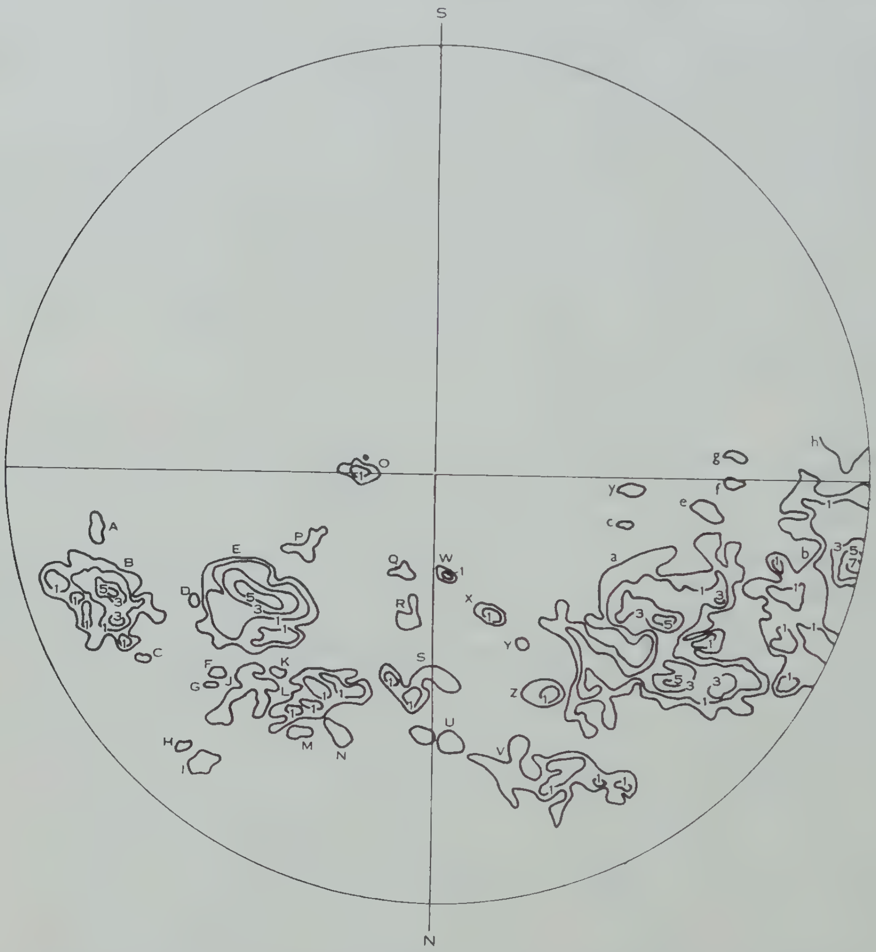

Fig. 5.—The distribution of optical plages as seen in the *K* line of calcium is shown. This was obtained by photometering the distribution shown in Plate 1 and compensating for the rotation of the Sun between the taking of Plate 1 and the time of the eclipse. The contour intervals are those described in Section IV (*a*). The outermost contours are not numbered and the letters attached to each region are used to label them for discussion.

In Figure 6 are plotted three curves. Curve *B* is obtained by artificially eclipsing the assumed quiet-Sun model; curve *C* by subtracting curve *B* from the eclipse curve in Figure 2. Curve *C* thus represents the eclipse record that would have been obtained if the quiet Sun had not been present and if the radio plages alone were eclipsed. Curve *A* is the result of artificially eclipsing the plage faculaire distribution derived and shown in Figure 5. From the arbitrary units in which Figure 5 is drawn this curve has been scaled by arranging that the maximum amount eclipsed is the same as that of curve *C*, i.e. 34%.

A general similarity in shape between *A* and *C* is apparent but the curves are displaced. It is of interest to note that the radio eclipse is earlier in the first part of the eclipse and later during the closing stages. This is to be expected, as the radio regions would be situated above the plages faculaires in the solar atmosphere.

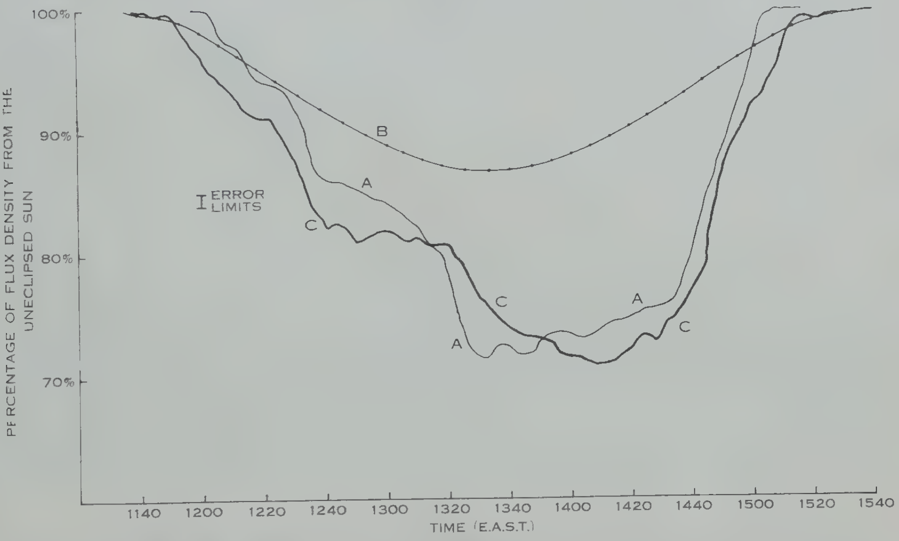

Fig. 6.—A comparison between the optical plage distribution and a radio plage distribution based on an assumed quiet-Sun distribution. The optical plage distribution was *not* compensated for height for this comparison. *A*, the curve obtained by eclipsing the optical distribution shown in Figure 5. *B*, the curve obtained by eclipsing an assumed quiet-Sun distribution ; in this case the one indicated for sunspot maximum by our array observations (Labrum 1960) and is described in Section IV (*c*). *C*, this curve is obtained by subtracting curve *B* from the eclipse curve in Figure 3. Curve *A* has been scaled so that the maximum power eclipsed is the same as for curve (*C*).

It is not possible from Figure 6 to derive the heights of the regions individually, as most of the time both eclipsing and uneclipsing of different regions is taking place. However, in the curves marked *A* shown in Figures 7 (*a*) to 7 (*d*) we have arranged for the contour diagram to be adjusted for a uniform height of the bright regions of 70 000 km, radially outwards from the centre of the Sun. This height was obtained by estimating the height of region *B* in Figure 5, from the differing time of eclipsing as shown by Figure 6. This height seemed reasonable to assume, as Christiansen and Mathewson (1958) have pointed out that heights can vary from 20 000 to 100 000 km. The bright regions were moved bodily by the amount appropriate to their centres ; no further adjustments to their shapes were made.

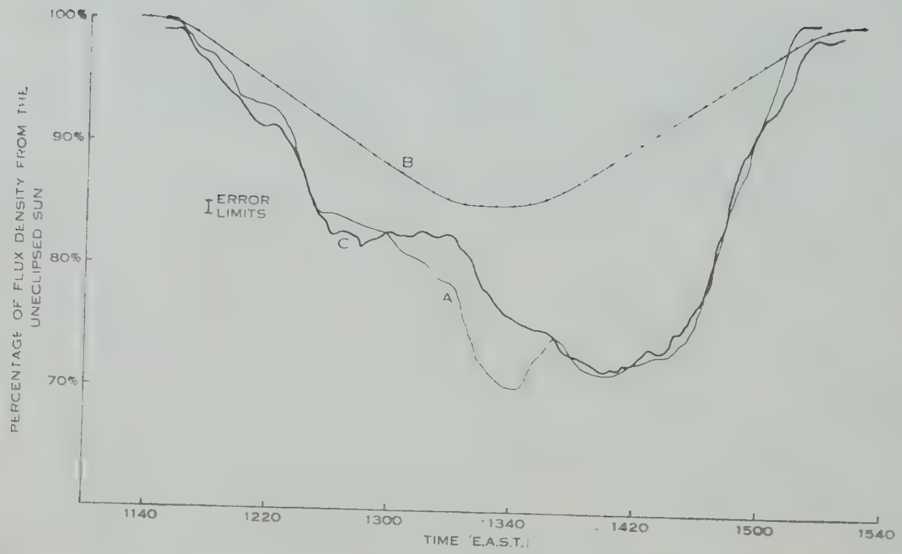

Fig. 7 (*a*).—These curves are obtained by methods similar to those of Figure 6 with two differences. All curves *A* are similar and are obtained by eclipsing the optical distribution of Figure 5 adjusted to lie radially at a height of 70 000 km above the photosphere. The four curves *B* in Figures 7 (*a*) to 7 (*d*) are obtained by eclipsing different models of the quiet Sun as described in Section IV (*c*) and whose distributions are shown with the same numbering in Figures 8 (*a*) and 8 (*b*). The four curves *C* are then obtained by subtracting curve *B* in every case from the eclipse curve of Figure 3.

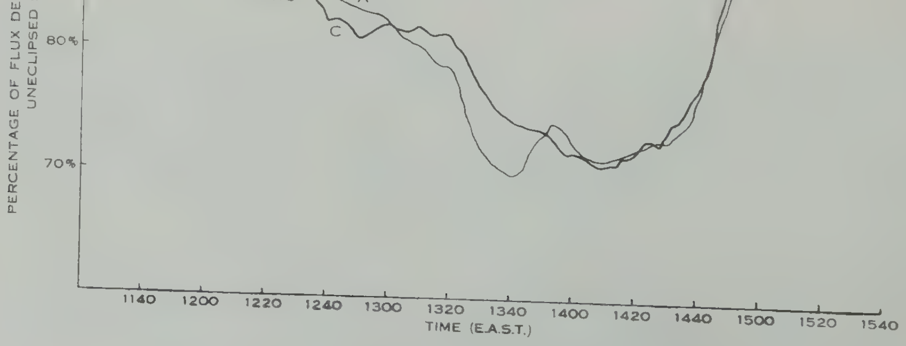

Fig. 7 (*b*).—For explanation see **Figure 7 (*a*).**

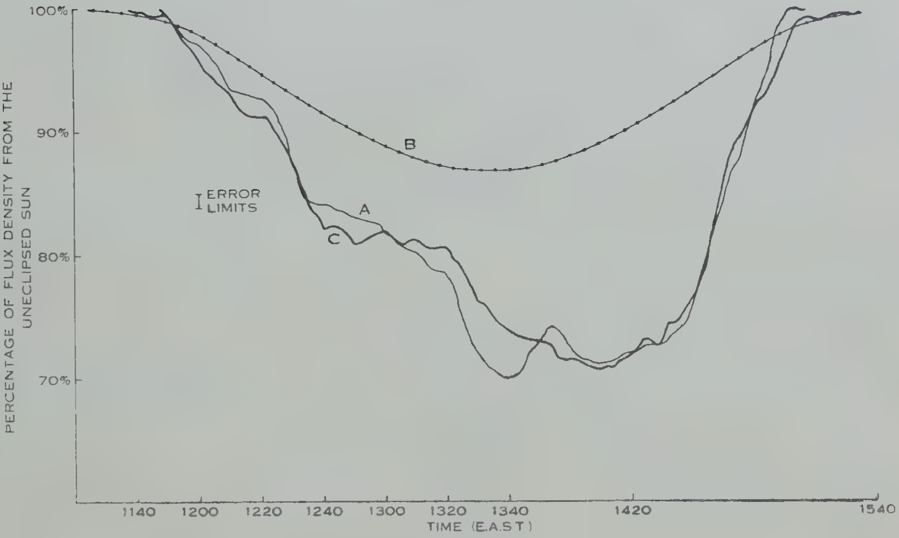

Fig. 7 (*c*).—For explanation see Figure 7 (*a*).

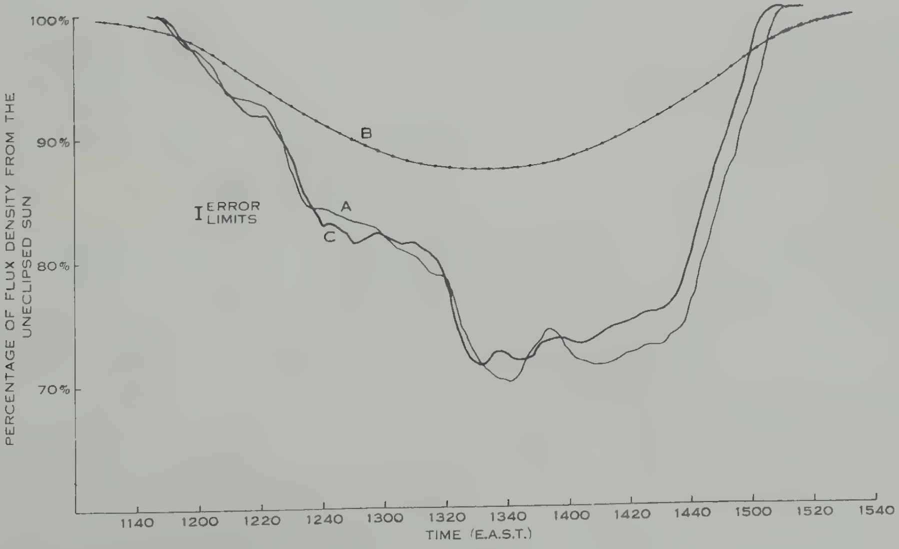

Fig. 7 (*d*).—For explanation see Figure 7 (*a*).

The four curves marked B have been obtained by artificially eclipsing four different models of the quiet Sun and subtracting the resultant curves from the eclipse record as was done for Figure 6. The flux density ascribed to the quiet Sun is in each case 40% of the flux from the uneclipsed Sun. The four models are:

(1) a uniform disk of radius $1\cdot3$ times the photospheric radius $R_\odot$,

(2) a uniform disk of radius $1\cdot2R_\odot$ containing 75% of the quiet-Sun flux with a narrow ring around it containing the remaining 25%,

(3) a Christiansen-Warburton (1955) type of distribution with the temperatures scaled up by a factor of approximately 2, and

(4) the same type of distribution as in (3) with the temperature gradient in the ear component alone scaled up by a factor of two.

The temperature distributions of all four models along the line joining the poles and along the line perpendicular to this direction are shown in Figures 8 (*a*) and 8 (*b*).

It will be seen that the agreement between curves A and C improves as we go down the list of models, until (4) gives the best fit. This is presumably due to the fact that an ear component with a steep gradient exists on the Sun.

There is still some disparity between the two curves in the closing stages of the eclipse; this would appear to be due to the fact that the intense bright region on the eastern limb of the Sun has a height greater than 70 000 km.

Model (4) was proposed mainly to reduce the disparity we have remarked on in subsection (*b*). It is tempting to improve on this model by increasing the temperature gradient in the ear component even more than in this model. However, it is doubtful whether such a step would have much extra validity, as any further adjustments would probably be within the limits of error of the eclipse data.

It would thus seem that the eclipse record can be explained by assuming a quiet-Sun distribution similar to that of Christiansen and Warburton for sunspot minimum, with the temperature gradient of the ear component stepped-up and having temperatures as shown by Model (4) of Figure 8, accompanied by a radio plage distribution identical to that of plages faculaires as seen in the K line of calcium but located radially above the plages at a height of about 70 000 km.

(*d*) *Brightness Temperatures of the Radio Plages*

With the brightness distribution of the radio plages assumed to be similar to that of optical plages it is possible to obtain temperatures for the contours marked in arbitrary units in Figure 5. For a source of uniform brightness the flux density S is related to the brightness temperature according to the relationship

$$S=2\cdot77\times10^{-23}T_b\Omega/\lambda^2\ \mathrm{Wm^{-2}\ (c/s)^{-1}},$$

where Ω is the solid angle subtended by the source and λ is the wavelength in metres. The brightness temperatures of the contours shown in Figure 5 are evaluated thus and the contour unit is equal to $3\cdot5\times10^5$ °K. Thus, that would be the temperature ascribed to the contour marked 1, the contour marked 2 is $7\cdot0\times10^5$ °K, and so on to the highest value 8 which is equivalent to a brightness temperature of 28×10^5 °K.

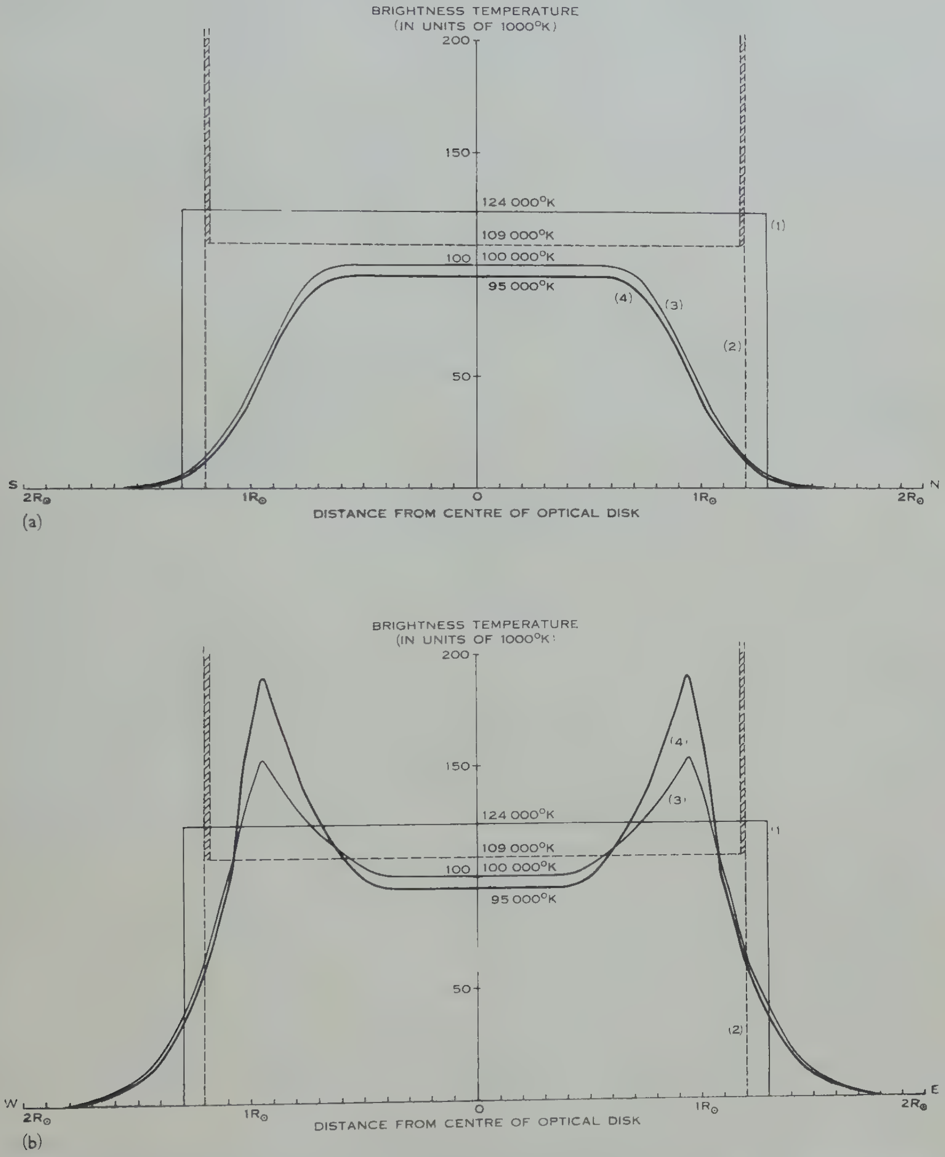

Fig. 8.—These depict the four quiet-Sun distributions used in the analysis. Distances from the centre of the optical disk are in units of the photospheric radius $R_{\odot}$. (*a*) is a plot of the distribution along the solar axia and (*b*) along a line perpendicular to the axis and passing through the centre of the disk. The distributions shown are: (1) A uniform disk of radius $1 \cdot 3$ times the photospheric radius $R_{\odot}$. (2) A uniform disk of radius $1 \cdot 2R_{\odot}$ containing 75% of the quiet-Sun flux with a narrow ring around it containing the remaining 25%. The narrow ring is shown but its extent is indeterminate. (3) A Christiansen-Warburton (1955) type of distribution with the temperatures scaled up by a factor of 2 for sunspot maximum. (4) The same type of distribution as in (3) with the temperature gradient in the ear component alone scaled up by a factor of 2.

A comparison between the distribution derived in this way and the cross map (Fig. 2) shows that for regions well inside the limb the eclipse observations show temperatures of about twice the values obtained from the cross. This is an indication of the extra information obtained due to the higher resolution.

For the region on the eastern limb the temperature that we have derived seems much higher than that from the cross. It should, however, be pointed out that the temperatures obtained from the eclipse are not as reliable for this region as for the others owing to its small apparent size due to foreshortening.

V. DISCUSSION

The quiet-Sun model that we have derived agrees with other observations in this laboratory (Labrum 1960) taken at sunspot maximum. While the method of analysis does not allow a very sensitive interpretation of the distribution of the quiet-Sun component, our result does seem to indicate limb brightening at the equator and the absence of limb brightening at the poles. The fact that the model with the gradient of the ear component stepped-up, fits best, indicates a limb-brightened model closer to those predicted theoretically than the Christiansen and Warburton (1955) model for sunspot minimum, and brings out the advantages of higher resolution obtained at eclipse observations. It is interesting in this connexion to note that Tanaka and Kakinuma (1959) in the interpretation of their eclipse observations of April 1958 (near sunspot maximum) have also been led to suggest an ear component.

The peak temperatures of the bright regions are of the order of $1 \cdot 5 \times 10^6$ °K for the large regions, which indicates that the regions are at normal coronal temperatures. The heights we have obtained also seem to indicate that the hypothesis that the slowly varying component originates in over-dense regions of the corona lying above plages faculaires is correct. In this connexion it is interesting to note that the small regions we have taken into account do not have any appreciable flux density. If they had they would have contributed fluctuations of short period in the observed eclipse curve (a source of size 1′ would exhibit a fluctuation in the curve of period 4 min of time).

The very close relationship on the day of the eclipse between the optical and radio plages, both in intensity and shape, has allowed us to derive the distributions. While such a relationship has been suspected before (Dodson 1954), a detailed correlation as demonstrated here had not been clearly shown until this observation. It is not possible from observation of the Sun on one day to say that this similarity always holds. It would be desirable to obtain comparable fan-beam observations of both radio plages and optical plages faculaires over a period of time. If the similarity is persistent, it will be possible with eclipse observations, of greater sensitivity and resolution than ours, to allow for the radio plage component and obtain detailed quiet-Sun distributions which would be of considerable theoretical interest.

VI. ACKNOWLEDGMENTS

This work was done with the enthusiastic cooperation of many others. In particular, we would like to thank Mr. G. Fairweather, Mr. E. Harting, Mr. C. Turrall, and Mr. M. Willing.

Other observatories provided much of the data and facilities. We are grateful to Mrs. Helen Dodson-Prince for her cooperation, and also to Herr Hachenburg of the Heinrich Hertz Institute, to Professor Bok of the Mount Stromlo Observatory, and to Miss Marie McCabe, C.S.I.R.O. Division of Physics, Sydney.

One of us (T. Krishnan) was indebted to the Government of the Commonwealth of Australia for the award of a Colombo Plan Senior Fellowship during the course of which this work was done.

Dr. J. L. Pawsey and Professor W. N. Christiansen gave us much encouragement and guidance, without which this study would not have been possible.

VII. References

Christiansen, W. N., *et al.* (1960).—*Ann. Astrophys.* **23**: 75.

Christiansen, W. N., Labrum, N. R., McAlister, K. R., and Mathewson, D. S. (1961).—*Proc. Instn. Elect. Engrs.* **108B**: 48.

Christiansen, W. N., and Mathewson, D. S. (1958).—I.A.U.–U.R.S.I. Radio Astronomy Symposium, Paris, 1958, p. 108.

Christiansen, W. N., and Warburton, J. A. (1953).—*Aust. J. Phys.* **6**: 190.

Christiansen, W. N., and Warburton, J. A. (1955).—*Aust. J. Phys.* **8**: 474.

Christiansen, W. N., Warburton, J. A., and Davies, R. D. (1957).—*Aust. J. Phys.* **10**: 491.

Christiansen, W. N., Yabsley, D. E., and Mills, B. Y. (1949).—*Aust. J. Sci. Res.* A **2**: 506.

Covington, A. E. (1947).—*Nature* **150**: 405.

Denisse, J. F. (1949).—*C.R. Acad. Sci., Paris* **228**: 1571.

Dodson, Helen W. (1954).—*Astrophys. J.* **119**: 564.

Labrum, N. R. (1960).—*Aust. J. Phys.* **13**: 700.

Pawsey, J. L., and Yabsley, D. E. (1949).—*Aust. J. Sci. Res.* A **2**: 198.

Smerd, S. F., and Wild, J. P. (1957).—I.A.U. Symposium No. IV on Radio Astronomy, held at Jodrell Bank, 1957, p. 290. (Cambridge Univ. Press.)

Tanaka, H., and Kakinuma, T. (1959).—*Proc. Res. Inst. Atmos. Nagoya University* **6**: 63.

Waldmeier, M., and Müller, H. (1950).—*Z. Astrophys.* **27**: 58.

ANHARMONICITY AND THE THERMAL EXPANSION OF SOLIDS

By G. C. Fletcher*

[*Manuscript received January 26, 1961*]

Summary

Using many-particle perturbation theory an attempt has been made to improve the author's previous calculation of the thermal expansion of sodium chloride and to assess the effect of including anharmonic terms in the crystal potential. The results are disappointing; agreement with experiment is poor except at low and moderate temperatures. One reason for this is the poor convergence of a method based on the series expansion of the crystal potential in terms of particle displacements, a point further illustrated by calculations of specific heat and compressibility.

I. Introduction

A previous calculation of the thermal expansion of sodium chloride by the author (Fletcher 1959; hereafter referred to as I) exhibited a large discrepancy between theory and experiment. The most likely reason for this appeared to be neglect of the anharmonicity of the interionic forces and in the present work a calculation has been made in which the lowest order anharmonic terms in the potential energy of the crystal have been included. In developing an expression for their contribution to the free energy of the crystal a development of many-particle perturbation theory by van Hove (1959; hereafter referred to as vH), designed to avoid spurious divergencies, has been used. In Section II a brief review is given of the notation used in I with certain changes made, bringing it more into conformity with that of vH. In Section III parts of vH which are essential for the present work are briefly summarized and in Section IV the specific formula used for the quartic contribution to the free energy in this work is derived. Practical details of the calculation of the thermal expansion, specific heat at constant volume, and isothermal compressibility of sodium chloride are given in Section V and a discussion of the results in Section VI.

II. Review of the Harmonic Problem

As in I, consider a crystal, in which unit cell of volume v_a is determined by lattice vectors $\mathbf{a}_1$, $\mathbf{a}_2$, $\mathbf{a}_3$ and contains s particles, whose positions in the cell are given by the basis vectors $\mathbf{r}_\varkappa$ ($\varkappa=1, 2, \ldots, s$). Let the $\varkappa$th particle of mass $m_\varkappa$ in cell $\mathbf{l}=(l_1, l_2, l_3)$ (l_i integral or zero), whose equilibrium position is

$$\mathring{\mathbf{r}}_\varkappa^{\mathbf{l}}=\mathbf{a}^{\mathbf{l}}+\mathring{\mathbf{r}}_\varkappa=l_1\mathbf{a}_1+l_2\mathbf{a}_2+l_3\mathbf{a}_3+\mathring{\mathbf{r}}_\varkappa, \tag{1}$$

suffer a displacement $\mathbf{u}_\varkappa^{\mathbf{l}}$ to the position $\mathbf{r}_\varkappa^{\mathbf{l}}$. Assuming central forces between pairs of particles, depending only on their distances apart, the total potential energy $\mathbf{\Phi}$ of the crystal may be expanded in powers of the Cartesian components $u^{\mathbf{l}}_{\varkappa\alpha}$ ($\alpha = x, y, z$) of the $\mathbf{u}^{\mathbf{l}}_{\varkappa}$, i.e. $\mathbf{\Phi} = \mathbf{\Phi}^{(0)} + \mathbf{\Phi}^{(2)} + \mathbf{\Phi}'$, where $\mathbf{\Phi}^{(0)}$, $\mathbf{\Phi}^{(2)}$ are as given by $\mathbf{\Phi}_0$, $\mathbf{\Phi}_2$ in I and $\mathbf{\Phi}' = \sum\limits_{\nu=3}^{\infty} \mathbf{\Phi}^{(\nu)}$, where

---

* Department of Applied Mathematics, University of Sydney.

$$\mathbf{\Phi}^{(\nu)} = \sum_{\mathbf{l}_1, \ldots, \mathbf{l}_\nu} \; \sum_{\varkappa_1 \ldots \varkappa_\nu} \; \sum_{\alpha_1 \ldots \alpha_\nu} C^{(\nu)}_{\mathbf{l}_1\varkappa_1\alpha_1, \ldots, \mathbf{l}_\nu\varkappa_\nu\alpha_\nu} u^{\mathbf{l}_1}_{\varkappa_1\alpha_1} \ldots u^{\mathbf{l}_\nu}_{\varkappa_\nu\alpha_\nu}. \tag{2}$$

The Hamiltonian of the system is then $H = H^{(2)} + \mathbf{\Phi}'$, where

$$H^{(2)} = \mathbf{\Phi}^{(0)} + \tfrac{1}{2} \sum_{\varkappa, \mathbf{l}} m_\varkappa \, | \, \dot{\mathbf{u}}^{\mathbf{l}}_{\varkappa} \, |^2 + \mathbf{\Phi}^{(2)} \tag{3}$$

will be termed the harmonic Hamiltonian. In general the expectation value of $\mathbf{\Phi}^{(\nu)}$ can be shown to be of order $\omega(u/d)^{\nu-2}$ per unit volume, where ω is a typical particle vibration frequency, u an average particle displacement for a given temperature T, and d the separation of the mean positions of two neighbouring particles. Thus this series expansion of $\mathbf{\Phi}$ and the subsequent treatment of $\mathbf{\Phi}'$ as a perturbation to the harmonic problem will only be valid when $u \ll d$, i.e. for T reasonably small compared with the melting point T_M of the crystal.

If $\mathbf{\Phi}'$ is neglected, normal solutions

$$\mathbf{u}^{\mathbf{l}}_{\varkappa} = (\alpha_{\mathbf{q}j} - \mathrm{i}\alpha'_{\mathbf{q}j}) \mathbf{V}_{\varkappa\mathbf{q}j} \exp \mathrm{i}\mathbf{q} \cdot \mathring{\mathbf{r}}^{\mathbf{l}}_{\varkappa} \tag{4}$$

of the Lagrangian equations of motion may be found as in I. As compared with I, $\mathbf{k}$ has been replaced by $\mathbf{q}/2\pi$ and $\mathbf{U}_\varkappa(\mathbf{k}, i) \exp[-\mathrm{i}\omega(\mathbf{k}, i)t]$ by $(\alpha_{\mathbf{q}j} - \mathrm{i}\alpha'_{\mathbf{q}j})\mathbf{V}_{\varkappa\mathbf{q}j}$, $\alpha_{\mathbf{q}j}$ and $\alpha'_{\mathbf{q}j}$ being real; the notation $\omega(\mathbf{k}, i)$ will be changed to $\omega_{\mathbf{q}j}$. $\mathbf{V}_{\varkappa\mathbf{q}j}$ corresponds to $\mathbf{e}^{(n)}_{\mathbf{q}j} - \mathrm{i}\mathbf{f}^{(n)}_{\mathbf{q}j}$ of vH so that $\mathbf{V}_{\varkappa, -\mathbf{q}j} = \mathbf{V}^*_{\varkappa\mathbf{q}j}$ while

$$\alpha_{-\mathbf{q}j} = \alpha_{\mathbf{q}j}\,; \quad \alpha'_{-\mathbf{q}j} = -\alpha'_{\mathbf{q}j}\,; \quad \dot{\alpha}_{-\mathbf{q}j} = \dot{\alpha}_{\mathbf{q}j}\,; \quad \dot{\alpha}'_{-\mathbf{q}j} = \dot{\alpha}'_{\mathbf{q}j}, \tag{5}$$

a dot denoting differentiation with respect to time t. It is assumed that

$$\ddot{\alpha}_{\mathbf{q}j} = -\omega^2_{\mathbf{q}j}\alpha_{\mathbf{q}j}\,; \quad \ddot{\alpha}'_{\mathbf{q}j} = -\omega^2_{\mathbf{q}j}\alpha'_{\mathbf{q}j}. \tag{6}$$

The usual cyclic boundary conditions restrict $\mathbf{q}$ to the vectors $\mathbf{q} = q_1\mathbf{b}_1 + q_2\mathbf{b}_2 + q_3\mathbf{b}_3$, where $\mathbf{a}_i \cdot \mathbf{b}_j = \delta_{ij}$, $q_i = 2\pi h_i/L$, ($h_i = 0, 1, \ldots, L-1$), and $L^3 = N$ is the number of cells in the lattice. A translation vector of the reciprocal lattice will be denoted by $\boldsymbol{\tau} = \tau_1\mathbf{b}_1 + \tau_2\mathbf{b}_2 + \tau_3\mathbf{b}_3$ (τ_i integral or zero) and α, α', $\dot{\alpha}$, and $\dot{\alpha}'$ are unaltered in changing $\mathbf{q}$ to $\mathbf{q} + 2\pi\boldsymbol{\tau}$.

There are $3s$ solutions of the form (4) for each vector $\mathbf{q}$, denoted by the suffix j ($j = 1, 2, \ldots, 3s$). The $\mathbf{V}_{\varkappa\mathbf{q}j}$ with weighting factors $m^{\frac{1}{2}}_\varkappa$ are orthogonal to one another for the same $\mathbf{q}$ and different j and may be assumed normalized to unity in the sense that

$$\sum_{\varkappa} m_\varkappa \mathbf{V}_{\varkappa\mathbf{q}j} \cdot \mathbf{V}_{\varkappa\mathbf{q}j'} = \delta_{jj'}. \tag{7}$$

A general solution of the harmonic problem may then be taken as a linear combination of solutions (4). For the quantum mechanical treatment of the problem the normal coordinates α, α' and their conjugate momenta $\dot{\alpha}$, $\dot{\alpha}'$ must be replaced by operators. The most convenient ones are combinations of the form

$$A_{\mathbf{q}j} = \tfrac{1}{2}(V/8\pi^3\hbar)^{\frac{1}{2}} [\omega^{\frac{1}{2}}_{\mathbf{q}j}(\alpha_{\mathbf{q}j} - \mathrm{i}\alpha'_{\mathbf{q}j}) + \mathrm{i}\omega^{-\frac{1}{2}}_{\mathbf{q}j}(\dot{\alpha}_{\mathbf{q}j} - \mathrm{i}\dot{\alpha}'_{\mathbf{q}j})], \tag{8}$$

and $A^{*}_{\mathbf{q}j}$, where $V=Nv_a$ ($\equiv\Omega$ of vH). These obey the commutation relations

$$[A_{\mathbf{q}j}, A^{*}_{\mathbf{q}'j'}]=\delta_{jj'}\Delta(\mathbf{q}-\mathbf{q}')\,; \quad [A_{\mathbf{q}j}, A_{\mathbf{q}'j'}]=[A^{*}_{\mathbf{q}j}, A^{*}_{\mathbf{q}'j'}]=0, \tag{9}$$

where $\Delta(\mathbf{q})=(V/8\pi^3)\delta_{\mathbf{q},\,2\pi\tau}$. The general solution of the harmonic problem then takes the form

$$\mathbf{u}^{\mathbf{l}}_{\varkappa}=(4\pi^3\hbar/NV)^{\frac{1}{2}}\sum_{\mathbf{q}j}\omega_{\mathbf{q}j}^{-\frac{1}{2}}(A_{\mathbf{q}j}+A^{*}_{-\mathbf{q}j})\,\mathbf{V}_{\varkappa\mathbf{q}j}\exp i\mathbf{q}\cdot\mathring{\mathbf{r}}^{\mathbf{l}}_{\varkappa}, \tag{10}$$

and the harmonic Hamiltonian the form

$$H^{(2)}=\mathbf{\Phi}^{(0)}+\sum_{\mathbf{q}j}[(8\pi^3/V)A^{*}_{\mathbf{q}j}A_{\mathbf{q}j}+\tfrac{1}{2}]\hbar\omega_{\mathbf{q}j}. \tag{11}$$

Now the eigenfunctions of this must be products of simple harmonic wave functions with eigenvalues

$$E^{(2)}_m=\mathbf{\Phi}^{(0)}+\sum_{\mathbf{q}j}(m_{\mathbf{q}j}+\tfrac{1}{2})\hbar\omega_{\mathbf{q}j} \tag{12}$$

($m_{\mathbf{q}j}$ positive integers or zero); they will be described by the numbers $m_{\mathbf{q}j}$ of quanta of energy $\hbar\omega_{\mathbf{q}j}$ (or simply phonons $(\mathbf{q}, j)$) that their eigenvalues contain and denoted by $|\,\Psi^{(2)}_m\rangle$ or more specifically by $|\,\mathbf{q}_1 j_1, \mathbf{q}_2 j_2, \ldots\rangle$. This is consistent with $A_{\mathbf{q}j}$, $A^{*}_{\mathbf{q}j}$ being annihilation and creation operators, i.e. with

$$A_{\mathbf{q}j}\,|\,\Psi^{(2)}_a\rangle=m_{\mathbf{q}j}(V/8\pi^3)\,|\,\Psi^{(2)}_c\rangle, \tag{13}$$

where the state $|\,\Psi^{(2)}_a\rangle$ contains $m_{\mathbf{q}j}$ phonons $(\mathbf{q}, j)$ and $|\,\Psi^{(2)}_c\rangle$ contains $m_{\mathbf{q}j}-1$, while $A^{*}_{\mathbf{q}j}\,|\,\Psi^{(2)}_c\rangle=(V/8\pi^3)\,|\,\Psi^{(2)}_a\rangle$. The ground (or vacuum) state eigenfunction $|\,0\rangle$ of $H^{(2)}$ involves no phonons (all $m_{\mathbf{q}j}$ zero) and will be assumed normalized to unity, i.e. $\langle 0\,|\,0\rangle=1$. Any other eigenfunction can be regarded as generated from this by creation operators, its normalization being so chosen that, in fact,

$$|\,\mathbf{q}_1 j_1, \mathbf{q}_2 j_2, \ldots, \mathbf{q}_m j_m\rangle=A^{*}_{\mathbf{q}_1 j_1}A^{*}_{\mathbf{q}_2 j_2}\ldots A^{*}_{\mathbf{q}_m j_m}\,|\,0\rangle. \tag{14}$$

It is convenient to put $H^{(2)}=\mathbf{\Phi}^{(0)}+\varepsilon_{zp}+H_0$, where $\varepsilon_{zp}=\frac{1}{2}\hbar\sum_{\mathbf{q}j}\omega_{\mathbf{q}j}$ and $H_0=(8\pi^3\hbar/V)\sum_{\mathbf{q}j}\omega_{\mathbf{q}j}A^{*}_{\mathbf{q}j}A_{\mathbf{q}j}$, and to note that

$$\exp(-\beta H_0)|\,\mathbf{q}_1 j_1\ldots\mathbf{q}_m j_m\rangle=\exp[-\beta\hbar(\omega_{\mathbf{q}_1 j_1}+\ldots+\omega_{\mathbf{q}_m j_m})]|\,\mathbf{q}_1 j_1\ldots\mathbf{q}_m j_m\rangle. \tag{15}$$

III. Free Energy of the Crystal

The free energy F of the crystal, which forms the basis for the calculations made, is derived as usual from the partition function $Z=\sum_{\mu}\exp(-\beta E_{\mu})$, where $\beta=1/kT$ and E_{μ} is the energy of the crystal in state $|\,\Psi_{\mu}\rangle$, summation being over all possible states. This may be written

$$Z=\sum_{\mu}\langle\Psi_{\mu}\,|\,\mathrm{e}^{-\beta H}\,|\,\Psi_{\mu}\rangle=\mathrm{Sp}\,\{\mathrm{e}^{-\beta H}\}, \tag{16}$$

i.e. as the spur of the operator $\mathrm{e}^{-\beta H}$ in the representation of the eigenfunctions $|\,\Psi_{\mu}\rangle$ of H. Since, however, the spur of a matrix is unaltered by a unitary transformation, Z is also equal to the spur of $\mathrm{e}^{-\beta H}$ in the representation of the eigenfunctions $|\,\Psi^{(2)}_m\rangle$ of $H^{(2)}$. Putting

$$Z=Z'\exp[-\beta(\mathbf{\Phi}^{(0)}+\varepsilon_{zp})], \tag{17}$$

one therefore has

$$Z'=\mathrm{Sp}\,\{\exp\,[-\beta(H_0+\mathbf{\Phi}')]\}$$
$$=\sum_{m=0}^{\infty}(1/m\,!)(8\pi^3/V)^m\times$$
$$\sum_{\mathbf{q}_1j_1\ldots\mathbf{q}_mj_m}\langle\mathbf{q}_mj_m\ldots\mathbf{q}_1j_1\,|\,\exp\,[-\beta(H_0+\mathbf{\Phi}')]|\,\mathbf{q}_1j_1\ldots\mathbf{q}_mj_m\rangle. \tag{18}$$

The first step in evaluating this is to expand the operator in powers of $\mathbf{\Phi}'$

$$\exp\,[-\beta(H_0+\mathbf{\Phi}')]$$
$$=e^{-\beta H_0}+\sum_{r=1}^{\infty}(-1)^r\int_0^{\beta}\int_0^{\beta_1}\ldots\int_0^{\beta_{r-1}}\exp\,[-(\beta-\beta_1)H_0]\mathbf{\Phi}'\exp\,[-(\beta_1-\beta_2)H_0]\mathbf{\Phi}'$$
$$\ldots\mathbf{\Phi}'\exp\,(-\beta_rH_0)\mathrm{d}\beta_r\ldots\mathrm{d}\beta_2\mathrm{d}\beta_1. \tag{19}$$

Considering next the operator $\mathbf{\Phi}'=\sum_{\nu=3}^{\infty}\mathbf{\Phi}^{(\nu)}$, substitution of (10) in (2) gives

$$\mathbf{\Phi}^{(\nu)}=\sum_{\mathbf{q}_1j_1\ldots\mathbf{q}_\nu j_\nu}B^{(\nu)}_{1,2,\ldots,\nu}(A_1+A^*_{-1})\ldots(A_\nu+A^*_{-\nu})\Delta_{\mathbf{q}_1+\mathbf{q}_2+\ldots+\mathbf{q}_\nu}, \tag{20}$$

where $\Delta_{\mathbf{q}}=1$ if $\mathbf{q}=2\pi\tau$ and is zero otherwise and the abbreviations i for $\mathbf{q}_ij_i$ and $-i$ for $-\mathbf{q}_ij_i$ have been used in the suffices of $A_{\mathbf{q}j}$ and $A^*_{\mathbf{q}j}$. The coefficients $B^{(\nu)}_{1,2,\ldots,\nu}$ differ slightly from those of van Hove but are still essentially the Fourier transforms of the $C^{(\nu)}_{l_1\kappa_1\alpha_1,\ldots,l_\nu\kappa_\nu\alpha_\nu}$ of (2). They involve factors $(\omega_1\,\omega_2\ldots\omega_\nu)^{-\frac{1}{2}}$ but the normal modes of zero frequency, which occur for $\mathbf{q}=0$, do not cause any problem since they are excluded from the calculations as being pure translations of the crystals as a whole. For small $\mathbf{q}$ some frequencies are small but it can be verified that other factors in the $B^{(\nu)}$ prevent them becoming unduly large.

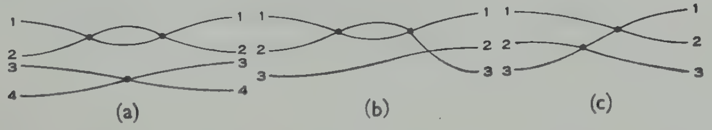

Fig. 1.—Perturbation diagrams (read from right to left). (*a*) Disconnected, (*b*) connected, (*c*) connected reduced.

After substitution of (19) and (20) in (18) it is obvious that the first quantities of interest have the form

$$\langle m,\ldots,1\,|\,\exp\,[-(\beta-\beta_1)H_0]A_iA^*_j\ldots\exp\,[-(\beta_1-\beta_2)H_0]\ldots$$
$$\ldots A^*_kA_l\ldots\exp\,(-\beta_rH_0)|\,1,\ldots,m\rangle. \tag{21}$$

Each of these may be represented by a diagram with a vertex for each operator $A_iA^*_j\ldots$, at which phonons $i,\ldots$ are annihilated and $j,\ldots$ created. Diagrams of the types shown in Figures 1 (*a*) and 1 (*b*) are termed disconnected and connected respectively by van Hove, who has shown that calculations may be made in terms of the latter only. There are still two essentially different types of connected diagrams, as illustrated in Figures 1 (*b*) and 1 (*c*). Van Hove terms the latter reduced diagrams and shows that only these need be considered if the operators A_i, A_i^* are replaced by

$$A_i[1-\exp(-\beta\hbar\omega_i)]^{-\frac{1}{2}},\ A_i^*[1-\exp(-\beta\hbar\omega_i)]^{-\frac{1}{2}}.$$

Denoting the complete operator so modified by $\exp[-\beta(H_0+\mathbf{\Phi}')]_r$ and summation over reduced diagrams by $\sum_{\text{red.}}$, the final expression for the free energy is

$$F=\mathbf{\Phi}^{(0)}+\tfrac{1}{2}\hbar\sum_{\mathbf{q}j}\omega_{\mathbf{q}j}+F', \tag{22}$$

where

$$\begin{aligned}F'&=-(1/\beta)\ln Z'\\&=F'^{(2)}-\frac{1}{\beta}\sum_{\text{red.}}\left(\frac{V}{8\pi^3}\right)^{n_r}\frac{1}{n_r!}\sum_{1,\ldots,n_r}\langle n_r\ldots 1\,|\exp[-\beta(H_0+\mathbf{\Phi}')]_r|\,1\ldots n_r\rangle\end{aligned} \tag{23}$$

where n_r is the number of initial (or final) phonons in a reduced diagram and $F'^{(2)}(\equiv\mathscr{T}$ of I) is the (harmonic) contribution from diagrams with no vertices, that is,

$$F'^{(2)}=\beta\sum_{\mathbf{q}j}\ln[1-\exp(-\beta\hbar\omega_{\mathbf{q}j})]. \tag{24}$$

IV. QUARTIC CONTRIBUTION TO F

The present calculation was made for a cubic crystal ($\mathbf{\Phi}^{(3)}=0$) and only the lowest order (quartic) anharmonic terms in the $\mathbf{u}_{\varkappa\alpha}^{\mathbf{l}}$ were included so that $\mathbf{\Phi}'=\mathbf{\Phi}^{(4)}$. In this case each annihilation-creation factor in (21) consists of a product of four operators A_i or A_j^* corresponding to a fourfold vertex. Diagrams involving any number of such vertices should be considered but each additional vertex reduces the contribution of a diagram considerably. (This arises from the fact that $\mathbf{\Phi}^{(4)}/\mathbf{\Phi}^{(2)}$ is of the order of u^2/d^2.) For this reason diagrams with more than one vertex were ignored and this left only the three reduced diagrams shown in Figures 2 (*a*), 2 (*b*), and 2 (*c*) to be considered. Furthermore, the only annihilation-creation operators of interest must contain two operators A_i, A_j and two corresponding ones A_i^*, A_j^* since $\langle\Psi_a^{(2)}|A_iA_j^*\ldots|\Psi_a^{(2)}\rangle=\langle\Psi_a^{(2)}|\Psi_b^{(2)}\rangle$ is zero unless $|\Psi_a^{(2)}\rangle$ and $|\Psi_b^{(2)}\rangle$ are the same state, owing to the orthogonality of the $|\Psi_m^{(2)}\rangle$. With this point in mind $\mathbf{\Phi}'=\mathbf{\Phi}^{(4)}$ may be replaced by

$$\sum_{\mathbf{q}_1j_1\ldots\mathbf{q}_4j_4}B^{(4)}_{1,2,3,4}(A_1+A^*_{-1})\ldots(A_4+A^*_{-4}), \tag{25}$$

where either (i) $3\equiv-1$, $4\equiv-2$, (ii) $2\equiv-1$, $4\equiv-3$, or (iii) $3\equiv-2$, $4\equiv-1$ (it is convenient to replace suffix 3 by 2 in (ii) so that in all cases there are just two different suffices 1 and 2). In each case one has a sum of 16 fourfold annihilation-creation factors, of which one corresponds to each of Figures 2 (*a*) and 2 (*c*) and two to Figure 2 (*b*) while the other 12 are of no interest.

In the practical calculation of the quartic contribution $F'^{(4)}$ to the free energy the coefficients $B^{(4)}_{1,2,3,4}$ remain to be evaluated. This was not done explicitly as it proved simpler to substitute (10) into the classical expression

$$\mathbf{\Phi}^{(4)}=\frac{1}{2}\frac{1}{4!}\sum_{\varkappa\varkappa'}\sum_{\mathbf{ll}'}{}'\sum_{\alpha_1\ldots\alpha_4}\left(\frac{\partial^4\mathbf{\Phi}^{\mathbf{ll}'}_{\varkappa\varkappa'}(r)}{\partial\alpha_1\partial\alpha_2\partial\alpha_3\partial\alpha_4}\right)_0(u^{\mathbf{l}}_{\varkappa\alpha_1}-u^{\mathbf{l}'}_{\varkappa'\alpha_1})\ldots(u^{\mathbf{l}}_{\varkappa\alpha_4}-u^{\mathbf{l}'}_{\varkappa'\alpha_4}) \tag{26}$$

(where $r^2=x^2+y^2+z^2$, each α_i may be x, y, or z, the differential coefficients are to be evaluated with $\mathbf{r}=\mathring{\mathbf{r}}^{\mathbf{l}}_{\varkappa}-\mathring{\mathbf{r}}^{\mathbf{l}'}_{\varkappa'}$, and the primed summation sign indicates that the case $\varkappa=\varkappa'$, $\mathbf{l}=\mathbf{l}'$ is omitted) and consider sets of terms with the same α_1, α_2, α_3, and α_4. Ignoring for the moment the factors $(4\pi^3\hbar/NV)^{\frac{1}{2}}\omega_{\mathbf{q}j}^{-\frac{1}{2}}(A_{\mathbf{q}j}+A^*_{-\mathbf{q}j})$ and the summations over $\mathbf{q}$ and j, consider the following cases.

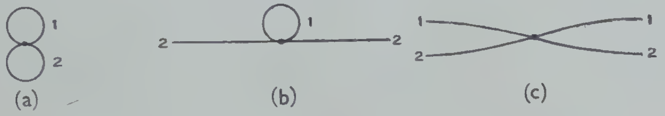

Fig. 2.—Perturbation diagrams (read from right to left).

(*a*) If $\alpha_1=\alpha_2=\alpha_3=\alpha_4=x$, the remaining factor in the contribution of such terms to $\mathbf{\Phi}^{(4)}$ may be reduced to

$$\frac{N}{2}\sum_{\varkappa\varkappa'}\sum_{\mathbf{l}}{}'\left(\frac{\partial^4\mathbf{\Phi}^{\mathbf{l}0}_{\varkappa\varkappa'}}{\partial x^4}\right)_0 f_x(\mathbf{l};\,\varkappa\varkappa';\,1)f_x(\mathbf{l};\,\varkappa\varkappa';\,2), \tag{27}$$

where

$$f_x(\mathbf{l};\,\varkappa\varkappa';\,i)=V^2_{\varkappa ix}-2V_{\varkappa ix}V_{\varkappa' ix}\cos\mathbf{q}_i\cdot(\mathring{\mathbf{r}}^{\mathbf{l}}_{\varkappa}-\mathring{\mathbf{r}}_{\varkappa'})+V^2_{\varkappa' ix}. \tag{28}$$

(*b*) If $\alpha_1=\alpha_2=\alpha_3=x$ and $\alpha_4=y$, say, the corresponding factor is a complicated one. In the case of a crystal of cubic symmetry, every part of it contains factors of the form $\cos\mathbf{q}\cdot(\mathring{\mathbf{r}}^{\mathbf{l}}_{\varkappa}-\mathring{\mathbf{r}}_{\varkappa'})$, which may be replaced by

$$\sin q_x(\mathring{r}^{\mathbf{l}}_{\varkappa x}-\mathring{r}_{\varkappa' x})\sin q_y\,(\mathring{r}^{\mathbf{l}}_{\varkappa y}-\mathring{r}_{\varkappa' y})\cos q_z\,(\mathring{r}^{\mathbf{l}}_{\varkappa z}-\mathring{r}_{\varkappa' z}).$$

(*c*) If $\alpha_1=\alpha_2=x$ and $\alpha_3=\alpha_4=y$, say, the corresponding factor is

$$\frac{N}{2}\sum_{\varkappa\varkappa'}\sum_{\mathbf{l}}{}'\left(\frac{\partial^4\mathbf{\Phi}^{\mathbf{l}0}_{\varkappa\varkappa'}}{\partial x^2\partial y^2}\right)_0 \{f_x(\mathbf{l};\,\varkappa\varkappa';\,1)f_y(\mathbf{l};\,\varkappa\varkappa';\,2)+f_y(\mathbf{l};\,\varkappa\varkappa';\,1)f_x(\mathbf{l};\,\varkappa\varkappa';\,2) \\ +4g_{xy}(\mathbf{l};\,\varkappa\varkappa';\,1)g_{xy}(\mathbf{l};\,\varkappa\varkappa';\,2)\}, \tag{29}$$

where

$$g_{xy}(\mathbf{l};\,\varkappa\varkappa';\,i)=V_{\varkappa ix}V_{\varkappa iy}-(V_{\varkappa ix}V_{\varkappa' iy}+V_{\varkappa' ix}V_{\varkappa iy})\cos\mathbf{q}_i\cdot(\mathring{\mathbf{r}}^{\mathbf{l}}_{\varkappa}-\mathring{\mathbf{r}}_{\varkappa'})+V_{\varkappa' ix}V_{\varkappa' iy}. \tag{30}$$

(*d*) If $\alpha_1=\alpha_2=x$, $\alpha_3=y$, $\alpha_4=z$, say, the factor is again a complicated one but again for cubic symmetry every part of it contains factors of the form $\cos\mathbf{q}\cdot(\mathring{\mathbf{r}}^{\mathbf{l}}_{\varkappa}-\mathring{\mathbf{r}}_{\varkappa'})$, which may be replaced by

$$\cos q_x(\mathring{r}^{\mathbf{l}}_{\varkappa x}-\mathring{r}_{\varkappa' x})\sin q_y(\mathring{r}^{\mathbf{l}}_{\varkappa y}-\mathring{r}_{\varkappa' y})\sin q_z(\mathring{r}^{\mathbf{l}}_{\varkappa z}-\mathring{r}_{\varkappa' z}).$$

In each of the cases (*a*)-(*d*) there are contributions from pairs of particles of the same type ($\varkappa=\varkappa'$) and from pairs of different types. For the former the notation

$$\sum_{\mathbf{l}}{}'\left(\frac{\partial^4\mathbf{\Phi}^{\mathbf{l}0}_{\varkappa\varkappa}}{\partial\alpha_1\partial\alpha_2\partial\alpha_3\partial\alpha_4}\right)_0=(\alpha_1\alpha_2\alpha_3\alpha_4;\,\mathbf{l})\,;\quad \sum_{\mathbf{l}}{}'\left(\frac{\partial^4\mathbf{\Phi}^{\mathbf{l}0}_{\varkappa\varkappa}}{\partial\alpha_1\partial\alpha_2\partial\alpha_3\partial\alpha_4}\right)_0\cos\mathbf{q}\cdot\mathring{\mathbf{r}}^{\mathbf{l}}_{\varkappa}=(\alpha_1\alpha_2\alpha_3\alpha_4;\,\mathbf{q};\,\mathbf{l})\,;$$

$$\sum_{\mathbf{l}}{}'\left(\frac{\partial^4\mathbf{\Phi}^{\mathbf{l}0}_{\varkappa\varkappa}}{\partial\alpha_1\partial\alpha_2\partial\alpha_3\partial\alpha_4}\right)_0\cos(\mathbf{q}_1+\mathbf{q}_2)\cdot\mathring{\mathbf{r}}^{\mathbf{l}}_{\varkappa}=(\alpha_1\alpha_2\alpha_3\alpha_4;\,\mathbf{q}_1,\,\mathbf{q}_2;\,\mathbf{l}) \tag{31}$$

will be introduced, while for the latter, for which there is no prime on the summation signs, $\mathbf{l}$ is replaced by $\boldsymbol{\lambda}$.

It was appreciated at this stage of the work that, despite the approximations made so far, the necessary calculation of $F'^{(4)}$ for several temperatures and volumes of the crystal would prove far too lengthy for the value of the results obtained without further approximation. It seemed necessary to simplify the dependence of expressions (*a*)-(*d*) on $\mathbf{q}_1$ and $\mathbf{q}_2$ and this was investigated for $\mathbf{q}_1=(q_{1x}, 0, 0)$, $\mathbf{q}_2=(q_{2x}, 0, 0)$ in the case of sodium chloride, for which $\mathbf{V}_{\varkappa\mathbf{q}j}$, $\mathbf{V}_{\varkappa'\mathbf{q}j}$ were known from the calculations of I. The following conclusions were reached.

(i) Expressions for $\varkappa\neq\varkappa'$ were larger than corresponding ones for $\varkappa=\varkappa'$ by factors ~ 100 except for a few values of q_x where both were small.

(ii)
$$\left.\begin{aligned} &(x^4; q_x; \boldsymbol{\lambda})\simeq(x^4; \boldsymbol{\lambda}) \cos \pi q_x; \qquad (y^4; q_x; \boldsymbol{\lambda})\simeq(x^4; \boldsymbol{\lambda}),\\ &(x^2y^2; q_x; \boldsymbol{\lambda})\simeq(x^2y^2; \boldsymbol{\lambda}) \cos \frac{\pi q_x}{2}; \quad (y^2z^2; q_x; \boldsymbol{\lambda})\simeq(y^2z^2; \boldsymbol{\lambda}),\end{aligned}\right\} \tag{32}$$
where $(x^4; \boldsymbol{\lambda})$ is $(x^4; q_x; \boldsymbol{\lambda})$ with $q_x=0$ etc.

(iii) All expressions involved in (*b*) and (*d*) were identically zero.

It was therefore decided, for all values of $\mathbf{q}_1$, $\mathbf{q}_2$, to neglect (*b*), (*d*) and the contributions to (*a*) and (*c*), for which $\varkappa=\varkappa'$. Further reduction of the remaining parts of (*a*) and (*c*) is then possible by use of crystal symmetry. Thus preliminary summation of these over the 48^2 wave-vector pairs obtained by applying cubic symmetry operations to $\mathbf{q}_1$ and $\mathbf{q}_2$ was carried out. Thereafter summation over a $\mathbf{q}$ could be restricted to a basic region of $\mathbf{q}$-space,

$$\pi/a\geqslant q_x\geqslant q_y\geqslant q_z\geqslant 0\,; \quad q_x+q_y+q_z\leqslant 3\pi/2a,$$

where a is the lattice constant of the crystal, i.e. $v_a=2a^3$. In carrying out this preliminary summation (denoted by $\sum_{\mathrm{e}}$) the symmetry permits the factor $\cos \mathbf{q}_1\cdot(\mathring{\mathbf{r}}^{\mathbf{l}}_{\varkappa}-\mathring{\mathbf{r}}_{\varkappa'}) \cos \mathbf{q}_2\cdot(\mathring{\mathbf{r}}^{\mathbf{l}}_{\varkappa}-\mathring{\mathbf{r}}_{\varkappa'})$ to be replaced by $\cos (\mathbf{q}_1+\mathbf{q}_2)\cdot(\mathring{\mathbf{r}}^{\mathbf{l}}_{\varkappa}-\mathring{\mathbf{r}}_{\varkappa'})$. Then from terms of type (*a*) one obtains

$$\begin{aligned}\frac{N}{2}\sum_{\mathrm{e}}\sum_{\varkappa\varkappa'}\sum_{\lambda}{}'\sum_{\alpha}\left(\frac{\partial^4\mathbf{\Phi}^{\lambda 0}_{\varkappa\varkappa'}}{\partial\alpha^4}\right)_0 f_\alpha(\boldsymbol{\lambda}; \varkappa\varkappa'; 1)f_\alpha(\boldsymbol{\lambda}; \varkappa\varkappa'; 2)&\\ =12N \operatorname{Re} \{(x^4; \boldsymbol{\lambda})P(\mathbf{q}_1j_1)P(\mathbf{q}_ij_i)\},&\end{aligned} \tag{33}$$
where
$$P(\mathbf{q}_j)=\mathbf{V}_{\varkappa\mathbf{q}j}\cdot\mathbf{V}_{\varkappa\mathbf{q}j}+\mathbf{V}_{\varkappa'\mathbf{q}j}\cdot\mathbf{V}_{\varkappa'\mathbf{q}j}-2\sum_{\alpha}V_{\varkappa\mathbf{q}j\alpha}V_{\varkappa'\mathbf{q}j\alpha}\mathrm{e}^{\mathrm{i}\pi q_\alpha}. \tag{34}$$
Similarly from terms of type (*c*) one obtains

$$\begin{aligned}\frac{N}{2}\sum_{\mathrm{e}}\sum_{\varkappa\varkappa'}\sum_{\lambda}\sum_{\alpha_1\alpha_2}\left(\frac{\partial^4\mathbf{\Phi}^{\lambda 0}_{\varkappa\varkappa'}}{\partial\alpha_1^2\partial\alpha_2^2}\right)_0 \{f_{\alpha_1}(\boldsymbol{\lambda}; \varkappa\varkappa'; 1)f_{\alpha_2}(\boldsymbol{\lambda}; \varkappa\varkappa'; 2)+f_{\alpha_2}(\boldsymbol{\lambda}; \varkappa\varkappa'; 1)f_{\alpha_1}(\boldsymbol{\lambda}; \varkappa\varkappa'; 2)&\\ +4g_{\alpha_1\alpha_2}(\boldsymbol{\lambda}; \varkappa\varkappa'; 1)g_{\alpha_1\alpha_2}(\boldsymbol{\lambda}; \varkappa\varkappa'; 2)\}&\\ =24N \operatorname{Re} \{(x^2y^2; \boldsymbol{\lambda})Q(\mathbf{q}_1j_1)Q(\mathbf{q}_2j_2)\} +48N \operatorname{Re} \{(x^2y^2; \boldsymbol{\lambda})R(\mathbf{q}_1j_1)R(\mathbf{q}_2j_2),&\end{aligned} \tag{35}$$
where
$$Q(\mathbf{q}j)=\mathbf{V}_{\varkappa\mathbf{q}j}\cdot\mathbf{V}_{\varkappa\mathbf{q}j}+\mathbf{V}_{\varkappa'\mathbf{q}j}\cdot\mathbf{V}_{\varkappa'\mathbf{q}j}-\sum_{\text{cyc.}}(V_{\varkappa\mathbf{q}jx}V_{\varkappa'\mathbf{q}jx}+V_{\varkappa\mathbf{q}jy}V_{\varkappa'\mathbf{q}jy})\mathrm{e}^{\mathrm{i}\pi(q_x+q_y)/2}, \tag{36}$$
and
$$R(\mathbf{q}j)=\sum_{\text{cyc.}}[V_{\varkappa\mathbf{q}j\varkappa}V_{\varkappa\mathbf{q}jy}+V_{\varkappa'\mathbf{q}jx}V_{\varkappa'\mathbf{q}jy}-(V_{\varkappa\mathbf{q}jx}V_{\varkappa'\mathbf{q}jy}+V_{\varkappa'\mathbf{q}jx}V_{\varkappa\mathbf{q}jy})\mathrm{e}^{\mathrm{i}\pi(q_x+q_y)/2}], \tag{37}$$

$\sum\limits_{\text{cyc.}}$ denoting cyclic permutation of x, y, and z. Thus the approximate expression for $\mathbf{\Phi}^{(4)}$ proves to be

$$\mathbf{\Phi}^{(4)} \simeq \frac{64N}{4!}\left(\frac{\hbar}{2N}\right)^2\left(\frac{8\pi^3}{V}\right)^2 \sum_{\mathbf{q}_1\mathbf{q}_2}^{\text{basic}} \sum_{j_1 j_2} \frac{12B_{1,2}^{(4)\prime}}{\omega_1\omega_2}(A_1A_2A_1^*A_2^*+\ldots), \tag{38}$$

where

$$B_{1,2}^{(4)\prime} = \operatorname{Re}\,\{(x^4;\boldsymbol{\lambda})P(1)P(2)+2(x^2y^2;\boldsymbol{\lambda})Q(1)Q(2)+4(x^2y^2;\boldsymbol{\lambda})R(1)R(2)\}, \tag{39}$$

and the final bracket of (38) contains 12 different fourfold operators, of which 3 correspond to Figure 2 (*a*), 6 to Figure 2 (*b*), and 3 to Figure 2 (*c*). This expression has to be substituted in the approximate quartic contribution to the free energy

$$F'^{(4)} \simeq \frac{1}{\beta}\sum_{\text{red.}}\left(\frac{V}{8\pi^3}\right)^{n_r}\frac{1}{n_r!}\sum_{\mathbf{q}_1 j_1\ldots\mathbf{q}_{n_r} j_{n_r}} \frac{\langle n_r\ldots 1|\int_0^\beta \mathrm{e}^{-(\beta-\beta_1)H_0}\mathbf{\Phi}^{(4)}\,\mathrm{e}^{-\beta_1 H_0}\mathrm{d}\beta_1|\,1\ldots n_r\rangle}{[1-\exp(-\beta\hbar\omega_1)][1-\exp(-\beta\hbar\omega_2)]}. \tag{40}$$

For the operators in $\mathbf{\Phi}^{(4)}$ corresponding to Figure 2 (*a*) $n_r=0$ and each one, e.g. $A_1A_2A_1^*A_2^*$, produces a term

$$\langle 0\,|\int_0^\beta \mathrm{e}^{-(\beta-\beta_1)H_0}A_1A_2A_1^*A_2^*\mathrm{e}^{-\beta_1H_0}\mathrm{d}\beta_1\,|\,0\rangle=\beta(V/8\pi^3)^2. \tag{41}$$

For an operator such as $A_1^*A_2A_1A_2^*$ corresponding to Figure 2 (*b*) $n_r=1$ and one similarly obtains

$$\left(\frac{V}{8\pi^3}\right)\langle 1\,|\int_0^\beta \mathrm{e}^{-(\beta-\beta_1)H_0}A_1^*A_2A_1A_2^*\mathrm{e}^{-\beta_1H_0}\mathrm{d}\beta_1\,|\,1\rangle=\beta\exp(-\beta\hbar\omega_1)(V/8\pi^3)^2. \tag{42}$$

For an operator such as $A_1^*A_2^*A_1A_2$ corresponding to Figure 2 (*c*) $n_r=2$ and one obtains

$$\left(\frac{V}{8\pi^3}\right)^2\frac{1}{2!}\langle 2,1|\int_0^\beta \mathrm{e}^{-(\beta-\beta_1)H_0}A_1^*A_2^*A_1A_2\mathrm{e}^{-\beta_1H_0}\mathrm{d}\beta_1|\,1,2\rangle=\frac{\beta}{2}\exp[-\beta\hbar(\omega_1+\omega_2)]\left(\frac{V}{8\pi^3}\right)^2. \tag{43}$$

It may be noted that in obtaining these results various positive and negative powers of $(V/8\pi^3)$ arise from (13), from the normalization of the harmonic eigenfunctions, and from the fact that, when a summation over $\mathbf{q}$ and j becomes redundant (e.g. for Figure 2 (*b*) one of the $\sum\limits_{\mathbf{q}j}$ in $\mathbf{\Phi}^{(4)}$ is redundant since it is duplicated by another $\sum\limits_{\mathbf{q}j}$ in $F'^{(4)}$), a factor $V/8\pi^3$ must be introduced (see vH). Substituting these results in (40), one obtains

$$F'^{(4)} = \frac{24\hbar^2}{N}\sum_{\mathbf{q}_1\mathbf{q}_2}^{\text{basic}}\sum_{j_1j_2} B_{1,2}^{(4)\prime}\frac{[1+\exp(-\beta\hbar\omega_1)][1+\exp(-\beta\hbar\omega_2)]}{\omega_1\omega_2[1-\exp(-\beta\hbar\omega_1)][1-\exp(-\beta\hbar\omega_2)]}. \tag{44}$$

Now $B_{1,2}^{(4)\prime}$ consists of three parts, each of which is separable in $\mathbf{q}_1$, $\mathbf{q}_2$ and the corresponding contribution to $F'^{(4)}$ can therefore be expressed as the square of a single sum over $\mathbf{q}, j$. Finally, if the real and imaginary parts of P, Q, and R are denoted by R_P, R_Q, R_R, I_P, I_Q, I_R respectively, one obtains

$$F'^{(4)}=\frac{24\hbar^2}{N}\sum_{k=P,Q,R}\left\{\left[\sum_{\mathbf{q}}^{\text{basic}}\sum_{j}\frac{R_k\coth(\beta\hbar\omega_{\mathbf{q}j}/2}{\omega_{\mathbf{q}j}}\right]^2-\left[\sum_{\mathbf{q}}^{\text{basic}}\sum_{j}\frac{I_k\coth(\beta\hbar\omega_{\mathbf{q}j}/2)}{\omega_{\mathbf{q}j}}\right]^2\right\}. \tag{45}$$

V. APPLICATION TO SODIUM CHLORIDE

The purpose of this work was to examine the effect of inclusion of the quartic terms in the expansion of $\mathbf{\Phi}$ on the theoretical thermal expansion of sodium chloride. Thus, as in I, solutions of the equation of state

$$p=-(\partial F/\partial V)_T \tag{46}$$

for various values of the lattice parameter a were sought, with the quartic contribution to the free energy included at all stages. Thus, one mole of the crystal was considered, for which $V=2Na^3$, N being Avogadro's number ; let $V/V_0=g$, where the suffix zero will always denote values for a standard value a_0 of a (the experimental value at $T=288$ °K). It was assumed that

$$\mathbf{\Phi}^{(0)}=N(-\alpha_M e^2a_0^{-1}g^{-1/3}+6ba_0^{-n}g^{-n/3}), \tag{47}$$

where α_M is the Madelung number for the lattice, e is the charge on an electron, and b, n are parameters ; as before the latter were replaced by

$$A=4n(n+1)be^{-2}a_0^{-n+1} \text{ and } B=-4nbe^{-2}a_0^{-n+1}.$$

A and B were determined as in I, i.e. by satisfying (46) and $\varkappa_T^{-1}=V(\partial^2F/\partial V^2)_{T,T}$ at $T=288$ °K, $p=0$ with the experimental values for a_0 ($2\cdot814\times10^{-8}$ cm) and the isothermal compressibility $\varkappa_T$ ($4\cdot16\times10^{-12}$ cm²/dyne). At each stage of the iterative procedure (see I for details) $F'^{(2)}$ and $F'^{(4)}$ were calculated for $T=288$ °K and six values of g by digital computer, as this proved simpler than a direct computation of their derivatives. A further approximation was made in the case of $F'^{(4)}$; it was decided that the dependence of R_k, I_k ($k=P, Q, R$) on g would be relatively small so that, in order to reduce the amount of computation, their values calculated for one value of g (and the 300 values of ($\mathbf{q}, j$) used in the further summations) were used for all g. The normal frequencies $\omega_{\mathbf{q}j}$ having only been calculated for about 50 points in the basic region of $\mathbf{q}$-space, summations were restricted to these values of $\mathbf{q}$ with suitable weighting factors (ΔK of I). The derivatives, e.g. $(\partial F'^{(2)}/\partial V)_T$, $(\partial^2F'^{(2)}/\partial V^2)_{T,T}$, were found numerically from

TABLE 1

COMPARISON OF VALUES OF PARAMETERS

	A	B	n	b
Kellermann ..	10·18	−1·165	7·738	$1\cdot148\times10^{-71}$
I	10·68	−1·048	9·188	$9\cdot902\times10^{-83}$
Present work..	10·40	−1·063	8·779	$1\cdot587\times10^{-78}$

difference tables prepared from the computations. The values obtained for A, B, n, and b are compared in Table 1 with those of Kellermann (who essentially ignored the dependence of the vibrational energy on g) and of the calculation I (where $F'^{(4)}$ was not included).

With these values of the parameters $F'^{(2)}$ and $F'^{(4)}$ were computed and $(\partial F'^{(2)}/\partial V)_T$ and $(\partial F'^{(4)}/\partial V)_T$ determined numerically for various values of g and T, and thereby pairs of values (g, T) determined for which (46) was satisfied (with $p=0$). In order that comparison with experiment could be made for temperatures below $T=288$ °K, normal frequencies for the crystal were computed for $g=0\cdot975(\cdot005)1\cdot000$. The theoretical curve so obtained is shown in comparison with the experimental results of Eucken and Dannöhl (1934) and of Srinivasan (1955) in Figure 3 ; also shown is the theoretical curve obtained in I.

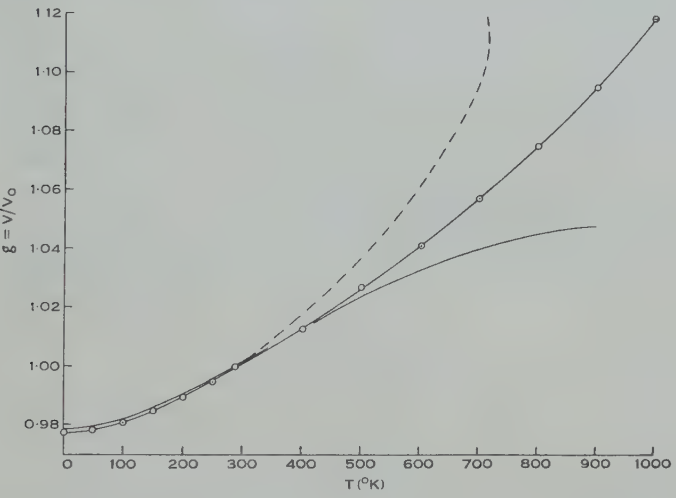

Fig. 3.—Expansion of sodium chloride. –⊙–⊙– Experimental (Eucken and Dannöhl 1934 ; Srinivasan 1955) ; —— theoretical (present work) ; ---- theoretical (I).

As in I there is wide discrepancy between theory and experiment at the higher temperatures and again it seemed of interest to calculate the specific heat C_v at constant volume and $\varkappa_T$, using the experimental figures for the thermal expansion to relate the values of g, for which the normal frequencies to be used had been calculated, to temperature T. They were both calculated numerically from suitable difference tables for $F'^{(2)}$ and $F'^{(4)}$ and the relations

$$C_v = -T(\partial^2 F/\partial T^2)_{v,v} \text{ and } \varkappa_T^{-1} = V(\partial^2 F/\partial V^2)_{T,T}.$$

(Note that the first group of terms in expression (31) for $\varkappa_T^{-1}$ in I is incorrect except when $g=1$.) The results are again compared with experiment in Figures 4 and 5. As an indication of the magnitude of the quartic contributions, curves, for which these have been omitted, have also been inserted. (They are, however, calculated with the values of A and B obtained by inclusion of quartic effects. If quartic effects are completely ignored, the curves of I are obtained.)

VI. Discussion of Results

As can be seen from Figure 3 agreement between theory and experiment has not been improved greatly by the inclusion of the lowest order anharmonic terms in this calculation of thermal expansion. Although a number of approximations were made in obtaining the expression (45) for $F'^{(4)}$, ultimately aimed

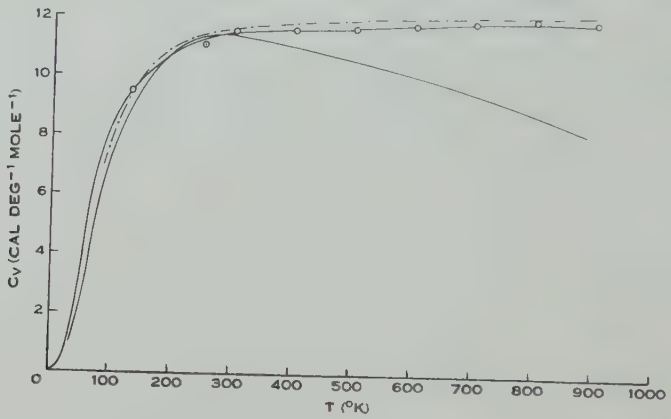

Fig. 4.—Specific heat of sodium chloride. -⊙-⊙- Experimental (Hunter and Siegel 1942 ; Clusius, Goldmann, and Perlick 1949) ; —— theoretical ; —·—·— anharmonic contribution omitted.

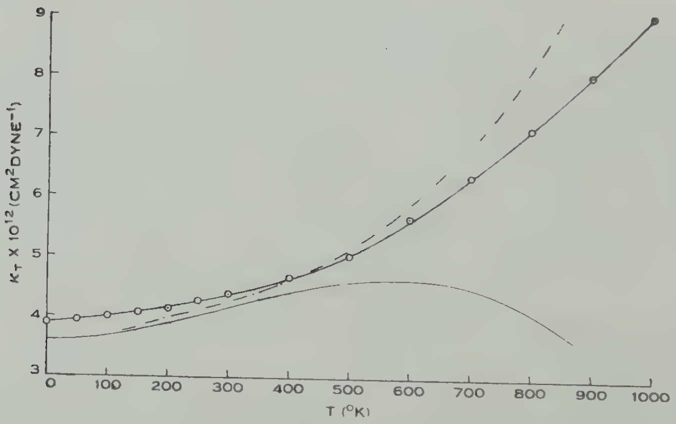

Fig. 5.—Compressibility of sodium chloride. -⊙-⊙- Experimental (Hunter and Siegel 1942 ; Overton and Swim 1951) ; —— theory ; —·—·— anharmonic contribution omitted.

at making its computation a reasonable proposition, these are not thought to have affected the result essentially. The factors

$$(\omega_1\omega_2)^{-1} \coth (\beta\hbar\omega_1/2) \coth (\beta\hbar\omega_2/2)$$

will obviously increase with T and the great majority with V also (since most $\partial\omega/\partial V < 0$). At high temperatures the arguments $\beta\hbar\omega/2$ are so small that the rate of increase of these factors with V causes $(\partial F'^{(4)}/\partial V)_T$ to outstrip

$-(\partial F'^{(2)}/\partial V)_T - \partial \mathbf{\Phi}^{(0)}/\partial V$ at all volumes, i.e. no equilibrium volume can be found. This stems originally from the use of a Taylor expansion for $\mathbf{\Phi}$ up to quartic terms only in the $u^1_{\varkappa\alpha}$. Inclusion of higher order terms, which would increase the computation enormously, might improve agreement with experiment but, as stated in Section II, the use of such an expansion for $\mathbf{\Phi}$ can never be satisfactory at high temperatures. At the lower temperatures (below $T = 288$ °K) agreement with experiment is reasonable but little better than is obtained by ignoring the quartic terms, as would also be expected. The unrealistic influence of the quartic terms at higher temperatures is also well illustrated by Figures 4 and 5.

It appears to the author that it would be unprofitable to proceed any further with the investigation of thermal expansion, even for ionic solids, on the basis of the expansion in powers of particle displacements of the form used here for the potential energy Φ of a crystal. Replacement of the repulsive term b/r^n in the interparticle potential by an exponential term might be worth while but it would probably be even more profitable to examine the effect of deviations from central symmetry in the interparticle forces (Born and Huang 1954, especially Chapter V).

VII. ACKNOWLEDGMENT

The author wishes to thank the Adolph Basser Computing Laboratory, University of Sydney, for the use of SILLIAC in making the computations necessary in this work.

VIII. REFERENCES

BORN, M., and HUANG, K. (1954).—"Dynamical Theory of Crystal Lattices." (Oxford Univ. Press.)

CLUSIUS, K., GOLDMANN, J., and PERLICK, A. (1949).—*Z. Naturf.* **4a**: 424.

EUCKEN, A., and DANNÖHL, W. (1934).—*Z. Electrochem.* **40**: 814.

FLETCHER, G. C. (1959).—*Aust. J. Phys.* **12**: 237.

VAN HOVE, L. (1959).—Solid-State and Molecular Theory Group, Massachusetts Institute of Technology, Tech. Rep. No. 11.

HUNTER, L., and SIEGEL, S. (1942).—*Phys. Rev.* **61**: 84.

OVERTON, W. C., and SWIM, R. T. (1951).—*Phys. Rev.* **84**: 758.

SRINIVASAN, R. (1955).—*J. Indian Inst. Sci.* A **37**: 232.

SHORT COMMUNICATIONS

INELASTIC SCATTERING OF PROTONS ON ^{12}C[†]

By V. R. McKenna[‡] and G. G. Shute[‡]

During the recent Variable Energy Cyclotron experiment involving the elastic scattering of protons on ^{12}C, the complete energy spectrum of the scattered protons was obtained by means of a 100-channel analyser (McKenna, Baxter, and Shute 1961, henceforth referred to as I). Two prominent peaks were obtained: the higher energy one corresponding to elastic scattering and the lower energy one to inelastic scattering with the residual carbon nucleus being left in its first excited state, 4·43 MeV. In I the elastic scattering results were reported briefly. The purpose of this short communication is to discuss the main features of the inelastic scattering.

Angular distributions for this inelastic process have been determined at approximately 5° intervals, between 170° and 25° scattering angles, over the energy range $11\frac{1}{2}$–8 MeV in 100 keV steps. Moreover, complete angular distributions were made, in 25 keV steps, over the known resonance region at 9·2 MeV, while runs at nine preferred angles, with 40 keV spacing, were later made over the 7·6, 8·2, and 10·5 MeV resonance regions. Below 8 MeV only fragmentary angular distributions were obtained. This was due to the low energy of the inelastic peak, especially at backward angles, which prevented correct reproduction by the kick-sorter. From 8 to 7 MeV, angular distributions were obtained only for angles less than 100°. Below 7 MeV no useful data were obtained, both because of the low proton energy at all angles, and because the inelastic cross section had become too small for the peak to be observed above the background.

None of the angular distributions exhibit any information between 55° and 25°. This is due to the masking of the inelastic peak, at these angles, by protons elastically scattered from the hydrogen content of the polythene target. This process has a relatively high cross section, and the energy of the scattered proton is a $\cos^2$ function of the detection angle. In order to keep the analyser counting rate low without using excessively small beam currents, the display of the non-elastic region was biased out; thus only elastic distributions are available between these angles. However, at 25° a separate run was made, using a reduced beam and no analyser bias, so that inelastic scattering information is available at this angle. This 25° point is of low accuracy ($\simeq 10\%$), due to poor statistics and high dead-time counting losses, but was persisted with because information at this forward angle is of assistance in judging the possible direct interaction contribution to the inelastic scattering process.

[†] Manuscript received May 4, 1961.

[‡] Physics Department, University of Melbourne.

In estimating the differential cross section from the spectrum displayed on the analyser, the background contribution of elastically scattered protons under the inelastic peak was allowed for. This reached a maximum value of 10% when there was a very large elastic cross section without a correspondingly large inelastic cross section. This elastic "tail", due to slit scattering, inelastic reactions in the scintillator, etc., is discussed by the Minnesota group (Stovall and Lee 1960).

Some of the angular distributions obtained are shown in Figure 1. Figure 1 (*a*) shows a rapid variation as the 9·2 MeV resonance is crossed. Figure 1 (*b*) shows the complete change of shape that occurs between 10·67 and 10·37 MeV, indicating the complexity of the level structure in this region.

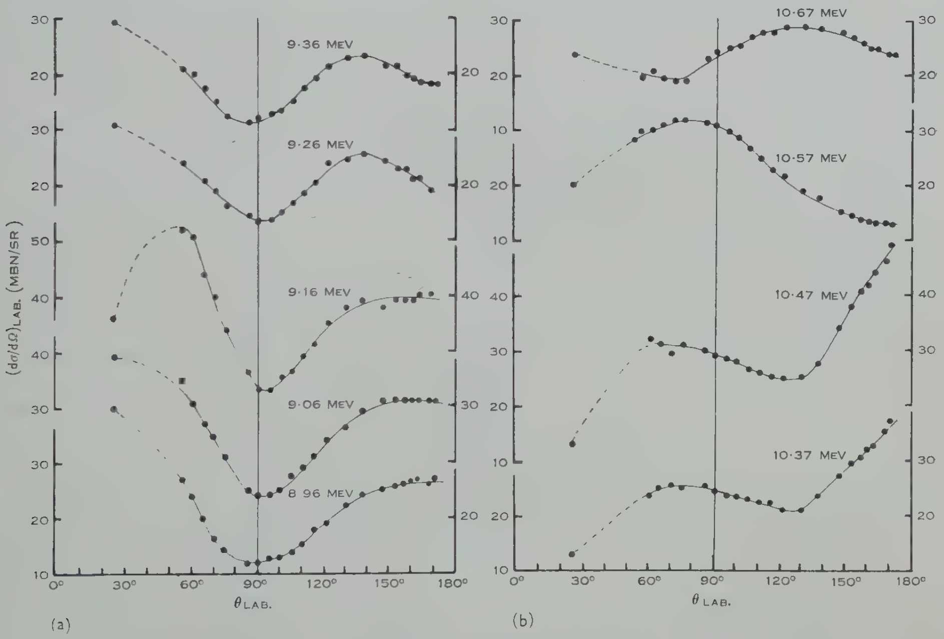

Fig. 1.—Angular distributions for $^{12}\mathrm{C}(p,p')^{12}\mathrm{C}^*$ 4·43 MeV, (*a*) in the region of 9·2 MeV incident proton energy; (*b*) in the region of 10·5 MeV incident proton energy. The smooth line indicates the trend of the experimental points. Relative accuracy of points: ±2%; absolute value of differential cross section: ±10%. All units in the laboratory system.

The behaviour of the cross section at fixed scattering angles for differing incident energies is obtainable from the above data. These excitation functions show resonance structure at energies corresponding to the recently discovered levels in $^{13}\mathrm{N}$ discussed in I. Similar resonances have also been observed when the de-excitation gamma ray is detected in coincidence with the inelastic proton (Adams *et al.* 1960).

Some of the excitation functions obtained are shown in Figure 2, for scattering angles of 65°, 85·3°, 137·6°, and 168°. In all cases differential cross section, angle, and incident energy are given in the laboratory system. The 7·6, 8·2, and 9·2 MeV resonances are clearly indicated ; between 10 and 11 MeV there appear to be at least 3 resonances, namely, 10·3, 10·5, and 11·0 MeV.

These inelastic scattering results are presented here in order to confirm the resonance structure reported in I. This additional information will be of assistance in the analysis of the elastic scattering, which is proceeding by means of a tentative two-channel multilevel type analysis.

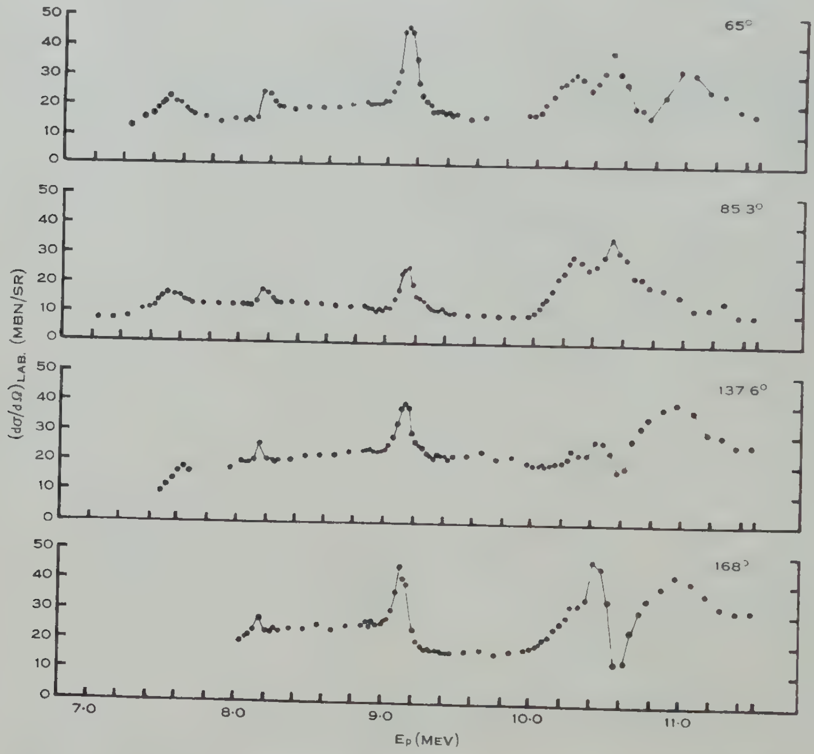

Fig. 2.—$^{12}C(p,p')^{12}C^*$ 4·43 MeV : differential cross section v. bombarding energy at four representative angles, showing resonance structure at 7·6, 8·2, 9·2, 10·3, 10·5, and 11·0 MeV. Absolute value of cross sections accurate to ±10%. All units in the laboratory system.

As in I, we acknowledge the assistance of the cyclotron group, led by Professor Caro.

Note added in Proof

The preliminary phase shift analysis which we have carried out on the elastic data below 8 MeV, confirms that the 5·38 MeV resonance in ^{13}N is $3/2^+$, $\Gamma \simeq 110$ keV. It shows, moreover, that the broad resonance at $6\frac{1}{2}$ MeV is also $3/2^+$, $\Gamma \simeq 2$ MeV. Confirmation of these assigned j^π values has been given in a personal communication from the Wisconsin group where analysis of polarization measurements produced similar level parameters.

In a recent article (INS34), Okai and Tamura of the Institute of Nuclear Study, Tokyo, indicate that the 8·2 MeV resonance, as seen in our elastic and inelastic data, could be due to an F-wave contribution on the grounds of the strong coupling between the competing elastic and inelastic channels. Phase contributions up to $l=3$ have been included in our analysis scheme, but as yet there is no confirmation of this possible assignment at 8·2 MeV.

We wish to thank Drs. W. Haeberli and S. Okai for the communications referred to here.

References

Adams, H. S., Becker, J. A., Fox, J. D., Heydenberg, N. P., and Temmer, G. M. (1960).—*Bull. Amer. Phys. Soc.* II, Vol. 5, No. 6.

McKenna, V. R., Baxter, A. M., and Shute, G. G. (1961).—*Aust. J. Phys.* **14** : 196.

Stovall, T., and Lee, L. L., Jr. (1960).—University of Minnesota Linear Accelerator Lab. Report 1960, p. 32.

CORRIGENDA

VOLUME 14, NUMBER 2, PAGES 279–94

" *The Influence of Thermoelectric Effects on the Maximum Temperature in a Radially Constricted Gas Discharge between Electrodes* "

Page 283, equation (3.2.15): For V read $\overline{V}$.

Page 283, equation (3.2.16): For T read $\overline{T}$.

AUSTRALASIAN MEDICAL PUBLISHING CO. LTD.
SEAMER AND ARUNDEL STS., GLEBE, SYDNEY

POLARIZATION IN NUCLEAR COLLISIONS WITH CHANNEL COUPLING

By C. B. O. Mohr* and C. A. Edvi-Illes*

[*Manuscript received July* 31, 1961]

Summary

The effect of the coupling between elastically and inelastically scattered waves on the polarization of particles scattered in nuclear collisions is considered for the simplest case of E0 excitations of the nucleus. The angular distribution of the polarization for elastic and inelastic collisions is found to be sensitive to the magnitude of the coupling parameter (the transition potential).

I. Introduction

With direct interaction established as the main mechanism operating in nuclear reactions at high energies, i.e. above the region where individual compound nucleus resonances play an independent part, there have been many calculations of differential scattering cross sections using the optical model and the Born approximation, either with simple plane waves or with distorted waves. With the inclusion of spin-orbit forces the work has been extended to the calculation of polarization produced in nuclear collisions.

Taking account of coupling between the elastically and inelastically scattered waves, however, causes appreciable changes in angular distributions (Mohr 1959 ; referred to later as paper I), and this throws doubt on the accuracy of nuclear parameters derived by fitting experimental angular distributions with curves calculated on the Born approximation.

In the present paper the channel coupling theory is extended to give the polarization in both elastic and inelastic collisions, for the simplest case of E0 excitations of the nucleus.

II. Theory

We use the obvious notation of paper I, suitably extended below, and the same simplifying assumptions to make the problem tractable, namely,

(i) the incident particles uncharged and the target nucleus spinless,
(ii) the excitation energy small compared with the incident energy E,
(iii) the nuclear potential $-V_{11}$ for the inelastically scattered particles the same as the nuclear potential $-V_{00}$ for the incident and elastically scattered particles,
(iv) the transition potential $-V_{01}$ spherically symmetrical (E0 excitations).

We introduce a spin-orbit term of the usual Thomas type to give the nuclear potential

$$-V_{00}+\gamma(h/2\pi mc)^2 r^{-1}(\mathrm{d}V_{00}/\mathrm{d}r)\mathbf{l}\cdot\mathbf{s},$$

---

* Physics Department, University of Melbourne.

where m is the mass of the pion, and $\mathbf{l}\cdot\mathbf{s}=l$ and $-(l+1)$ for $j=l+\frac{1}{2}$ and $l-\frac{1}{2}$ respectively. We take for $-V_{00}$ a square well of radius R, and then the spin-orbit term has the form of a Dirac δ function at $r=R$.

If we disregard channel coupling and spin-orbit coupling, the interior solution $F_l(r)$ of the radial wave equation for the incident and elastically scattered waves of order l will be a wave acted on by the attractive potential $-V_{00}$ and having at infinity a phase shift η_l.

With channel coupling, the coupled equations for the elastically and inelastically scattered waves $F_l^0(r)$ and $F_l^1(r)$ respectively have interior solutions $F_l^+(r)$ and $F_l^-(r)$ corresponding to waves in potential wells of depth $V_{00}+V_{01}$ and $V_{00}-V_{01}$ respectively. If these two solutions are extended beyond the nuclear boundary to large distances, they will have phase shifts η_l^+ and η_l^- respectively. Then the general solutions are (paper I, equations (13) and (15)):

$$F_l^0=LF_l^+ +MF_l^-, \tag{1a}$$
$$F_l^1=LF_l^+ -MF_l^-, \tag{1b}$$

where L and M are numerical coefficients.

If the spin-orbit potential, of δ function form at $r=R$, is now allowed to act on the two coupled interior waves as they reach the distance R, the slopes of each wave are changed at this point by amounts proportional to l and $-(l+1)$ for $j=l+\frac{1}{2}$ and $l-\frac{1}{2}$ respectively. If the four resulting waves F_l^{++}, F_l^{+-}, F_l^{-+}, and F_l^{--} are now integrated out to infinity, they will have phase shifts η_l^{++}, η_l^{+-}, η_l^{-+}, and η_l^{--}, where the second suffix $+$ or $-$ refers to the case of $j=l+\frac{1}{2}$ or $l-\frac{1}{2}$ respectively. These phases are most readily obtained in the usual way by fitting each of the four interior solutions at $r=R$ smoothly to the general exterior form

$$\cos\eta_l j_l(kr)+(-)^l\sin\eta_l n_l(kr),$$

and then

$$F_l\sim(kr)^{-1}\sin(kr-\tfrac{1}{2}l\pi+\eta_l). \tag{2}$$

Taking into account the angular dependence of the lth order wave functions, the four interior solutions have to be combined in the following proportions (Mott and Massey 1949):

$$\left.\begin{array}{ll}(l+1)F_l^{++}P_l(\cos\theta), & lF_l^{+-}P_l(\cos\theta)\\ (l+1)F_l^{-+}P_l(\cos\theta), & lF_l^{--}P_l(\cos\theta)\end{array}\right\}\text{ for }\psi_{3el}, \tag{3a}$$

$$\left.\begin{array}{ll}-F_l^{++}P_l^1(\cos\theta)\exp i\varphi, & F_l^{+-}P_l^1(\cos\theta)\exp i\varphi\\ -F_l^{-+}P_l^1(\cos\theta)\exp i\varphi, & F_l^{--}P_l^1(\cos\theta)\exp i\varphi\end{array}\right\}\text{ for }\psi_{4el}, \tag{3b}$$

and a similar combination for ψ_{3in} and ψ_{4in}, with opposite signs for the terms in F_l^{-+} and F_l^{--} on account of (1).

ψ_3 and ψ_4 are the "large components" of the four-component Dirac wave function describing the elastically or inelastically scattered waves, denoted respectively by the suffixes "*el*" and "*in*". They have the asymptotic form:

$$\psi_{3el}\sim e^{ikz}+r^{-1}e^{ikr}f_{el}(\theta), \tag{4a}$$
$$\psi_{4el}\sim r^{-1}e^{ikr}g_{el}(\theta), \tag{4b}$$
$$\psi_{3in}\sim r^{-1}e^{ikr}f_{in}(\theta)\exp i\varphi, \tag{4c}$$
$$\psi_{4in}\sim r^{-1}e^{ikr}g_{in}(\theta)\exp i\varphi, \tag{4d}$$

with the z axis taken along the incident beam, where

$$f_{el}=\Sigma_l k^{-1}(2l+1)\alpha_l P_l\,(\cos\theta),\qquad f_{in}=\Sigma_l k^{-1}(2l+1)\beta_l P_l\,(\cos\theta),\tag{5a}$$
$$g_{el}=\Sigma_l k^{-1}(2l+1)\alpha_l^s P_l^1\,(\cos\theta),\qquad g_{in}=\Sigma_l k^{-1}(2l+1)\beta_l^s P_l^1\,(\cos\theta).\tag{5b}$$

Taking linear combinations of the four interior solutions (3) for each of ψ_{3el}, ψ_{4el}, ψ_{3in}, and ψ_{4in} in their asymptotic form (2), and equating them to the corresponding asymptotic form (5) of the exterior solutions (4), we have

$$a(l+1)F_l^{++}+blF_l^{+-}+c(l+1)F_l^{-+}+dlF_l^{--}=i^l(2l+1)\{\sin(kr-\tfrac{1}{2}l\pi)+\alpha_l\exp ikr\},\tag{6a}$$
$$-aF_l^{++}+bF_l^{+-}-cF_l^{-+}+dF_l^{--}=i^l(2l+1)\alpha_l^s\exp ikr,\tag{6b}$$
$$a(l+1)F_l^{++}+blF_l^{+-}-c(l+1)F_l^{-+}-dlF_l^{--}=i^l(2l+1)\beta_l\exp ikr,\tag{6c}$$
$$-aF_l^{++}+bF_l^{+-}+cF_l^{-+}-dF_l^{--}=i^l(2l+1)\beta_l^s\exp ikr,\tag{6d}$$

where, for brevity of notation, the F's here denote their asymptotic forms (2), and a, b, c, and d are arbitrary (complex) coefficients. The correct combination of signs before the F's in (6a) and (6c) is indicated by (3a) and (1), and the combination of signs in (6b) and (6d) follows from (3b); but this result may be confirmed by employing the alternative method of projection operators used in the weak coupling case (Lepore 1950). A further set of four similar equations may be obtained by equating the *slopes* of the wave functions at the nuclear boundary.

We thus have eight equations to determine the eight unknown constants a, b, c, d, α_l, α_l^s, β_l, and β_l^s, though only the last four interest us. The equations may be solved without difficulty, using the properties of determinants, to give:

$$\alpha_l=\{(l+1)(E^{++}-1)+l(E^{+-}-1)+(l+1)(E^{-+}-1)+l(E^{--}-1)\}/4i(2l+1),\tag{7a}$$
$$\beta_l=\{(l+1)(E^{++}-1)+l(E^{+-}-1)-(l+1)(E^{-+}-1)-l(E^{--}-1)\}/4i(2l+1),\tag{7b}$$
$$\alpha_l^s=(-E^{++}+E^{+-}-E^{-+}+E^{--})/4i(2l+1),\tag{7c}$$
$$\beta_l^s=(-E^{++}+E^{+-}+E^{-+}-E^{--})/4i(2l+1),\tag{7d}$$

where $E^{++}=\exp 2i\eta_l^{++}$, etc.

The polarization P for either elastic or inelastic collisions is given by

$$P=(fg^*-f^*g)/i(ff^*+gg^*),\tag{8}$$

where the values of f and g are given by (5a) and (5b) with (7).

In the limiting case of zero coupling between the two channels ($V_{01}=0$), we have $\eta_l^{++}=\eta_l^{-+}=\eta_l^{0+}$ (say), $\eta_l^{+-}=\eta_l^{--}=\eta_l^{0-}$ (say), and (7) reduce to the well-known results (Mott and Massey 1949):

$$\alpha_l=\{(l+1)(\exp 2i\eta_l^{0+}-1)+l(\exp 2i\eta_l^{0-}-1)\}/2i(2l+1),\tag{9a}$$
$$\alpha_l^s=(-\exp 2i\eta_l^{0+}+\exp 2i\eta_l^{0-})/2i(2l+1),\tag{9b}$$
$$\beta_l=0=\beta_l^s.\tag{9c}$$

In the limiting case of zero spin-orbit coupling, $\eta_l^{++}=\eta_l^{+-}=\eta_l^{+0}$ (say), $\eta_l^{-+}=\eta_l^{--}=\eta_l^{-0}$ (say), and (7) reduce to

$$\alpha_l=(\exp 2i\eta_l^{+0}+\exp 2i\eta_l^{-0}-2)/2i,\tag{10a}$$
$$\beta_l=(\exp 2i\eta_l^{+0}-\exp 2i\eta_l^{-0})/2i,\tag{10b}$$
$$\alpha_l^s=0=\beta_l^s.\tag{10c}$$

Some remarks are necessary about the possibility of eliminating the simplifying assumptions made in the above theory. The elimination of the assumptions $k_1=k$ and $V_{11}=V_{00}$ still allows the general method of paper I to be extended to the problem of polarization, but the determinants obtained in the solution of (6) no longer reduce to simple expressions. The use of rounded-off potential wells for V_{00} and V_{01} causes the spin-orbit potential to overlap the potentials V_{00} and V_{01}, and a clean-cut separation of the effects of channel coupling and spin-orbit coupling on the interior wave functions is no longer possible: spin-orbit terms must be included in the coupled equations themselves, and this complicates the analysis. The consideration of excitations of higher multipolarity than E0 adds very greatly to the complexity of the problem, even with the neglect of spin-orbit forces (Mohr 1961), while the introduction of target nucleus spin will introduce further difficulty.

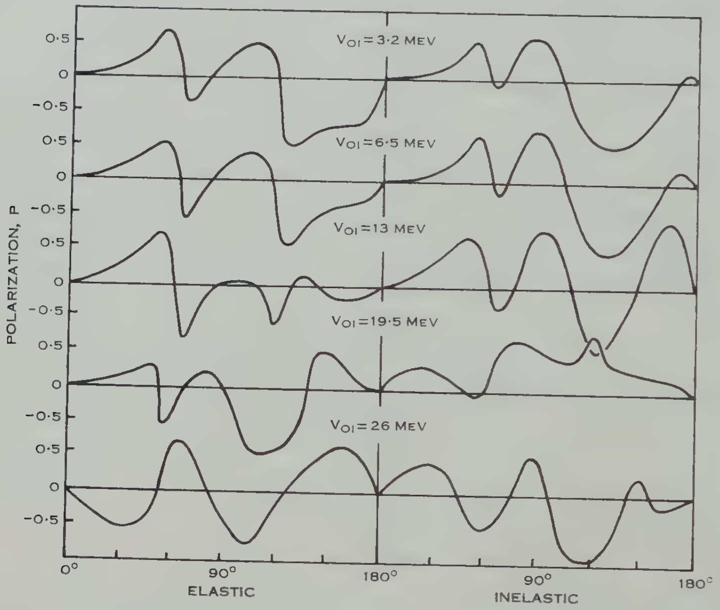

Fig. 1.—Angular distribution of the polarization of 18 MeV neutrons after elastic or inelastic collision with a light nucleus represented by a square well of radius $R=2\cdot 9$ fermi and depth $V_{00}=47$ MeV, and spin-orbit coupling parameter $\gamma=0\cdot 17$, for various values of the spherically symmetrical transition potential V_{01} indicated on the curves.

In view of all these difficulties and the fact that cases of strong E0 transitions are not found in the experiments, no direct comparison with experiment of theoretical angular distributions of polarization calculated with channel coupling can be attempted at the present time. Our purpose has been to estimate the magnitude of the effect of channel coupling on polarization, and to show that in general the effect is too large to be disregarded.

III. Results and Discussion

The parameters chosen for numerical calculations were $R=2\cdot9$ fermi (corresponding to carbon), $V_{00}=V_{11}=47$ MeV, incident energy $E=18$ MeV, as in paper I, in order to permit comparison of the effect of channel coupling on the polarization and on the scattering cross section. In paper I it was found that the magnitudes of β_0, β_1, β_2, and β_3 reached their maximum value of $0\cdot5$ for values of V_{01} of 15, 23, 25, and 5 MeV respectively, so in this work we took values of V_{01} between 0 and 26 MeV. The values chosen for the spin-orbit parameter were taken in the range of values used in Born approximation calculations for a light nucleus like carbon.

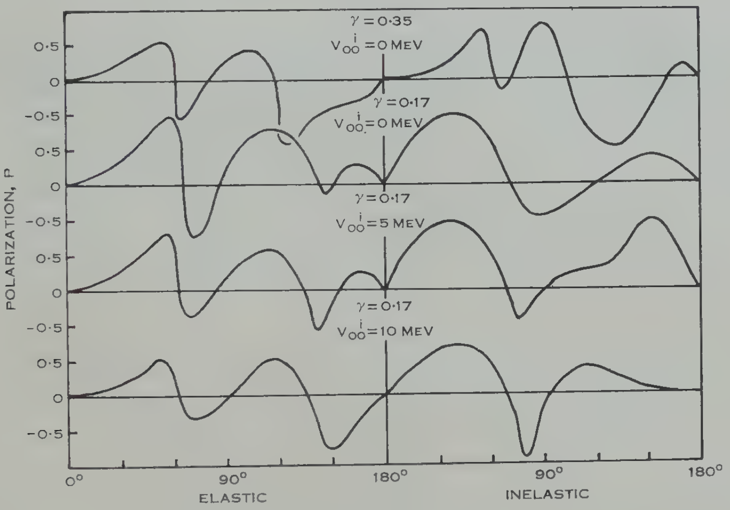

Fig. 2.—Angular distribution of the polarization of 18 MeV neutrons, for the same square well as for Figure 1. The top two curves show the effect of altering the spin-orbit coupling parameter γ. The bottom three curves show the effect of introducing increasing amounts of an imaginary component V^{i}_{00} and V^{i}_{11} into the nuclear potentials V_{00} and V_{11}.

The effect of varying the channel coupling is shown in Figure 1. The smallest two values of the transition potential V_{01} give practically the same angular distribution of the polarization, and this is not unexpected, since the form of the distribution will tend more and more closely to that given by the Born approximation as V_{01} tends to zero. The curves for $V_{01}=19\cdot5$ and 26 MeV are considerably different, however, especially at the larger angles.

The effect of increasing the spin-orbit coupling parameter γ from $0\cdot17$ to $0\cdot35$ is shown by the top two curves in Figure 2, a marked change being produced in the inelastic polarization. The effect of introducing an imaginary component $V^{i}_{00}=V^{i}_{11}$ into the nuclear potentials V_{00} and V_{11} to allow for nuclear absorption of the incident particles is shown in the bottom three curves of Figure 2. The inelastic polarization is seen to be very sensitive to the value of V^{i}_{00}, the elastic polarization much less so.

It appears, then, that the polarization is as sensitive to the channel coupling as the scattering, for E0 excitations. For E2 excitations, however, the scattering is even more sensitive (Mohr 1961), and it is likely that the polarization will similarly be more sensitive.

Channel coupling therefore cannot be ignored, and it introduces still another variable into this work. Any attempt to use a less crude model for channel coupling than that considered here, and to alter the many adjustable nuclear parameters to obtain a unique fit with experimental curves would seem to require a prohibitive amount of work.

IV. References

Lepore, J. V. (1950).—*Phys. Rev.* **79** : 137.

Mohr, C. B. O. (1959).—*Proc. Phys. Soc. Lond.* **73** : 894.

Mohr, C. B. O. (1961).—*Proc. Phys. Soc. Lond.* (In press.)

Mott, N. F., and Massey, H. S. W. (1949).—"The Theory of Atomic Collisions." 2nd Ed. Chap. IV, Section 4. (Oxford Univ. Press.)

GAMMA-RADIATION ABSORPTION COEFFICIENTS OF VARIOUS MATERIALS ALLOWING FOR BREMSSTRAHLUNG AND OTHER SECONDARY RADIATIONS

By J. W. ALLISON*

[*Manuscript received May* 25, 1961]

Summary

Existing calculations of the total absorption coefficient are generally based on the assumption that all the primary radiation energy which is converted into Compton-scattered radiation escapes from the material without significant absorption. This paper extends this basic assumption to include fluorescent and annihilation radiation and bremsstrahlung, and new values of the photoelectric, Compton, pair production, and total absorption coefficients are determined in the energy range 0·01–100 MeV for hydrogen, nitrogen, oxygen, argon, aluminium, iron, lead, air, and water. For comparison purposes revised values of the total absorption coefficient, allowing for the Compton radiation energy loss only, are also determined for these materials, using the most recent data for the component coefficients.

I. INTRODUCTION

When a beam of radiation passes through a material, photoelectric absorption, Compton scattering, and (above 1·02 MeV) pair production take place, as a result of which photons are removed from the beam and energy is absorbed in the material. The fractional loss of photons from an ideally narrow beam of monochromatic radiation per unit path length, and the corresponding fraction of the incident energy which is actually absorbed in the material, are respectively termed the total linear attenuation and total absorption coefficients, μ and μ_a,† of the material. The values of both these coefficients, or cross sections, depend on the radiation energy as well as on the material. Since some of the energy of the photons removed from the beam is not absorbed but escapes in the form of secondary radiation, $\mu_a<\mu$.

Multiplication of the linear coefficient μ_a by the factors $A/\rho N_0$, $A/\rho N_0 Z$, and $1/\rho$, where A, Z, and ρ are the atomic weight, atomic number, and density in g/cm³, and N_0 is Avogadro's number, gives corresponding coefficients per atom, per electron, and per unit mass, ${}_a\mu_a$, ${}_e\mu_a$, and μ_a/ρ respectively. Corresponding expressions hold for the other linear coefficients occurring in this work.

Apart from its importance in measuring the absorption of energy in materials, the absorption coefficient is also of considerable interest in studies of broad-beam attenuation. Under broad-beam conditions the effect of an absorber of thickness x cm is to reduce the dose rate at a given point by the factor $\exp(-\mu_{\text{eff.}}x)$, where

---

* Australian Defence Scientific Service, Defence Standards Laboratories, Department of Supply, Melbourne.

† These coefficients are frequently referred to in the literature as the absorption and the "real" or "true" absorption coefficients, respectively.

$\mu_{\text{eff.}}$ is an effective attenuation coefficient. Since secondary radiation contributes to the dose rate, $\mu_{\text{eff.}}$ must be less than the narrow-beam attenuation coefficient μ, the precise value depending on the absorber geometry. Evans and Evans (1948) have found experimentally that for ^{60}Co gamma-rays, where Compton scattering is the major attenuation process, $\mu_{\text{eff.}}=\mu-0\cdot 8\sigma_s=\mu_a+0\cdot 2\sigma_s$, where σ_s is the Compton coefficient relating to the energy carried away by the scattered photons, both when the source is enclosed in a close-fitting cylindrical lead absorber and when a large plane slab of absorber is placed directly against the source. The inequality $\mu_{\text{eff.}}>\mu_a$ found in this example is shown in the Appendix to hold in other cases where broad-beam conditions apply and where, in addition to Compton-scattered radiation, the secondary radiation is taken to include fluorescent radiation and bremsstrahlung. Thus in all cases μ and μ_a may be regarded as upper and lower limits to the value of $\mu_{\text{eff.}}$ required to describe the effect of the absorber in reducing the dose-rate. In this sense the coefficients μ and μ_a are of equal interest in problems of broad-beam attenuation.

Grodstein (1957) has made a detailed analysis of theoretical and experimental evidence and has published values of the total mass attenuation coefficient μ/ρ, and the component coefficients τ, σ, and $\varkappa$, relating to photoelectric absorption, Compton scattering, and pair production respectively. Her work, together with some subsequent revisions by McGinnies (1959), represents the most recent data available and covers a wide range of materials for the energy range 0·01–100 MeV. The results obtained for hydrogen, nitrogen, oxygen, argon, aluminium, iron, lead, air, and water are included in Tables 2 (*a*), 2 (*b*), 4, and 5, for comparison with the absorption coefficients calculated for these materials in this paper.

Unlike the attenuation coefficient, which simply represents the probability that a photon will undergo one or other of the three interaction processes, the absorption coefficient cannot be specified uniquely. This is because it is necessary to allow for absorption of the secondary radiations in the material and for escape of the secondary electrons before their energy is dissipated. However, a first approximation may be obtained by assuming that the dimensions of the material are sufficiently great for all the energy of the secondary electrons to be absorbed, but that the secondary radiations escape without significant absorption. The extent to which this basic assumption is realized in practice depends on the dimensions of the material and the energy of the primary radiation.

Existing calculations of the absorption coefficient make use of this assumption to take into account the escape of energy from the material in the form of Compton-scattered radiation. Thus Evans (1955, p. 713) has given graphs of μ_a/ρ for air, water, aluminium, lead, and sodium iodide for the energy range 0·01–100 MeV, which were plotted from the equation

$$\mu_a/\rho=\tau/\rho+\varkappa/\rho+\sigma_a/\rho, \tag{1}$$

where $\sigma_a=\sigma-\sigma_s$ is the Compton absorption coefficient relating to the energy which is converted into kinetic energy of secondary electrons in the material.

This calculation takes no account of the fluorescent radiation that is associated with the photoelectric process. In this process a photoelectron is ejected from the atom and, when the resulting vacancy is filled by an outer shell electron, either an X-ray photon or an Auger electron is emitted by the atom. In heavy materials the emission of radiation predominates: for example, the *K* fluorescent yield, that is, the number of photons which are emitted by the atom per *K* electron vacancy, is about 96% for lead. Also, since electron binding energies are relatively large in such materials, each X-ray photon carries an appreciable amount of energy: about 88 keV for the *K* radiation of lead. Hence an appreciable fraction of the total energy of the primary photons that take part in photoelectric collisions is converted into fluorescent radiation. Moreover, this radiation is sufficiently penetrating for it to travel some distance from its point of origin and should therefore be regarded as escaping from the material like the Compton-scattered radiation. For heavy materials the photoelectric absorption coefficient τ_a is thus substantially less than the attenuation coefficient τ, and at low energies, where the photoelectric process predominates, values of μ_a/ρ calculated from equation (1) are therefore too high.

Following each pair production process two annihilation quanta of total energy $2m_0c^2$, or $1\cdot02$ MeV, are produced when the positron, after losing most of its initial kinetic energy, is finally annihilated by an electron. Since this annihilation radiation forms part of the secondary radiation and should also be regarded as escaping from the material, the pair production absorption coefficient $\varkappa_a$ is less than the attenuation coefficient $\varkappa$. However, although this difference is very large at energies of a few MeV, the error in the total coefficient μ_a/ρ calculated from equation (1) is not more than about 2% since at such energies Compton scattering is the predominant attenuation process. The loss of energy from the material in the form of annihilation radiation is thus relatively unimportant in determinations of the total absorption coefficient.

In discussing the physical significance of the absorption coefficient Evans pointed out that the energy carried away from the primary collisions in the form of degraded secondary photons is not absorbed energy. He also defined energy absorption to mean the photon energy which is converted into kinetic energy of secondary electrons, and stated that this energy is eventually dissipated in the material as heat which could in principle be measured with a calorimeter. At low energies where the energy loss of electrons is predominantly by ionization this view is correct. However, at high energies electrons lose a large part of their energy in the production of bremsstrahlung, that is, secondary radiation emitted when the electron is decelerated or deflected in a nuclear field. Indeed, Heitler (1954, p. 253) has shown that the rate of energy loss per unit path length due to the emission of radiation equals the rate of loss due to ionization at about 10 MeV for lead and at about 125 MeV for water. Thus at high energies, and particularly for heavy materials, an appreciable part of the kinetic energy of the secondary electrons is not dissipated as heat, and it appears that due allowance should be made for this fact.

Some calculations of the total absorption coefficient allowing for all secondary radiations were briefly described by Fano (1953), who published results for water, aluminium, iron, and lead in the energy range $0\cdot088$–10 MeV. For heavy materials these results are substantially less than those calculated by taking

Compton-scattered radiation only into account, as would be expected from the above discussion. However, although Evans (1955) dealt with a wider energy range, 0·01–100 MeV, where the effects of fluorescent radiation and bremsstrahlung would be even greater, he did not allow for either of these secondary radiations. Since the results given by Evans have also been included in another textbook by Hine and Brownell (1956), it appears that the importance of fluorescent radiation and bremsstrahlung has not been generally recognized.

The purpose of the present paper is to present new and detailed calculations of the photoelectric, Compton-scattering, pair production, and total absorption coefficients which take into account the loss of energy from the material due to fluorescent radiation, annihilation radiation, and bremsstrahlung, in addition to Compton-scattered radiation. These calculations are based on the underlying assumption referred to earlier. In view of the application of the absorption coefficient in problems concerning the absorption of energy in materials and the fact that this coefficient is also associated with the study of broad-beam attenuation, it is thought that this work should prove of general interest.

II. BREMSSTRAHLUNG CORRECTION FACTORS, $\zeta(T_0)$

In this section, after a brief summary* of existing theoretical results for the probability that an electron of kinetic energy T MeV will produce radiation of energy k MeV, the intensity distribution of the bremsstrahlung is determined for several materials. From this work the rate of radiation energy loss per unit path of the electron $(\mathrm{d}T/\mathrm{d}s)_{\mathrm{rad}}$ is calculated in units of MeV cm²/g. This is followed by a calculation of the rate of ionization energy loss per unit path of the electron $(\mathrm{d}T/\mathrm{d}s)_{\mathrm{coll}}$ MeV cm²/g. The values of $(\mathrm{d}T/\mathrm{d}s)_{\mathrm{rad}}$ and $(\mathrm{d}T/\mathrm{d}s)_{\mathrm{coll}}$ thus obtained are used to determine the total amount of energy which is spent in ionization when an electron of initial kinetic energy T_0 MeV is brought to rest in each material. Each result is expressed as a bremsstrahlung correction factor $\zeta(T_0)$, which is defined as the ratio of the energy actually absorbed in the material to the initial kinetic energy of the electron. These correction factors, which do not appear to have been determined previously, are employed in the calculations of the photoelectric, Compton-scattering, and pair production absorption coefficients at high radiation energies in the three subsequent sections of this paper. This section concludes with a calculation of the intensity distributions of the total amount of bremsstrahlung emitted when an electron of initial kinetic energy T_0 MeV is brought to rest in each material.

Bethe and Heitler (1934) have shown that in the extreme relativistic region (energies much greater than $\mu_0=m_0c^2=0\cdot51098$ MeV) the cross section $\varphi'(k)\mathrm{d}k$ for the emission of a quantum of energy between k and $k+\mathrm{d}k$ by an electron of total energy $E=T+\mu_0$ is given by

$$\varphi'(k)\mathrm{d}k=\frac{4r_0^2Z^2}{137}\left(1+\frac{E_f^2}{E^2}-\frac{2E_f}{3E}\right)\left(\ln\frac{2EE_f}{k\mu_0}-\frac{1}{2}\right)\frac{\mathrm{d}k}{k}, \tag{2}$$

where $r_0=e^2/\mu_0=2\cdot8178\times10^{-13}$ cm and E_f is the final total energy of the electron, provided screening of the nuclear field by the atomic electrons is negligible. At high energies and with materials of high atomic number the probability of the radiation process taking place at large distances from the nucleus is increased and equation (2) must be modified to take screening into account. For this purpose Bethe and Heitler assumed a Thomas-Fermi distribution of atomic electrons and obtained:

---

* A comprehensive review has been given by Koch and Motz (1959).

$$2<\gamma<15,\quad \varphi'(k)\mathrm{d}k=\frac{4r_0^2Z^2}{137}\left(1+\frac{E_f^2}{E^2}-\frac{2E_f}{3E}\right)\left[\ln\frac{2EE_f}{k\mu_0}-\frac{1}{2}-c(\gamma)\right]\frac{\mathrm{d}k}{k},\tag{3}$$

$$\gamma<2,\quad \varphi'(k)\mathrm{d}k=\frac{4r_0^2Z^2}{137}\left\{\left(1+\frac{E_f^2}{E^2}\right)\left[\frac{\varphi_1(\gamma)}{4}-\frac{\ln Z}{3}\right]-\frac{2E_f}{3E}\left[\frac{\varphi_2(\gamma)}{4}-\frac{\ln Z}{3}\right]\right\}\frac{\mathrm{d}k}{k},\tag{4}$$

where $\gamma=100k\mu_0/EE_fZ^{1/3}$ and $\varphi_1(\gamma)$, $\varphi_2(\gamma)$, and $c(\gamma)$ are functions of γ given in Figure 1 and Table 1 of their paper. γ is a measure of the screening: $\gamma\gg1$ corresponds to the case of no screening; $2<\gamma<15$ to that of only slight screening, the function $c(\gamma)$ in equation (3) being a small correction to equation (2); and $\gamma<2$ to the case where screening is quite appreciable. In the limit of complete screening $\gamma=0$ and the expression within braces of equation (4) reduces to

$$\{(1+E_f^2/E^2-2E_f/3E)\ln(183Z^{-1/3})+E_f/9E\}.$$

Heitler (1954, p. 254) has considered the various approximations made in the derivation of the preceding equations and has concluded that the only serious error arises from the use of the Born approximation. This approximation has been corrected for in the present work by adding to the expressions the correction δ derived by Davies and Bethe (1952), namely,

$$\delta=-\frac{4\cdot828r_0^2Z^2}{137}\left(1+\frac{E_f^2}{E^2}-\frac{2E_f}{3E}\right)f(Z)\frac{\mathrm{d}k}{k},\tag{5}$$

where $f(Z)=(Z/137)^2$ for light materials and $f(Z)=0\cdot67$ for lead.

In addition to radiation in the field of the nucleus, radiation in the field of the atomic electrons should also be considered. Borsellino (1947) has shown that for the lower energies in the extreme relativistic region where screening is negligible, equation (2) also holds for electrons provided Z^2 is replaced by Z. Thus in this energy region the total cross section is proportional to $Z(Z+1)$. Wheeler and Lamb (1939, 1956) have treated the case of higher energies where screening is appreciable. Assuming a Thomas-Fermi distribution of atomic electrons they found that the cross section $\varphi''(k)\mathrm{d}k$ for the emission of a quantum of energy between k and $k+\mathrm{d}k$ is given by

$$\varepsilon<2,\quad \varphi''(k)\mathrm{d}k=\frac{4r_0^2Z}{137}\left\{\left(1+\frac{E_f^2}{E^2}\right)\left[\frac{\psi_1(\varepsilon)}{4}-\frac{2\ln Z}{3}\right]-\frac{2E_f}{3E}\left[\frac{\psi_2(\varepsilon)}{4}-\frac{2\ln Z}{3}\right]\right\}\frac{\mathrm{d}k}{k},\tag{6}$$

where $\varepsilon=100k\mu_0/EE_fZ^{2/3}$ and $\psi_1(\varepsilon)$ and $\psi_2(\varepsilon)$ are functions of ε given in Figure 1 of their 1956 paper. In the limit of complete screening $\varepsilon=0$ and the expression within braces of equation (6) reduces to

$$\{(1+E_f^2/E^2-2E_f/3E)\ln(1440Z^{-2/3})+E_f/9E\}.$$

As a check on the accuracy of the Fermi-Thomas model Wheeler and Lamb used atomic wave functions to recalculate their screening functions ψ_1 and ψ_2 and the corresponding Bethe and Heitler functions φ_1 and φ_2 for nitrogen in the limiting case of high energies (complete screening) and for hydrogen at all energies. This check illustrated the inadequacy of the Fermi-Thomas model for light materials. In the present work the Wheeler and Lamb recalculated values of ψ_1, ψ_2, φ_1, and φ_2 were employed when dealing with hydrogen.

Joseph and Rohrlich (1958) have recently considered the emission of bremsstrahlung, and the analogous process of pair production, where these processes take place in the field of the atomic electrons. Their work indicated that the Wheeler and Lamb calculations are subject to an appreciable error at low energies owing to the neglect of the exchange effect which arises from the similarity of the incident and recoil particles. On the other hand, McGinnies (1959, p. 3) has pointed out that current experimental evidence for pair production supports the Wheeler and Lamb calculations. For this reason the exchange correction derived by Joseph and Rohrlich was not applied in the present work.*

The total intensity $k\varphi(k)$ was calculated in the present investigation for electrons with kinetic energies of 100, 80, 40, 20, 10, and 5 MeV for hydrogen, nitrogen, oxygen, argon, aluminium, iron, and lead. The results for hydrogen, aluminium, and lead, shown graphically in Figure 1, illustrate the intensity distribution of the bremsstrahlung. For convenience the intensity is plotted as a function of k/T, which varies from 0 to 1, rather than of k itself. The curves for lead agree with those given by Heitler (1954, p. 250, Fig. 12) if allowance is made for the fact that his curves do not include the Born correction.

The areas under the intensity distribution curves are a measure of the radiation energy loss $(\mathrm{d}T/\mathrm{d}s)_{\mathrm{rad}}$ since, in units of MeV cm²/g, this is given by

$$\left(\frac{\mathrm{d}T}{\mathrm{d}s}\right)_{\mathrm{rad}}=-\frac{N_0}{A}\int_0^1 Tk\varphi(k)\mathrm{d}\left(\frac{k}{T}\right). \tag{7}$$

Using numerical integration this equation was evaluated for each of the seven materials at the five energies given above. In addition a value of $(\mathrm{d}T/\mathrm{d}s)_{\mathrm{rad}}$ for an electron with a kinetic energy of $0\cdot 1$ MeV was obtained from the equation (see Heitler, pp. 251–2, equations (28) and (32))

$$\left(\frac{\mathrm{d}T}{\mathrm{d}s}\right)_{\mathrm{rad}}=-\frac{16r_0^2Z^2N_0T}{411A}, \tag{8}$$

which holds in the non-relativistic region (energies much less than μ_0). The values of $(\mathrm{d}T/\mathrm{d}s)_{\mathrm{rad}}$ so obtained for each material were plotted in units of A/N_0T

---

* Even if the exchange correction were appropriate its omission would not affect the results for the bremsstrahlung correction factors to any significant degree. For heavy materials, radiation in the field of the electrons is small compared with that in the field of the nucleus so that no significant error would occur in the total intensity $\varphi(k)=\varphi'(k)+\varphi''(k)$. In the case of light materials bremsstrahlung in the field of the electrons is more important: indeed for hydrogen it is nearly equal to that in the field of the nucleus. However, the radiation energy loss for this material is small compared with the ionization energy loss so that again no significant error would result in the bremsstrahlung correction factors.

as functions of the energy T and fitted by smooth curves. The results given in Tables 1 (a) and 1 (b) for $(\mathrm{d}T/\mathrm{d}s)_{\mathrm{rad}}$ in the energy range 0·1–100 MeV were read from these curves, except the results for water which were derived from those for hydrogen and oxygen.

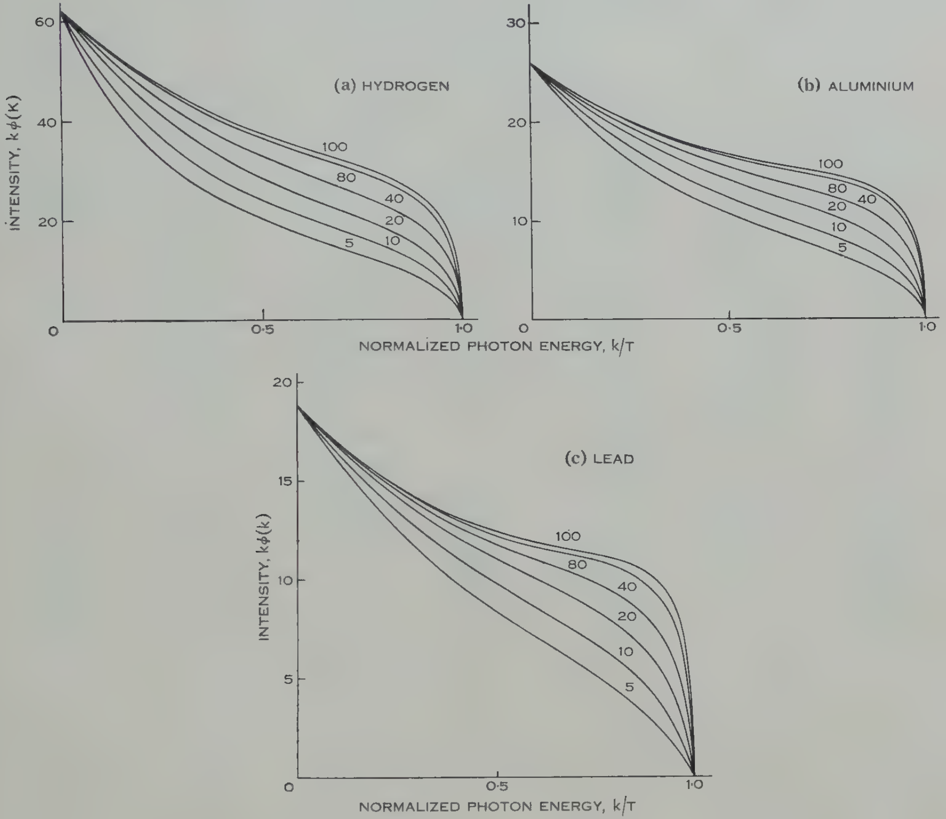

Fig. 1.—Intensity distribution of bremsstrahlung produced by a fast electron. (The ordinates are in units of $r_0^2Z^2/137$, k is the photon energy, and the numbers affixed to the curves refer to the electron's kinetic energy T MeV.)

The average energy loss per unit path length $(\mathrm{d}T/\mathrm{d}s)_{\mathrm{coll}}$ of an electron due to excitation and ionization of the atoms of the material through which it travels is given, in units of MeV cm^2/g, by the Bethe equation (see Bethe and Ashkin 1953)

$$\left(\frac{\mathrm{d}T}{\mathrm{d}s}\right)_{\mathrm{coll}}=\frac{2\pi e^4N_0Z}{Am_0v^2}\left\{\ln\left[\frac{m_0v^2T}{2I^2\lambda^2}\right]-(2\lambda-\lambda^2)\ln 2+\lambda^2+\tfrac{1}{8}(1-\lambda)^2\right\}, \qquad (9)$$

where v is the velocity of the electron, $\lambda^2=1-(v/c)^2$, and I is the mean excitation potential of the atom. In the present work the ionization loss was calculated for the materials in Tables 1 (a) and 1 (b) using the values of I which Bethe and Ashkin derived from the experimental work of Bakker and Segrè (1951). Values for water were derived from those for hydrogen and oxygen.

Table 1 (*a*)

RADIATION AND COLLISION ENERGY LOSSES OF AN ELECTRON PER UNIT PATH, $(\mathrm{d}T/\mathrm{d}s)_{\mathrm{rad}}$ AND $(\mathrm{d}T/\mathrm{d}s)_{\mathrm{coll}}$, FOR GASES*

Units are MeV cm^2/g

Kinetic Energy (MeV)	Hydrogen			Nitrogen		
	Radiation Loss	Collision Loss	Polarization Correction	Radiation Loss	Collision Loss	Polarization Correction
0·1	0·000	8·946		0·001	3·625	
0·2	0·000	5·984		0·001	2·466	
0·5	0·001	4·279		0·003	1·800	
1·0	0·002	3·886		0·008	1·659	
2·0	0·009	3·890		0·022	1·683	
5·0	0·041	4·168		0·078	1·832	
10·0	0·095	4·452		0·177	1·977	
20·0	0·215	4·761		0·390	2·133	
30·0	0·344	4·944	—0·001	0·618	2·226	
40·0	0·477	5·045	—0·029	0·853	2·284	—0·007
50·0	0·617	5·113	—0·065	1·095	2·327	—0·016
60·0	0·756	5·157	—0·103	1·336	2·359	—0·026
80·0	1·042	5·221	—0·170	1·835	2·403	—0·045
100·0	1·334	5·262	—0·231	2·330	2·433	—0·069
	Oxygen			Argon		
	Radiation Loss	Collision Loss	Polarization Correction	Radiation Loss	Collision Loss	Polarization Correction
0·1	0·001	3·570		0·002	2·908	
0·2	0·001	2·404		0·003	2·000	
0·5	0·004	1·778		0·008	1·477	
1·0	0·009	1·640		0·017	1·373	
2·0	0·025	1·666		0·048	1·404	
5·0	0·087	1·816		0·160	1·543	
10·0	0·196	1·961		0·361	1·674	
20·0	0·435	2·117		0·792	1·815	
30·0	0·691	2·206		1·250	1·900	
40·0	0·954	2·275		1·721	1·958	
50·0	1·225	2·325	—0·002	2·202	2·003	
60·0	1·496	2·359	—0·010	2·683	2·037	—0·005
80·0	2·052	2·412	—0·023	3·664	2·086	—0·015
100·0	2·600	2·445	—0·041	4·661	2·122	—0·026

---

* Values of the collision loss given in this table include the polarization correction.

TABLE 1 (*b*)

RADIATION AND COLLISION ENERGY LOSSES OF AN ELECTRON PER UNIT PATH, $(\mathrm{d}T/\mathrm{d}s)_{\mathrm{rad}}$ AND $(\mathrm{d}T/\mathrm{d}s)_{\mathrm{coll}}$, FOR CONDENSED MATERIALS*

Units are MeV cm^2/g

Kinetic Energy (MeV)	Water			Aluminium		
	Radiation Loss	Collision Loss	Polarization Correction	Radiation Loss	Collision Loss	Polarization Correction
0·1	0·001	4·172		0·001	3·231	
0·2	0·001	2·805		0·002	2·214	
0·5	0·004	2·054	—0·004	0·006	1·629	
1·0	0·008	1·865	—0·026	0·014	1·491	—0·003
2·0	0·023	1·849	—0·066	0·038	1·506	—0·034
5·0	0·082	1·925	—0·154	0·128	1·585	—0·102
10·0	0·184	1·996	—0·244	0·287	1·654	—0·173
20·0	0·411	2·063	—0·350	0·636	1·719	—0·258
30·0	0·653	2·096	—0·416	1·005	1·755	—0·312
40·0	0·901	2·124	—0·464	1·382	1·779	—0·351
50·0	1·157	2·144	—0·502	1·772	1·798	—0·382
60·0	1·413	2·160	—0·533	2·161	1·812	—0·408
80·0	1·939	2·184	—0·581	2·946	1·834	—0·449
100·0	2·458	2·203	—0·619	3·741	1·851	—0·482

Kinetic Energy (MeV)	Iron			Lead		
	Radiation Loss	Collision Loss	Polarization Correction	Radiation Loss	Collision Loss	Polarization Correction
0·1	0·002	2·896		0·01	2·027	
0·2	0·005	1·969		0·01	1·429	
0·5	0·011	1·471	—0·011	0·03	1·085	
1·0	0·027	1·352	—0·030	0·07	1·024	—0·003
2·0	0·074	1·357	—0·060	0·17	1·056	—0·012
5·0	0·231	1·427	—0·123	0·50	1·152	—0·043
10·0	0·511	1·509	—0·188	1·13	1·230	—0·081
20·0	1·144	1·579	—0·264	2·50	1·305	—0·130
30·0	1·781	1·615	—0·314	3·92	1·345	—0·164
40·0	2·447	1·640	—0·350	5·38	1·371	—0·190
50·0	3·132	1·656	—0·382	6·87	1·390	—0·212
60·0	3·813	1·669	—0·408	8·35	1·405	—0·230
80·0	5·197	1·691	—0·447	11·35	1·428	—0·259
100·0	6·587	1·707	—0·479	14·45	1·445	—0·283

* Values of the collision loss given in this table include the polarization correction.

At high energies the ionization energy loss is appreciably reduced by the shielding effect of the polarization of the medium. This effect has been treated in detail by Sternheimer (1952), who derived a theoretical equation for the correction $(\mathrm{d}T/\mathrm{d}s)_{\mathrm{pol}}$ which must be added to the values of $(\mathrm{d}T/\mathrm{d}s)_{\mathrm{coll}}$ obtained from equation (9). The correction is given by

$$\left(\frac{\mathrm{d}T}{\mathrm{d}s}\right)_{\mathrm{pol}}=-\frac{2\pi e^4 N_0 Z}{A m_0 v^2}\sum_i\left[f_i \ln\left(\frac{\bar{\nu}_i^2+l^2}{\bar{\nu}_i^2}\right)-l^2\lambda^2\right], \tag{10}$$

where f_i is the number of electrons in the ith shell divided by Z, and l is a solution of the equation

$$\frac{\lambda^2}{1-\lambda^2}=\sum_i\frac{f_i}{\bar{\nu}_i^2+l^2}. \tag{11}$$

The frequency $\bar{\nu}_i$ in equations (10) and (11) is given by Sternheimer as

$$\bar{\nu}_i=(\pi m_0 A/e^2 N_0 Z)^{\frac{1}{2}} B\nu_i, \tag{12}$$

where $h\nu_i$ is the excitation potential of the ith shell and B is an empirical correction factor equal to the ratio of the mean excitation potential $I=h\nu_m$ of the atom determined experimentally by Bakker and Segrè to the value deduced from the equation

$$\ln \nu_m=\sum_i f_i \ln \nu_i. \tag{13}$$

Sternheimer calculated the polarization correction for a number of materials and fitted his results by an empirical equation. This empirical equation was used in the present work for the materials in Tables 1 (*a*) and 1 (*b*), other than oxygen, for which the values of the coefficients in the empirical equation were not available and the polarization correction was calculated directly from equation (10).

The results obtained in the present work for the ionization loss corrected for polarization are given in Tables 1 (*a*) and 1 (*b*), together with results for the polarization correction itself. The values for water and lead agree with those given in graphical form by Heitler (1954, p. 373, Fig. 26). With hydrogen the radiation loss is about 25% of the collision loss for 100 MeV electrons. For heavier materials the radiation loss is even more important. Thus, for 100 MeV electrons, the ratio of the radiation loss to the ionization loss is nearly unity for nitrogen, is about 3·8 for iron, and is as high as 10 for lead.

The energy which is actually absorbed in each material from electrons of energies up to 100 MeV can be derived from the data assembled in Tables 1 (*a*) and 1 (*b*). Since the average energy absorbed in a path length ds is given by

$$(\mathrm{d}T)_{\mathrm{coll}}=(\mathrm{d}T/\mathrm{d}s)_{\mathrm{coll}}\mathrm{d}s=(\mathrm{d}T/\mathrm{d}s)_{\mathrm{coll}}(\mathrm{d}s/\mathrm{d}T)_{\mathrm{total}}(\mathrm{d}T)_{\mathrm{total}}, \tag{14}$$

it follows that the average fraction $\zeta(T_0)$ of the initial kinetic energy T_0 MeV which is absorbed when the electron is brought to rest is given by

$$\zeta(T_0)=\frac{1}{T_0}\int_0^{T_0}\left(\frac{\mathrm{d}T}{\mathrm{d}s}\right)_{\mathrm{coll}}\left(\frac{\mathrm{d}s}{\mathrm{d}T}\right)_{\mathrm{total}}\mathrm{d}T. \tag{15}$$

This integral was evaluated numerically in the present work for the various materials dealt with in this section and the results are given graphically in Figure 2.

This figure shows that for 10 MeV electrons the percentage of energy absorbed in the material due to ionization processes is 99% for hydrogen, 96% for nitrogen, 87% for iron, and 71% for lead. For 100 MeV electrons these percentages become 90, 70, 42, and 23% respectively. It is clear that at high energies, and especially for heavy materials, a substantial part of the initial kinetic energy of the secondary electrons produced in the various radiation attenuation processes is transformed into secondary radiation as the electrons are brought to rest.

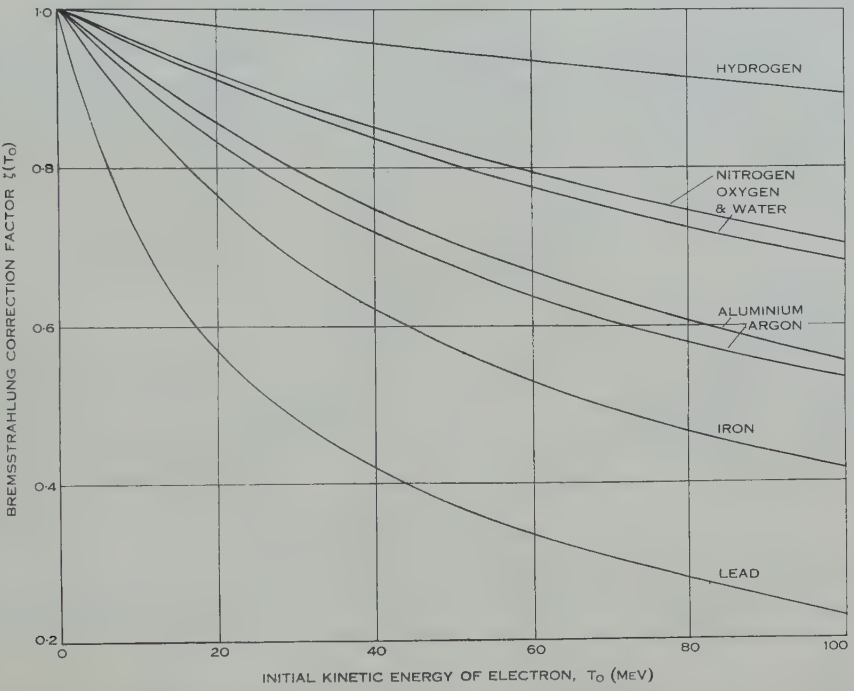

Fig. 2.—Bremsstrahlung correction factors $\zeta(T_0)$ for determining the energy absorbed in a material in which an electron of initial kinetic energy T_0 MeV is brought to rest.

The energy distribution of this radiation may now be derived. As a preliminary step it is necessary to obtain the electron's kinetic energy as a function of the distance travelled by it through the material. When both collision and radiation energy losses are taken into account the distance s, in units of g/cm², which the electron has travelled when its energy has fallen to T MeV, is given by the equation

$$s=\int_{T}^{T_0}\left\{1\bigg/\left(\frac{\mathrm{d}T}{\mathrm{d}s}\right)_{\text{total}}\right\}\mathrm{d}T. \tag{16}$$

Using values of $(\mathrm{d}T/\mathrm{d}s)_{\text{total}}=(\mathrm{d}T/\mathrm{d}s)_{\text{coll}}+(\mathrm{d}T/\mathrm{d}s)_{\text{rad}}$ from Tables 1 (*a*) and 1 (*b*) this integral can be evaluated numerically for various values of T and T_0 and the required relation between T and s obtained. Thus at each point in its range the kinetic energy of the electron can be found and, from the curves in Figure 1, the corresponding intensity $k\varphi(k)$ for the emission of photons of energy k. The total intensity $k\Phi(k)$ for the emission of photons of energy k as the electron is brought to rest is then given by the equation

$$k\Phi(k)=\frac{N_0}{A}\int_0^{R_0} k\varphi(k)\mathrm{d}s, \tag{17}$$

where R_0 g/cm², the maximum range of the electron, is given by

$$R_0=\int_0^{T_0}\left\{1\Big/\left(\frac{\mathrm{d}T}{\mathrm{d}s}\right)_{\text{total}}\right\}\mathrm{d}T. \tag{18}$$

In the present work $k\Phi(k)$ was calculated for initial electron energies of 10, 20, 40, 60, and 100 MeV. The results for aluminium and lead, shown graphically in Figure 3, illustrate the bremsstrahlung intensity distribution. It may be noted that the areas under these curves are a measure of the total amount of energy E_R MeV converted into radiation, since this is given by

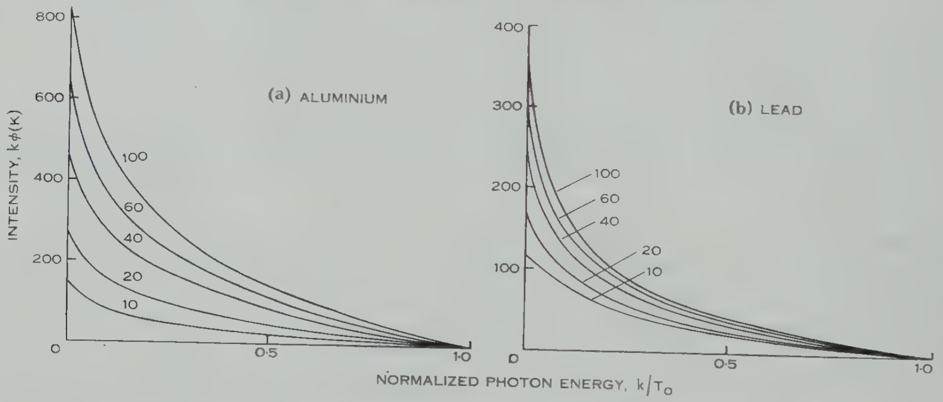

Fig. 3.—Intensity distribution of bremsstrahlung produced by an electron as it is brought to rest. (The ordinates are in units of $r_0^2Z^2N_0/137A$, k is the photon energy, and the numbers affixed to the curves refer to the electron's initial kinetic energy T_0 MeV.)

$$E_R=\int_0^1 T_0k\Phi(k)\mathrm{d}\left(\frac{k}{T_0}\right). \tag{19}$$

The bremsstrahlung correction factors $\zeta(T_0)$, which are simply equal to $(T_0-E_R)/T_0$, may therefore be obtained from the results illustrated in Figure 3. However, the preceding calculation of these factors is more direct and more accurate.

III. Photoelectric Absorption Coefficient

Values of the photoelectric absorption coefficient τ_a are derived in this section of the paper from those for the attenuation coefficient τ given by Grodstein and McGinnies (see Tables 2 (*a*) and 2 (*b*)) by applying a correction for the escape of energy in the form of fluorescent radiation from each material. A further correction is made in the case of lead to allow for the energy carried away in the form of bremsstrahlung, since for this material the photoelectric process remains significant up to fairly high energies.

The amount of primary energy which is converted into fluorescent radiation is negligible at all energies for the materials in Table 2 (*a*), since, firstly, the production of Auger electrons (Burhop 1954) predominates over that of X-ray photons, that is, only a few photoelectric collisions are accompanied by the emission of radiation, and secondly, electron binding energies are small so that each X-ray photon which is emitted carries only a small amount of energy. For example, for 10 keV primary radiation, and for aluminium which has a *K* fluorescent yield of about 0·031 and a *K* electron binding energy of about 1·56 keV, only about 0·5% of the primary energy is transformed into fluorescent radiation. This proportion is even less for greater primary energies, or for lighter materials which have smaller fluorescent yields and electron binding energies. Moreover, even the small amount of fluorescent radiation which is produced cannot be considered as escaping from the material since, because of its softness, it is absorbed within a very short distance of its point of origin. Thus for all the materials in Table 2 (*a*) the fluorescent radiation correction is negligible and the photoelectric absorption and attenuation coefficients are equal.

Appreciable corrections are required for the heavier materials in Table 2 (*b*) which have greater fluorescent yields and electron binding energies. For primary radiation energies greater than the *K* absorption limit of the material the photoelectron can be ejected from any of the shells of the atom so that *K*, *L*, *M*, . . . fluorescent radiations are produced. However, the fluorescent yield, the binding energy of an electron, and the probability for the photoelectric process itself

TABLE 2 (*a*)

MASS PHOTOELECTRIC ATTENUATION COEFFICIENTS τ/ρ FOR LIGHT MATERIALS*†

Energy (MeV)	τ/ρ (cm²/g)					
	Hydrogen	Nitrogen	Oxygen	Aluminium	Air	Water
0·01	0·0027	3·31	5·34	25·56	4·55	4·75
0·015	0·0007	0·877	1·44	7·48	1·25	1·28
0·02		0·345	0·561	3·04	0·495	0·498
0·03		0·0912	0·152	0·855	0·135	0·135
0·04		0·0340	0·0557	0·324	0·0505	0·0495
0·05		0·0159	0·0263	0·156	0·0240	0·0234
0·06		0·0086	0·0147	0·0870	0·0133	0·0130
0·08		0·0034	0·0056	0·0350	0·0052	0·0050
0·10		0·0017	0·0026	0·0172	0·0026	0·0024
0·15		0·0004	0·0008	0·0047	0·0007	0·0007
0·20			0·0004	0·0018	0·0002	0·0003
0·30				0·0004		
0·40				0·0002		

---

* All values are directly from Grodstein (1957) and McGinnies (1959), except the values for air which are derived from those for nitrogen, oxygen, and argon.

† For these materials the photoelectric absorption coefficient τ_a/ρ equals the attenuation coefficient.

TABLE 2 (*b*)

MASS PHOTOELECTRIC ATTENUATION AND ABSORPTION COEFFICIENTS, τ/ρ AND τ_a/ρ, FOR HEAVY MATERIALS*

Units are cm^2/g

Energy (MeV)	Argon		Iron		Lead†	
	τ/ρ	τ_a/ρ	τ/ρ	τ_a/ρ	τ/ρ	τ_a/ρ
0·01	64·0	62·0	179	141	137	137
0·01307					67·6	67·6
0·015	19·6	19·2	57·7	49·4		
0·01589					168	115
0·02	8·19	8·07	25·0	22·2	90·0	68·1
0·03	2·43	2·40	7·74	7·19	30·5	25·7
0·04	0·935	0·929	3·30	3·13	14·3	12·5
0·05	0·460	0·457	1·64	1·57	7·82	7·09
0·06	0·264	0·262	0·960	0·926	4·59	4·24
0·08	0·107	0·107	0·404	0·303	2·00	1·88
0·08823					1·52 7·30	1·44 1·36
0·10	0·054	0·054	0·204	0·199	5·17	1·49
0·15	0·0148	0·015	0·058	0·057	1·73	0·886
0·20	0·0062	0·0062	0·0240	0·0238	0·799	0·501
0·30	0·0018	0·0018	0·0071	0·0071	0·272	0·204
0·40	0·0008	0·0008	0·0031	0·0031	0·133	0·107
0·50	0·0005	0·0005	0·0017	0·0017	0·0759	0·0641
0·60	0·0003	0·0003	0·0011	0·0011	0·0503	0·0435
0·80			0·0005	0·0005	0·0276	0·0244
1·0			0·0003	0·0003	0·0180	0·0161
1·5					0·0087	0·0080
2·0					0·0058	0·0051
3·0					0·0032	0·0029
4·0					0·0023	0·0020
5·0					0·0017	0·0014
6·0					0·0014	0·0011
8·0					0·0010	0·0010
10					0·0008	0·0006
15					0·0005	0·0003
20					0·0004	0·0002
30					0·0003	0·0002
40					0·0002	0·0001
50					0·0001	0·0001

---

* Values of τ/ρ are from Grodstein (1957) and McGinnies (1959).

† For this material the values given for 0·01 and 0·01307 MeV (L_3 edge) are for the *M* shell; from 0·01589 MeV (L_1 edge) to 0·08823 MeV (*K* edge) they are for the *L* and *M* shells; and from 0·08823 MeV upwards they are for the *K*, *L*, and *M* shells.

are all less for an outer shell than for the K shell, so that little energy is converted into radiations other than the K. Hence it is only necessary to allow for the escape of K radiation. In the case of lead the energy range 0·01–100 MeV extends below both the K and L absorption limits (0·08823 and 0·01307 MeV). For this material and energies in the range 0·01307–0·08823 MeV the L fluorescent radiation must be taken into account since, firstly, the photoelectric process occurs predominantly in the L shell and secondly, the energy of the L radiation (about 15 keV) is appreciable compared to the primary energy. For energies less than 0·01307 MeV the photoelectric process occurs predominantly in the M shell and, since the fluorescent yield of this shell is very small (Burhop quotes the value 0·06 for uranium), the fluorescent radiation correction is negligible.

Hence for primary energies $h\nu$ greater than the K absorption limit of the material, and for energies between the K and L absorption limits in the case of lead, the photoelectric absorption coefficient is given by the respective equations

$$\frac{\tau_a}{\rho}=\frac{h\nu-p_K\omega_K I_K}{h\nu}\,\frac{\tau}{\rho}, \tag{20}$$

and

$$\frac{\tau_a}{\rho}=\frac{h\nu-p_L\omega_L I_L}{h\nu}\,\frac{\tau}{\rho}, \tag{21}$$

where $p_K=\tau_K/\tau_{K+L+M}$ and $p_L=\tau_L/\tau_{L+M}$ are the fractions of the total number of photoelectric collisions which occur in the K and L shells, ω_K and ω_L are the K and L fluorescent yields, and I_K and I_L are the ionization potentials of the K and L shells.

For the present calculation, values of I_K and I_L, ω_K, and p_K were obtained from the works of Hill, Church, and Mihelich (1952), Broyles, Thomas, and Haynes (1953), and Grodstein (1957, p. 18, Table V) respectively. The value of ω_L required in equation (21) was obtained from the early work of Lay (1934), who used X-ray excitation to find the fluorescent yields of several materials.* No information was available in the literature for the fraction p_L required in equation (21) and this was calculated with the aid of the Hall (1936) equations for the photoelectric attenuation coefficients of the L and M shells. These equations are respectively

$$\tau_L=\frac{2^{14}A_0}{(Z-s_2)^2}\nu_2^4(1+6\nu_2+8\nu_2^2)\,\frac{\exp\{-8(v_1/v)\arctan(v/v_1)\}}{1-\exp(-4\pi v_1/v)}, \tag{22}$$

and

$$\tau_M=\frac{2^9A_03^3}{(Z-s_3)^2}\nu_3^4(1+8\nu_3)(27+136\nu_3+208\nu_3^2+96\nu_3^3)\,\frac{\exp\{-4n_3\arctan(3/n_3)\}}{1-\exp(-2\pi n_3)}, \tag{23}$$

* Although the determination of K fluorescent yields has been the subject of considerable work, little information is available concerning the yields of outer shells. Lay's work has recently been supported by a value of ω_L for lead obtained by Patronis, Braden, and Wyly (1957). On the other hand values of ω_L published by Robinson and Fink (1955) for several materials do not agree with Lay's results, possibly because nuclear rather than X-ray excitation was employed.

where $A_0=h^3N_0\rho/12\pi m_0^2cAe^2$, $\nu_2=(Z-s_2)^2/4\nu$, $v_1=\pi e^2(Z-s_2)/h$, $v/v_1=(1/\nu_2-1)^{\frac{1}{2}}$, $\nu_3=(Z-s_3)^2/9\nu$, $n_3=3(1/\nu_3-1)^{-\frac{1}{2}}$, and s_2 and s_3 are Slater screening constants. A check on the calculation of τ_L and τ_M was provided by the fact that the sum $\tau_L+\tau_M$ was found to be in good agreement with the values of τ calculated independently by Grodstein.

The results obtained for the photoelectric absorption coefficients of argon, iron, and lead are given in Table 2 (*b*). In the case of lead these results include a correction for the bremsstrahlung produced in this material by high energy photoelectrons. This correction was made by subtracting an amount

$$\frac{E_R}{h\nu}\frac{\tau}{\rho}=\frac{T_0}{h\nu}[1-\zeta(T_0)]\frac{\tau}{\rho}, \tag{24}$$

where $T_0=h\nu-I_K$, from the values of τ_a/ρ obtained from equation (20).

Comparison of the values of τ_a/ρ and τ/ρ given in Table 2 (*b*) indicates the effect of taking fluorescent radiation and bremsstrahlung into account. The greatest change is for lead; for an energy just greater than the K absorption limit of this material, τ_a/ρ is only 19% of τ/ρ.

IV. Compton Absorption Coefficient

Although the variation in the energy and the number of Compton-scattered photons with the angle through which they are scattered have been considered frequently in the literature, the most comprehensive treatment being that of Nelms (1953), no information appears to be available giving the intensity distribution as a function of the radiation energy. This distribution is of interest in the present work, since the validity of the assumption that the scattered radiation escapes from the material without significant absorption depends on the energy of the radiation. This section contains a derivation of the radiation energy distribution, and a new calculation of the Compton absorption coefficient which allows for the loss of energy from the material in the form of bremsstrahlung.

The number of photons $g(\theta)\mathrm{d}\Omega$ which are scattered by an electron through an angle θ into a small solid angle $\mathrm{d}\Omega$ is given by the well known Klein-Nishina equation

$$g(\theta)\mathrm{d}\Omega=\frac{r_0^2}{2}\left\{\frac{(1+\cos^2\theta)[1+\alpha(1-\cos\theta)]+\alpha^2(1-\cos\theta)^2}{[1+\alpha(1-\cos\theta)]^3}\right\}\mathrm{d}\Omega, \tag{25}$$

where $\alpha=h\nu/\mu_0$ and $h\nu$ is the primary radiation energy. The energy $h\nu'$ of the scattered photon is given by the Compton equation

$$h\nu'=h\nu/[1+\alpha(1-\cos\theta)]. \tag{26}$$

From equations (25) and (26) it can be shown that the number of photons $g(h\nu')\mathrm{d}(h\nu')$ which are scattered per electron so that they have an energy between $h\nu'$ and $h\nu'+\mathrm{d}(h\nu')$ is given by the equation

$$g(h\nu')\mathrm{d}(h\nu')=\frac{\pi r_0^2}{\alpha h\nu}\left[\frac{1}{\alpha^2}\left(\frac{h\nu}{h\nu'}\right)^2+\left(1-\frac{2}{\alpha}-\frac{2}{\alpha^2}\right)\frac{h\nu}{h\nu'}+\left(\frac{2}{\alpha}+\frac{1}{\alpha^2}\right)+\frac{h\nu'}{h\nu}\right]\mathrm{d}(h\nu'). \tag{27}$$

The required cross section $g'(h\nu')\mathrm{d}(h\nu')$ for the energy scattered per electron in the range $\mathrm{d}(h\nu')$ is given by the equation

$$g'(h\nu')\mathrm{d}(h\nu')=(h\nu'/h\nu)g(h\nu')\mathrm{d}(h\nu'). \tag{28}$$

The intensity $g'(h\nu')$ was calculated in the present work for primary radiation energies of 0·1, 1, 10, and 100 MeV. The results, given graphically in Figure 4, illustrate the energy distribution of the Compton-scattered radiation. For convenience the intensity is plotted as a function of $h\nu'/h\nu$, which varies from 0 to 1, rather than of $h\nu'$ itself.

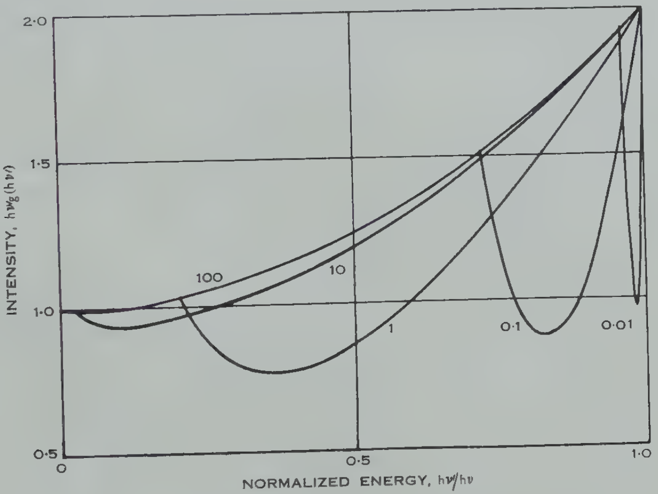

Fig. 4.—Intensity distribution of Compton-scattered photons. (The ordinates are in units of $\pi r_0^2/\alpha$, $h\nu'$ is the energy of the scattered photon, and the numbers affixed to the curves refer to the primary radiation energy $h\nu$ in MeV.)

Reference to Figure 4 shows that at high primary energies the scattered radiation contains a considerable amount of relatively soft photons. Thus, whereas for 0·01 MeV radiation the minimum scattered photon energy is about 96% of the primary energy, for 0·1, 1, 10, and 100 MeV radiation it falls to about 75, 20, 2·5, and 0·25% respectively. Again, consideration of the areas* under the curves in this figure shows that for primary energies of 10 and 100 MeV about 30 and 40% respectively of the total scattered energy are carried by photons with energies less than half the primary energy.

---

* The total area under each of these curves represents the Compton cross section ${}_e\sigma_s$ for the total amount of energy which is scattered by each electron in the material. However, this cross section is better obtained analytically from the equation

$${}_e\sigma_s=\int_0^1 h\nu' g(h\nu')\mathrm{d}(h\nu'/h\nu).$$

The cross-section $g''(h\nu')\mathrm{d}(h\nu')$ for the energy converted into kinetic energy of secondary electrons in the range $\mathrm{d}(h\nu')$ is given by the equation

$$g''(h\nu')\mathrm{d}(h\nu')=\{(h\nu-h\nu')/h\nu\}g(h\nu')\mathrm{d}(h\nu'). \tag{29}$$

Analytical integration gives the well known Klein-Nishina equation for the total cross section ${}_e\sigma_a$, namely,

$${}_e\sigma_a=\pi r_0^2\left[\frac{-20\alpha^4+102\alpha^3+186\alpha^2+102\alpha+18}{3\alpha^2(1+2\alpha)^3}+\frac{\alpha^2-2\alpha-3}{\alpha^3}\ln(1+2\alpha)\right]. \tag{30}$$

TABLE 3

COMPTON MASS ABSORPTION COEFFICIENT σ_a/ρ ALLOWING FOR THE ESCAPE FROM THE MATERIAL OF (*a*) SCATTERED RADIATION ONLY AND (*b*) SCATTERED RADIATION AND BREMSSTRAHLUNG

Units are cm²/g

Energy (MeV)	σ_a/ρ													
	Hydrogen		Nitrogen, Oxygen, and Air		Aluminium		Argon		Iron		Lead		Water	
	(*a*)	(*b*)	(*a*)	(*b*)	(*a*)	(*b*)	(*a*)	(*b*)	(*a*)	(*b*)	(*a*)	(*b*)	(*a*)	(*b*)
0·01	0·0072	0·0072	0·0036	0·0036	0·0035	0·0035	0·0033	0·0033	0·0034	0·0034	0·0029	0·0029	0·0040	0·0040
0·01307											0·0036	0·0036		
0·015	0·0104	0·0104	0·0052	0·0052	0·0050	0·0050	0·0047	0·0047	0·0049	0·0049	0·0041	0·0041	0·0058	0·0058
0·01589											0·0044	0·0044		
0·02	0·0133	0·0133	0·0068	0·0068	0·0065	0·0065	0·0061	0·0061	0·0062	0·0062	0·0053	0·0053	0·0074	0·0074
0·03	0·0186	0·0186	0·0094	0·0094	0·0090	0·0090	0·0084	0·0084	0·0087	0·0087	0·0074	0·0074	0·0104	0·0104
0·04	0·0231	0·0231	0·0116	0·0116	0·0112	0·0112	0·0105	0·0105	0·0108	0·0108	0·0092	0·0092	0·0129	0·0129
0·05	0·0271	0·0271	0·0136	0·0136	0·0132	0·0132	0·0123	0·0123	0·0127	0·0127	0·0108	0·0108	0·0152	0·0152
0·06	0·0305	0·0305	0·0154	0·0154	0·0148	0·0148	0·0139	0·0139	0·0143	0·0143	0·0122	0·0122	0·0171	0·0171
0·08	0·0362	0·0362	0·0182	0·0182	0·0176	0·0176	0·0164	0·0164	0·0170	0·0170	0·0144	0·0144	0·0203	0·0203
0·08823											0·0151	0·0151		
0·10	0·0406	0·0406	0·0205	0·0205	0·0197	0·0197	0·0185	0·0185	0·0191	0·0191	0·0162	0·0162	0·0227	0·0227
0·15	0·0481	0·0481	0·0242	0·0242	0·0234	0·0234	0·0219	0·0219	0·0226	0·0226	0·0192	0·0192	0·0269	0·0269
0·20	0·0525	0·0525	0·0265	0·0265	0·0255	0·0255	0·0239	0·0239	0·0246	0·0246	0·0210	0·0210	0·0294	0·0294
0·30	0·0569	0·0569	0·0287	0·0287	0·0277	0·0277	0·0259	0·0259	0·0267	0·0267	0·0227	0·0227	0·0319	0·0319
0·40	0·0586	0·0586	0·0295	0·0295	0·0285	0·0285	0·0266	0·0266	0·0275	0·0275	0·0234	0·0234	0·0328	0·0328
0·50	0·0590	0·0590	0·0297	0·0297	0·0286	0·0286	0·0268	0·0268	0·0277	0·0277	0·0235	0·0235	0·0330	0·0330
0·60	0·0587	0·0587	0·0296	0·0296	0·0285	0·0285	0·0267	0·0267	0·0276	0·0276	0·0234	0·0234	0·0329	0·0329
0·80	0·0574	0·0574	0·0289	0·0289	0·0279	0·0279	0·0261	0·0261	0·0269	0·0269	0·0229	0·0227	0·0321	0·0321
1·0	0·0555	0·0555	0·0280	0·0280	0·0270	0·0269	0·0252	0·0252	0·0260	0·0260	0·0222	0·0218	0·0311	0·0311
1·5	0·0507	0·0507	0·0255	0·0255	0·0246	0·0246	0·0230	0·0230	0·0238	0·0237	0·0202	0·0197	0·0284	0·0284
2·0	0·0464	0·0464	0·0234	0·0234	0·0225	0·0224	0·0211	0·0210	0·0218	0·0215	0·0185	0·0176	0·0260	0·0260
3·0	0·0397	0·0397	0·0200	0·0199	0·0193	0·0190	0·0180	0·0177	0·0186	0·0182	0·0158	0·0148	0·0222	0·0222
4·0	0·0348	0·0348	0·0175	0·0174	0·0169	0·0166	0·0158	0·0154	0·0163	0·0157	0·0139	0·0125	0·0195	0·0193
5·0	0·0311	0·0311	0·0157	0·0155	0·0151	0·0147	0·0141	0·0137	0·0146	0·0139	0·0124	0·0109	0·0174	0·0172
6·0	0·0282	0·0282	0·0142	0·0140	0·0137	0·0132	0·0128	0·0123	0·0132	0·0125	0·0112	0·0097	0·0158	0·0156
8·0	0·0239	0·0238	0·0120	0·0118	0·0116	0·0111	0·0108	0·0103	0·0112	0·0103	0·0095	0·0076	0·0134	0·0131
10	0·0208	0·0208	0·0105	0·0103	0·0101	0·0095	0·0095	0·0089	0·0098	0·0088	0·0083	0·0062	0·0117	0·0113
15	0·0160	0·0159	0·0081	0·0075	0·0078	0·0071	0·0072	0·0066	0·0075	0·0064	0·0064	0·0043	0·0089	0·0083
20	0·0131	0·0130	0·0066	0·0062	0·0064	0·0056	0·0060	0·0052	0·0062	0·0050	0·0052	0·0032	0·0073	0·0069
30	0·0098	0·0096	0·0049	0·0044	0·0048	0·0039	0·0045	0·0038	0·0046	0·0033	0·0039	0·0021	0·0055	0·0049
40	0·0079	0·0077	0·0040	0·0034	0·0039	0·0031	0·0036	0·0027	0·0037	0·0021	0·0032	0·0015	0·0044	0·0038
50	0·0067	0·0064	0·0034	0·0028	0·0033	0·0024	0·0030	0·0021	0·0031	0·0017	0·0027	0·0011	0·0037	0·0031
60	0·0058	0·0055	0·0029	0·0023	0·0028	0·0019	0·0026	0·0017	0·0027	0·0013	0·0023	0·0008	0·0033	0·0026
80	0·0046	0·0043	0·0023	0·0018	0·0023	0·0014	0·0021	0·0013	0·0022	0·0009	0·0019	0·0004	0·0026	0·0020
100	0·0039	0·0035	0·0020	0·0015	0·0019	0·0012	0·0018	0·0010	0·0018	0·0008	0·0016	0·0004	·0022	0·0016

To allow for the loss of energy in the form of bremsstrahlung it is necessary to use the bremsstrahlung correction factors $\zeta(T_0)$, illustrated in Figure 2, to weight the intensity $g''(h\nu')$ in equation (29). When this is done the cross section ${}_e\sigma_a$ is given by the equation

$$ {}_e\sigma_a=\int_{h\nu/(1+2\alpha)}^{h\nu} \frac{h\nu-h\nu'}{h\nu}\zeta(h\nu-h\nu')g(h\nu')\mathrm{d}(h\nu'), \tag{31} $$

which must be evaluated numerically.

In the present work, for purposes of comparison, values of ${}_e\sigma_a$ were calculated from both equations (30) and (31). The two sets of results for the various materials dealt with in this paper are given in mass units in columns (*a*) and (*b*) respectively of Table 3. The results for air were derived from those for nitrogen, oxygen, and argon. This table shows that for heavy materials and high energies the value of the Compton absorption coefficient is substantially reduced when bremsstrahlung is taken into account. Thus for aluminium and primary energies of 1, 10, and 100 MeV the new values (equation (31)) are about 100, 94, and 63% respectively of the Klein-Nishina values (equation (30)). For lead and the same energies these percentages are about 98, 75, and 25 respectively.

V. Pair Production Absorption Coefficient

In this section values of the pair production absorption coefficient are derived from those for the attenuation coefficient given by Grodstein (see Table 4), by applying corrections for the escape of energy in the form of bremsstrahlung and annihilation radiation.

In the pair production process a portion $2\mu_0$ of the energy of the incident photon is converted into a positron and an electron, and the remaining energy is shared, not necessarily equally, between these two particles in the form of kinetic energy. The attenuation coefficient ${}_a\varkappa$ is determined by integrating the cross section $\varphi(E_+)\mathrm{d}E_+$ for the creation of a positron with a total energy between E_+ and $E_++\mathrm{d}E_+$, and an electron with corresponding energy between E_- and $E_--\mathrm{d}E_-$, over all possible energies of the positron. Thus

$$ {}_a\varkappa=\int_{\mu_0}^{h\nu-\mu_0} \varphi(E_+)\mathrm{d}E_+. \tag{32} $$

For the present determination of the absorption coefficient ${}_a\varkappa_a$, bremsstrahlung energy losses were taken into account by using the bremsstrahlung correction factors (see Fig. 2) to weight the intensity $\varphi(E_+)$ in equation (32). Thus

$$ \begin{aligned} {}_a\varkappa_a&=\int_{\mu_0}^{h\nu-\mu_0} \frac{\zeta(E_+-\mu_0)E_++\zeta(E_--\mu_0)E_-}{h\nu}\varphi(E_+)\mathrm{d}E_+ \\ &=\frac{2}{h\nu}\int_{\mu_0}^{h\nu-\mu_0} \zeta(E_+-\mu_0)E_+\varphi(E_+)\mathrm{d}E_+. \end{aligned} \tag{33} $$

When the primary energy is sufficiently low for the radiation energy loss to be negligible compared to the ionization energy loss, $\zeta(E_+-\mu_0)=\zeta(E_--\mu_0)=1$ and equation (33) reduces to equation (32).

TABLE 4

PAIR PRODUCTION MASS ATTENUATION AND ABSORPTION COEFFICIENTS, $\varkappa/\rho$ AND $\varkappa_a/\rho$*

Units are cm^2/g

Energy (MeV)	Hydrogen		Nitrogen		Oxygen		Aluminium		Argon		Iron		Lead		Air		Water	
	$\varkappa/\rho$	$\varkappa_a/\rho$	$\varkappa/\rho$	$\varkappa_a/\rho$	$\varkappa/\rho$	$\varkappa_a/\rho$	$\varkappa/\rho$	$\varkappa_a/\rho$	$\varkappa/\rho$	$\varkappa_a/\rho$	$\varkappa/\rho$	$\varkappa_a/\rho$	$\varkappa/\rho$	$\varkappa_a/\rho$	$\varkappa/\rho$	$\varkappa_a/\rho$	$\varkappa/\rho$	$\varkappa_a/\rho$
1·5	0·0000	0·0000	0·0001	0·0000	0·0001	0·0000	0·0002	0·0001	0·0002	0·0001	0·0003	0·0001	0·0016	0·0003	0·0001	0·0000	0·0001	0·0000
2·0	0·0001	0·0001	0·0004	0·0002	0·0004	0·0002	0·0007	0·0003	0·0009	0·0004	0·0013	0·0005	0·0050	0·0015	0·0004	0·0002	0·0004	0·0002
3·0	0·0003	0·0002	0·0011	0·0007	0·0012	0·0008	0·0019	0·0013	0·0026	0·0017	0·0038	0·0022	0·0114	0·0061	0·0011	0·0008	0·0011	0·0007
4·0	0·0005	0·0004	0·0017	0·0013	0·0020	0·0015	0·0031	0·0023	0·0041	0·0029	0·0060	0·0041	0·0168	0·0103	0·0018	0·0014	0·0019	0·0014
5·0	0·0007	0·0005	0·0024	0·0019	0·0027	0·0021	0·0042	0·0033	0·0055	0·0040	0·0081	0·0059	0·0211	0·0135	0·0025	0·0019	0·0024	0·0019
6·0	0·0009	0·0007	0·0029	0·0024	0·0033	0·0028	0·0051	0·0042	0·0067	0·0050	0·0099	0·0076	0·0247	0·0170	0·0030	0·0025	0·0030	0·0025
8·0	0·0013	0·0011	0·0038	0·0034	0·0043	0·0038	0·0067	0·0058	0·0086	0·0070	0·0127	0·0104	0·0306	0·0220	0·0040	0·0035	0·0040	0·0034
10	0·0016	0·0014	0·0046	0·0040	0·0052	0·0046	0·0081	0·0069	0·0103	0·0087	0·0152	0·0124	0·0359	0·0257	0·0048	0·0043	0·0048	0·0042
15	0·0023	0·0020	0·0061	0·0056	0·0069	0·0061	0·0106	0·0092	0·0134	0·0117	0·0198	0·0159	0·0459	0·0306	0·0064	0·0058	0·0064	0·0058
20	0·0029	0·0026	0·0072	0·0067	0·0082	0·0073	0·0125	0·0107	0·0158	0·0135	0·0231	0·0180	0·0536	0·0333	0·0075	0·0069	0·0076	0·0067
30	0·0036	0·0034	0·0088	0·0079	0·0100	0·0087	0·0150	0·0125	0·0191	0·0155	0·0277	0·0204	0·0642	0·0353	0·0092	0·0082	0·0092	0·0082
40	0·0042	0·0039	0·0099	0·0086	0·0113	0·0096	0·0169	0·0135	0·0214	0·0166	0·0310	0·0214	0·0715	0·0356	0·0104	0·0090	0·0103	0·0090
50	0·0046	0·0043	0·0108	0·0092	0·0122	0·0101	0·0183	0·0140	0·0231	0·0171	0·0335	0·0217	0·0769	0·0355	0·0113	0·0095	0·0112	0·0096
60	0·0050	0·0047	0·0115	0·0095	0·0129	0·0105	0·0194	0·0142	0·0246	0·0174	0·0355	0·0218	0·0813	0·0350	0·0120	0·0098	0·0119	0·0100
80	0·0056	0·0052	0·0125	0·0100	0·0141	0·0110	0·0211	0·0145	0·0265	0·0175	0·0384	0·0215	0·0875	0·0330	0·0130	0·0104	0·0130	0·0105
100	0·0060	0·0056	0·0133	0·0104	0·0150	0·0112	0·0223	0·0144	0·0280	0·0174	0·0404	0·0208	0·0920	0·0297	0·0139	0·0107	0·0138	0·0108

* Values of $\varkappa/\rho$ are from Grodstein (1957).

The cross section $\varphi(E_+)\mathrm{d}E_+$ required in equations (32) and (33) has been derived by Bethe and Heitler (1934) for the case of pair production in the field of the nucleus. Their results, which are analogous to equations (2), (3), and (4) for the bremsstrahlung, are

$$\gamma_p \gg 1, \quad \varphi(E_+)\mathrm{d}E_+ = \frac{4r_0^2Z^2}{137(h\nu)^3}(E_+^2+E_-^2+\tfrac{2}{3}E_+E_-)\left(\ln\frac{2E_+E_-}{h\nu\mu_0}-\tfrac{1}{2}\right)\mathrm{d}E_+, \tag{34}$$

$$2<\gamma_p<15, \quad \varphi(E_+)\mathrm{d}E_+ = \frac{4r_0^2Z^2}{137(h\nu)^3}(E_+^2+E_-^2+\tfrac{2}{3}E_+E_-)\left[\ln\frac{2E_+E_-}{h\nu\mu_0}-\tfrac{1}{2}-c(\gamma_p)\right]\mathrm{d}E_+, \tag{35}$$

and

$$\gamma_p<2, \quad \varphi(E_+)\mathrm{d}E_+ = \frac{4r_0^2Z^2}{137(h\nu)^3}\left\{(E_+^2+E_-^2)\left[\frac{\varphi_1(\gamma_p)}{4}-\frac{\ln Z}{3}\right] + \tfrac{2}{3}E_+E_-\left[\frac{\varphi_2(\gamma_p)}{4}-\frac{\ln Z}{3}\right]\right\}\mathrm{d}E_+. \tag{36}$$

where $\gamma_p=100h\nu\mu_0/E_+E_-Z^{1/3}$ is a measure of the screening. For complete screening $\gamma_p=0$ and the expression in the braces of equation (36) reduces to

$$\{(E_+^2+E_-^2+2E_+E_-/3)\ln(183Z^{-1/3})-E_+E_-/9\}.$$

Using equations (34), (35), and (36) to obtain $\varphi(E_+)$, the weighted intensity $\varphi(E_+)\zeta(E_+-\mu_0)E_+$ was determined for each material and ${}_a\varkappa_a$ calculated from equation (33) by numerical integration. In the case of water, equation (33) was evaluated using values of the bremsstrahlung correction factor for this material, and values of the intensity $\varphi(E_+)$ given by $2\varphi_{\mathrm{H}}(E_+)+\varphi_{\mathrm{O}}(E_+)$, where $\varphi_{\mathrm{H}}(E_+)$ and $\varphi_{\mathrm{O}}(E_+)$ are the intensities for hydrogen and oxygen. The results for the weighted intensity for hydrogen, aluminium, and lead are shown graphically in Figure 5 for various primary energies. For convenience the intensity is plotted as a function of $(E_+-\mu_0)/(h\nu-2\mu_0)$ rather than of E_+.

The results for ${}_a\varkappa_a$ must be corrected for the Born approximation and also for the fact that pair production occurs in the field of the atomic electrons. These corrections were made with the aid of Grodstein's published results for the pair production cross sections in the fields of the nucleus and the atomic electrons, ${}_a\varkappa'$ and ${}_a\varkappa''$ respectively. Grodstein's results for ${}_a\varkappa'$ include a correction ${}_a\varkappa'_{\mathrm{Born}}$ for the Born approximation given by the equation

$${}_a\varkappa'_{\mathrm{Born}} = -\Delta\sigma_c+(a^2\mu_0/h\nu)\ln(h\nu/\mu_0), \tag{37}$$

where $\Delta\sigma_c$ and a^2 are functions of Z given in her Table 7. A corresponding correction was therefore made in the present work by multiplying the values of ${}_a\varkappa_a$ from equation (33) by the factor ${}_a\varkappa'/({}_a\varkappa'-{}_a\varkappa'_{\mathrm{Born}})$. To allow for pair production in the field of the atomic electrons the resulting values were multiplied by $({}_a\varkappa'+{}_a\varkappa'')/{}_a\varkappa'$.

As stated in the introduction, the annihilation radiation correction is very large at energies of a few MeV. In order to obtain accurate values of the pair absorption coefficient this energy loss was taken into account in the present work by subtracting the amount $(2\mu_0/h\nu)_a\varkappa$ from the values of ${}_a\varkappa_a$ obtained above, where ${}_a\varkappa={}_a\varkappa'+{}_a\varkappa''$ is the total Grodstein pair attenuation coefficient.

The final results for the pair production absorption coefficient for the various materials dealt with in this paper are given in Table 4. The results for air were derived from those for nitrogen, oxygen, and argon. Reference to this table shows the effect of taking bremsstrahlung and annihilation radiation into account. For example, for hydrogen, iron, and lead and 10 MeV radiation, the pair production absorption coefficients are respectively only about 88, 82, and 72% of the attenuation coefficients. For 100 MeV radiation these percentages become about 93, 52, and 32 respectively.

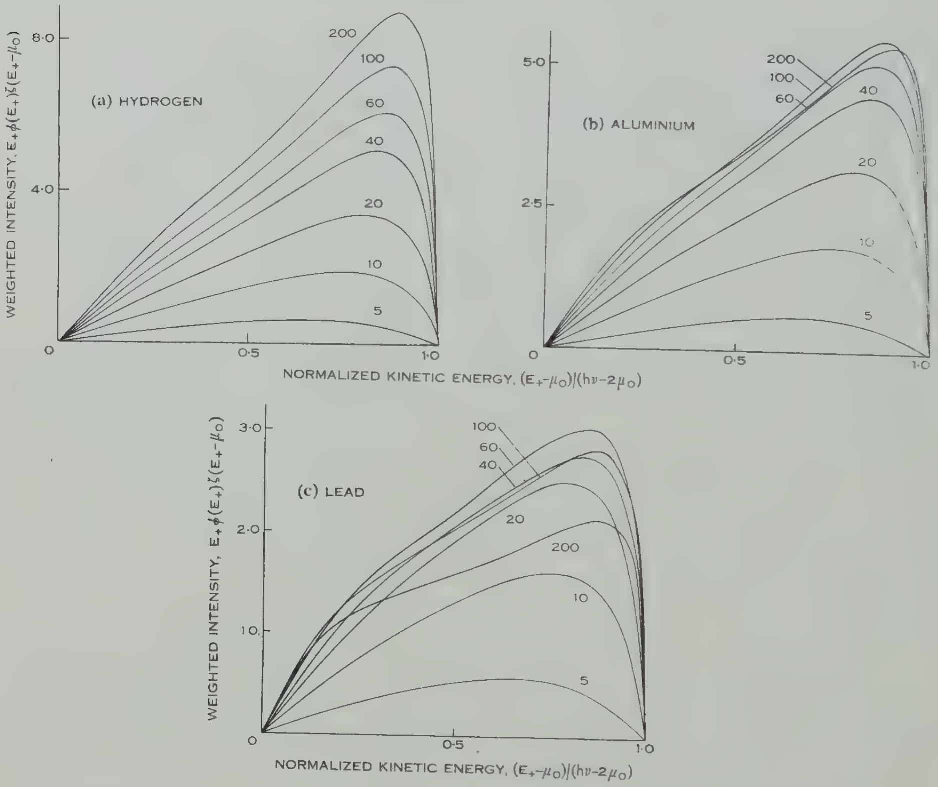

Fig. 5.—Intensity distribution of pair production positrons weighted to allow for bremsstrahlung energy losses. (The ordinates are in units of $2r_0^2Z^2/137h\nu$, E_+ is the total energy of the positron, and the numbers affixed to the curves refer to the primary radiation energy $h\nu$ in units of $\mu_0=m_0c^2$).

VI. Total Absorption Coefficient

Addition of the photoelectric, Compton, and pair production absorption coefficients determined in the previous section by taking into account the loss of energy from the material in the form of fluorescent and annihilation radiation and bremsstrahlung, in addition to Compton-scattered radiation, gives the new values for the total absorption coefficient listed in Table 5.

It is interesting to compare these results with values obtained from equation (1), which allows for the Compton-scattered radiation only. For this purpose the work of Evans (1955), which was based on the tables of atomic cross sections given by White (1952), was extended to include the various materials dealt with in this paper and revised using the more recent tables of τ and $\varkappa$ given by Grodstein (1957) and McGinnies (1959) (see Tables 2 (*a*) and 2 (*b*) and Table 4) together with values of σ_a calculated from the Klein-Nishina equation (see columns (*a*) of Table 3). The revised values, given in columns (*a*) of Table 5, differ from those of Evans at low energies because the values of τ given by McGinnies are substantially greater than those given by White; for example, for lead and an energy of 0·01 MeV the revised value is about 70% greater than Evans's value. Values of the total mass attenuation given by Grodstein and McGinnies are also included in Table 5.

TABLE 5

TOTAL MASS ATTENUATION AND ABSORPTION COEFFICIENTS μ/ρ AND μ_a/ρ*

The two sets of values for the absorption coefficient allow for the escape from the material of (*a*) scattered radiation only and (*b*) all secondary radiations. Units are cm²/g

Energy (MeV)	Hydrogen			Nitrogen			Oxygen			Aluminium		
	μ/ρ	μ_a/ρ (*a*)	μ_a/ρ (*b*)	μ/ρ	μ_a/ρ (*a*)	μ_a/ρ (*b*)	μ/ρ	μ_a/ρ (*a*)	μ_a/ρ (*b*)	μ/ρ	μ_a/ρ (*a*)	μ_a/ρ (*b*)
0·01	0·385	0·0099	0·0099	3·50	3·32	3·32	5·54	5·35	5·35	25·8	25·6	25·6
0·015	0·377	0·0111	0·0111	1·07	0·882	0·882	1·63	1·44	1·44	7·67	7·48	7·48
0·02	0·369	0·0133	0·0133	0·531	0·352	0·352	0·747	0·568	0·568	3·22	3·04	3·04
0·03	0·357	0·0186	0·0186	0·271	0·101	0·101	0·332	0·161	0·161	1·03	0·864	0·864
0·04	0·345	0·0231	0·0231	0·208	0·0456	0·0456	0·230	0·0674	0·0674	0·492	0·335	0·335
0·05	0·335	0·0271	0·0271	0·185	0·0295	0·0295	0·195	0·0399	0·0399	0·319	0·170	0·170
0·06	0·326	0·0305	0·0305	0·173	0·0240	0·0240	0·179	0·0301	0·0301	0·246	0·102	0·102
0·08	0·309	0·0362	0·0362	0·159	0·0217	0·0217	0·162	0·0239	0·0239	0·185	0·0527	0·0527
0·10	0·295	0·0406	0·0406	0·150	0·0222	0·0222	0·151	0·0231	0·0231	0·160	0·0369	0·0369
0·15	0·265	0·0481	0·0481	0·134	0·0246	0·0246	0·134	0·0250	0·0250	0·134	0·0281	0·0281
0·20	0·243	0·0525	0·0525	0·123	0·0265	0·0265	0·123	0·0269	0·0269	0·120	0·0273	0·0273
0·30	0·212	0·0569	0·0569	0·106	0·0287	0·0287	0·107	0·0287	0·0287	0·103	0·0281	0·0281
0·40	0·189	0·0586	0·0586	0·0955	0·0295	0·0295	0·0953	0·0295	0·0295	0·0922	0·0287	0·0287
0·50	0·173	0·0590	0·0590	0·0869	0·0297	0·0297	0·0870	0·0297	0·0297	0·0840	0·0286	0·0286
0·60	0·160	0·0587	0·0587	0·0805	0·0296	0·0296	0·0806	0·0296	0·0296	0·0777	0·0285	0·0285
0·80	0·140	0·0574	0·0574	0·0707	0·0289	0·0289	0·0708	0·0289	0·0289	0·0683	0·0279	0·0279
1·0	0·126	0·0555	0·0555	0·0636	0·0280	0·0280	0·0636	0·0280	0·0280	0·0614	0·0270	0·0269
1·5	0·103	0·0507	0·0507	0·0517	0·0256	0·0255	0·0518	0·0257	0·0255	0·0500	0·0248	0·0246
2·0	0·0876	0·0465	0·0465	0·0445	0·0238	0·0235	0·0445	0·0238	0·0236	0·0432	0·0232	0·0227
3·0	0·0691	0·0399	0·0399	0·0357	0·0211	0·0206	0·0359	0·0212	0·0207	0·0353	0·0212	0·0203
4·0	0·0579	0·0353	0·0353	0·0306	0·0193	0·0187	0·0309	0·0196	0·0189	0·0310	0·0200	0·0189
5·0	0·0502	0·0318	0·0316	0·0273	0·0180	0·0174	0·0276	0·0183	0·0177	0·0282	0·0193	0·0180
6·0	0·0446	0·0291	0·0289	0·0249	0·0171	0·0164	0·0254	0·0175	0·0167	0·0264	0·0188	0·0174
8·0	0·0371	0·0252	0·0248	0·0218	0·0159	0·0152	0·0224	0·0164	0·0156	0·0241	0·0183	0·0168
10	0·0321	0·0224	0·0222	0·0200	0·0151	0·0143	0·0206	0·0157	0·0148	0·0229	0·0182	0·0164
15	0·0249	0·0183	0·0179	0·0175	0·0142	0·0131	0·0183	0·0149	0·0136	0·0215	0·0183	0·0163
20	0·0209	0·0160	0·0156	0·0163	0·0139	0·0128	0·0173	0·0148	0·0135	0·0212	0·0188	0·0162
30	0·0168	0·0135	0·0130	0·0154	0·0138	0·0123	0·0166	0·0149	0·0131	0·0214	0·0198	0·0164
40	0·0147	0·0121	0·0116	0·0152	0·0139	0·0121	0·0165	0·0152	0·0130	0·0220	0·0208	0·0166
50	0·0133	0·0113	0·0107	0·0152	0·0142	0·0119	0·0165	0·0156	0·0129	0·0225	0·0216	0·0164
60	0·0125	0·0108	0·0102	0·0153	0·0144	0·0118	0·0167	0·0159	0·0129	0·0231	0·0222	0·0161
80	0·0115	0·0103	0·0095	0·0154	0·0148	0·0118	0·0171	0·0164	0·0127	0·0240	0·0233	0·0159
100	0·0109	0·0099	0·0092	0·0158	0·0153	0·0119	0·0175	0·0169	0·0127	0·0247	0·0242	0·0156

* Values of μ/ρ are from Grodstein (1957) and McGinnies (1959).

TABLE 5 (*Continued*)

Energy (MeV)	Argon μ/ρ	Argon μ_a/ρ (*a*)	Argon μ_a/ρ (*b*)	Iron μ/ρ	Iron μ_a/ρ (*a*)	Iron μ_a/ρ (*b*)	Lead† μ/ρ	Lead† μ_a/ρ (*a*)	Lead† μ_a/ρ (*b*)	Air μ/ρ	Air μ_a/ρ (*a*)	Air μ_a/ρ (*b*)	Water μ/ρ	Water μ_a/ρ (*a*)	Water
0·01	64·0	64·0	62·0	179	179	141	137	137	137	4·76	4·56	4·56	4·96	4·75	4·7
0·01307							67·6	67·6	67·6						
0·015	19·6	19·6	19·2	57·7	57·7	49·4				1·44	1·25	1·25	1·49	1·28	1·2
0·01589							168	168	115						
0·02	8·36	8·20	8·07	25·0	25·0	22·2	90	90	68·1	0·683	0·501	0·501	0·705	0·506	0·5
0·03	2·59	2·44	2·41	7·91	7·75	7·20	30·6	30·5	25·7	0·315	0·144	0·144	0·335	0·146	0·1
0·04	1·09	0·946	0·939	3·46	3·31	3·14	14·3	14·2	12·5	0·225	0·0620	0·0620	0·243	0·0624	0·0
0·05	0·612	0·472	0·469	1·80	1·65	1·59	7·96	7·83	7·10	0·193	0·0375	0·0375	0·211	0·0385	0·0
0·06	0·412	0·278	0·276	1·11	0·975	0·940	4·72	4·60	4·25	0·177	0·0286	0·0286	0·196	0·0301	0·0
0·08	0·247	0·124	0·124	0·550	0·421	0·411	2·12	2·01	1·89	0·161	0·0235	0·0235	0·178	0·0253	0·0
0·08823							1·64	1·54	1·46						
							7·42	7·32	1·38						
0·10	0·188	0·0725	0·0725	0·342	0·224	0·219	5·29	5·19	1·51	0·151	0·0231	0·0231	0·167	0·0251	0·0
0·15	0·135	0·0367	0·0367	0·183	0·0808	0·0797	1·84	1·753	0·906	0·134	0·0249	0·0249	0·149	0·0276	0·0
0·20	0·117	0·0301	0·0301	0·138	0·0487	0·0485	0·896	0·820	0·522	0·123	0·0267	0·0267	0·136	0·0297	0·0
0·30	0·0977	0·0277	0·0277	0·106	0·0338	0·0338	0·356	0·295	0·226	0·106	0·0287	0·0287	0·118	0·0319	0·0
0·40	0·0867	0·0274	0·0274	0·0919	0·0306	0·0306	0·208	0·156	0·131	0·0953	0·0295	0·0295	0·106	0·0328	0·0
0·50	0·0790	0·0272	0·0272	0·0828	0·0294	0·0294	0·145	0·0994	0·0876	0·0868	0·0297	0·0297	0·0966	0·0330	0·0
0·60	0·0730	0·0270	0·0270	0·0762	0·0287	0·0287	0·114	0·0737	0·0669	0·0804	0·0296	0·0296	0·0896	0·0329	0·0
0·80	0·0638	0·0261	0·0261	0·0664	0·0275	0·0275	0·0836	0·0505	0·0471	0·0706	0·0289	0·0289	0·0786	0·0321	0·0
1·0	0·0573	0·0252	0·0252	0·0595	0·0263	0·0263	0·0684	0·0402	0·0378	0·0635	0·0280	0·0280	0·0706	0·0311	0·0
1·5	0·0468	0·0233	0·0231	0·0485	0·0241	0·0238	0·0512	0·0306	0·0279	0·0517	0·0256	0·0255	0·0575	0·0285	0·0
2·0	0·0407	0·0220	0·0214	0·0424	0·0231	0·0220	0·0457	0·0293	0·0242	0·0445	0·0238	0·0235	0·0493	0·0263	0·0
3·0	0·0338	0·0206	0·0194	0·0360	0·0224	0·0205	0·0421	0·0305	0·0238	0·0357	0·0211	0·0206	0·0396	0·0233	0·0
4·0	0·0301	0·0199	0·0184	0·0330	0·0224	0·0198	0·0420	0·0330	0·0249	0·0307	0·0194	0·0188	0·0339	0·0213	0·0
5·0	0·0279	0·0196	0·0176	0·0313	0·0227	0·0198	0·0426	0·0353	0·0258	0·0274	0·0181	0·0174	0·0301	0·0198	0·01
6·0	0·0266	0·0195	0·0173	0·0304	0·0231	0·0201	0·0436	0·0374	0·0278	0·0250	0·0172	0·0165	0·0275	0·0188	0·01
8·0	0·0248	0·0194	0·0174	0·0295	0·0239	0·0207	0·0459	0·0412	0·0305	0·0220	0·0160	0·0153	0·0240	0·0173	0·01
10	0·0241	0·0197	0·0176	0·0294	0·0249	0·0212	0·0489	0·0450	0·0324	0·0202	0·0154	0·0145	0·0219	0·0165	0·01
15	0·0237	0·0207	0·0183	0·0304	0·0273	0·0223	0·0554	0·0527	0·0352	0·0178	0·0145	0·0132	0·0190	0·0153	0·01
20	0·0240	0·0218	0·0187	0·0315	0·0292	0·0230	0·0611	0·0592	0·0367	0·0166	0·0141	0·0131	0·0177	0·0149	0·01
30	0·0251	0·0236	0·0192	0·0339	0·0324	0·0236	0·0697	0·0683	0·0375	0·0158	0·0141	0·0126	0·0166	0·0147	0·01
40	0·0261	0·0250	0·0192	0·0359	0·0347	0·0235	0·0759	0·0749	0·0372	0·0156	0·0143	0·0124	0·0162	0·0148	0·01
50	0·0271	0·0262	0·0192	0·0376	0·0366	0·0234	0·0805	0·0797	0·0366	0·0157	0·0147	0·0122	0·0161	0·0150	0·01
60	0·0280	0·0272	0·0190	0·0391	0·0383	0·0230	0·0843	0·0836	0·0357	0·0158	0·0148	0·0122	0·0161	0·0151	0·01
80	0·0292	0·0286	0·0188	0·0412	0·0405	0·0233	0·0899	0·0894	0·0334	0·0160	0·0154	0·0121	0·0163	0·0156	0·01
100	0·0302	0·0298	0·0184	0·0427	0·0423	0·0217	0·0939	0·0936	0·0301	0·0164	0·0159	0·0121	0·0166	0·0160	0·01

† For this material the values given for 0·01 and 0·01307 MeV (L_3 edge) are for the *M* shell; from 0·01589 MeV (L_1 edge) to 0·08823 M (*K* edge) they are for the *L* and *M* shells; and from 0·08823 MeV upwards they are for the *K*, *L*, and *M* shells.

For low energies and heavy materials the values of the absorption coefficients in columns (*b*) of Table 5 are appreciably less than those in columns (*a*) owing to taking fluorescent radiation into account. For example, for an energy of 0·01 MeV the column (*b*) values are about 97 and 79% of the column (*a*) values for argon and iron respectively. For lead, and energies just above the L_1 and *K* absorption edges, these proportions fall to about 68 and 19% respectively. At high energies the effect of taking bremsstrahlung into consideration is evident. For example, for an energy of 10 MeV the column (*b*) values are about 99, 95, 90, 85, and 72% of the column (*a*) values for hydrogen, nitrogen, aluminium, iron, and lead respectively. For an energy of 100 MeV and the same materials these proportions are about 93, 78, 64, 51, and 32% respectively.

VII. ACKNOWLEDGMENTS

The author is grateful to Mr. R. G. Ackland for his valuable assistance in the preparation of this paper. Thanks are also due to Miss N. Rushford for carrying out many of the calculations.

This paper is published with the permission of the Chief Scientist, Australian Defence Scientific Service, Department of Supply, Melbourne, Australia.

VIII. REFERENCES

BAKKER, C. J., and SEGRÈ, E. (1951).—*Phys. Rev.* **81** : 489–92.

BETHE, H. A., and ASHKIN, J. (1953).—" Experimental Nuclear Physics." (Ed. E. Segrè.) Vol. I, Part II. (Wiley : New York.)

BETHE, H. A., and HEITLER, W. (1934).—*Proc. Roy. Soc.* A **146** : 83–112.

BORSELLINO, A. (1947).—*Nuovo Cim.* **4** : 112 ; *Rev. univ. nac. Tucumán* **A6** : 7. (Ref. from " Experimental Nuclear Physics." (Ed. E. Segrè.) Vol. I, p. 261. (Wiley : New York.))

BROYLES, C. D., THOMAS, D. A., and HAYNES, S. K. (1953).—*Phys. Rev.* **89** : 715–24.

BURHOP, E. H. S. (1954).—" The Auger Effect and Other Radiationless Transitions." (Cambridge Univ. Press.)

DAVIES, H., and BETHE, H. A. (1952).—*Phys. Rev.* **87** : 156–7.

EVANS, R. D. (1955).—" The Atomic Nucleus." (McGraw-Hill : New York.)

EVANS, R. D., and EVANS, R. O. (1948).—*Rev. Mod. Phys.* **20** : 305–26.

FANO, U. (1953).—*Nucleonics* **11** : 8–12.

GRODSTEIN, G. W. (1957).—X-ray attenuation coefficients from 10 keV to 100 MeV. Circ. Nat. Bur. Stand. 583.

HALL, H. (1936).—*Rev. Mod. Phys.* **8** : 358–97.

HEITLER, W. (1954).—" The Quantum Theory of Radiation." 3rd Ed. (Oxford Univ. Press.)

HILL, R. D., CHURCH, E. L., and MIHELICH, J. W. (1952).—*Rev. Sci. Instrum.* **23** : 523–8.

HINE, G. J., and BROWNELL, G. L. (1956).—" Radiation Dosimetry." (Academic Press : New York.)

JOSEPH, J., and ROHRLICH, F. (1958).—*Rev. Mod. Phys.* **30** : 354–68.

KOCH, H. W., and MOTZ, J. W. (1959).—*Rev. Mod. Phys.* **31** : 920–55.

LAY, H. (1934).—*Z. Phys.* **91** : 533.

MCGINNIES, R. T. (1959).—X-ray attenuation coefficients from 10 keV to 100 MeV. Circ. Nat. Bur. Stand. 583, Supplement.

NELMS, A. T. (1953).—Graphs of the Compton energy-angle relationship and the Klein-Nishina formula from 10 keV to 500 MeV. Circ. Nat. Bur. Stand. 542.

PATRONIS, E. T., BRADEN, C. H., and WYLY, L. D. (1957).—*Phys. Rev.* **105** : 681–2.

ROBINSON, B. L., and FINK, R. W. (1955).—*Rev. Mod. Phys.* **27** : 424–30.

STERNHEIMER, R. M. (1952).—*Phys. Rev.* **88** : 851–9.

WHEELER, J. A., and LAMB, W. E. (1939).—*Phys. Rev.* **55** : 858–62.

WHEELER, J. A., and LAMB, W. E. (1956).—*Phys. Rev.* **101** : 1836.

WHITE, G. R. (1952).—X-ray attenuation coefficients from 10 keV to 100 MeV. Nat. Bur. Stand. Rep. No. 1003 (unpublished). (The information in this report has been published in " Beta and Gamma-ray Spectroscopy." (Ed. K. Seigbahn.) (North-Holland Publishing Co. : Amsterdam, 1955.))

APPENDIX

Broad-beam Attenuation

As a typical example, consider the attenuation of a parallel beam of radiation by a large plane slab of absorber (see Fig. 6). From the geometry it can be seen that the amount of energy which is lost at A from the direct beam crossing the spherical volume element $\mathrm{d}V$, and which is converted into secondary radiation travelling in a forward direction within a conical shell of semivertical angle between θ and $\theta+\mathrm{d}\theta$, is just balanced by the amount of secondary radiation directed towards $\mathrm{d}V$ from corresponding points B lying in a circle around A.

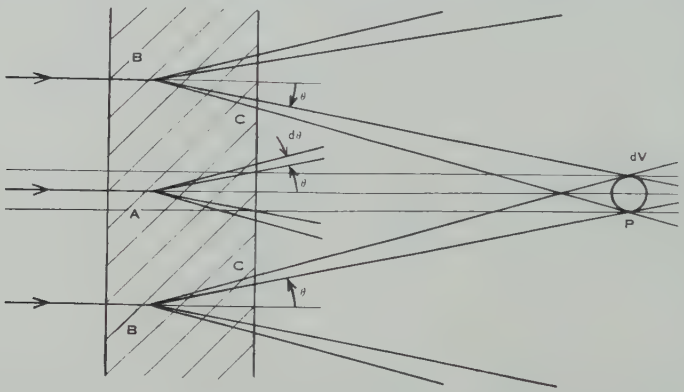

Fig. 6.—Attenuation of a parallel beam of radiation by a plane slab of absorber.

However, since the secondary radiation directed towards $\mathrm{d}V$ is attenuated in traversing the distance BC in the absorber, and also since some of the primary energy converted at A into secondary radiation travels in the backwards direction ($\theta \geqslant \frac{1}{2}\pi$), the total amount of secondary radiation arriving at $\mathrm{d}V$ from all points in the absorber must be less than the total amount of direct beam energy converted into secondary radiation. It follows that $\mu_a < \mu_{\text{eff.}} < \mu$. Similar considerations in other examples of broad-beam attenuation give the same result.

AN INVESTIGATION ON THE THERMAL CONDUCTIVITY OF POROUS MATERIALS AND ITS APPLICATION TO POROUS ROCK

By A. Sugawara* and Y. Yoshizawa*

[*Manuscript received March* 27, 1961]

Summary

The thermal conductivity of porous materials, particularly the effect of porosity and of temperature on thermal conductivity, has been investigated. A " comparison method " was used for measurement and the experiment was carried out with three types of models. A generalized formula for thermal conductivity is derived empirically. This formula can represent other formulas on the thermal conductivity of porous materials, and the formula can be applied to sandstones having different porosity as a typical example of porous materials.

I. Introduction

Owing to recent developments in science and engineering, such as geophysics, soil science, and mechanical and chemical engineering, the study of the thermal conductivity of porous materials is becoming increasingly important. The amount of pores in porous materials plays an important role among the many factors which influence thermal conductivity. However, no formulas are known that represent reasonably the relationship between thermal conductivity and porosity. Therefore correct formulation of the effect of porosity on thermal conductivity is of great importance.

This effect has been studied extensively, and numerous attempts (Euchen 1932; Russell 1935; Ribaud 1937; Waddams 1944; Francl and Kingery 1954; Loeb 1954; Krischer and Esdorn 1956; Kingery and Klein 1958; Somerton 1958) have been made to derive simplified relationships by approximating the complex effect of pore space. It has been known that not only the porosity but also the size, the shape, the orientation of the pore, and the emissivity in the pore have considerable effects on thermal conductivity. Even if these effects were known separately, it is impossible to analyse theoretically these effects because of three-dimensional irregularity of the above factors. Eventually therefore, all the formulas on thermal conductivity influenced by porosity had to be empirical and expressed as a function of porosity alone (Euchen 1932; Russell 1935; Ribaud 1937; Francl and Kingery 1954; Krischer and Esdorn 1956) with a shortcoming of not representing satisfactorily the actual state of thermal conductivity.

In the present paper a rather more reasonable formula relating thermal conductivity than any of those previously published is obtained from the results of fundamental experiments. By varying the empirical exponent " n " in this formula, the actual overall thermal conductivity can be represented more correctly than by any other formula.

---

* Department of Mining, Faculty of Engineering, Tohoku University, Sendai, Japan.

II. METHOD

In the present work the comparison method by linear heat flow has been adopted to measure the thermal conductivity. A sample material and a standard material, both in the form of plates, are brought face to face in close contact and a steady heat flow is sent through the plates, establishing a steady linear flow through the plate centres. From the measured values of the temperature gradients in the two plates and from the known thermal conductivity of the standard material, the thermal conductivity of the sample material is obtained.

The comparison method has an inherent defect as applied to the relatively thick sample; lateral heat loss to the surroundings reduces the accuracy of measurement. To limit the error thus caused to 1%, the thickness is required to satisfy the condition given by Tanazawa's (1932) theory that the diameters of the standard and sample plates should be more than five times their combined thickness.

Since in the steady state the temperature gradients in the two plates are obtained in the forms of $(\Delta T/d)$ and $(\Delta T_0/d_0)$, the thermal conductivity of the sample is given by

$$\lambda=\lambda_0\left(\frac{\Delta T_0}{d_0}\right)\left(\frac{d}{\Delta T}\right), \qquad (1)$$

where λ, λ_0=thermal conductivities of sample and standard plates respectively, in kcal/m hr degC,

ΔT, ΔT_0=temperature differences between the two faces of the sample and standard plates respectively, in degC,

d, d_0=thickness of sample and standard plates respectively, in mm.

A diagram of the experimental apparatus has been published and explained in detail by Sugawara (1961).

III. SAMPLE PREPARATION

Each sample was made to conform to the condition required by Tanazawa's theory; the shape was a flat circular disk with surfaces finished as smooth as possible. Attention was paid to having the thickness constant at every point.

The samples used were as follows.

(*a*) *An Aggregation of Glass Balls having Small Diameter*

An aggregation of small glass balls is considered most ideal as the model of porous material and very convenient to explain actual phenomena, but in the natural piled up state as shown in Figure 1 (*a*), called the cubic type, the porosity is 26·0% regardless of ball diameter. So, in order to obtain a different porosity, balls were linked together with very fine threads of the same glass as the ball, as shown in Figure 1 (*b*). The porosity was varied by changing the distance between the balls.

The diameter of the glass balls used was 3·1 mm, and the porosity was 26·0% for the natural piled up state and was 80·0% for the linked balls.

The most serious drawback in this experiment is the uncertainty of the conductivity of the solid constituent of the material as a basis for calculation.

Many cases are known in which the method of determining such conductivity is that a more or less straight line relationship between the overall thermal conductivity and the porosity is assumed and, by the use of a few samples of different porosity and by extrapolation to zero volume fraction, the required conductivity is obtained. In the present case, the glass balls were melted down and glass plates were cast with which the conductivity of the glass was determined.

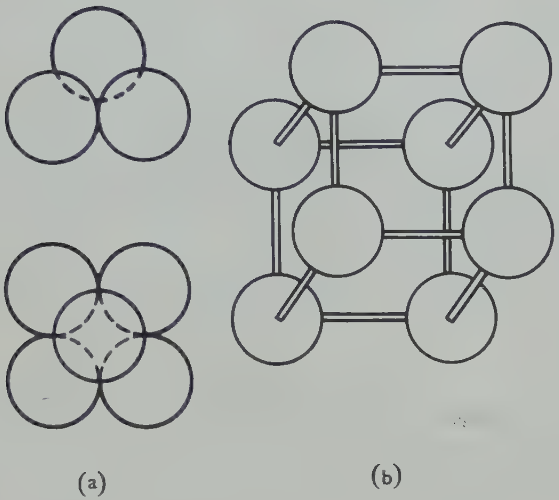

Fig. 1.—Glass ball samples.

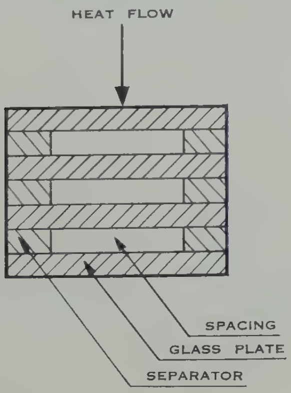

Fig. 2.—Multilayered glass sample.

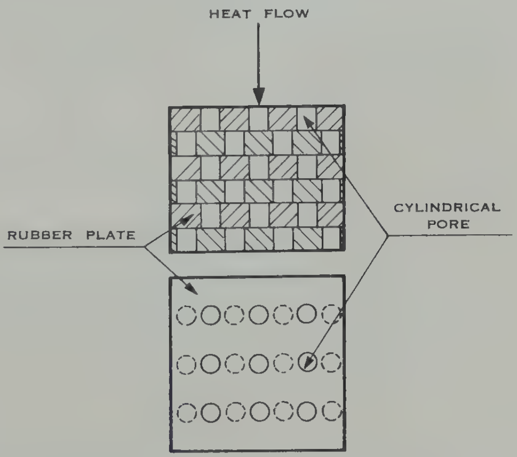

Fig. 3.—Pored rubber plate sample.

(*b*) *Multilayered Glass Plates*

Krischer and Esdorn (1956) showed that, in measuring thermal conductivity, porous materials can be simulated by multilayered plates of glass. This idea was followed up and a set of multilayered glass (as shown in Fig. 2) was prepared.

Several glass plates were placed face-parallel, the spacing between plates was kept constant by means of a separator fixed around the edges, the ratio of the total sum of the spacing to the total volume of the glass array representing the porosity of the array.

The porosities used in this experiment were 25·0, 50·0, and 75·0%.

(c) *Cylindrical-pored Rubber Plates*

A piled set of flat and smooth rubber plates was prepared as a sample. Cylindrical pores 2·0 mm in diameter were drilled through every plate with a given pitch regularly over its whole surface. In piling the plates, every other plate is shifted half the pitch so that all the pores are closed off by adjacent plates as shown in Figure 3.

For varying the porosity, the pitch between the pores was changed. The porosities used were 12·5, 26·0, and 50·0%.

IV. RESULTS

Experiments were made on the above three types of samples under given porosities. The fluids with which the pores were filled were dry air and distilled water. Thermal conductivity was obtained as a function of temperature with porosity as parameter.

From the results of the measurement, thermal conductivity (λ) versus temperature (t) diagrams and thermal conductivity (λ) versus porosity (ψ) diagrams were drawn.

(a) λ *versus* t *Diagrams*

λ versus t diagrams obtained on the glass ball, the multilayered glass, and the pored rubber plates are shown in Figures 4, 5, and 6 respectively with porosity as parameter.

In Figures 4 and 5

$$\lambda_{sg} > \lambda_w > \lambda_a,$$

in Figure 6

$$\lambda_w > \lambda_{sr} > \lambda_a,$$

where suffixes are a, air ; sg, glass ; sr, rubber ; w, water.

In each case the relationship between (λ) and (t) is linear. In Figures 4 and 5, the lines placed above the line (λ_w) and in Figure 6, the lines above the line (λ_{sr}) show the case when water was used as the filling fluid. The lines below them relate to when air was used.

(b) λ *versus* ψ *Diagrams*

λ versus ψ diagrams with temperature as parameter can be obtained by tracing λ versus t diagrams vertically. λ versus ψ curves for the glass ball, the multilayered glass, and the pored rubber plate samples are shown in Figures 7, 8, and 9 respectively. When the thermal conductivity of the solid constituent is greater than that of the fluid in the pores, the λ verus ψ curves are convex against the ψ axes as shown in Figures 7 and 8 and when otherwise, λ versus ψ curves are concave as shown in the case of water saturation of Figure 9.

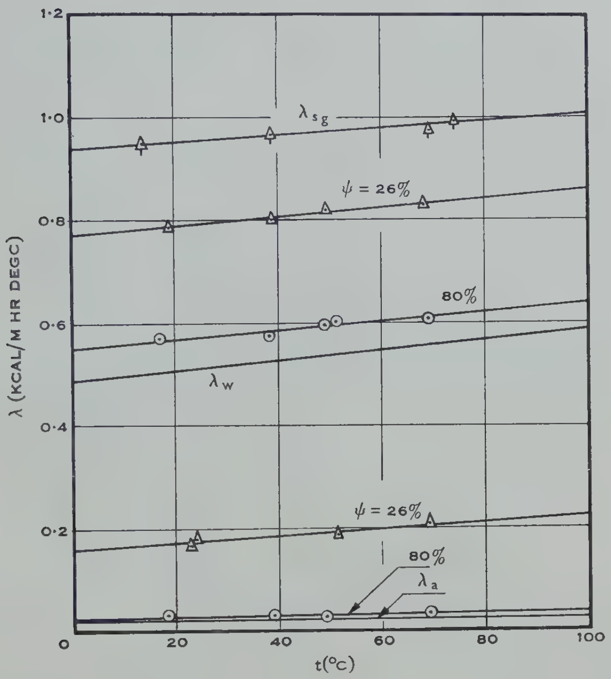

Fig. 4.—λ versus *t* diagram obtained on glass ball samples.

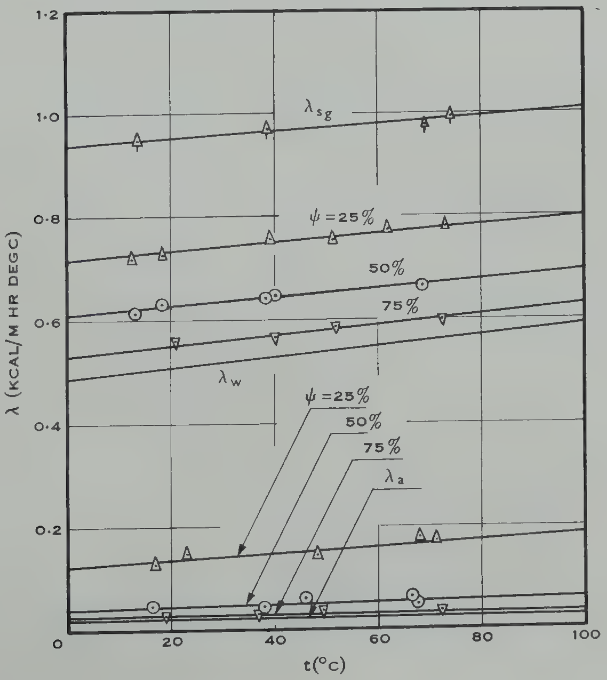

Fig. 5.—λ versus *t* diagram obtained on multilayered glass sample.

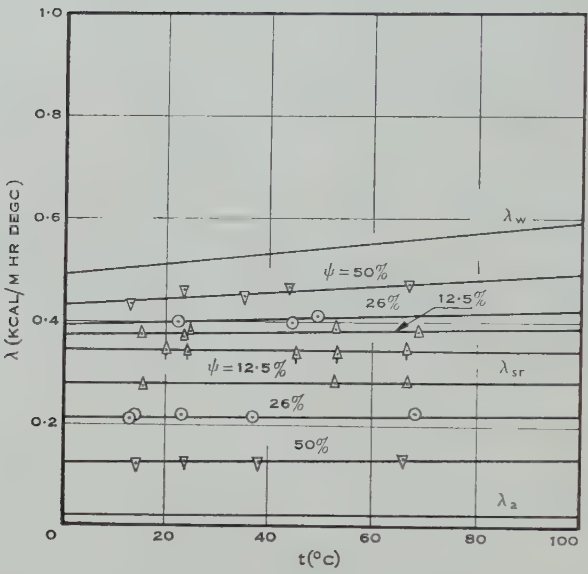

Fig. 6.—λ versus t diagram obtained on pored rubber plate sample.

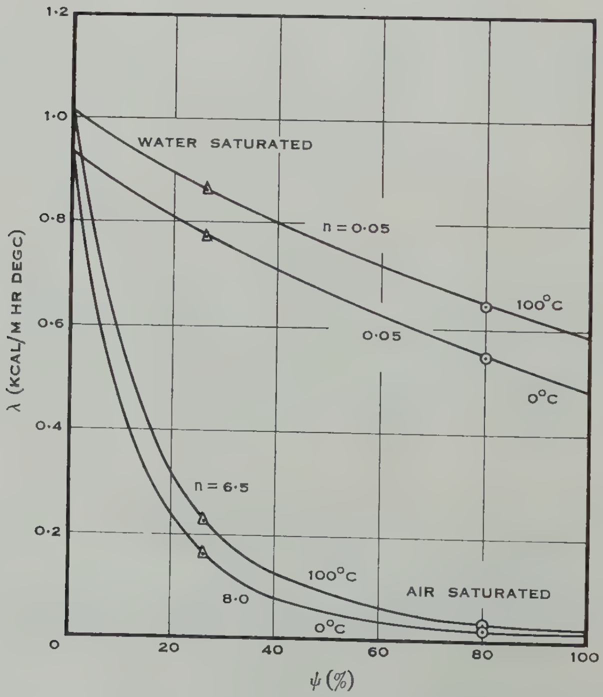

Fig. 7.—λ versus ψ diagram obtained on glass ball samples.

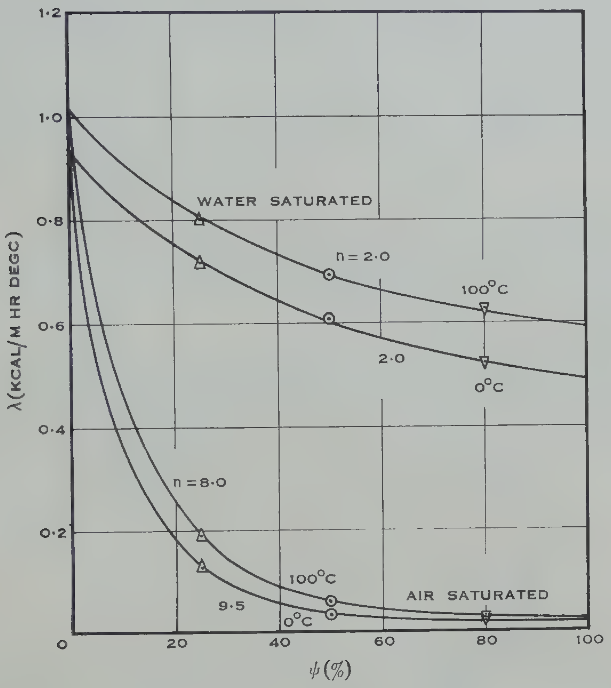

Fig. 8.—λ versus ψ diagram obtained on multilayered glass sample.

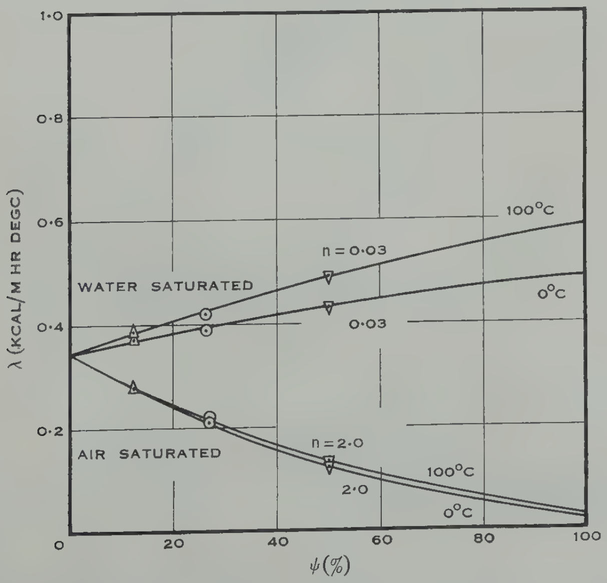

Fig. 9.—λ versus ψ diagram obtained on pored rubber plate sample.

Generally, it can be seen that the porosity and the fluid that fills the pores influence the thermal conductivity very much, the porosity in particular when the difference between the conductivity of solid constituent and that of the fluid is very great.

From these diagrams, the following general formula is derived,

$$\lambda=(1-A)\lambda_s+A\lambda_f \quad \text{kcal/m hr degC}, \tag{2}$$

where $A=\dfrac{2^n}{2^n-1}\left\{1-\dfrac{1}{(1+\psi)^n}\right\}$,

λ=overall thermal conductivity of porous materials,

λ_f, λ_s=thermal conductivity of fluid and solid constituent respectively,

ψ=porosity,

n=empirical exponent determined by mode of packing, pore size, pore shape, and emissivity inside of the pore, and $n>0$.

The values of n for each λ versus ψ curve are shown in Figures 7, 8, and 9.

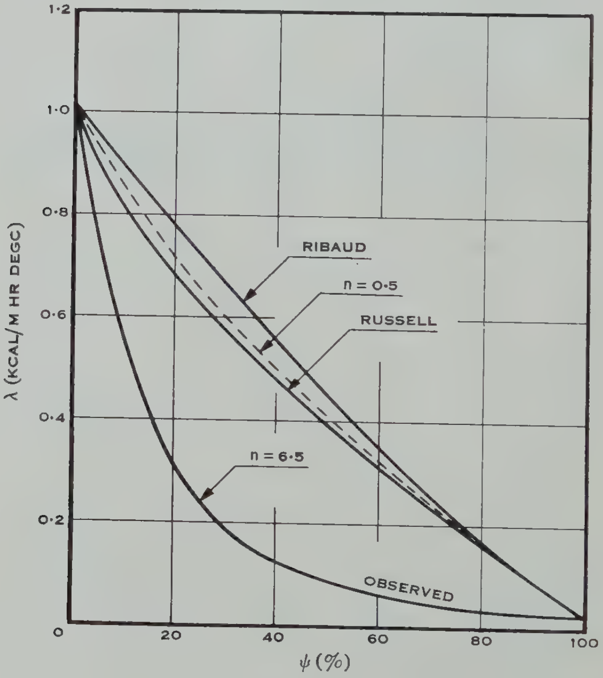

Fig. 10.—λ versus ψ diagram compared with other results.

V. Comparison with Other Results

There are many formulas concerning the relationship between thermal conductivity and porosity; representative are those of Eucken (1932), Russell (1935), Ribaud (1937), and Loeb (1954).

By Ribaud's and Russell's formulas applied to the case of the air-filled glass ball specimen and by the use of the values of λ_s and λ_a at 100 °C mentioned above, λ versus ψ curves were obtained by calculation and are shown in Figure 10, on which the curve obtained in the present experiment is given, marked " Observed ", for comparison.

The very great difference between these curves can probably be attributed to the fact that all those authors referred to above treated the thermal conductivity as a function of porosity alone and ignored the influence of pore size, pore shape, material structure, etc.

Ribaud's and Russell's formulas are as follows :

$$\lambda=\lambda_a\psi^{\frac{2}{3}}+\lambda_s(1-\psi^{\frac{2}{3}}), \qquad \text{Ribaud}$$

$$\lambda=\lambda_s\frac{\psi^{\frac{2}{3}}+Q(1-\psi^{\frac{2}{3}})}{\psi^{\frac{2}{3}}-\psi+Q(1-\psi^{\frac{2}{3}}+\psi)}, \qquad \text{Russell}$$

where $Q=\lambda_s/\lambda_a$.

Other formulas have similar tendencies to the above two in deviating from the observed curve shown in Figure 10.

Allowing a small percentage of error, if we represent the two calculated curves of Figure 10 by a curve shown by the dotted line in the figure, the value of n of this curve becomes $0 \cdot 5$. So the formula (2) can cover any other formula on the thermal conductivity of porous material.

VI. APPLICATION TO POROUS ROCK

For applying formula (2) to practical cases, we choose sandstones having different porosities as a typical example of porous material. The sandstone is sedimentary rock which consists of aggregations of small particles. The sandstone used, called " Nanaura ", was obtained from the Yotsuyama Colliery, Mitsui Mining Co., located in Fukuoka Prefecture.

The characteristics of the sandstones by visual observation were as follows :

grain size ; medium (diameter $\frac{1}{2}\sim\frac{1}{4}$ mm by U.S. Bureau of Soils Classification)
matrix ; calcareous
sorting ; well and uniform
colour ; grey and light grey.

Measurements were carried out for two cases on each sample, one was dry (did not contain moisture) and the other was water-saturated. In order to obtain the dry sample, it was dried for 2 hr in an air oven at 110 °C and was put into a closed vessel in which the measurement was carried out. On the other hand, in order to saturate the pore space with water, the sample was supported as shown in Figure 11 ; one face of the flat sample is in air and the other is in water. In this case, water was introduced into the pore space by capillary pressure through the pores and the air in the pores was driven out from the open face. Thus we obtained a fully water-saturated sample.

On measuring the thermal conductivity of the water-saturated sample, to prevent any convection effect caused by water movement (sometimes moisture movement) due to a temperature gradient in the sample, the temperature difference between the two faces of the sample plate was kept as small as possible during the measurement.

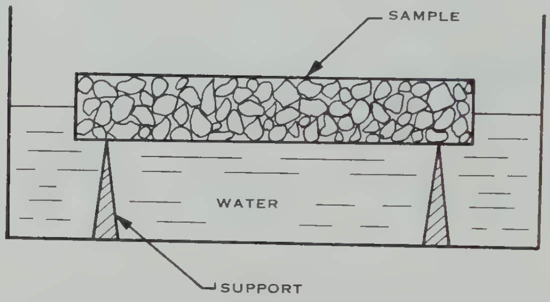

Fig. 11.—Cross section of diagram for saturating the pore spaces of sandstone specimen with water.

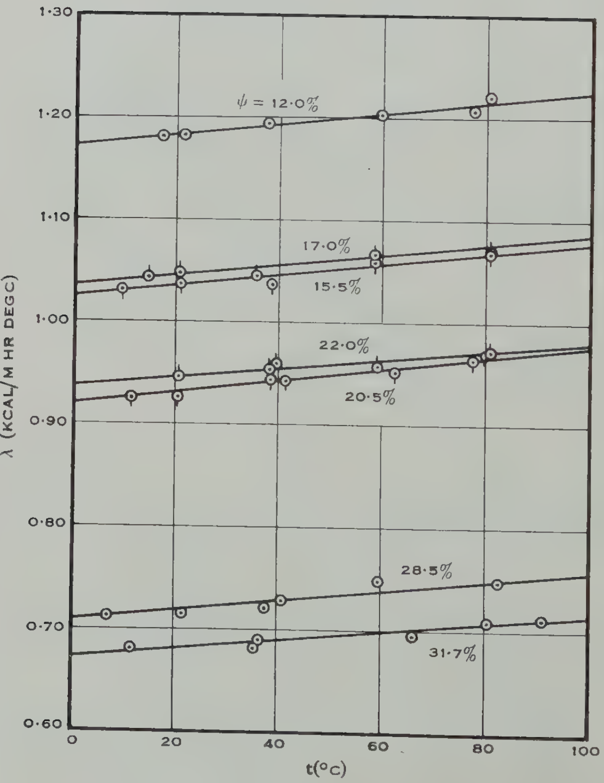

Fig. 12.—λ versus t diagram obtained on sandstones saturated with air.

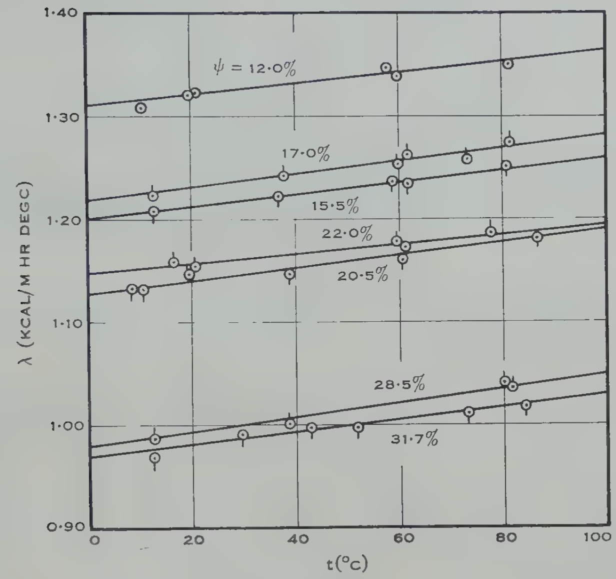

Fig. 13.—λ versus *t* diagram obtained on sandstones saturated with water.

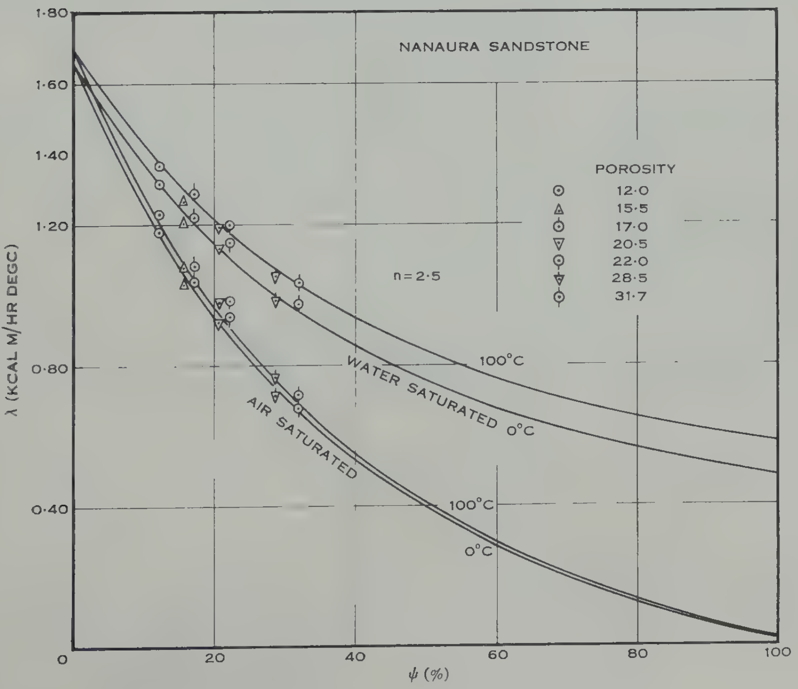

Fig. 14.—λ versus ψ diagram obtained on sandstones.

Results of measurements are shown in Figures 12 and 13. From these two λ versus t diagrams with porosity as parameter it can be recognized that the relationship between thermal conductivity and temperature is linear also; thermal conductivity increases with rise in temperature.

The λ versus ψ diagram with temperature as parameter can be drawn by tracing λ versus t diagrams vertically, and it is shown in Figure 14. Thus, applying formula (2) to these four curves, the value of n becomes $2 \cdot 5$.

This fact shows that formula (2) is in complete agreement with the experimental results and that this formula can apply immediately to practical examples.

VII. Conclusion

The effect of porosity on thermal conductivity is confirmed experimentally for porous materials and following facts are shown.

(1) If the thermal conductivity of the solid constituent is larger than that of the fluid in the pores, the thermal conductivity of a porous material is decreased with porosity increment.

(2) If the thermal conductivity of the solid constituent is smaller than that of the fluid, the thermal conductivity of a porous material is increased with porosity increment.

The generalized formula (2), with which above two cases can be covered simply by varying the value of n, has been obtained empirically.

This formula can represent any other formula on thermal conductivity of porous material by varying n as stated in Section V. We show that this formula is in complete agreement with the experimental results.

VIII. References

Eucken, A. (1932).—*V.D.I. Forschungsheft* **3** (353): 16.
Francl, J., and Kingery, W. D. (1954).—*J. Amer. Ceram. Soc.* **37**: 99–107.
Kingery, W. D., and Klein, L. (1958).—*Trans. Amer. Soc. Mech. Engrs.* **80**: 705–10.
Krischer, O., and Esdorn, H. (1956).—*Forsch. IngWes.* **22**: 1–8.
Loeb, A. L. (1954).—*J. Amer. Ceram. Soc.* **37**: 96–9.
Ribaud, M. (1937).—*Chal. et Industr.* **18**: 36–43.
Russell, H. W. (1935).—*J. Amer. Ceram. Soc.* **18**: 1–5.
Somerton, W. H. (1958).—*J. Petrol. Tech.* **10** (5): 61–4.
Sugawara, A. (1961).—*J. Appl. Phys. Japan* **30**: 17–23.
Tanazawa, Y. (1932).—*J. Japan Soc. Mech, Engrs.* **35**: 325–32.
Waddams, A. L. (1944).—*J. Soc. Chem. Ind., Lond.* **63**: 357.

THE PHASE SPEED OF A TRAVELLING DISTURBANCE IN THE *F* REGION OF THE IONOSPHERE AND ITS COMPARISON WITH GROUP VELOCITY

By L. H. Heisler* and J. D. Whitehead*

[*Manuscript received July* 10, 1961]

Summary

Three methods of measuring the phase speed of a disturbance in the *F* region, that is, the speed of a peak or trough in the isoionic contours, are given using ionograms records from one station. The analysis has been applied to one such disturbance whose group velocity was known to be 10 km/min. All three methods gave the phase speed to be about half of this. The theoretical explanation of this observation is discussed.

I. Introduction

Travelling ionospheric disturbances pertinent to this discussion have been previously described by Munro and Heisler (1956), and cause gross distortions on ionogram records, due to ripples formed in isoionic contours. The velocity of the disturbances has been measured to be about 10 km/min (Heisler 1958) by observations at stations spaced the order of 1000 km apart. As the stations were spaced much more widely than a wavelength of the ripples, this velocity is evidently the group velocity of the ripples, that is, the velocity with which a patch of large distortion of the contours moves regardless of the detailed movement within the patch. Recently, however, Heisler (1959) and Heisler and Whitehead (1960) found that travelling disturbances are associated with the appearance of sporadic *E*. This relationship is all the more puzzling when it is realized that the velocity of sporadic *E* clouds measured at relatively closely spaced stations (Harvey 1955) is only about half the velocity of *F* disturbances. However, sporadic *E* clouds may be associated not with the travelling disturbance as a whole, but with a particular phase (i.e. a peak or trough) of the isoionic ripples, as suggested by an observation by Bowman (1960*a*). Such an association would be feasible if the *phase velocity* of the ripples was equal to that of the sporadic *E* clouds.

The purpose of this paper is to describe three methods used to measure this phase velocity, or rather speed, for we do not determine the direction of the movement, and to show that the results support the hypothesis, as previously reported by Heisler and Whitehead (1961).

* Radio Research Board Laboratory, School of Electrical Engineering, University of Sydney.

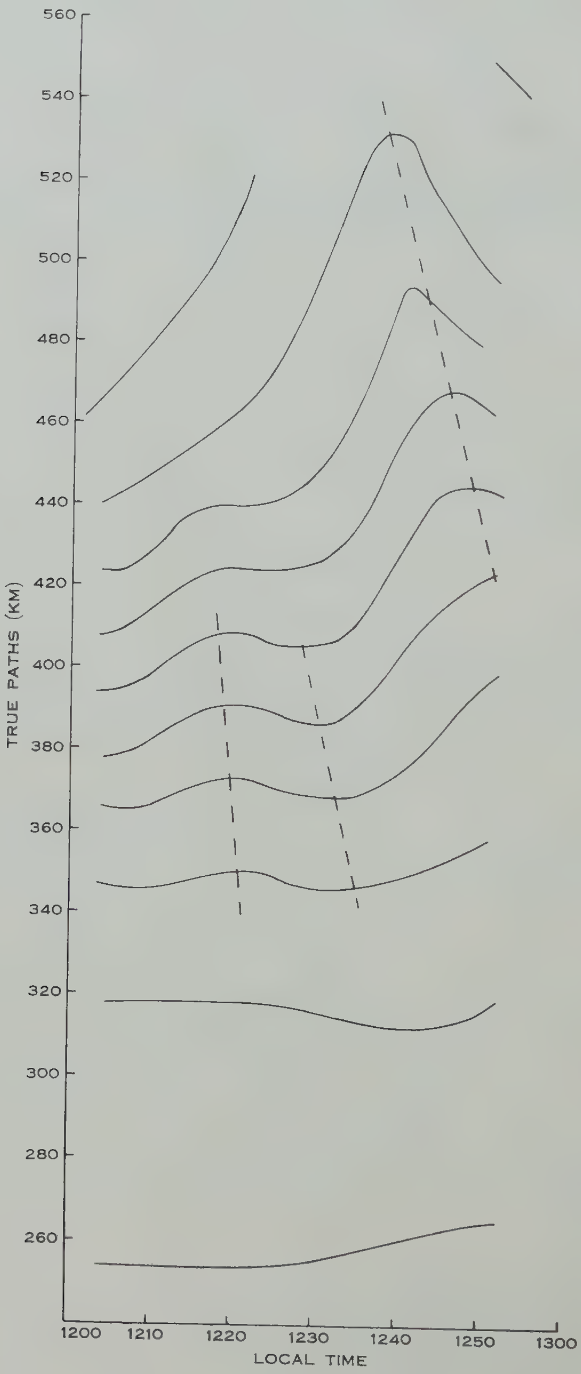

Fig. 1.—Isoionic curves showing true path against time for each electron density.

II. DERIVATION OF THE ISOIONIC CURVES AND THEIR RELATION TO THE ISOIONIC CONTOURS

Ionogram records taken every two minutes were used in the analysis and suitable records were chosen on the following basis.

(1) Ionogram records existed for Canberra (35° 18′ S., 149° E.), Sydney (33° 52′ S., 151° 11′ E.), Brisbane (27° 30′ S., 153° E.), and Townsville (19° 10′ S., 146° 58′ E.) and gave a non-ambiguous group velocity.

(2) The Brisbane records which were used in the phase speed analysis had a well-defined second echo.

(3) The first echo on these records showed little or no splitting (implying a relatively small disturbance) so that a true height reduction could be carried out without ambiguity.

After inspecting several thousand ionogram records, we consider ourselves fortunate in finding one disturbance which satisfied all three conditions.

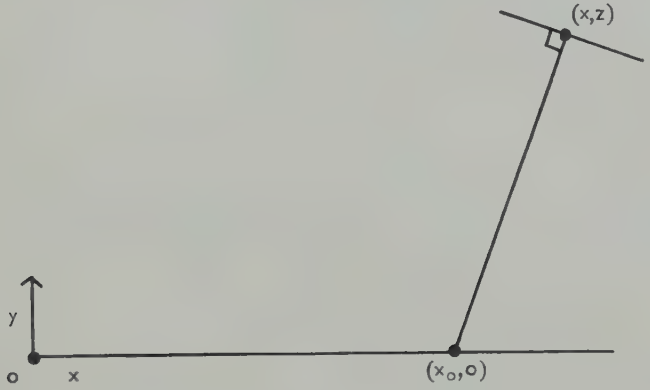

Fig. 2.—The geometry of off-vertical reflections.

The next step was to reduce the ionograms to electron density : true path curves by Duncan's (1958) method which takes the Earth's magnetic field into account. Note the term " true path " rather than " true height ", because in general the echoes do not return from the vertical. Errors due to this deviation (which changes the angle between the direction of propagation and magnetic field) and to the fact that all echoes recorded on one ionogram do not come from the same direction are likely to be quite small because the deviation is only a few degrees and the group delay is determined principally by the electron density gradient at the reflection level.

It is now possible to construct a diagram showing how the true path P for each value of electron density varies with time. These isoionic curves are shown in Figure 1 and are simply related to the isoionic *contours* in space once the phase velocity is known. For instance, in Figure 2, (x, z) is the reflecting point when the ionosonde is at a distance x_0 along the ground, z being the distance of the point above the ground. Then we have

$$P^2=4\{z^2+(x_0-x)^2\}, \tag{1}$$

and

$$x_0=z\mathrm{d}z/\mathrm{d}x+x. \tag{2}$$

Differentiating equation (1) with respect to x_0,

$$P\cdot\frac{\mathrm{d}P}{\mathrm{d}x_0}=4\left[z\cdot\frac{\mathrm{d}z}{\mathrm{d}x}\cdot\frac{\mathrm{d}x}{\mathrm{d}x_0}+(x_0-x)\left(1-\frac{\mathrm{d}x}{\mathrm{d}x_0}\right)\right]$$

$$=4(x_0-x), \tag{3}$$

from (2). Therefore

$$x=x_0-\tfrac{1}{4}P\cdot\mathrm{d}P/\mathrm{d}x_0, \tag{4}$$

and

$$z^2=\tfrac{1}{4}P^2\{1-\tfrac{1}{4}(\mathrm{d}P/\mathrm{d}x_0)^2\}. \tag{5}$$

But

$$\mathrm{d}P/\mathrm{d}x_0=(1/V)\mathrm{d}P/\mathrm{d}t,$$

where V=phase velocity. Hence from equations (4) and (5)

$$x=x_0-(P/4V)\mathrm{d}P/\mathrm{d}t, \tag{6}$$

and

$$z^2=\tfrac{1}{4}P^2\{1-(1/4V^2)(\mathrm{d}P/\mathrm{d}t)^2\}. \tag{7}$$

Equations (6) and (7) enable us to calculate the isoionic contours (x, z) once V is known. In particular, the radius of curvature R of the contours (positive when concave downwards) is given by

$$1/R\approx\mathrm{d}^2z/\mathrm{d}x^2 \text{ as } (\mathrm{d}z/\mathrm{d}x)^2\ll 1.$$

But from equations (2) and (3)

$$z\mathrm{d}z/\mathrm{d}x=\tfrac{1}{4}P\mathrm{d}P/\mathrm{d}x_0.$$

Therefore

$$z\mathrm{d}^2z/\mathrm{d}x^2\approx\tfrac{1}{4}P(\mathrm{d}^2P/\mathrm{d}x_0^2)\mathrm{d}x_0/\mathrm{d}x$$

$$=\tfrac{1}{4}P\frac{\mathrm{d}^2P}{\mathrm{d}x_0^2}\cdot\frac{1}{1-\frac{1}{4}P\mathrm{d}^2P/\mathrm{d}x_0^2},$$

from equation (4). But $z\approx\frac{1}{2}P$, therefore

$$R=\frac{P\mathrm{d}^2P/\mathrm{d}t^2-4V^2}{2\mathrm{d}^2P/\mathrm{d}t^2},$$

or

$$V^2=\tfrac{1}{4}(P-2R)\mathrm{d}^2P/\mathrm{d}t^2. \tag{8}$$

III. THE PHASE SPEED FROM A KNOWLEDGE OF R

The first method of calculating V relies on the fact that R may be estimated from the splitting of the various order echoes. If R is greater than the height of the layer, the first echo will not be split (Munro 1953) but if it is less than twice this, the second echo will be split. This situation occurred during the travelling disturbance under discussion. Hence when the second echo is split $\frac{1}{2}P<R<P$ and $V^2<\frac{1}{4}P(-\mathrm{d}^2P/\mathrm{d}t^2)$ the quantity $\mathrm{d}^2P/\mathrm{d}t^2$ being negative when $R>\frac{1}{2}P$. At the lowest frequency at which splitting of the second echo occurred during the disturbance, $\mathrm{d}^2P/\mathrm{d}t^2\approx-0\cdot22$ km/min², giving $V<4\cdot5$ km/min.

IV. Calculating V from the Relative Group Paths of the First and Second Echoes

The second method of calculating the phase speed is based on the fact that the second echo is not in general reflected from the same point as the first. It is usually more off-vertical than the first and therefore even more unreliable than the first as regards the conditions directly overhead—in contrast to the assumption by Wright (1959) that the second echo gives the more reliable data under these circumstances. Thus the second echo has true and group paths not equal to twice those of the first echo. Figure 3 shows the simple situation when the isoionic contours are straight and parallel but not horizontal (when $\mathrm{d}^2P/\mathrm{d}t^2=0$ but $\mathrm{d}P/\mathrm{d}t\neq0$). If the first echo path inclined at angle θ to the vertical is P_1 and the group path is P_1', and the second echo group path is P_2', we have

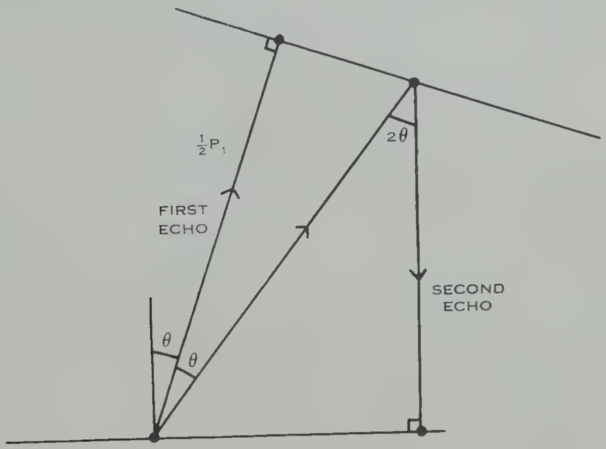

Fig. 3.—The paths of first and second echoes when the isoionic contours are straight lines.

$$P_2'=\frac{P_1}{\cos\theta}+\frac{P_1\cos 2\theta}{\cos\theta}+\frac{2(P_1'-P_1)}{\cos\theta},$$

or approximately

$$2P_1'-P_2'=\theta^2(2P_1-P_1'),$$

allowing θ to be calculated. V may then be found from the relation

$$V=(1/2\theta)\cdot(\mathrm{d}P/\mathrm{d}t).$$

The analysis was extended to the case where $\mathrm{d}^2P/\mathrm{d}t^2\neq0$ by assuming that the contours form concentric circles: the validity of this assumption depends on there being only a small change in the curvature of the contours over a horizontal distance of $\frac{1}{2}P_1\theta$. During the disturbance, this amounted to as much as 25 km, making single measurements unreliable. A systematic error seems unlikely from this course, but may occur in the measurement of $2P'_1-P'_2$, should the height marks on the ionograms have a zero error. By noting the variations with time and probing frequency, this zero error was found to be about 3 km, making a difference of 6 km in $2P'_1-P'_2$ which had a value not greater than 60 km. The random error in $2P'_1-P'_2$ was about the same order.

This method gave a mean value for V of 4 ± 1 km/min.

V. Calculating V from the Slope of the Front

This method makes use of the evidence that wave fronts of travelling disturbances tend to lie along the Earth's magnetic field (Munro and Heisler 1956 ; Bowman 1960*b*). It must be admitted that the present disturbance is probably much larger in amplitude than those investigated. However, it is known that the wave front slopes forward for disturbances moving towards the equator, that is, in the same sense as the magnetic field slope, and thus it appears not unlikely that the slope is along the magnetic field lines. From the isoionic curves, it is possible to trace out the sloping wavefronts (shown as dotted lines in Fig. 1). If the fronts are to lie along the magnetic field then $V=5\pm2$ km/min.

VI. The Mean Phase Velocity

Whilst it could be argued that each one of the three methods given for measuring the phase speed has some uncertainty about it, yet the fact that all three gave similar values for V is very strong evidence in favour of their veracity. It is not suggested that these methods could be used on a systematic basis and there is need for further experimental verification. Indeed, the difficulty introduced by having to choose suitable records and analysis involving many true path calculations precludes the general application of the method. The purpose in describing the methods is to display their validity in arriving at the final result that the phase speed of the disturbance was 4·5 km/min whereas its group velocity was about twice this at 10 km/min travelling 6° E. of N.

This result confirms the indication we had of two velocities relevant to travelling disturbances, and thus removes one stumbling block to the understanding of the disturbance : sporadic *E* association.

Furthermore, inspection of the methods used to estimate the velocity of " fronts ", which cause " satellite " traces on ionogram records, shows that this is the phase velocity. Its magnitude of $\sim$4 km/min (McNicol, Webster, and Bowman 1956) agrees well with our value and makes it more certain that the satellite traces are just another manifestation of travelling disturbances.

Waves moving with this large dispersion will change form rapidly. Indeed, the lifetime of a single ripple would only be about one period—the order of half an hour. Such a lifetime was found by Gusev *et al.* (1960) for observations of radio phase path changes at fairly closely spaced stations. The changes in form should not be completely random and further stations more widely spaced could be used to follow this change of form.

VII. Theoretical Implications of the Observed Dispersion

The reported dispersion does not agree with that given by Hines (1960) for internal gravity waves which he regards as the cause of *F*-region disturbances. His dispersion in fact has an opposite sign.

One explanation is, however, possible which retains Hines's gravity waves in the *E* region as the basic cause of the *F*-region disturbance, that is, if they give rise to ionization movements in the *F* region by virtue of the electric fields they generate in the *E* region rather than by neutral air movements in the *F* region. The electric fields in the *E* region are generated by movements of the neutral air which drive ionized material across the Earth's magnetic field. The details are discussed by Whitehead (1961), from which paper it may be seen that the electric fields are proportional to a mean horizontal velocity $\overline{U}$ of the neutral air in the *E* region given by

$$\overline{U}=\int UNf(\nu_i)\mathrm{d}h/\int Nf(\nu_i)\mathrm{d}h,$$

where N = electron density,

ν_i = ionic collision frequency,

U = horizontal velocity of neutral air,

and $f(\nu_i)$ is a function of ν_i which becomes small above 130 km.

For a particular electron density distribution in the *E* region, the total electric field generated by two wind systems is the sum of the electric fields generated by each. However, each wind system itself changes the electron density distribution and thus so far as the electric field is concerned, and hence *F*-region ionization movements, there is considerable interaction between the systems.

Now suppose a short gravity wave only generates an appreciable electric field for the electron density distribution appearing at a particular phase of a long gravity wave. Then the corresponding disturbance in the *F* region will have a " phase velocity " equal to the actual velocity of the short wave but a " group velocity " equal to that of the long wave. Hines predicts a velocity increasing with wavelength, and so this interaction mechanism may provide an explanation of an apparent phase velocity in the *F* region being less than the apparent group velocity.

VIII. General Comment

The fact that two distinct velocities have been shown to be associated with the same disturbance illustrates that great care must be exercised in comparing velocities of movements using different methods. For instance, Thomas (1959) estimated height gradients of horizontal velocities to be the order of 2×10^{-3}/s in the *F* region from four average velocities found by using three different methods variously at three places. Clearly this height gradient is inconsistent with the observation that wavefronts of travelling disturbances maintain their slopes fairly constant for several hours, for Thomas's height gradient would lead to a front rotating at about one revolution per hour. Our result shows that one might expect different velocities when using different methods of observation even though this may be only a matter of the spacing of the observing stations. Single-station observations by Heisler (1960) would suggest that such a height gradient is non-existent.

IX. Conclusions

It has been shown that the phase speed of a particular travelling disturbance was 4·5 km/min whereas its group velocity was 10 km/min. The validity of the result rests principally on the consistency of the three independent methods used in deriving it. One possible explanation of the result is given which retains gravity waves in the *E* region as the prime cause of travelling disturbances in the *F* region.

X. Acknowledgments

This investigation has been carried out in the School of Electrical Engineering of the University of Sydney as part of the research programme sponsored by the Radio Research Board of the Commonwealth Scientific and Industrial Research Organization. We wish to express our appreciation to the University of Sydney and in particular to Professor W. N. Christiansen for the provision of facilities in the School of Electrical Engineering, and to the Ionospheric Prediction Service who kindly supplied the ionograms used in the analysis. The authors are also particularly indebted to Mr. R. A. Duncan of the Upper Atmosphere Section of the Commonwealth Scientific and Industrial Research Organization for provision of the program used in SILLIAC for analysis of data.

XI. References

Bowman, G. G. (1960*a*).—*Planet. Space Sci.* **2**: 195.
Bowman, G. G. (1960*b*).—*Planet. Space Sci.* **2**: 133.
Duncan, R. A. (1958).—*J. Geophys. Res.* **63**: 491.
Gusev, V. D., Mirkotan, S. F., Berezin, I. B., and Kiyanovsky, M. P. (1960).—"Some Ionospheric Results obtained during the I.G.Y." (Ed. W. J. B. Beynon). p. 304. (Elsevier Publishing Co.: Amsterdam.)
Harvey, J. A. (1955).—*Aust. J. Phys.* **8**: 523.
Heisler, L. H. (1958).—*Aust. J. Phys.* **11**: 79.
Heisler, L. H. (1959).—*Nature* **184**: 1788.
Heisler, L. H. (1960).—*Aust. J. Phys.* **13**: 655.
Heisler, L. H., and Whitehead, J. D. (1960).—*J. Geophys. Res.* **65**: 2767.
Heisler, L. H., and Whitehead, J. D. (1961).—*Nature* **191**: 157.
Hines, C. O. (1960).—*Canad. J. Phys.* **38**: 1441.
McNicol, R. W. E., Webster, H. C., and Bowman, G. G. (1956).—*Aust. J. Phys.* **9**: 247
Munro, G. H. (1953).—*Proc. Roy. Soc.* A **219**: 447.
Munro, G. H., and Heisler, L. H. (1956).—*Aust. J. Phys.* **9**: 359.
Thomas, L. (1959).—*J. Atmos. Terr. Phys.* **14**: 123.
Whitehead, J. D. (1961).—*J. Atmos. Terr. Phys.* **20**: 49.
Wright, J. W. (1959).—*J. Geophys. Res.* **64**: 1631.

SYSTEMS FOR SIMULTANEOUS IMAGE FORMATION WITH RADIO TELESCOPES

By D. J. McLean* and J. P. Wild*

[*Manuscript received May* 17, 1961]

Summary

The large arrays of aerials often necessary for high resolution in radio astronomy are generally used to observe a brightness distribution in an area of the sky by scanning the aerial beam, point by point, across the area. In this paper we investigate the possibility of observing the complete distribution simultaneously over a given area. Two possible analogue systems capable in principle of forming such images, are described; in one, the analogue image is formed optically, in the other with ultrasonic methods. The problems and limitations of the two systems are examined and it is concluded that further technical developments are required before practical systems with useful sensitivity and resolution can be achieved.

I. Introduction

The recording of radio brightness distributions in the sky is the ultimate observational aim of many radio astronomical investigations. For a variety of reasons it may be desirable to make these observations rapidly—for instance to avoid the effects, important at metre wavelengths, due to variations in the ionosphere; to observe variable sources, such as solar or Jovian bursts; or simply to collect a large amount of data in a reasonable period of time. In the present paper we aim to investigate a number of possible rapid systems, especially as they might be applied to the observation of solar bursts. However, the generalization to other situations is obvious.

More precisely, we aim to find a system capable of observing the Sun, quiet or active, at metre wavelengths in a time comparable with the time scale of the fastest observed bursts. We can take this time to be about one second. The resolution required to observe details of the Sun at metre wavelengths makes a full aperture system, such as a steerable paraboloid reflector or even a circle filled with closely spaced dipoles, quite impracticable (2 km would be a typical diameter). Instead we must use what we term a *dilute* aerial array, such as the Mills Cross (Mills and Little 1953) or circular-array (Wild 1961). With both aerial systems, sharp " pencil " beams emerge as the result of taking the difference between two directivity patterns, both possessing widespread side lobes but only one having appreciable response in the central beam. In the course of the subtraction process, the mean *power* of signals received in the widespread side lobes cancel one another but the noise *fluctuations* do not. Hence with neither system is it possible to improve the signal-to-noise ratio beyond a certain limit fixed by radiation from the surrounding Sun and cosmic background entering the side lobes. The result is that the observations must be integrated,

---

* Division of Radiophysics, C.S.I.R.O., University Grounds, Chippendale, N.S.W.

at each point, over a period which ranges from about $0 \cdot 1$ s to several seconds depending on the bandwidth of the associated receivers and the image quality required. This is of the same order as the total time available. It appears therefore that the most satisfactory solution to our problem would be a system which produces and integrates an image of the whole distribution simultaneously, as a lens and film do for the optical astronomer. The requirements are similar to those which led to the development of the iconoscope for television.

In what follows we shall confine our discussion largely to the simple case of a circular (i.e. annular) array. Most of the results can be applied in principle to any other suitable array.

II. CONCEIVABLE SYSTEMS

One way to scan the beam of an aerial array across a source is to vary the lengths of line connecting the different elements of the array to the receiver. In the same way it is possible to observe in several different directions with the same array by means of several receivers joined to the elements of the array through appropriate lengths of line. In principle this leads to a possible solution of the problem : all points of the distribution can be observed simultaneously by having a separate receiver and detector to observe each point. However, since a useful picture requires observations at each of several thousand independent points and hence several thousand receivers, this system is scarcely practicable as it stands.

It is possible, however, to use a simpler system consisting of a much smaller number of receivers, the beams of which are swept together along parallel lines to observe the distribution in a number of simultaneous parallel scans. Under certain circumstances, this may represent an adequate compromise between rapidity of observation and complexity of equipment.

Again, in principle, the intensity distribution could be calculated with a digital computer from the instantaneous amplitudes and phases of the signals at the various aerials. However, for an array of 10^2 elements and a bandwidth of 10^6 c/s, this computer would have to accept about 10^8 amplitudes per second, calculate about 10^6 intensity distributions per second (each distribution consisting of 10^4 independent points, a total of 10^{10} calculated values of intensity per second), and then average these 10^6 intensity distributions to supply an output of 10^4 values of intensity per second.

These numbers are so great that we must surely reject the idea of a digital computer and seek some sort of analogue computer which will not be daunted by the enormous rate at which information must be handled. The analogy which interests us most is the obvious one of an optical telescope and a photographic plate. This is developed in the next section.

III. AN OPTICAL ANALOGUE SYSTEM

We wish to observe the intensity distribution which would be observed by scanning the beam of the circular array (shown in Fig. 1 (*a*)) across the source. This distribution is the same as that produced at the image plane of the hypothetical arrangement shown in Figure 1 (*b*). Basically the arrangement consists of a lens which focuses the radio waves on an image plane. To make the image identical* with the distribution observed by scanning the source with the annular array of discrete aerials, an opaque screen is placed in front of the lens with holes cut in the screen at the positions occupied by the aerials of the array.

The system of image formation depicted in Figure 1 (*b*) is possible at optical wavelengths but becomes quite impracticable at radio wavelengths of several metres. Figure 2 shows a proposed equivalent system, in which we convert the received radio signals to light waves, which are then focused to form a complete image in monochromatic light of the radio brightness distribution. In Figure 2 the undetected radio-frequency signals from each aerial are used to modulate the transmission and phase of an optical aperture or *pupil* in step with the amplitude and phase of the radio signals. The pupils are arranged on the otherwise opaque screen in the same pattern as the corresponding aerials.

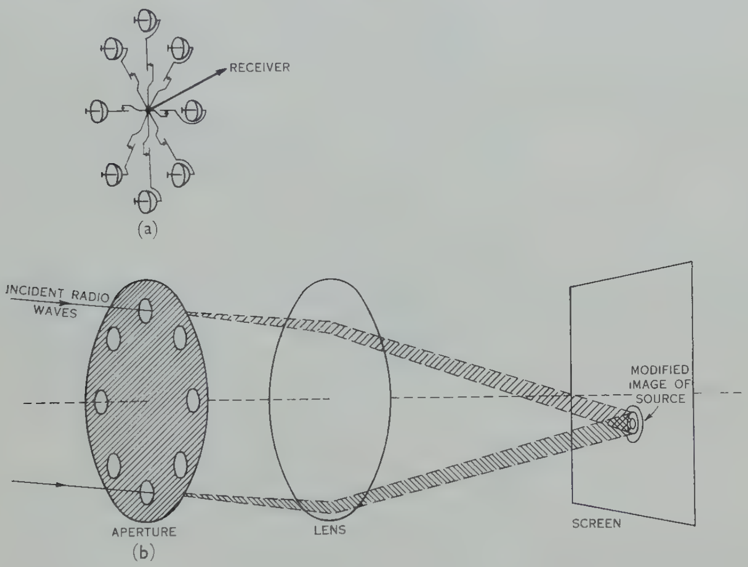

Fig. 1 (*a*).—Circular array of radio aerials, capable of giving an image by point-by-point scanning.

Fig. 1 (*b*).—Hypothetical system for focusing radio waves to yield an image identical with that of (*a*).

The *pupil array* is illuminated with a parallel beam of light (from a point source and collimating lens) and the light which passes through the pupil array is focused on the image plane. Since the light, after passing through the pupil array, has the same amplitude and relative phase as the radio waves incident on the aerials, the image formed is the same as that formed in the hypothetical system of Figure 1 (*b*) as desired. The only effect of varying the scale of the pupil array is to vary the scale of the image.

---

* The proof of the identity of the two image distributions in the case of a point source follows at once from the well-known equivalence of the polar diagram of an aerial system and the diffraction pattern of its aperture.

It is possible at least in principle to build up a pupil which will produce the desired effect. One such pupil, using interference between beams reflected from piezo-electric crystals, driven by the radio signals, is shown in Figure 3. It should be noted that a few of the critical dimensions, especially those in the pupils, must be maintained accurately, to a small fraction of a wavelength. Also, the maximum bandwidth of the radio-frequency circuits is limited (but not severely) by dispersion effects in the system. On the other hand, it is permissible to use frequency changing between the aerials and the pupils, provided only that the new frequency is greater than the bandwidth.

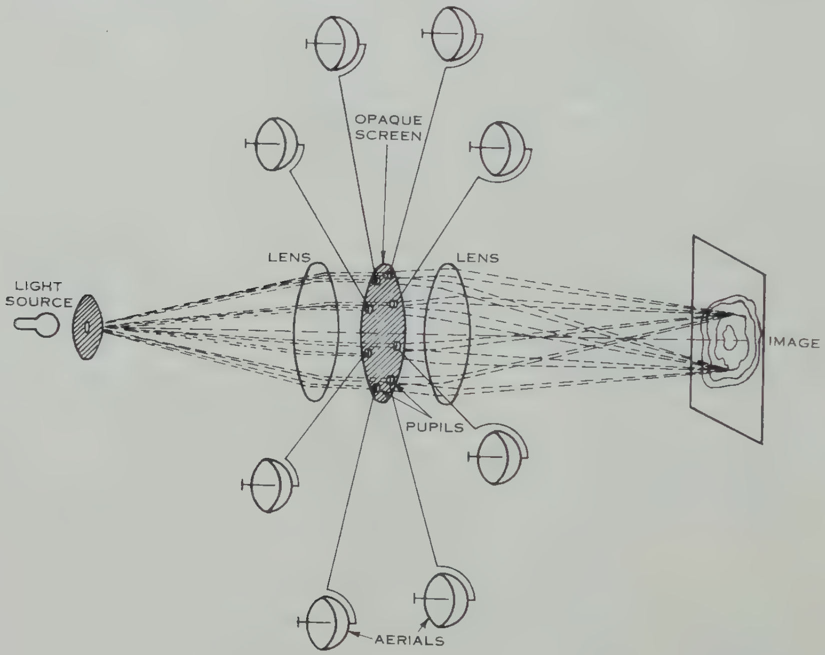

Fig. 2.—Principle of the optical system of forming an image of radio brightness. Note the analogy with Figure 1.

It is interesting to note the analogy between the optical system of Figure 2 and the system containing a large number of receivers or detectors fed through different lengths of feeder (see Section II). In the optical system the detectors are replaced by small areas of photographic emulsion and the lengths of feeders by the optical paths from the pupils to the different points of the image plane.

Now the image yielded directly by a circular array or annular aperture is distorted and requires modification or *correction* to suppress unwanted diffraction or side-lobe effects. The correction process proposed by Wild (1961) consists of cross-correlating the recorded image with a special two-dimensional correction function, which has been obtained analytically; the corrected image is then identical with that which would be given by a uniform aperture having the same radius as the annular aperture used. The correction function assumes both positive and negative values and so the process involves more than simple smoothing.

The process of correction is desirably incorporated in the observing instrument so that the recorded images are fully corrected. Fortunately, the optical system described above can be simply adapted to function in this way, since to cross-correlate the image with any given two-dimensional function G, one merely replaces the point source of light by an extended light source whose intensity distribution is given by G. Essentially this arrangement has been employed by McLean (1961) to demonstrate the feasibility of the correction process.

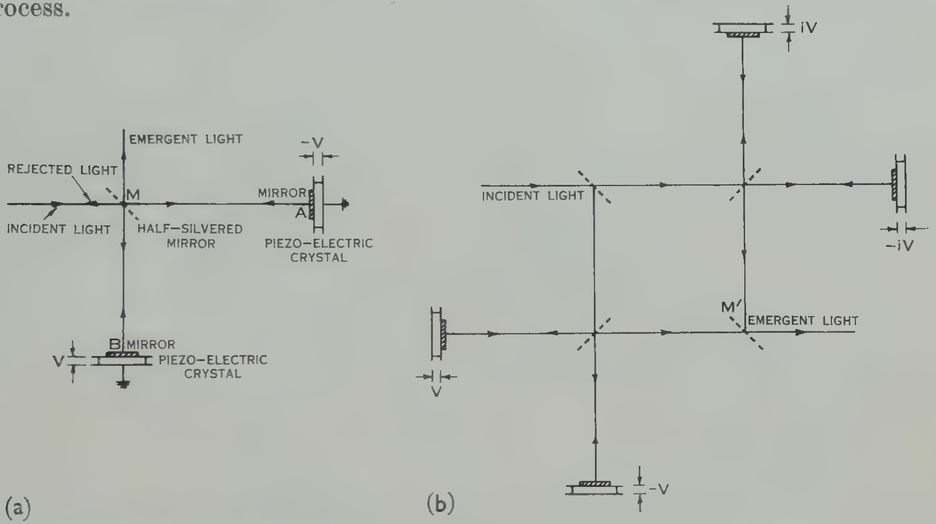

Fig. 3.—Illustrating one possible design for a pupil by which the phase and amplitude of an applied radio-frequency signal is imposed on a coherent beam of monochromatic light. The complete unit is shown in (*b*) ; it consists of two amplitude modulators of the type (*a*) operated in phase quadrature. In (*a*), the rays reflected from A and B interfere at the half-silvered mirror with phases which are varied by displacements of the mirrors A and B. These displacements are controlled by applying radio-frequency voltages across the pair of piezo-electric crystals. The two crystals are fed in anti-phase and, with proper adjustment (i.e. paths for zero volts differing by $\lambda/2$), the amplitude of the emergent beam is proportional to the instantaneous voltage (if not too large) while the phase is constant. In (*b*), the two pairs of crystals are fed in phase quadrature and it may easily be shown that, if the two modulated light beams are also combined in phase quadrature, the emergent beam possesses both the relative amplitude and phase of the applied signal.

In Figure 4 we show one complete arrangement which includes the correction process in the optical system. It is the same as Figure 2 except that the point source of light is replaced by two widely-separated extended sources, in one of which the brightness distribution is given by the positive part of the correction function, in the other by the negative part. These produce two non-overlapping image distributions ; the difference between these two distributions is the required distribution. The difference is obtained by obscuring alternate strips of both images with coarse gratings, then combining the two images optically so that the unobscured parts of one image fall on the obscured parts of the other, and vice versa. If this interlaced image is now scanned at right-angles to the grating by a TV image tube, the output will contain an alternating component proportional to the required difference.

Unfortunately, this optical system falls short of ideal owing to the noise introduced by the system itself. It can be seen, for instance, that most of the available light falls on the opaque screen of Figure 4, while the light which passes through the pupil array must be spread over an area considerably larger than that of the useful image. The image is therefore very weak and so fluctuations in the number of quanta striking a given area will introduce noise. This effect is enhanced by the correction process, in which the small difference between two almost equal intensities is taken. We have calculated that the signal-to-noise ratio of the system expected for the final image is given by*

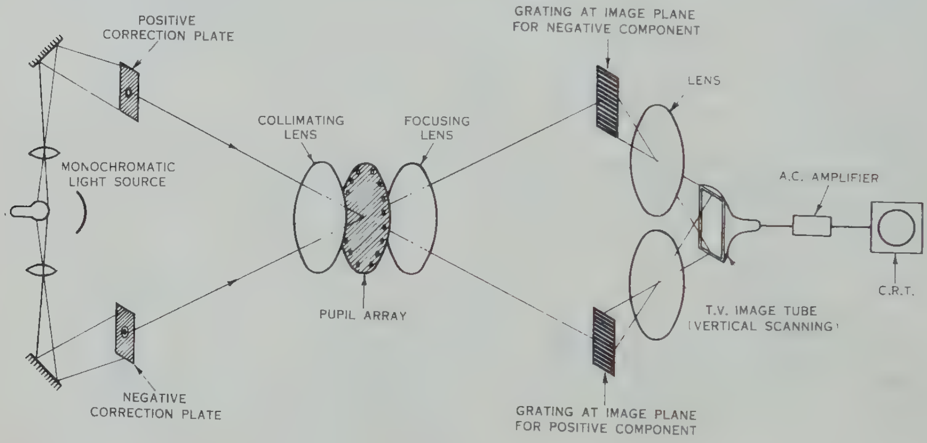
POSITIVE CORRECTION PLATE
GRATING AT IMAGE PLANE FOR NEGATIVE COMPONENT
LENS
COLLIMATING LENS
FOCUSING LENS
MONOCHROMATIC LIGHT SOURCE
A.C. AMPLIFIER
C.R.T.
PUPIL ARRAY
T.V. IMAGE TUBE (VERTICAL SCANNING)
NEGATIVE CORRECTION PLATE
GRATING AT IMAGE PLANE FOR POSITIVE COMPONENT

Fig. 4.—The complete optical system with the correction process included.

$$\frac{\text{signal}}{\text{noise}} \simeq \left(\frac{\alpha k \gamma \lambda^3 \overline{B}\,T}{hcn^5}\right)^{\frac{1}{2}}, \qquad (1)$$

where k is the efficiency of a pupil (estimated to be $k \simeq 0 \cdot 2$),

γ is the efficiency of all other optical parts ($\gamma \simeq 0 \cdot 5$),

α is the quantum efficiency of the optical detector ($\alpha \simeq 0 \cdot 1$ for a sensitive TV image tube),

λ is the wavelength of light to be used ($\lambda \simeq 5 \times 10^{-5}$ cm),

$\overline{B}$ is the mean brightness of the positive part of the correction plate ($\overline{B} \simeq 0 \cdot 75 \times 10^8$ erg cm^{-2} steradian^{-1} ($= 0 \cdot 5 \times 10^4$ candles cm^{-2}) for one line of a bright mercury arc),

T is the integration time in seconds,

n is the number of array elements or pupils,

c is the velocity of light,

h is Planck's constant.

---

* This formula assumes that, for a given diameter, d, of the complete pupil array, the individual pupils are made as large as possible. It is interesting to note that the result is independent of the magnitude of d. This is because an increase in d (and hence the area of the aperture) demands that the solid angle subtended by the correction plate at the aperture must be correspondingly reduced.

Substituting the numerical values suggested above yields

$$\frac{\text{signal}}{\text{noise}} \simeq 2\cdot 4\times 10^{4} T^{\frac{1}{2}} n^{-5/2}. \tag{2}$$

It has been shown (Wild 1961) that the maximum resolution with which a given area of the sky can be observed is proportional to n.* Equation (2) therefore indicates the compromise which must be made between resolution and the effects of noise introduced by the optical imaging system when the brightest available light source is used. For instance, if we require a signal-to-noise ratio of 30 and an integration time of 1 s, then we must have $n<15$, which implies severely restricted resolution. Without introducing further elaborate complexities into the optical system, we believe that this limitation can only be overcome by the use of much brighter light sources than are currently available. It is possible that the development of light amplifiers such as optical masers could provide the answer.

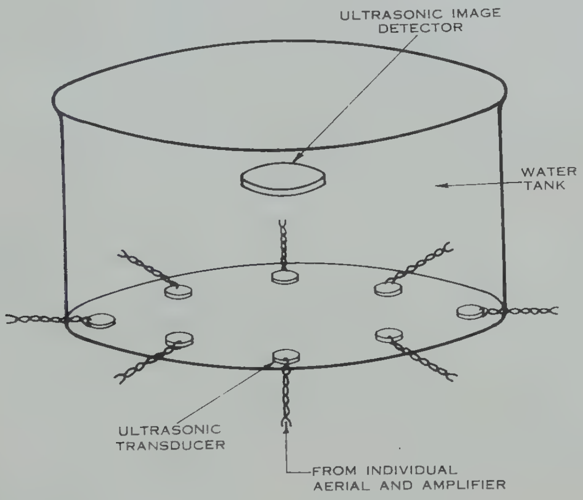
ULTRASONIC IMAGE DETECTOR
WATER TANK
ULTRASONIC TRANSDUCER
FROM INDIVIDUAL AERIAL AND AMPLIFIER

Fig. 5.—Showing the basic arrangement of an ultrasonic system.

IV. An Ultrasonic System

We have seen that with currently available techniques the optical system has two main drawbacks; firstly, the poor signal-to-noise ratio of the image, which is essentially the result of the inefficient use of the light flux generated by the source; and secondly, the great technical difficulties to be expected in the construction of the pupils—a result of the extremely short wavelength of light. The first of these problems could be overcome if the point source and pupil array were replaced by an array of coherent, modulated sources ; the emitted waves may be of any physical kind provided their interference pattern is capable of detection. Nearly all the radiated intensity can then be used in the formation of the image, and so the efficiency is enormously improved. However, the abandonment of the system of Figure 4 would mean that a different means of aerial correction would have to be incorporated, presumably at a later stage of the system. The second problem may be directly overcome by the choice of waves of convenient wavelength (e.g. 1 mm).

---

* This is because a ring of n discrete aerials introduces a set of side lobes into the polar diagram which are not present in the polar diagram of a continuous annulus. If these side lobes are not to introduce highly undesirable effects the diameter of the aerial array must be small enough to keep the secondary side lobes outside the area in which it is expected to observe strong sources. This of course restricts the available resolution when a field of given angular area is viewed with a system containing a given number of aerials.

Systems incorporating both the above modifications are conceivable with both microwaves and ultrasonic waves, although in both cases the problem of image detection is clumsy or requires techniques which have not yet been properly developed. Of the two, the ultrasonic system seems simpler and the remaining discussion will be restricted to it.

Figure 5 shows a possible arrangement using ultrasonic waves. In place of a pupil array we have an array of quartz transducers. After amplification and coherent frequency changing* (but before detection), the signals from the aerials are used to drive the transducers. Here we see one of the advantages of a circular array : instead of using a lens, it is only necessary to tilt the crystals towards the centre of the desired image. The image is then formed as a distribution of ultrasonic intensity across a plane in the medium (e.g. water) surrounding the crystals.

There remains the problem of detecting or rendering visible such a distribution in a suitable manner. A detection system is required to fulfil the same function as the photographic plate or TV pick-up tube of the optical system : the system must be one in which the image is integrated simultaneously over the whole picture, it must be quantitatively faithful in reproduction, and it must be rapid enough to register in periods of the order of one second. The various methods which have so far been developed for observing ultrasonic images scarcely satisfy these requirements.

While the ultrasonic system must await the possible development of a suitable detector, its potential advantages over the optical system are very great. Firstly, no fundamental limitations in detection sensitivity exist, so that the corresponding restrictions on resolution are removed ; secondly, with wavelengths of ~1 mm the constructional problems are much less exacting ; and thirdly, the transducer elements are simple in comparison with the intricate pupil elements of the optical system.

V. REFERENCES

McLEAN, D. J. (1961).—*Proc. Roy. Soc.* A (In press).
MILLS, B. Y., and LITTLE, A. G. (1953).—*Aust. J. Phys.* **6** : 272.
WILD, J. P. (1961).—*Proc. Roy. Soc.* A **262** : 84.

---

* It is desirable to change the frequency down to about 10 Mc/s, or lower because the attenuation of ultrasonic waves is excessive at higher frequencies. However, the procedure of frequency changing can be shown to impose restrictions on the usable frequency bandwidth of the system owing to dispersion effects in the analogue image. The greater the fractional frequency change, the less the allowable bandwidth. Hence an ultrasonic frequency of 10 Mc/s may be regarded as an acceptable compromise. At this frequency the wavelength in water is 0·14 mm.

A CATALOGUE OF RADIO SOURCES BETWEEN DECLINATIONS —50° AND —80°

By B. Y. Mills,*† O. B. Slee,* and E. R. Hill*

[*Manuscript received June* 13, 1961]

Summary

A catalogue has been prepared of the radio sources observed between declinations —50° and —80°, using the Sydney cross-type radio telescope at a wavelength of 3·5 m; a total of 219 sources is listed. This supplements the earlier catalogues for the declination ranges +10° to —20° and —20° to —50°. In addition to the positions and intensities of the sources, angular sizes of 42 of the strongest sources are given. As before, identifications with bright optical objects have been sought, and a number of possible identifications with emission nebulae and bright galaxies are listed. Because of the small area of sky covered by the present catalogue, the numbers of sources are small (compared with those in our earlier catalogues) so that the statistical analysis of their distribution has comparatively low weight. However, the analysis gives results consistent with those obtained using the earlier catalogues. Finally, the present state of the identification of sources in our catalogues is briefly reviewed.

I. Introduction

Catalogues of radio sources observed with the Sydney 3·5 m cross-type radio telescope covering declinations +10° to —50° have been published (Mills, Slee, and Hill 1958, 1960). The present catalogue concludes this series by extending the area to —80°. In a paper in preparation an attempt will be made to assess the general accuracy of our catalogues in performing their intended function, and a number of alterations which have been found necessary in previous catalogues will also be included.

The southernmost area is particularly difficult to catalogue because of spurious responses, which are here more obtrusive than usual. The geometry of the situation is such that strongly emitting regions are within the fan-beams of the cross, where side lobes tend to be higher, for a greatly increased proportion of the observing time. This effect has been discussed in an earlier paper (Mills, Little, Sheridan, and Slee 1958) which contains a diagram showing the regions most likely to be affected.

Because of the above difficulty, combined with the small total area of the region, fewer sources are listed in the present catalogue. The total is 219 which, in the area of 1·36 steradians, corresponds to 161 sources per steradian, or approximately half the source density of the earlier catalogues. The total number of sources listed in the whole area, +10° to —80°, is 2270. The additional sources in the present catalogue are too few to affect the source count statistics

---

* Division of Radiophysics, C.S.I.R.O., University Grounds, Chippendale, N.S.W.

† Present address: School of Physics, University of Sydney.

presented in our last paper (Mills, Slee, and Hill 1960), so that no further analysis is given here. It may be noted, however, that there are no significant divergences from earlier results.

II. The Catalogue

Preparation of the catalogue follows the methods described in the earlier papers. The catalogue is divided into three zones covering declinations −50° to −60°, −60° to −70°, and −70° to −80° ; these are given in Tables 1, 2, and 3 respectively. The usual scheme of reference numbers is adopted for identifying a radio source, that is, the first two digits of the reference number denote the hour of the Right Ascension ; these are followed by the sign of the declination and the tens digit measured in degrees and, finally, an italicized serial number arranged in order of increasing Right Ascension within the 1-hr period. Only the latter italicized numbers are given in Tables 1, 2, and 3 as the others are evident ; for example, in Table 1 the third source would be referred to as 00–5*3*. As before, the probable error in the final digit of a measured position is indicated by a superscript.

Radio sources resolved by the aerial beam have been treated as before, both their peak flux density and their integrated flux being given, the former in parentheses. Such sources have been called " extended " sources, while others which may have been resolved have been described as " perhaps extended ", or words to that effect. However, our interpretation of the word " extended " given in the preliminary catalogue (Mills and Slee 1957) needs to be re-emphasized—it is that " these (extended or perhaps extended sources) may either be sources of large angular size, or blends of two or more small sources "—it is not possible from a pencil-beam survey alone to differentiate between these two possibilities if the blending sources are close enough to one another.

Angular sizes, when they are quoted in the footnotes, have been derived from the radio link interferometer (Goddard, Watkinson, and Mills 1960). These measurements are preliminary and are likely to be improved later.

Possible identifications with bright nebulae and galaxies are also given in the footnotes ; they have been taken mainly from the catalogues of Becvar (1951). When the catalogue number of the nebula is in parentheses there is no reason for thinking that this is other than an accidental coincidence in position. The catalogues of Bok, Bester, and Wade (1955) and Gum (1955) have been used to supplement the information about emission nebulae in the Becvar catalogues.

III. Identifications

Although the area included in the present catalogue is much less than in our previous catalogues, a reasonable number of identifications with bright nebulae may be suggested. This situation arises principally because the southern regions of the Milky Way, rich in H II regions but comparatively low in radio brightness, are included in the catalogue area. Several such H II regions may be recognized as radio sources ; the data relating to them are collected in Table 4, and, in Table 5, the bright external galaxies for which possible identifications exist are also listed. There is also noted in the catalogue a globular cluster

TABLE 1

SOURCES BETWEEN DECLINATIONS —50° AND —60°

Sources which may be "extended", that is resolvable, are indicated by a dagger. A colon is placed beside uncertain flux densities. Angular sizes, where available, are indicated in the footnotes

Ref. No.	Position (1950)		Flux Density (10^{-26} Wm^{-2} (c/s)$^{-1}$)
	R.A. h m	Dec. S. ° ′	
	00		
1	02·7^{4}	56 28^{6}	19†
2	27·2^{6}	55 12^{6}	12
3	36·1^{3}	51 36^{6}	11
4	58·1^{3}	50 41^{6}	10
	01		
1	01·0^{6}	55 58^{8}	8
2	15·2^{5}	52 05^{6}	15
3	19·9^{3}	50 24^{6}	12
4	26·1^{5}	53 02^{6}	11
5	29·6^{8}	51 12^{8}	8
6	41·5^{8}	54 56^{6}	9:
7	44·9^{5}	52 12^{7}	13†
8	47·1^{5}	57 53^{6}	20
	02		
1	16·1^{4}	57 42^{5}	9
2	26·0^{4}	52 43^{7}	11†(1)
3	42·3^{3}	51 23^{5}	37(2)
4	45·8^{2}	55 52^{4}	48(3)
5	49·7^{4}	54 24^{6}	15
6	56·4^{5}	52 37^{7}	11
	03		
1	36·7^{5}	57 35^{6}	11
2	44·3^{4}	53 16^{7}	18†
3	46·6^{4}	52 20^{6}	13
	04		
1	00·3^{4}	50 30^{7}	11
2	11·1^{4}	56 04^{6}	16
3	22·7^{5}	52 57^{7}	14†
4	28·0^{2}	53 59^{3}	50(4)
5	43·1^{8}	51 22^{7}	8
	05		
1	36·0^{4}	51 30^{7}	10
2	37·9^{10}	52 56^{8}	9
3	53·6^{4}	54 08^{6}	12
	06		
1	05·3^{3}	50 32^{7}	13
2	09·6^{5}	58 33^{6}	12†
3	20·7^{3}	52 35^{5}	30
4	22·3^{6}	50 15^{7}	8
5	25·4^{1}	53 44^{4}	*172* (113)(5)
6	42·2^{4}	54 00^{6}	9
7	50·7^{4}	56 55^{7}	18
	07		
1	00·5^{4}	59 21^{6}	15
2	06·2^{4}	50 19^{6}	10
3	18·3^{3}	55 33^{5}	24
4	20·0^{3}	52 42^{6}	13
5	29·7^{3}	52 43^{6}	12
6	40·6^{8}	54 07^{10}	*18*: (11)(6)
7	48·2^{5}	57 42^{6}	10
8	53·5^{6}	56 14^{8}	8

(1) A doubtful source.

(2) <10″.

(3) ⩾40″.

(4) I 2082>40″.

(5) Perhaps two sources, 20″.

(6) Perhaps two sources.

Table 1 (*Continued*)

Ref. No.	Position (1950) R.A. h m	Position (1950) Dec. S. ° ′	Flux Density (10^{-26} Wm^{-2} $(c/s)^{-1}$)
	08		
1	$12\cdot 7^{4}$	$53\ 44^{8}$	15†
2	$27\cdot 6^{6}$	$51\ 07^{8}$	10
3	$44\cdot 7^{3}$	$57\ 20^{7}$	30(7)
	09		
1	$05\cdot 7^{5}$	$53\ 05^{5}$	8
2	$16\cdot 4^{3}$	$54\ 38^{5}$	36†(8)
3	$26\cdot 8^{5}$	$50\ 15^{7}$	14
4	$38\cdot 1^{5}$	$53\ 25^{7}$	23†(9)
5	$39\cdot 6^{6}$	$57\ 02^{6}$	9:
	10		
1	$05\cdot 6^{4}$	$56\ 53^{7}$	*68* (47)
2	$06\cdot 2^{5}$	$55\ 31^{7}$	26†
3	$17\cdot 2^{6}$	$58\ 50^{10}$	71:†(10)
4	$20\cdot 3^{5}$	$57\ 34^{6}$	*151* (96)(11)
5	$38\cdot 1^{4}$	$53\ 41^{6}$	9:
6	$41\cdot 3^{5}$	$51\ 55^{7}$	9
7	$43\cdot 5^{2}$	$59\ 30^{3}$	*339* (242)(12)
8	$53\cdot 0^{4}$	$56\ 26^{7}$	19
9	$54\cdot 8^{5}$	$58\ 10^{6}$	20
10	$59\cdot 6^{4}$	$51\ 07^{7}$	13
	11		
1	$05\cdot 7^{3}$	$53\ 49^{6}$	12
2	$07\cdot 7^{6}$	$57\ 09^{6}$	15
3	$18\cdot 9^{4}$	$50\ 40^{6}$	14
4	$22\cdot 2^{4}$	$59\ 10^{6}$	39
5	$24\cdot 1^{3}$	$56\ 04^{5}$	30
6	$49\cdot 7^{3}$	$54\ 05^{5}$	16(13)
	12		
1	$08\cdot 1^{3}$	$52\ 20^{5}$	*182* (114)(14)
2	$28\cdot 1^{4}$	$59\ 59^{6}$	19
3	$36\cdot 0^{4}$	$55\ 29^{8}$	16
4	$43\cdot 3^{4}$	$53\ 25^{6}$	17
5	$59\cdot 1^{4}$	$52\ 10^{6}$	22†
	13		
1	$51\cdot 7^{5}$	$52\ 10^{6}$	18
2	$59\cdot 6^{8}$	$57\ 56^{10}$	*71* (35)
	14		
1	$03\cdot 6^{4}$	$54\ 27^{5}$	12
2	$05\cdot 7^{4}$	$51\ 20^{7}$	39
3	$05\cdot 7^{8}$	$59\ 08^{10}$	44:†
4	$14\cdot 7^{5}$	$52\ 25^{6}$	18
5	$19\cdot 6^{3}$	$55\ 53^{5}$	36(15)
6	$26\cdot 2^{5}$	$50\ 56^{5}$	15
7	$37\cdot 8^{4}$	$59\ 44^{4}$	*167* (133)(16)
8	$50\cdot 0^{5}$	$59\ 03^{5}$	71:†(17)
	15		
1	$08\cdot 7^{4}$	$50\ 28^{6}$	27†
2	$11\cdot 5^{5}$	$58\ 55^{6}$	*252* (190)(18)
3	$15\cdot 6^{5}$	$57\ 30^{6}$	55
4	$28\cdot 3^{6}$	$56\ 08^{6}$	50:†
5	$44\cdot 0^{3}$	$54\ 30^{7}$	70†(19)
6	$48\cdot 6^{3}$	$55\ 56^{4}$	*323* (270)(20)
7	$50\cdot 8^{4}$	$53\ 14^{5}$	146:(21)
8	$58\cdot 0^{2}$	$52\ 07^{4}$	91(22)

---

(7) Perhaps extended or two sources, >30″.

(8) >30″.

(9) A doubtful source ; perhaps a galactic irregularity.

(10) >30″.

(11) (S 29).

(12) η Carinae nebula NGC 3372.

(13) Perhaps a side lobe of 17S2A.

(14) Perhaps two sources, >40″.

(15) >40″.

(16) >55″.

(17) >30″.

(18) BWW228*02*, <30″.

(19) >40″.

(20) >50″.

(21) >60″.

(22) >45″.

TABLE 1 (*Continued*)

Ref. No.	Position (1950) R.A. h m	Position (1950) Dec. S. ° ′	Flux Density (10^{-26} Wm^{-2} (c/s)$^{-1}$)
	16		
1	$11\cdot5^{4}$	50 40^{5}	256†(23)
2	$13\cdot9^{6}$	54 00^{8}	33
3	$26\cdot5^{6}$	52 10^{7}	32
	17		
1	$55\cdot0^{4}$	59 45^{6}	25:
	18		
1	$05\cdot8^{6}$	50 56^{8}	20:†
2	$14\cdot5^{6}$	51 59^{5}	27(24)
3	$18\cdot8^{3}$	55 32^{7}	23†
4	$41\cdot6^{3}$	55 05^{5}	12
	19		
1	$15\cdot5^{6}$	53 02^{5}	16
2	$17\cdot7^{5}$	54 30^{5}	27
3	$22\cdot5^{4}$	57 47^{6}	16
4	$23\cdot6^{5}$	51 27^{7}	17
5	$25\cdot8^{6}$	52 25^{8}	10
6	$34\cdot5^{4}$	58 31^{5}	17
7	$54\cdot3^{3}$	55 16^{4}	54(25)
	20		
1	$03\cdot4^{6}$	53 59^{6}	12:
2	$06\cdot8^{2}$	56 39^{4}	81(26)
3	$10\cdot3^{4}$	52 21^{6}	14
4	$13\cdot4^{4}$	55 37^{6}	19
5	$20\cdot3^{4}$	57 33^{5}	36(27)
6	$40\cdot8^{6}$	51 17^{8}	9
7	$46\cdot6^{8}$	57 23^{8}	12:(28)
	21		
1	$13\cdot7^{4}$	50 54^{5}	13
2	$22\cdot4^{6}$	55 32^{7}	17
3	$25\cdot5^{5}$	58 04^{6}	17
4	$30\cdot1^{5}$	53 44^{7}	20
5	$37\cdot6^{6}$	51 28^{8}	10†
6	$41\cdot0^{6}$	56 52^{8}	18:
7	$49\cdot8^{5}$	58 26^{7}	13
8	$50\cdot9^{3}$	51 53^{5}	28(29)
	22		
1	$18\cdot5^{4}$	50 32^{6}	16
2	$23\cdot7^{3}$	52 45^{5}	30(30)
3	$45\cdot4^{6}$	51 17^{7}	7
4	$53\cdot2^{3}$	53 02^{5}	22
5	$54\cdot5^{4}$	52 15^{5}	28(31)
	23		
1	$25\cdot1^{6}$	52 18^{7}	9
2	$38\cdot9^{4}$	58 34^{5}	25

(23) $>60''$.
(24) (NGC 6584), $<15''$.
(25) $>40''$.
(26) $\geqslant 35''$.
(27) $<15''$.
(28) I 5063.
(29) $30''$.
(30) $\sim 15''$.
(31) $\leqslant 15''$.

TABLE 2

SOURCES BETWEEN DECLINATIONS $-60°$ AND $-70°$

Sources which may be "extended", that is resolvable, are indicated by a dagger. A colon is placed beside uncertain flux densities. Angular sizes, where available, are indicated in the footnotes

Ref. No.	Position (1950) R.A. h m	Position (1950) Dec. S. ° ′	Flux Density (10^{-26} $\mathrm{Wm^{-2}\,(c/s)^{-1}}$)
	00		
1	13·4^{4}	63 20^{5}	27
	01		
1	20·2^{4}	63 14^{5}	22
2	28·7^{5}	61 37^{6}	17
3	38·9^{5}	69 58^{6}	22
4	59·5^{6}	60 55^{6}	14
	02		
1	00·9^{8}	60 38^{7}	10:
2	08·3^{5}	62 11^{7}	11
3	31·1^{6}	66 25^{7}	13
4	48·0^{3}	60 17^{5}	19
5	51·7^{5}	67 42^{5}	34†(1)
	03		
1	46·0^{6}	68 00^{7}	10:
	04		
1	02·5^{4}	63 44^{9}	14
2	07·1^{3}	65 58^{5}	36(2)
3	19·9^{2}	62 29^{5}	38(3)
4	29·3^{3}	61 31^{5}	35†
5	37·0^{4}	64 47^{6}	16
6	49·0^{6}	62 08^{6}	9
	05		
1	05·5^{3}	61 07^{6}	14
2	08·2^{5}	62 21^{8}	11
3	17:	69 18:	4000 (100)(4)
4	25·4^{4}	65 58^{5}	34(5)
5	31·0^{5}	63 41^{10}	10
6	39·8^{4}	69 20^{5}	108†(6)
	06		
1	07·8^{5}	65 58^{7}	14:
2	09·2^{6}	60 40^{6}	16
3	50·8^{5}	60 28^{8}	9::
4	57·6^{4}	65 38^{6}	17
5	59·5^{5}	67 15^{7}	14
	07		
1	11·6^{3}	64 27^{7}	16
2	22·5^{8}	65 14^{7}	8
	09		
1	04·1^{8}	65 40^{6}	8::
2	08·4^{6}	63 24^{6}	15(7)
3	37·0^{5}	62 35^{6}	16
4	57·0^{6}	66 48^{5}	9:
	10		
1	10·0^{3}	64 34^{7}	19

(1) $>35''$.

(2) $<15''$.

(3) $20''$.

(4) Large Magellanic Cloud, the position is that of the centroid.

(5) $\sim 30''$.

(6) 30 Doradus, $>40''$.

(7) Perhaps a side lobe of 03S3A.

TABLE 2 (*Continued*)

Ref. No.	Position (1950)		Flux Density (10^{-26} Wm^{-2} (c/s)$^{-1}$)
	R.A. h m	Dec. S. ° ′	
	11		
1	00·0^{3}	60 36^{4}	162(8)
2	10·2^{6}	60 38^{6}	42(9)
3	34·0^{7}	62 26^{8}	100: (50)(9a)
4	36·4^{6}	67 54^{7}	34(10)
5	37·0^{5}	63 02^{7}	38(11)
6	51·8^{6}	69 17^{6}	15
	12		
1	10·5^{3}	62 25^{5}	*140* (112)
2	15·3^{5}	61 29^{5}	18
3	17·4^{8}	63 40^{8}	30:
4	39·7^{5}	61 42^{5}	26
	13		
1	10·0^{4}	64 08^{5}	24
2	43·4^{1}	60 07^{2}	795(12)
3	57·7^{5}	63 41^{6}	20:(13)
	14		
1	06·3^{5}	61 24^{6}	*196*: (69)
2	09·9^{5}	65 05^{7}	35:
3	38·9^{3}	62 24^{6}	110(14)
4	51·9^{8}	60 50^{10}	*147* : (84)
	15		
1	28·0^{4}	60 50^{7}	*81* (55)(15)
	16		
1	10·2^{1}	60 45^{2}	1190(16)
2	33·8^{8}	61 47^{7}	30::
3	59·9^{5}	62 32^{6}	18(17)
	17		
1	13·4^{8}	62 10^{6}	35:(18)
	18		
1	16·2^{3}	64 00^{4}	71(19)
2	42·4^{8}	60 40^{7}	9
	19		
1	21·3^{5}	62 30^{10}	12†
	20		
1	41·2^{3}	60 23^{4}	55(20)
2	59·2^{4}	64 03^{6}	17
	21		
1	00·2^{8}	61 36^{7}	8
2	17·5^{8}	67 00^{10}	9:
3	26·5::	61 13::	8:
4	52·9^{2}	69 58^{3}	253(21)
	22		
1	17·1^{8}	63 52^{10}	11
2	38·3^{5}	61 01^{5}	14
3	53·9^{4}	65 14^{6}	19
4	55·8^{5}	67 54^{8}	13
5	56·1^{8}	63 52^{10}	8
	23		
1	13·3^{4}	62 24^{8}	14:
2	20·1^{6}	60 50^{10}	10
3	33·0^{6}	66 55^{6}	26
4	56·0^{2}	61 08^{3}	296(22)

(8) NGC 3503, >50″.

(9) (S38a), >40″.

(9a) BBW2620.

(10) >35″.

(11) >35″.

(12) IAU 13S6A, 65″.

(13) Possibly interference from IAU 16S6A.

(14) >40″.

(15) Perhaps a galactic irregularity.

(16) IAU 16S6A, ⩾70″.

(17) Perhaps a background irregularity.

(18) Perhaps a background irregularity.

(19) ⩽20″.

(20) <15″.

(21) 25″.

(22) 40″.

TABLE 3

SOURCES SOUTH OF DECLINATION —70°

Sources which may be "extended", that is resolvable, are indicated by a dagger. A colon is placed beside uncertain flux densities. Angular sizes, where available, are indicated in the footnotes

Ref. No.	Position (1950) R.A. h m	Position (1950) Dec. S. ° ′	Flux Density (10^{-26} Wm^{-2} (c/s)$^{-1}$)
	00		
1	54 :	72 42 :	*550*: (37)(1)
	01		
1	59·7^{10}	76 02^{10}	18:†
	02		
1	21·3^{5}	70 50^{7}	30
2	52·0^{6}	70 52^{8}	7:
	04		
1	09·4^{3}	75 08^{4}	87(2)
2	24·3^{6}	72 39^{8}	11
	06		
1	36·0^{6}	75 04^{7}	20
	07		
1	28·7^{5}	70 11^{8}	11
	08		
1	43·1^{5}	75 31^{7}	58(3)
	12		
1	28·1^{8}	70 16^{8}	19
	15		
1	28·9^{5}	74 07^{7}	20(4)
	16		
1	22·6^{8}	75 11^{7}	38
	17		
1	21·2^{5}	70 01^{8}	46
	18		
1	11·8^{10}	77 25^{10}	18:(5)
	20		
1	28·0^{8}	73 13^{6}	18:(6)
	22		
1	44·3^{8}	77 19^{10}	43(7)

(1) Small Magellanic Cloud, the position is that of the centroid.

(2) <20″.

(3) <20″.

(4) Perhaps a background irregularity.

(5) A doubtful source.

(6) A doubtful source.

(7) A doubtful source.

NGC 6584, comparatively close to the radio source 18–*52*; however, there is no reason for thinking that this is other than an accidental coincidence.

Examination of the tables shows that the new possible identifications are not numerous. Only one galaxy has not been noted before (I 5063), although there are four new H II regions observed. In general, comparisons of radio and optical catalogues are not very satisfactory for studying H II regions because these are often not isolated objects. It is usually better to compare radio and optical isophotes, e.g. for the region of this catalogue the radio isophotes of Hill, Slee, and Mills (1958) and the Hα isophotes of Johnson (1960).

TABLE 4

POSSIBLE IDENTIFICATIONS WITH EMISSION NEBULAE

Radio Source	Emission Nebulae	Notes
05–6*6*	NGC 2270	30 Doradus, an emission nebula in the Large Magellanic Cloud. This is a well-known identification
10–5*7*	NGC 3372	η Carinae nebula, a well-known identification
11–6*1*	NGC 3503	An area displaying a complex H II distribution
11–6*2*	S 38a*	
11–6*3*	BBW 26201†	This is given as two separate nebulae, S 40* and S 42,* by Gum
15–5*2*	BBW 28802†	

* Gum (1955).

† Bok, Bester, and Wade (1955).

A number of fields containing radio sources listed in the catalogue have been photographed by Basinski, Bok, and Gottlieb (1959). No clear identifications emerge from these photographs, although in a few cases the radio positions correspond with clusters of galaxies, i.e. the sources 04–5*4* (probably identified with a cluster member I 2082—see Table 5), 16–6*1*, and 23–6*4*: these sources undoubtedly need further investigation. The sources 04–5*4* and 03–5*2* have previously been noted as corresponding with cluster positions (Mills 1959).

IV. DISCUSSION

The number of radio sources included in the present catalogue represents only about one-tenth of the total: consequently the effect of adding these results to the previous statistics (Mills, Slee, and Hill 1960) is negligible. The conclusion reached before is therefore not altered; that is, the statistics of the

TABLE 5

POSSIBLE IDENTIFICATIONS WITH BRIGHT GALAXIES

Radio Source	Galaxy Catalogue No.	Type	$m_{1\cdot 9}-m_p$	Notes
00–7*1*	S.M.C.	Irr.	2·8	The Small Magellanic Cloud is a well-known identification
04–5*4*	I 2082		—7	A double galaxy of about magnitude 15 in a cluster: this appears a very probable identification
05–6*3*	L.M.C.	Irr.	3·0	The Large Magellanic Cloud is a well-known identification
20–5*7*	I 5063	E 2	—2·8	The position agreement is relatively close, but there is no confirmatory evidence

source counts, when due allowance is made for instrumental effects, show no significant departures from those expected with a random distribution of sources in a static Euclidean universe. They are also not inconsistent with the counts expected in a relativistic expanding universe. The sensitivity of the instrument is inadequate for a definitive result in cosmology based on source counts alone: it seems likely that this method will require numbers of well-determined radio sources approaching 10 000 per steradian, at least, to succeed.

Summarizing the identification situation, we find that in the three published catalogues, totalling 2270 sources, some 28 bright galaxies, 11 emission nebulae, and 2 supernovae remnants have been listed as possible identifications. We have also found two relatively close coincidences with globular clusters, but this is about the number expected by chance. A search for identifications involving fainter galaxies and clusters of galaxies has been carried out in selected portions of the catalogues (Mills 1960); this has produced about 90 additional possible identifications with faint galaxies (many of them double systems) and 55 possible identifications with clusters of galaxies (or individual galaxies within the cluster). A certain proportion of all these possible identifications represent chance coincidences, as discussed in the papers concerned. The great majority of radio sources, however, remain unidentified.

At high galactic latitudes the sparsity of identification is consistent with the form of radio luminosity function proposed by Mills (1960) and subsequently elaborated by Bolton (1960) and Minkowski (1961). At low latitudes, however, the small number of identifications with galactic objects requires explanation. There is a complete absence of identifications with optical emission nebulae at longitudes greater than 288° (old system) extending through the centre to our northern limit, at longitude 13°. This arises because, at our wavelength of 3·5 m, the nearby bright emission nebulae in this region are seen against a background temperature equal to or greater than their electron temperature and consequently are observed in absorption or not at all: NGC 6357 and probably M8 are in the former category.

In northern declinations inaccessible to our instruments, about a dozen galactic non-thermal sources have been identified with filamentary nebulosities, apparently old supernova remnants. In our southern catalogues, however, only two sources, 08–*44* and 17–2*11* (Kepler's supernova), can be so identified. This may be due partly to the absence of wide-angle photographic plates of the necessary quality but principally, we feel, to the richness and heavy obscuration of the southern Milky Way, which makes the detection of such objects more difficult.

Finally, we point out that the angular size data included in our catalogues are incomplete (in fact absent in the region +10° to −20°). It is proposed to include the complete observational data in a later publication.

V. References

Basinski, J., Bok, B. J., and Gottlieb, K. (1959).—" Paris Symposium on Radioastronomy." Vol. 9, p. 514. (Stanford Univ. Press.)

Becvar, A. (1951).—" Atlas Coeli Skalnate Pleso." (Prirodovedecke Vydavatelstvi : Prague.)

Bok, B. J., Bester, M. J., and Wade, C. M. (1955).—*Daedalus* **86** : 9.

Bolton, J. G. (1960).—Observations of the C.I.T. Radio Observatory No. 5.

Goddard, B. R., Watkinson, A., and Mills, O. B. (1960).—*Aust. J. Phys.* **13** : 665.

Gum, C. S. (1955).—*Mem. R. Astr. Soc.* **67** : 155.

Hill, E. R., Slee, O. B., and Mills, B. Y. (1958).—*Aust. J. Phys.* **11** : 530.

Johnson, H. M. (1960).—*Mem. Mount Stromlo Obs.* **3**, No. 15.

Mills, B. Y. (1959).—" Handbuch der Physik." Vol. 52, p. 239. (Springer-Verlag : Berlin.)

Mills, B. Y. (1960).—*Aust. J. Phys.* **13** : 550.

Mills, B. Y., Little, A. G., Sheridan, K. V., and Slee, O. B. (1958).—*Proc. Inst. Radio Engrs., N.Y.* **46** : 67.

Mills, B. Y., and Slee, O. B. (1957).—*Aust. J. Phys.* **10** : 162.

Mills, B. Y., Slee, O. B., and Hill, E. R. (1958).—*Aust. J. Phys.* **11** : 360.

Mills, B. Y., Slee, O. B., and Hill, E. R. (1960).—*Aust. J. Phys.* **13** : 676.

Minkowski, R. L. (1961).—Luminosity function of extragalactic radio sources. (In press.)

A HIGH RESOLUTION GALACTIC SURVEY AT 19·7 Mc/s

By The Late C. A. Shain,* M. M. Komesaroff,† and C. S. Higgins†

[*Manuscript received August* 16, 1961]

Summary

An extensive strip of the Southern Milky Way has been surveyed at 19·7 Mc/s, using a Mills Cross with a pencil beam 1·4° wide. The radio contours show a number of dark areas whose positions agree with those of optically-observed H II regions which at this frequency are seen in absorption. In addition, an intensity minimum along the galactic equator appears to represent the effect of absorption due to many H II regions extending to great distances in the galactic plane.

I. Introduction

Observations of the galactic radio emission around 20 Mc/s provide a striking confirmation of conclusions which have been drawn from work at much higher frequencies. A number of high resolution surveys have been made at frequencies well above 20 Mc/s and these show a broad band of emission concentrated towards the galactic plane, on which is superimposed a narrow and intense band only a few degrees wide, following the plane quite closely.

In order to explain this narrow band at least two processes must be considered. One component of the radiation is due to thermal emission from ionized interstellar hydrogen regions (H II regions) which are known to be concentrated towards the galactic plane. Optical observations provide estimates of the electron densities and temperatures in these regions, and from these the expected radio emission can be roughly estimated. At frequencies above 1000 Mc/s the predicted and observed intensities agree in general magnitude.

However, the observed intensity increases with decreasing frequency at a rate far too rapid to be compatible with a purely thermal origin. Some non-thermal component must also be present, and it is generally thought that this is due to " synchrotron " emission from electrons of relativistic energies gyrating in very weak magnetic fields in interstellar space.

---

* The work described in this paper was initiated by the late C. A. Shain, who had taken it to the stage at which the contour maps were nearly complete before his untimely death in February 1960. His two colleagues, the remaining authors, who had worked with him for some time prior to his death, completed the observation of certain areas, carried out the remainder of the reductions, and wrote this paper. Because of these circumstances, some of the discussion is less complete than might be desired. In particular this applies to the description of calibration techniques. This is based largely on Shain's notes, but it has not been possible to elucidate all the details.

† Division of Radiophysics, C.S.I.R.O., University Grounds, Chippendale, N.S.W.

Shain's observations at low frequencies have vividly confirmed the twofold origin of the galactic emission. Below 20 Mc/s the non-thermal component of brightness temperature often exceeds 100 000 °K. Since the electron temperatures of H II regions are commonly about 10 000 °K and since their optical depths are considerable at these frequencies, they appear in absorption against a very bright background. The first experimental evidence of absorption was found by Shain (1951, 1954) and Shain and Higgins (1954), who carried out galactic surveys at 18·3 Mc/s, using very broad-beam aerial systems. It was found that the ratio of brightness temperature at 18·3 Mc/s to that at 100 Mc/s (as measured by Bolton and Westfold 1950) was lower towards the galactic centre than in other directions.

In order to progress further, better angular resolution was required, and Shain therefore adapted the Mills Cross principle to low frequency observations. The instrument he designed had a pencil beam 1·4° wide and operated at 19·7 Mc/s. With this it was possible to explore the region near the galactic equator in considerable detail.

In contrast with high frequency results, he found an intensity minimum along the equator where ionized hydrogen is known to be concentrated, and, in addition, he found a number of discrete radio " dark " areas corresponding in position with optically-visible H II regions. He was also able to confirm Mills's (1955) conclusion that the bright band observed near the equator at 85 Mc/s is mainly of non-thermal origin. Preliminary accounts of this work over restricted areas have been given previously (Shain 1957, 1959).

It was Shain's aim to survey a large section of the Southern Milky Way, but difficulties associated with the low observing frequency made the program a very lengthy one. The 18·3 Mc/s work had shown that ionospheric absorption can be quite severe, and, accordingly, the 19·7 Mc/s observations were taken in the pre-dawn period when absorption is low. Ionospheric refraction was still considerable, however, and a separate investigation of this effect had to be undertaken. It was found possible to calculate refraction corrections provided data were available from two or more appropriately located ionospheric sounding stations for the time of observation. The most serious experimental difficulty was the severe loss of observation time due to short-wave interference.

Despite these difficulties, Shain had completed most of the work before his untimely death in early 1960. The observations required to fill the remaining gaps in the contours were attempted after his death, but as they were all in high southerly declinations where conditions are most unfavourable, not much was added to his survey.

The main aim of the present paper is to present Shain's results in the substantially complete form in which he left them. The survey covers an area extending between $l^{\mathrm{I}}=224°$ to 16° and over 10° of latitude. A chart of optically-observed H II regions is presented with the radio map and from this the good correlation between H II and radio " dark " areas can be seen.

In areas where the radio contours are unaffected by " nearby " H II regions or strong non-thermal sources, a comparison of the present results with high frequency observations yields information about the non-thermal radio spectrum and the large-scale relative distribution of thermal and non-thermal emission. This question is discussed in a companion paper (Komesaroff 1961).

II. OBSERVATIONS

(*a*) *Procedures and Difficulties*

The observational program was carried out between 1956 and mid 1960. The instrument is of the Mills Cross type and has a beamwidth of 1·4°. The general principles of operation have been described by Mills, Little, and Sheridan (1956), and Shain (1958) has outlined the features peculiar to the low frequency instrument; in particular these include a set of narrow-band tunable i.f. amplifiers which permit utilization of the maximum frequency band while avoiding interference from short-wave transmitters.

Calibration of an instrument of this type presents considerable difficulties. Little (1958) has described a method by which the gains of larger antenna systems can be compared with the known gain of a half-wave dipole, but this technique was found unworkable at 19·7 Mc/s, due to the effect of ionospheric scintillations. The method finally adopted involved determining two sets of parameters.

(i) The directivity diagrams of the individual arrays, which were derived from their known complex current distributions and from the diagram of a single half-wave dipole.

(ii) Efficiency factors, computed by comparing observed aerial temperatures with those to be expected from the earlier 18·3 Mc/s observations of Shain and Higgins (1954).

By combining the results of (i) and (ii), it was possible to derive a calibration procedure along the lines described by Mills *et al.* (1958). The absolute calibration was estimated to have a possible error of about 20%, but the relative accuracy was thought to be considerably better.

The "scanning" system of observation was used almost exclusively throughout. This gives quasi-simultaneous records on each of five declinations spaced at intervals of about $\frac{1}{2}$–$\frac{3}{4}$°, depending on zenith distance. In the subsequent analysis mean values of "beam temperature" were taken at intervals of 4 min (sidereal time). Since the aerial beamwidth is 1·4°, this led to no significant degradation of the original information.

The low observing frequency of 19·7 Mc/s entailed a number of difficulties which were enhanced by the fact that observations were taken during a period of exceptionally great sunspot activity.

Firstly, the spectral density of short-wave signals, mostly from long distances, was very high. In order to avoid them it was necessary to use the system of tunable i.f. amplifiers mentioned earlier and described in greater detail by Shain (1958). Interference at a high level was easily recognized, but at a low level it could be quite insidious, requiring a beat-frequency oscillator for its detection, and necessitating continuous aural monitoring throughout the observing period.

Secondly, ionospheric refraction was often severe, sometimes exceeding 1°. To correct for the "steady" component of refraction, formulae derived by

Komesaroff (1960) were used, expressing the refraction in terms of measurable ionospheric parameters. Scintillation effects could not be estimated, but were mitigated by the time-averaging procedure mentioned earlier. Duplication of records provided a cross-check on refraction and it is believed that residual errors were only of the order of 10′ of arc.

To minimize the above effects and also that of ionospheric absorption, recording was mainly restricted to the period between 2200 h and 0600 h local time. Even at this time, a percentage of records was rendered useless by short-wave interference and atmospherics. Nevertheless, several " good " records were obtained on each of the declinations covered. It was therefore possible to check their mutual consistency and also to improve the signal-to-noise ratio by averaging.

(*b*) *Analysis of Results*

In their paper describing the original 85 Mc/s Mills Cross, Mills *et al.* (1958) showed that, in order to determine the brightness temperature in the direction of the main beam, two quantities must be measured. These are the mean product of the voltages from the individual arrays (the pencil-beam temperature) and the power from the north-south array. The required brightness temperature is the sum of these two terms multiplied by appropriate weighting factors.

In the 19·7 Mc/s equipment, the two quantities are recorded independently. The record of pencil-beam temperature consists of a sawtooth pattern, the height of each " tooth " being proportional to the beam temperature integrated over 12 s (sidereal time). Adjacent " teeth " represent adjacent declinations in the five-position cycle. The output of the north-south array appears on a separate recorder.

In the first step of the analysis, the five declinations of the pencil-beam record were separated, and for each of these constant-declination profiles, the average temperature was computed at 4-min intervals ; this last step was to reduce the effect of scintillations. The north-south component was then added, giving five constant declination profiles of brightness temperature.

The measured declinations and Right Ascensions were then corrected for refraction effects. In an earlier paper (Komesaroff 1960) it was shown that refraction corrections can be calculated using hourly values of critical frequency measured at a number of ionospheric sounding stations. When sufficient ionospheric data could be obtained, refraction corrections were first applied and then all the available records on each (corrected) declination were averaged, in order to achieve the best signal-to-noise ratio. In a number of instances, however, the hourly ionospheric data were incomplete or unavailable. In these cases the records were fitted together empirically and averaged, and corrections were computed from the predicted monthly mean values of critical frequency.

The next step was to transfer the mean values of brightness temperature from the corrected records to a rectangular grid of Lund galactic coordinates, on which lines of constant declination and Right Ascension were drawn for guidance. When this had been done a further correction had to be applied to allow for the effect of the aerial side lobes. This question has been discussed in some detail by Mills *et al.* (1958) and the system of correction used for the 19·7 Mc/s results was essentially similar to the one they describe. The final step was to draw smooth contour lines through points of equal brightness temperature.

III. RESULTS

The results of the survey are shown in Plate 1. Contour lines of equal brightness temperature at intervals of 50 000 °K are drawn on a grid of Lund galactic coordinates. A considerably coarser grid of equatorial coordinates (epoch 1958) is also included. The galactic equator according to the new I.A.U. system (1958 revision) is indicated by a dashed line.

The map covers a strip of the Milky Way about 10° wide extending over a considerable range of longitudes (l^I=224–16°) on either side of the galactic centre. The gaps in the contours between l^I=234° and 282° arise from the great observational difficulties in this region. This is the most extreme southerly declination of the survey and had to be observed near midsummer. Consequently ionospheric effects and interference—both atmospheric and man-made—were at their most severe. For several of the declinations it was found that the degree of correlation between successive records was too poor to warrant their inclusion, and it was decided to publish the map in its incomplete form. It should be noted that the region between about l^I=290° and 318° was also observed under difficulties and may be somewhat less reliable than the region beyond the galactic centre.* Finally, the break in the contours near l^I=288° indicates what appears to be a discontinuity, presumably of instrumental origin. The discrepancy is about 20% of the mean level.

IV. COMPARISON WITH OPTICAL OBSERVATIONS

The transparent overlay accompanying Plate 1 shows the distribution of optically-observed ionized hydrogen along the Milky Way, according to the work of Rodgers *et al.* (1960). Areas containing Hα-emission are enclosed by a dashed line and, within these, more intense emission is outlined with a full line. Smaller regions, believed to be separate, but seen against the broader areas, are indicated in black.

On comparing Plate 1 with the transparent overlay, a very good correlation is noted between optically-observed H II regions and localized radio "dark" areas. Conversely, between longitudes 328·5 and 332°, where the optical data show a break in the H II distribution, there is a maximum of radio brightness. Thus the observations provide a striking illustration of the absorption of low radio frequencies in ionized hydrogen. Two radio features which are apparently unrelated to the optical data are the dark areas near longitudes 287° and 5°. In the next paper (Komesaroff 1961) it is shown that these are not produced by absorption but by a deficiency of emission.

It might not have been expected that the two sets of data would show such good agreement considering the vast dust clouds—opaque to optical wavelengths but transparent to radio waves—which lie along the galactic plane. Despite the obscuration, however, the optical observations appear to delineate the distribution of " nearby " ionized hydrogen fairly completely. It must be emphasized that this can only be said of regions whose angular dimensions exceed about $\frac{3}{4}$° ; owing to the finite resolution of our aerial smaller regions would scarcely be detectable.

---

* Most of the records were taken in one month at a time when ionospheric conditions were adverse and when ionospheric sounding data were incomplete.

The electron temperature of an H II region is only about 10 000 °K (Mills, Little, and Sheridan 1956), and Shain (1957) has shown that even H II regions which are faint by optical standards are nearly opaque at 19·7 Mc/s. In all cases, however, the 19·7 Mc/s brightness temperatures in the direction of H II regions greatly exceed 10 000 °K. Part of this temperature excess arises because generally an individual region does not fill the aerial beam, but another part represents " foreground " radiation generated between the obscuring region and the observer. Shain (1959) has correlated values of " foreground temperature " with optically-derived distance estimates and draws the tentative conclusion that an upper limiting value of 50 000 °K is reached at a distance of about 600 parsecs. This suggests that the emission is fairly strongly concentrated in spiral arms. It is hoped to investigate this problem further, using more extensive data ; however, it will not be discussed further in the present paper.

Away from the galactic centre and where the radio contours are unaffected by nearby absorbing regions, they show an extended minimum following the equator quite closely out to longitudes of about ±35° from the centre. This would appear to be the integrated effect of many H II regions extending to such vast distances that they are not individually distinguishable. Radio-spectral studies of this region can provide information about its structure in depth. This question is discussed in detail in the next paper (Komesaroff 1961).

V. Acknowledgments

The present results represent the combined efforts of a number of workers. In particular, Mr. C. F. Attwood and Mr. L. F. Clague took many of the observations and also contributed to the development and maintenance of equipment. Mrs. J. Raengel carried out much of the laborious record analysis, a task which was taken over in its later stages by Miss W. Wolfe.

We also wish to acknowledge the advice and help of Professor B. J. Bok, Dr. A. W. Rodgers, Mr. J. B. Whiteoak, and other members of the Mt. Stromlo Observatory staff who were engaged in the preparation of their Milky Way Atlas during the course of this work.

VI. References

Bolton, J. G., and Westfold, K. C. (1950).—*Aust. J. Sci. Res.* A **3** : 19.

Komesaroff, M. M. (1960).—*Aust. J. Phys.* **13** : 153.

Komesaroff, M. M. (1961).—*Aust. J. Phys.* **14** : 515.

Little, A. G. (1958).—*Aust. J. Phys.* **11** : 70.

Mills, B. Y. (1955).—*Aust. J. Phys.* **8** : 368.

Mills, B. Y., Little, A. G., and Sheridan, K. V. (1956).—*Aust. J. Phys.* **9** : 218.

Mills, B. Y., Little, A. G., Sheridan, K. V., and Slee, O. B. (1958).—*Proc. Inst. Radio Engrs., N.Y.* **46** : 67.

Rodgers, A. W., Campbell, C. T., Whiteoak, J. B., Bailey, H. H., and Hunt, V. O. (1960).—"An Atlas of Hα Emission in the Southern Milky Way." (Aust. National University: Canberra.)

Shain, C. A. (1951).—*Aust. J. Sci. Res.* A **4**: 258.

Shain, C. A., and Higgins, C. S. (1954).—*Aust. J. Phys.* **7**: 130.

Shain, C. A. (1954).—*Aust. J. Phys.* **7**: 150.

Shain, C. A. (1957).—*Aust. J. Phys.* **10**: 195.

Shain, C. A. (1958).—*Proc. Inst. Radio Engrs., N.Y.* **46**: 85.

Shain, C. A. (1959).—"Paris Symposium on Radio Astronomy." (Ed. R. N. Bracewell.) p. 451. (Stanford Univ. Press.)

EXPLANATION OF PLATE 1

Contours of brightness temperatures at 19·7 Mc/s. The main grid is in Lund galactic coordinates. The galactic equator according to the new I.A.U. system (1958 revision) is indicated by a dotted line. The coarser grid gives equatorial coordinates (epoch 1958). Between $l^{\mathrm{I}}=290°$ and 318°, the contours may be less reliable than elsewhere: and the break near $l^{\mathrm{I}}=290°$ indicates what appears to be a discontinuity of instrumental origin in the contours. The transparent overlay gives the distribution of ionized hydrogen, according to Rodgers *et al.* (1960).

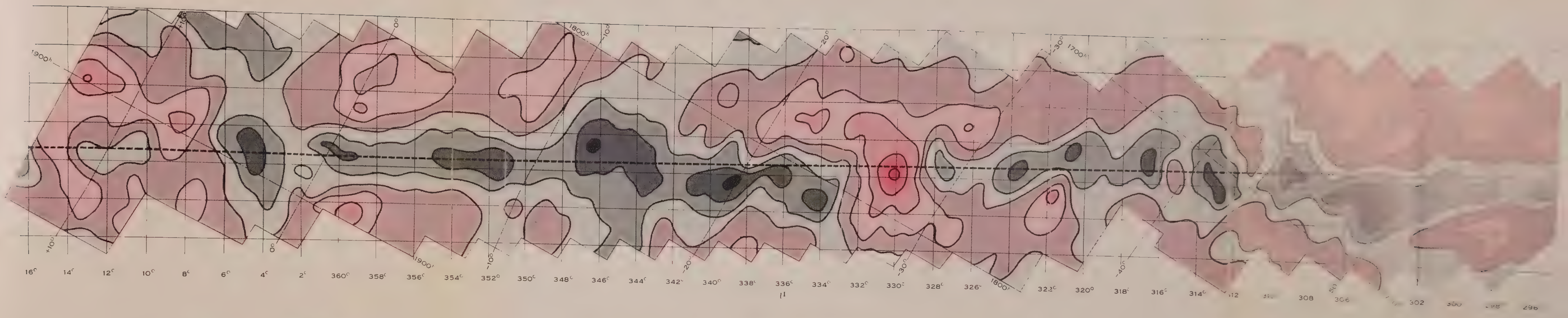
1900h
+10°
0°
1800h
-10°
-20°
-30°
1700h
-40°
50
16°
14°
12°
10°
8°
6°
4°
2°
360°
358°
356°
354°
352°
350°
348°
346°
344°
342°
340°
338°
336°
334°
332°
330°
328°
326°
322°
320°
318°
316°
314°
312
308
306
302
300
298
296
l^I

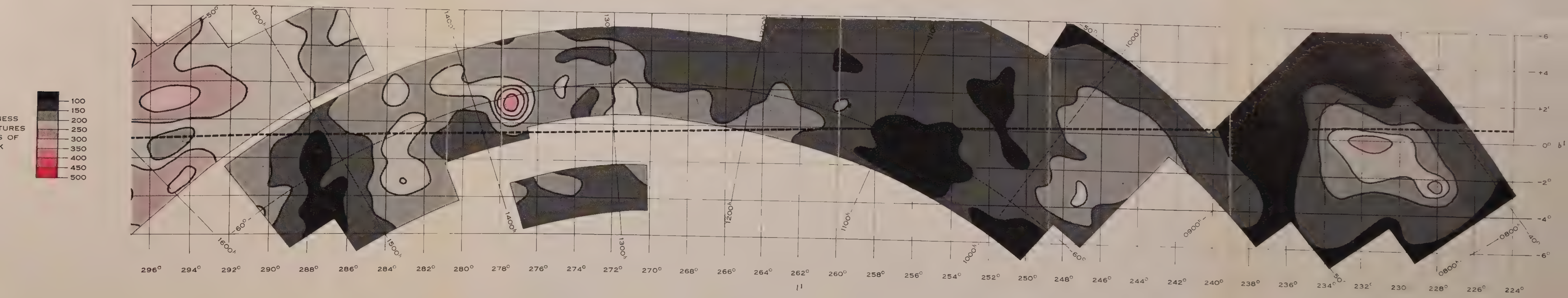
NESS
TURES
S OF
K
100
150
200
250
300
350
400
450
500
-50°
1500h
1400h
1300h
1200h
-60°
1600h
1100h
1000h
50°
0900h
0800h
-40°
+6
+4
+2°
0°
b^I
-2°
-4°
-6°
296°
294°
292°
290°
288°
286°
284°
282°
280°
278°
276°
274°
272°
270°
268°
266°
264°
262°
260°
258°
256°
254°
252°
250°
248°
246°
244°
242°
240°
238°
236°
234°
232°
230
228°
226°
224°
l^I

THE GALACTIC RADIO SPECTRUM DOWN TO 19·7 Mc/s

By M. M. Komesaroff*

[*Manuscript received August* 16, 1961]

Summary

Studies of the galactic radio spectrum have been carried out using results of a number of surveys between 19·7 and 1390 Mc/s. About 4–5° from the equator the spectrum is non-thermal and the temperature spectral index has a constant value of $2\cdot 6 \pm 0\cdot 1$.

The form of the spectrum changes with decreasing latitude, and at the lowest frequency an intensity minimum is observed along the equator. It is shown that the observations are fully consistent with a model consisting of two components:

(i) non-thermal sources of constant spectral index
(ii) ionized hydrogen of constant temperature.

The results yield some information about the distribution of thermal and non-thermal emissivity in the galactic plane, and provide qualitative support for results which Westerhout has drawn from more limited spectral data.

I. Introduction

Below about 100 Mc/s, the galactic radio emission is mainly of non-thermal origin and has a concentration towards the galactic equator. In low latitudes the observed intensity is modified by ionized hydrogen regions which both absorb the background radiation and contribute their own component of thermal emission. They appear in absorption at very low frequencies, and in a companion paper it is shown (Shain, Komesaroff, and Higgins 1961) that individual H II regions may be distinguished as radio " dark " areas at 19·7 Mc/s.

The present paper is chiefly concerned with studying the galactic emission near the equator in directions where optical observations give no indication of H II regions, but where, nevertheless, there is an intensity minimum in the 19·7 Mc/s contours, presumably due to many H II regions beyond the range of optical observation. This is a line of investigation which Shain had intended to pursue.

If complete radio spectra for each point in the sky were available, it would be possible, subject to certain assumptions, to determine for each line of sight the magnitudes of the thermal and non-thermal components of emission and also some information about their relative distribution in depth.

At very high frequencies the optical depth of the Galaxy is generally much less than unity and the total brightness is simply the sum of the thermal and non-thermal components; because these have different spectra they can be individually determined from a number of high frequency observations. It

---

* Division of Radiophysics, C.S.I.R.O., University Grounds, Chippendale, N.S.W.

is only at low frequencies, for which the Galaxy is optically thick, that brightness temperatures depend on the form of the distribution in depth, and, conversely, it is only from studies of the low frequency end of the spectrum that information about the form of this distribution may be derived.

Westerhout (1958) has separated the galactic emission into thermal and non-thermal components by comparing his own 1390 Mc/s observations with those of Mills at 85 Mc/s. In effecting this separation he made the following assumptions :

(i) Within the area covered by the two surveys the non-thermal radiation is everywhere characterized by a constant spectral index,

(ii) Spectral variations are entirely due to thermal absorption in ionized hydrogen at a temperature of 10 000 °K.

Westerhout's analysis was based on only two spectral points for each direction in space ; the data were therefore inadequate to check the validity of his assumptions. The 19·7 Mc/s observations (Shain, Komesaroff, and Higgins 1961), having also been taken with a high resolution instrument, provide a third spectral point, and allow Westerhout's assumptions and conclusions to be tested over a range of 70 : 1 in frequency.

The main aim of the present paper is to show that for a number of directions near the equator the values of brightness temperature measured at 19·7 Mc/s lie well within the limits predicted from the high frequency results according to assumptions (i) and (ii) above. In addition, the low frequency observations provide a check on a further assumption that Westerhout makes, namely, that along any line of sight the ratio of non-thermal to thermal emissivity is constant. From his analysis, based on this assumption, Westerhout was led to the conclusion that ionized hydrogen is concentrated in a ring 3–4 kiloparsecs in diameter, around the galactic centre. As there is no evidence to suggest a corresponding concentration of non-thermal emission, his assumption and conclusion seem mutually contradictory. However, even at 85 Mc/s the optical depth of the Galaxy rarely exceeds 0·3 ; this means, as will be shown subsequently, that his results are fairly insensitive to the form of the assumed distribution, and therefore the contradiction does not invalidate his conclusion. At 19·7 Mc/s, on the other hand, optical depths are many times greater, and brightness temperatures depend quite critically on the relative disposition of the two components. Thus by comparing the three surveys we can derive additional information about the distribution in depth.

Lack of resolution, however, introduces difficulties in making the comparison. The beamwidth of the 19·7 Mc/s aerial is 1·4°, and the half-width of the intensity minimum along the equator is only about 3°. Where the observed contours are regular, it can be shown that the errors in measured equatorial temperatures due to aerial smoothing are not likely to exceed about 20%. However, the contours are often complicated by a number of " nearby " H II regions 1° or more wide ; these appear in emission at the higher frequencies as do a number of discrete non-thermal sources. The analysis has, therefore, been carried out only for areas free of strong discrete sources. There are five such areas in the overlapping sections of the three surveys, and they are the ones which have been discussed previously by Westerhout. Mathewson, Healey, and Rome are at present engaged in a 1440 Mc/s survey of the Southern Milky Way. When their results become available it may be possible to extend this type of analysis over a greater area.

II. Theory of Radio Spectra

In this section we consider the way in which the observed brightness temperature in any direction is related to the distribution of emission and absorption along the line of sight. For the moment we leave out of account the physical mechanisms underlying these processes.

Let η and $\varkappa$ be functions of spatial coordinates, and represent the total emission per unit volume and total absorption coefficient respectively. Then, if the refractive index of the medium is unity, it follows from the Rayleigh-Jeans law that the brightness temperature at a frequency f Mc/s is given by

$$T_b=\frac{c^2}{2kf^2\times10^{12}}\int_0^\infty \eta \exp(-\tau')\mathrm{d}s, \tag{1}$$

where $\tau'=\int \varkappa \mathrm{d}s$, c is the velocity of light *in vacuo*, k is Boltzmann's constant, and the integrals with respect to distance s are carried out along the observer's line of sight.

(a) *Non-thermal Emission*

Away from the galactic equator, brightness temperature is found to depend on frequency according to a simple power law. This is illustrated by Figure 1 in which $\log T_b$ is plotted against $\log f$ for various points in latitudes $b^{\mathrm{I}}=+4°$ and $-6°$. The brightness temperatures are taken from a number of narrow-beam surveys at the following frequencies, 19·7 Mc/s (Shain, Komesaroff, and Higgins 1961), 85 Mc/s (Hill, Slee, and Mills 1958), 240 Mc/s (Kraus and Ko 1957), 400 Mc/s (Seeger, Stumpers, and van Hurck 1960), 910 Mc/s (Denisse, Leroux, and Steinberg 1955, 1957), and 1390 Mc/s (Westerhout 1958). These results indicate that a good approximation to the spectral law is given by

$$T_b \propto f^{-2\cdot6}. \tag{2}$$

Taking into account both the scatter in the measured values of spectral index, and also the possibility of a 20 per cent. systematic error in the measured temperatures across the frequency range, the probable error in the spectral index is about ±0·1.

Various estimates of the spectral index have been quoted in previous papers. In particular, Adgie and Smith (1956) and Costain (1960), working with scaled aerial systems, have derived the values $2\cdot5\pm0\cdot1$ and $2\cdot37\pm0\cdot04$ respectively. Both workers used broad-beam aerial systems, so that the values they quote are averages over fairly large areas of the sky. The discrepancy between the present value and Costain's could be due to a true variation with galactic latitude, with higher values of spectral index being observed near the equator than elsewhere.

Westerhout (1958) finds that the ratio of brightness temperatures at 85 and 1390 Mc/s supports a value of 2·6 but on other grounds concludes that it should be 2·7.

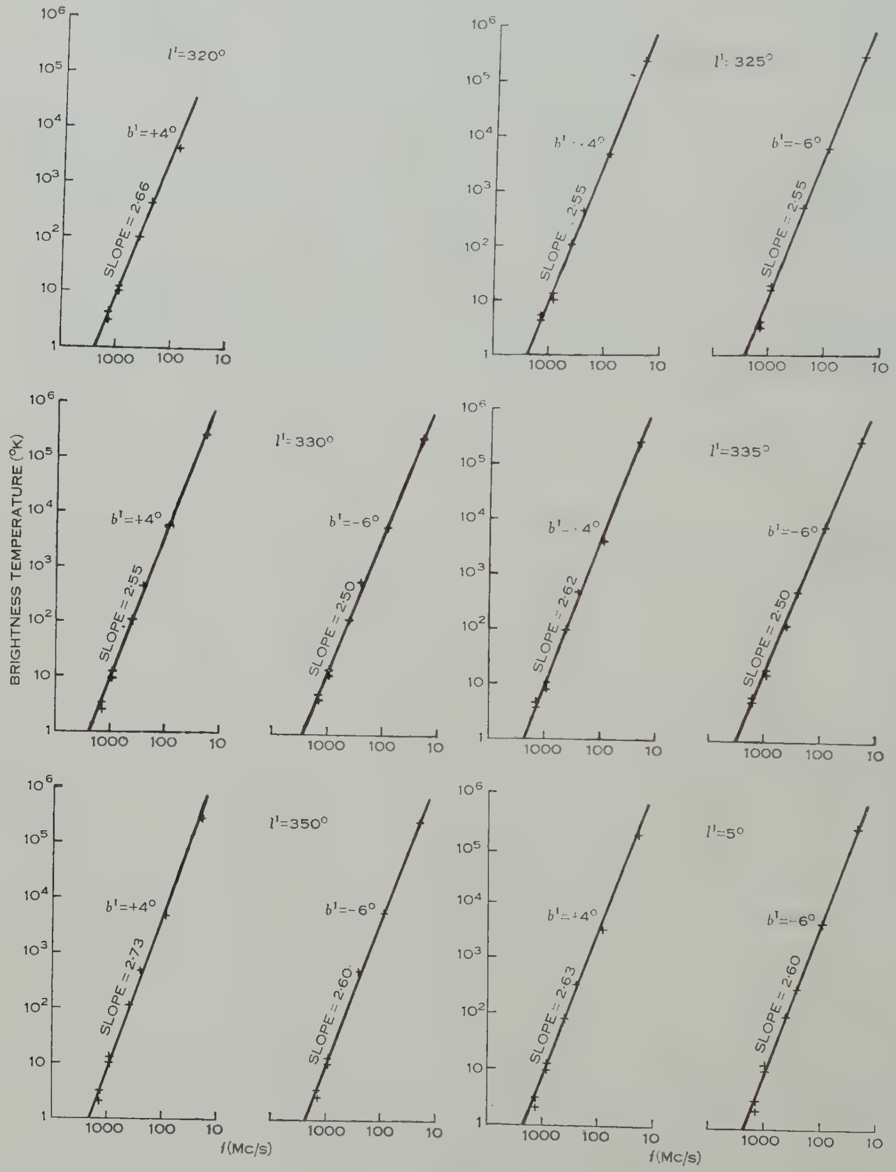

Fig. 1.—Spectra at a number of points away from the galactic equator. Brightness temperatures have been measured at the following frequencies: 19·7, 85, 250, 400, 910, and 1390 Mc/s. On each graph the Lund coordinates are given, together with an estimate of the spectral index.

The fact that the index is substantially greater than 2 indicates that the radiation is of non-thermal origin (see Piddington 1951). Equation 2 provides strong evidence that the non-thermal medium is optically thin. For, whatever the mechanism of emission, it is to be expected that η and τ' in equation (1) should depend on both frequency and direction. Therefore the most plausible assumption on which (1) and (2) can be reconciled is that

$$\tau' \ll 1.$$

(*b*) *Thermal Processes in Ionized Hydrogen*

Within a few degrees of the equator a simple relation like (2) no longer holds, since thermal emission and absorption in ionized hydrogen become important. Following Mills, Little, and Sheridan (1956), we assume that the electron temperature of this gas is 10 000 °K. Then, according to a recent calculation by Scheuer (1960) which takes into account the dissipative effect of both binary and multiple electron-ion collisions, the absorption coefficient per parsec is given by

$$\varkappa = (0\cdot532 - 0\cdot069 \log_{10} f) f^{-2} N^2, \tag{3}$$

where N cm^{-3} is the electron density. Then

$$\tau' = (0\cdot532 - 0\cdot069 \log_{10} f) f^{-2} E, \tag{4}$$

E being the "emission measure" in cm^{-6} parsec. These equations can be written in the form

$$\varkappa_f / \varkappa_{19\cdot7} = \tau'_f / \tau'_{19\cdot7} = p(f). \tag{5}$$

Numerical values of the frequency-dependent functions in (2), (3), (4), and (5) are given in Table 1.

TABLE 1

FREQUENCY-DEPENDENT TERMS USED IN THE ANALYSIS

f (Mc/s)	$\left(\frac{f}{19\cdot7}\right)^{2\cdot6}$	$\frac{\varkappa}{N^2} = \frac{\tau}{E}$	$\frac{\varkappa}{\varkappa_{19\cdot7}} = \frac{\tau}{\tau_{19\cdot7}}$ *
19·7	1	$1\cdot14 \times 10^{-3}$	1·0
85	45	$5\cdot52 \times 10^{-5}$	$4\cdot84 \times 10^{-2}$
1390	$6\cdot4 \times 10^{4}$	$1\cdot63 \times 10^{-7}$	$1\cdot43 \times 10^{-4}$

* According to the inverse-square law which is often quoted, the values are 1·0, $5\cdot4 \times 10^{-2}$, and $2\cdot0 \times 10^{-4}$.

Since the electron temperature associated with the ionized hydrogen is 10^4 °K, equation (1) may be written

$$T_b = \int_0^\infty (J + 10^4 \varkappa) \exp(-\tau') \mathrm{d}s. \tag{6}$$

The quantity J is related to the non-thermal brightness temperature T_n which would be observed in the absence of absorption, by the relation

$$T_n = \int_0^\infty J \, \mathrm{d}s.$$

In terms of the non-thermal volume emissivity η_n,

$$J = (c^2 \eta_n / 2kf^2 \times 10^{12}).$$

It has previously been shown that for directions a few degrees from the galactic equator, and over a wide range of longitudes, the non-thermal spectral index has a constant value of 2·6. In the subsequent argument it will be assumed that this value applies in all directions covered by the 19·7 Mc/s survey and that departures of the observed spectral law from equation (2) are due to thermal absorption. It is then convenient to introduce a " scaled up " brightness temperature $\mathscr{T}_{19\cdot7}(f)$, referred to 19·7 Mc/s, and defined by

$$\mathscr{T}_{19\cdot7}(f)=\left(\frac{f}{19\cdot7}\right)^{2\cdot6}T_b(f). \tag{7}$$

For directions in which there is no absorption, $\mathscr{T}_{19\cdot7}(f)$ is independent of frequency and equal to the measured 19·7 Mc/s brightness temperature. As we will now show, in the directions of absorbing regions, $\mathscr{T}_{19\cdot7}(f)$ increases with frequency, so that for $f>19\cdot7$,

$$T_b(19\cdot7)<\mathscr{T}_{19\cdot7}(f)\,;$$

the difference between the two quantities depends on the total optical depth of the absorbing medium, as well as its distribution in relation to the sources of non-thermal emission.

From equations (3), (4), (5), (6), (7), and the relation $\mathrm{d}s=\mathrm{d}\tau'/\varkappa$, it follows that

$$\mathscr{T}_{19\cdot7}(f)=\int_0^{\tau_{19\cdot7}}(J_{19\cdot7}/\varkappa_{19\cdot7})\exp\left[-p(f)\tau'_{19\cdot7}\right]\mathrm{d}\tau'_{19\cdot7}+(f/19\cdot7)^{2\cdot6}T_t, \tag{8}$$

where $T_t(f)$, the thermal component of brightness temperature, is given by

$$T_t(f)=10^4\{1-\exp\left[-p(f)\tau_{19\cdot7}\right]\}.$$

For very high frequencies, such that $p(f)\tau_{19\cdot7}\ll1$, we can write

$$\mathscr{T}_{19\cdot7}(f)=T_n(19\cdot7)+10^4(f/19\cdot7)^{2\cdot6}p(f)\tau_{19\cdot7}. \tag{9}$$

Since the function $p(f)$ is known, we can determine $T_n(19\cdot7)$ and $\tau_{19\cdot7}$ separately from two high frequency observations. From $\tau_{19\cdot7}$, $T_t(f)$ can then be calculated for all values of f.

(c) *Relative Distribution of the Two Components*

From what has been said, it follows that if the spectrum of the radiation is known, the integral term on the right-hand side of equation (8), which we will designate $L_{19\cdot7}(p)$, may be determined as a function of frequency. Now it may be shown that no loss of generality is incurred if an infinite upper limit replaces $\tau_{19\cdot7}$ in this integral (since $J_{19\cdot7}/\varkappa_{19\cdot7}$ is non-zero only when $\tau'_{19\cdot7}<\tau_{19\cdot7}$). Accordingly we may write

$$L_{19\cdot7}(p)=\int_0^{\infty}J_{19\cdot7}/\varkappa_{19\cdot7}\exp\left[-p(f)\tau'_{19\cdot7}\right]\mathrm{d}\tau'_{19\cdot7}.$$

This integral is a Laplace Transform. Knowing the way it varies with p, we can, by inverse transformation, determine $J_{19\cdot7}/\varkappa_{19\cdot7}$ as a function of optical depth $\tau'_{19\cdot7}$ for any line of sight. The available evidence suggests that $J_{19\cdot7}/\varkappa_{19\cdot7}$

varies quite markedly within each spiral arm, having its lowest values in absorbing regions and showing maxima where the ionized hydrogen density is low. Thus spectral studies provide, at least in principle, another approach to the elucidation of spiral structure. However, to derive detailed information about the variation of $J_{19\cdot7}/\varkappa_{19\cdot7}$ we need to know the values of $L_{19\cdot7}(p)$ down to such low frequencies (of the order of 10 Mc/s for directions near the equator) that $p(f)\tau_{19\cdot7}$ is many times greater than unity. At present there is not a sufficient number of galactic surveys of the requisite angular resolution in the relevant frequency range for this to be done in detail, but a comparison of the 19·7 Mc/s results (Shain, Komesaroff, and Higgins 1961) with observations at higher frequencies should enable us to determine, for example, whether the mean value of $J_{19\cdot7}/\varkappa_{19\cdot7}$ in the solar neighbourhood is of the same order as for the whole Galaxy.

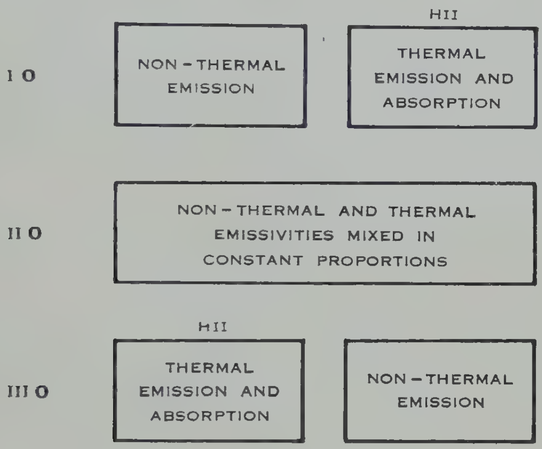
HII
I O
NON-THERMAL EMISSION
THERMAL EMISSION AND ABSORPTION
II O
NON-THERMAL AND THERMAL EMISSIVITIES MIXED IN CONSTANT PROPORTIONS
HII
III O
THERMAL EMISSION AND ABSORPTION
NON-THERMAL EMISSION

Fig. 2.—Three possible galactic models, described in the text. In each the distribution of non-thermal emission and ionized hydrogen is shown in relation to an observer at O.

In Section III, the 19·7 Mc/s results are compared with those at 85 and 1390 Mc/s. Before this comparison is made, let us consider some simplified models giving the possible large-scale depth distribution of the quantity $J_{19\cdot7}/\varkappa_{19\cdot7}$. The three models to be considered are illustrated in Figure 2.

(d) *Three Simplified Galactic Models*

Model I "Distant H II"—It is assumed that all the non-thermal emission takes place between the observer and the ionized hydrogen. Equation (8) becomes

$$\mathscr{T}_{19\cdot7}(f)=T_n(19\cdot7)+10^4(f/19\cdot7)^{2\cdot6}\{1-\exp[-p(f)\tau_{19\cdot7}]\}. \tag{10}$$

Model II "Perfect Mixing".—The ratio of non-thermal to thermal emissivity does not change along the line of sight. From equation (8)

$$\begin{aligned}\mathscr{T}_{19\cdot7}(f)&=\{[J_{19\cdot7}/p(f)\varkappa_{19\cdot7}]+10^4(f/19\cdot7)^{2\cdot6}\}\{1-\exp[-p(f)\tau_{19\cdot7}]\} \quad (11)\\&=\{[T_n(19\cdot7)/p(f)\tau_{19\cdot7}]+10^4(f/19\cdot7)^{2\cdot6}\}\{1-\exp[-p(f)\tau_{19\cdot7}]\}. \quad (12)\end{aligned}$$

For large values of $[p(f)\tau_{19\cdot7}]$, $\mathscr{T}_{19\cdot7}(f)$ approaches the limiting value of

$$T_n(19\cdot7)/p(f)\tau_{19\cdot7}+10^4(f/19\cdot7)^{2\cdot6}.$$

Equation (12) has been used by Westerhout (1958) in separating the thermal and non-thermal components of brightness observed at 85 and 1390 Mc/s.

Model III "*Nearby H* II".—Here we assume that all the H II lies between the observer and the non-thermal medium. Equation (8) must be written

$$\mathscr{T}_{19\cdot7}(f)=T_n(19\cdot7)\exp[-p(f)\tau_{19\cdot7}]+10^4(f/19\cdot7)^{2\cdot6}\{1-\exp[-p(f)\tau_{19\cdot7}]\} \quad (13)$$

It is easily seen that for fixed values of $T_n(19\cdot7)$ and $\tau_{19\cdot7}$, the value of $\mathscr{T}_{19\cdot7}(f)$ decreases towards the lower frequencies at a rate which is least for model I and greatest for model III. In the next section a number of galactic "crossings" are considered, and for each of these, observed values of $T_b(19\cdot7)$ are compared with values calculated from the 85 and 1390 Mc/s observations according to each of the above models in turn.

III. Comparison of Three Radio Surveys

(a) *Five Galactic Profiles*

To apply the type of analysis just outlined we need to select areas free of strong non-thermal sources or dense localized H II regions. Suitable areas close to the equator are rare, and those which have been chosen are five previously discussed by Westerhout (1958). These are 1–2° wide and centred on $l^{\mathrm{I}}=323\cdot5$, 332, 339, 354, and 5°. In Figure 3 the average value of $\mathscr{T}_{19\cdot7}(f)$ is shown as a function of b^{I} for each longitude for the frequencies 19·7, 85, and 1390 Mc/s. It can be seen that for each longitude the profiles converge at high latitudes, but that towards the equator there is a relative decrease in $\mathscr{T}_{19\cdot7}(f)$ at the lower frequencies. This is due to absorption.

In Figure 4 the observed values of $T_b(19\cdot7)$ are again shown, together with calculated values derived from the higher frequency results according to each of the models previously described. The data on which these curves are based are given in Table 2. It is apparent that near the equator the 19·7 Mc/s results lie well within the limits given by the extreme models, I and III, and show fairly good agreement with model II. This consistency over a 70 : 1 frequency range provides excellent confirmation of the assumption on which the analysis is based, namely, that the non-thermal spectral index along the galactic plane agrees with its value measured elsewhere, and that spectral differences can be accounted for in terms of free-free transitions in ionized hydrogen. It is not to be expected that the observations should agree exactly with model II, since this is obviously an over-simplification.

In all cases the observed temperature at the equator is greater than predicted on model II. The limited resolution of the 19·7 Mc/s aerial, whose beamwidth is 1·4° (compared with 0·57° at 1390 Mc/s and 0·8° at 85 Mc/s) would tend to increase the equatorial temperatures, but from the smoothness of the profiles it can be shown that the resultant error is not likely to exceed about 20%, whereas the actual discrepancies are considerably greater; furthermore, if the effects of " nearby " H II at $l^{\mathrm{I}}=323\cdot5$, 332, and 339°, could be allowed for, the discrepancies would be greater still.

The results are therefore consistent with a galactic distribution lying between models I and II. This implies that beyond several kiloparsecs ($\tau_{19\cdot7}>1$), the ratio of thermal to non-thermal emissivity is greater than it is in the solar neighbourhood, and this is particularly the case for longitudes 323·5, 332, and 354°. According to Westerhout, the latter direction is tangential to a ring of ionized hydrogen 3–4 kiloparsecs from the galactic centre, so that the present results, although incomplete, provide qualitative support for Westerhout's conclusion.

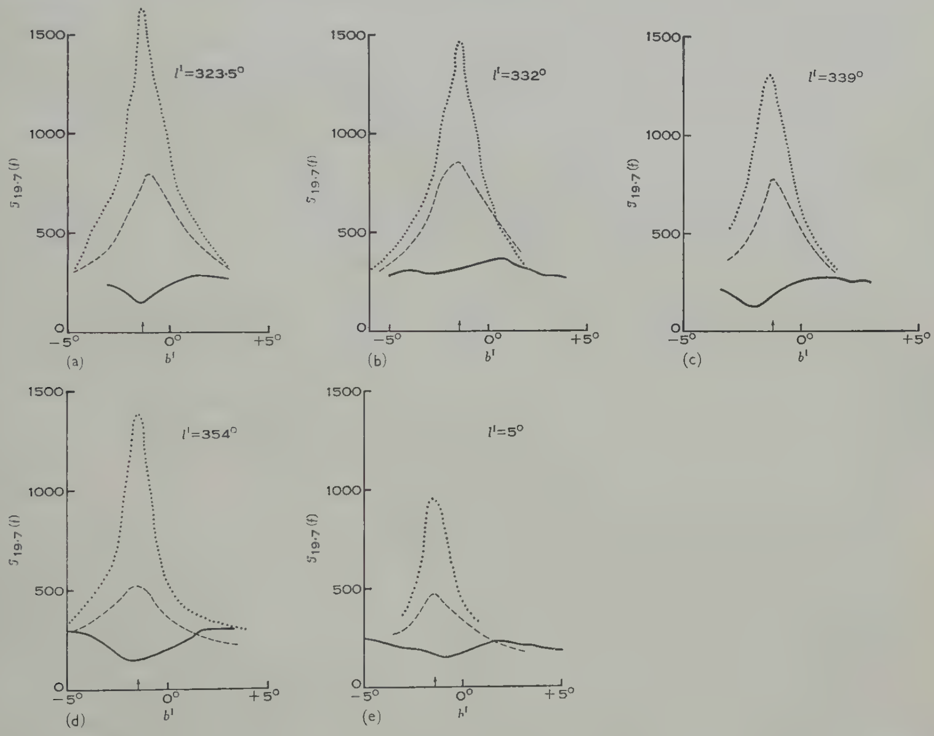

Fig. 3.—Variation of the " scaled-up " brightness temperature $\mathcal{T}_{19\cdot7}(f)$ (unit 10^3 °K), defined by $\mathcal{T}_{19\cdot7}(f)=(f/19\cdot7)^{2\cdot6}T_b$. For each of five longitudes the variation of $\mathcal{T}_{19\cdot7}(f)$ with latitude is shown for the frequencies 19·7, 85, and 1390 Mc/s : —— 19·7 Mc/s, - - - 85 Mc/s, · · · 1390 Mc/s. The equator according to the new I.A.U. system of galactic coordinates (1958 revision) is indicated by arrows.

(*b*) *Estimates of Emission Measures and Non-thermal Brightness Temperatures*

It has been shown that the observations are consistent with a galactic model in which in each direction the thermal and non-thermal emissivities have a roughly constant ratio. Table 2 indicates that, even if this were not the case, a separation of the 1390 and 85 Mc/s results into the two components according to this assumption, would not be seriously in error, since the limiting values of $T_n(19\cdot7)$ and $\tau_{19\cdot7}$ derived from models I and III, do not differ drastically from the model II values.

TABLE 2

PARAMETERS DERIVED ACCORDING TO THE THREE MODELS

(Temperature unit 10^3 °K)

l^{I}	b^{I}	$\mathscr{T}_{19\cdot7}(85)$*	$\mathscr{T}_{19\cdot7}(1390)$*	Model I			Model II			Model III		
				$\tau_{19\cdot7}$	$T_n(19\cdot7)$	$T_b(19\cdot7)$	$\tau_{19\cdot7}$	$T_n(19\cdot7)$	$T_b(19\cdot7)$	$\tau_{19\cdot7}$	$T_n(19\cdot7)$	$T_b(19\cdot7)$
323·5°	+3·2	330	300	—	—	—	—	—	—	—	—	—
	+1·6	440	510	1·1	410	420	0·9	430	280	0·9	430	190
	+0·5	570	720	2·0	530	540	1·7	550	270	1·5	580	140
	—0·4	750	1140	5·4	650	660	4·5	730	170	3·7	800	30
	—1·1	800	1550	10·0	640	650	8·3	790	110	6·7	940	10
	—1·25	780	1630	11·4	590	600	9·5	760	90	7·7	930	10
	—1·5	710	1550	11·3	520	530	9·5	680	80	7·9	830	10
	—2·0	610	1140	7·2	480	490	6·2	570	100	5·3	660	10
	—2·25	570	930	5·1	460	470	4·5	520	120	3·7	590	30
	—2·8	450	720	3·7	380	390	3·3	410	130	2·9	450	40
	—3·8	360	510	2·1	320	330	2·0	330	150	1·7	360	80
	—4·8	310	300	—	—	—	—	—	—	—	—	—
332°	+2·1	360	300	—	—	—	—	—	—	—	—	—
	+0·8	510	510	0	510	510	0	510	510	0	510	510
	+0·0	640	720	1·1	620	620	0·9	630	410	0·7	650	340
	—0·85	760	1140	5·2	670	680	4·5	730	170	3·5	820	40
	—1·2	830	1340	7·0	700	170	5·7	820	160	4·5	928	20
	—1·45	860	1470	8·3	710	720	7·0	830	130	5·4	980	10
	—1·65	860	1340	6·7	730	740	5·4	850	160	4·2	960	20
	—2·2	810	1140	4·6	720	730	3·8	790	220	3·0	870	50
	—3·0	580	720	1·9	540	550	1·6	570	280	1·4	590	160
	—4·0	430	510	1·2	400	410	1·0	420	270	1·0	420	170
	—6·0	290	300	0·2	280	280	0·2	280	260	0·2	280	240

* $\mathscr{T}_{19\cdot7}(85)$ defined as $(85/19\cdot7)^{2\cdot6}T_b(85)$ etc.

TABLE 2 (*Continued*)

l^{I}	b^{I}	$\mathscr{T}_{19\cdot 7}(85)$*	$\mathscr{T}_{19\cdot 7}(1390)$*	Model I			Model II			Model III		
				$\tau_{19\cdot 7}$	$T_n(19\cdot 7)$	$T_b(19\cdot 7)$	$\tau_{19\cdot 7}$	$T_n(19\cdot 7)$	$T_b(19\cdot 7)$	$\tau_{19\cdot 7}$	$T_n(19\cdot 7)$	$T_b(19\cdot 7)$
339°	+2·0	260	300	0·5	260	260	0·4	260	220	0·4	260	190
	+0·5	450	510	0·8	440	450	0·7	450	320	0·7	450	250
	—0·2	570	720	2·1	520	530	1·7	560	270	1·5	580	140
	—1·1	750	1140	5·4	650	660	4·5	730	170	3·7	800	30
	—1·6	740	1300	7·7	600	610	6·5	710	120	5·2	820	20
	—2·0	610	1140	7·2	480	490	6·1	580	110	5·3	660	10
	—2·85	450	720	3·7	370	380	3·2	420	140	2·9	450	40
	—3·6	370	510	2·0	330	340	1·7	360	180	1·6	370	80
354°	+3·7	200	300	1·4	170	180	1·3	180	110	1·2	190	70
	+0·1	350	510	2·2	310	320	2·0	330	150	1·7	360	80
	—0·5	430	720	4·1	340	350	3·6	390	110	3·3	420	30
	—1·0	500	1140	8·6	350	360	7·7	440	70	6·8	520	10
	—1·5	530	1390	11·5	340	350	10·3	450	50	8·0	660	10
	—2·0	490	1140	8·7	340	350	7·9	420	60	6·9	510	10
	—2·6	430	720	4·0	350	360	3·5	400	120	3·2	420	30
	—3·4	360	510	2·1	320	330	1·8	350	160	1·7	360	80
	—5·2	280	300	0·2	280	290	0·2	280	260	0·2	280	240
5°	+0·2	310	390	1·1	290	300	1·0	300	200	0·9	300	130
	—0·6	400	600	2·9	330	340	2·6	360	140	2·4	380	50
	—1·0	440	810	5·2	330	340	4·5	400	100	4·1	420	20
	—1·55	470	950	6·6	350	360	5·9	410	80	5·2	480	10
	—1·95	430	810	5·3	320	330	4·7	380	90	4·3	410	20
	—2·2	390	600	3·0	325	340	2·7	350	130	2·5	370	40
	—2·9	300	390	1·3	270	280	1·2	280	170	1·0	300	120

---

* $\mathscr{T}_{19\cdot 7}(85)$ defined as $(85/19\cdot 7)^{2\cdot 6}T_b(85)$ etc.

Westerhout (1958) has made a similar separation of the 1390 and 85 Mc/s results, based on the " perfect mixing " model, but using the following expression for optical depth,

$$\tau = (0 \cdot 36/f^2)E,$$

rather than equation (4). Values of $T_n(19 \cdot 7)$ and E on the equator, from the present analysis and from Westerhout's are given in Table 3.

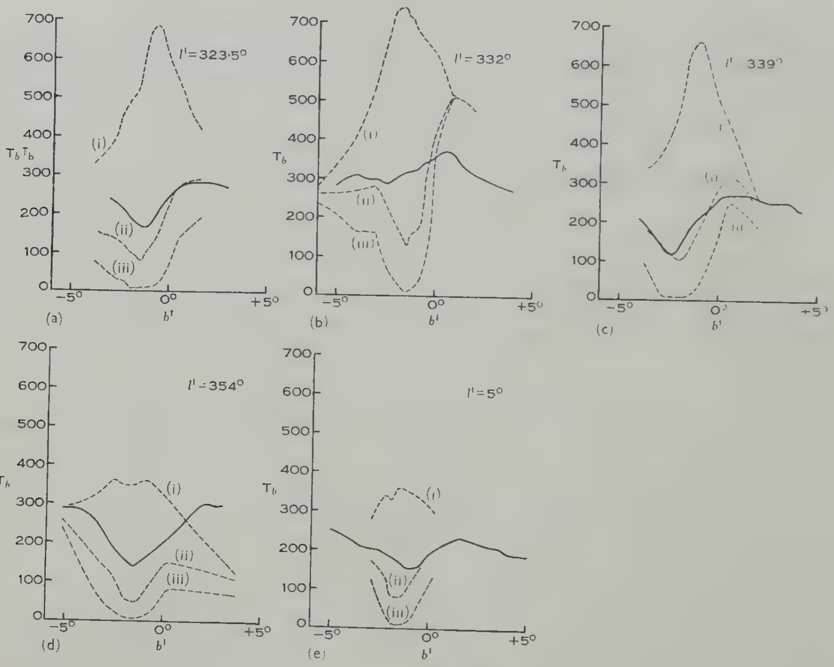

Fig. 4.—Observed (full line) and computed (dotted line) values of brightness temperature at $19 \cdot 7$ Mc/s (unit 10^3 °K). Curve (i) refers to model I, (ii) to model II, and (iii) to model III.

(c) *The Minima near* $l^{\mathrm{I}}=287°$ *and* $l^{\mathrm{I}}=5°$

In the companion paper (Shain, Komesaroff, and Higgins 1961) attention was drawn to the extensive " dark " areas crossing the galactic equator near longitudes 287° and 5° at $19 \cdot 7$ Mc/s. The optical observations indicate no large-scale H II in either direction ; furthermore it can be seen from Figure 3 (*e*) that for $l^{\mathrm{I}}=5°$ the values of $\mathscr{T}_{19 \cdot 7}(f)$ away from the equator agree at the three frequencies, supporting the idea that absorption is negligible. Westerhout's survey does not extend as far south as the minimum near $l^{\mathrm{I}}=287°$, but a comparison of the 85 and $19 \cdot 7$ Mc/s results indicates that a similar conclusion applies here also. Values of $\mathscr{T}_{19 \cdot 7}(f)$ have been determined at $19 \cdot 7$ and 85 Mc/s for a number of longitudes at $b^{\mathrm{I}}=+3°$. In general, values at the two frequencies do not agree exactly, as we should expect them to do in the absence of absorption (part of the discrepancy is probably due to measuring error), but at $l^{\mathrm{I}}=5°$ and 287° the agreement is rather better than at most other longitudes, which supports our previous conclusion.

TABLE 3

COMPARISON OF THE PRESENT RESULTS WITH THOSE OF WESTERHOUT

l^{I}	b^{I}	Present Analysis		Westerhout's Analysis	
		E (cm^{-6} parsec)	$T_n(19\cdot7)$ $\times10^{-3}$	E (cm^{-6} parsec)	$T_n(19\cdot7)$ $\times10^{-3}$
323·5	—1·5	$8\cdot3\times10^3$	680	$7\cdot4\times10^3$	670
332	—1·45	$6\cdot1\times10^3$	830	$5\cdot3\times10^3$	860
339	—1·6	$5\cdot7\times10^3$	710	$4\cdot9\times10^3$	720
354	—1·5	$9\cdot0\times10^3$	450	$7\cdot8\times10^3$	460
5	—1·55	$5\cdot2\times10^3$	410	$4\cdot5\times10^3$	420

The near symmetry of the two longitudes about the galactic centre suggests that a large-scale feature of galactic structure is involved. According to the galactic model derived by Mills (1959), at these longitudes the line of sight passes between the two spiral arms nearest to the local one, towards the galactic centre. At moderate latitudes, therefore, a minimum might be expected. However, as was shown in a recent paper by Hanbury-Brown and Hazard (1960), the exact form of the distribution in longitude depends on a number of parameters which at present must be conjectional, so a more detailed interpretation will not be attempted.

IV. CONCLUSIONS

(i) About 4–5° from the equator, over a wide range of longitudes, the galactic radio spectrum is non-thermal and over a range of 70 : 1 in frequency follows the simple power law

$$T_b \propto f^{-2\cdot6}.$$

(ii) Nearer the equator, low frequency values of brightness temperature are consistently lower than this law predicts and, in fact, $T_b(19\cdot7)$ exhibits a minimum along the equator in contrast with the maximum observed at higher frequencies. This can be explained entirely in terms of thermal processes in ionized hydrogen, without invoking changes in the non-thermal spectrum.

(iii) Spectral studies provide some information about the distribution in depth of the thermal and non-thermal components. Although the present results do not give an unambiguous answer to this question, they are consistent with a model in which the ratio of non-thermal to thermal emissivity is roughly constant along any line of sight, but higher near the Sun than towards the centre of the Galaxy. On the assumption that the non-thermal emissivity is more uniformly distributed than the thermal, this is in qualitative agreement with Westerhout's conclusion that ionized hydrogen is concentrated in a ring around the galactic centre.

V. ACKNOWLEDGMENTS

The author wishes to thank Dr. J. L. Pawsey for much helpful criticism and advice while this paper was in preparation. He also thanks Mr. S. F. Smerd, who pointed out that the radio spectrum could be represented as a Laplace Transform.

VI. References

Adgie, R., and Smith, F. G. (1956).—*Observatory* **76** : 181.

Costain, C. H. (1960).—*Mon. Not. R. Astr. Soc.* **120** : 248.

Denisse, J. F., Leroux, E., and Steinberg, J. L. (1955).—*C.R. Acad. Sci., Paris* **240** : 278.

Denisse, J. F., Leroux, E., and Steinberg, J. L. (1957).—*C.R. Acad. Sci., Paris* **244** : 3030.

Hanbury-Brown, R., and Hazard, C. (1960).—*Observatory* **80** : 137.

Hill, E. R., Slee, O. B., and Mills, B. Y. (1958).—*Aust. J. Phys.* **11** : 530.

Kraus, J. D., and Ko, H. C. (1957).—Celestial radio radiation. R.F. Project 673. Sci. Rep. No. 1 Ohio.

Mills, B. Y. (1959).—" Paris Symposium on Radio Astronomy." (Ed. R. N. Bracewell.) p. 431. (Stanford Univ. Press.)

Mills, B. Y., Little, A. G., and Sheridan, K. V. (1956).—*Aust. J. Phys.* **9** : 218.

Piddington, J. H. (1951).—*Mon. Not. R. Astr. Soc.* **111** : 45.

Scheuer, P. A. G. (1960).—*Mon. Not. R. Astr. Soc.* **120** : 231.

Seeger, C. L., Stumpers, F. L. H. M., and van Hurck, N. (1960).—*Philips Tech. Rev.* **21** : 317.

Shain, C. A., Komesaroff, M. M., and Higgins, C. S. (1961).—*Aust. J. Phys.* **14** : 508.

Westerhout, G. (1958).—*Bull. Astr. Inst. Netherlds.* **14** : 215.

FREE CONVECTION IN A VERTICAL TUBE WITH A LINEAR WALL TEMPERATURE GRADIENT

By I. G. Donaldson*

[*Manuscript received July* 18, 1961]

Summary

The paper discusses convection in a vertical tube closed at both ends in which the temperature of the walls is arranged to increase linearly with depth. For the purposes of the theory, the convective flow is assumed to be radially symmetrical about the axis of the tube.

The temperature and velocity distributions in the pipe are found to be dependent on a non-dimensional modified Rayleigh number H. Experiments conducted at values of H between 90 and 30 000 agree with theoretical predictions for values of H below 300 and above 3000. Negative temperature gradients occurring along the axis for values of H between 700 and 950 indicate that in this range the flow cannot be radially symmetric. This non-symmetric flow would develop first, as H is increased from zero, and it is suggested that the agreement between the experimental and theoretical results for $H<300$ shows that the critical value of H for the non-symmetrical flow does not differ greatly from the value (142) obtained theoretically for the symmetric regime. Presumably it is at values of H of 3000 and above that the flow takes an axially symmetric form. This higher range is appropriate to bores in the New Zealand thermal regions.

I. Introduction

Ever since the first bores were drilled at Wairakei, N.Z., for steam for power production, temperature measurements have been made using a geothermograph at 100 ft intervals down closed bores. These temperatures are one of the few physical measurements that can be made at depth in the field, but up to the present time there has been considerable doubt as to whether the temperatures measured indicate closely the temperatures of the surrounding ground at the same depth. It is probable that these temperatures will be related in some manner to the steady-state temperatures of the surrounding ground, but many man-introduced factors (e.g. bore history) may have a controlling influence.

Since a bore is at a higher temperature at the bottom, it is probable that free convection will occur within it. This convective flow will have the effect of transferring heat from one region of the surrounding ground to another at a different level, thus temperatures measured in the bore are likely to be different from those that would exist in the ground originally, i.e. the temperature isotherms will be displaced in the vicinity of a bore. It will also cause some variation of temperature with radial distance.

---

*Dominion Physical Laboratory, Department of Scientific and Industrial Research, Lower Hutt, New Zealand.

II. Previous Work

Ostrach (1957) reviews most of the available literature about convection phenomena in fluids heated from below. In the bibliography at the end of this paper it is seen that there is very little previous work on convection in vertical pipes. Ostrach (1952) discusses free convection in vertical channels (between parallel plates), which enables him to introduce some simplification not available when studying tubes. The few papers in existence concerning free convection in vertical pipes have arisen because of the problem of cooling turbine blades by free convection of the fluid in channels in the blades. Of these papers, only two have dealt with the theoretical side, Lighthill (1953) and Eckert and Jackson (1950). Both these papers deal with a vertical pipe at constant wall temperature fed at the top by a reservoir of cool fluid. The work of Lighthill has been verified experimentally by Martin and Cohen (1954).

III. Assumptions

In order to build up a mathematical theory it has been necessary to make many assumptions that to some degree divorce the problem from that of a bore drilled in a thermal area. This is regrettable, but it is possible to obtain an indication of the parameters involved and the effect of the temperature and to design further experiments from which it may be possible to estimate empirically the effect in bores.

The following assumptions were made:

(1) A pipe of length h and radius a, closed at both ends, is so maintained that the temperature gradient at the wall is linear, the higher temperature being at the lower end.

(2) There is a point on the axis at which the flow velocity is zero—this point is taken as the origin of coordinates.

(3) The length of the pipe is much greater than the radius.

(4) The kinematic viscosity, the thermal diffusivity, and the coefficient of volumetric expansion are all independent of temperature.

(5) The law of variation of density with temperature is

$$\rho^{-1}=\rho_0^{-1}\{1+\beta(T-T_0)\}, \tag{1}$$

where ρ is the density at a temperature T,
ρ_0 is the density at a temperature T_0,
β is the coefficient of volumetric expansion of water at T_0,
T_0 is the temperature at the origin.

(6) The boundary layer approximations apply, i.e. the gradient of a quantity along the tube is neglected in comparison with its gradient along a radius. This may be justified by the large length/radius ratio.

(7) The flow is symmetrical about the axis. At the time when the theoretical approach was done this was felt to be a logical assumption. Some of the experimental results, however, could only be accounted for by a non-symmetric flow pattern. A. McNabb (personal communication) has since shown from stability

theory that this non-symmetric flow regime would occur, as the controlling parameter H is increased from zero, before the axially symmetric flow regime.

The non-symmetric flow regime is not discussed theoretically in this paper as it is outside the limits expected to be met in bores.

IV. Theoretical Discussion

Inside the pipe in the vicinity of the origin, the equations of conservation of mass, momentum, and heat which apply to the liquid for steady axi-symmetrical flow, and with the boundary layer approximation, are (Lighthill 1953):

$$\frac{\partial U}{\partial X}+\frac{\partial V}{\partial R}+\frac{V}{R}=0, \tag{2}$$

$$U\frac{\partial U}{\partial X}+V\frac{\partial U}{\partial R}=-g-\frac{1}{\rho}\,\frac{\partial p}{\partial X}+\nu\left(\frac{\partial^2 U}{\partial R^2}+\frac{1}{R}\,\frac{\partial U}{\partial R}\right), \tag{3}$$

$$\frac{\partial p}{\partial R}=0, \tag{4}$$

$$U\frac{\partial T}{\partial X}+V\frac{\partial T}{\partial R}=\alpha\left(\frac{\partial^2 T}{\partial R^2}+\frac{1}{R}\,\frac{\partial T}{\partial R}\right), \tag{5}$$

where X is the vertical distance measured upwards from the origin,
R is the radial distance,
U is the axial velocity upwards of the liquid,
V is the radial velocity of the liquid,
g is the acceleration due to gravity,
ρ is the density of the liquid,
p is the pressure,
ν is the kinematic viscosity (viscosity/density) of the liquid,
α is the thermal diffusivity of the liquid.

The boundary conditions are:

$$\left.\begin{array}{lll} U=0, & V=0, & \text{at } R=a, \\ & U=0, & \text{at } X=0, \\ & T=T_s(X), & \text{at } R=a, \\ & T=T_0, & \text{at } X=0. \end{array}\right\} \tag{6}$$

From the boundary conditions, since at $R=a$, $U=0$, $V=0$, equation (3) reduces to

$$0=-g-\frac{1}{\rho_s}\,\frac{\partial p}{\partial X}+\nu\left(\frac{\partial^2 U}{\partial R^2}+\frac{1}{R}\,\frac{\partial U}{\partial R}\right)_{R=a}; \tag{7}$$

hence allowing for the variation of density (1), and substituting for $\partial p/\partial X$,

$$U\frac{\partial U}{\partial X}+V\frac{\partial U}{\partial R}=g\beta(T-T_s(X))+\nu\left(\frac{\partial^2 U}{\partial R^2}+\frac{1}{R}\,\frac{\partial U}{\partial R}\right)_a^R. \tag{8}$$

It is possible to reduce the equations and boundary conditions simultaneously to a non-dimensional form by the following substitutions :

$$\left.\begin{aligned} U&=(\alpha h/a^2)u,\\ V&=(\alpha/a)v,\\ R&=ar,\\ X&=hx,\\ T-T_0&=-(\nu\alpha h/\beta g a^4)\theta,\\ T_s(X)-T_0&=-(\nu\alpha h/\beta g a^4)\theta_s(x), \end{aligned}\right\} \tag{9}$$

The equations become

$$\frac{\partial u}{\partial x}+\frac{\partial v}{\partial r}+\frac{v}{r}=0, \tag{10}$$

$$\frac{1}{\sigma}\left(u\frac{\partial u}{\partial x}+v\frac{\partial u}{\partial r}\right)=-(\theta-\theta_s)+\left(\frac{\partial^2 u}{\partial r^2}+\frac{1}{r}\,\frac{\partial u}{\partial r}\right)_1^r, \tag{11}$$

$$u\frac{\partial\theta}{\partial x}+v\frac{\partial\theta}{\partial r}=\left(\frac{\partial^2\theta}{\partial r^2}+\frac{1}{r}\,\frac{\partial\theta}{\partial r}\right), \tag{12}$$

and the boundary conditions are

$$\left.\begin{aligned} u=0,\quad v&=0, && \text{at } r=1,\\ u&=0, && \text{at } x=0,\\ \theta&=\theta_s(x), && \text{at } r=1,\\ \theta&=0, && \text{at } x=0. \end{aligned}\right\} \tag{13}$$

The equations (10), (11), (12) may be integrated over a cross section to give

$$\int_0^1 ru\,dr=0, \tag{14}$$

$$\frac{\partial}{\partial x}\int_0^1 ru\theta\,dr=\left(\frac{\partial\theta}{\partial r}\right)_{r=1}, \tag{15}$$

$$\int_0^1 r\theta\,dr=\tfrac{1}{2}\left(\frac{\partial u}{\partial r}-\frac{\partial^2 u}{\partial r^2}\right)_{r=1}. \tag{16}$$

Since experimental measurements were made only at the wall of the pipe and along the central axis, equations (10), (11), and (12) may be simplified to read

$$\left(\frac{\partial^2\theta}{\partial r^2}+\frac{1}{r}\,\frac{\partial\theta}{\partial r}\right)_{r=1}=0, \tag{17}$$

$$\left(u\frac{\partial\theta}{\partial x}\right)_{r=0}=\left(\frac{\partial^2\theta}{\partial r^2}+\frac{1}{r}\,\frac{\partial\theta}{\partial r}\right)_{r=0}, \tag{18}$$

$$(\theta-\theta_s)_{r=0}=\left(\frac{\partial^2 u}{\partial r^2}+\frac{1}{r}\,\frac{\partial u}{\partial r}\right)_1^0, \tag{19}$$

and these equations, (17), (18), and (19), together with (14), (15), and (16), are the equations for which a solution is required.

As throughout the pipe $\theta_s(x)=Hx$, where H is the modified Rayleigh number, $\beta g a^4(T_2-T_1)/\nu\alpha h$, T_1 and T_2 being the temperature at top and bottom of the pipe respectively, the solution for θ and u in the vicinity of the origin must be linear with respect to x. Hence θ and u may be replaced by

$$\theta=x(\alpha_0+\alpha_1 r^2+\alpha_2 r^4+\alpha_3 r^6)+Hx, \tag{20}$$
$$u=x(\beta_0+\beta_1 r^2+\beta_2 r^4+\beta_3 r^6). \tag{21}$$

Then from the boundary conditions (13) and the equations (14), (16), (17), and (19),

$$\alpha_0+\alpha_1+\alpha_2+\alpha_3=0, \tag{22}$$
$$\beta_0+\beta_1+\beta_2+\beta_3=0, \tag{23}$$
$$12\beta_0+8\beta_1+4\beta_2+3\beta_3=0, \tag{24}$$
$$12\alpha_0+8\alpha_1+4\alpha_2+3\alpha_3+12H=-12(8\beta_2+24\beta_3), \tag{25}$$
$$\alpha_1+4\alpha_2+9\alpha_3=0, \tag{26}$$
$$\alpha_0=-(16\beta_2+36\beta_3). \tag{27}$$

Solving for all the unknowns in terms of α_0, α_1, and H,

$$\theta=x\left(\alpha_0+\alpha_1 r^2-\frac{9\alpha_0+8\alpha_1}{5}r^4+\frac{4\alpha_0+3\alpha_1}{5}r^6\right)+Hx, \tag{28}$$

$$\begin{aligned} u=\frac{x}{1440}\{&(-66\alpha_0+68\alpha_1+240H)+(126\alpha_0-153\alpha_1-540H)r^2\\ &+(-36\alpha_0+153\alpha_1+540H)r^4+(-24\alpha_0-68\alpha_1-240H)r^6\}, \end{aligned} \tag{29}$$

and substituting in (18)

$$\{5760-68(\alpha_0+H)\}\alpha_1=(-66\alpha_0+240H)(\alpha_0+H) \tag{30}$$

and in (15)

$$\begin{aligned} &\alpha_0(1\cdot 239\alpha_0-2\cdot 439\alpha_1-8\cdot 614H)\\ &+\alpha_1(-1\cdot 258\alpha_0+1\cdot 535\alpha_1+5\cdot 414H)=-1152(3\alpha_0+\alpha_1). \end{aligned} \tag{31}$$

From (30) it is possible to obtain a unique value of α_1, in terms of α_0 and H which may be substituted in (31) to give

$$\begin{aligned} &\{68(\alpha_0+H)-5760\}^2(1\cdot 239\alpha_0^2-8\cdot 614\alpha_0 H+3456\alpha_0)\\ &+\{68(\alpha_0+H)-5760\}(66\alpha_0-240H)(\alpha_0+H)(-3\cdot 697\alpha_0+5\cdot 414H+1152)\\ &+(66\alpha_0-240H)^2(\alpha_0+H)^2\times 1\cdot 535=0. \end{aligned} \tag{32}$$

Multiplying this out and substituting

$$\mu=\alpha_0/H, \tag{33}$$

then

$$\begin{aligned} &4\cdot 177\mu^4+(12\cdot 180-21\cdot 585\times 10^3H^{-1})\mu^3+(11\cdot 771-10\cdot 017\times 10^3H^{-1}\\ &+3\cdot 104\times 10^6H^{-2})\mu^2+(3\cdot 708+22\cdot 883\times 10^3H^{-1}+1\cdot 838\times 10^6H^{-2}\\ &-0\cdot 115\times 10^9H^{-3})\mu+(-0\cdot 060+11\cdot 317\times 10^3H^{-1}-1\cdot 593\times 10^6H^{-2})=0 \end{aligned} \tag{34}$$

is obtained.

From this it is possible to obtain solutions for μ for various values of H. For the axially symmetric flow regime considered, convection would have the effect of reducing the temperature gradient and hence α_0 would lie in the range $0\geqslant\alpha_0\geqslant -H$. Thus only solutions for μ in the range $0\geqslant\mu\geqslant -1$ are considered.

V. Results

Table 1 lists the value of μ, α_0, and the non-dimensional axial temperature gradient for various values of the non-dimensional wall temperature gradient H.

Table 1

THEORETICAL RELATIONSHIP BETWEEN WALL AND AXIAL TEMPERATURE GRADIENTS

All units are non-dimensional

Wall Temperature Gradient H	μ	α_0	Axial Temperature Gradient
0	0	0	0
142	0	0	142
250	—0·177	—44	206
500	—0·332	—161	339
750	—0·366	—275	475
1 000	—0·391	—391	609
1 250	—0·405	—506	744
2 000	—0·420	—840	1 160
2 500	—0·422	—1 055	1 445
5 000	—0·395	—1 975	3 025
7 500	—0·345	—2 588	4 912
10 000	—0·293	—2 930	7 070
25 000	—0·112	—2 800	22 200
50 000	—0·046	—2 280	47 700
75 000	—0·024	—1 830	73 200
100 000	—0·014	—1 350	98 700

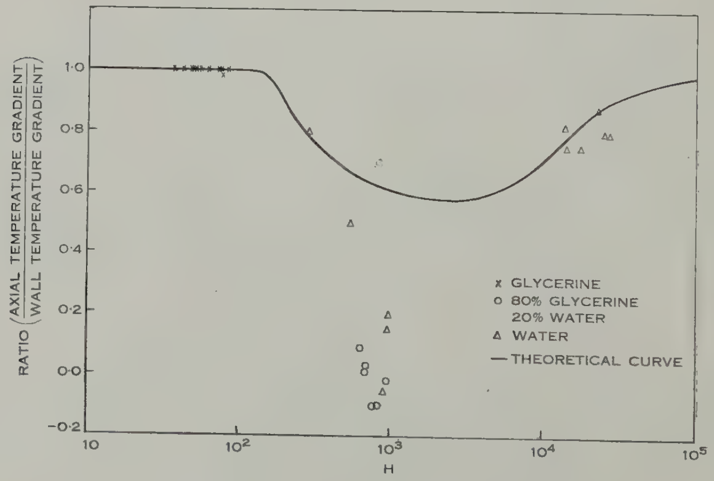

Fig. 1.—Comparison of theoretical and experimental results.

The ratio of the non-dimensional axial temperature gradient to the non-dimensional wall temperature gradient is plotted against H in Figure 1—experimental results are displayed on the same graph.

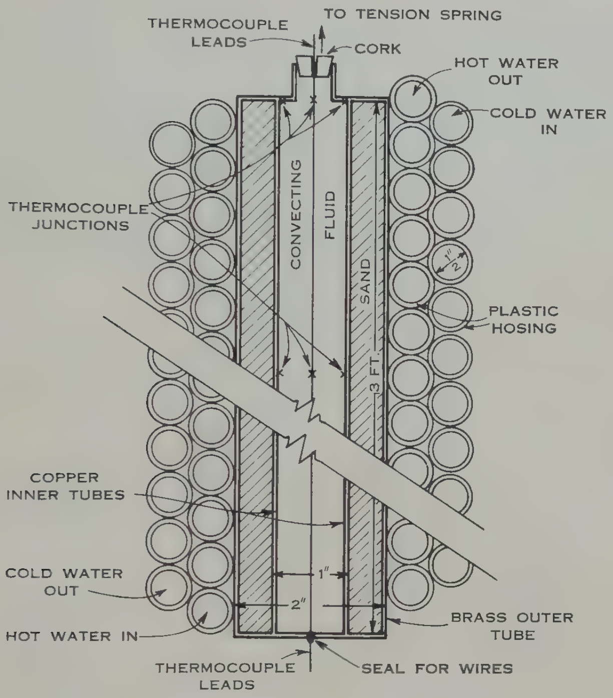

Fig. 2 (*a*).—The experimental apparatus, lengthwise central section.

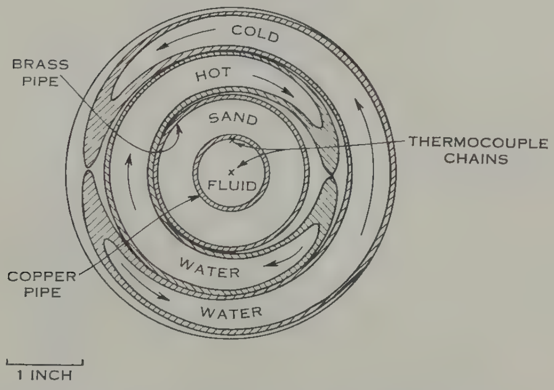

Fig. 2 (*b*).—The experimental apparatus, section perpendicular to axis.

VI. Experimental Procedure

The convection pipe used in the experiment consisted of a copper tube 36 in. long and of internal diameter 1 in., closed at both ends by a copper plate. Temperatures were measured by thermojunctions arrayed along the axis of the tube and along the wall. Holes were provided for filling the tube. The arrangement is shown in Figure 2 (*a*).

This tube was sealed within a larger brass tube, also 36 in. long, but 2 in. in diameter, the intervening space being filled with dry sand. Two layers of plastic hosing, ½ in. internal diameter, were close-wound about the outer tube. Hot water from a constant temperature, constant flow reservoir was fed upwards through the inner coil, and cold water from another controlled reservoir was fed downwards through the outer coil. The hot water was therefore cooled

TABLE 2

EXPERIMENTALLY DETERMINED RELATIONSHIP BETWEEL WALL AND CENTRAL TEMPERATURE GRADIENTS

Convecting Fluid	Run No.	Non-dimensional Wall Temp. Grad. (*H*)	Non-dimensional Central Temp. Grad.	Difference
Glycerine	1	51	51	0
	2	49	49	0
	4	72	72	0
	5	37	37	0
	6	50	50	0
	8	73	73	0
	9	55	55	0
	10	43	43	0
	12	49	49	0
	13	62	62	0
	14	84	84	0
	15	78	76·5	—1·5
80% Glycerine 20% Water	18	685	7	—678
	19	685	20	—665
	20	775	—80	—855
	21	650	58	—592
	22	860	—89	—951
	23	945	—19	—963
Water	24	25 900	20 700	—5 170
	25	27 350	21 900	—5 464
	26	14 500	10 900	—3 430
	27	17 800	13 500	—4 300
	28	14 200	11 600	—2 600
	29	23 300	20 500	—2 800
	30 31	290	233	—57
	32 33	550	275	—275
	34 35 36	970	145	—835
	37 38	990	200	—790
	39 40	910	—45	—955

as it ascended and by this means it proved possible to create temperature gradients ranging from 0·4 degC to 24 degC per 3 ft of pipe. A cross-sectional view of the arrangement is shown in Figure 2 (*b*).

Eleven thermojunctions were set at equal spacing along the wall of the inner tube and 11 others were arranged along the axis of the inner tube, matching those in the wall.

By the use of glycerine, water, or a mixture of the two it was possible to adapt the modified Rayleigh number H to a wide range of values, between 40 and 3×10^4.

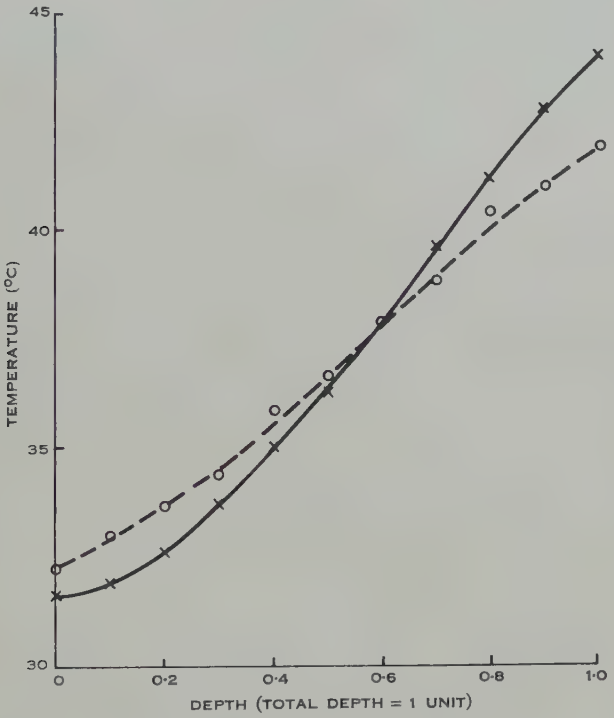

Fig. 3.—Typical profiles, —— along wall and - - - - along axis for large values of H. This case is run No. 26 with $H = 14\,500$. Here the flow is believed to be axially symmetric.

VII. Experimental Results

The experimental results are given in Table 2.

The H values are the product of the temperature gradients and the physical constants of the liquid. As these physical constants have been taken at the mean temperature of the fluid, based on the thermocouple readings, the H values are only approximate. The axial temperature gradient is estimated in the central section of the pipe, around the point where the axial and wall temperatures are equal.

Figures 3 and 4 show typical results.

VIII. Conclusion

For H less than 300 and greater than 3000 the theoretical results appear to agree with the experimental ones as closely as would be expected taking into account the approximations involved. Between these values the experimental results differ considerably from those calculated from the theory. In particular at values of H between 700 and 950, negative temperature gradients occur on the axis. Figure 4 illustrates this regime. Such a flow cannot have radial symmetry. The fluid must be rising up one side of the pipe and descending on the other. As mentioned earlier, McNabb (personal communication) states that, according to instability theory, this non-symmetric flow would develop first, as H is increased from zero, and that the radially symmetric regime discussed here would occur at higher values of H. It would appear that the experimental results support this view. The agreement between the experimental and theoretical results for H below 300 indicates that the critical value for this non-symmetric flow is not greatly different from that determined theoretically for the radially symmetrical flow (i.e. 142).

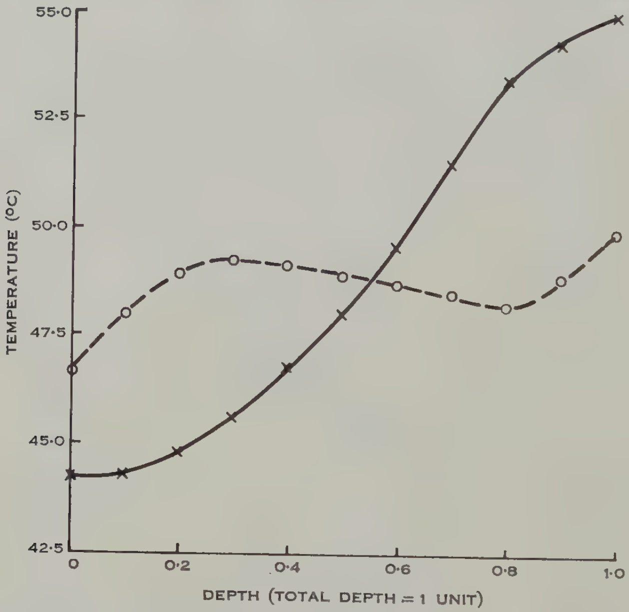

Fig. 4.—Typical profiles, —— along wall and ---- along axis for medium values of H. Here the flow is believed to be up one side of the pipe and down the other. This case is run No. 20, for H=775.

It is seen that the temperature effects (and thus the velocity and heat flow effects) are controlled by the value of the modified Rayleigh number

$$H=\frac{\beta g a^4(T_2-T_1)}{\nu\alpha h}.$$

Thus by determining this for the various bores we are able to determine the effects inside the bore, although not as yet in the ground surrounding it. For the bores, in almost all cases, H is greater than 10^5. Thus we see from the theory that, for the section under consideration, the temperatures measured in the bores will be a good indication of the temperatures at the wall of the bores, within 2 degC for $H=10^6$, but not necessarily of the temperature in the ground at the same depth. For H as large as 10^6, however, it is possible that turbulent flow might occur within the bore. In this event the temperature difference between the measuring instrument and the wall of the bore will be very small, and the pipe and the convecting fluid may be regarded as a very good conductor. The author, in an earlier paper (Donaldson 1959), determined the effect of a metal probe inserted into the ground on the temperatures in the ground. For a 3000 ft long probe, 10 in. in diameter, having a thermal conductivity of 8·4 joule cm^{-1} sec^{-1} degC^{-1} (about twice that of copper) embedded in ground in which the temperature increases by 250 degC in 1000 ft, the maximum temperature discrepancy would be approximately 0·75 degC.

IX. References

Donaldson, I. G. (1959).—Temperature errors introduced by temperature-measuring probes. *Brit. J. Appl. Phys.* **10** : 252–5.

Eckert, E. R. G., and Jackson, T. W. (1950).—Analytical investigation of flow and heat transfer in coolant passages of free convection liquid cooled turbines. NACA RM E50D25.

Lighthill, M. J. (1953).—Theoretical considerations on free convection in tubes. *Quart. J. Mech. & Appl. Maths.* **6** : 398–439.

Martin, B. W., and Cohen, H. (1954).—Heat transfer by free convection in an open thermosyphon tube. *Brit. J. Appl. Phys.* **5** : 91–6.

Ostrach, S. (1952).—Laminar natural convection flow and heat transfer of fluids with and without heat sources in channels with constant wall temperatures. NACA TN 2863.

Ostrach, S. (1957).—Convection phenomena in fluids heated from below. *Trans. ASME* **79** : 299.

SHORT COMMUNICATIONS

EVIDENCE FOR THE TRANSFER OF CORPUSCLES TO DISTANT PARTS OF THE SUN FOLLOWING A SOLAR RADIO BURST*

By R. F. Mullaly†

The brightness distribution of 21-cm radiation over the Sun's surface has been studied for the past four years with the Christiansen crossed-grating interferometer (Christiansen *et al.* 1961) at Fleurs near Sydney. The observations described here were made using one arm of this cross as a simple grating interferometer, providing a transit instrument with a fan beam of about 2′ of arc resolution to half-power points in the east-west direction and very low resolution north-south. The Sun was scanned repeatedly from east to west at time intervals of approximately 4 min.

Observations have been made for several hours a day on most days during the past few years. The most prominent features of these records are the peaks due to the slowly varying bright regions on the Sun with an average lifetime of some weeks. In addition a number (35) of bursts have been seen, located always near the position of a previously existing radio bright region. Simultaneously with the bursts, and in the same vicinity, flares are often observed optically. During burst events the level of radiation suddenly increases for a period of from a few minutes to a few hours. The high level typically fluctuates, sometimes violently, and on different occasions the peak intensity has ranged from less than twice up to several hundred times the previous steady level. These observations will be described in detail elsewhere.

On three occasions it was found that, on the second scan after the onset of a small burst (8 or 9 min later) another bright region, distant about a solar radius, showed a small but definite increase in its emission. In one instance (December 13, 1958) this was noted on only one scan, after which the augmented region returned to its previous level; on another (July 29, 1958) the increase persisted for at least four scans (after which observation came to an end); and, in the third case (May 13, 1959) the increase certainly persisted for many scans. (See Fig. 1.)

Before accepting these secondary increases as physically associated with the main bursts it is necessary to inquire if they might not be due to independent small bursts or to receiver gain fluctuations, which happened by chance to occur at almost the same time as the main bursts. Over 600 east-west scans were examined for evidence of such small increases when no other burst had occurred. None were found (confirming a subjective impression from a much larger sample

---

* Manuscript received August 24, 1961.

† Division of Radiophysics, C.S.I.R.O., University Grounds, Chippendale, N.S.W.

that they are very rare). Let p be the probability of a random small increase occurring in a single scan. To estimate an upper bound for p, suppose that the occurrence of no increase in a sample of 600 is a *rare* event, say with a probability of 0·001. Then $(1-p)^{600}=0\cdot 001$, giving $p=0\cdot 01$; there is only one chance in 10^3 that p exceeds this value. Out of 35 scans each next but one after the scan on which a burst was first seen, three show small increases; the probability of this happening by chance is

$$\binom{35}{3}(1-p)^{32}p^3,$$

which, with the above value for p, is about 0·006. The possibility that the observed small increases might be due to side lobes in the instrument must also be discussed. The answer is twofold: first, that the side lobes are known to be much too small, both in theory and from the absence of side-lobe effects even comparable to our increases with many much larger bursts; secondly, that the amount of the enhanced emission in the three cases being considered shows no kind of proportionality to the simultaneous level of the main burst.

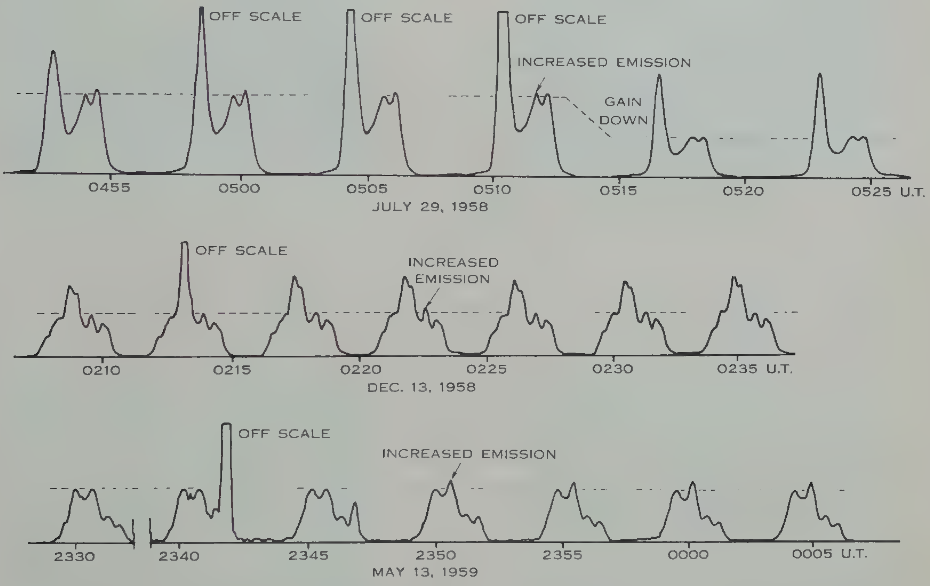

Fig. 1.—East-west strip scans of the Sun at 21 cm. Beamwidth about 2′ of arc east-west. In each case a burst is followed, two scans later, by a small increase in the emission from a distant bright region.

The immediate deduction from the observations is that the secondary increases are stimulated by something (e.g. a plasma cloud or a shock wave) propagated from the region of the main burst. The velocity of propagation appears in all cases to lie between 1000 and 2000 km/s; uncertainty in the precise time interval and in the path (which might follow the Sun's surface or arch high into the corona) precludes more exact calculation.

For two of the three events optical data are available. For December 13, 1958 a class 1 flare was observed at 0° N., 21° W. during the period $02^h\ 12^m$ to $02^h\ 47^m$ U.T. and this was accompanied by a surge. Photographs of this event taken by the C.S.I.R.O. Division of Physics are shown on Plate 1. The probable region of the augmented radio emission was scrutinized on a number of photographs but no definite evidence of brightening or change could be detected. For May 13, 1959 a class 1+ flare accompanied by a bright surge going over the limb was observed (I.G.Y. World Data Centre A 1959) commencing $23^h\ 40^m$ U.T. and situated at 8° S., 87° E. The positions of the flares and the radio bursts coincide well for both these days, and the direction of motion of the surge of December 13, 1958 appears to be roughly towards the assumed seat of the secondary enhanced radiation.

The surges at the time of the two above events represent matter with a line of sight velocity much less than 1000 km/s, otherwise the Doppler shift would have made them invisible. Very recently, however, Moreton (Athay and Moreton 1961; Moreton 1961), using an extremely wide-band filter, has reported disturbances, which he believes to be plasma clouds, moving out from the region of flares with velocities of from 1000 km/s to as high as 2500 km/s. Further, he states that on some such occasions sudden optical changes have been observed in filaments distant as much as 700 000 km from the seat of the main disturbance.

The radio observations we have described suggest that, when the burst occurred, matter was ejected or escaped from the active region, followed some trajectory, perhaps an arched one guided by the lines of force of the leakage flux between magnetic fields near the two regions, and descended on the second region, augmenting its emission, either by some heating or other effect of impact or simply by increasing the amount of hot gas present. Since certainly two of the three events were associated with optical surges it might plausibly be suggested that such secondary radio activity may be associated with surge flares. Some support for this idea comes from the facts that, while most radio bursts are associated with flares (though not most flares with bursts), only a small fraction (about 10% on our data) of bursts give enhanced emission of distant regions and only a minority of flares are seen to be accompanied by surges. Moreton's observations show that with at least some surge flares, plasma clouds as he thinks, or possibly shock waves, are ejected to great distances with velocities of the right order (1000–2000 km/s) to agree with the radio results. The long persistence of the augmented brightness of the 1959 event and, with less certainty, of the event of July 29, 1958 suggests as the mechanism the transfer of a substantial mass of corpuscles rather than the propagation of a shock wave. The event of December 13, 1958, for which the augmentation is small, and seen on only one scan, is more open to a shock-wave or impact interpretation. Possibly two different mechanisms operate on different occasions.

Thanks are due to Dr. J. L. Pawsey for his advice and encouragement in the preparation of this paper, and to Miss Marie McCabe of the Division of Physics for most helpful discussions and information on the optical aspects of the work; also to Mr. T. Krishnan and Mr. N. Labrum.

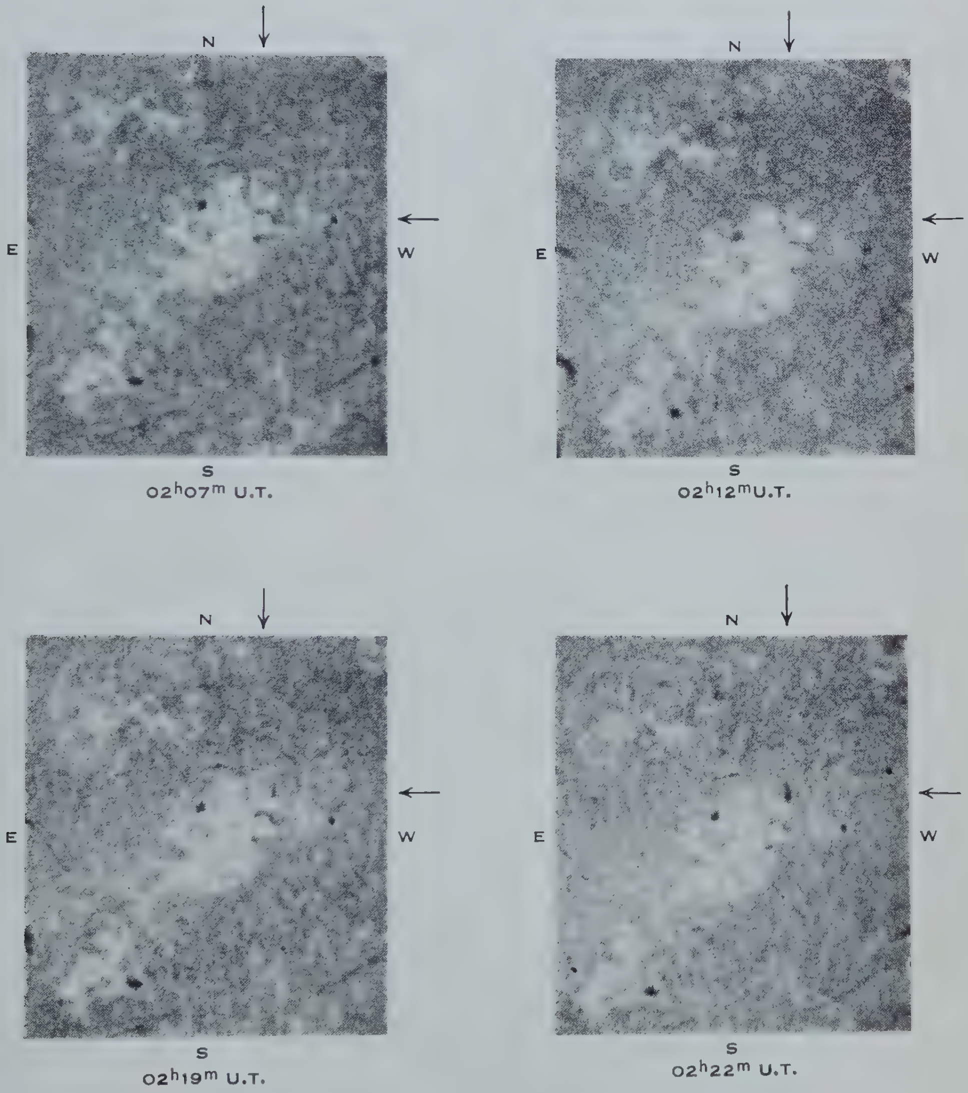

$02^{\mathrm{h}}07^{\mathrm{m}}$ U.T.

$02^{\mathrm{h}}12^{\mathrm{m}}$ U.T.

$02^{\mathrm{h}}19^{\mathrm{m}}$ U.T.

$02^{\mathrm{h}}22^{\mathrm{m}}$ U.T.

Photographs in Hα light of a surge flare on December 13, 1958. The surge is seen on the third and fourth photographs as a dark streak extending roughly to the north of the position of the bright flare. (Photographs by courtesy of the Division of Physics, C.S.I.R.O.)

References

Athay, R. G., and Moreton, G. E. (1961).—*Astrophys. J.* **133**: 935.

Christiansen, W. N., Labrum, N. R., McAlister, K. R., and Mathewson, D. S. (1961).—*Proc. Inst. Elect. Engrs.* **108 B**: 48.

I.G.Y. World Data Centre A (1959).—Solar Activity, Report Series. Intermediate Report No. 9 (April–June 1959).

Moreton, G. E. (1961).—*Sky & Telesc.* **21** (3): 145.

4

3 8198 303 614 554
THE UNIVERSITY OF ILLINOIS AT CHICAGO